Royal Netherlands
Meteorological Institute
Ministry of Infrastructure
and Water Management

KNMI National Climate Scenarios 2023 for the Netherlands

R. van Dorland, J. Beersma, J. Bessembinder, N. Bloemendaal, H. van den Brink
M. Brotons Blanes, S. Drijfhout, R. Groenland, R. Haarsma, C. Homan, I. Keizer,
F. Krikken, D. Le Bars, G. Lenderink, E. van Meijgaard, J. F. Meirink, B. Overbeek,
T. Reerink, F. Selten, C. Severijns, P. Siegmund, A. Sterl, C. de Valk, P. van
Velthoven, H. de Vries, M. van Weele, B. Wichers Schreur, K. van der Wiel

De Bilt, 2023 | Scientific report; WR-23-02

KNMI National Climate Scenarios 2023 for the Netherlands

Rob van Dorland Jules Beersma Janette Bessembinder
Nadia Bloemendaal Henk van den Brink Marta Brotons Blanes
Sybren Drijfhout Rob Groenland Rein Haarsma Carine Homan
Iris Keizer Folmer Krikken Dewi Le Bars Geert Lenderink
Erik van Meijgaard Jan Fokke Meirink Bernadet Overbeek
Thomas Reerink Frank Selten Camiel Severijns Peter Siegmund
Andreas Sterl Cees de Valk Peter van Velthoven Hylke de Vries
Michiel van Weele Ben Wichers Schreur Karin van der Wiel

October 6, 2023

Abstract

This is the scientific report, which supports the Dutch 'gebruikersrapport' with more background information on methods, results, and evaluation of the KNMI'23 national climate scenarios. The methodology described in this report has been submitted for publication in the peer-reviewed literature.

The figures including data and scripts to produce them are stored in KNMI gitlab.

Contents

Introduction

This report documents and motivates the KNMI'23 climate change scenarios for the Netherlands. It underpins the information given in the public report and at the website (www.knmi23.nl). It contains the description of design criteria and choices, the underlying assumptions, the technical procedure to construct the scenario data, and descriptions of the final results and additional products. Much effort has been put in data and script management in order to make the results traceable, transparent and reproducible, and last but not least to serve as a starting point for next generations of climate scenarios.

Our choices during the development of the KNMI'23 climate scenarios, the basis for the resulting data, the generic scenario table values, as well as the themes to be highlighted in the report, have been discussed with a consultative group, consisting of Dutch experts of various knowledge institutions, policy makers from the Ministries, end users and communication experts. Furthermore, we discussed and verified choices with an advisory board, in which climate experts from surrounding countries (sometimes involved in making national climate scenarios for their countries) were represented. Also, a number of workshops for stakeholders have been organized to get feedback on the planning, scoping and communication of the KNMI'23 climate scenarios.

The timing of the KNMI climate scenarios is dictated by the IPCC assessment cycles, such that we make use of the latest generation of climate models and the new insights in climate change for our national climate information. Leading for the KNMI'23 climate scenarios is the Working Group I contribution to the IPCC sixth assessment cycle, which was released in August 2021 after approval of its Summary for Policy Makers: (IPCC, 2021b). In this report climate scenarios were based on the Coupled Model Intercomparison Project (CMIP6) model suite in combination with the updated range in climate sensitivity from multiple lines of evidence. The CMIP6 model runs were performed for a common set of future emissions of greenhouse gasses and land use scenarios of the so-called Shared Socioeconomic Pathways (SSPs) in order to make comparison of the model results possible.

The KNMI'23 climate scenarios are based on the same CMIP6 model runs. We also take into account the progress that has been made regarding estimates of climate sensitivity. Here we use the most likely warming based on the IPCC best estimate (i.e. median value) of climate sensitivity at the KNMI'23 time horizons. This choice removes the uncertainty range in climate sensitivity from the scenario products. This range can be taken into account a posteriori by shifting the time horizons either forward (low sensitivity case) or backward (high sensitivity case). We may also scale the results at the given time horizons with the global warming level for the lower and upper bound of the very likely range of climate sensitivity. The CMIP6 runs provide the range of change of a number of meteorological parameters for the Netherlands and the Rhine-Meuse basin for each SSP. Two storylines of regional climate change are developed that span a large portion of the CMIP6 model uncertainty range. The two scenarios of regional climate change are focussed on the spread in precipitation, and as such have strong implications for future water availability and water safety (e.g., through low and high river discharge). The global CMIP6 models are too coarse to provide detailed regional climate information. Therefore, we generated a large ensemble of climate simulations with the KNMI global climate model EC-Earth3, and used the KNMI regional climate model RACMO to dynamically downscale these simulations to a 12×12 km scale resolution over Europe. The RACMO model better resolves land-sea contrasts, the topography, and improves the simulation of convective systems. Using a resampling technique we reconstructed the climate

change signal of the two storylines based on the CMIP6 range of regional climate change by making use of the internal variability that is present in the EC-Earth-RACMO ensemble. The idea is that by selecting, for instance, more frequently drier future summers, one is able to represent a drier future summer climate, and similarly one could reconstruct a relatively wet future summer climate.

Preparations of EC-Earth3 and RACMO, included both historical and future model simulations with 16 ensemble members for three SSP scenarios up to the year 2165. These took about two years of computational time. The fact that the release of the CMIP6 climate runs was delayed as compared to the previous IPCC cycles, and the time needed for this computational exercise and the consequent analyses leading to the KNMI'23 scenario data, gave rise to the publication of the KNMI'23 climate scenarios for the Netherlands in 2023. To accommodate the need for communication of the main findings in the AR6 IPCC WGI report, KNMI published in 2021 the public report 'Klimaatsignaal'21', i.e. Climate Signal'21. This also provided an indication of how KNMI'23 would differ from KNMI'14, based solely on analyses of the differences between CMIP6 and CMIP5 projections (KNMI'14 was based on the CMIP5 model runs).

Basically, we follow the same approach in creating new climate scenarios as done for KNMI'14. However, the choices and underlying assumptions we made for the KNMI'23 climate scenarios differ from those made for KNMI'14. Firstly, because of the Paris Climate Agreement in 2015 where the majority of countries agreed to limit global warming to well below 2 °C and preferably not more than 1.5 °C relative to the pre-industrial era. As a consequence countries made pledges (National Determined Contributions or NDCs) to mitigate their greenhouse gas emissions. The world is by far not on track to reach this goal, even when the more recent, more ambitious promised emission reductions are taken into account. Present estimates suggest a global warming of approximately 2.5 °C at the end of this century based on the current climate policy ambitions. Nevertheless, we lowered the lower end of the KNMI'23 climate scenarios to recognise the political will to mitigate climate change, and to recognise that meeting the Paris goals still remains a possibility. Secondly, we wished to decouple uncertainties in (global) climate policy from uncertainties due to incomplete scientific knowledge about how the physical climate system responds to the changes in atmospheric composition and land-use. This makes the approach and choices made more transparent, and helps in communicating how a change in human actions now can limit future climate change. The range of global temperature change in the KNMI'23 scenarios is therefor based on the Shared Socioeconomic Pathways (SSPs). In KNMI'14 this range was based on the range of global warming outcomes of the CMIP5 models for three RCP scenarios that were deemed equally likely (RCP4.5, RCP6.0 and RCP8.5). The lower emission scenario (RCP2.6) was not considered realistic at the time, given the lack of international agreement on emission reductions when the KNMI'14 climate scenarios were developed. Thirdly, a different choice is made to represent the uncertainty in the regional response. In KNMI'23 a storyline approach is followed with a focus on the uncertainty in the precipitation response and the implications for water safety and water availability. This choice leads to a Wet scenario with a strong wetting trend in winter, moderate drying in summer, and a Dry scenario with moderate wetting in winter and a strong drying trend in summer. In KNMI'14 the choice was made to construct two scenarios that captured a large portion of the CMIP5 spread in regional changes of winter and summer temperature and precipitation, and large changes in both seasons were combined in a single scenario.

In the Netherlands a strong tradition in constructing national climate change scenarios has developed over the past decades (Können (2001), Van den Hurk et al. (2007), Lenderink et al. (2014)). Frequent updates of these scenarios are desirable, as both scientific insights and user requirements develop over time. Starting point is to deliver a limited set of generic climate scenarios, preferably an even number as to avoid the use of a single scenario somewhere in the middle of the range, which could -mistakingly- easily be considered as the most plausible forecast of the future climate. Furthermore, the set of climate scenarios should span a plausible range of climate change in the Netherlands. Although individual scenarios cannot be labelled with a probability, the complete set of climate scenarios may be recognized as a likely range of climate change in our region.

Chapter 1 describes the motivation of the choices we made in the construction of the climate scenarios, choices that were discussed and evaluated with a consultative group of stakeholders and

the international advisory board. The chapter concludes with a final section providing a reading guide for this report.

Chapter 1

Scope of the climate change scenarios

1.1 Climate change and drivers

Climate refers to the long-term patterns of weather conditions in a particular region or on the planet as a whole. Climate is defined typically over a 30-year period and varies spatially and in time. The observed rate of global temperature change of about 0.6 °C over the last 30-year period indicates that even over this climatological time frame climate show trends, which should be taken into account. The Earth's climate is the state of a complex system, which consists of the atmosphere, ocean, cryosphere (snow and ice), land surface and the biosphere. It includes many physical, chemical and biological processes interacting on a huge range of spatial and time scales. The interactions between the various components of the climate system give rise to complex behaviour.

The climate system is primarily driven by the energy it receives from the sun. About 30 % of the incoming solar radiation is reflected and lost to space. The remaining part is absorbed within the atmosphere and at the Earth surface, and is converted into heat which eventually leaves the system as infrared radiation. If the globally averaged net incoming short-wave radiation and outgoing long-wave radiation are not in balance at the top of the atmosphere, the global mean temperature adjusts and restores this balance. Conservation of energy, as one of the fundamental physical laws, is a strong boundary condition for climate on the global scale, and the dependence of long-wave radiation on temperature is a strong, stabilizing, climate feedback.

The climate system naturally varies in time due to the turbulent flows in atmosphere and ocean and redistribution of heat, water and momentum across the planet and between the different components of the climate system (land, ocean atmosphere, cryosphere, biosphere). We distinguish internal variability and forced variability. Forced variability is due to variations in external factors. The internal variations are often referred to as climate noise. On a global scale spectra of temperature variations generally have a red noise character, indicating that fluctuations are larger for longer time-scale. These spectra also show resonant peaks, indicating the existence of typical time scales of feedback mechanisms.

Internal variability causes temperature fluctuations on numerous time scales as the result of interactions between the ocean, atmosphere, cryosphere and biosphere. Changes in ocean circulation may cause changes in sea ice extent altering the Earth's planetary albedo. These changes may also trigger anomalous circulation patterns in the atmosphere leading to (long lasting) changes in regional precipitation, cloud amount and snow cover. In addition the length of the growing season may be affected. A well-known manifestation of internal variability is the occurrence of El Niño/La Niña, a result of the complex interaction between the tropical Pacific ocean and the atmosphere above. On average once every three to seven years the ocean surface waters west of Peru undergo a rapid warming. The atmosphere responds to this warming with large-scale

shifts in clouds and precipitation patterns leading to large seasonal anomalies in temperature and precipitation in specific areas around the world. Finally, also global mean temperatures respond during El Niño years with a temperature rise by several tenths of a degree.

In contrast, changes in external factors lead to forced variations in the climate. Examples are the anthropogenic emissions of greenhouse gases (GHG) and anthropogenic land-use changes. Examples of external forcings of natural origin are aerosol and GHG emissions from volcanic eruptions or variations in the energy flux from the sun. It is sometimes difficult to separate internal variability and externally forced variations due to the fact that the spatial structures, time scales and amplitudes of both are often very similar.

Changes relative to the current climate can be expected from forced climate change related to prolonged GHG and aerosol emissions and land use change, and natural variability at multi-decadal time scales. The amplitude of natural variations becomes smaller when taking an average over longer time periods, but even for 30 year averages –the usual period to define a climate– variations occur just by chance (i.e. internal variability). Internal variations on (multi-)decadal timescales are inherently unpredictable and represent noise. They are larger for precipitation than for temperature, larger for extremes than for the mean, and larger for the climate of the Netherlands than for the global climate.

Given that we know the timing and magnitude of external forcing, the variations due to external forcings are predictable. We refer to this externally forced climate change as the *climate signal*. Variations due to internal variability are referred to as climate noise. In KNMI'23 we quantify the climate signal, conditioned on the greenhouse gas emissions based on the different Shared Socioeconomic Pathways (SSPs), as used in the IPCC sixth assessment report (IPCC, 2021b), and present an estimate of the climate noise in each meteorological parameter.

1.2 Uncertainty framework for regional climate change

When making assessments of the future climate at a regional level, one has to make assumptions about future changes in external forcings and assess the uncertainty in the climate response to these forcings. The external forcings have both a natural (solar variability and volcanic eruptions) and an anthropogenic origin. Solar variability (length and amplitude of the 11-year sunspot cycle) and volcanic eruptions are unpredictable in nature. Therefore, a plausible future evolution of the 11-year solar cycle has been constructed and a mean background of volcanic aerosols has been chosen as volcanic forcing for the future. The anthropogenic forcing has been derived from storylines of socioeconomic developments (see next Section 1.2.1).

1.2.1 Uncertainty in future anthropogenic forcings

The amount of future GHG emissions and other anthropogenic activities, such as the emission of (precursors of) aerosols and land-use changes, is strongly dependent on the sum of the national climate policies in conjunction with demographic, technological and socioeconomic development. The scientific community developed a set of Shared Socioeconomic Pathways (SSPs), which can be grouped into five storylines:

- SSP1: sustainability ('the green road')
- SSP2: the middle of the road
- SSP3: regional rivalry ('a rocky road')
- SSP4: inequality ('a divided road')
- SSP5: fossil-fuelled development ('taking the highway')

Integrated assessment models have been employed to calculate future emissions and land-use changes based on these storylines, and the CMIP6 modelling groups have calculated the climate

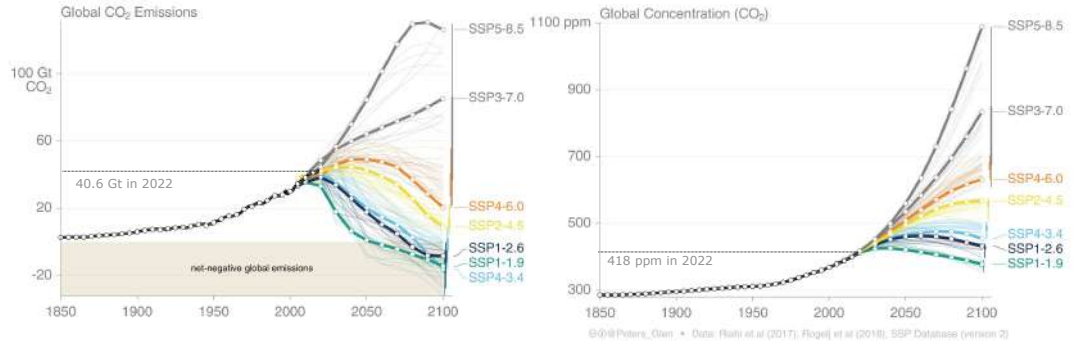

Figure 1.1: CO_2 emissions per year (left) and concentrations (right) of representative SSPs. Figure based on data from Riahi et al. (2017) and Rogelj et al. (2018)

response on the basis of the anthropogenic radiative forcings. In fact, these are the SSP-RCPs, where RCP is the abbreviation for Representative Concentration Pathways followed by a number indicating the radiative forcing at the end of this century. Throughout this report we use the term SSPn-rf instead of repeating SSP-RCP, where n is the number of the pathway and rf is the radiative forcing. These illustrative pathways are well documented and used in the IPCC reports (Fig. 1.1). SSP1-1.9 is the pathway with the lowest emissions, resulting in a 50 % likelihood of a global warming of 1.5 °C at the end of the century relative to pre-industrial conditions conform the Paris climate agreement. SSP5-8.5 is the highest emission scenario and serves as a benchmark of no mitigation of climate change at all, although many countries have already implemented mitigation measures. Hence, the SSP5-8.5 pathway should be considered as an upper bound of greenhouse gas emissions. It can be useful for risk analyses in the context of climate adaptation in the sense of the precautionary principle. In the scientific literature the plausibility of SSP5-8.5 is debated (Hausfather and Peters, 2020). Some researchers argue that SSP5.8.5 could be more likely than was originally proposed. This is because some important feedback effects — such as the release of greenhouse gases from thawing permafrost (Friedlingstein et al., 2014; Lenton et al., 2014) might be much larger than has been estimated by current climate models. Since in KNMI'23 we use the median global warming level (and not the upper bound of the climate sensitivity range) the radiative forcing of 8.5 W/m2 at the end of this century may also be reached with lower greenhouse gas emissions in combination with a high climate sensitivity. For the KNMI'23 climate scenarios we selected SSP1-2.6, resulting in a 50 % likelihood of 1.7 °C global warming in 2100 (note that IPCC AR6 uses the 67 % probability to connect the 2 °C in 2100 with the SSP1-2.6), and SSP5-8.5, resulting in a 50 % likelihood of 4.9 °C global warming in 2100 as assessed in CMIP6 using the best estimate of climate sensitivity. Since the gap between the climate impacts of the SSP1-2.6 and SSP5-8.5 pathways at the end of this century and beyond is large, we also calculated the climate response for the middle of the road SSP2-4.5, resulting in a warming of 2.8 °C in 2100. This addition is made on request by the water community (sea level and river discharge) in the Netherlands, but is held outside the generic climate scenarios for general use. All temperature changes noted here are relative to the pre-industrial baseline.

1.2.2 Uncertainty in the climate response

On a global scale there is scientific uncertainty in the temperature response due to an imposed radiative forcing (as a result of GHG emissions). The magnitude of the global temperature change in response to a doubling of the CO_2 concentration is referred to as the climate sensitivity. The range of estimates of climate sensitivity is determined by the uncertainties in climate feedbacks, like changes in the water vapour amount in the atmosphere and in the properties of clouds. Much progress has been made in understanding and quantifying the climate feedbacks using the

combination of modelled processes and observations, which resulted in narrowing the range in climate sensitivity by a factor of two. In (IPCC, 2021b) the likely (67 %) range of climate sensitivity is 2.5 to 4 °C. When assessing climate change for a specific SSP storyline, this range may either be included as a bandwidth around the best estimates of the projected variables through scaling with the global temperature with the median value (i.e. lower bound 2.5/3 and upper bound 4/3 times of the calculated effects of climate change of the median value of 3 °C) or as a time shift in the occurrence of the calculated future climate. However, for slow onsets like sea level rise this method of scaling is not applicable. For that reason we will use the bandwidth of climate sensitivity explicitly around the median values of sea level rise.

On a regional scale, climate change depends on shifts in circulation and regional forcings and feedbacks (such as aerosols, ozone, land use, soil moisture). For example, there are indications that global warming results in a poleward shift of the jetstream in winter, though many factors related to global warming contribute to circulation changes, for instance reductions in sea-ice cover (Screen et al., 2022). Climate models differ in the way relevant processes are parameterized and this influences interactions and feedbacks leading to different regional responses.

1.2.3 Internal variability

Internal variability at various time and spatial scales introduces deviations from the anticipated mean climate signal. In model simulations, the mean climate signal can be found using multiple realizations, named ensemble members, of individual climate models differing only in the initial condition (single model initial condition large ensembles, SMILEs), and that way average out the climate noise. Climate noise thus contributes to observed climate trends, making statements regarding the cause of observed trends, or statements regarding individual model quality based on their agreement with available observations, inherently difficult since the real forced climate trend is not known. Natural variability on the local scale can be quite large, e.g. the standard deviation in winter-mean temperatures in the Netherlands is about 1.3 °C.

CMIP6 model runs can be used to estimate the range in regional climate response including the natural variability. It is hard to distinguish between the forced climate signal and the unforced climate noise in the absence of SMILEs. We will see later, that, for some variables like winter precipitation, the internal variability at the regional scale in a 16-member EC-Earth3 ensemble approaches the range in the CMIP6 climate response.

1.3 Strategic choices and criteria for the KNMI'23 climate scenarios

The KNMI'23 climate change scenarios are designed to give a quantitative visualization of a range of climate states to which our country and its surroundings might be exposed in the coming one-and-a-half century. The aim of the KNMI'23 scenarios is not fundamentally different from the aim of previous generations, i.e., KNMI'06 and KNMI'14. In the construction of the KNMI'23 scenarios some fundamental design changes were made. We have built on the experience gained and lessons learned from previous generations of KNMI climate scenarios. Also we took into account changed user requirements for both adaptation and mitigation questions, and made an attempt to incorporate the changed world (since 2014) with respect to agreements in mitigation policies. The choices made for KNMI'23 have been discussed with the consultative group of stakeholders and the international advisory board. In this section we present an overview of the strategic choices, a detailed account of the full KNMI'23 methodology is given in Chapter 2.

1.3.1 Criteria for the KNMI'23 climate scenarios

The KNMI'23 scenarios are designed to provide a scientific set of plausible, (internally) consistent and relevant future climate conditions, to be used as a reference framework for a multitude of societal impact assessments of different scope and origin.

Scenarios are defined by IPCC (IPCC, 2021b) as "plausible descriptions of how the future may develop based on a coherent and internally consistent set of assumptions about key driving forces (e.g., rate of technological change, prices) and relationships. Note that scenarios are neither predictions nor forecasts, but are used to provide a view of the implications of developments and actions". The scenarios form the basis of the SSPs and concentration pathways, which serve as input for climate models to calculate climate projections. Climate projections often serve as the raw material for constructing climate scenarios, but climate scenarios usually require additional information such as the observed current climate. A climate change scenario is the difference between a climate scenario and the current climate. Climate (change) scenarios should be possible, plausible, and internally consistent, but not necessarily probable, developments of the future climate state. A set of scenarios can be constructed that together provide a plausible description of how the future may develop. But as for projections: when quantitative probabilities are not given to the key driving forces of the scenarios, they cannot be considered to be probabilistic forecasts of the future.

Internal consistency implies that the climate scenarios are physically consistent and well understood, and are supported by quantitative evidence obtained from models and observations. In KNMI'23 internal consistency is imposed by deriving quantities that are physically related from a similar set of climate simulations, grouped in samples reflecting the assumed large scale steering variables for each scenario This grouping of ensemble simulations from a single regional climate model, driven by a single global climate model ensured that coherent patterns of temperature, precipitation, winds, evaporation, radiation and other derived quantities could be compiled for each scenario.

Relevance is ensured by generating climate change variables that are considered useful by a large group of users. A generic set of climate scenarios in KNMI'23 (as was also the case for KNMI'06 and KNMI'14) cannot ensure relevance to all users of these scenarios, as many climate indicators become relevant at different spatial or temporal scales for different users. Relevance is therefore often increased by application of further tailoring the scenarios to the users' needs.

Since the KNMI'06 climate scenarios (and also in the last phase of its production) more effort is invested in tailoring climate information for various user groups and societal sectors, whose information need is very diverse. The publication of the KNMI'06 climate change scenarios resulted in many requests for additional information and guidance of these scenarios and their implications for society stakeholders. The experience with the user requests and their use of the available climate information were documented (Bessembinder et al., 2014) and cross-checked in two user consultation workshops and a climate scenario user working group. In the user requirements surveys new types of information are requested, among others:

- more climate variables
- more information on natural (year-to-year) variability
- information on the relation between scenarios and observed trends
- scenarios for 2030
- more regional detail in the climate change information
- sub-daily (hourly) extreme conditions
- probabilistic assessment of the various scenarios
- visual illustration of the manifestation of climate change and its possible impacts
- time series associated with the scenarios

These user requests were taken into account in the construction and production of the KNMI'14 climate scenarios, while stakeholders consultations became a structural part in the making of KNMI climate scenarios for the Netherlands. This approach was extended for the KNMI'23

climate scenarios as the result of the use of the KNMI'14 scenarios in the National Adaptation Strategy (NAS), which was initiated in 2012 by the Ministry of Infrastructure and Environment and documented in 2015 (Van Oostenbrugge et al., 2015). Within the framework of the NAS seven societal sectors (agriculture, fishery, nature, health, transport and infrastructure, energy infrastructure, and ICT) were prioritized for an inquiry of risk analyses in which the KNMI'14 climate scenarios played an important role. It implied an increasing effort of investment in tailoring climate information for various user groups and societal sectors, whose information need is very diverse.

In addition, the Dutch Delta program focusing on the three pillars of water safety, fresh water availability and spatial adaptation, became increasingly interested in the new scientific findings on the possibility of much higher sea level rise at the end of the century than on the basis of the modelled slow onsets using the SSPs due to increased melting processes at Antarctica and of the more frequent occurrence and severity of droughts in the Netherlands. Also, the increased heat stress in urban areas is a focus in the Dutch Delta program in close collaboration with the NAS.

The design and evaluation of measures aiming at a robust Delta infrastructure are guided by the so-called Delta Scenarios (Bruggeman et al., 2015) in which key indicators of both future climate and socio-economic conditions are quantified. These Deltascenarios are based on a selection (and modification) of the KNMI'06 climate scenarios. In 2024 a new set of Deltascenarios will be published. It has been decided that these will be based on a selection of the KNMI'23 climate scenarios and combined with the new national socioeconomic scenarios, prepared by PBL.

Twice a year the consultative group of stakeholders was invited to put forward ideas and give feedback on the plans for the themes, variables and methodical issues of the KNMI'23 climate scenarios. Taking into account the feedback and requests of a large group of users it is ensured that the KNMI'23 scenarios are relevant.

Besides the inputs from the stakeholders the KNMI'23 scientific team regularly consulted an international scientific advisory board, consisting of experts from Germany, Belgium, France, Switzerland, UK and the Netherlands, involved in their national production of climate scenarios or in climate modelling in general. This advisory board gave useful feedback on the methodological issues in producing the KNMI'23 climate scenarios. Ideas of the stakeholders were input to the KNMI'23 science team to judge feasibility and scientific accountability and then discussed with the advisory board. Decisions were finally taken by the KNMI'23 steering group, consisting of the managers of the team, the KNMI business manager on climate and the project leaders of KNMI'23.

1.3.2 Reference period

It has been decided to use the most recent WMO climatological normal period, 1991-2020, as a reference period for the KNMI'23 climate scenarios. This reference period is shifted 10 years compared to the reference period used in KNMI'14. When comparing scenario table values this change in the reference period and the associated climate normal should be taken into account. Furthermore, for some purposes it is advisable to use the pre-industrial period (1850-1900) as a reference, especially when comparing results with (IPCC, 2021b). In terms of global-mean annual-mean temperature, the difference between the pre-industrial and the period 1991-2020 is approximately 0.85 °C.

1.3.3 Time horizons

We decided to develop climate scenarios for the time horizons 2050, 2100 and 2150, following comments and advise from users. The KNMI'14 climate scenarios were produced for 2050 and 2085. Though these time horizons are referred to as a single year, we actually consider the 30-year climatological values around these time horizons to also take into account internal variability, in the same way as is done in the reference period. The 2050 time horizon thus refers to the 30-year period 2036-2065. It should be made clear that uncertainties increase with time, therefore scenario values for 2150 will have a different status than those for 2050 and 2100. Increased uncertainty

is for example because CMIP6 model experiments do not go beyond the year 2100. For the time horizon 2150 we then calculated the extrapolated bandwidth of the CMIP6 models at the end of this century scaled with the global warming level in 2150 for the two SSPs. In addition, the underlying assumptions of the SSPs further into the future are more uncertain. Note our in-house EC-Earth3 and RACMO simulations have been continued unto 2165, this will be discussed in more detail later.

In addition to the time horizons above, the user community requested an outlook for the climate change in the near future. We therefore decided to also provide values for the time horizon 2033. According to (IPCC, 2021b) in the SSP scenarios the 1.5 °C global warming level will be reached around that year. Similar to the WMO climate normals, the IPCC defines reaching 1.5 °C based on a longer period, in this case the 20-year period centered around the year of mentioning.

1.3.4 Four climate scenarios based on two SSPs and two modes of regional responses

Based on feedback from the users we decided to maintain the two-axis scenario framework similar to KNMI'06 and KNMI'14, resulting in four scenarios for future climate in the Netherlands. We intend to improve the coherency of the climate characteristics between scenarios across a range of desired variables, and spatial and temporal scales. The four scenarios framework prevents an unintended selection of a 'middle' scenario as the best estimate of climate change in the Netherlands. Estimates of likelihood or probability can not be assigned to the scenarios. The four scenarios are set up along two main axes of uncertainty for regional climate change, and provide plausible and physically consistent storylines or pathways of climate change in our region. We choose as upper and lower bound of projected global climate change (and associated global temperature change as the driver of regional climate change) a scenario for sustainable development (SSP1-2.6) and a scenario for fossil-fuel intensive development (SSP5-8.5). We discarded SSP1-1.9 as lowest emissions scenario, since it is highly debated whether this emission scenario has the potential of being actually being realized. On the second axis of uncertainty, we choose to develop storylines of regional climate change based on uncertainties in the regional precipitation response.

The future emission or SSP-axis

Rationale for developing separate scenarios for two SSP scenarios is to decouple policy uncertainty and scientific uncertainty. In addition, this makes comparison of KNMI'23 scenarios with global projections from, e.g., IPCC possible, as these are also based on the SSPs. These chosen upper and lower boundaries of future emission are the SSP5-8.5 pathway, with a 50 % likelihood of reaching 4.9 °C global warming in 2100 as compared to the pre-industrial period, and the SSP1-2.6 pathway, with a 50 % likelihood of 1.7 °C warming in 2100. This upper bound can be considered as the base line of not taking any mitigation measures at all, the lower bound is close to the mitigation pathway as aimed for in the Paris Agreement. We opted for a large bandwidth between the KNMI'23 high and low emission scenario to emphasize the consequences of the international choices of mitigation policies, and to have a framework for national risk assessments. Climate change in Netherlands will likely evolve within the given bandwidth, although it is not possible to label a likelihood to either the high or the low emission scenarios. On request of several professional users of the KNMI'23 climate scenario's we also calculated the changes for the SSP2-4.5 pathway using the same methodology as for SSP5-8.5 and SSP1-2.6.

Given a SSP scenario, we take the median value of the IPCC range of climate sensitivity to determine the most likely value of global temperature changes within a SSP. Through this choice for the median climate sensitivity, we can further separate remaining uncertainty (after removing emission uncertainty) due to climate sensitivity and uncertainty in the regional response (second axis, next section). As stated before, the effect of the uncertainty in climate sensitivity on the final scenario values can be evaluated a posteriori.

To arrive at multi-model estimates of regional climate change at the median value of climate sensitivity, we translate the SSPs into a warming level at the time horizon used and use these

warming levels to compute the multi-model range of regional climate change. Values for warming levels at the time horizons are determined by using the median value of IPCC 'assessed range' (50% likelihood of reaching that warming level) of the global temperature for a given SSP, corrected for the observed global temperature increase between preindustrial and the reference period (1991-2020). The IPCC assessed range of the global temperature projections differ from raw CMIP6 model ensemble mean, both in magnitude as in spread. There is a broad consensus that the CMIP6 ensemble overestimates the climate sensitivity.

Uncertainty in regional climate response: the dry-wet axis

The second axis of uncertainty spans part of the uncertainty in regional climate change conditional on a SSP or level of global climate change (warming level). We decided to take a storyline approach, which allows the construction of physically consistent scenarios. The two storylines are designed to span the CMIP6 model spread in precipitation changes in the Netherlands and Rhine and Meuse basins (see section 1.3.5. Precipitation changes are very relevant for adaptation questions, e.g. adapting to possible higher likelihoods of high river discharge in case of significant increases in winter precipitation, or adapting to possible higher likelihoods of drought and associated water shortages in case of decreases in summer precipitation. We took into account advice and requests from experts and stakeholders in the decision making process that led to the choice of the storylines based on the precipitation response. This choice implies that model uncertainties in the response of other variables besides precipitation, like temperature, radiation, wind, are less optimal represented. Per SSP emission scenario the range in the climate response in these variables may be underestimated, but note that especially at the end of the century the range in the climate response is dominated by the uncertainty in future emissions, not by model uncertainty, and this range is well captured by the high and low emission scenarios. For impact modelers interested in scenarios that better represent model uncertainty in temperature, radiation or wind, other storylines could be developed along similar lines.

CMIP6 models consistently project increasing winter precipitation and decreasing summer precipitation, though the magnitude of these changes, and consequently the sign and magnitude of the annual total precipitation change, varies between models. To arrive at two physically consistent and plausible storylines, our selection of 33 CMIP6 models was split into three groups of 11 models each. Group assignment was such that they best captured the CMIP6 spread in winter (December-January-February, DJF), summer (June-July-August, JJA) and annual total precipitation change. We took into account that for water safety and availability, it is relevant to provide two scenarios most relevant for each. Thus, one scenario for water safety combines strongest wetting in winter and least drying in summer, the other for water availability, strongest drying in summer, and least wetting in winter. The first projects increased annual precipitation, the second decreased, relevant for multi-year droughts. The composite group response for each SSP and time horizon was then used to define a 'Dry' and 'Wet' scenario.

This choice for the development of precipitation-based storyline scenarios differs from the scenario construction approach in KNMI'14. In KNMI'14 a more probabilistic approach was taken, with the aim to capture a large portion of the model spread in regional climate change. Then, both regional precipitation and regional temperature change were used to construct the scenario-axes/spread, and the winter and summer seasons were considered separately. For water management applications the KNMI'23 scenarios might provide new insights: KNMI'14 combined relatively large increases in winter precipitation and relatively large reductions in summer precipitation. In contrast, KNMI'23 combines relatively large increases in winter with relatively small decreases in summer, and vice versa. This might have consequences for, e.g., the restoring of groundwater tables after future dry summers. A more detailed description of the methodological differences between KNMI'23 and KNMI'14 is provided in Chapter 2.

1.3.5 Area of focus

In the estimation of regional climate change, we decided to analyse the area of the Netherlands in combination with the upstream parts of the catchments of the Rhine and Meuse rivers. The rationale for this choice, which is different from KNMI'14, is to achieve better consistency between the KNMI'23 scenario values and associated projections of river discharge, which depend on precipitation and evaporation in the upstream basin areas as well. The combination of information on climate change in the Netherlands and river discharge at, e.g., Lobith is relevant for, e.g., water management, water safety and river transport.

1.3.6 Additional climate scenarios for professional users

Since the gap between the climate response based on SSP1-2.6 and SSP5-8.5 is quite large, we also define a moderate climate scenario based on SSP2-4.5 in response to requests for this scenario by professional users. This climate scenario is constructed following the exact same methodology as for the other two SSP's, thus resulting in an additional Dry and Wet scenario. The set of 6 scenarios (3 SSPs, 2 Dry-Wet) matches the setup of the scenarios for sea level rise (next section) which have been constructed separately, but which will make use of the same three given SSPs. Here having three SSP scenarios, with overlapping uncertainty bands is especially relevant for water management and safety. The moderate scenario will only be presented on the website and in this scientific report, but will be left out of the general report for the general audience.

1.3.7 Transformed and bias corrected time series

Impact studies often make use of time series of present and future climate to calculate the consequences of climate change for various sectors, e.g. water management, health, agriculture, infrastructure. These time series include information on temperature, precipitation, wind, evaporation and solar insolation on a daily basis. The future times series can be generated in two ways: 1. Transform the observed time series using the output of climate models such that the statistics match the statistics of the future climate (time series transformation) or 2. Use directly the time series from future climate runs and correct them for biases with respect to the observed statistics (bias corrected time series). Both approaches are based on the same RACMO model projections that are used to derive the scenario table values. Both sets of time series will be available within KNMI'23 to be used by professional users to calculate impacts of climate change in the Netherlands.

From the simple methods, the Quantile Delta Mapping was selected for the bias corrected time series because it is relatively robust (except possibly in the extreme ranges, like all other methods), has produced good results in other studies (e.g. Cannon et al., 2015) and shows relatively good performance in tests based on historical weather data over two different periods. Moreover, Quantile Delta Mapping can also be used to transform observational timeseries to a future climate, and the results of bias-correction and time-series transformation using Quantile Delta Mapping are highly compatible.

1.3.8 Sea level rise scenarios

Scenarios for sea level rise at the Dutch coast are be part of the generic climate scenario table. As in KNMI'14 there is no distinction of sea level rise values between the dry and the wet scenarios. Like all other variables in the KNMI'23 scenario table, the sea level rise numbers are directly conditioned on the same greenhouse-gas emission scenarios (SSPs). However, the presentation of the results includes the uncertainty due to climate sensitivity in contrast to the presentation of the meteorological variables in the scenario table where we use the median global warming levels conditioned on the SSPs.

The KNMI'23 scenarios of sea-level change along the Dutch coast are based on chapter 9 of the sixth assessment report (AR6) from the Intergovernmental Panel on Climate Change (IPCC) on

the physics of climate change (Fox-Kemper et al., 2021). While the method of AR6 projections is constrained by the fact that it should work for all oceans in the world we adjust our scenarios to the Dutch coast. For the first time, these adjustments are informed by a closed sea-level budget based on recent advances in the field (Frederikse et al., 2016, 2020). Our goal is to develop scenarios that overlap with observations over the period 1993-2021, and seamlessly continue into the future. An additional requirement is that such a good connection between observation and scenarios not only holds for total sea level but also for each individual contributor (e.g., Antarctica, ocean-dynamic sea level...). This increases our confidence in the ability of models to also provide reliable century projections.

Furthermore, we include Low Likelihood High Impact (LLHI) scenarios. Those scenarios are either based on physical processes (mostly ice dynamics in ice sheets) not yet well-understood or difficult to quantify, or Structured Expert Judgement (SEJ), a different way to assess expert opinions. These LLHI scenarios are mostly conditioned on processes not yet observed in Antarctica, but physically plausible and, either observed in Greenland, or derived from geological evidence of past changes.

1.4 Additional products in KNMI'23

Besides the generic KNMI'23 climate scenarios for the Netherlands several other topics are covered separately in the KNMI'23 products. These topics and their motivation are:

1.4.1 Climate scenarios for the Caribbean

Bonaire, St. Eustatius and Saba, known as the BES islands, located in the Caribbean Sea, are municipalities of the Netherlands. We therefore examine the past, current and future climate of the BES islands and include climate scenarios for the region. We use basically the same methodology as for the European part of the Netherlands, although we did not downscale the CMIP6/EC-Earth response dynamically with RACMO. Instead we use a statistical downscaling technique by comparing observations with the outcomes of the global models at coarse grid level for the historical period. Also, seasons are defined differently as dry and wet seasons are commonly used in (sub)tropical regions, and in the case of the Caribbean heavily influenced by ENSO. Apart from temperature and precipitation changes we focus on tropical cyclones (wind and extreme precipitation) and local sea level rise.

1.4.2 Extreme summer precipitation, thunderstorms, hail and wind gusts

Triggered by observed climate trends we also focus on extreme summer precipitation, thunderstorms, wind gusts and hail in the Netherlands. As these intense rain showers have a duration of only a few hours and occur at relatively small spatial scales, the models used to derive the large scale and daily precipitation changes (EC-Earth and RACMO) are not fit for the job due to the coarse spatial and time resolution. Instead we make use of high resolution convective permitting models (CPMs) to investigate future changes in extreme precipitation. Results are given for global warming levels of 1, 2 and 4 degrees in addition to the warming levels at the time horizons of the generic scenario tables. In addition to the scenario table values for hourly and daily rainfall, we also looked more qualitatively at a some other aspects of convective cloud systems, like the size of the events and other weather phenomena related to convective clouds: wind gusts, hail and lightning. It should be noted that these aspects are still very uncertain given the present-day knowledge and modeling capacity.

1.4.3 Climate change in the Netherlands for a 1.5 degrees warmer world

In December 2015, after the release of the KNMI'14 climate scenarios, the Paris Climate agreement was established to maintain the global temperature change well below the 2 degrees and preferably

not more than 1.5 degree with respect to preindustrial level (average global temperature over the period 1850-1900). The global warming will reach the 1.5 degree level in 2033, following the best estimate and definition of IPCC AR6 (IPCC, 2021b), irrespective of the SSPs due to historical emissions of greenhouse gases and the unavoidable future emissions. In KNMI'23 we consider the climate of a 1.5 degrees warmer world set in 2033. This is done using the same procedure as described in Section 2.1, prescribing a warming level of 1.5°C above pre-industrial (or 0.6°C above the reference period 1991–2020).

1.4.4 Cities and climate change

A large part of the Dutch population lives and works in cities. Cities as centers of economic activity are main contributors to climate change. At the same time the effects of climate change on for instance health and economical activities are felt substantially within cities. This is due to the fact that global warming intensifies the urban heat island effect. Therefore, climate change is a real challenge for urban areas. It is a well-known fact that cities through the way they are built modify the local energy and water balance and thus affect the local and regional weather and climate. To study urban climate change and its impact in the framework of the KNMI climate scenario's the full range of scales from global to local must be bridged. This can only be achieved through downscaling using a chain of models. The highest resolution of data available came from the mesoscale climate model HCLIM that was used to downscale information from the RACMO regional climate model, provided from the EU-CORDEX regional downscaling experiment based on RCP8.5 runs of CMIP5. HCLIM provided results for a historic period 1995-2005, a mid-century period 2040-2050 and an end-century period 2090-2100. HCLIM contains a town energy balance module (Masson, 2000) that models the modification of the local climate by cities. This urban effect is not represented by the larger scales of the global and regional models.

1.4.5 Future Weather case of the hottest day in the Netherlands

Historic weather and climate extremes are important (benchmark) events. Especially if their impact on society was large they might trigger policy action by the government. The stories surrounding such events also tend to stick in the people's minds for a long time. For these and other reasons they can be quite useful as a communication and illustration tool. In "Future Weather" we revisit such historic high-impact cases and transform them in a dynamically consistent way to a future (warmer) climate. In the previous KNMI'14 scenarios, for example, we described an extreme rainfall event and showed how it could get both more intense and more spatially extended in a warmer climate.

In the KNMI'23 scenarios we focus on the record breaking heat wave of July 2019. As is well known, summertime heat waves are extreme meteorological events with a high societal impact (heat stress, tropical nights, increased mortality, etc). They can be characterized by three aspects: intensity, duration and spatial extent. All three are expected to change for the worse in a warming world. Here we illustrate how these changes could play out for the heat wave that produced the hottest day to date in the Netherlands (40.7 °C, Gilze-Rijen 25 July 2019). This is done using a chain of regional climate models in combination with the Pseudo Global Warming (PGW) approach. In this way we can simulate in detail how the 2019 summer would appear in a +2 degree warmer climate, how much hotter the days would potentially get, how much longer the resulting heat wave(s) could last and how spatially extended it would be.

1.5 Reading guide to the scientific report on the KNMI'23 climate scenarios for the Netherlands

This scientific report describes all products within the framework of the KNMI'23 climate scenarios for the Netherlands including the methodological aspects. In this chapter we have described the motivation for the criteria and our strategic choices for the KNMI'23 climate scenarios.

In chapter 2 we describe the general structure and the methodology of the generic climate scenarios for the atmospheric climate variables. The generic climate scenarios are based on the spread in the CMIP6 projections of relevant parameters and on the representation of this spread using an ensemble of runs of the EC-Earth global climate model, dynamically downscaled using the high resolution regional atmospheric climate mode RACMO. On the basis of these runs the scenario table values are calculated and the bias correction and time series transformation routines derived. Observations of the climate in the Netherlands are used to determine the climatology in the reference period (1991-2020) as well as the rate of climate change in the historical period.

Chapter 3 describes the observed trends and the scenario values at the chosen time horizons (2050, 2100 and 2150) for selected atmospheric climate variables: temperature, precipitation, wind and storm, solar radiation, clouds, fog, aerosols, drought and evaporation, both for changes in the mean and in extremes. Besides the scenario table values for the four generic climate scenarios based on SSP1-2.6 and SSP5-8.5 and the wet and dry variants it also includes the two climate scenario's for moderate emissions based on SSP2-4.5 and again for the dry and wet variant for the professional users.

Chapter 4 describes sea level rise for all KNMI'23 emission scenarios (no distinction between the dry and the wet variants), including their pathways until 2300 and the possible low likelihood high impact outcome due to dynamical Antarctic ice cap processes. The values of sea level rise for 2050 and 2100 are also part of the KNMI'23 scenario table.

Chapter 5 is devoted to small scale convective precipitation. It analyzes the summer showers, wind gusts, hail and lighting simulated by very high resolution models, the so-called convection permitting models. These models are used to also get an impression of the sub daily (hourly) extreme rainfall in summer, which is important for impact analyses. It thus follows a different method as compared to the scenario values for the atmospheric climate variables described in chapter 3, but the values of (extreme) summer precipitation have been scaled to the warming levels at the time horizons in the generic climate scenarios and included in the scenario table.

Chapter 6 describes the climate issues in urban areas, mainly the urban heat island effect and precipitation. It considers the present situation and future following the climate scenarios. It describes the key parameters in cities determining the anomalies as compared to their surroundings.

Chapter 7 focusses on the future weather case for the warmest day in the Netherlands, based on the situation of 25 July 2019 when for the first time temperatures above 40 °C were recorded. This weather situation has been transformed to a 2 °C and 4 °C warmer world to illustrate the severity, duration and areal extend of future heat waves.

In Chapter 8 we describe the temperature increase and changes in temperature indices such as the number of summer days in the Netherlands when globally the 1.5 °C level is reached relative to the preindustrial era using the same methodology as for the scenario table values for other time horizons. This temperature limit is important in the context of the Paris Agreement of 2015. According to the IPCC AR6 report (IPCC, 2021b) the year of reaching the 1.5 °C is likely around 2033 defined as the midst of the 20 year period in which the average temperature reaches the 1.5 °C warming level.

In Chapter 9 we describe the present climate and climate scenarios for the BES islands (Bonaire, St. Eustace and Saba) in the Caribbean region. Rationale for this is the fact that these islands became part of the Netherlands. We focus on temperature, precipitation, wind and sea level with a special attention to the occurrence and severity of hurricanes. The same methodology as for the Netherlands in Europe has been followed except that a statistical downscaling has been applied to translate regional values into island values instead of a dynamical downscaling.

In Chapter 10 we describe the dissemination of the KNMI'23 climate scenarios. This scientific report underpins all the work of KNMI'23. In addition, publications on several topics of KNMI'23 will be published in the scientific literature. To facilitate the public and users of climate scenarios for impact studies we have several additional products: the public report and the website covering all data of the KNMI'23 scenarios, including the data for professional users. Finally we address the locations of where to find the background information in the scientific report of the topics described in the public report.

In the last Chapter 11 we provide a guidance for use of the KNMI'23 climate scenarios. Since many users of climate information also used the KNMI'14 climate scenarios, we describe the differences between the outcomes of KNMI'14 and KNMI'23 as a consequence of different methodological choices, the new generation of climate models (CMIP6 versus CMIP5), and the new insights as summarized in the IPCC AR6 report. Also, we describe the differences between the KNMI'23 climate scenarios for the Netherlands and the national climate scenarios of surrounding countries.

Diagram KNMI'23 climate scenarios for the Netherlands

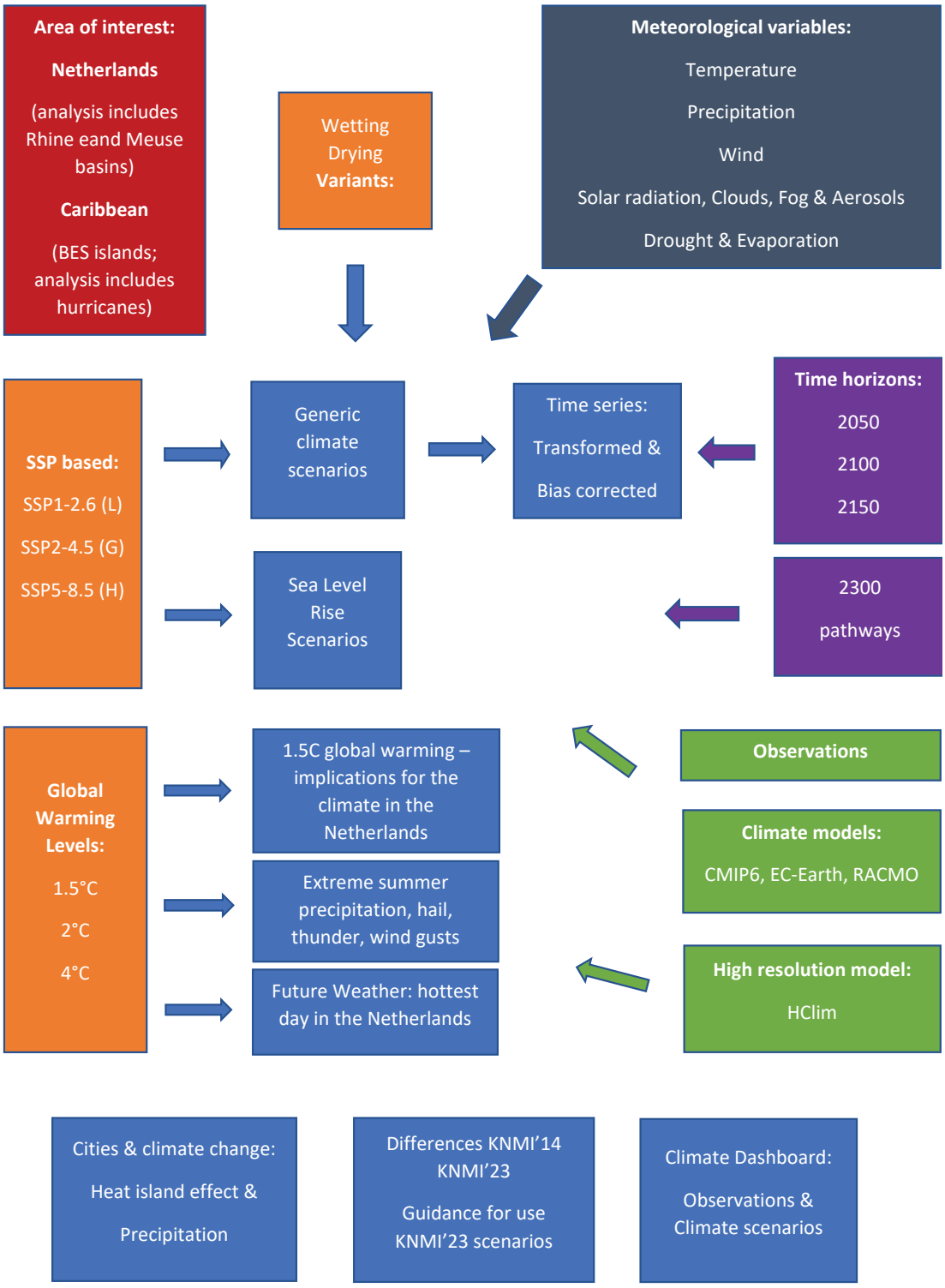

Figure 1.2: Caption on the following page.

Figure 1.2: Diagram of the KNMI'23 climate scenarios. In blue the various products of KNMI'23 described in this scientific report. Key products are the generic climate scenario's for the Netherlands consisting of the scenario table, transformed time series and bias corrected timeseries, calculated for the meteorological variables listed in the gray box, and sea level rise scenarios. All are calculated for the Netherlands (European part) and the Caribbean part (Bonaire, St. Eustace and Saba) as listed in the red box. The analyses include the catchments of Rhine and Meuse, although the scenario table values are confined to the Dutch area. The generic climate scenarios are based on the median global warming values for the time horizons 2050, 2100 and 2150 (purple box) using the SSP1-2.6 and SSP5-8.5 (orange boxes). For sea level rise also the values are given for 2300 while pathways are graphically displayed (purple box). For these products observations, EC-Earth (global climate model) and RACMO (high resolution regional climate model for dynamical downscaling) have been used (green boxes). For the professional users also the median global warming estimates for SSP2-4.5 have been tabulated, but are considered outside the generic climate scenarios. Other KNMI'23 scenario products are the climate change in the Netherlands, when globally the 1.5 °C warming has been reached (although we have also calculated these values using the same methods as for the generic climate scenario's), extreme summer precipitation using the high resolution convective permitting models (CPM, green box), and a future weather case for the hottest day in the Netherlands using the very resolution HCLIM model (green box). These products are based on warming levels of 1.5, 2 and 4 °C (orange box) instead of at the time horizons based on SSPs. However, extreme summer precipitation has been scaled to also the warming levels used at the time horizons of the KNMI'23 scenarios. These numbers have been included in the scenario table. Special products within KNMI'23 are the analyses of climate change in cities and the comparison between the previous climate scenarios for the Netherlands, KNMI'14, and KNMI'23. All products, including extensions, have been listed and described at our website.

Chapter 2

General structure of KNMI'23

In this chapter we will describe in detail the construction procedure of the generic KNMI'23 scenarios and related products. The rationale behind the approach, including the choices that were made, was introduced in the previous chapter (Sections 1.2 and 1.3). Here we discuss the scenario methods in full detail, and will refer to the relevant sections from the previous chapter throughout. A schematic overview of the different methodologic steps in the construction of the scenarios is provided in Figure 2.1. The scenarios developed for the Caribbean islands follow a similar procedure, details can be found in 9.4.2.

2.1 The KNMI'23 scenario construction procedure

2.1.1 Global warming levels for the chosen SSP emission scenarios and time horizons

The KNMI'23 climate scenarios have been developed for pre-selected scenarios of global socio-economic development (SSP scenarios, see Section 1.3.4) that capture the uncertainty in future human emissions (policy uncertainty, socio-economic developments). For each of these SSP scenarios, the IPCC AR6 report provides projections of the Global Surface Air Temperature (GSAT). These are based on multiple lines of evidence regarding climate sensitivity to constrain the raw model projections. The IPCC refers to their constrained projections of global mean temperature change as the 'ΔGSAT assessed range'. Note that these projections thus differ from a straightforward CMIP6 multi-model mean, or model-democracy approach, which would provide higher values for ΔGSAT (IPCC, 2021b).

The IPCC follows a two-part method to calculate the ΔGSAT assessed range. The first line of evidence consists of applying observational constraints to CMIP6 simulations, consisting of the average constraints from three independent estimates: Liang et al. (2020), Tokarska et al. (2020) and Ribes et al. (2021). As a second line of evidence, a 2-layer energy balance model is used, or emulator, using IPCC derived estimates of equilibrium climate sensitivity and the transient climate response, to make ΔGSAT projections. The 'assessed range' is the average of these two methods for calculating the change in GSAT. Since the CMIP6 scenario runs end in 2100, these estimates are only available up to the year 2100 (Figure 2.2). Beyond 2100, socioeconomic developments were not modelled (C. Smith, chapter scientist IPCC chapter 7, pers.comm.) and the described method can therefore not be applied for this period. Instead, IPCC has extrapolated the assessed range using a tuned version of the FAIR model (Smith et al., 2018), providing ΔGSAT projections beyond 2100 that are largely consistent with those before 2100. In the IPCC report these are only used for sea level projections, but here we also use them for the development of regional climate change scenarios beyond 2100.

The KNMI'23 warming levels, based on values of ΔGSAT are derived from this IPCC data. We take the median value of the ΔGSAT assessed range as the most likely warming level for each

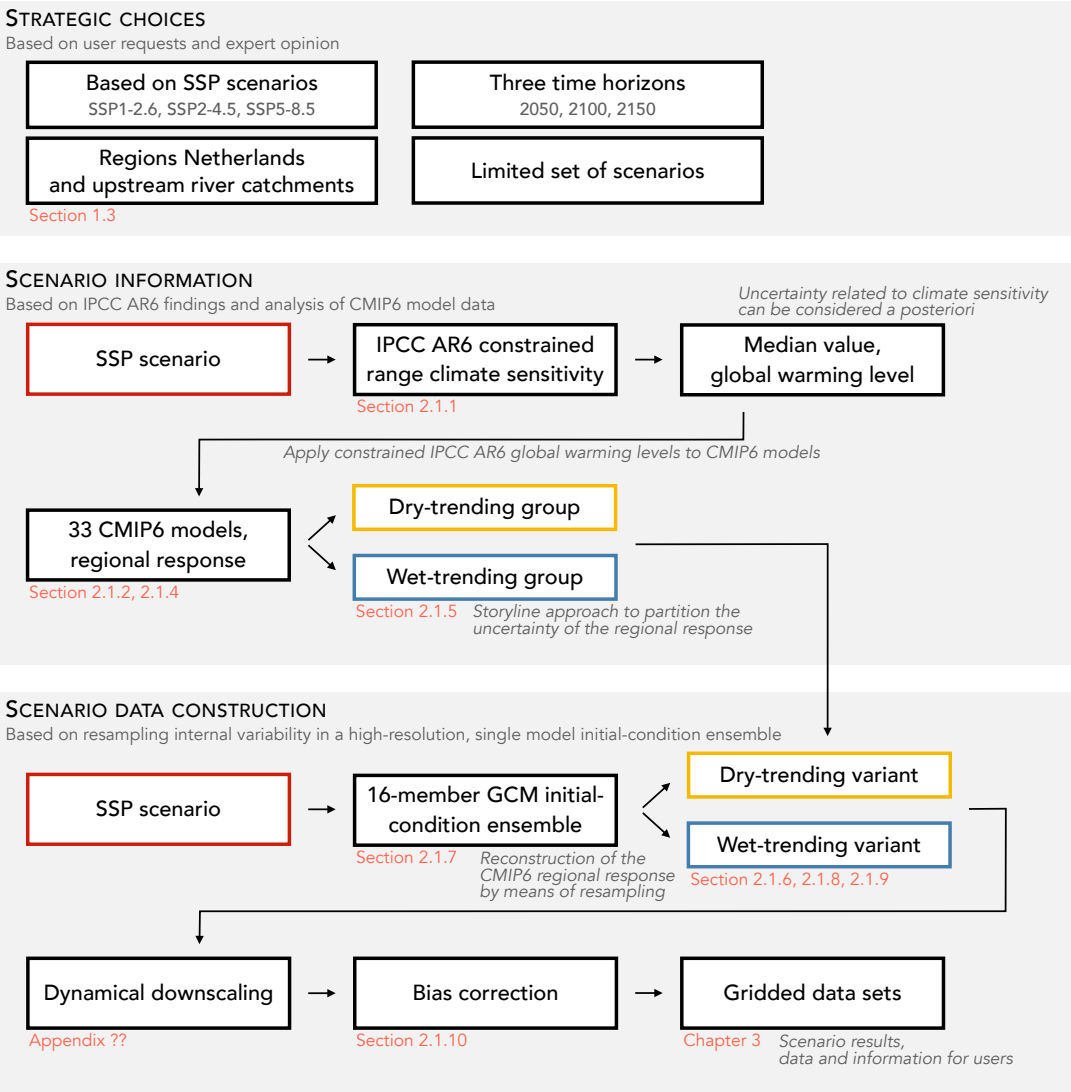

Figure 2.1: Schematic diagram of the KNMI'23 climate scenario methodology, noting strategic choices (top), scenario information (middle) and scenario data construction (bottom). Red text refers to specific sections in this report.

time horizon (Table 2.1). The time horizons for KNMI'23 are the 30 year periods around 2050 (2036-2065), 2100 (2086-2115) and 2150 (2136-2165). The period 1991-2020 is the reference period for the present-day climate. Note that IPCC uses averages over a 20-year period rather than over 30-year periods as is advised by the WMO and is standard practice at KNMI. We have taken the IPCC 20-year periods in the center of the KNMI'23 30-year periods, the differences in ΔGSAT due to this methodological difference is very small (less than 0.05 K). Note that the values of ΔGSAT here are relative to the IPCC period 1996-2015, equivalent to the latest climate normal period of 1991-2020. In the Paris agreement, climate targets are defined relative to a pre-industrial background state. The warming from pre-industrial to the 1996-2015 reference period is 0.85 °C (IPCC best estimate of warming since 1850-1900, (IPCC, 2021b)).

Since each global climate model in the CMIP6 ensemble has a different climate sensitivity, the simulated time at which different models reach the KNMI'23 warming levels is model dependent. High sensitivity models warm faster and reach the warming levels earlier in their simulation than low sensitivity models that warm relatively slow. In order to assess the projected regional climate

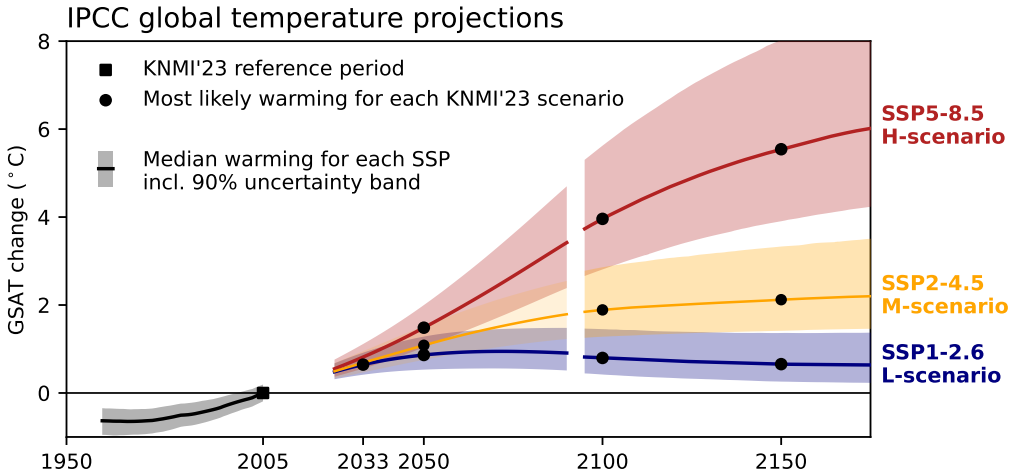

Figure 2.2: Projections of Global Surface Air Temperature change (ΔGSAT) relative to 1996-2015 [°C] based on the IPCC 'assessed range'. Solid lines show the median warming for each SSP scenario, shading shows the 90 % uncertainty range ($5-95$ %), a 20-yr running mean was applied to all data. Black circles show most likely GSAT value at the KNMI'23 time horizons, the black square shows the KNMI'23 reference period (1996-2015 here). The projections are split in two sections, 2015-2090 and 2090-onwards respectively, see Section 2.1.1 for details. Colours: black/grey historical, red SSP5-8.5 (H-scenario), blue SSP1-2.6 (L-scenario) and yellow SSP2-4.5 (M-scenario for professional users). Data sources: Fyfe et al. (2021) and Smith (2021).

Emission uncertainty	Scenario name	Time horizons			
		2033	2050	2100	2150
SSP1-2.6	L	0.6 (0.4 – 0.9)	0.9 (0.5 – 1.3)	0.8 (0.4 – 1.5)	0.7 (0.3 – 1.4)
SSP2-4.5	M		1.1 (0.8 – 1.6)	1.9 (1.3 – 2.9)	2.1 (1.4 – 3.3)
SSP5-8.5	H		1.5 (1.0 – 2.0)	4.0 (2.8 – 5.6)	5.5 (3.9 – 8.0)

Table 2.1: KNMI'23 global warming levels, based on the the median value of the IPCC 'assessed range' of Global Surface Air Temperature change (ΔGSAT) relative to 1996-2015 [°C], for different SSP scenarios at the KNMI'23 time horizons, in brackets the 90 % confidence interval ($5-95$ %).

change at the KNMI'23 warming levels, we shift each model in time such that the warming in that model matches the warming level of choice (Hausfather et al., 2022). This procedure will be referred to as 'matched warming'. The resulting data set is used to evaluate the CMIP6 spread of projected changes over the region of interest (Section 2.1.4).

The choice for the most likely warming (i.e. median warming) at the KNMI'23 time horizons removes the uncertainty in climate sensitivity from the scenario products. If one is interested in this uncertainty, it can be considered in a couple of ways. First, if climate sensitivity is larger than the IPCC best estimate, the time horizons of KNMI'23 will move forward (earlier in time), similarly for lower values of climate sensitivity the time horizons move backward (later in time). E.g., taking into account the 90 % uncertainty range of climate sensitivity, the SSP5-8.5 2100 warming level of 4.0 °C will be reached somewhere between 2080 and 2155 (Figure 2.2). The SSP5-8.5 scenario in 2100 can thus also be considered as a high climate sensitivity scenario in 2080. Second, in first order projected regional changes scale with ΔGSAT (Section 2.1.8). As such, the KNMI'23 scenario values for regional climate change can be scaled to higher and lower warming levels if a higher or lower level of climate sensitivity is considered. Following these lines of thinking, the 2150 time horizon of SSP5-8.5 (warming level 5.5 °C) is approximately equal to the high climate sensitivity-uncertainty estimate in 2100 (warming level 5.6 °C, Table 2.1). The scenario for SSP5-8.5 2150 scenario can thus be considered as an approximation for the high-climate sensitivity case in SSP5-8.5 2100.

2.1.2 Selection of CMIP6 models for the assessment of the regional climate change

To assess regional climate change for the chosen SSP scenarios and warming levels, we use a set of simulations of 33 CMIP6 models (Table 2.2), referred to as the 'CMIP6 standard set'. The models were selected on the basis of data availability alone. The requirements were the availability of historical and scenario runs (SSP1-2.6, SSP2-4.5, SSP5-8.5) with the same variant-id to ensure a continuous evolution from the past into the future, and the availability of all variables of interest (near-surface temperature, TAS, precipitation, PR, incoming solar radiation, RSDS, and surface pressure, PSL). A set of 33 CMIP6 models matched these criteria for the main data set (monthly data). For some purposes daily data were required. Of the 33 models selected, 26 models had the required daily data on-line (noted in Table 2.2). To prevent issues due to the unequal sampling of natural variability between models, because the models differ in the number of ensemble members published, we use a single run from each model, even when more are available.

2.1.3 Regions of interest: Netherlands and basins of rivers Rhine and Meuse

We consider two spatial regions for our regional climate assessment: 1) The Netherlands (European area), referred to as 'NL', and 2) the combined area of The Netherlands (European area, not the Caribbean islands, these are treated separately, see Section 9) and the upstream parts of the catchments of the Rhine and Meuse, referred to as 'NL+RM'. The CMIP6 models, and also the RACMO regional model, have a lower spatial resolution than the detailed outline of these regions. We have therefore mapped these regions onto each model's horizontal grid in order to calculate basin averages (Figure 2.3a,b). First a high-resolution mask at 0.1° resolution was created. The fractional overlap between the coarse model grids and the high-resolution mask was used to weigh the data on the coarse grid in the calculation of basin averages. In case the coarse model grid has a land fraction (Figure 2.3c) that is lower than this fractional overlap of the high-resolution mask, the land fraction value is chosen to weigh the contribution of that grid cell to the basin average

Model name	Variant-id	Data	Model name	Variant-id	Data
ACCESS-CM2	r1i1p1f1	M,D	GFDL-ESM4	r1i1p1f1	M,D
ACCESS-ESM1-5	r1i1p1f1	M,D	GISS-E2-1-G	r1i1p3f1	M
AWI-CM-1-1-MR	r1i1p1f1	M,D	HadGEM3-GC31-LL	r1i1p1f3	M,D
BCC-CSM2-MR	r1i1p1f1	M,D	INM-CM4-8	r1i1p1f1	M,D
CanESM5	r10i1p1f1	M,D	INM-CM5-0	r1i1p1f1	M,D
CanESM5-CanOE	r1i1p2f1	M	IPSL-CM6A-LR	r1i1p1f1	M,D
CESM2	r4i1p1f1	M,D	KACE-1-0-G	r1i1p1f1	M,D
CESM2-WACCM	r1i1p1f1	M,D	MIROC6	r1i1p1f1	M,D
CIESM	r1i1p1f1	M	MIROC-ES2L	r1i1p1f2	M,D
CMCC-CM2-SR5	r1i1p1f1	M,D	MPI-ESM1-2-HR	r1i1p1f1	M,D
CNRM-CM6-1	r1i1p1f2	M,D	MPI-ESM1-2-LR	r10i1p1f1	M,D
CNRM-CM6-1-HR	r1i1p1f2	M,D	MRI-ESM2-0	r1i1p1f1	M,D
CNRM-ESM2-1	r1i1p1f2	M,D	NESM3	r1i1p1f1	M,D
EC-Earth3	r1i1p1f1	M	NorESM2-LM	r1i1p1f1	M,D
EC-Earth3-Veg	r1i1p1f1	M	NorESM2-MM	r1i1p1f1	M,D
FGOALS-f3-L	r1i1p1f1	M	UKESM1-0-LL	r1i1p1f2	M,D
FGOALS-g3	r1i1p1f1	M			

Table 2.2: CMIP6 models included in the KNMI'23 CMIP6 standard set. Noted are model names, the specific variant-id of the published run, and temporal resolution of data available (monthly and/or daily).

(Equation 2.1):

$$\overline{P}_{\text{basin}} = \frac{\sum_{i,j} \left[P(i,j) \cdot w(i,j) \cdot \text{area}(i,j)\right]}{\sum_{i,j} \left[w(i,j) \cdot \text{area}(i,j)\right]},$$
$$w(i,j) = \min\left(\text{landfraction}(i,j), \text{overlap}(i,j)\right), \tag{2.1}$$

in which P is the meteorological variable of interest, w is the grid cell weight determined by either the fractional overlap or land fraction value, and area is the grid cell area. i and j are grid indices in latitudinal and longitudinal direction, respectively. The basin averaged time series form the basis for the assessment of the spread in the regional climate projections (Section 2.1.4).

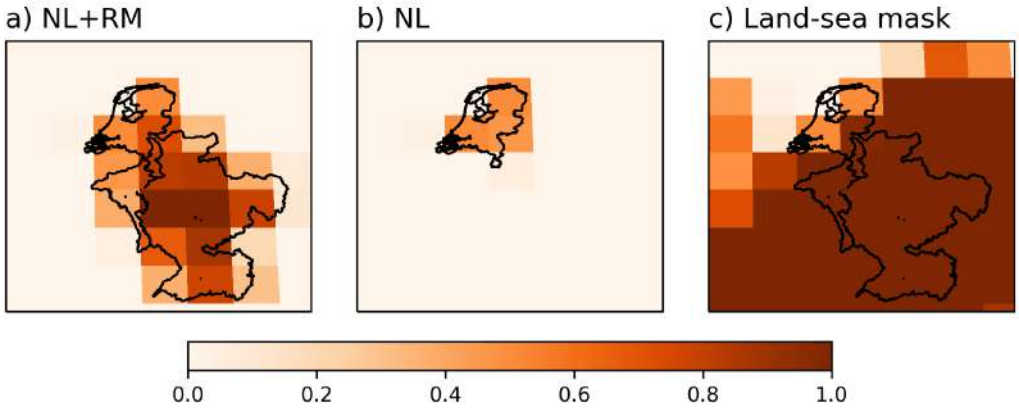

Figure 2.3: Model masks used to generate regional time series from global data, shown here for the ACCESS-CM2 model. (a) Netherlands plus upstream Rhine and Meuse catchments (NL+RM), (b) Netherlands (NL), (c) model land-sea mask. Shaded squares show the horizontal model grid, coloured by the fraction of the grid cell that lies within the mask (a,b), or the fraction of land within the cell (c), black outline shows the spatial region considered.

2.1.4 CMIP6 projections of regional climate change

The CMIP6 standard set is used to determine the spread in the area-averaged climate response for the NL+RM and NL regions (Section 2.1.3) at all warming levels (Section 2.1.1). To determine the regional response at the specified warming levels, we apply the 'matched warming' approach, in which we determine for each model the 30-year period that has the same global warming level as the ΔGSAT-warming level, and use this period to evaluate the regional climate response (see also Section 2.1.1). The multi-model projection of regional climate change at that warming level is found by averaging the results. A similar procedure is also followed in the 'IPCC WGI Interactive Atlas' which provides information on regional climate change for different warming levels, and is advocated for in Hausfather et al. (2022).

In case a model with low climate sensitivity does not reach the specified warming level, we regress its response to ΔGSAT and linearly extrapolate the response to the warming level. An example of this procedure is given in Figure 2.4, the extrapolation based on the linear regression looks reasonable. The assumption of a linear dependence is better satisfied for the regional temperature response than for the precipitation response shown here. Note that extrapolation is not required for the 2050 time horizon. For the SSP5-8.5 scenarios, extrapolation is required for about half of the models in 2100, and for all models for the warming levels in 2150. This is due to the CMIP6 models runs ending in 2100, and no model reaching the required warming level of 5.5 °C by 2100.

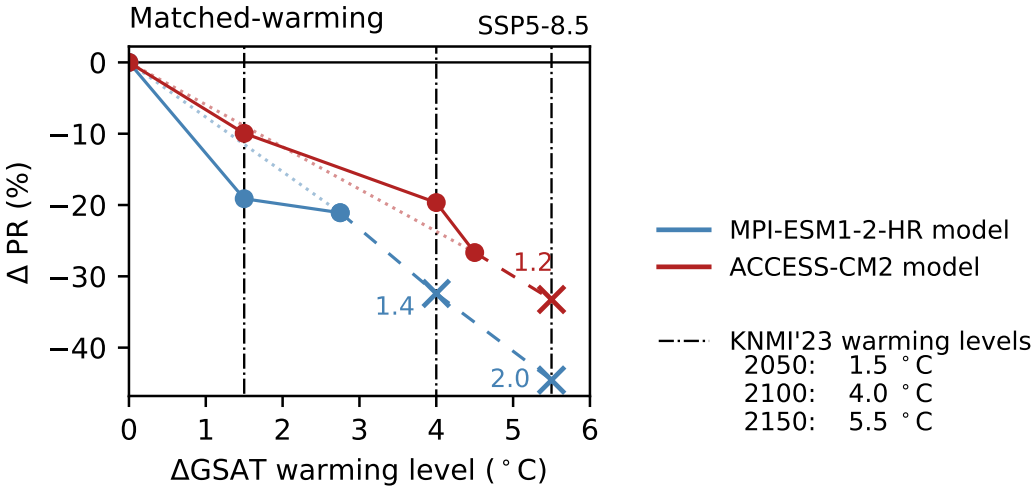

Figure 2.4: Illustration of the procedure to scale the regional response of low-sensitivity climate models to the specified warming levels. Coloured dots show the modelled response at the KNMI'23 warming levels, and in case of scaling the warming level associated with their end-of-century period (2071-2100). These last points are then scaled to the warming level of interest, shown by a dashed line and coloured cross. The printed number shows the applied scaling factor. This example shows the summer precipitation response in NL+RM in SSP5-8.5 for different warming levels, for MPI-ESM1-2-HR (scaling for 2100 and 2150 time horizon, blue) and ACCESS-CM2 (scaling only for 2150 time horizon, red).

The mean projection of European climate change for the SSP5-8.5 scenario at the end of the century (time horizon 2100, 4.0 °C warming level) for the CMIP6 standard set is shown in the large panels of Figure 2.5. For precipitation a seesaw pattern is projected, with increased precipitation in the north and decreased precipitation in the south. In winter the border between positive and negative changes is situated just north of the Mediterranean, in summer it is situated in Scandinavia (Figures 2.5a,c). Temperatures are projected to increase everywhere and in all seasons, with slightly larger trends in summer than in winter. There is substantial model uncertainty in the pattern and the magnitude of the projected trends. This is illustrated in the smaller panels

of Figure 2.5, which for each variable and season show two individual models with very different regional responses.

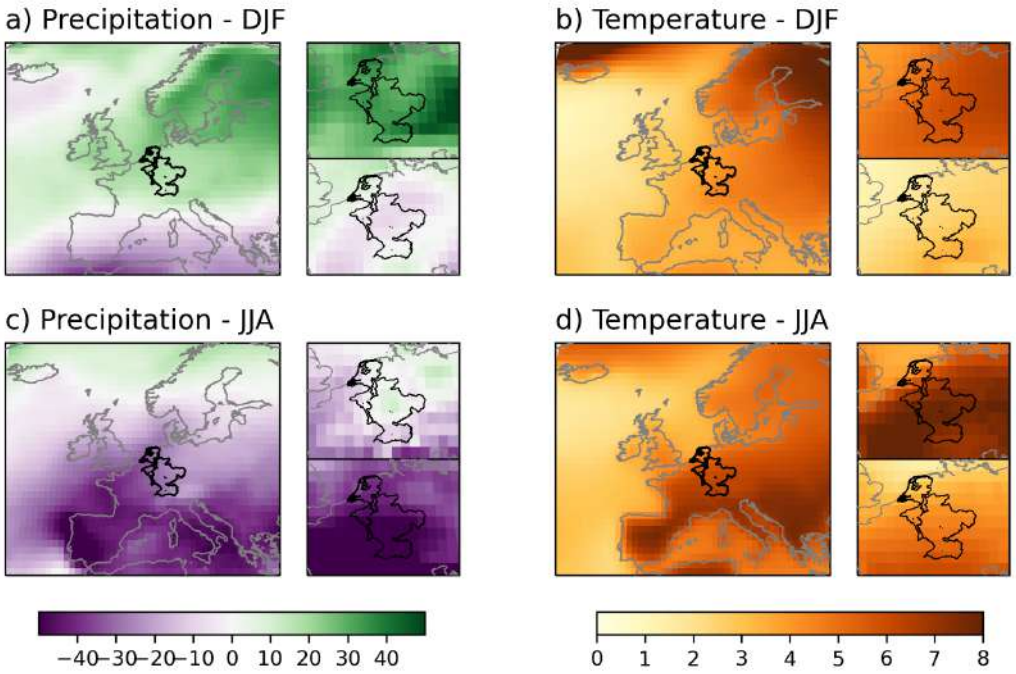

Figure 2.5: Large panels: CMIP6 multi-model mean projected regional climate change in Europe for SSP5-8.5 in 2100 (ΔGSAT = 4.0 °C), for (a,c) precipitation [%], (b,d) 2 m temperature (°C), and (a,b) in the winter season (DJF), (c,d) in the summer season (JJA). Small panels show the models with the largest and smallest trend in the NL+RM region, note these are different models for each variable/season. NL+RM region outlined in black.

Note that internal variability contributes substantially to an individual model's response pattern. This is due to the fact that the response is calculated based on the difference between two 30-year periods, and that for some variables internal variability significantly impacts a single realisation of a 30-year mean climate. As an illustration of this we show projections of winter precipitation of a 16-member ensemble of SSP5-8.5 simulations with the EC-Earth3$_{\text{p5}}$ model (Figure 2.6). The 16 ensemble members have been set up exactly the same except for a different initial condition (taken from different years in a long pre-industrial run, see Section 2.3). Differences are thus solely due to internal variability. In the ensemble mean the contribution from internal variability is reduced by a factor of four ($1/\sqrt{N}$). The large variations of single estimates of the winter precipitation response illustrate that for this variable the contribution of internal variability cannot be neglected. The spread in responses in the CMIP6 standard set is thus due to a combination of model uncertainty and internal variability, and consequently the full range of regional responses should not be interpreted as the spread due to model uncertainty alone. In the construction of the KNMI'23 scenarios we take this into account, and remove the contribution of internal variability as much as possible (Section 2.1.8).

For the NL+RM region, the multi-model mean shows no change in annual mean precipitation and a 4.6 °C increase in 2 m air temperature (Figure 2.7). The spread around these values is substantial, e.g., the range for precipitation is from an increase of 11.9 % to a decrease of 12.3 %, for temperature the increase varies between models from 3.1 to 5.6 °C. Seasonal changes are different to the changes in the annual mean, e.g., in winter an increase of precipitation is projected (multi-model mean: 16.9 %, Figures 2.5a, 2.7a), whereas for the summer months a strong decrease is projected (multi-model mean: -27.9 %, Figures 2.5c, 2.7a). The summer reduction

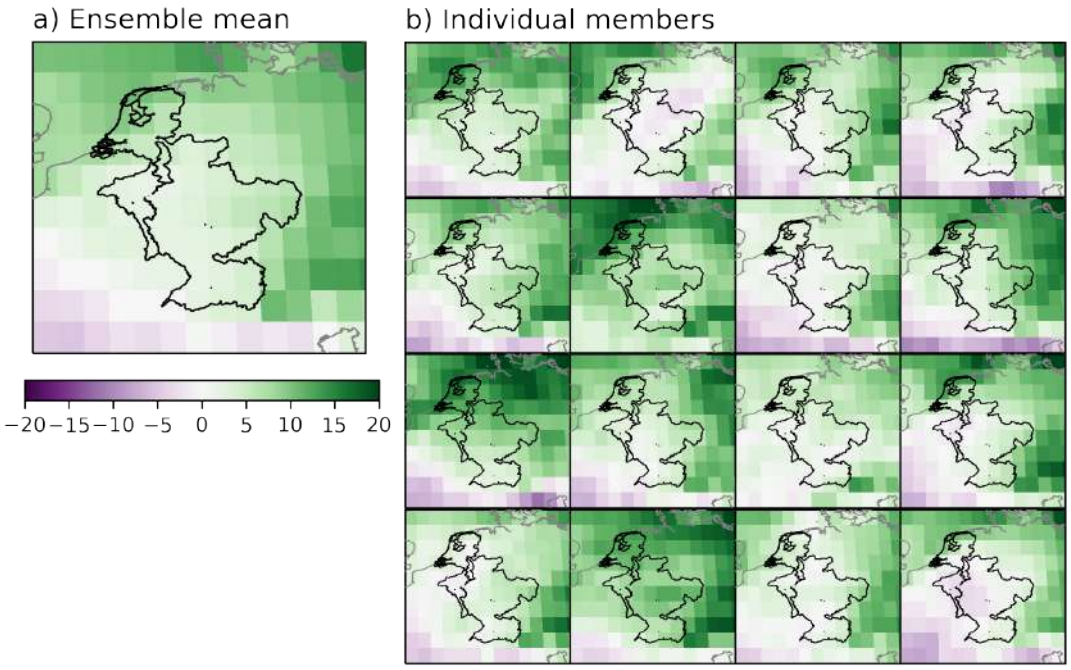

Figure 2.6: As Figure 2.5a but here for annual mean precipitation change [%] in an 16-member initial-condition ensemble simulation with the EC-Earth3$_{p5}$ model. (a) Shows the 16-member ensemble mean response, (b) shows the response in the 16 individual runs.

of precipitation is accompanied by a strong temperature and incoming solar radiation increase (Figures 2.7b,c). Rising temperatures and increasing solar radiation fuel evapotranspiration if there is water available in the soil. Reduced precipitation and increased evapotranspiration make for a drier summer climate. In terms of the water balance, the cumulative difference between Makkink reference evapotranspiration and precipitation from 1st of April onwards, there is a mean projected increase in the September value of 187 mm (Figure 2.7d). For more details on the water balance index and potential evapotranspiration, see Section 3.5. Also these seasonal change have substantial uncertainty and model spread.

The spread in the seasonal responses are for a large part due to model uncertainty. Besides the contribution from internal variability, the differences in individual model's responses are, for example, due to different representations of parameterised processes in the atmosphere, land and ocean (such as convection in atmosphere and ocean, cloud micro-physics and the effect of clouds on radiation, and evapotranspiration over land). The model spread reflects remaining uncertainties in scientific understanding and modelling of these processes (e.g., Selten et al., 2020).

The regional responses in the NL+RM and in the NL regions are closely related, but not always the same. Differences in the trends in the two regions have impact on the balance between fresh water sources, i.e. local precipitation/evapotranspiration versus water 'imported' through the rivers Rhine and Meuse. Precipitation trends are slightly larger in NL than in NL+RM, while temperature trends are smaller in NL than in NL+RM (Figure 2.8). For temperature this is due to the relatively larger projected trends in southern Europe than in northern Europe, and further inland on the continent (Figure 2.5b,d). Because the NL+RM region reaches further south and east, this results in larger trends for the NL+RM region. The winter precipitation increase is a bit larger in NL, probably due to the more northerly location. For summer, the difference in precipitation reduction is small, albeit slightly stronger in NL (Figure 2.8a). Projected trends towards a drier summer climate, measured through the water balance, are stronger in NL+RM than in NL (Figure 2.8)d. Both the stronger temperature and solar radiation increase contribute to a stronger increase in potential evapotranspiration in NL+RM.

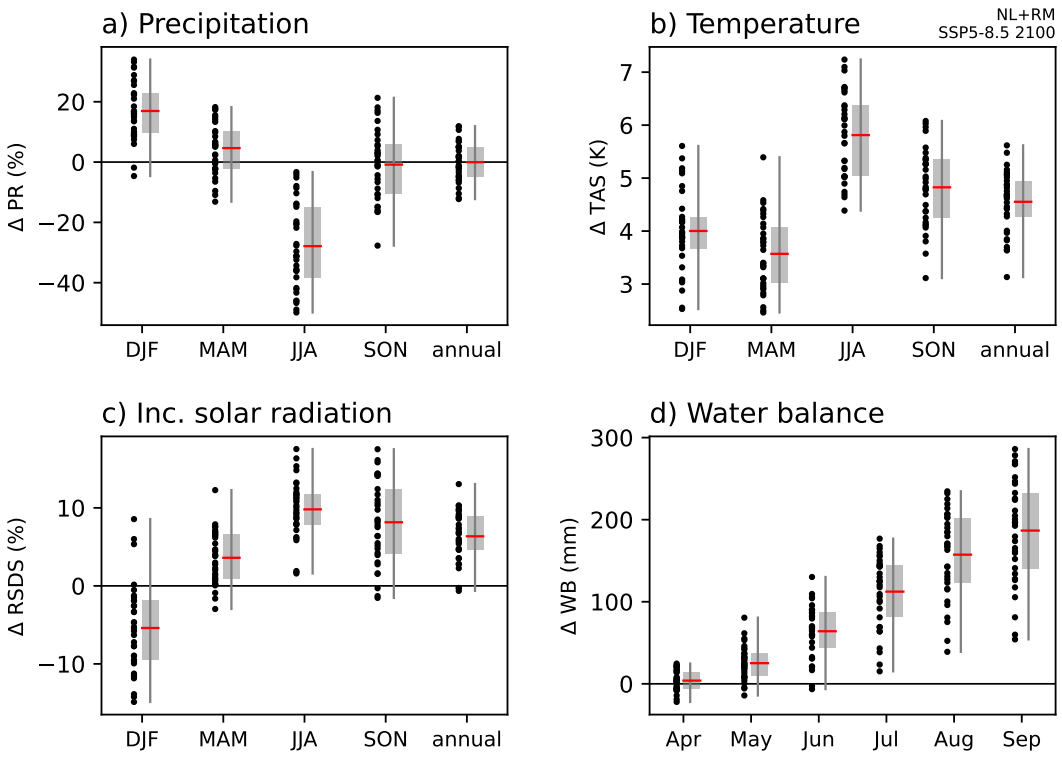

Figure 2.7: CMIP6 multi-model projected regional climate change in NL+RM region for SSP5-8.5 in 2100 (ΔGSAT = 4.0 °C), relative to present-day climate. For (a) precipitation (%) (b) 2 m temperature (°C), (c) incoming solar radiation (%), (d) cumulative water balance (mm), i.e. Makkink reference evapotranspiration minus precipitation, cumulative from 1 April. Shown are the 33 individual models in the CMIP6 standard set (black dots), their distribution (in grey, vertical line shows minimum and maximum, bar shows 25th to 75th percentile), and their mean (red line).

A similar analysis provides the spread in the response of the CMIP6 standard set for the other SSP scenarios and time horizons. The response patterns are quite similar, the main difference is the magnitude of the regional response. Generally, the magnitude of regional change is smaller for lower emission scenarios (smaller changes in SSP1-2.6 and SSP2-4.5 than in SSP5-8.5) and for earlier time horizons (i.e. smaller projected changes in 2050, than in 2100 and 2150). An exception to this is the SSP1-2.6 scenario, in which the GSAT peaks around 2075 (Figure 2.2), and consequently the KNMI'23 GSAT targets are lower for 2100 and 2150 than they are in 2050 (Table 2.1). Figure 2.9 shows the regional response in different SSP scenarios and for different time horizons for selected variables, Figure 2.10 shows the same, but plotted against global warming level.

From Figure 2.9 it is obvious that the projections for the different time horizons under SSP1-2.6 have large overlap. This is due to the warming levels for this scenario, which are almost indistinguishable (Table 2.1). Given our matched-warming assumption, in which regional climate response only depends on the value of GSAT (Figure 2.10), we expect that the regional responses will also not be distinct. To further check the validity of this assumption, we have investigated the difference in the regional responses for 2100 and 2050 in temperature, sea level pressure and precipitation over a large North Atlantic-European region (Figure 2.11). With the exception of the Nordic Seas, where sea-ice changes may play a strong role, the differences are small, verifying our assumption. It has therefore been decided to create just one set of scenarios data for SSP1-2.6, which is valid for all three time horizons. We use a warming level of 0.8 °C, associated with the

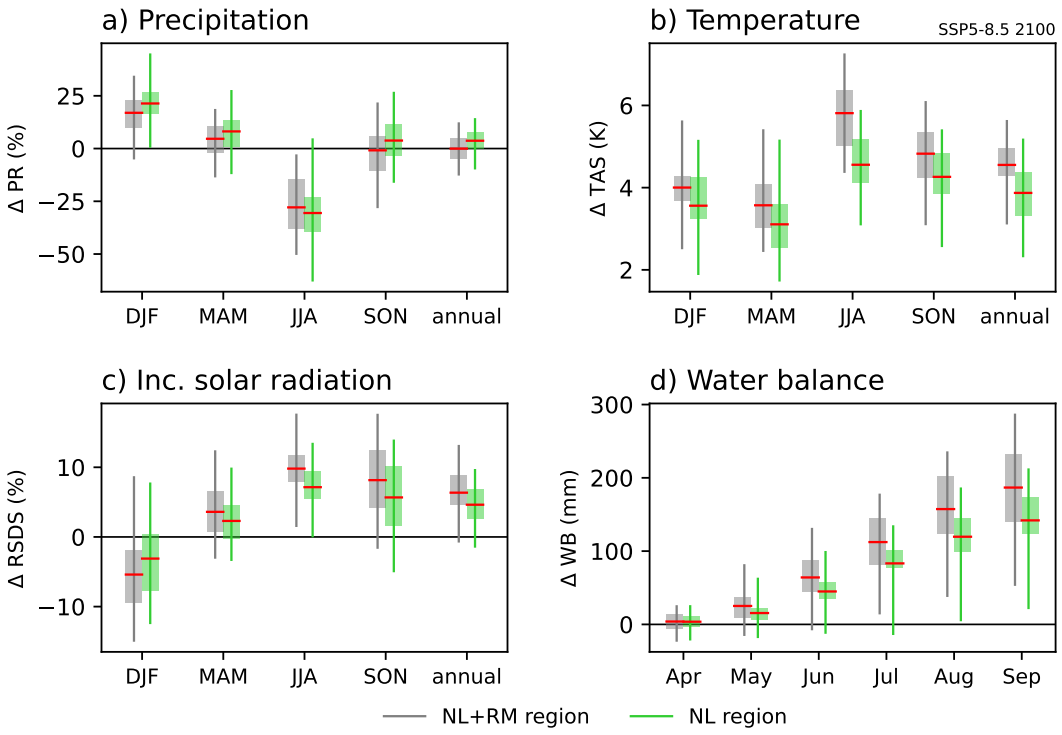

Figure 2.8: As Figure 2.7, but here comparing the NL+RM (grey) and NL (green) region.

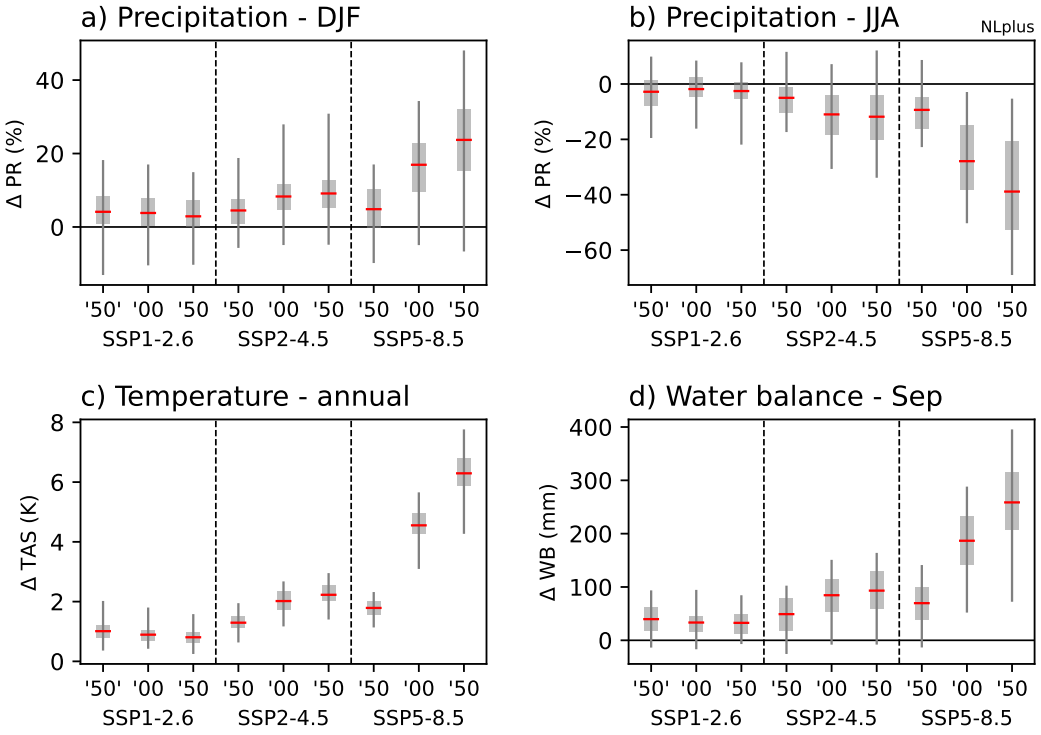

Figure 2.9: As Figure 2.7, but here comparing different time horizons (2050, 2100 and 2150) for SSP1-2.6, SSP2-4.5 and SSP5-8.5, for (a) DJF precipitation, (b) JJA precipitation, (c) annual temperature, (d) September water balance.

2100 time horizon, for this scenario. It should be stressed that the assumption of full dependence on GSAT is not valid for sea level rise, as in the 50 years of time between the time horizons in this scenario the warming of the ocean and the melting of glaciers and ice sheets continues, resulting in continuing sea level rise (see Chapter 4).

2.1.5 Two storyline scenarios to capture the spread in the regional climate projections

The spread in the regional climate projections of the CMIP6 standard set is substantial (Figures 2.5, 2.7, 2.8, 2.9). We wish to represent the contribution of model uncertainty to this spread in just two distinct and relevant scenarios. Inevitably, the choice on how to achieve this is subjective. The uncertainty in the regional climate projections is by definition multi-dimensional. E.g., if we limit the uncertainty only to seasonal and annual means of precipitation and temperature (10 variables), we are faced with the challenge to pick two points in a 10-dimensional space, such that the two points cover a relevant and substantial portion of the total spread. With the limitation of creating two scenarios that describe the model uncertainty, it is clear that these scenarios will not be able to cover the spread in all seasons and all climate variables. We therefore choose a story-line approach. Storylines, in this case, are physically self-consistent unfoldings of plausible future pathways, and are used to provide a physical basis for partitioning uncertainty (Shepherd et al., 2018).

The two storylines, which we will refer to as two scenarios, are designed to cover the spread in the projected precipitation change in the NL+RM region in the winter, the summer and the annual mean. This choice is motivated by the fact that the precipitation change, according to experts consulted, is most relevant for climate adaptation in the Netherlands (see Section 1.3.4). Higher probabilities of high river discharge due to increased winter precipitation, and/or higher probabilities of drought and water shortage due to decreased summer precipitation, require substantial adaptation. Furthermore, the spread in the projected change of precipitation is substantial and allows the formation of distinct storylines, with some models projecting an increase of annual total precipitation and others projecting a decrease (Figure 2.7a).

The projections of seasonal precipitation in NL+RM include a reduction of summer precipitation, and for most models an increase in winter precipitation (Figure 2.7a). The magnitude of this summer reduction and winter increase varies strongly between models (Figure 2.12a), though the correlation of these projected seasonal changes is such that the total annual precipitation will either increase or decrease. We define three groups of models by the combined projected change in winter (December-January-February, DJF), summer (June-July-August, JJA) and the annual sum (Figure 2.12a). We normalise the projected changes in each season by the standard-deviation of the projected changes in that season (Figure 2.12b). This way, each season contributes equally to the sum of the three (Figure 2.12c). The groups are defined on the basis of this normalised sum:

- a 'dry-trending group' containing the 11 models that project the largest trends towards a drier future climate (decrease of annual total precipitation, strong trend towards reduced summer precipitation, relatively small increase in winter precipitation),
- a 'wet-trending group' containing the 11 models that project the largest trends towards a wetter future climate (increase of annual total precipitation, large trend towards increased winter precipitation, relatively small decrease in summer precipitation),
- and a third group of the remaining 11 models.

The composite mean climate signals of the dry-trending and wet-trending groups form the basis for spanning the uncertainty in the regional climate response for a given warming level. We define the groups at the 2100 time horizon for the highest emissions scenario SSP5-8.5. The same groups are used as the basis for the model uncertainty quantification for the other emission scenarios and other time horizons. The motivation for this choice is that the signal to noise ratio is largest for

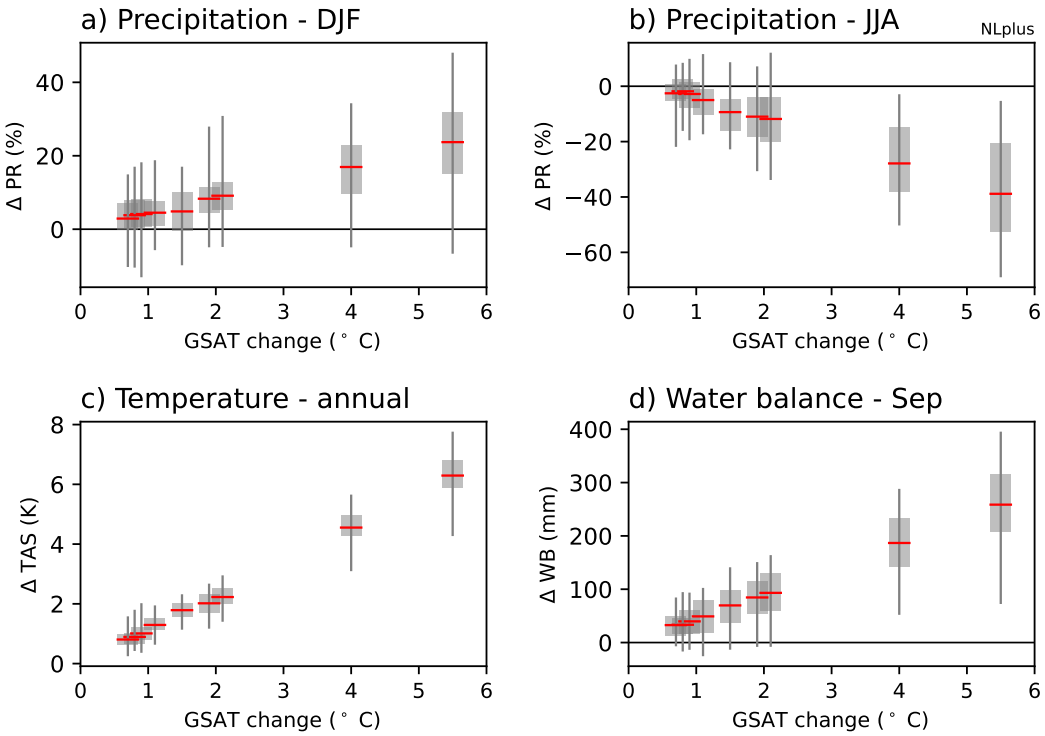

Figure 2.10: As Figure 2.9, but here plotted against the change in global surface air temperature.

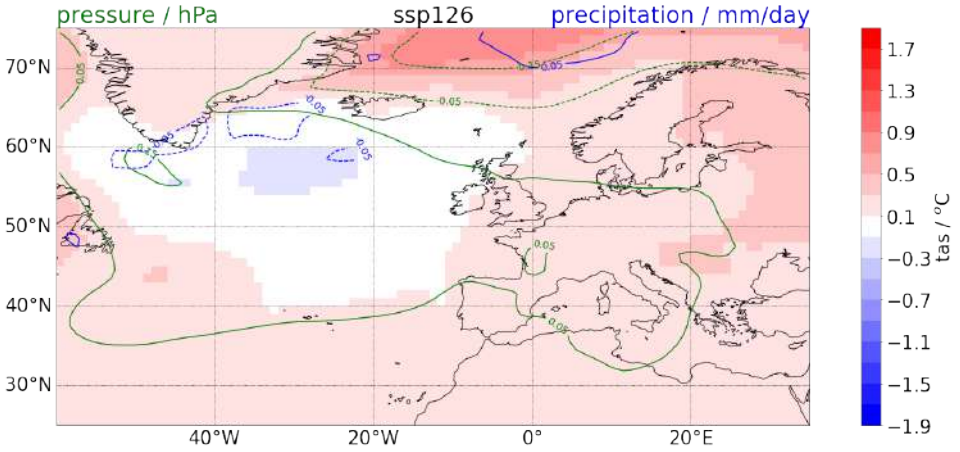

Figure 2.11: Differences between the changes until 2100 and until 2050, both calculated according to the matched-warming approach, of annual-mean near-surface temperature (tas, colours), sea level pressure (psl, green contours) and precipitation (pr, blue contours) over the North Atlantic region in the CMIP6 standard set for SSP1-2.6. The absolute precipitation changes shown in the plot correspond to relative differences of less than 2%.

the highest emission scenario in 2100 and we assume that to first order the climate change signal is proportional to the accumulated emissions (see figure TS.18 of IPCC, 2021b).

The composition of the groups is listed in Table 2.3. MPI-ESM1-2-LR projects the largest precipitation decrease in the NL+RM region, CanESM5-CanOE the largest increase. Note that both groups contain a number of models that share certain parts of the model code and cannot be treated as completely independent, such as EC-Earth and CNRM in the wet-trending group (ECMWF family), and UKESM1-0 and ACCESS-ESM1-5 in the dry-trending group (HadAM3 family) (Kuma et al., 2023).

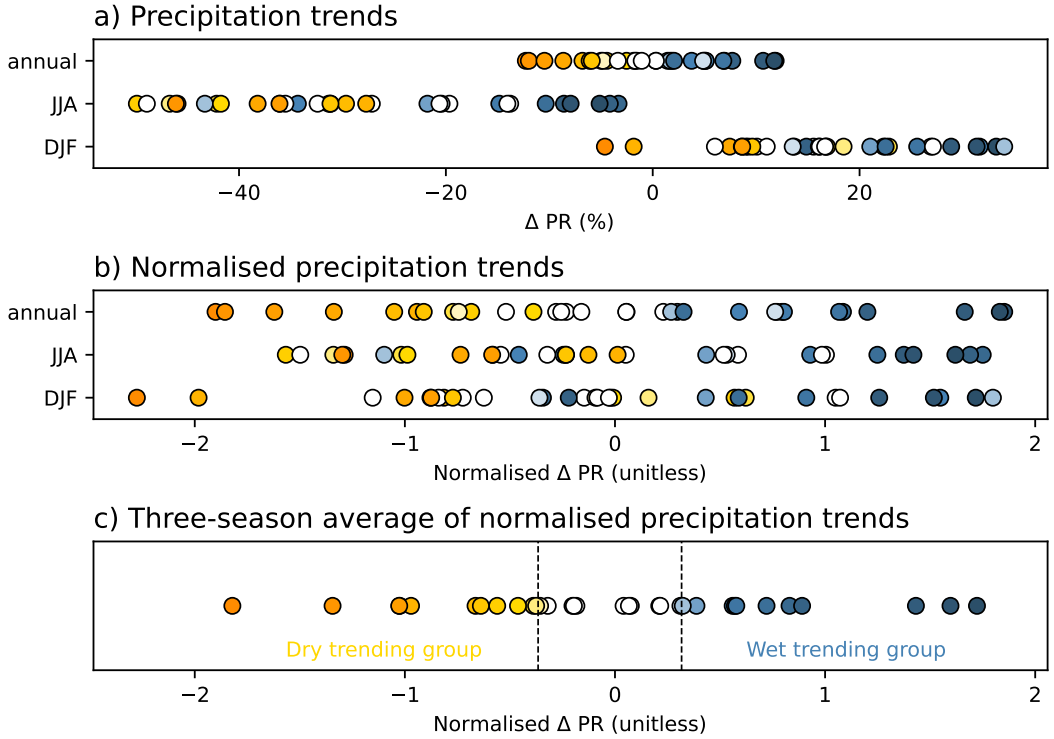

Figure 2.12: CMIP6 model projections of precipitation change in NL+RM for SSP5-8.5 in 2100. Shown are (a) actual values, (b) normalised values (assuming a normal distribution), (c) three 'seasons' average of the normalised values in (b). Vertical dashed lines in (c) show the separation of the 33 models into three groups of 11 models (Table 2.3). In all panels, individual models (dots) are coloured by their value in (c).

The composite mean response of each group forms the basis for the two regional climate scenarios. For precipitation, these composite means cover approximately 60 % of the full spread of the precipitation response in the CMIP6 standard set (Figures 2.13a, 2.14). The composite responses are approximately positioned at the 20th and the 80th percentiles of the multi-model distribution, (Figure 2.14). The separation of the two groups is largest in the seasons used to define the groups (annual, JJA, DJF) and is smaller in the shoulder seasons (March-April-May, MAM, and September-October-November, SON). In the shoulder seasons they span approximately 40 % of the full CMIP6 model spread. Note that the full CMIP6 spread includes a contribution from internal variability, and thus the spread of the forced climate response is smaller. The two groups span a larger range of the spread in the true CMIP6 forced climate response than is suggested by these numbers.

The groups are less distinct with respect to the temperature response (Figure 2.13b) and span less of the full ensemble spread (Figure 2.14). The regional warming is smaller in the wet-trending group than in the dry-trending group in all seasons except winter (DJF). In the annual mean, the groups are positioned at the 40th (wet-trending) and 60th (dry-trending) percentile of the range

Dry trending group		Wet trending group		Remaining models	
MPI-ESM1-2-LR	-1.82	CanESM5-CanOE	1.72	GISS-E2-1-G	-0.36
NorESM2-MM	-1.34	CanESM5	1.60	CESM2-WACCM	-0.32
UKESM1-0-LL	-1.03	CNRM-CM6-1	1.43	MPI-ESM1-2-HR	-0.20
ACCESS-ESM1-5	-1.02	CNRM-ESM2-1	0.89	NorESM2-LM	-0.20
MRI-ESM2-0	-0.97	CNRM-CM6-1-HR	0.83	MIROC6	-0.18
HadGEM3-GC31-LL	-0.66	IPSL-CM6A-LR	0.72	GFDL-ESM4	0.04
NESM3	-0.64	FGOALS-f3-L	0.58	MIROC-ES2L	0.07
BCC-CSM2-MR	-0.56	EC-Earth3-Veg	0.57	CMCC-CM2-SR5	0.08
KACE-1-0-G	-0.46	CESM2	0.56	ACCESS-CM2	0.21
AWI-CM-1-1-MR	-0.39	EC-Earth3	0.39	CIESM	0.22
INM-CM4-8	-0.38	INM-CM5-0	0.32	FGOALS-g3	0.31

Table 2.3: Partitioning of the CMIP6 standard set in the 'dry trending group' and the 'wet trending group', based on the sign and magnitude of their projection of annual, DJF and JJA precipitation trends in NL+RM in the SSP5-8.5 2100 scenario. Numeric values show the grouping variable (as in Figure 2.12c).

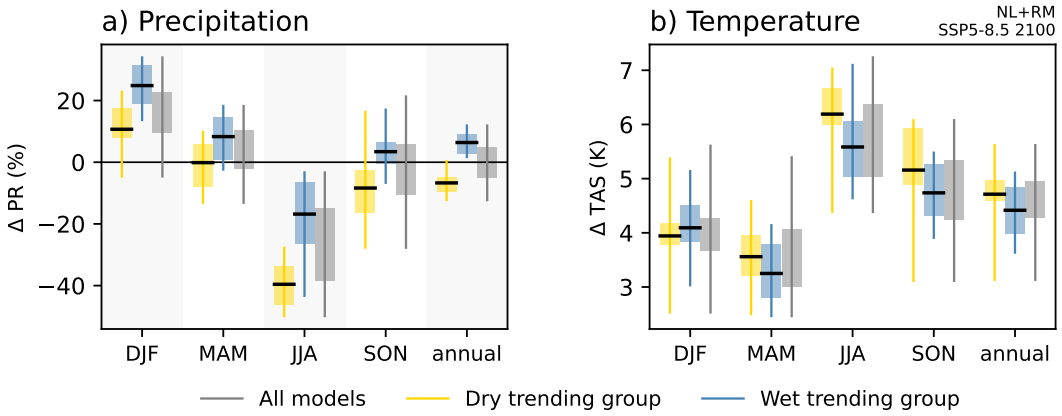

Figure 2.13: Same as Figure 2.7, but here showing the distribution of projections from all models (grey), and the projections in the dry-trending group (yellow) and wet-trending group (blue), see text for details. Black horizontal lines show the mean of a group. Light grey shading in (a) highlights the seasons and variable (i.e. precipitation) which were used to define the groups.

of the CMIP6 standard set. Correlations between the regional precipitation and temperature responses are weak, with the exception of the summer season (JJA), and to a lesser extent the autumn season (SON). The summer is therefore the season in which the two groups are most distinct in their temperature response (30th and 70th percentile of the CMIP6 range).

There are several advantages of spanning regional uncertainty by means of the composite response of two distinct groups of models. First, the composite climate signal preserves physical consistency in each of the two scenarios. Relationships between variables or seasons, e.g. covariance or lagged effects, that are present in the individual models are preserved in the composite. This is not the case if one would treat seasons and/or variables separately, and chooses specific values for the climate response of different variables in the different seasons for the two scenarios on the basis of expert judgement, or based on specific percentiles (e.g., 20th/80th percentile for all variables in each season). Such approaches might introduce correlations between the climate response in different seasons and variables that are not necessarily physically consistent. The composite response in summer for instance is consistent between temperature and precipitation. The dry-trending group projects a stronger reduction in precipitation and a stronger warming. We will see that this is physically consistent with stronger easterlies, larger precipitation deficits

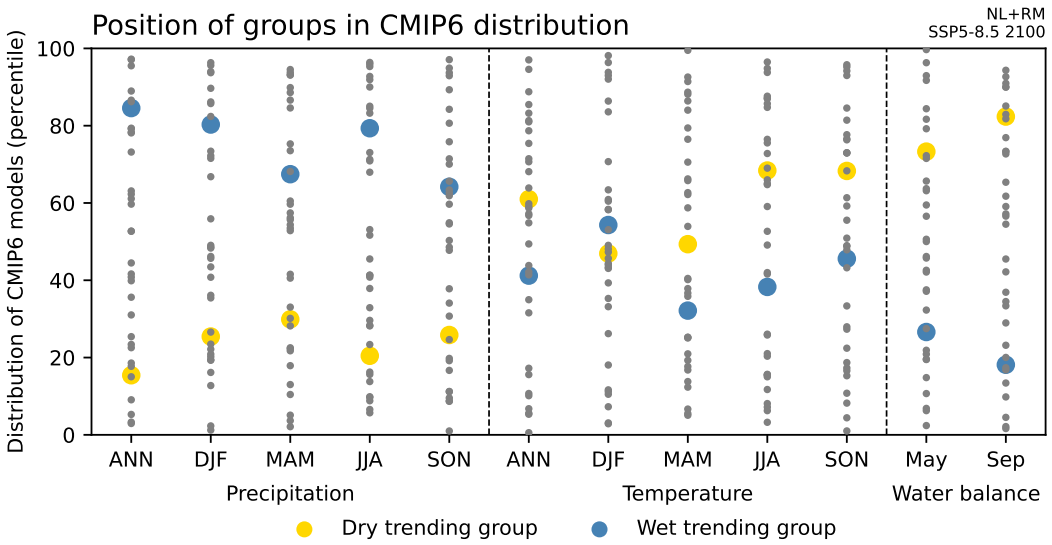

Figure 2.14: Percentile position of the means of the dry trending group and wet trending group (yellow and blue, respectively) within the full distribution of 33 CMIP6 models (grey). A normal distribution is assumed to compute the percentiles. The X-axis shows different variables and seasons, the y-axis shows the distribution of 33 CMIP6 models in percentiles.

and a stronger increase in solar radiation as compared to the wet-trending group. A downside of his methodological choice for physical consistency in the two scenarios, is that it limits the ability to span the full spread of the CMIP6 standard set in temperature and precipitation in all seasons. A second advantage of taking the composite mean over 11 modelled responses is that the contribution of internal climate variability to the calculated response is reduced by a factor of $1/\sqrt{11}$ (see also Section 2.1.4, Figure 2.6). A third advantage is that it is generally found that results from multi-model assessments have smaller biases than results from individual models (Tebaldi and Knutti, 2007).

Finally, we note that the 'distillation' of climate information as is done in this scenario process is subjective to context and values. The choices made in the development of the KNMI'23 national climate scenarios are such that the resulting scenarios are relevant for a wide range of stakeholders and users. Priority was given to adequately represent uncertainties in the regional climate response that have implications for water management applications (water safety and availability). A different choice for the defining variable(s) would lead to different, but equally valid scenarios. Despite this focus on water safety, we emphasize that these are general climate scenarios, which are relevant for a wide range of stakeholders and users. In the application of these scenarios we advise to check how much of the CMIP6 spread in the climate variables of relevance to the specific application is covered by the scenarios. For some applications it might be more appropriate to develop and use tailor-made scenarios.

2.1.6 Rationale for regional modelling and resampling from a single GCM

The two groups based on the regional precipitation response in the CMIP6 standard set (dry-trending group and wet-trending group, Figure 2.13) form the basis of the KNMI'23 climate scenarios. However, because there is a strong need for detailed regional climate change information, more detailed than the Global Climate Models (GCMs) of the CMIP6 standard set allow, we will use data from a Regional Climate Model (RCM) for the final scenario products. Dynamical downscaling with a RCM requires transfer of information from the steering GCM to the RCM at the RCM boundaries. Unfortunately, this information is not available for most GCM's in the

CMIP6 standard set. Furthermore, even if the information had been available, it would have been computationally too expensive to dynamically downscale all 33 GCM's and SSP's considered with a regional climate model.

To solve this issue, we use a resampling technique which aims to reconstruct the regional climate response in the two groups of the CMIP6 standard set using a 16-member initial condition ensemble of a single GCM. The GCM used here is a retuned version (see Section 2.3 of the EC-Earth model v3 (Döscher et al., 2022), which is run in-house and for which all experiments have been down-scaled with the RCM RACMO (Meijgaard et al., 2012) (see next Section). The resampling technique uses internal variability in the EC-Earth model to represent the climate change response in the two CMIP6-based groups. For example, in order to construct a future climate with a stronger summer drying trend than is the case in the EC-Earth model, the resampling preferentially selects years with drier than average summers. With 16-members, for the future period of interest, 480 summers are available for selection (16×30). The resampling modifies the statistics of the internal variations by selecting 240 years in the reference period and 240 years in the future period (8×30), such that the statistics of the difference matches the climate response in the wet-trending or the dry-trending groups. We aim to reconstruct the composite mean response for selection of variables and seasons. For these variables and seasons, we compute the composite mean change which will serve as constraints for the resampling tool that was developed for the KNMI'23 scenario project. More details on the exact resampling constraints are provided in Section 2.1.8. The resampling tool is described in full detail in Section 2.2.

2.1.7 EC-Earth and RACMO ensemble experiments

As noted in the previous section, we have used in-house EC-Earth3 and RACMO simulations to reconstruct the regional response in the dry-trending and wet-trending groups through resampling. The EC-Earth3 model version that is part of CMIP6 (later referred to as EC-Earth3$_{\text{p1}}$) has a cold temperature bias over land regions and in the Northern Hemisphere, and a strong warm bias over the Southern Ocean and Antarctica (Döscher et al., 2022). For the KNMI'23 scenario project the simulated climate over western Europe should be as realistic as possible. Therefore, the model was re-tuned in order to decrease the cold bias in the Northern Hemisphere and over Europe. This has resulted in an additional version of EC-Earth3, referred to as EC-Earth3$_{\text{p5}}$. Details on the re-tuning procedure and remaining model biases in EC-Earth3$_{\text{p5}}$ can be found in Section 2.3.

The EC-Earth3$_{\text{p5}}$ experiments were dynamically downscaled with RACMO v2.3, which is an updated version of RACMO v2.2 (Meijgaard et al., 2012). The most significant differences between v2.2 and v2.3 are the external forcings. In v2.3 greenhouse gas forcing follows CMIP6 protocols, aerosol forcing is fully compliant with EC-Earth3$_{\text{p5}}$, and land-use changes are taken from LUCAS-LUC (Hoffmann et al., 2022). The EC-Earth3$_{\text{p5}}$ compliant aerosol forcing required a change to the short wave radiation scheme (SRTM with 14 bands in v2.3). Some inconsistencies were found regarding the land-use forcing in the simulations, see Section 2.4 for details.

The ensemble simulations were set up following CMIP6 protocols. A pre-industrial EC-Earth3$_{\text{p5}}$ run of 1800 years was performed, and from this run 16 transient runs were initialised at 25 model year intervals at the end of the pre-industrial run. These transient runs were forced with the CMIP6 historical forcing. At the end of model year 2014, these 16 historical runs were continued with 16 runs for each of SSP1-2.6, SSP2-4.5 and SSP5-8.5 up to the year 2165. All members were downscaled with RACMO from year 1950 up to 2120, and for the SSP5-8.5 runs up to 2165.

The 16 members of the EC-Earth3$_{\text{p5}}$ ensemble sample internal variability in the climate system. Figure 2.15 shows the magnitude of this variability in the ensemble, and how it compares to the regional climate change response in the dry-trending and wet-trending groups. For some variables and seasons the spread between the 16 members of the EC-Earth3$_{\text{p5}}$ model approaches the model uncertainty within the groups, e.g. for temperature in the winter. The spread in the 16 member EC-Earth3$_{\text{p5}}$ ensemble is substantial and is solely due to internal variability. The year-to-year variations due to internal variability is exploited in the resampling procedure, such that the resulting resampled data represents the climate response of the dry-trending and wet-

trending groups. Large differences between the EC-Earth3$_{p5}$ response and the CMIP6 group responses reduce the ability of the resampling procedure to represent the desired CMIP6-based response in the resampled data. This is for example the case for precipitation in the summer, where EC-Earth3$_{p5}$ does not have much overlap with the dry-trending group.

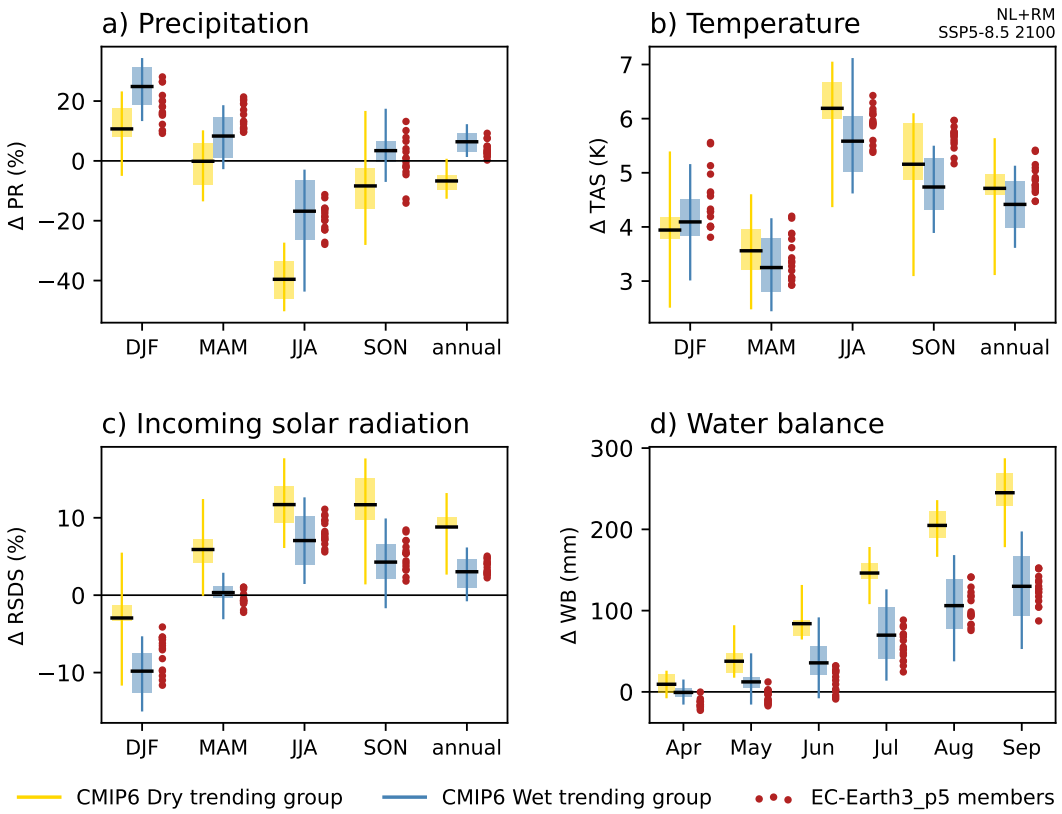

Figure 2.15: As Figure 2.13, but here with additionally the 16 EC-Earth3$_{p5}$ ensemble members shown as red dots.

2.1.8 CMIP6-based target values for the resampling procedure

In the resampling procedure, we aim to reconstruct the composite mean regional climate response of the two model groups (dry trending and wet trending, Section 2.1.5), using the EC-Earth3$_{p5}$ ensemble simulations. To achieve this, we provide target values of the response ('criteria' or 'constraints') to the resampling tool (Section 2.2.

We expect the regional climate signal to depend smoothly on global warming levels since the prescribed climate forcing depends smoothly on time. Additionally, we expect the regional climate response to first order to depend only on the global warming level, not on the speed of climate change. Together, this leads to the expectation of a similar climate response at a particular warming level for the three SSP-scenarios considered (SSP1-2.6, SSP2-4.5 and SSP5-8.5). To obtain this consistent climate signal across SSPs and time horizons, we aim to remove the contribution from internal variability in the estimate of the climate signal. First, for both the dry-trending and wet-trending group of 11 models (Table 2.3), we determined the composite mean regional climate response using the matched warming approach for three SSP-scenarios (SSP1-2.6, SSP2-4.5 and SSP5-8.5) and for a range of warming levels (from 0 to 1.2, 2.5 and 5.6 K respectively, in steps of 0.1 K). Given our assumptions that the regional climate response does not depend on the speed of global warming, we combine the regional responses of the three SSP emission scenarios

(Figure 2.16). The composite climate response as a function of warming level is not smooth due to the contribution from internal variability. A third order polynomial fit filters this noise from the composite responses and we assume that the fitted response is a better estimate of the climate signal. We force the fit through the origin, as we expect the true regional climate change signal to be zero at zero global warming. Finally, for the construction of a specific scenario we take the warming level associated with the SSP and time horizon (Table 2.1), and use the fitted curves to determine the exact constraints for the resampling procedure.

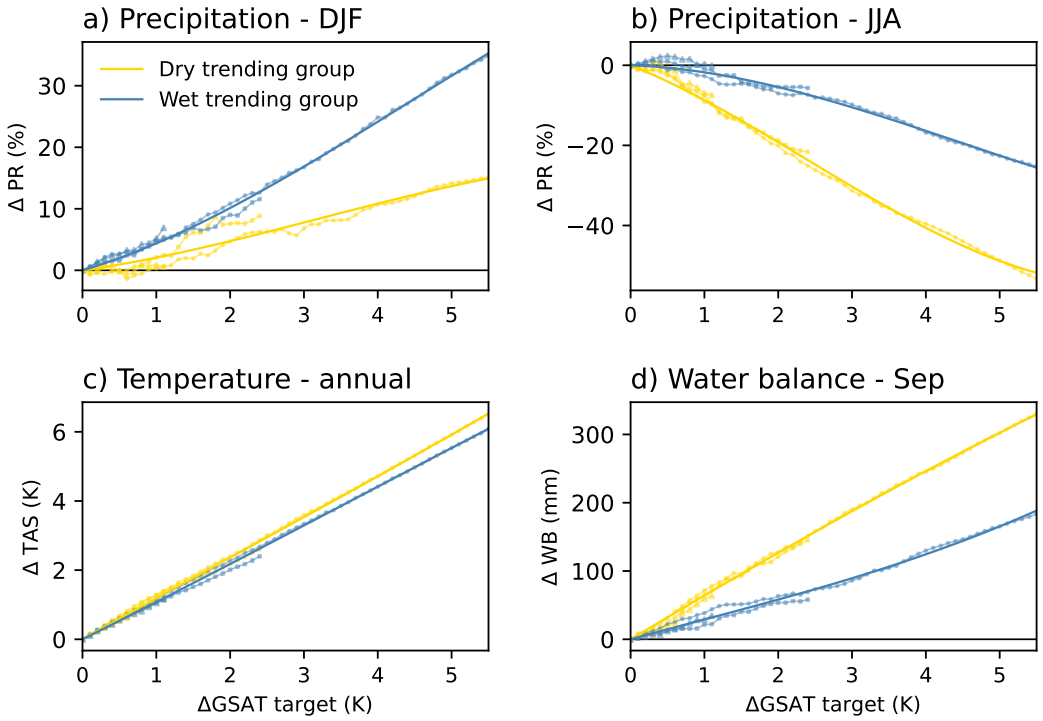

Figure 2.16: 3rd order polynomial fit, forced through the origin, of the mean regional climate change response in the wet trending (blue) and dry trending (yellow) group. Three SSP-scenarios, SSP1-2.6 (triangles), SSP2-4.5 (squares) and SSP5-8.5 (circles) are considered in the final fit (solid line). For (a) winter precipitation [%], (b) summer precipitation, (c) annual temperature [K], and (d) water balance in September [mm].

For each scenario we apply 18 constraints. These are the composite responses according to the polynomial fits for each variable, season and region listed in Table 2.4. Precipitation and temperature constraints are based on the seasonal and annual mean values, the water balance constraint is based on the cumulative difference between Makkink reference evapotranspiration and precipitation from the 1st of April onwards. The 10-day maximum precipitation constraint corresponds to the 1-in-10 year wettest sequence of 10-days in a year, estimated from the full ensemble. Note that this is the only constraint that requires daily CMIP6 data from the standard set. Not all models in the CMIP6 standard set had daily data available (Table 2.2), consequently the constraint values for this criterion are based on fewer models. In the wet trending group this means that the value is based on 7 rather than 11 models, in the dry trending all models had daily data available.

The rationale behind the choice for these 18 constraints is that they are relevant for climate change adaptation in the Netherlands. We use the NL+RM region as it is of importance for river discharge values. For precipitation, constraints for the NL region were added to improve NL-region consistency across time horizons and SSP emission scenarios, and to better reproduce the CMIP6-based spatial patterns of change. The water balance variable was added as a constraint

Variable	Season	Region	Target values		Tolerance
			Dry trending	Wet trending	
Precipitation	Annual	NL+RM	−6.9 %	6.4 %	5/2/1 %
	DJF		10.8 %	24.2 %	
	MAM		0.1 %	8.9 %	
	JJA		−40.6 %	−16.4 %	
	SON		−8.6 %	3.2 %	
Precipitation	Annual	NL	−2.8 %	10.1 %	5/2/1 %
	DJF		15.0 %	29.1 %	
	MAM		4.3 %	11.3 %	
	JJA		−41.9 %	−19.4 %	
	SON		−4.5 %	9.0 %	
2 m temperature	Annual	NL+RM	4.7 K	4.4 K	0.3 K
	DJF		3.9 K	4.1 K	
	MAM		3.6 K	3.3 K	
	JJA		6.2 K	5.6 K	
	SON		5.2 K	4.7 K	
Water balance	May	NL+RM	37 mm	10 mm	5 mm
	September		246 mm	125 mm	10 mm
10-d max. precipitation	Annual	NL+RM	7.8 %	17.7 %	1/2/1 %

Table 2.4: CMIP6-based target values (constraints) applied in the resampling procedure for the SSP5-8.5 scenario and 2100 time horizon. Constraint values are shown for both the dry trending and wet trending groups, including the applied tolerance values (see main text for details).

as an indicator for the occurrence of meteorological drought. It is a temporally compounding variable with seasonal memory. Finally, the 10-day precipitation extremes in the NL+RM region was added as a constraint as an indicator related to the probability of high river discharge.

The choice of a group size of 11 models is of course rather arbitrary. In order to assess the sensitivity of the constraints to this group definition, we repeated the estimate of the composite climate signal for different group sizes. For group sizes of 8 models and larger, the composite climate signal hardly changes. We thus conclude the choice of group size is not critical in the scenario construction. This also implies that the scenario construction is robust to the models that are part of the CMIP6 standard set. We therefore did not bother to exclude specific models on the basis of a somewhat subjective criterium related to the model's ability to reproduce the historical climate.

The optimal resamples that are produced by the resampling tool depend on the relative weight that is given to each constraint. We use the relative size of the internal variability in the variables to define the weights or tolerances. For example, a one standard deviation mismatch in the DJF precipitation change over the NL region receives the same penalty as a one standard deviation mismatch in the September water balance over the NL+RM region. Table 2.4 shows the constraints for the 2100 time horizon in the SSP5-8.5 scenario and the associated tolerances for both the dry-trending and wet-trending groups. For other SSP scenarios and time horizons, these tables can be found on the KNMI Gitlab. Resamples were calculated for three tolerance levels for the precipitation-related constraints. The reason for this will be explained in the following paragraph. The tolerance levels are similar for all SSP scenarios and time horizons with the exception of 2150, for which larger tolerances were used because the 2150 projected climate response of the dry-trending and the wet-trending groups is larger, and has a larger uncertainty associated with it (more spread within the group). The constraints are therefore less strictly defined, and larger tolerance values make sense.

It is found that there are many optimal resamples that satify the constraints equally well. Different random seeds in the tool thus result in resamples that are qualitatively similar, but do have some differences. In the validation of the resampling results we noticed that the final

projected change for two extreme precipitation indices varied quite a bit between resamples that were started from different seeds. This uncertainty was dealt with in the following way. For each time horizon and SSP, a total of 33 resamples were calculated (11 with each of the three tolerance levels for precipitation in Table 2.4, for SSP5-8.5 2150 only the 5 % tolerance levels were used). Next, the mean projected change in the 1-in-10-year summer maximum 1-day precipitation sum in the NL region and in the 1-in-10-year annual maximum 10-day precipitation sum over the NL+RM region of the 33 resamples was calculated and the resample with a projected change in these two indices that lies closest to their center of gravity was selected as the final resample. Figure 2.17 illustrates the procedure for the SSP5-8.5 wet-trending scenarios. The same procedure is applied for the other SSP based and dry-trending scenario's.

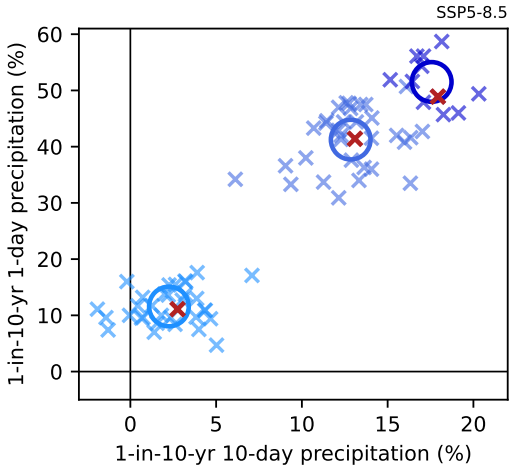

Figure 2.17: Example seed selection for SSP5-8.5 wet-trending scenarios (2050, 2100, 2150; light, middle and dark blue respectively). Blue crosses show the 33 resamples generated with different random seeds (11 resamples for 2150), the blue large circle shows their center of gravity, the red cross shows the selected final resample. See main text for details.

2.1.9 Results of resampling procedure

Characteristics of the resampled dataset

The resampling tool creates 8 members of 30 years each by selecting subsequent years from different members of the 16 member EC-Earth3$_{p5}$ ensemble (illustrated in Figure 2.18). The resampling tool aims to find an optimal selection to match the CMIP6-based constraints (Section 2.1.8). This is more complex for cases where the difference between the CMIP6-based constraint values and the change in the EC-Earth3$_{p5}$ dataset are large (Figure 2.15, e.g., for the water balance constraints in the dry-trending group). Furthermore, two other criteria are of relevance. First, the number of consecutive years selected in the resampling procedure should be large enough in order to preserve the correct year-to-year variability in the resamples and reduce the number of discontinuous December to January transitions. In order to achieve this, the resampling tool applies a penalty if only a small number of consecutive years is selected. Second, it can happen that the same year from the same original ensemble member is selected multiple times. The number of such duplicates should be as low as possible. This is because duplicates impact the statistical properties of the resamples, especially if the selected year has an extreme event of interest. The return time of this extreme will be underestimated in the resamples if the event is present multiple times. Again, the resampling tool applies a penalty if a duplicate year is selected.

By applying the CMIP6-based constraints, and the penalties for short resample parts and duplicates, a trade-off is to be found between the quality of the match between the resampled

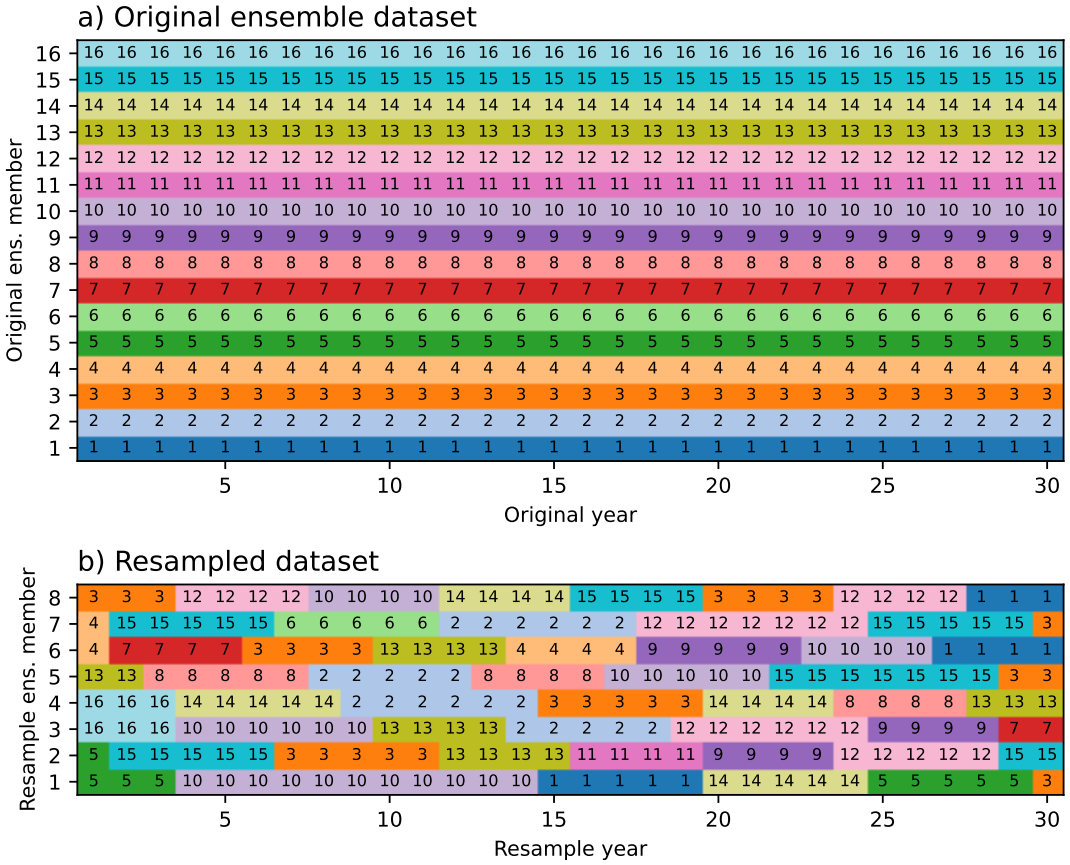

Figure 2.18: a) Schematic image of the original 16-member EC-Earth3$_{p5}$ ensemble dataset, b) schematic image of a resampled dataset (SSP5-8.5 2100, dry-trending group, future period). Displayed numbers and colours refer to the ensemble member of the original ensemble dataset.

dataset and the CMIP6-based constraints on the one hand and the characteristics of the resampled dataset on the other. Figure 2.18b shows an example of a resampled dataset.There are long parts (in this case maximum length of 11) and short 1 year parts at the beginning or end of the resampled period. Overall, the mean length of the parts is 6.5 years and the minimum length is at least 4 years. The dry-trending resampled datasets for SSP5-8.5 in 2100 and 2150 deviate from this with a mean part length of 5.4 years and a minimum length in 2150 of 3 years. This is expected since EC-Earth3$_{p5}$ acts more like the wet-trending group than the dry-trending group. Figure 2.19 again shows a resampled dataset, but now highlighting the duplicates. The total number of duplicates is limited, and again higher in the dry-trending resample than in the wet-trending resample. Finally, Figure 2.20 illustrates the effect of duplicates on the statistics of extreme events. The horizontal line segments in these Gumbel plots clearly show that the same yearly extreme is selected multiple times. However, the influence of the horizontal line segments on the general form of the Gumbel plot is limited, which allows general statements on return times of extreme events.

Comparison of the climate response in resamples and the corresponding CMIP6 group

Given the constraints deduced from a dry-trending or wet-trending CMIP6 group, the resampling tool produces two datasets: 8 members of 30 years each, one for the present-day and one for the future period (1991-2020, and centered around the time horizon of interest, 2050, 2100 or 2150). The climatological difference between these datasets defines the resampled climate response, which

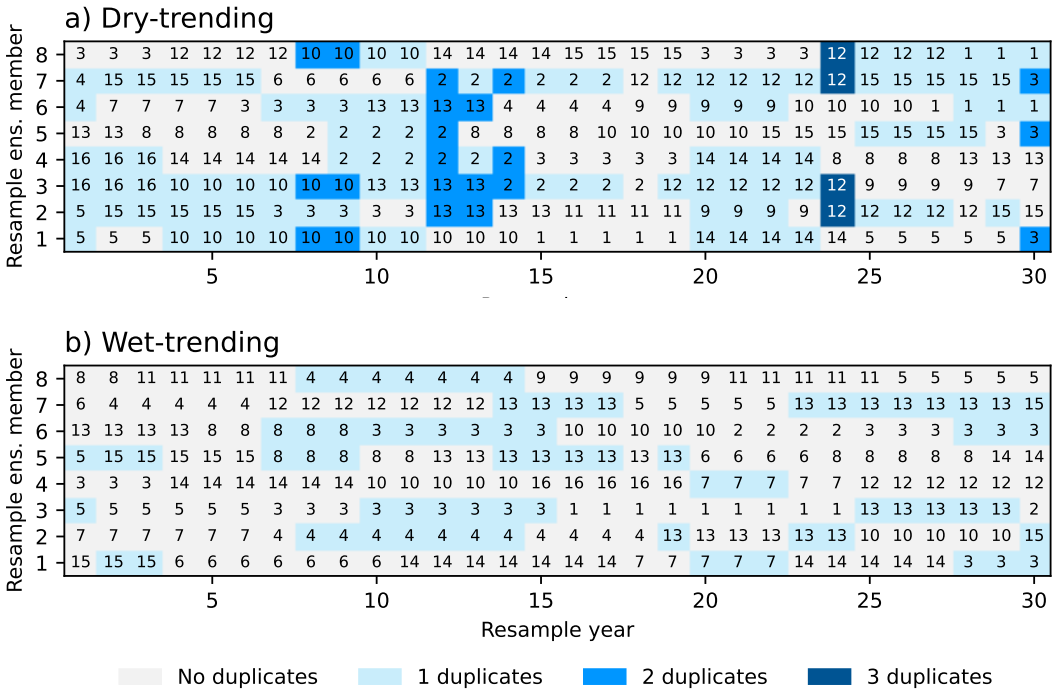

Figure 2.19: As Figure 2.18b, but here the colours show the number of duplicates across ensemble members of the resampled dataset. a) SSP5-8.5 2100, dry-trending, future period, b) SSP5-8.5 2100, wet-trending, future period.

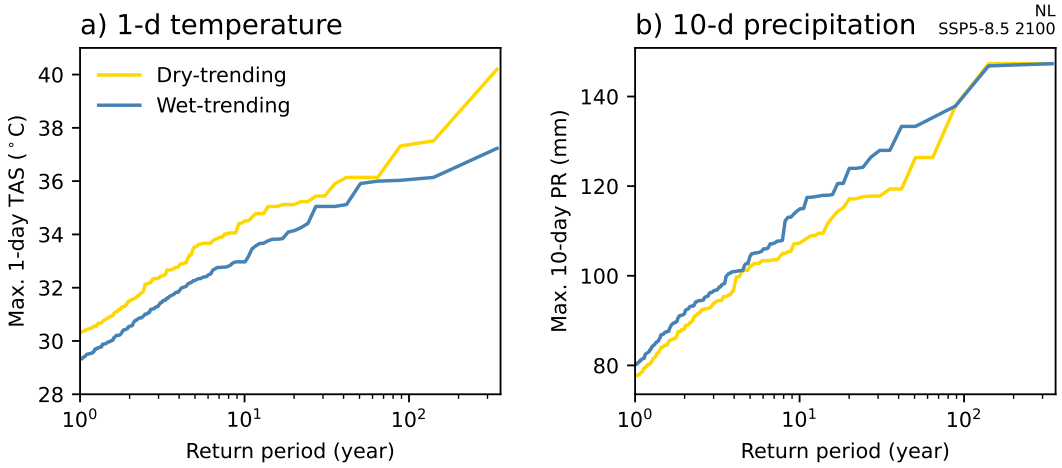

Figure 2.20: Gumbel plots for the hottest day of the year (left) and the highest 10-day precipitation sum of the year (right) for the dry and the wet resample for SSP5-8.5 in 2100.

for the constrained variables is as close as possible to the applied constraints based on the CMIP6 group of choice. Variables that were not constrained, have a physically consistent climate response and can also be evaluated. The resampled datasets form a detailed storyline of a plausible future climate of the Netherlands.

For the SSP5-8.5 scenario, Figure 2.21 compares the climate response in the EC-Earth3$_{p5}$ resampled datasets with the CMIP6-based target values. In general, the resampled response is very close to the constraint values, much closer than the original EC-Earth3$_{p5}$ response (Figure 2.15). The resampling procedure succeeds in reconstructing the desired CMIP6 responses. The match between CMIP6-based constraints and the resamples is especially close for precipitation and water balance, with only a slight underestimation of the summer precipitation decrease. In terms of 2 m temperature there are slightly larger differences, with the summer and autumn seasons warming more in the resamples than in the CMIP6-groups.

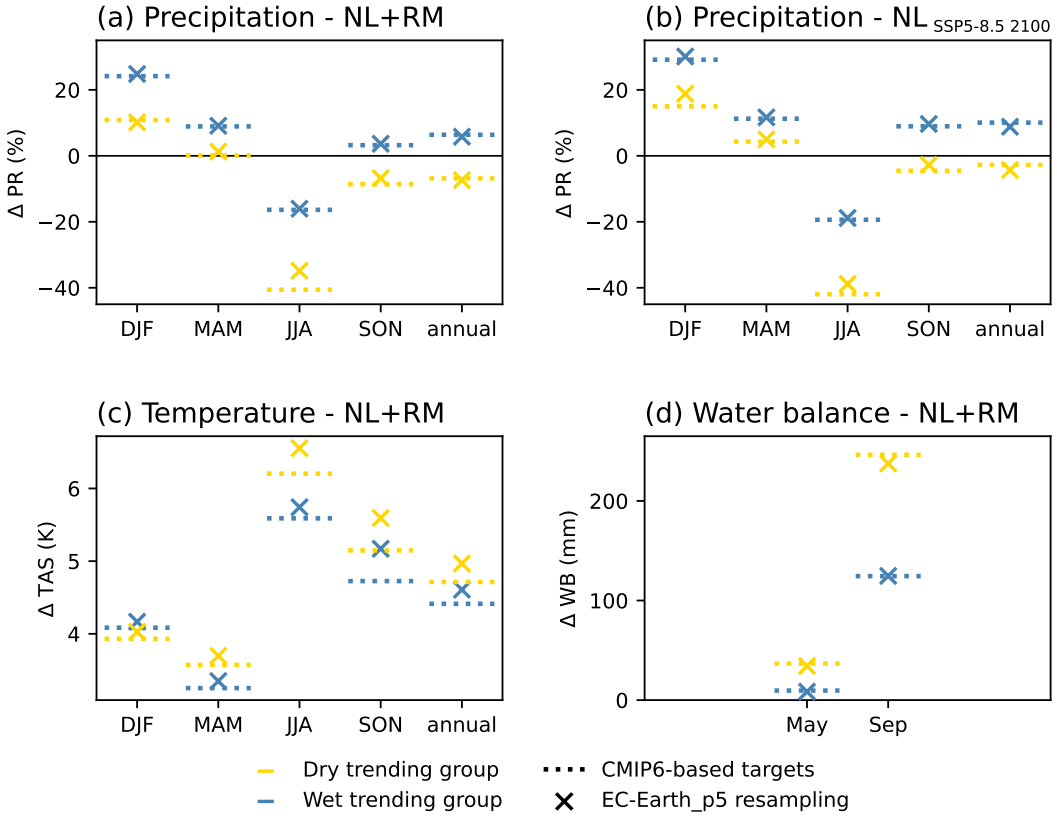

Figure 2.21: Applied constraints (dashed lines) and the resampling result (crosses) for 17 out of 18 constraints applied, for the SSP5-8.5 2100 scenarios (dry-trending group in yellow, wet-trending group in blue). Shown constraints: (a) Precipitation in NL+RM region, (b) precipitation in NL region, (c) temperature in NL+RM region, (d) water balance in NL+RM region. Not included is the 10-day precipitation constraint, which was shown in Figure 2.17.

Figures 2.22 and 2.23 show the spatial pattern of precipitation, temperature and sea level pressure changes in the CMIP6-based groups and the resamples. Remember that no spatial constraints have been applied in the construction of the resamples. The spatial structure of the climate response in the resamples follows from a careful subselection of years from the 16-member EC-Earth ensemble such that the climate response averaged over the NL+RM and NL regions satisfy the constraints. The spatial structure of the climate response in the CMIP6 groups arises from the response of the regional climate and circulation to global warming, which is subject to model uncertainty. In winter, higher pressure develops over the Mediterranean, lower pressure

over Scandinavia. For our region this means increased westerly winds and associated higher precipitation. The exact position and strength of these changes differ in the dry- and wet-trending groups. The resampling procedure reproduces these patterns quite well, including the differences between the two groups. In summer, a trend towards higher pressure is found over the British isles, and a trend towards lower pressure over the Mediterranean. For the Netherlands, this leads to increased easterlies, which bring drier and warmer winds from the continent. These trends are stronger in the dry-trending group, leading to stronger drying over the NL+RM region. Again, the resampled datasets reproduce this pattern relatively well, including the relative magnitude of the trends in the two groups. The resampling procedure using EC-Earth3 $_{\text{p5}}$ data appears to be able to reconstruct the climate response in both CMIP6 groups in a physically consistent way.

The model uncertainty in the winter circulation response is discussed in Haarsma et al. (2013) and is due to a competition between upper level subtropic warming in the descending branch of the Hadley circulation in the North-Atlantic region and the reduced warming in the region of the sub-polar gyre. In summer, the strength of the high-pressure response west of the British Isles correlates with the strength of the reduced warming in the sub-polar gyre region (Haarsma et al., 2015). The strength of the low-pressure response in Southern Europe correlates with the amount of soil drying and related enhanced warming in Southern Europe (Haarsma et al., 2009). Both pressure responses control the response of the easterly winds over Europe that bring dry continental air masses and lead to increased drying and heating. Models project a slow-down of the Atlantic Meridional Overturning Circulation leading to reduced warming in the sub-polar gyre region, but disagree on the rate of the slow-down and strength of the reduce warming. Models also disagree on the amount of soil drying and the strength of the heat-low response in Southern Europe.

Effect of RACMO downscaling

The EC-Earth resamples closely match the constraints of both CMIP6 groups. The dynamical downscaling with RACMO leads to changes in the values of regional resions (Figure 2.24). The summer drying is less pronounced in RACMO. Consistent with the reduced summer drying we see a somewhat reduced summer warming. The winter precipitation response is slightly less. More details about the effect of the RACMO downscaling is presented in Section 2.4.

Fog

Since RACMO does not explicitly model fog conditions, we followed a slightly different approach to obtain quantitative estimates of future fog conditions. Fog conditions are likely to occur under stable and humid boundary layer conditions. Given a historical RACMO simulation using ERA5 boundary conditions and observations of fog on a number of Dutch stations, we first deduce a conditional probability of the occurrence of fog given certain boundary layer characteristics in RACMO. Next we apply this conditional probability on EC-Earth-RACMO states to calculate to probability of the occurrence of fog. We do this for the wet-trending and dry-trending resamples corresponding to the different time horizons and emission scenarios and are thus able to quantify the projected change in the probability of the occurrence of fog. More details can be found in Section 3.4.2.

2.1.10 Bias correction of resampling output

Introduction

There are several reasons why the RACMO climatology differs from the observed climatology

- due to natural variability, the climatology of RACMO will always differ from the observed climatology. This effect will be most pronounced for the extremes.
- due to difference in resolution: the observations are local, whereas RACMO values are averaged over 12×12 km.

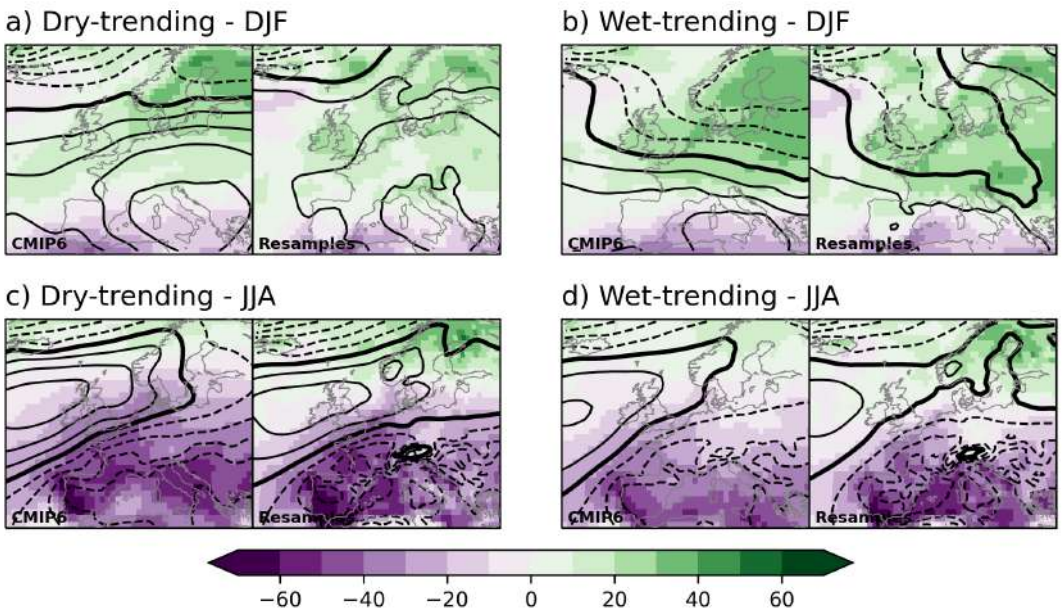

Figure 2.22: Maps comparing the climatic response in the CMIP6-based groups and the resample datasets (left and right panels, respectively). Variables shown: precipitation (colours, %) and sea level pressure (contours, solid lines negative change, dashed lines positive change, thick line no change, contour interval 1 Pa). (a,c) Dry-trending groups/resamples and (b,d) wet-trending groups/resamples, for the (a,b) winter season and (c,d) summer season.

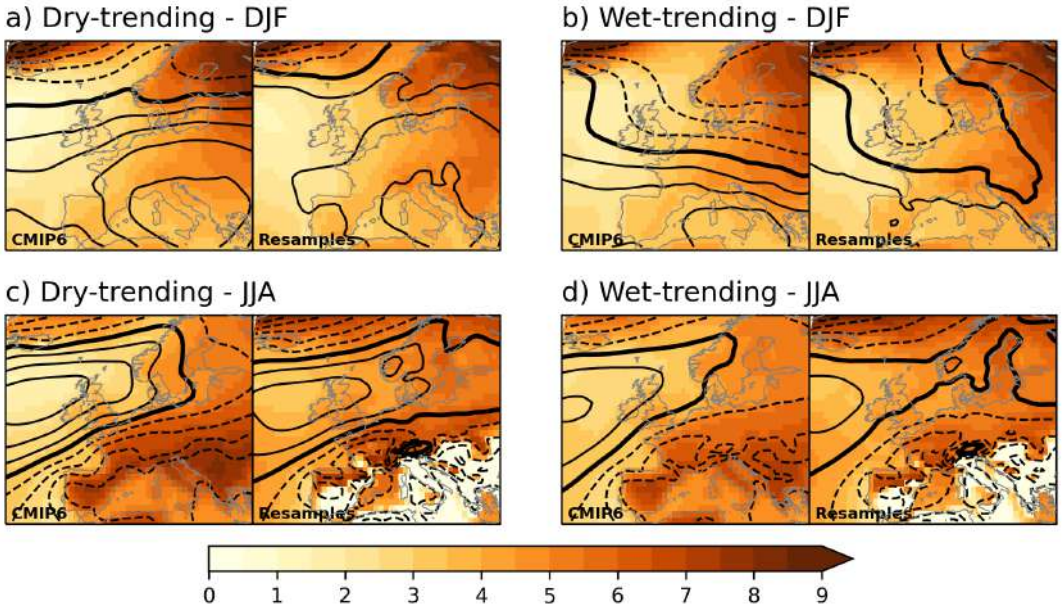

Figure 2.23: As Figure 2.22, but here showing the temperature response in colours (°C).

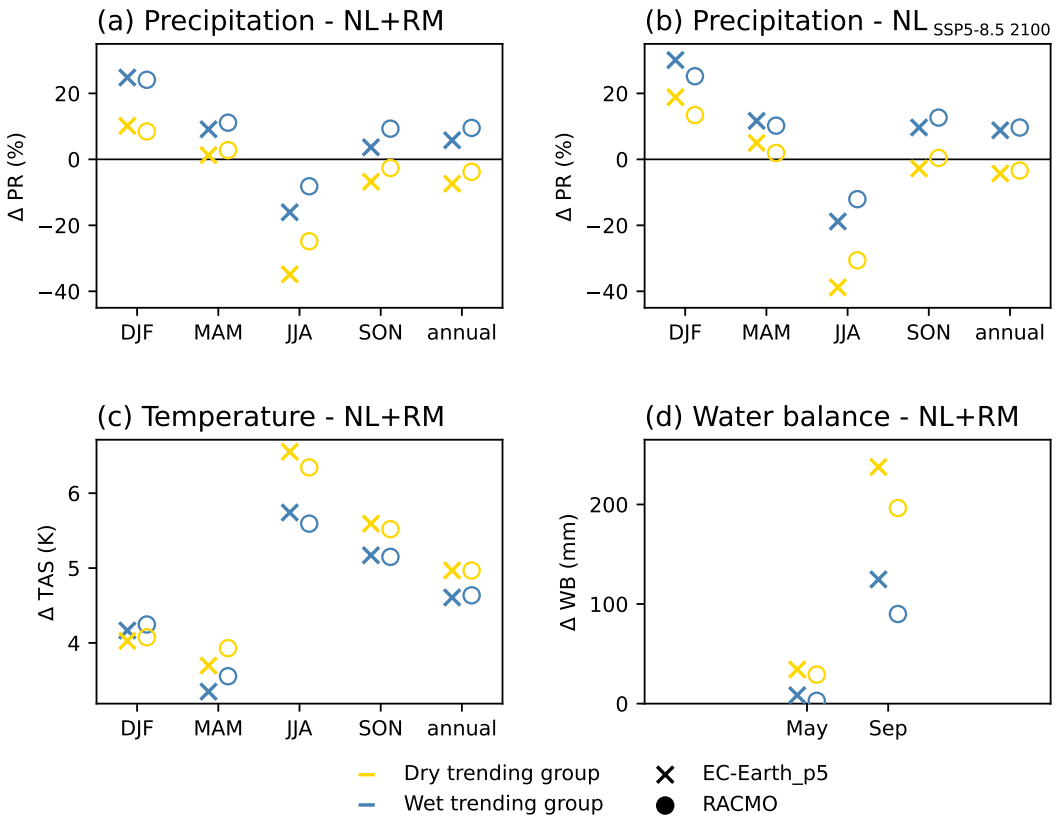

Figure 2.24: As Figure 2.21, but here comparing the EC-Earth3$_{p5}$ resample data and the data after dynamical downscaling with RACMO.

- some meteorological processes (e.g. convection) are poorly resolved by RACMO, which may lead to underestimation of extreme (summer) precipitation.
- the roughness map of RACMO may differ from reality (e.g. by seasonal changes due to more or less leafs on the trees).
- the orography of RACMO may - especially in the Alps - be too low, again due to averaging over the grid size. This may influence variables like temperature (too high in RACMO) and precipitation (too low in RACMO).
- The climatological forcing from EC-Earth3bis may be wrong, which leads to biases in the climatology of RACMO.
- the resampling is optimised to resemble the *signal* from the CMIP6 models; a part of this signal may be achieved by distorting the control climate.

For these reasons, bias in the RACMO data is corrected. We applied bias correction to each variable, month and location separately, using the Quantile Delta Mapping (QDM) from Cannon et al., 2015 (see also chapter 5 in Feigenwinter et al., 2018 for an extensive description):

- For each probability in (0,1), the difference or ratio (the "delta") of the quantiles of the observations ("truth") and the RACMO output is assumed to be the same in the present and the future climate. This determines the quantiles of the bias-corrected RACMO output for the future climate for all these probabilities.
- Then the uncorrected RACMO output for the future climate is adjusted to match these quantiles.

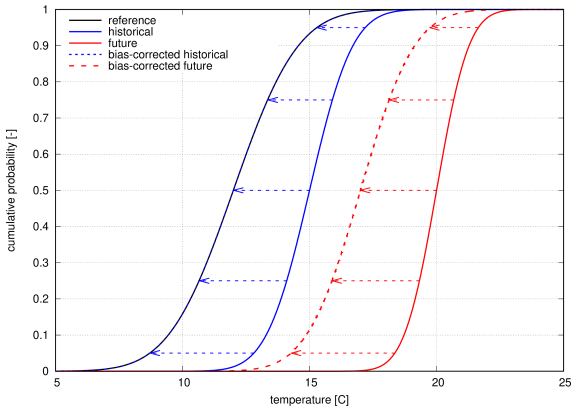

Figure 2.25: Explanation of the Quantile Delta Mapping method.

Methodology for bias correction

Quantile Delta Mapping The method of Quantile Delta Mapping (Cannon et al., 2015) is illustrated in Figure 2.25. The black line shows the empirical cumulative distribution function (ECDF) of (in this illustration) the observed temperature, which is the reference. The blue line is the ECDF of the historical RACMO temperature, which shows a positive bias that depends on the quantile. The blue arrows (the "deltas") indicate how much the temperature quantiles for the probabilities of 0.05, 0.25, 0.50, 0.75 and 0.95 need to be adjusted in order to agree with the reference quantiles.

The red curve in Figure 2.25 represents the ECDF of the uncorrected RACMO data for the future run (solid red line). It maps each uncorrected RACMO temperature for the future to a probability. Then the blue arrow (delta) for this probability is added to the temperature to yield the bias-corrected temperature. The bias-corrected future temperatures therefore have the ECDF indicated by the dashed red curve in Figure 2.25.

For temperature, mslp and humidity, the *differences* of the quantiles of the observations and of the RACMO output for the historical period (the arrows in Figure 2.25) are preserved in the future climate for every probability, as described above. However, for precipitation, surface wind and radiation, we preserve the *ratios* (except for zero values; see details below). This can be reduced to the previous case by taking logarithms.

Comparing the bias-corrected model output to the observations (our reference), the climate signal from the RACMO simulations of temperature, mslp and humidity is preserved in the following sense (see Figure 2.25): for every probability, the horizontal differences between the dashed red and solid black lines are identical to the corresponding horizontal differences between the solid red and blue lines. In other words, the *absolute* changes in quantiles computed by RACMO constitute the preserved climate signal. Similarly, for precipitation, surface wind and radiation, the *relative* changes in the quantiles computed by RACMO are now the preserved climate signal.

The Quantile Delta Mapping is approximated by computing only the quantiles and the changes in quantiles (differences or ratios) for the following probabilities: 0, 0.001, 0.01, 0.05, 0.1, 0.15, 0.2, 0.25, 0.3, 0.35, 0.4, 0.45, 0.5, 0.55, 0.6, 0.65, 0.7, 0.75, 0.8, 0.85, 0.9, 0.95, 0.99, 0.999, 0.9999. For other probabilities, the changes in quantiles are obtained by linear interpolation. The following comments are made:

- the 0.99, 0.999 and 0.9999 quantiles are not directly calculated, but extrapolated from the 0.90 and 0.95 quantiles. For precipitation, we use the exponential distribution for this extrapolation, for the wind, the Weibull distribution, and for the temperature, the Gaussian distribution is applied. In this way, stochastic uncertainty in the extreme quantiles is reduced. However, despite this, one cannot expect that the mapping of extreme values will be accurate.

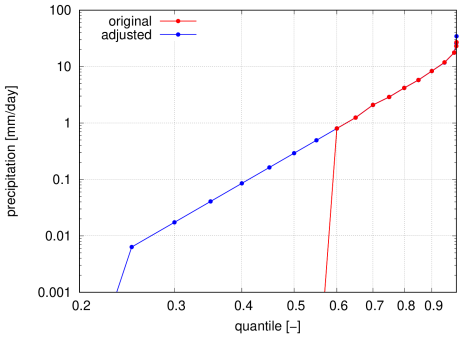

Figure 2.26: Illustration of the wetting of the quantiles that indicate no precipitation. Both axes are logarithmic.

For the other variables (humidity, mslp, radiation), no extrapolation is applied (as here the extremes are not very relevant).

- the gridded observational data for precipitation is discretized in steps of 0.05 mm, which distorts the bias correction for low precipitation amounts, and consequently the number of dry days (often defined as days with less than 0.1 mm). The largest quantiles that indicate no precipitation are therefore adjusted to small precipitation amounts (i.e. drizzle). This is done by extrapolating from the lowest wet quantiles, as long as the adjusted precipitation is larger than 0.005 mm. These quantiles are adjusted by linear extrapolation on a logarithmic scale. The adjustment is graphically explained in Figure 2.26. In this example, the original (red) ECDF indicates 'dry' for quantiles of 0.55 and below. The quantiles of 0.6 and 0.65 are used for the extrapolation down to the threshold of 0.005 mm.

Besides the Quantile Delta Mapping, a number of other methods have been proposed for bias-correction: other simple univariate methods (e.g., ordinary Quantile Mapping or simple linear transformations, e.g. Cannon et al., 2015, Casanueva et al., 2020) but also complex multivariate bias-correction methods; see e.g. François et al., 2020, Whan et al., 2021.

For the present study, it was decided to select a simple univariate method and to test it on indices derived from multiple variables such as multi-day averages, computed river discharge, precipitation deficit and fire weather index, in order to find out if the selected method is good enough for the climate scenarios.

From the simple methods, the Quantile Delta Mapping was selected because it is relatively robust (except possibly in the extreme ranges, like all other methods), has produced good results in other studies (e.g. Cannon et al., 2015) and shows relatively good performance in tests based on historical weather data over two different periods. Moreover, Quantile Delta Mapping can also be used for transformation of time-series of observations to a future climate (see Section 2.5.1), and the results of bias-correction and time-series transformation using Quantile Delta Mapping are highly compatible.

Description of the gridded observations

Table 2.5 lists the variables that are bias-corrected, as well as the datasets of gridded observations used for this purpose.

EOBSv26e The data set covers the period back to 1950 and provides gridded fields at a spacing of $0.1 \times 0.1°$ in regular latitude/longitude coordinates. The EOBS dataset is described in Cornes et al. (2018).

variable:	dataset:
minimum temperature	EOBSv26e
maximum temperature	EOBSv26e
mean temperature	EOBSv26e
wind speed	EOBSv26e
precipitation	HYRAS3.0-PR (+EOBSv26e)
radiation	SARAH-3

Table 2.5: variables that are bias-corrected, and the gridded dataset used.

HYRAS3.0 The HYRAS3.0 dataset represents daily high-resolution (×5 km) grids of mean, minimum, and maximum temperature and relative humidity for Germany and its catchment areas, from 1951 to 2015. In addition to temperature and relative humidity, HYRAS-2015 also comprises a precipitation dataset (HYRAS-PR). This is an extension of the HYRAS-2006 version, presented in Rauthe et al. (2013).

The HYRAS3.0-PR dataset is preferred over the EOBSv26e dataset because of its higher spatial resolution, which is of importance especially in the Alps. In order to extend this dataset to the 1991-2020 period, quantiles were derived from the 1986-2015 period for both HYRAS3.0-PR and EOBSv26e and applied to the 2016-2020 period of EOBSv26e. These bias-corrected data were concatenated to the 1991-2015 HYRAS3.0-PR data. For the areas outside the HYRAS3.0-PR domain, EOBSv26e was used.

We acknowledge the DWD for the use of the HYRAS dataset.

SARAH SARAH-3 was produced by the Satellite Application Facility on Climate Monitoring (CM SAF) from Meteosat geostationary satellite observations. It spans the years 1983 until present. The data record is not yet publicly available. It was kindly provided by Jörg Trentmann (Deutscher Wetterdienst).

The quantiles of the observational datasets are calculated on the original grids, and then regridded to the RACMO grid. In this way the influence of the regridding is minimized, as the spatial fields of the quantiles are much smoother than the fields of individual time steps (especially of precipitation).

The EOBS and HYRAS datasets only cover land. The missing values of the quantiles over sea are filled with the nearest land points. This implies that we assume that the climate signal over sea is similar to the signal in the coastal area. It may be clear that this assumption fails far from the coast, especially for e.g. temperature.

Results

Illustration Figure 2.27 shows, for an arbitrary grid point in The Netherlands, the biases in the RACMO data (for the 2100Hn control resample[1]) with respect to the observations for January, April, July and October. The high ratios in winter for precipitation indicate that RACMO has considerable amount of drizzle, which is absent in summer. For extreme daily precipitation, the bias in RACMO is relatively small: the ratios tend to 1. The bias in temperature depends both on the season and on the quantile. In this example, the bias is small in July, except for the extremes, which are 1K too warm. The cold days in January are too cold in RACMO. Also for minimum and maximum temperature the biases are mostly within 1K. The deviation in radiation can be up to 20% in winter; however, here the values are small and of minor importance compared to summer values. The relative humidity values differ up to 5%-point in July.

Here we show how some relevant variables compare to the climatology of the gridded observations before and after bias correction.

[1] 2100Hn stands for wet ('nat') variant of the high scenario (i.e. SSP5-8.5) in 2100. See Table 3.3 for a more detailed description of the KNMI'23 climate scenarios names.

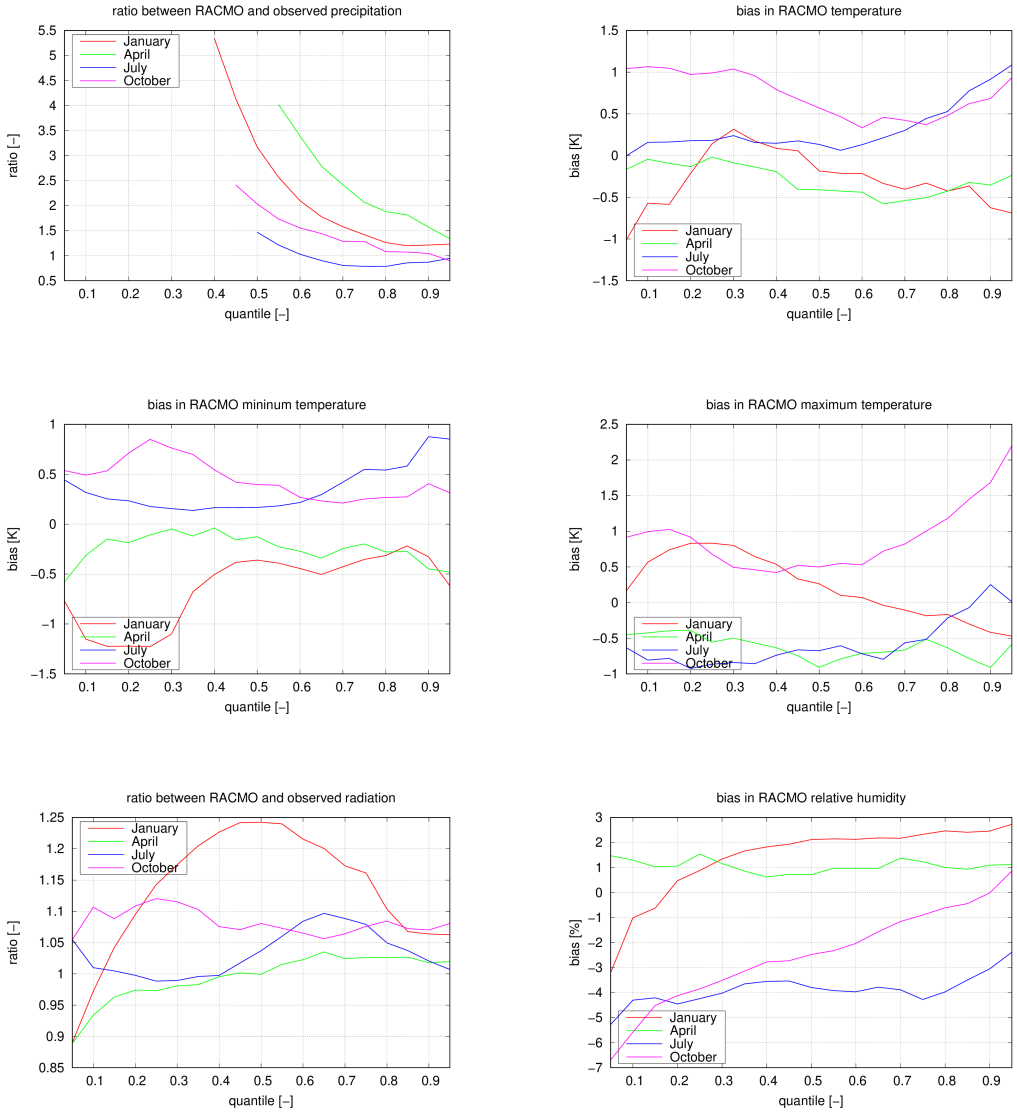

Figure 2.27: Comparison of the quantiles in the observations and RACMO for an arbitrary grid point in The Netherlands. Shown are the lines for January, April, July and October for precipitation (a), temperature (b), minimum temperature (c) and maximum temperature (d), radiation (e) and relative humidity (f).

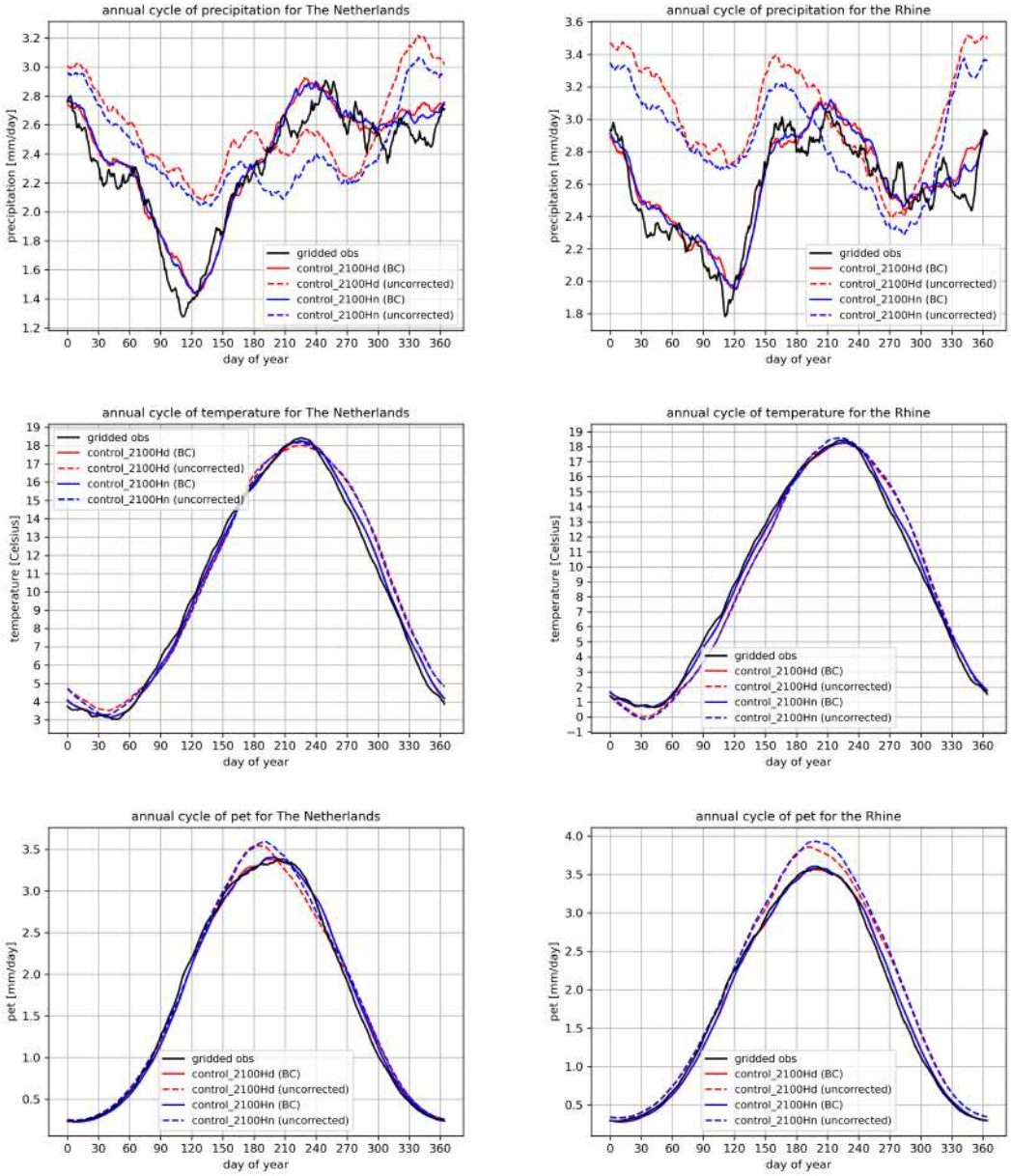

Figure 2.28: Annual cycle of the precipitation, temperature and Potential Evapotranspiration (PET) for The Netherlands (left) and the Rhine (right). The dashed lines indicate the unbiased values for Hd (red) and Hn (blue), the solid lines are the bias-corrected lines.

annual cycle The annual cycle of the precipitation, temperature and PET are shown in Figure 2.28. In all cases, the bias is reduced, especially for the precipitation (which shows in the unbiased situations too high precipitation amounts in the winter and too low amounts in the summer.

Figure 2.29 shows, for the temperature in July, how well the 5%, 50% and 99.9% quantiles of the gridded observations compare to the quantiles that are calculated after bias-correction (ideally they should be equal). The left column shows in colors the gridded observations (EOBSv26e), and in contours the bias-corrected RACMO results. The right column shows the bias in K. The figure shows that the biases after correction are very small (and are partly due to the effect of

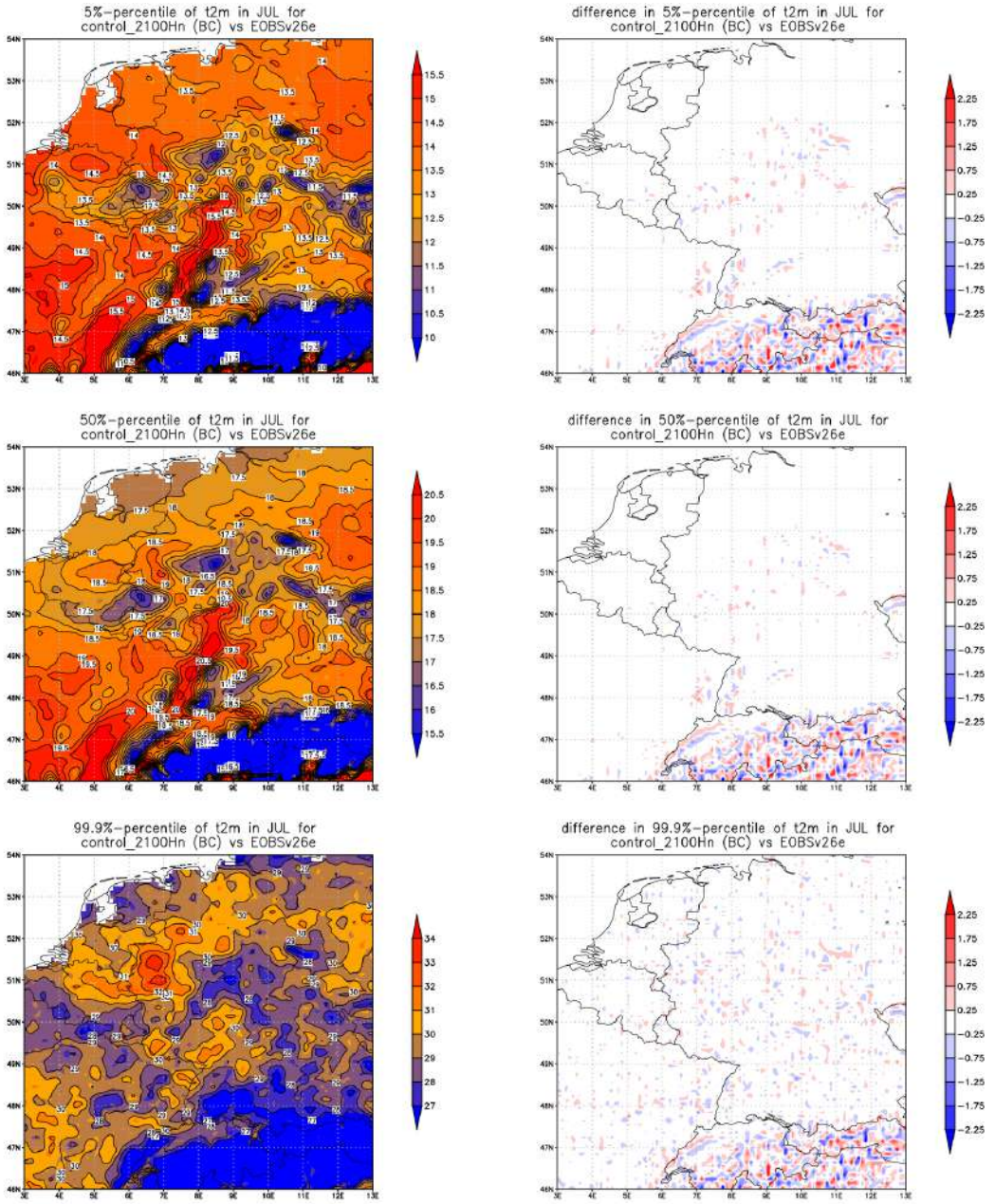

Figure 2.29: Quantiles of the temperature in July for the gridded observations (EOBSv26e, shaded) and RACMO (contours), and the difference between RACMO and EOBSv26e (right).

regridding, which is clearly visible in the Alps). Even for the 99.9% the biases are mostly small, and randomly distributed.

Figure 2.30 shows the 95, 99 and 99.9% quantiles of the precipitation in July (we choose higher quantiles than for temperature, as the lower quantiles indicate no precipitation). The right column shows the ratio between RACMO and EOBSv26e. The figure shows that the biases after correction are small (and are partly due to the effect of regridding). Even for the 99.9% the biases are fairly small, and randomly distributed.

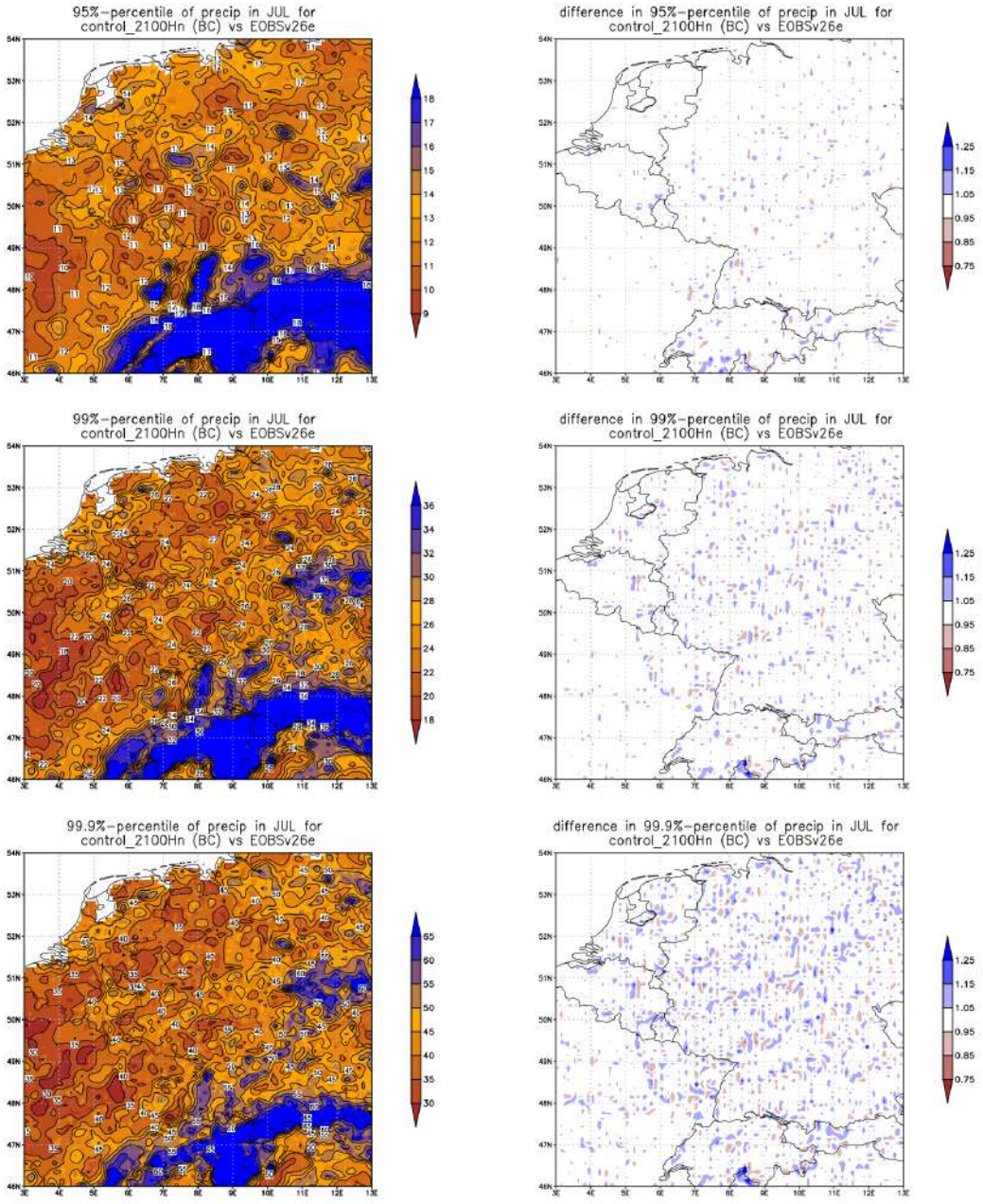

Figure 2.30: Quantiles of the precipitation in July for the gridded observations (EOBSv26e, shaded) and RACMO (contours), and the ratio between RACMO and EOBSv26e (right).

Extremes

Precipitation extremes Figure 2.31 shows the Gumbel plots of the 1-day and 10-day precipitation amounts averaged over The Netherlands, the Vecht and the Rhine, resp. The dashed lines are the unbiased values, the solid lines the bias-corrected values. The black lines show the observational data. The plots for The Netherlands indicates that the biascorrection improves the once-a-year value, but seems to worsen the values for more extreme amounts. Although the effect is less pronounced for the 10-day values, it is still present. It is remarkable that the bias correction works well for the Vecht - although this river basin is smaller than The Netherlands. And for the Rhine, the bias correction seems to have no effect on the 1-day extremes; however is considerably improves the 10-day extremes.

We conclude that it is very hard to correct extremes with return periods larger than once a year. This is mainly due to the large statistical uncertainty that is present (mainly in the short observational set). Nevertheless, the bias correction performs well for the Vecht and The Rhine basins (also for the Meuse, not shown), and improves the Gumbel plots for the accumulated precipitation over multiple days (which is important for river discharges).

Temperature maxima Figure 2.32 shows the Gumbel plots of the 1-day and 10-day averaged temperatures over The Netherlands, the Vecht and the Rhine, resp. The dashed lines are the unbiased values, the solid lines the bias-corrected values. The black lines show the observational data. The biases in the extreme temperatures are small, and well corrected.

Temperature minima Figure 2.33 shows the Gumbel plots of the 1-day and 10-day averaged minimum temperatures over The Netherlands, the Vecht and the Rhine, resp. The dashed lines are the unbiased values, the solid lines the bias-corrected values. The black lines show the observational data. The biases in the low temperatures are small, and the effect of the bias correction is small.

precipitation deficit Figure 2.34 shows the Gumbel plots of the minima of the cumulative precipitation over 90 days over The Netherlands and The Rhine basin. The right column shows the minimum values of the 90-day accumulated precipitation deficit (i.e., the cumulative amount of precipitation minus potential Evapotranspiration (pet)). The figure shows that the bias correction doesn't fully correct the overestimation of the most extreme precipitation minima (especially for The Netherlands), but that the precipitation deficit performs very well.

Figure 2.35 shows the temporal evolution through the year of the precipitation deficit for the grid point (6°E,52°N) for the uncorrected (left) and the biased scenarios. It shows that the bias is removed from the precipitation deficit for all three percentiles, for all three scenarios: after bias-correction they become indistinguishable in climatological sense. This indicates that RACMO represents realistic correlations both in time as well between the variables precipitation, radiation and temperature (which all influence the precipitation deficit).

River discharges In cooperation with Deltares, several bias-corrected 240-year runs each are used to calculate the discharges at Lobith (Rhine) and Borgharen (Meuse). This is done with the HBV model (Buiteveld and Eberle, 2005), as well with the (more advanced) model Wflow (Verseveld et al., 2022). The Gumbel plots are shown in Figure 2.36. All Gumbel lines are similar (except the most extreme events, due to statistical uncertainty). This is an extra confirmation that the bias-corrected meteorological variables have realistic correlations in time and space.

2.1.11 Computation of scenario table values

The climate normals in the scenario tables are calculated following the WMO guidelines regarding averaging and rounding of intermediate results. The climate normals for the reference period are based on station data. For the country average, we use the five main stations (LH5). We calculate the climate change value, the delta, by subtracting the bias-corrected, area-averaged value over

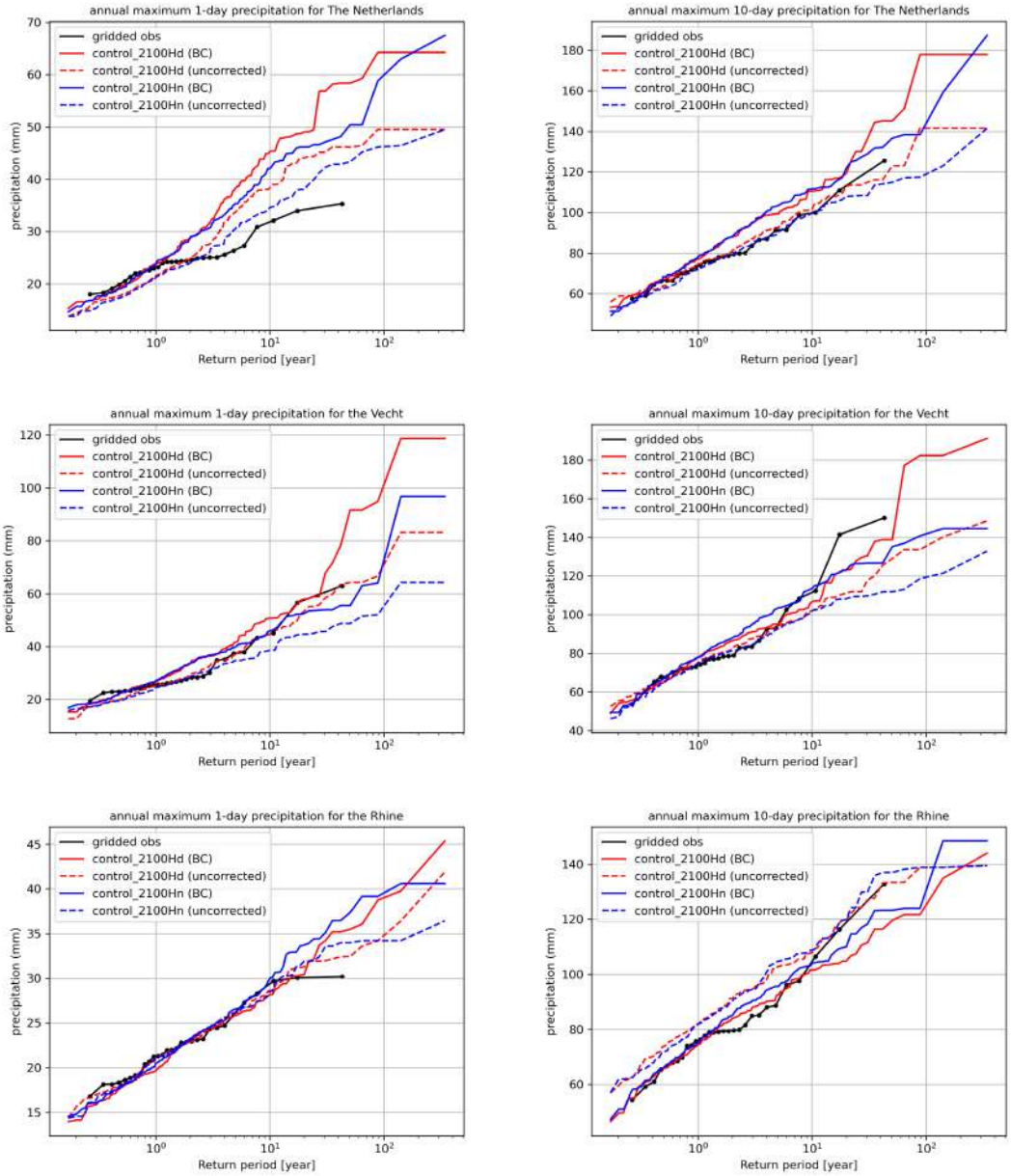

Figure 2.31: Gumbel plots of the 1-day (left) and 10-day (right) precipitation for The Netherlands (upper), The Vecht (middle) and the Rhine (bottom). The dashed lines indicate the unbiased values for Hd (red) and Hn (blue), the solid lines are the bias-corrected lines.

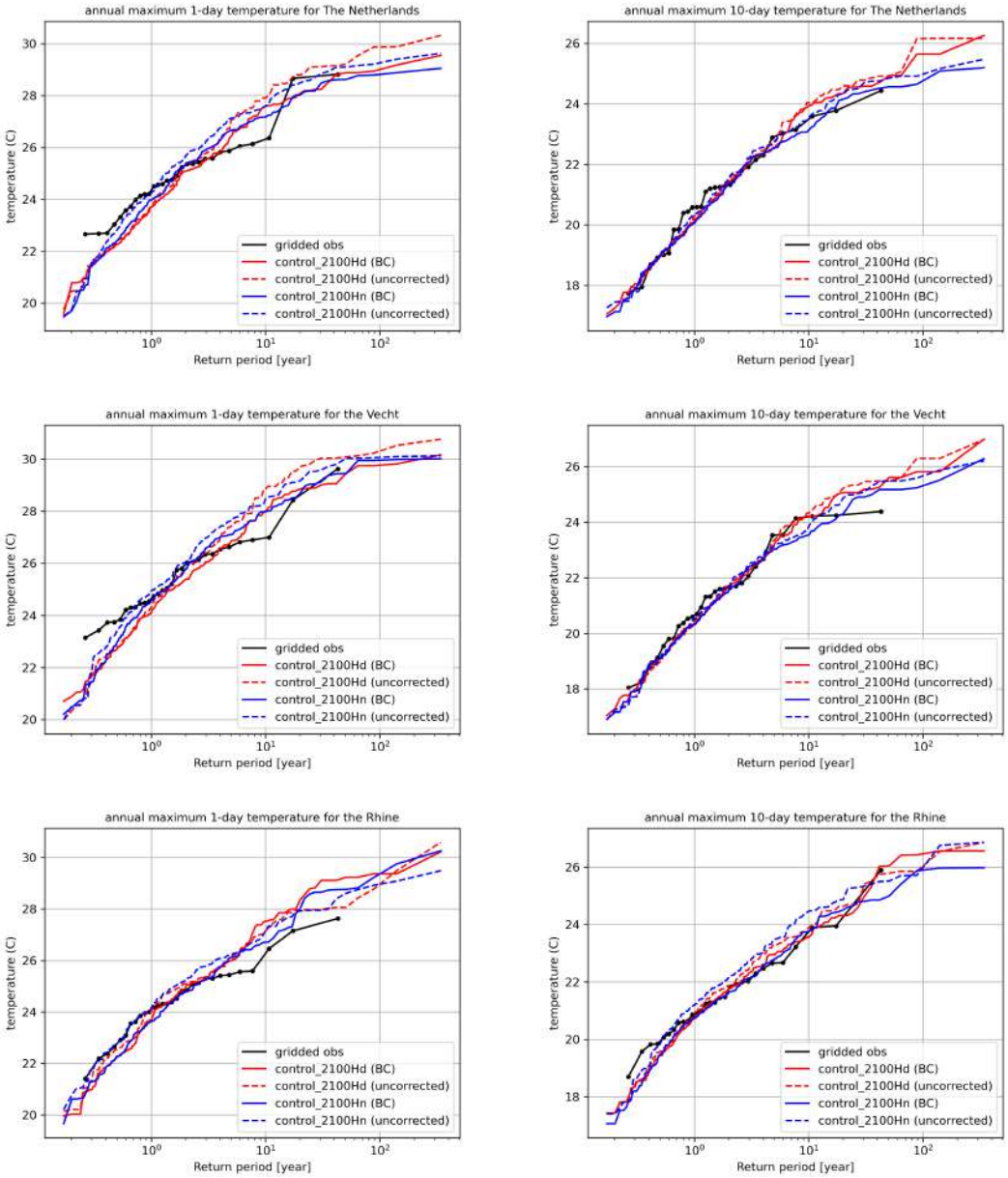

Figure 2.32: Gumbel plots of the 1-day (left) and 10-day (right) temperature for The Netherlands (upper), The Vecht (middle) and the Rhine (bottom). The dashed lines indicate the unbiased values for 2100Hd (red) and 2100Hn (blue), the solid lines are the bias-corrected lines.

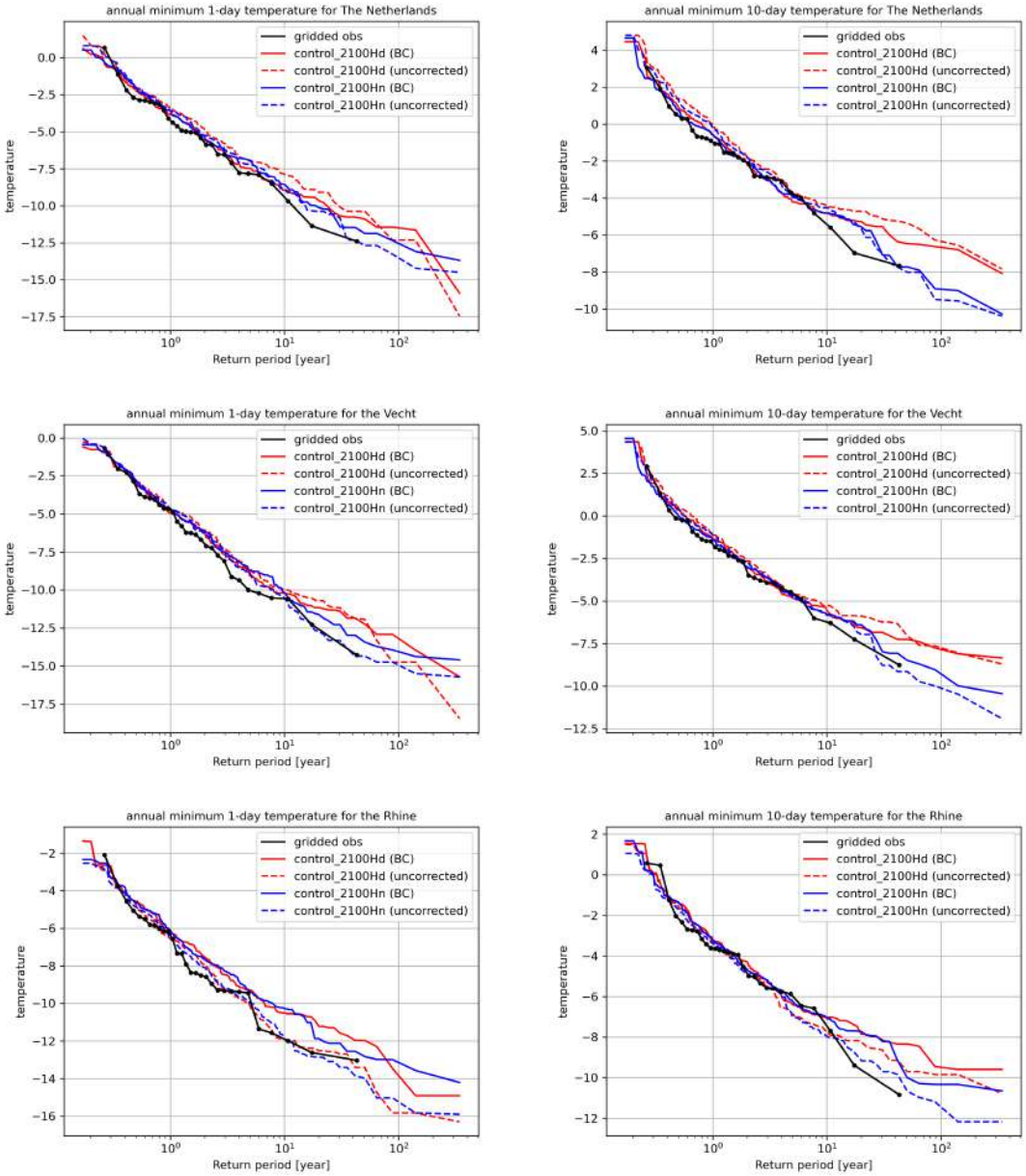

Figure 2.33: Gumbel plots of the 1-day (left) and 10-day (right) minimum temperature for The Netherlands (upper), The Vecht (middle) and the Rhine (bottom). The dashed lines indicate the unbiased values for 2100Hd (red) and 2100Hn (blue), the solid lines are the bias-corrected lines.

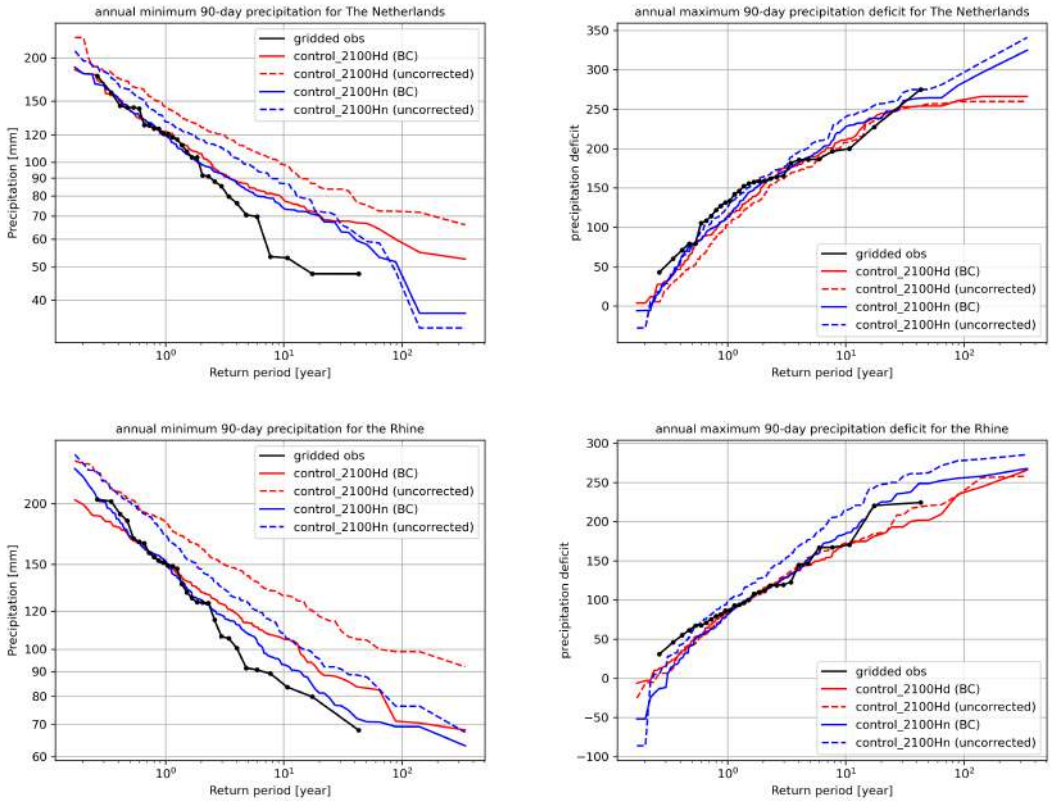

Figure 2.34: Gumbel plots of the 90-day minimum precipitation (left) and precipitation deficit (right) for The Netherlands (upper) and the Rhine (bottom). The dashed lines indicate the unbiased values for 2100Hd (red) and 2100Hn (blue), the solid lines are the bias-corrected lines.

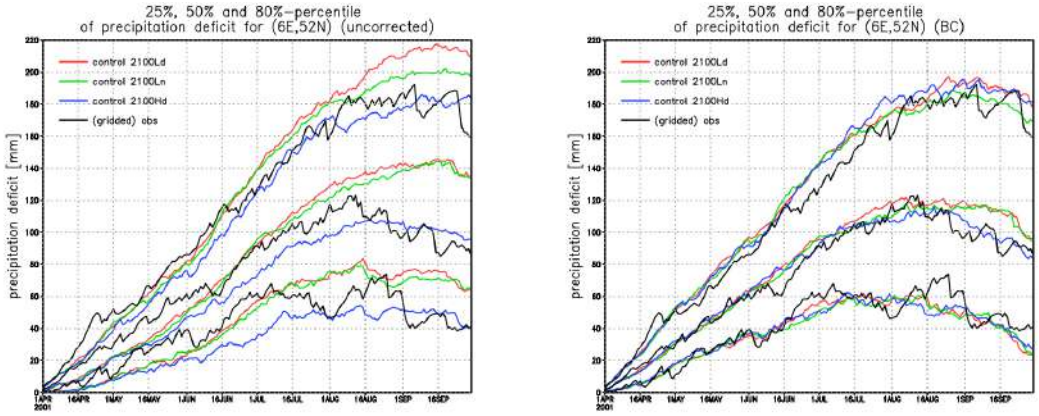

Figure 2.35: Precipitation deficit without (left) and with (right) bias correction for the 25%, 50% and 80% percentiles for the gridded observations (black), and three control scenario's.

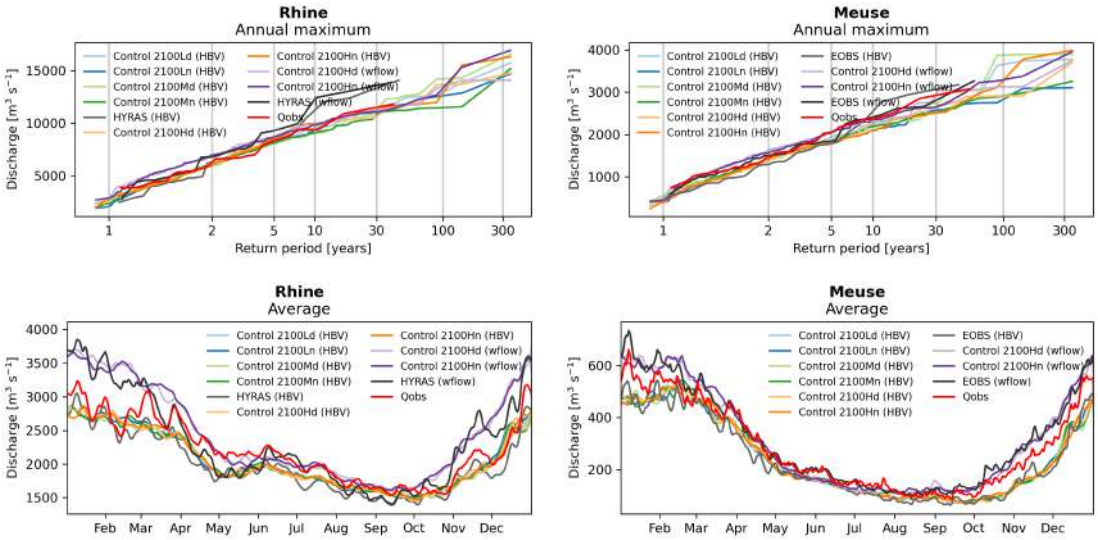

Figure 2.36: Gumbel plots (top) of the extreme discharges in the Rhine (left) and the Meuse (left), and for the annual cycle (bottom).

the Netherlands averaged over the 240 years of resampled RACMO data of the future time horizon from the reference period. Future values are found by adding the delta to the reference climate normal value. For specific station locations, we select the RACMO grid cell nearest to the station location.

Short-duration convective precipitation extremes are not well represented in RACMO. Therefor we base scenario values for changes in hourly and daily precipitation extremes on results from convection permitting models (CPM's), following a different methodology. See section 5 for a detailed description.

2.1.12 Methodological differences with the KNMI'14 scenarios

The methodology of KNMI'23 is somewhat comparable to the methodology of the previous version the national climate scenarios, KNMI'14 (Lenderink et al., 2014), though there are some fundamental differences. These will be discussed in this section, a short overview is provided in Table 2.6. In both cases a resampling technique was used to span the CMIP range of regional climate projections (then CMIP5, now CMIP6) through subselecting years from a single GCM ensemble (then EC-Earth2.3, now EC-Earth3 $_{p5}$) and dynamically downscale the GCM with the regional climate model RACMO. Furthermore, the general aim of both scenario projects was the same, which is to provide a quantitative description of a range of plausible future climate states to which The Netherlands and its surroundings might be exposed upto 2150 (then 2100). In the construction of the KNMI'23 scenarios, we have made some different choices based on feedback from users and lessons learned from previous generations of KNMI climate scenarios (KNMI'14, KNMI'06).

Global warming levels and climate sensitivity

A major difference between the fifth and sixth IPCC assessment report is that we now have a constrained estimate of the Earth's climate sensitivity. Also, there is a broad consensus that the CMIP6 ensemble overestimates the climate sensitivity. The global warming levels for KNMI'14 were assessed directly from the CMIP5 projections, this time we had to take a different approach because a direct assessment from the CMIP6 projections would lead to an overestimation of the projected warming. In addition, users expressed a preference to disentangle the uncertainty

Table 2.6: Overview of methodological differences between KNMI'14 and KNMI'23. Full details in the main text.

KNMI'14	KNMI'23
Conditional on global warming level	Conditional on SSP scenario
Mix of emission uncertainty, model uncertainty (both global and regional), and internal variability	Disentangle uncertainty due to emissions, global climate sensitivity, regional climate processes, and internal variability
No constraint on climate sensitivity, full range considered	Constrained climate sensitivity, IPCC best estimate
Based on RCP4.5 and RCP8.5	Based on SSP1-2.6, SSP2-4.5, and SSP5-8.5
Aimed at spanning univariate CMIP6 range in DJF and JJA, in PR and TAS	Aimed at spanning the multivariate response in PR, TAS and WB in all seasons, of two groups defined by PR response

in future emissions and the uncertainty in modelled climate response to the different emission pathways. So KNMI'23 differs from KNMI'14 in how the global warming levels (ΔGSAT) are deduced.

For KNMI'14 the ΔGSAT global warming levels were derived directly from the range of projected warming levels by the CMIP5 ensemble under the RCP4.5, RCP6.0 and RCP8.5 emission scenarios (multiple ensemble members of a particular model were included if available). Lower emission scenarios were not considered because the world had not yet agreed on climate policies aimed at reducing emissions at a rate sufficient to limit global warming to below 2 °C warming (the Paris Agreement). The 10th and 90th percentiles of the range of projected warming levels rounded to the nearest 0.5 °C defined the global warming levels of the high and the low scenarios of KNMI'14 (referred to as W and G scenario respectively).

In KNMI'23 we took the median value of the IPCC assessed range of ΔGSAT at each of the SSP scenarios considered: SSP5-8.5 for the high scenario (H scenario), SSP2-4.5 for the middle scenario (M scenario) and SSP1-2.6 for the low scenario (L scenario). Despite this very different approach, the global warming levels in the KNMI'23 scenarios are quantitatively close to KNMI'14 (Figure 2.37). The ΔGSAT values of the KNMI'14 W-scenarios are close to the SSP5-8.5 scenario, the ΔGSAT values of the KNMI'14 G-scenarios are close to the SSP1-2.6 scenario (L-scenario in KNMI'23). Note that the end-of-century time horizon has been shifted from 2085 to 2100, resulting in a higher value of ΔGSAT for the SSP5-8.5 end-of-century scenario. The lower value for the lower bound of the GSAT-change in 2100 in KNMI'23 is partly due to the choice of the SSP1-2.6 scenario for the lower bound of future emissions. This scenario assumes more climate mitigation and consequently lower emissions than the RCP4.5 scenario used in KNMI'14.

In KNMI'14 the uncertainty due to uncertainty in climate sensitivity and regional climate feedbacks was mixed with the uncertainty due to uncertainty in projections of future socio-economic activities and related emissions (RCPs/SSPs). In KNMI'23 these are disentangled. The KNMI'23 scenarios are conditional on the SSP scenarios, and take the most likely warming level (corresponding to the most likely value of climate sensitivity) for that emission scenario. The matched-warming procedure in addition disentangles the uncertainty due to climate sensitivity and regional climate feedbacks (see next section).

Determining and representing the spread in regional climate projections

In KNMI'14 the focus was to construct two scenarios that represented most of the spread in the regional climate projection of temperature and precipitation in summer and winter. In KNMI'23 we followed a story-line approach with a focus on physical consistency and implications for future water availability and safety. The advantage of KNMI'14 is that the two scenarios represent a larger part of the full CMIP range of projected changes in temperature and precipitation in winter and summer. The disadvantage is you loose part of the physical consistency of the climate change signal in the different seasons.

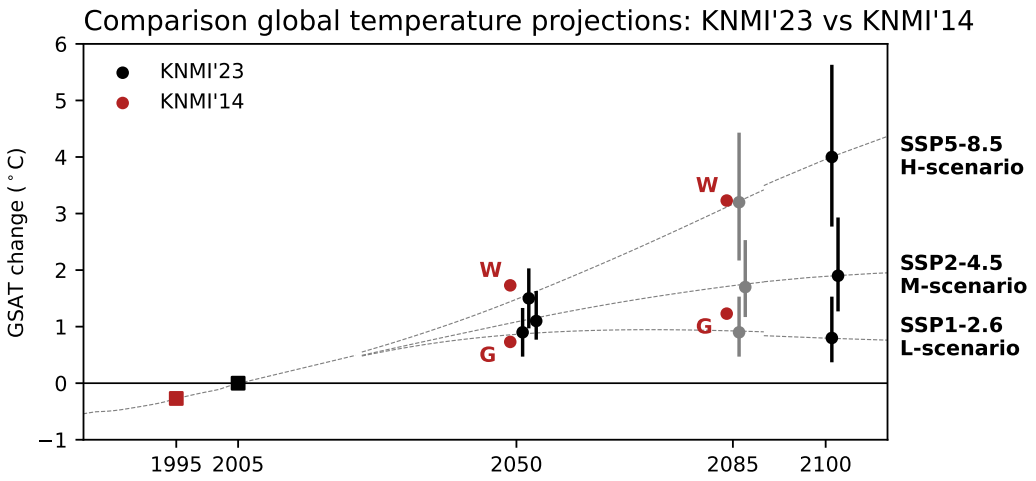

Figure 2.37: Comparison of the projections of Global Surface Air Temperature (GSAT) in KNMI'23 (black/grey markers) and KNMI'14 (red markers). Values shown are relative to 1996-2015, resulting in a negative GSAT change for the KNMI'14 reference period. Markers: squares reference period, circles scenarios, black/grey vertical lines 90 % uncertainty range.

In KNMI'14 the aim of the resampling procedure was to maximise the differences between the projected changes in the four scenarios in temperature and precipitation in the winter and summer seasons, and represent a large portion of the spread in the regional climate projections of CMIP5 (again combining the regional projections under RCP4.5, RCP6.0, and RCP8.5). Constraints for the resampling for the winter and summer precipitation and temperature change were chosen such that the lower values corresponded to about the 10th percentile and the upper values to the 90th percentile of the model spread in regional change. The scenarios for the lower values corresponded to climate projections with weak circulation changes (WL, GL), the scenarios for the higher values with stronger circulation changes (WH, GH): more westerly flows in winter, leading to stronger warming and wettening and more easterly flows in summer, leading to stronger warming and drying. These choices were not optimal for long term water budgets and did not represent the projected spread in annual rainfall. This was a consequence of the choice of combining wetter winters with dryer summers in the 2014-H scenario and not constraining the spring and autumn seasons in the resampling procedure. The choice of combining wetter winters and dryer summers in a single scenario was consistent with the national climate scenarios issued in 2006.

For KNMI'23 the choice concerning the correlation between precipitation changes in winter and summer has been revisited. In addition to representing the spread in winter and summer precipitation changes, we aim to represent the model uncertainty in changes in the annual total precipitation in two scenarios. Consequently, large summer drying is combined with weak winter wettening and vice versa, as this leads to the largest changes on annual precipitation sums. This choice follows advise from experts and stakeholders, who note that precipitation trends, including those across seasons, are relevant for climate adaptation in the Netherlands. Multi-year droughts for instance are more likely in case annual precipitation decreases. In order to construct two scenarios with temperature and precipitation changes in all seasons that are physically consistent, we choose in KNMI'23 to base the constraints for the resampling on the composite climate signal of a dry-trending and a wet-trending group of models. In KNMI'14 the constraints for temperature and precipitation were derived seperately without taking covariances between both variables and between the projected changes in the different seasons into account. We note that the correlations between the projected changes in the different seasons are small. It is also possible to choose two group of models, one with the smallest winter precipitation increase and summer precipitation decrease and one with the largest precipitation changes winter and summer (like the KNMI'14 L

and H scenarios) and base the constraints for the resampling of the composite climate signal of these groups.

The resampling procedure in KNMI'14 explicitly aimed to span the CMIP5 range of temperature (and precipitation as discussed). In the KNMI'23 procedure, the grouping of CMIP6 models was done based on the precipitation response alone. This has consequences for the spread in temperature, which is less pronounced in the new scenario set. We note however, that the main source of uncertainty in the regional temperature response is the emission pathway. Model uncertainty in the regional temperature response, conditional on a SSP scenario, is less well represented in the KNMI'23 scenarios than the model uncertainty in the precipitation response (Section 2.1.5, Figure 2.14).

In KNMI'23 we take more care in removing the contribution of natural variability from the estimate of the climate response (by taking the composite of 11 models and by smoothing the dependence of the composite climate response on warming level before their application as constraints in resampling). In KNMI'14 it was assumed that most of the spread in the climate response, assessed by taking differences in 30 year mean values between the future and reference period, was due to model uncertainty. This likely overestimates the model uncertainty.

A final difference is the estimate of the spread in the regional climate response. In KNMI'14, the regional climate response was evaluated for a given 30-year window around the future time horizon. The global warming levels at a fixed time in the future are different in models with different climate sensitivities. This difference contributes to the assessed spread in the regional response. In KNMI'23 we shift models in time until they reach the required global warming level and then assess the regional climate response. Due to the matched-warming approach, differences in climate sensitivity do not contribute to the assessed spread in the regional climate response. Uncertainty due to climate sensitivity can be translated in reaching a scenario for 2050 a number of years earlier or later in the century or by scaling the regional response for a given time-horizon by a factor larger than one in case the climate sensitivity is higher than the median estimate or smaller than one in case the climate sensitivity is lower (see Section 2.1.1).

2.2 Resampling procedure

The Selection Procedure of Model Samples

The aim of the resample tool is to rearrange the output from the EC-Earth3$_{\text{p5}}$ ensemble to best comply with a number of constraints that are derived from the CMIP6 ensemble. The input data consists of thirty year long time series of monthly data from the EC-Earth3$_{\text{p5}}$ ensemble for the reference and future periods. These time series are divided into thirty samples of one year. The resample tool combines a subset of these samples into a resampled ensemble while maintaining the time order of the samples so that trends due to climate change within the period of thirty years are preserved. The constraints are imposed on the absolute or relative change of quantities between the control and future periods in the resampled ensemble. Each quantity is either a mean, quantile, or maximum value for the whole year or for an individual month or season.

To compute the constraint for a specific variable, first algorithm 1 is used to construct the time series for the members of the resampled ensemble in the control and future periods. Note that this algorithm also produces an array with all time series values in ascending order which is convenient when computing constraints on quantile statistics of the resampled ensemble. The time series values can be sorted once in a preprocessing step during which the map from indices in the unsorted array to indices in the sorted array can be computed as well. Thereafter, the required statistics is computed from these time series for the two periods. For mean and quantile values this is straightforward. Algorithm 2 is used to compute the maximum value.

In addition to satisfying a set of constraints on quantities, the resampled ensemble should have realistic inter-annual variability and variance over its members. This can be realised by selecting in each time series of the resampled ensemble as many consecutive samples from the same EC-Earth3$_{\text{p5}}$ member as possible, and by using for each year samples from different EC-Earth3$_{\text{p5}}$ members as much as possible. The former is implemented by a constraint that penalises cases

where less than five consecutive samples from the same EC-Earth3$_{\text{p5}}$ member are used as shown in algorithm 3. The latter is implemented by a constraint, that adds a penalty when a sample from an EC-Earth3$_{\text{p5}}$ member for a specific year is used more than twice according to algorithm 4. Constructing a resampled ensemble with less members than the EC-Earth3$_{\text{p5}}$ ensemble also helps to limit the number of such duplicates.

Together the type of input data and the constraints define an optimisation problem in which the search space consisting of all possible resampled ensembles is discrete. For this type of optimisation problem, the global optimum can be approximated by means of simulated annealing (*Simulated Annealing* 2022). This procedure resembles the annealing procedure from, e.g., metallurgy: it approximates the minimum of an energy function by gradually changing a state while a temperature is being lowered. In our case, the state is the resampled ensemble and the energy function $E(s)$ is given by:

$$E(s) = \sum_i C_i^2(s) \tag{2.2}$$

where s is the current resampled ensemble and $\{C_i(s)\}$ is the set of constraints that it should satisfy. The state changes are computed by algorithm 5. This algorithm randomly selects a sample in the resampled ensemble and either replaces it by a sample from another member of the model ensemble or sets it to the member just before or after it. The latter increases the number of consecutive samples while the former reduces it.

Algorithm 1: Resample Ensemble

Data: $K \geq M$, the number of members in the model ensemble
Data: $M \geq 2$, the number of members in the resampled ensemble
Data: $N \geq 2$, the number of samples along the time axis in the model and resampled ensemble
Data: $T \geq 1$, the number of time series values along the time axis in each sample
Data: $V = N.K.T$, the total number of values in the model ensemble
Data: *count*, counts how often each of the V values is referred to by s
Input: s, the current resampled ensemble of $N \times M$ values from $0, ..., K-1$
Input: *values*, the V time series values from the model ensemble in ascending order
Input: *map*, the map consisting of $N \times K \times T$ indices in the range $0, ..., V-1$ into *values*
Output: *sorted*, the resampled ensemble as $N.T.M$ values in ascending order
Output: *member*, the resampled ensemble as $(N.T) \times M$ values, time series per member

```
for i ← 0 to V − 1 do count_i ← 0;
for n ← 0 to N − 1 do
    for m ← 0 to M − 1 do
        for i ← 0 to T − 1 do
            k ← map_{n,s_{n,m},i} ;
            count_k ← count_k + 1 ;
            member_{n.T+i,m} ← values_k ;
        end
    end
end
j ← 0 ;
for i ← 0 to V − 1 do
    for k ← 0 to count_i do
        sorted_j ← values_i ;
        j ← j + 1
    end
end
return member, sorted
```

Algorithm 2: Maximum Value

Data: $M \geq 2$, the number of members in the resampled ensemble
Data: $N \geq 2$, the length of the time series
Data: $W < N$, the size of the sliding window
Data: w, the windowed timeseries of $(N - W + 1) \times M \times W$ values
Data: m, the maximum over the last dimension of w, $(N - W + 1) \times M$ values
Input: t, the time series of the resampled ensemble, a total of $N \times M$ values for the control or future period
Output: r, the maximum value

$w \leftarrow$ Apply a sliding window of width W to t ;
$m \leftarrow \max_i(w_{0\ldots N-W+1,0\ldots M-1,i})$;
$r \leftarrow \frac{\sum_{i,j} m_{i,j}}{(N-W+1)M}$;
return r

Algorithm 3: Constraint on Consecutive Samples

Data: $K \geq M$, the number of members in the model ensemble
Data: $M \geq 2$, the number of members in the resampled ensemble
Data: $N \geq 2$, the number of samples in the time series of both the model and resampled ensemble in each period
Data: $P = 2$, the number of periods: 0 = control, 1 = future
Input: s, the current state of $P \times N \times M$ values from $0, ..., K - 1$
Input: $L = 5$, the desired minimum number of consecutive samples from the same model ensemble member
Input: $w \geq 0$, the weight of this constraint relative to the other constraints
Output: e, the energy value for this constraint

$e \leftarrow 0$;
for $p \leftarrow 0$ **to** $P - 1$ **do**
  for $m \leftarrow 0$ **to** $M - 1$ **do**
    Compute the run-length encoding $\{(m_i, l_i)\}$, $i = 0, ..., I - 1$, of $s_{p,0\ldots N-1,m}$;
    $\{\delta_i\} \leftarrow \{\texttt{min}(l_i - L, 0)\}$;
    $e \leftarrow e + \sum_{i=1}^{I-2} \delta_i^2$
  end
end
$e \leftarrow e/M$;
return $w.e$

Algorithm 4: Constraint on Duplicate Samples

Data: $K \geq M$, the number of members in the model ensemble
Data: $M \geq 2$, the number of members in the resampled ensemble
Data: $N \geq 2$, the number of samples in the time series of both the model and resampled ensemble in each period
Data: $P = 2$, the number of periods: 0 = control, 1 = future
Input: s, the current state of $P \times N \times M$ values from $0, ..., K-1$
Input: $D = 2$, the allowed maximum number of samples from the same model ensemble member
Input: $w \geq 0$, the weight of this constraint relative to the other constraints
Output: e, the energy value for this constraint

$e \leftarrow 0$;
for $p \leftarrow 0$ **to** $P-1$ **do**
  for $n \leftarrow 0$ **to** $N-1$ **do**
    $\{c_i\} \leftarrow$ Number of occurrences, c_i, of m_i $(i = 0, ..., I-1,\ I \leq M)$ in $s_{p,n,0...M-1}$;
    $\{d_i\} \leftarrow \{\texttt{max}(c_i - D, 0)\}$;
    $e \leftarrow e + \sum_i d_i^2$
  end
end
$e \leftarrow e/N$;
return $w.e$

Algorithm 5: Change Resampled Ensemble

Data: $K \geq M$, the number of members in the model ensemble
Data: $M \geq 2$, the number of members in the resampled ensemble
Data: $N \geq 2$, the number of samples in the time series of both the model and resampled ensemble in each period
Data: $P = 2$, the number of periods: 0 = control, 1 = future
Input: s, the current state of $P \times N \times M$ values from $0, ..., K-1$
Output: $\hat{s}$, the new state of $P \times N \times M$ values from $0, ..., K-1$

$m, n, p \leftarrow \texttt{random}(0, ..., M-1), \texttt{random}(0, ..., N-1), \texttt{random}(0, ..., P-1)$;
$n^-, n^+ \leftarrow \texttt{max}(n-1, 0), \texttt{min}(n+1, N-1)$;
// Replace by another sample, always or in case of equal samples n^-, n, n^+
if $\texttt{random}(true, false) \vee (s_{p,n,m} = s_{p,n^-,m} \wedge s_{p,n,m} = s_{p,n^+,m})$ **then**
  $v \leftarrow \texttt{random}(0, ..., s_{p,n,m}-1, s_{p,n,m}+1, ..., K-1)$;
else // Grow preceding or following group of consecutive samples
  if $s_{p,n,m} \neq s_{p,n^-,m} \wedge s_{p,n,m} \neq s_{p,n^+,m}$ **then**
    $v \leftarrow \texttt{random}(s_{p,n^-,m}, s_{p,n^+,m})$
  else if $s_{p,n,m} \neq s_{p,n^-,m}$ **then**
    $v \leftarrow s_{p,n^-,m}$
  else
    $v \leftarrow s_{p,n^+,m}$
  end
end
$\hat{s} \leftarrow s$;
$\hat{s}_{p,n,m} \leftarrow v$;
return $\hat{s}$

2.3 Retuning EC-Earth3 for KNMI'23 purposes

The CMIP6 version of EC-Earth3 has been retuned with the aim of reducing the negative temperature bias that is seen in the simulations with the control version over large parts of the Northern Hemisphere, including Europe. This bias can be associated to the intermittent occurrence of profoundly cold stages which coincide with the absence of deep convection in areas like the Labrador Sea. In several members such cold stages can be identified until the end of the historical simulations with the control version. In the retuned version the frequency of occurrence of cold stages and their intensity in the piControl simulation is substantially reduced, although not entirely suppressed. In the 16 member ensemble of historical simulations initialized in 1850 from piControl states the cold or low convective stages are absent in all members after 1975 and in all but two members after 1950. The NH cold bias has nearly vanished for the retuned version at the expense of a global mean temperature increase of about 1° in comparison to the control version.

For the purpose of dynamical downscaling the EC-Earth3 output with a regional climate model, in casu KNMI-RACMO, 6-hourly resolved multi-level atmospheric fields were stored from the model year 1949 onwards. A huge reduction in the output data volume (about 75 % implying several Peta bytes) could be achieved by using an alternative approach in which an optimal set of 23 pressure levels is used for the prognostic multi-level variables required as forcing data for the downscaling as opposed to the standard approach where GCM model level data (91 levels in case EC-Earth3) as multi-level forcings.

In this section we describe the motivation for the retuning, how it was done, the result and the details of the set of 16 member ensembles that was run for the KNMI'23 scenario project.

Note that variables and their names are conform the CMOR3 conventions (2023) & CMIP6 CMOR Tables (2023) in this section.

2.3.1 Retuning the EC-Earth3 CMIP6 version

The tuning of the CMIP6 EC-Earth3 version

Like most other coupled climate models EC-Earth shows substantial warm biases around the Southern Ocean area (Hyder et al., 2018; Sallée et al., 2013; Meijers, 2014). In the recent EC-Earth3 CMIP6 version (Döscher et al., 2022) this bias was even found significantly increased compared to the EC-Earth2 CMIP5 version (Hazeleger et al., 2012). At the same time the EC-Earth3 CMIP6 version shows a cold bias for large parts of the NH including Europe, compared to the ERA5 reanalysis (Hersbach et al., 2020). During the tuning of the EC-Earth3 CMIP6 version it appeared difficult to find a set of suitable tuning parameters with which a cooling of the SH could be achieved without affecting the NH, i.e. without cooling the NH as well, and vice versa. This was once more confirmed during the tuning of the EC-Earth3-AerChem version (Noije et al., 2021). In order to end up with a correct global mean temperature and to keep this southern warm bias limited, effectively, the NH has been tuned too cold in the EC-Earth3 CMIP6 version. Moreover, the cold NH bias most likely is related to the large variability in the Atlantic Meridional Overturning Circulation (AMOC) which has been identified to occur in the piControl and historical simulations with the EC-Earth3 CMIP6 version (Döscher et al., 2022; Meccia et al., 2022) and is very similar to the multicentennial variability found in the IPSL-CM6-LR model (Jiang et al., 2021). This is reflected in the oscillations in the global mean temperature, which show an amplitude in the piControl run of 0.9 K (while ∼0.25 K is expected) associated to irregular fluctuations between cold and warm states with episode lengths varying from a few decades up to about two centuries. When the model is in the cold state, the deep convection is absent in the Labrador Sea, shown by very small mixed layer depth numbers (see Fig. 2.38) coinciding with the occurrence of unrealistic (timing of) sea ice patterns. To ensure that this claim is not highly sensitive to the relative arbritary selected area section, we included two areas (see Fig. 2.39), however the fact that the blue and red curve in Fig. 2.38 nearly lie on top of each other show that this is not the case.

At the time of the release of the EC-Earth3 CMIP6 version, the EC-Earth Consortium found itself under time pressure because the CMIP6 simulations had to start. Due to the IPCC6 / CMIP6 deadline there was no time left at that moment for further investigation and to improve the tuning after the large variability showed up in the piControl run.

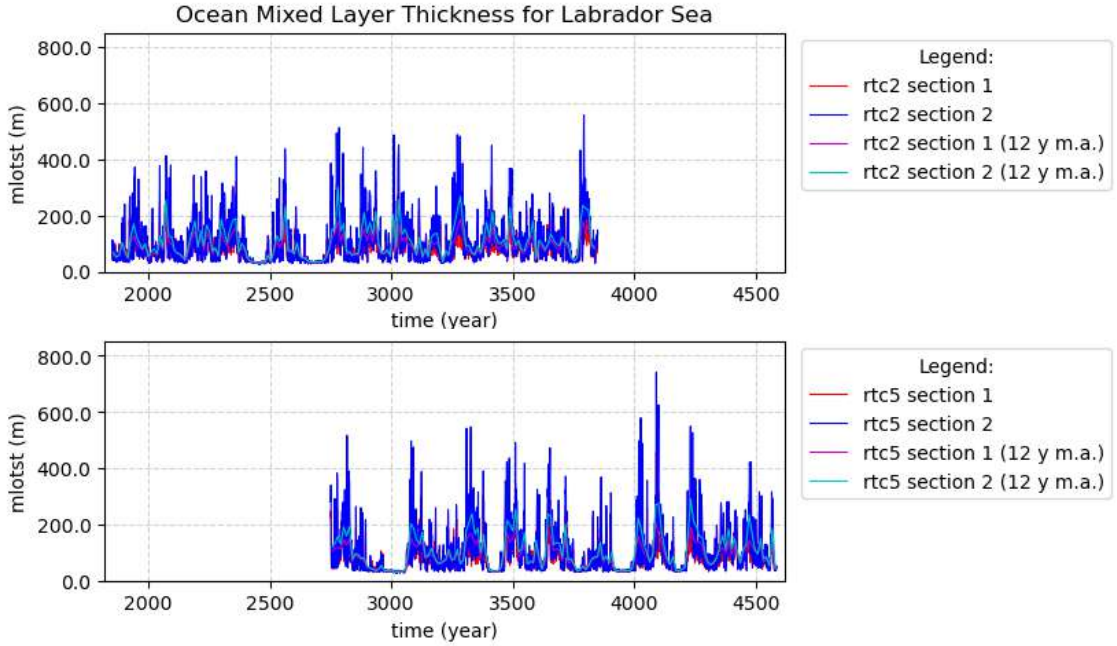

Figure 2.38: The ocean mixed layer thickness mean over two sections within the Labrador Sea (see Fig. 2.39) for two retune runs rtc2 & rtc5. The rtc2 run is an earlier retune attempt which finally warmed too much, the rtc5 is split off at year 2750 from the rtc2 run, and is our pre-industrial control run based on our final selected tune parameter set and values. The initial conditions for the historical ensemble are created from the last 600 year interval of the rtc5 run (see Fig. 2.41). The cold stages are visible by the absence of deep convection in various episodes, where in the second part of the rtc2 run the deep convection is no longer interrupted because, as pointed out in the text, it was warming more than acceptable.

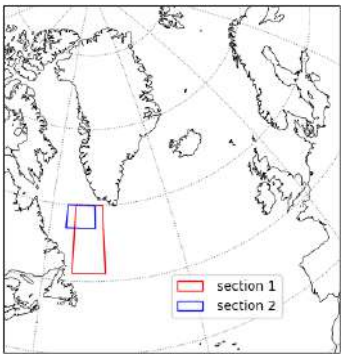

Figure 2.39: Labrador Sea sections

However, these oscillations are not only present in the piControl simulation but also in the historical simulations. Many of the historical members show them even up to 2010, though getting gradually less frequent and diminishing in length due to the onset of warming towards the end

of the historical period. EC-Earth3-Veg, which in general effectively behaves slightly cooler than EC-Earth3, remained during its piControl run more often in the cold and low convective state, however also this version faces the oscillations, certainly during the historical simulations when under slowly but progressively warming conditions the model is most exposed to the switch from the warm to the cold state regime and vice versa.

The EC-Earth3 requirements for the KNMI'23 project

For the KNMI'23 project these oscillations and the cold bias for Europe are difficult issues to cope with. In the KNMI'23 project the forcing boundaries from an EC-Earth3 ensemble of 16 members is used for downscaling with an RCM which is RACMO (Meijgaard et al., 2008, 2012) in the KNMI'23 project. The RACMO historical runs start in 1949, where the first year is considered as spin-up time. In the KNMI'23 project 1991-2020 is used as reference climatology for the future scenarios (SSP5-8.5, SSP2-4.5 & SSP1-2.6), where resampling time chunks of EC-Earth output forms the basis of emulating the entire CMIP6 model ensemble which is achieved by applying constraints given by the CMIP6 model ensemble itself on the resampling (see section 2.1.8). The aim is to provide a CMIP6 driven downscaling for Europe (with a focus on The Netherlands and its upstream river basins: the Rhine-Meuse catchments) for the historical part from 1950 onwards and for a few future time windows for three scenarios with the latest window around 2150. Because the output configuration of EC-Earth3 is in our own control we can exactly determine the required data for the downscaling with our RCM.

RACMO uses the KEXT12 domain (see Fig. 2.40 and Table 2.7) for the KNMI'23 ensemble.

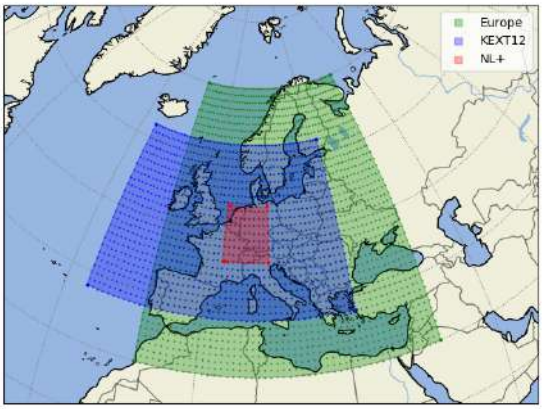

Figure 2.40: Selected areas, with the cmorised (regridded) grid points at which the EC-Earth3 data is available. For instance the KEXT12 RACMO domain is blue shaded and the EC-Earth3 grid points in this area are blue dotted. For grid corner coördinates see Table 2.7.

area	lon west	lon east	lat south	lat north	additional description
nlplus	3.4	12	46	53.6	proxy for KNMI'23 NL+ area
kext12	-21	27	38	62	proxy for KNMI'23 RACMO domain
europe	-10	40	30	70	
n30-70	0	360	30	70	30° to 70° North
norhem	0	360	0	90	Northern Hemisphere
global	0	360	-90	90	

Table 2.7: Corner coördinates of the selected areas for which climatologies & seasonal means have been computed.

Aim of retuning

However, recalling that it did not turn out straightforward to find a set of tuning parameter deltas with which we can cool the SH and warm the NH independently, and noticing that while tuning the EC-Earth3 CMIP6 version a cold NH bias could not be avoided in order to limit the SH warm bias and keep the global temperature mean correct, we decided to retune the EC-Earth3 version with a strict focus on NH conditions, relaxing constraints elsewhere, hence implying the following goals and consequences: 1. We accept that the global mean temperature will be too high, as our model has a substantial warm bias over the southern ocean and over the Antarctic region as well; we can not expect differently. 2. We accept that the warm bias at the SH will even get worse, admitting the model is far off anyway below 30° south. 3. Minimize the cold NH bias relative to ERA5. 4. Reduce the large amplitude in global mean temperature, i.e. eliminate the occurrence of a switch towards a cold and low convective state, and thus stabilizing the AMOC.

Idealiter point 4 is achieved for the retuned piControl run itself, second best this goal is reached from 1950 onwards, and at the least this goal must be achieved prior to 1991, being the initial year of the reference period defined in the KNMI'23 project.

Which tune parameters can accomplish our purpose?

There is no straightforward recipe for tuning coupled climate models, therefore reporting it is all the more important (Mauritsen et al., 2012; Hourdin et al., 2017). Because a main source of uncertainty in climate models originates from microphysics (Chen et al., 2021; Houghton et al., 2001; Morrison et al., 2020; Yin et al., 2022; Forbes and Ahlgrimm, 2014), cloud process related parameters are obvious candidates for tuning as they have a relatively wide range of uncertainty with significant impact on the model. Pre-industrial and historical simulations are used to constrain the tuning parameters and the model. Related to that, cloud microphysics remains one of the largest sources of uncertainty in understanding how the climate will change due to global warming (Sec. 1.5.3.1.2 in Chen et al. (2021)).

The autoconversion from supercooled cloud droplets or ice particles to rain or snow, is one of the cloud microphysics processes that are parameterized in large-scale weather and climate models. It is connected to the collision-coalescence process and the Wegener-Bergeron-Findeisen process (Findeisen et al., 1938; Storelvmo and Tan, 2015), the latter is a process of ice crystal growth in clouds that contain a mixture of supercooled water and ice. At a same temperature, the saturation vapor pressure over water slightly exceeds the lower saturation vapor pressure over ice, leading to a subsaturated environment for liquid water and a supersaturated environment for ice. If the ambient vapor pressure is in between, this causes rapid evaporation of liquid water from cloud droplets and at the same time rapid growth of ice crystals through vapor deposition. Provided the density of liquid water particles is large compared to that of ice, the ice crystals will then grow large enough to start falling out of the cloud as snow or graupel and, if temperatures at lower levels are high enough for melting, eventually as rain.

The threshold value of cloud content at which the conversion of cloud condensate through autoconversion into snow or rain becomes efficient is one of the key tuning parameters in the cloud microphysics. A typical value is $\sim 5 \times 10^{-5}$ kg kg^{-1} for warm clouds but it is considerably lower in mixed-phase clouds when the formation of snow is governed by the Wegener-Bergeron-Findeisen process. Another important tuning parameter is the terminal fall speed of large ice crystals in clouds and eventually into the cloud free environment below cloud base. This relatively slow vertical motion (∼15 cm per second) results from a balance between gravity and air resistance (of convective updraughts). The values of these two tuning parameters have been modified for the retuned EC-Earth3 version in the KNMI'23 project.

Intermezzo: Labeling the retuned EC-Earth3 version

When climate simulations are cmorised a *Variant Label* or *ripf* label (e.g.: variant_label = **r**1**i**1**p**1**f**1) is assigned to the metadata of each dataset which exists of four pieces: The ***r****ealization index*, ***i****nitialization index*, ***p****hysics index* & ***f****orcing index*. For instance the ***r****ealization index* is used

to bookkeep the ensemble numbers. Because with our retune exercise we slightly changed physical tune parameters, we decided to change the ***p****hysics index* for each of our retune cases, where ***p1*** is reserved for the original EC-Earth3 CMIP6 version. Form ***p2*** - ***p7***, the final selected retune case corresponds with ***p5***. Therefore the EC-Earth3 retuned version is labeled as EC-Earth3$_{\text{p5}}$ and the EC-Earth3 CMIP6 version as EC-Earth3$_{\text{p1}}$. The EC-Earth3$_{\text{p5}}$ version has been often referenced within the KNMI'23 team as EC-Earth3bis. Another option would have been to register a new EC-Earth3 model configuration within the official CMOR table administration (CMIP6 CMOR Tables, 2023), but for various retune parameter sets this would result in a lot of new EC-Earth3 configurations which is not really desirable.

The adjusted tuning parameters in the retuning

In setting up the retuning we investigated the adjustment of several parameter combinations and varied their values, this part will be reported in Reerink et al. (2023) but left out here. For now, we focus on the final selected set of two modified tuning parameters *RVICE* & *RLCRITSNOW* (see Table 2.8) and assess the impact of the retuning on the piControl simulation and on the 16-member ensemble of 16 historical simulations.

tuning parameter	**unit**	**IFS CY36R4**	**EC-Earth3$_{\text{p1}}$**	**EC-Earth3$_{\text{p5}}$**	**description**
RLCRITSNOW	kg kg^{-1}	5×10^{-5}	4.0×10^{-5}	4.6×10^{-5}	Threshold for snow autoconversion
RVICE	m s^{-1}	0.15	0.137	0.1328	Fall speed of ice particles in clouds

Table 2.8: The tuning parameters which are adjusted for the retuning and their values for the IFS CY36R4, the CMIP6 EC-Earth3$_{\text{p1}}$ and the retuned EC-Earth3$_{\text{p5}}$ version.

The atmosphere component of the EC-Earth model is based on the Integrated Forecast System (IFS) CY36R4 of the European Centre for Medium-Range Weather Forecasts (ECMWF) and solves the hydrostatic primitive equations. The parameterization of cloud and large-scale precipitation processes are described in Chapter 7 *Clouds and large-scale precipitation* of the IFS documentation (ECMWF, 2010), and Tiedtke (1993) describes in detail the scheme of the prognostic equations for cloud liquid water or ice and cloud fraction, and the diagnostic relations for precipitation.

For the autoconversion process from liquid cloud water to rain, and also from cloud ice to snow, a parametrization following Sundqvist (1978) is used. The conversion rate from cloud (water+ice) into precipitation (rain+snow) , see Eq. (7.37) in ECMWF (2010), contains the parameter $l_{\text{crit}} = l^*_{\text{crit}}/(F_1 F_2)$ that is referred to as the *critical autoconversion threshold for snow in large-scale precipitation*. It controls the amount of cloud water/ice at which the generation of precipitation becomes efficient. Here $l^*_{\text{crit}} = RLCRITSNOW$ is the tuning parameter, and F_1 and F_2 account for the collision-coalescence of cloud ice particles with snow nuclei and the the growth of snow nuclei via the Wegener-Bergeron-Findeisen process fed by the deposition of supercooled liquid droplets respectively. l^*_{crit} has been used as a tuning parameter (see Sec. 7.1.3 (i) Rain and snow autoconversion in (ECMWF, 2010)). The l^*_{crit} for ice-to-snow autoconversion is, based on model tuning, set to 3×10^{-5} and to 5×10^{-5} kg kg^{-1} in CY36R1 and CY36R4 respectively. The value of this tuning parameter l^*_{crit} has been modified within its uncertainty range for our retuning purpose.

The lower value of the tuned l^*_{crit}, used in CY36R1, seems to be in agreement with Rotstayn (2000), who reports that autoconversion is usually derived in GCMs from the mean in-cloud value of the liquid-water mixing ratio. He argues that this biases the calculated autoconversion rate, and may explain why it usually seems necessary to reduce the autoconversion threshold to an unrealistically low value to obtain a realistic simulation in a GCM (Rotstayn, 2000).

Increasing the critical autoconversion threshold l_{crit} for snow affects the high altitude clouds: The generation of precipitation will be delayed because the cloud ice particles will remain floating for a longer time as accretion becomes less effective. The higher abundance of ice particles in high clouds will cause a higher and, therefore, cooler upper cloud level, which will reduce the outgoing longwave radiation from the cloud top level into space. Moreover, because the albedo of

ice particles is lower than the albedo of water droplets the effective albedo slightly decreases, both leading to effective warming below the cloud top.

The reduced value of the terminal fall speed of cloud ice particles (*RVICE*), the second adjusted tuning parameter, also impacts primarily on high-level ice clouds by keeping the cloud ice particles longer floating, thereby effectively extending the cloud life time. Consequently, the same line of arguing applies: higher cloud tops and more high clouds will lead to effective warming as well.

These two parameters, *RLCRITSNOW* & *RVICE*, have, among others, also been used to tune the CMIP6 EC-Earth3$_{\text{p1}}$ version (see Table 6 in Döscher et al. (2022)). Note, that the reported 4.2×10^{-5} for *RLCRITSNOW* in EC-Earth3$_{\text{p1}}$ in this Table 6 in Döscher et al. (2022) is incorrect and should have been 4.0×10^{-5}, as in Table 2.8.

Pragmatic approach despite link between bias and microphysics

Though it would be preferable to follow an approach in which a set of tuning parameters and adjustments are determined that reduce the biases over the Southern Ocean without affecting the Northern Hemisphere negatively, we have chosen a pragmatic approach to reduce the two main practical issues we are facing, being a cold NH bias associated to a large AMOC variability, despite the fact that we recognize that the considered tuning parameters are also linked to the underlying causes of the bias itself.

2.3.2 The KNMI'23 pre-industrial control retuning simulation

The spin-up history

For the spin-up and pre-industrial control simulations, the CMIP piControl experiment setup of the CMIP6 Diagnostic, Evaluation and Characterization of Klima (DECK) (Eyring et al., 2016) protocol is followed. For details see (Döscher et al., 2022; ES-DOC/EC-Earth3, 2023).

Table 2.9 lists the spin-up ancestor history of the until the point at which the Initial Conditions (ICs) have been created from the KNMI'23 pre-industrial control (piControl) run; it shows the branching from parent experiments including the branching year.

experiment	period	exp. ID	p-index	parent ID & branch year
spin-up	2160-2760	t264	p1	eveg at 1850
spin-up	1850-3849	rtc2	p2	t264 at 2760
piControl	2750-4585	rtc5	p5	rtc2 at 2750
piControl	2850-4585	rt5b	p5	rtc2 at 2850
create ICs		ir5a	p5	rtc5 at 4000, 4025, .. 4550
create ICs		ir5b	p5	rtc5 at 4000, 4025, .. 4550

Table 2.9: The Dutch Climate Scenario (*KNMI*23) pre-industrial control (piControl) experiments. The last 600 years of the rtc5 run is used as the actual piControl run for the *KNMI*23 project; the ICs are sampled from that last 600 year interval with a 25 year frequency (see Fig. 2.41).

A compact data request for the retune spin-up simulations

For the long spin-up retuning experiments we have constructed a suitable light weight compact data request which considerably reduces the I/O costs and the stored data volume. With that compact request we are able to achieve 20 simulated year per day. A substantial amount of computing resources has been used for the retuning simulations, in total about 11 thousand simulated years with limited data storage: only monthly climatological data has been saved.

The KNMI'23 initial conditions

Fig. 2.41 shows the last 600 year of the 1835-year long rtc5 spin-up / piControl run for the global mean of Near-Surface Air Temperature. The initial conditions (ICs) for the KNMI'23 historical simulations are created from this last 600-year rtc5 run. In red the 16 used ICs for the 16 KNMI'23 ensemble members are indicated, the circles show the actual picked state. In purple a few reserve

ICs are indicated, they have not been used. The number designated to each IC corresponds with the ensemble member that is used for specifying ***r*** (***r***ealisation index) in the CMOR ***ripf*** label (see Sect. 2.3.1). Fig. 2.41 shows that the IC states are well spread with respect to the global mean temperature record of this piControl run.

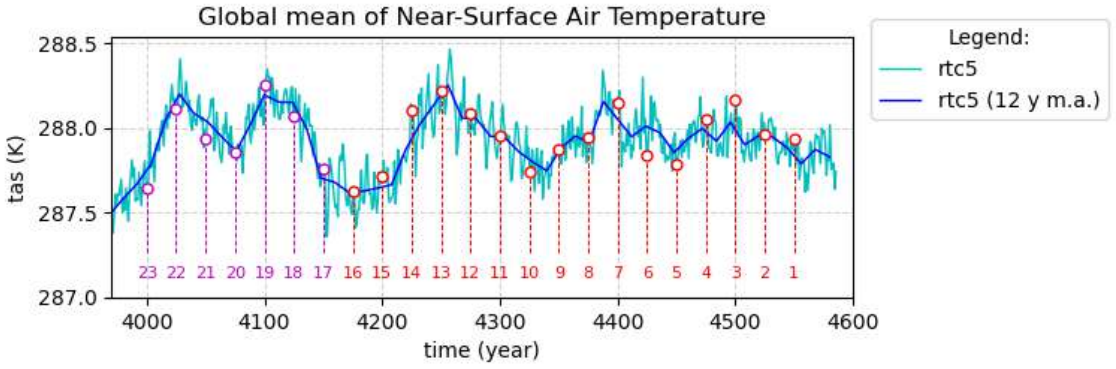

Figure 2.41: The global mean of Near-Surface Air Temperature (tas) produced by the piControl rtc5 simulation which uses the p5-set of retuned parameters, for the interval in which all KNMI'23 ICs are created for the KNMI'23 historical members (member numbers in figure).

2.3.3 The KNMI'23 ensemble

The KNMI'23 ensemble description

For the historical simulation the CMIP historical experiment setup of the DECK (Eyring et al., 2016) protocol is followed. The scenario simulations, ssp119 (SSP1-1.9) ssp126 (SSP1-2.6), ssp245 (SSP2-4.5), ssp370 (SSP3-7.0) & ssp585 (SSP5-8.5) follow the ScenarioMIP (O'Neill et al., 2016) protocol. For details see (Döscher et al., 2022; ES-DOC/EC-Earth3, 2023).

Table 2.10 provides an overview of the KNMI'23 ensemble. EC-Earth experiments use four characters as identification (ID). In the KNMI'23 ensemble the last two characters are reserved for the member number ranging from 01 until 16, while the first two characters are reserved for a short experiment label, for instance **ha** labels the **h**istorical experiment which is a continuation of a first retune experiment (rtc5) which uses the p5 parameter set from which initial conditions (ICs) have been created in ir5**a** (this in contrast to ir5b which is based on a second member rt5b which uses the same p5 set).

experiment	period	ensemble size	exp. IDs	member until 2301
historical	1850-2014	16 members	ha01-ha16	
SSP1-1.9	2015-2167	6 members	s001-s006	s001
SSP1-2.6	2015-2167	16 members	s101-s116	s101
SSP2-4.5	2015-2167	16 members	s201-s216	s201
SSP3-7.0	2015-2167	16 members	s301-s316	s301
SSP5-8.5	2015-2167	16 members	s501-s516	s501

Table 2.10: The Dutch Climate Scenario ($KNMI23$) ensemble of historical & SSP simulations. Except for SSP1-1.9 which has 6 members, all other $KNMI23$ ensembles have 16 members.

The data request for the KNMI'23 ensemble and a description how and where it is archived can be found in Appendix A. In total, the KNMI'23 ensemble consists of 14 thousand years of simulation.

The forcing beyond 2100

We continued the SSP-simulations until the year 2167, after SMHI at our request had extended one member of their EC-Earth3-Veg simulations until 2167 (later they continued the simulation

even until 2300) in order to provide the ICMCL files containing the vegetation forcing fields (#984) for all scenarios. Forcing data for GHG are available for all SSPs until 2300, and following the ScenarioMIP protocol, all other atmospheric forcings (aerosol, ozone, etc) have been kept constant at the 2100 level. The 2100 state of the Land Use Harmonization (LUH2) forcing dataset is used after 2100 because that is the latest available record. The colleagues from Lund confirmed that this has only a minimal effect while it provides consistency across the scenarios as availability of land use differs among the scenarios.

Production of the KNMI'23 ensemble

The data request for the KNMI'23 ensemble is shown in Listing A.1 in Appendix A.

A production branch for the KNMI'23 EC-Earth3$_{p5}$ ensemble runs is created within the EC-Earth svn repository:

```
https://svn.ec-earth.org/ecearth3/branches/projects/knmi23-dutch-climate-scenarios
```

The EC-Earth portal issue #907 describes the development of this production branch.

Part of the workflow is that for each member of the ensemble and for each experiment we do a checkout of the run-platform (the submit environment) whereafter via the *set-ensemble-member-changes.sh* script the experiment and member specific configuration is determined for EC-Earth. Moreover, these submit directories contain also the cmorisation configuration for each experiment - member combination for ece2cmor3. All submit directories have been archived. The yearly written restart files in EC-Earth3 do, unfortunately, not guarantee a bitwise identical result if the run is continued more than one year after the restart, therefore the "save_ic" option is configured in the EC-Earth KNMI'23 runs such that at 10-year intervals and in a few special years (1949, 2015 & 2165) initial conditions (ICs) are written. With these ICs bitwise identical results can be guaranteed over the entire time integration as long as the same computing platform and the same number of cores per component are used. These ICs also allow a restart on other platforms and/or the use of a different number of cores per component. Though the results won't be bitwise identical in that case, the same ensemble climate is guaranteed. Once an experiment has been completed and the cmorisation has finished, an extensive technical validation procedure follows. After a successful completion of the validation, a *sha256 checksum* of that member is computed.

2.3.4 Comparing the EC-Earth3 retuned and CMIP6 versions with ERA5

The piControl compared to ERA5

In order to judge the results of the retuned pre-industrial (piControl) simulation, we compare them with an estimate of the ERA5 Near-Surface Air Temperature for pre-industrial. This estimate has been constructed by taking the ERA5 1979-1989 mean and applying a latitude-only depending correction based on a fit to the GISTEMP dataset (Lenssen et al., 2019; GISTEMP Team, 2023) which is shown in Fig. 2.42 including the fit function and the parameter values.

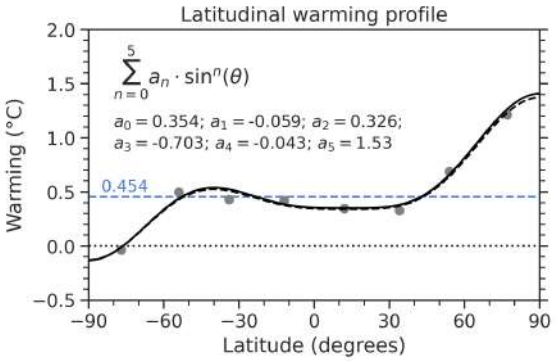

Figure 2.42: Fit to the GISTEMP data that have been used in applying a latitude correction to the ERA5 data in order to derive an ERA5 estimate for the pre-industrial state.

The left and right panel in Fig. 2.43 show *tas* for EC-Earth3$_{\text{p1}}$ (500 year mean) and for EC-Earth3$_{\text{p5}}$ (1000 year mean) of the piControl simulations relative to the ERA5 piControl estimate. It clearly shows a reduction of the NH cold bias for the retuned EC-Earth3$_{\text{p5}}$ version. In particular, the KEXT12 RACMO domain (see Fig. 2.40) area show very small temperature biases for the retuned p5 version. As expected, the warm bias in the Southern Hemisphere is also considerably increased in the retuned version.

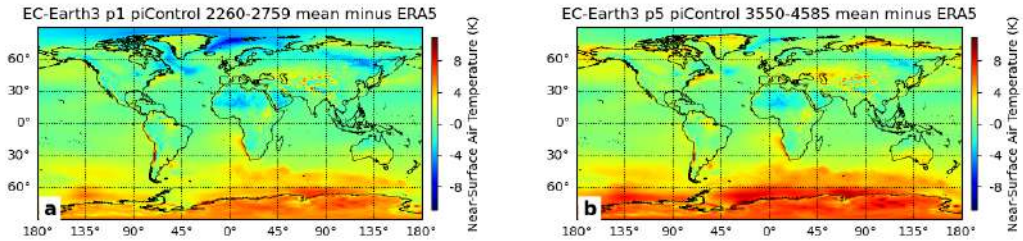

Figure 2.43: The Near-Surface Air Temperature (*tas*) relative to the ERA5 piControl estimate for the piControl simulations of a) EC-Earth3$_{\text{p1}}$ (500 year mean) and b) EC-Earth3$_{\text{p5}}$ (1000 year mean).

In Fig. 2.44 the zonal mean (left panel) and the zonal mean relative to the ERA5 piControl estimate (right panel) curves for *tas*, show the warming effect at the NH and the warming at the SH for EC-Earth3$_{\text{p5}}$ compared to EC-Earth3$_{\text{p1}}$ and compared to the CMIP6 EC-Earth3-Veg simulation. The latter is even considerably colder at the NH. As a reference, results from other CMIP6 models have been plotted in gray in the background. The ERA5 (1979-1989) without the GISTEMP correction is plotted in purple as a reference as well. These type of figures (Fig. 2.38 and Figs. 2.43-2.44) have been guiding the retuning. With the target to get the red EC-Earth3$_{\text{p5}}$ line around zero for the NH and for the Europe latitude in particular.

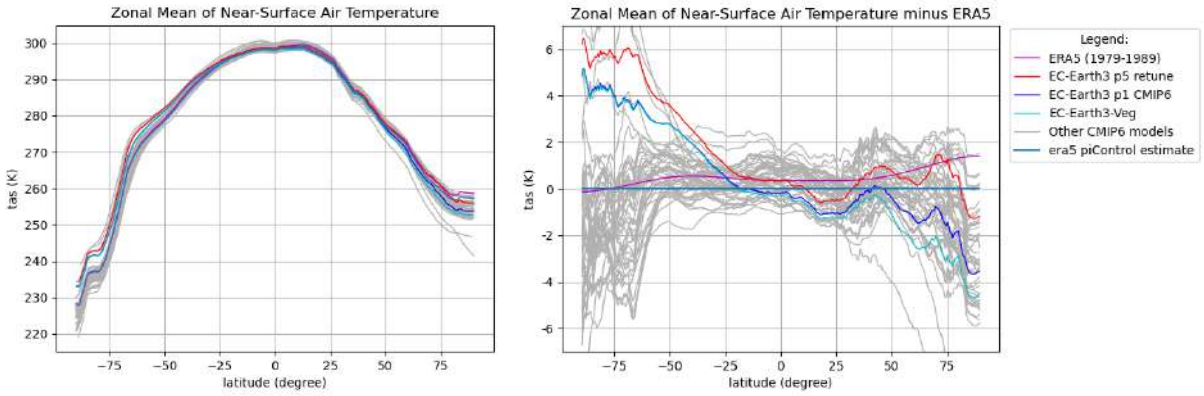

Figure 2.44: The figure shows the zonal mean *tas* (left panel) and the zonal mean *tas* relative to the ERA5 piControl estimate (right panel). The ERA5 piControl estimate is constructed with help of the GISTEMP fit (see Fig. 2.42). The right panel clearly shows the SH warm bias for EC-Earth3, and the cold bias reduction at the NH with EC-Earth3$_{\mathrm{p5}}$.

Historical EC-Earth3 p1 & p5 ensembles compared with ERA5

Fig. 2.45 contains the global mean Near-Surface Temperature for all historical and SSP members of the KNMI'23 ensemble as listed in Table 2.10, and labeled by their experiment ID. Fig. 2.45 shows that the ensemble spread reduces in time, but it mainly reduces when global mean temperature is increasing, in line with our expectation and retune rationale.

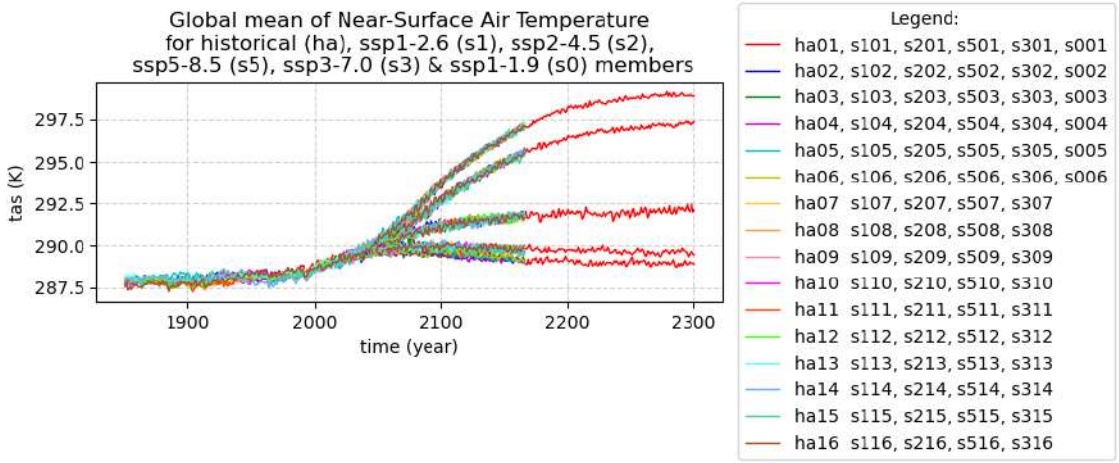

Figure 2.45: The global mean of Near-Surface Air Temperature (tas) of all KNMI'23 ensemble members, labeled by their experiment IDs. After year 2167 only the first member of each scenario (s001, s101, s201, s301 & s501) has been continued (shown in red) until year 2301 with a reduced data request (monthly output only).

The EC-Earth3$_{\mathrm{p5}}$ and EC-Earth3$_{\mathrm{p1}}$ available ensembles consisits of 16 and 19 ensemble members respectively. Because of their similar size, they can be used for comparison purpose. The variability in the ensemble of global mean *tas*, shown in Fig. 2.46 by the shaded areas between the ensemble p0-p100, p10-p90 and p25-p75 percentiles, is reduced for the EC-Earth3$_{\mathrm{p5}}$ version compared to EC-Earth3$_{\mathrm{p1}}$. This confirms that the likelihood of transitioning into the cold and low convective state is reduced towards the end of the historical period. However, Fig. 2.46 also shows

that for EC-Earth3$_{p5}$ a rather large variability continues to be present until about 1970. This indicates that transitions to the low convective state did still occur in the historical simulations, while ideally the retuning would have caused this state to be entirely absent right from the start of the historical runs. Furthermore, Fig. 2.46 indeed clearly shows that the global mean temperature of the retuned version EC-Earth3$_{p5}$ is about one degree higher than the reference simulation, a drawback we accepted on forehand.

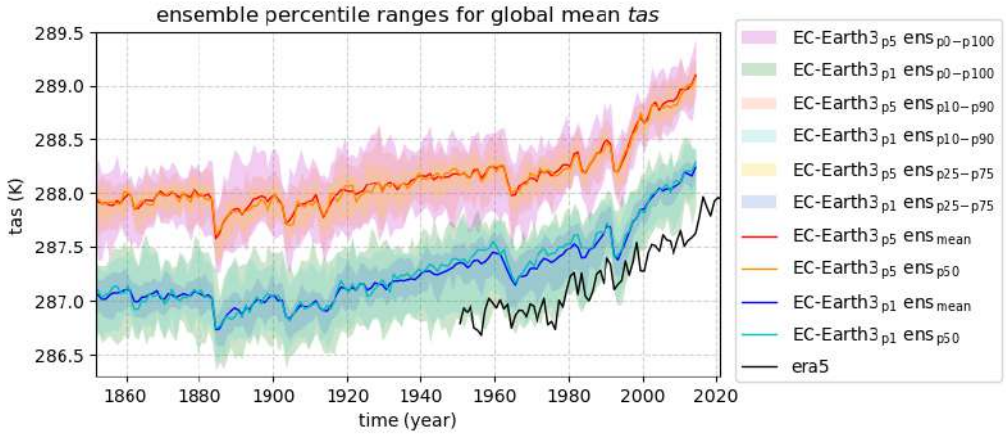

Figure 2.46: The amplitude in global mean *tas* has been reduced for the historical ensemble with the EC-Earth3$_{p5}$ version; c.f. the p0-p100, p10-p90 and p25-p75 shaded percentile ranges of both versions.

A decrease in the ensemble range (ρ) and ensemble standard deviation (σ) of the EC-Earth3$_{p5}$ global mean *tas* compared to EC-Earth3$_{p1}$ is visible in Fig. 2.47 between 1950-2000, especially when the 20 year running mean is plotted. Where ρ (t) equals the ensemble maximum minus the ensemble minimum as a function of time.

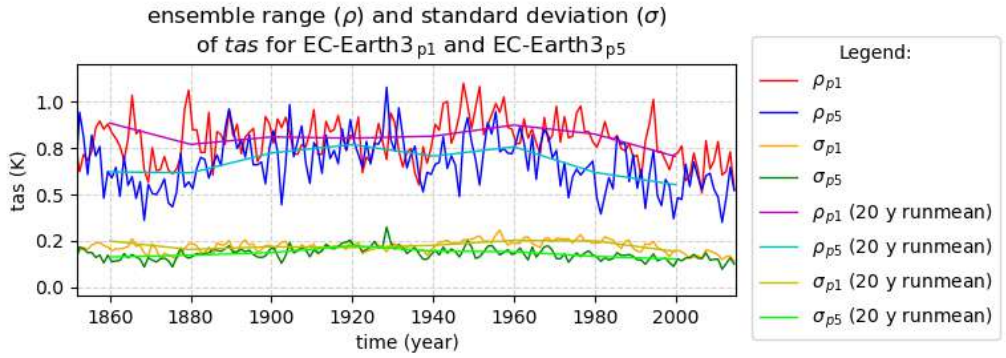

Figure 2.47: The ensemble range for EC-Earth3$_{p5}$ (ρ_{p5}) and the standard deviation for EC-Earth3$_{p5}$ (σ_{p5}) of the global mean *tas* are both reduced compared to ρ_{p1} and σ_{p1}, the ones for EC-Earth3$_{p1}$. The 20 year running means are plotted as well for convenience.

The percentage fraction of (the yearly data of) ρ and σ for EC-Earth3$_{p5}$ with respect to EC-Earth3$_{p1}$ are given here by

$$f_\rho = 100\,\frac{\rho_{p5}}{\rho_{p1}} \qquad \& \qquad f_\sigma = 100\,\frac{\sigma_{p5}}{\sigma_{p1}} \tag{2.3}$$

and the 12-year running mean of both f_ρ and f_σ are shown in Fig. 2.48. Both, f_ρ and f_σ, show a substantial reduction of the ensemble variability, certainly for the essential part from 1950-2000 where for instance f_σ shows a $20-35\%$ reduction with the EC-Earth3$_{\rm p5}$ version. Note that an increase towards 100% of the fractions is expected from 2010 onwards because thereafter the EC-Earth3$_{\rm p1}$ version shows a reduced variability itself (see Fig. 2.47).

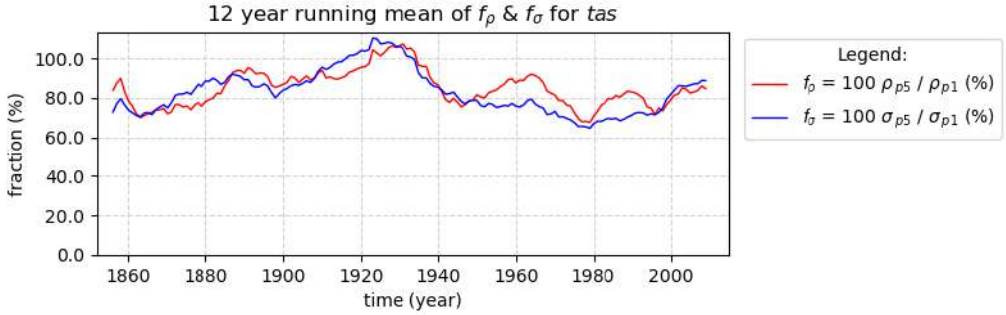

Figure 2.48: The 12-year running mean of the fractions f_ρ (red) and f_σ (blue) of global mean *tas*. It thus concenrs the fraction of the Fig. 2.47 curves for ρ and σ respectively.

Fourteen of the KNMI'23 members do not enter into a low convective state in the Labrador Sea after 1950, while none of them do this after 1975; the same applies to the cold global mean *tas* excursions. In Fig. 2.49 the time records of the ocean mixed layer thickness for the spatial mean in two Labrador Sea sections (see Fig. 2.39) are shown for two historical members. The first member (ha01) shows a typical episode in which the deep convection is absent, while the second member (ha02) has not encountered such an episode during the entire run.

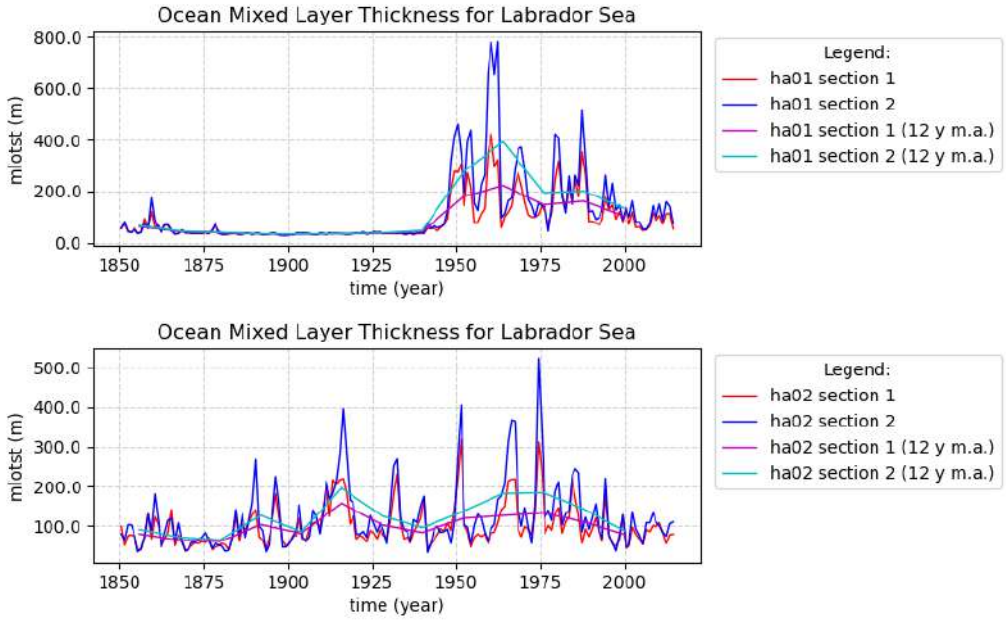

Figure 2.49: The Ocean Mixed Layer Thickness (*mlotst*) which is averaged over two Labrador Sea sections (see Fig. 2.39), is shown for two members. Member 01 shows an episode of absence of the deep convection in the Labrador Sea while member 02 did encounter such an episode during the entire historical period.

Figs. 2.50-2.56 show the ensemble mean for the 1991-2020 climatology, the season record relative to ERA5, the season record and the 1991-2020 mean for EC-Earth3$_{p5}$ & EC-Earth3$_{p1}$ for a number of variables and areas that are listed in Table 2.7. For a given variable, the climatology and season plots are produced with equal scaling across areas. The Europe, KEXT12 & NL+ area selections are shown in Fig. 2.40.

Fig. 2.50 and Figs. B.1-B.5 in the appendix show that the Near-Surface Air Temperature (*tas*) has improved for EC-Earth3$_{p5}$, the cold bias for the NH areas has been reduced and nearly vanished (see Fig. B.2). The captions describe this in more detail. The SH deteriorates (and is even warmer) for EC-Earth3$_{p5}$. These figures confirm that the aim of the retuning has been achieved.

The Surface Downwelling Shortwave Radiation (*rsds*) is rather similar for EC-Earth3$_{p5}$ and EC-Earth3$_{p1}$ and both overestimate ERA5 (most in NH summer) as shown in Fig. 2.51 and Figs. B.6-B.7 in the appendix. EC-Earth3$_{p1}$ is sligtly closer for NH spring, while EC-Earth3$_{p5}$ is slightly closer for NH autumn. All NH selections allign with this picture.

The Water Vapor Path (*prw*) has improved in EC-Earth3$_{p5}$ for all NH selections as illustrated in Fig. 2.52 compared to EC-Earth3$_{p1}$, and ended up closely to ERA5. In agreement with the fact that the water content increases by about 7% for per degree warming.

In general the Near-Surface Relative Humidity (*hurs*) is rather similar for EC-Earth3$_{p5}$ and EC-Earth3$_{p1}$ compared to their difference with ERA5, which is illustrated in Fig. 2.53 for the Europe selection. For both the KEXT12 and Europe selection EC-Earth3$_{p5}$ and EC-Earth3$_{p1}$ overestimate ERA5 in NH spring, while underestimating ERA5 in NH autumn. For other area selections this picture with respect to ERA5 is not exactly the same.

In general the Precipitation (*pr*) is rather similar for EC-Earth3$_{p5}$ and EC-Earth3$_{p1}$ compared to their difference with ERA5 for the NH selections, as shown by Fig. 2.54 and Figs. B.9-B.12 in the appendix. EC-Earth3$_{p5}$ and EC-Earth3$_{p5}$ underestimate ERA5 during NH summer and autumn for the area around Europe, though this shifts towards spring and summer for the NH as a whole.

As shown by Fig. 2.55 both EC-Earth3$_{p5}$ and EC-Earth3$_{p1}$ are similar for Near-Surface Wind Speed ($sfcWind$) and overestimate ERA5, where EC-Earth3$_{p5}$ is slightly lower and thus closer to ERA5. This applies to all NH selected areas.

The Sea-Ice Area Percentage (on Atmospheric Grid) (*siconca*) for the NH obtained with the retuned version is clearly closer to ERA5 than the result from the CMIP6-version, while almost equal for the SH (see Fig. 2.56 and Figs. B.13-B.14 in the appendix). The increase in NH sea-ice (in the correct direction, though limited) with EC-Earth3$_{p5}$ can be considered remarkable because the retuning implied a NH warming. An explanation might be that when the deep convection in the Labrador Sea is recovered, this prevents heat transport more north with the result that the sea-ice concentrations around the Arctic become more realistic again.

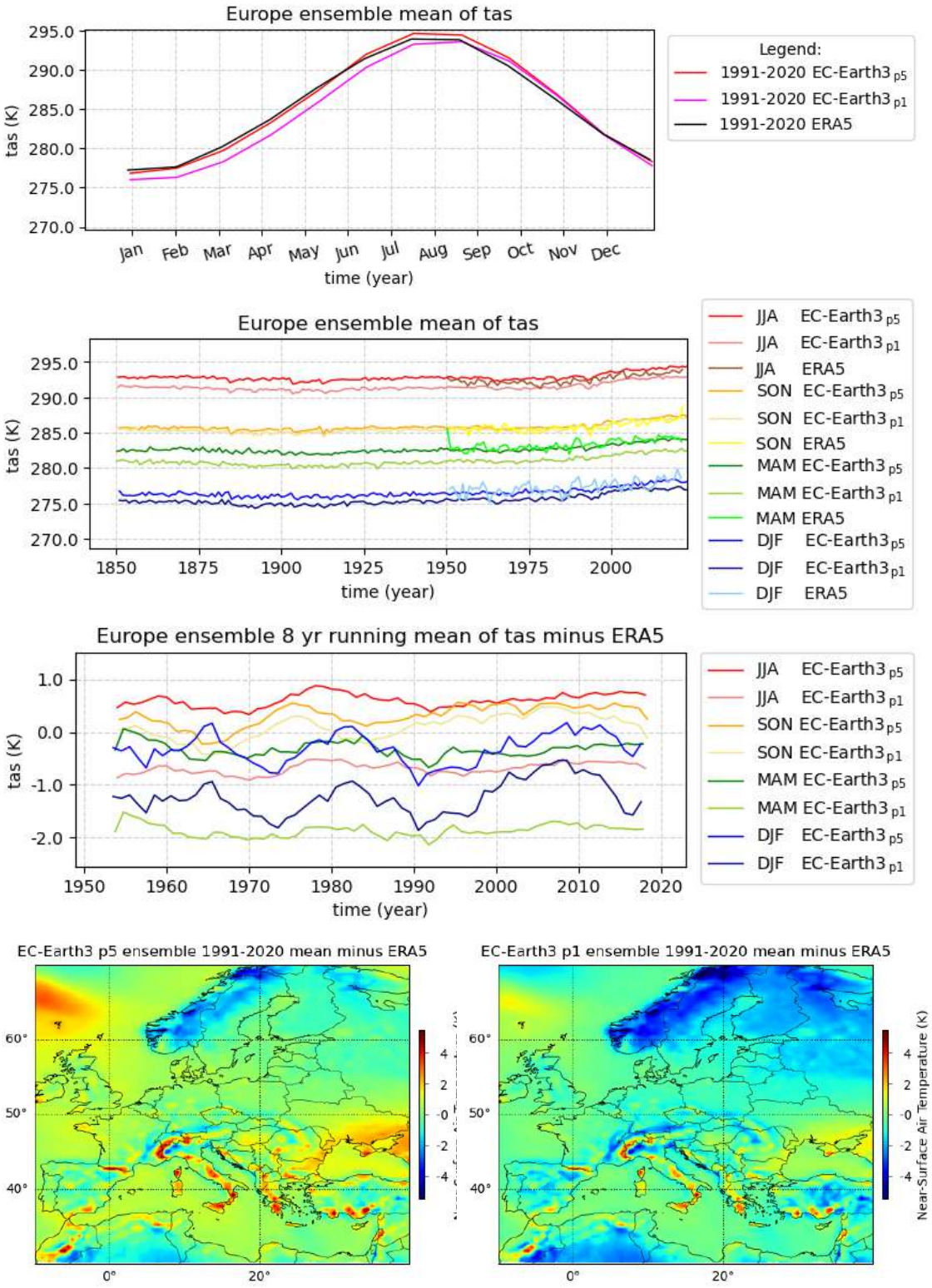

Figure 2.50: Near-Surface Air Temperature (**tas**) for **Europe**. The ensemble mean for the **1991-2020** climatology, the season record relative to ERA5, the season record and the 1991-2020 mean for p5 & p1. Observations: MAM & DJF warmer and closer to ERA5 with p5 (for AS p1 bit closer to ERA5, JJA overcorrected). The NH has improved with p5, while as expected, the SH deteriorates (even warmer) for p5. Tuning aim confirmed.

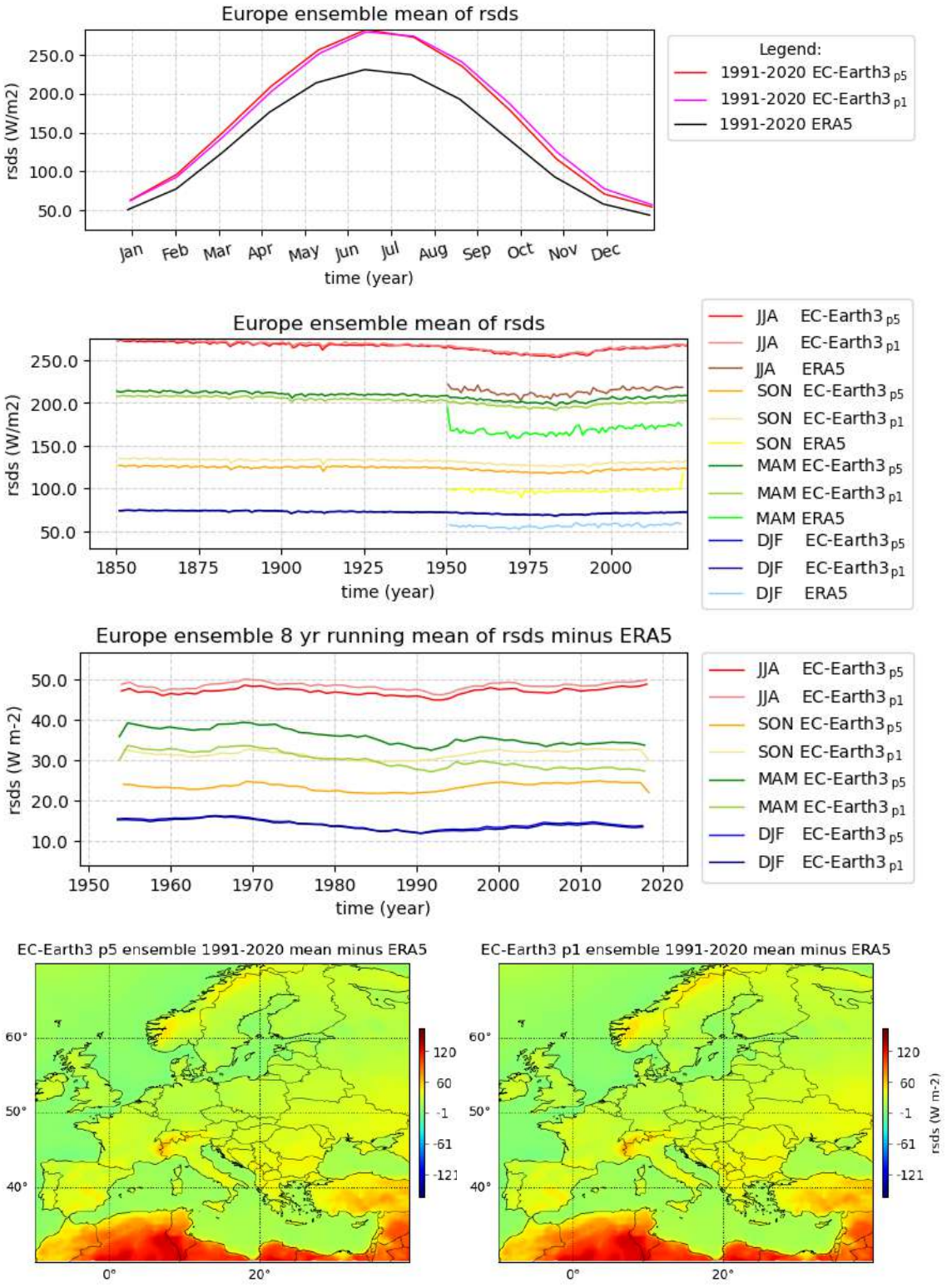

Figure 2.51: Surface Downwelling Shortwave Radiation (**rsds**) for **Europe**. The ensemble mean for the **1991-2020** climatology, the season record relative to ERA5, the season record and the 1991-2020 mean for p5 & p1. Observations: Both p5 & p1 are similar and overestimate ERA5 (most in NH-summer). For MAM p1 is sligthly closer to ERA5. For ASOND p5 is sligthly closer to ERA5.

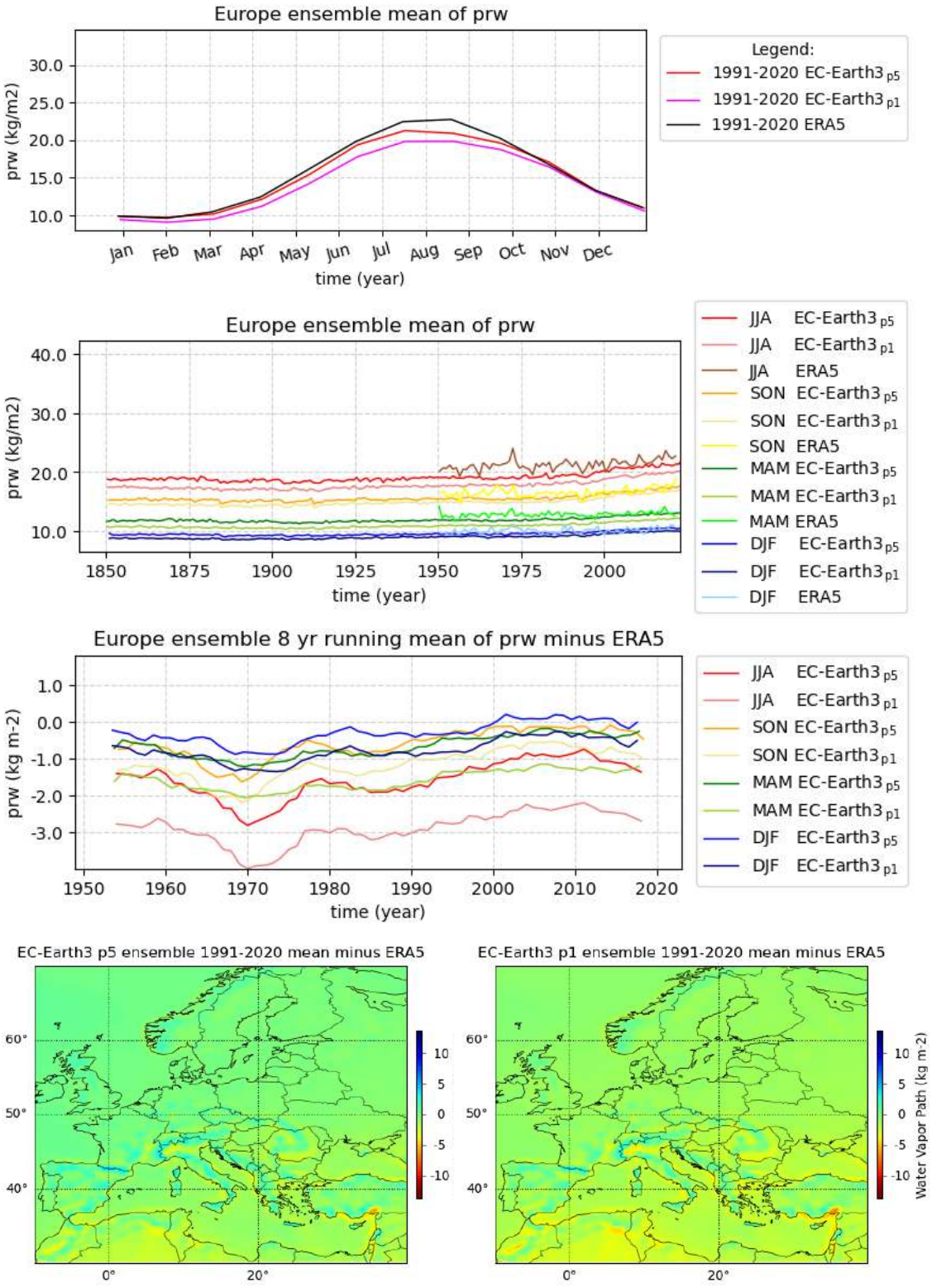

Figure 2.52: Water Vapor Path (**prw**) for **Europe**. The ensemble mean for the **1991-2020** climatology, the season record relative to ERA5, the season record and the 1991-2020 mean for p5 & p1. Observations: NH, N30-70, Europe, KEXT12 & NL+ are closer to ERA5 with p5.

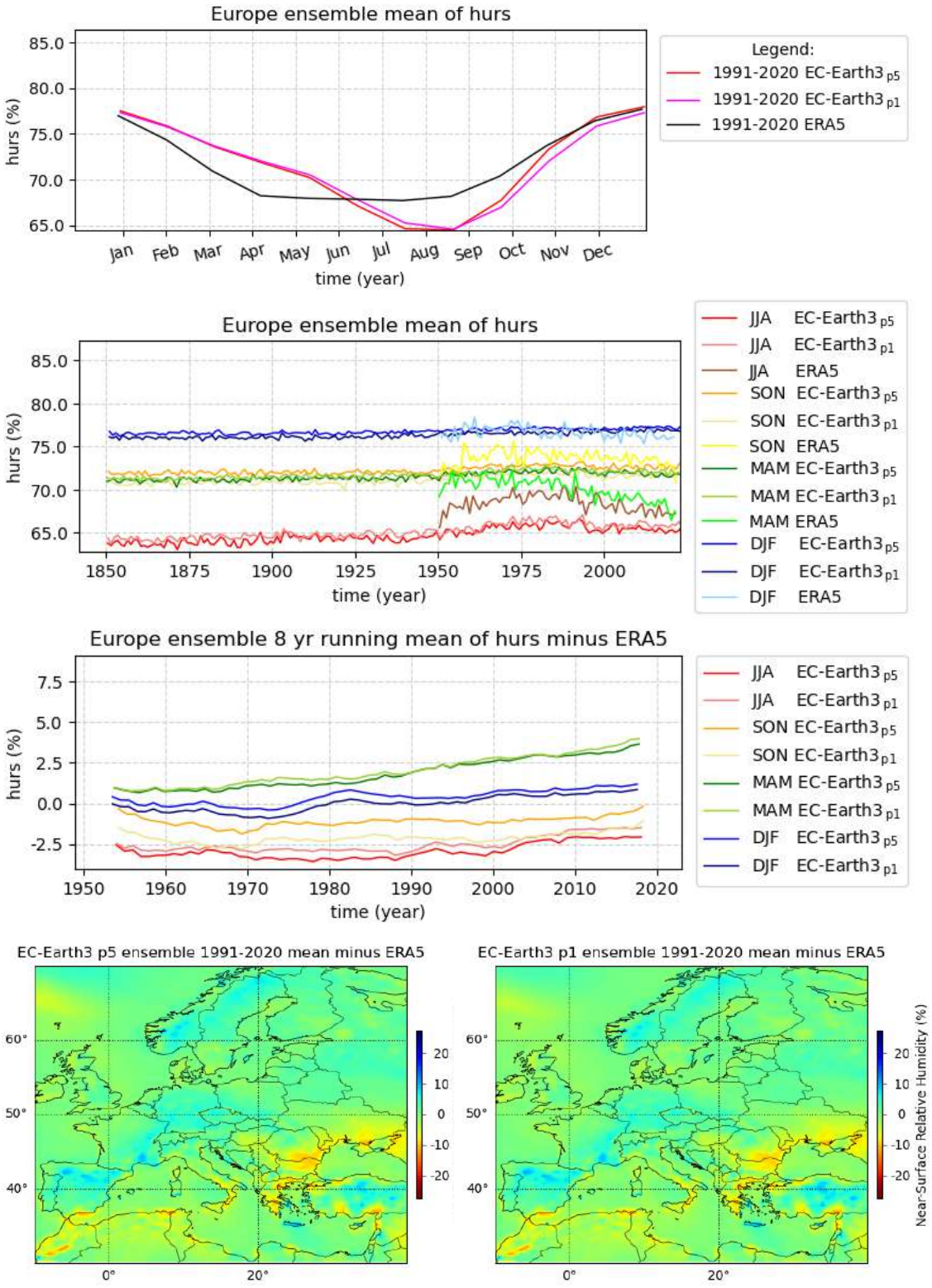

Figure 2.53: Near-Surface Relative Humidity (**hurs**) for **Europe**. The ensemble mean for the **1991-2020** climatology, the season record relative to ERA5, the season record and the 1991-2020 mean for p5 & p1. Observations: Both p5 & p1 are rather similar and overestimate ERA5 in JFMAM and underestimate JASO. SON slightly improved with p5.

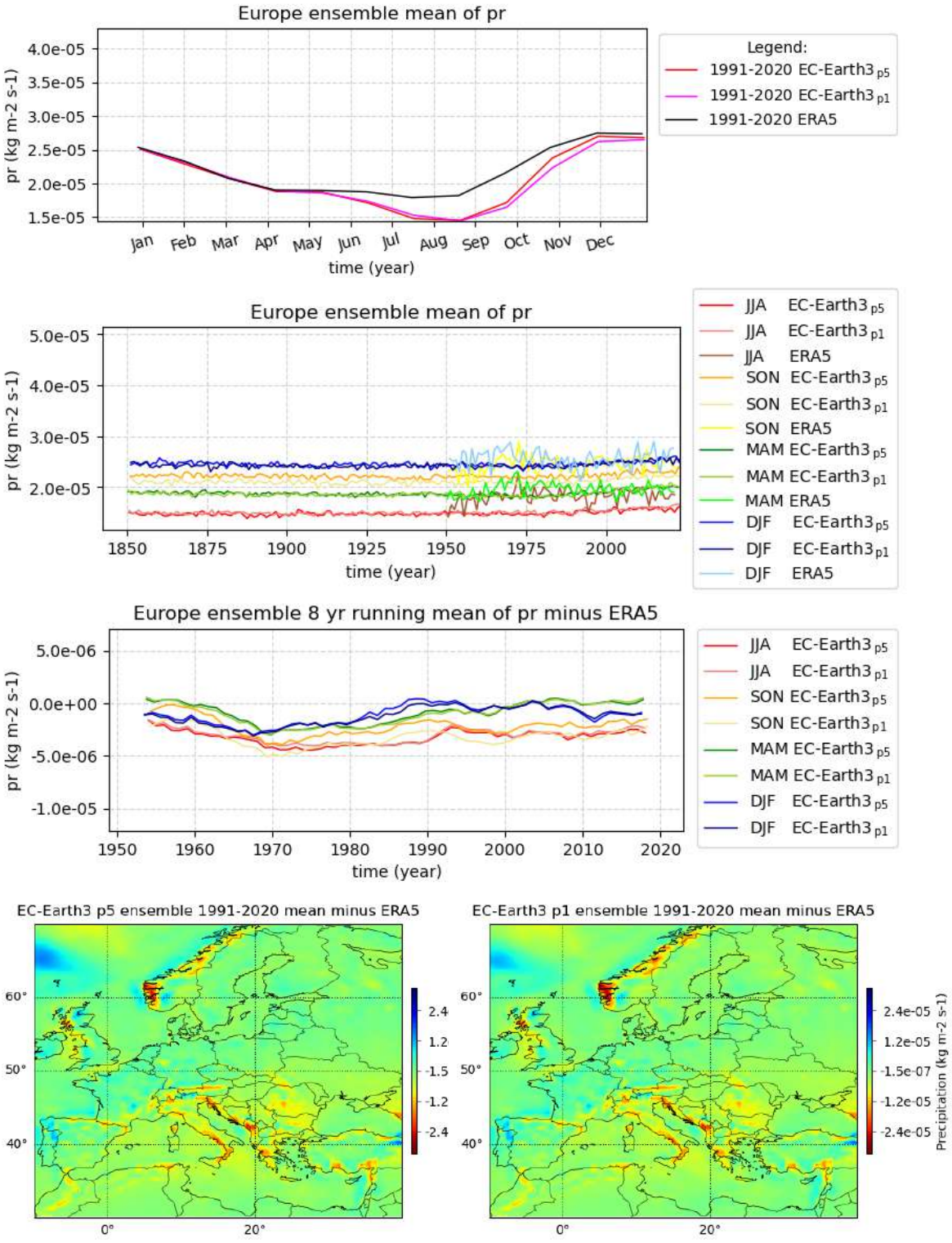

Figure 2.54: Precipitation (**pr**) for **Europe**. The ensemble mean for the **1991-2020** climatology, the season record relative to ERA5, the season record and the 1991-2020 mean for p5 & p1. Observations: For JJASON p5 & p1 underestimate ERA5. For SON p5 is wetter & better (closer to ERA5). For JFMA p5, p1 & ERA are nearly equal.

Note that ERA5 pr is considered less reliable than ERA5 tas.

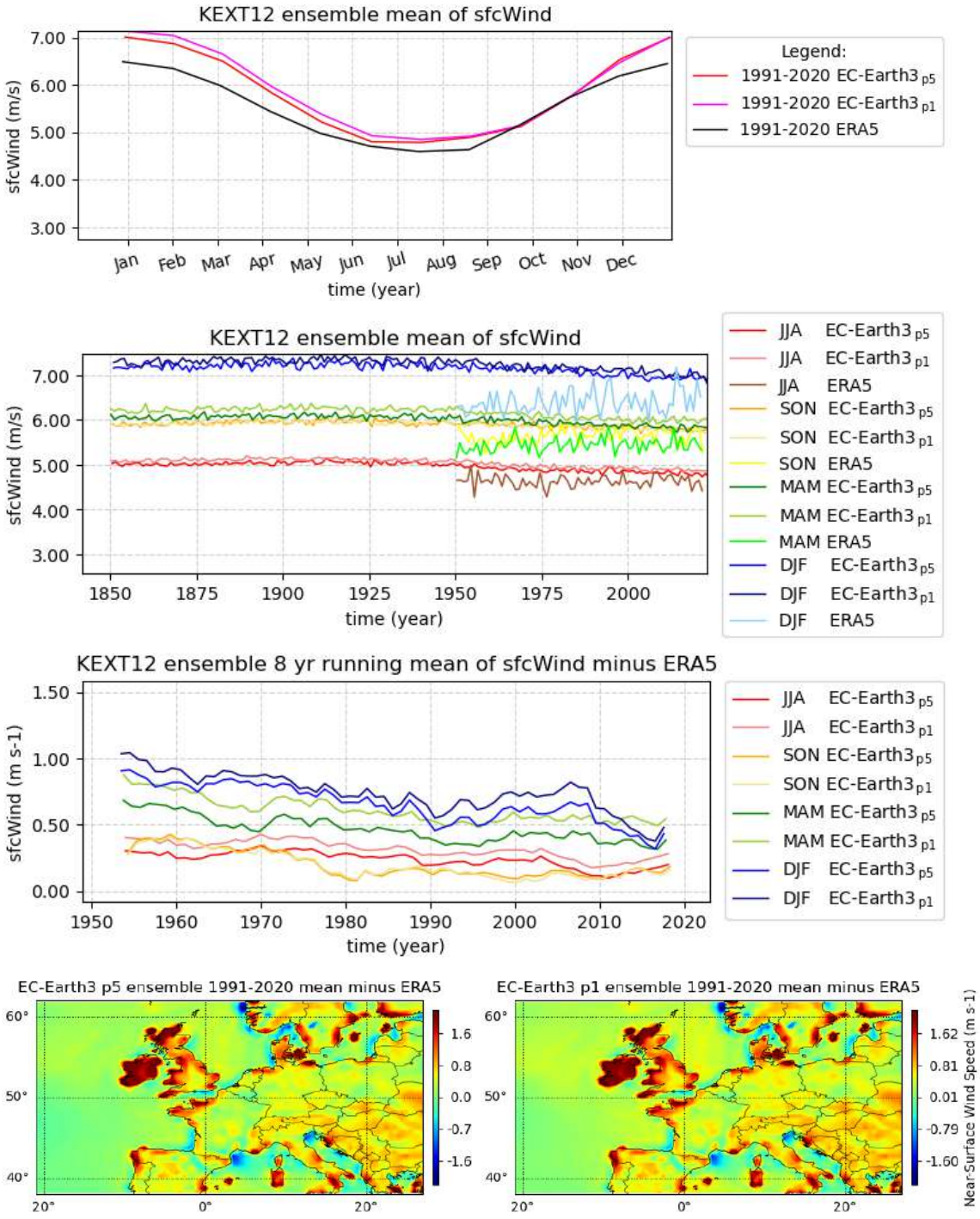

Figure 2.55: Near-Surface Wind Speed (**sfcWind**) for **KEXT12**. The ensemble mean for the **1991-2020** climatology, the season record relative to ERA5, the season record and the 1991-2020 mean for p5 & p1. Observations: Both p5 & p1 are similar and overestimate ERA5, where p5 is slightly lower and thus closer to ERA5.

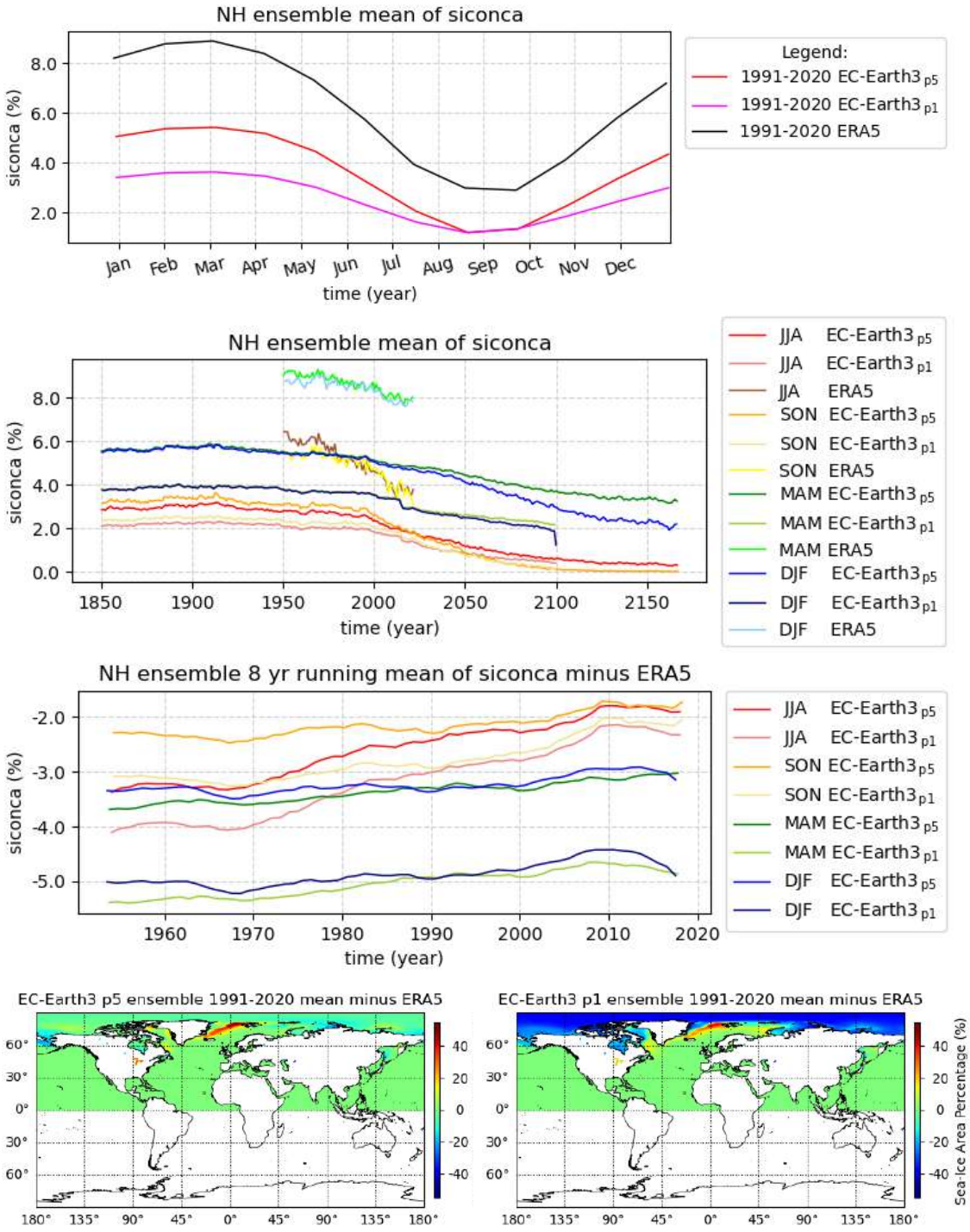

Figure 2.56: Sea-Ice Area Percentage (Atmospheric Grid) (**siconca**) for **NH**. The ensemble mean for the **1991-2020** climatology, the season record relative to ERA5, the season record and the 1991-2020 mean for p5 & p1. Observations: NH is closer to ERA5 and less underestimated with p5. Almost equal for SH.

Remarkable for this warmed NH tuning.

A more exhaustive comparison (more area selections) is provided in Appendix B.

The KNMI'23 ensemble for 2100

The comparison of the historical members (green) with the ERA5 record (black) in Fig. 2.57 clearly illustrates the warm bias of EC-Earth3$_{p5}$ at the Southern Hemisphere: far too warm and the sea-ice extent is much less than observed. So the asymmetry between SH and NH is largely due to the present-day bias in the SH; consequently the warming and sea-ice decline in the SH is less visible in the simulations forced by the future scenarios. For the high-end scenario SSP5-8.5, Fig. 2.57 shows an arctic increase in *tas* of ∼21° C around 2100, while Fig. 2.58 shows an even larger increase of ∼23° C for the Minimum Near-Surface Air Temperature (*tasmin*) and an only slightly lower increase of ∼19° C for the Maximum Near-Surface Air Temperature (*tasmax*) for that area around that time. Note that with Arctic we refer to the change at the North-Pole, not the area-mean north of 60 degree North.

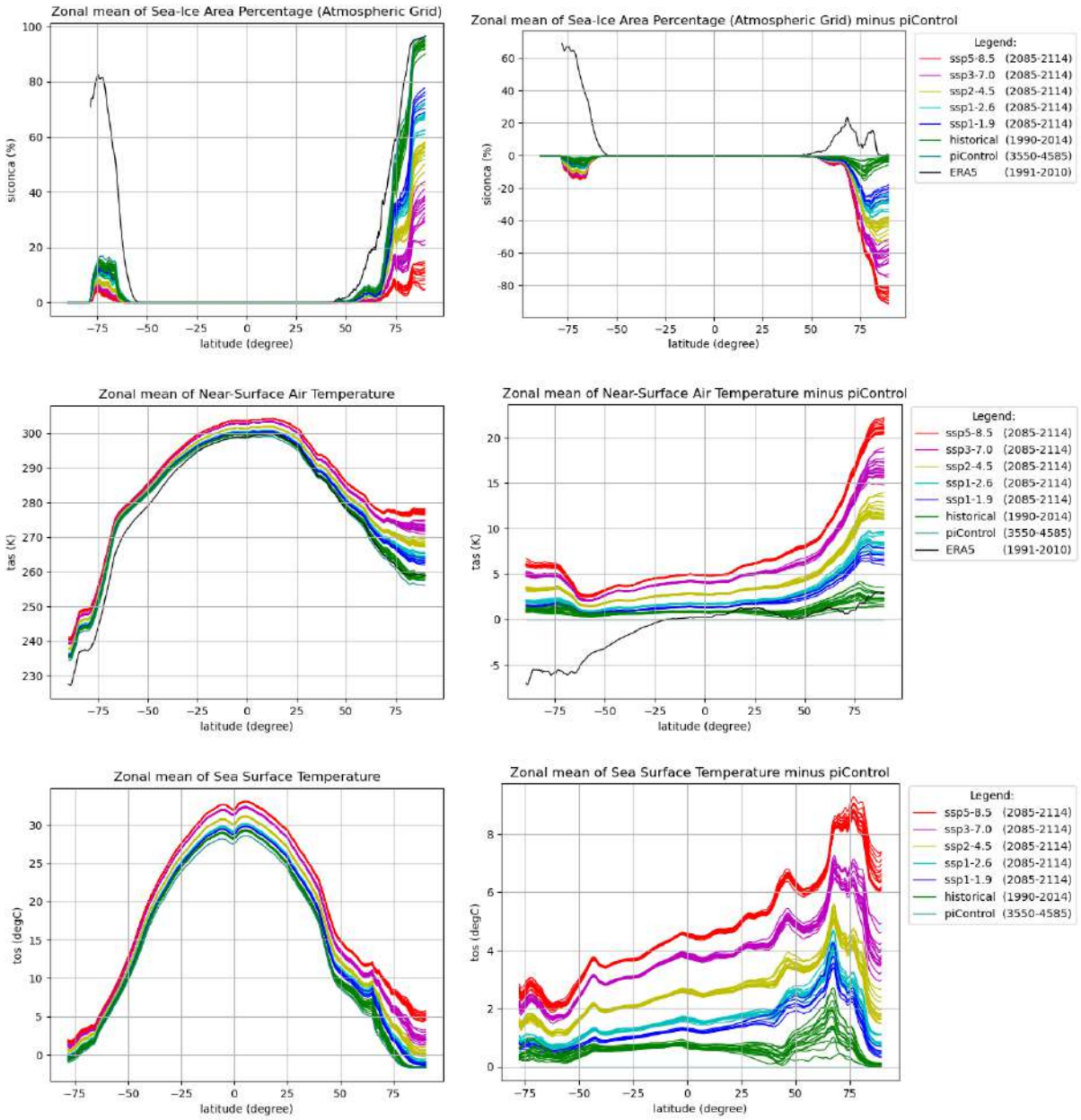

Figure 2.57: Zonal mean (left panels) and zonal mean relative to the pre-industrial level (right panels) of the Sea-Ice Area Percentage (*siconca*), Near-Surface Air Temperature (*tas*) and Sea Surface Temperature (*tos*) from top to bottom for the historical (1991-2020 mean) and the five SSP scenario (2085-2114 mean) ensembles. ERA5 (1991-2010 mean) is shown as reference. A 1000-year mean of the piControl is taken, the start and end time are chosen arbitrarily, because a constant pre-industrial 1850-forcing is applied during the entire experiment.

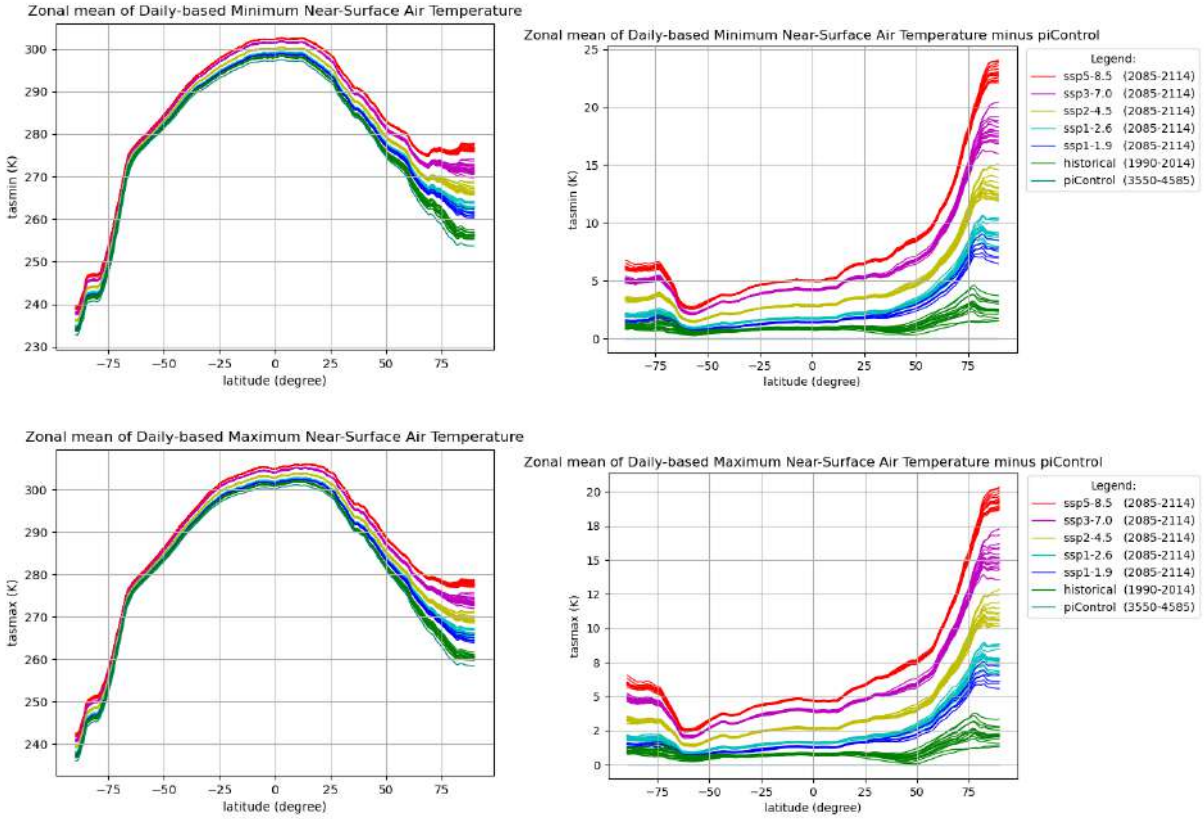

Figure 2.58: Like Fig. 2.57, but for Minimum Near-Surface Air Temperature (*tasmin*) and Maximum Near-Surface Air Temperature (*tasmax*) shown in top and bottom row, respectively.

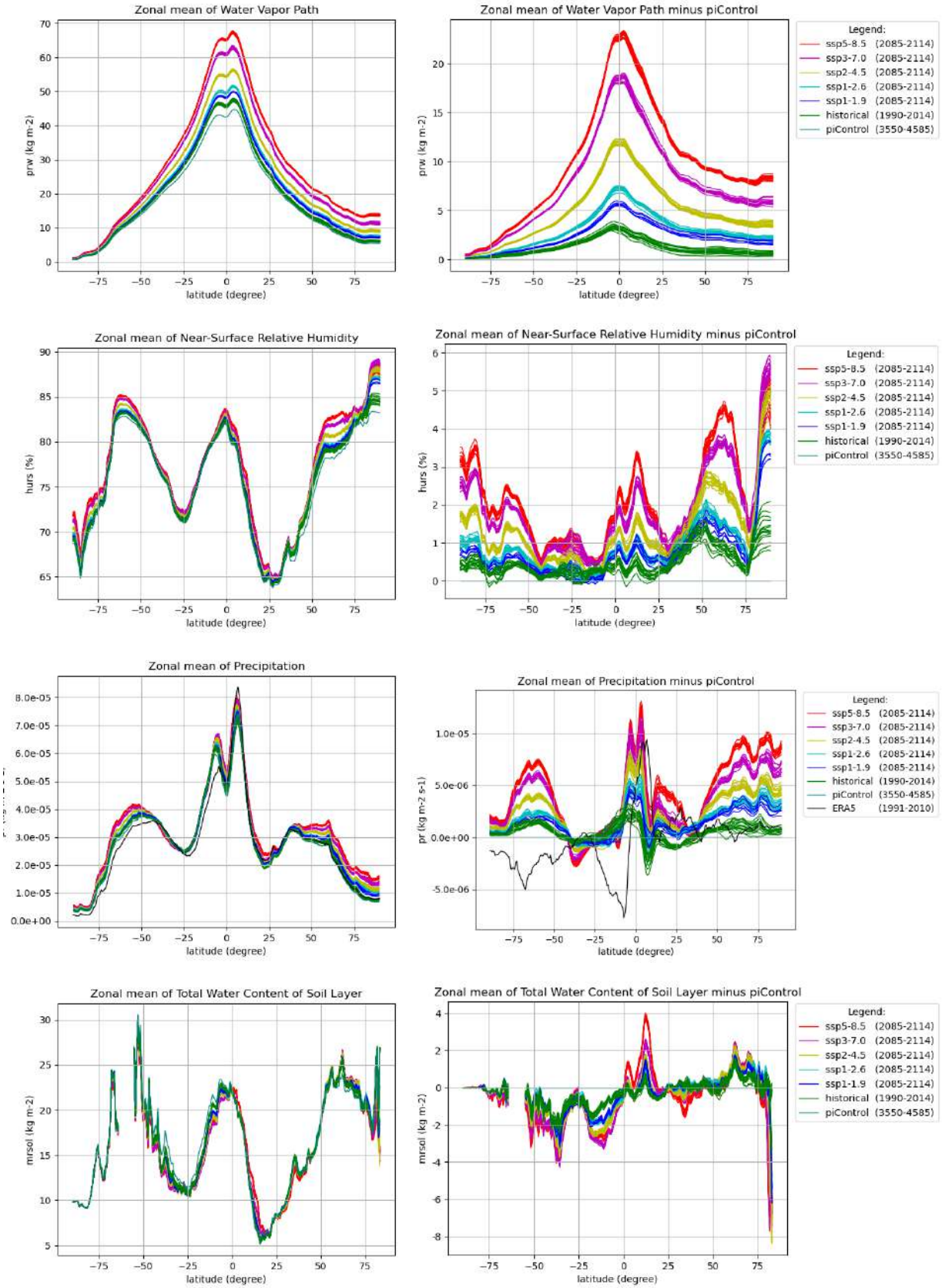

Figure 2.59: Like Fig. 2.57, but for Water Vapor Path (*prw*), Near-Surface Relative Humidity (*hurs*), Precipitation (*pr*) and Total Water Content of Soil Layer (*mrsol*) shown from top to bottom row, respectively.

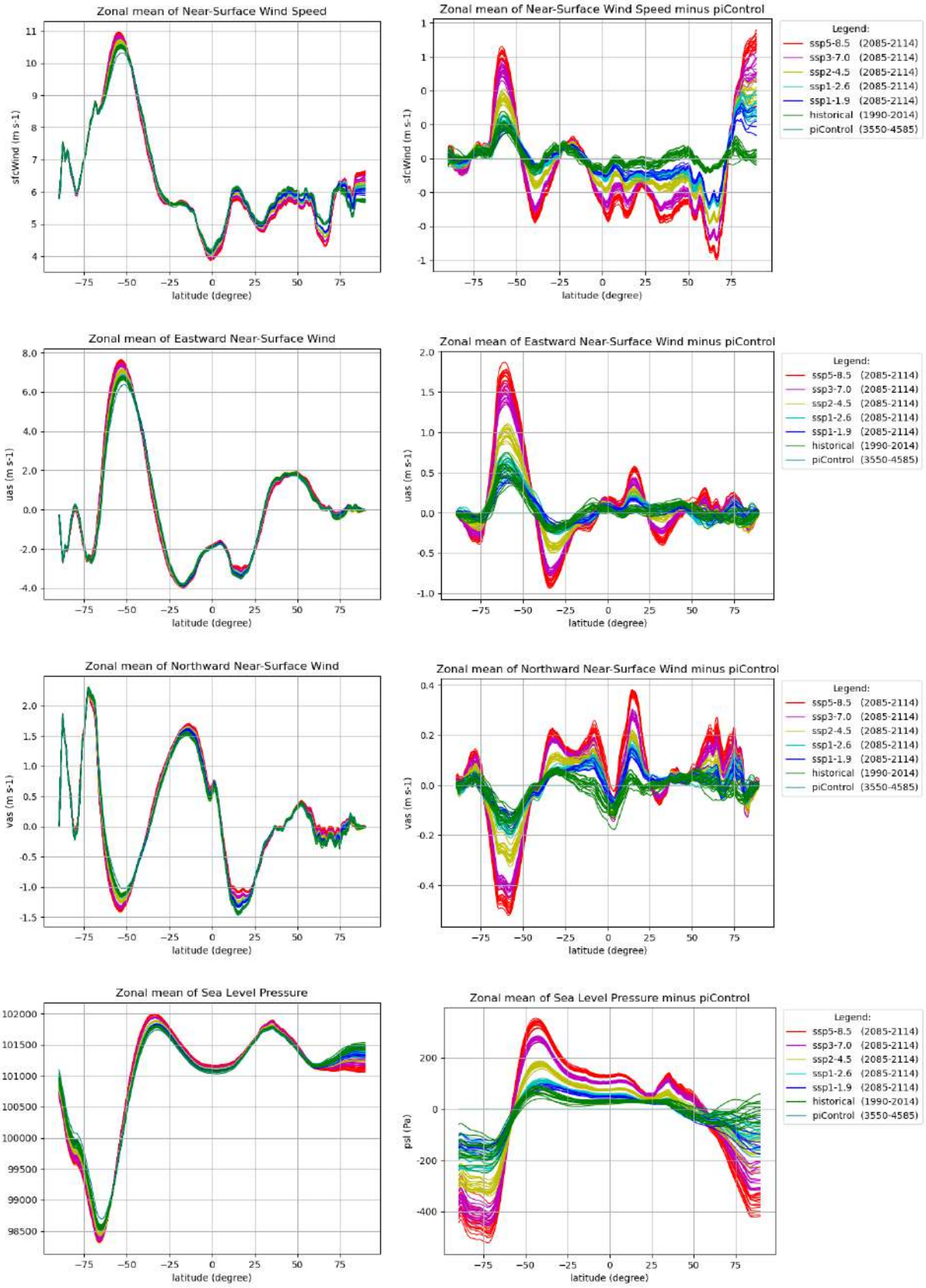

Figure 2.60: Like Fig. 2.57, but for Near-Surface Wind Speed (*sfcWind*), Eastward Near-Surface Wind (*uas*), Northward Near-Surface Wind (*vas*) and Sea Level Pressure (*psl*) shown from top to bottom row, respectively.

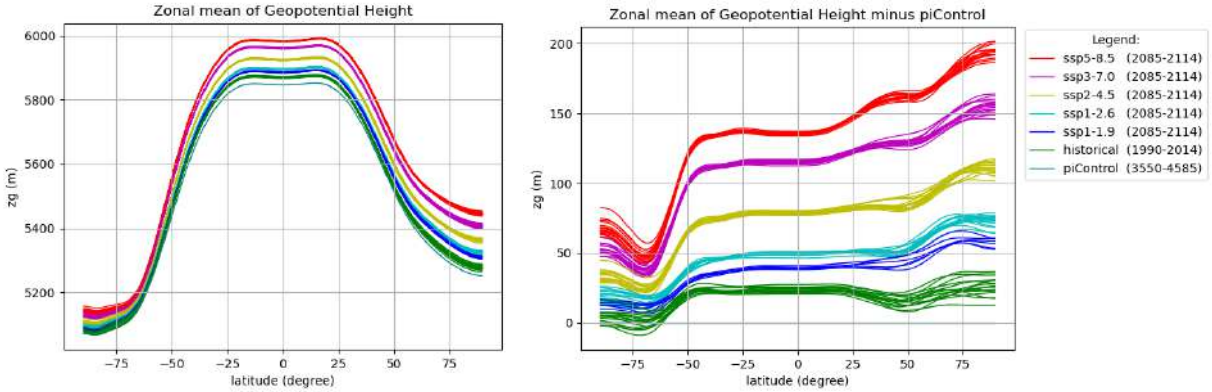

Figure 2.61: Like Fig. 2.57, but for Geopotential Height (zg).

The KNMI'23 ensemble for 2150

Fig. 2.62 shows the results for 30-year time slices around 2150 obtained from extended transient simulations forced by the various scenarios. For the SSP5-8.5 & SSP3-7.0 the decrease in sea-ice extent continued beyond 2100 (c.f. Fig. 2.57) and, as a result, has nearly entirely vanished in 2150, whereby these two scenarios predict 25 degree warming or more in the arctic region around that time.

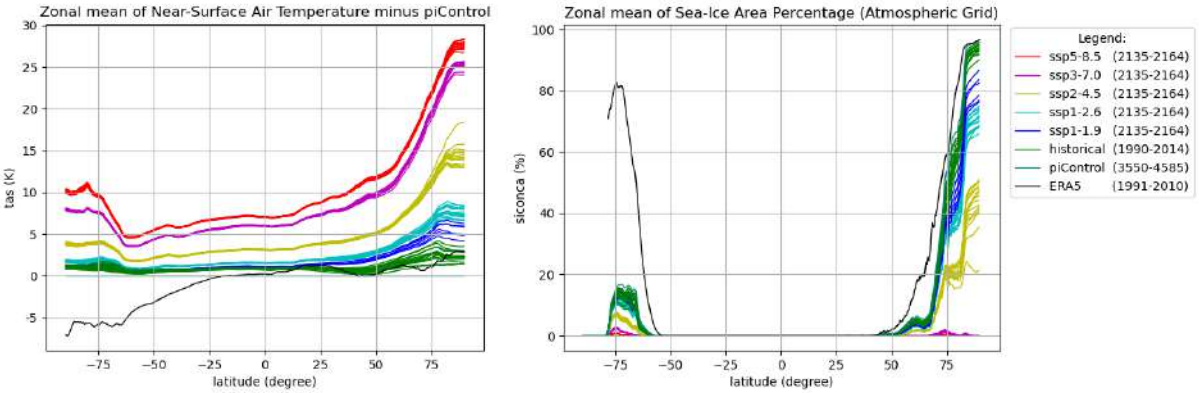

Figure 2.62: The zonal mean of the Near-Surface Air Temperature relative to piControl (left panel) and the zonal mean of the Sea-Ice Area Percentage (right panel) for the historical (1991-2020 mean) and the five SSP scenario (2135-2164 mean) ensembles. The ERA5 (1991-2010 mean) is shown as reference. A 1000-year mean of the piControl is taken, the start and end time are chosen arbitrarily, because a constant pre-industrial 1850-forcing is applied during the entire experiment.

Climate Sensitivity: ECS & TCR

The Equilibrium Climate Sensitivity (ECS) is a standard Earth System Model (ESM) metric measuring its response to increased CO2. The transient climate response (TCR), defined as the global temperature change at the time of CO2 doubling via a time path in which the CO2 is increased by 1% per year, is another standard climate sensitivity metric. The simulations which are required to compute the ECS and TCR metrics are since CMIP6 part of the standard Diagnostic, Evaluation and Characterization of Klima (DECK) experiments (Eyring et al., 2016).

The current generation of ESMs show the widest range in climate sensitivity with ECS values ranging from 1.8 to 5.6 K (Meehl et al., 2020) which is attributed to the diversity and uncertainty in

parameterisations concerning the aerosol–cloud microphysics despite recent improvements (Meehl et al., 2020). An ECS range of 2.0-5.7 has been limited according to Sherwood et al. (2020) to a 2.3-4.7 K range where paleo evidence is the strongest factor in reducing the upper bound.

Cloud feedback mechanisms were identified to be among the most important sources of uncertainty for the ECS for the past generation of climate models (Andrews et al., 2012). The World Climate Research Programme (WCRP) Grand Challenge on Clouds, Circulation, and Climate Sensitivity (WCRP, 2017) underlines the relevance of improved understanding of cloud microphysics in order to further limit the range in climate sensitivity spanned by coupled climate models.

The ECS of the EC-Earth model has increased from 3.3 K in CMIP5 to 4.3 K in CMIP6 (Wyser et al., 2020). This increase can be attributed to the more advanced treatment of aerosols, with the largest contribution coming from the effect of aerosols on cloud microphysics (cloud lifetime or second indirect effect), while it appeared to be unrelated to model tuning (Wyser et al., 2020).

Because the climate sensitivity of climate models is often linked to the uncertainties in cloud microphysics, we want to evaluate the impact of the applied adjustments in the tune parameters for the retuning. In order to determine the climate sensitivity of EC-Earth3$_{\mathrm{p5}}$ we have carried out two more CMIP6 DECK experiments: the CMIP 1pctCO2 experiment for determining the TCR and the CMIP abrupt-4×CO2 experiment for determining the ECS.

Both the TCR & ECS are slightly lower for EC-Earth3$_{\mathrm{p5}}$ than for EC-Earth3$_{\mathrm{p1}}$, with that the climate sensitivity of EC-Earth3$_{\mathrm{p5}}$ is closer to the CMIP6 multi-model mean: The transient climate response (TCR) is 2.1 K for EC-Earth3$_{\mathrm{p5}}$ (c.f. 2.3 K for EC-Earth3$_{\mathrm{p1}}$ and 2.0 K for the multi-model mean). The model's effective climate sensitivity (ECS) is 4.0 K for EC-Earth3$_{\mathrm{p5}}$ (c.f. 4.3 K for EC-Earth3$_{\mathrm{p1}}$ and 3.7 K for the multi-model mean).

2.3.5 Discussion of the retuning results

The NH cold bias is reduced, the large oscillations in global mean temperature are absent after 1975 for the entire 16 member ensemble. Two members still show cold stages within the 1949-1975 period, note that the downscaling with RACMO starts at 1949. And that the 1991-2020 interval is taken as the historical reference period for the KNMI'23 project.

The very long record of spin-up / piControl simulations, over 2000 additional years of integration for the various retuning experiments (see Reerink et al. (2023)), often show, despite a balance in the TOA radiative fluxes, episodes with an unexpected warming trend. This is probably caused by the slow response of the ocean component. It is found to be less straightforward than initially expected to conclude in an early stage whether a piControl run has reached an equilibrium. A lesson learned from our retuning experiments is that after 500 years of integration with slightly modified tuning parameters, an ostensible equilibrium is often still followed by an additional slow warming lasting several 100s of years before really flattening when the integration is continued for another 1000 years.

Our initial aim to retune EC-Earth3 such that a 0.5° warming of the NH is achieved, appeared not sufficient to avoid excursions into a low convective cold stage. That forced us to apply modifications in the tuning that resulted in more warming, and thus an even higher global mean of the temperature; a compromise in order to reduce the AMOC variability and with that to stabilize the last decades of the historical experiment for all ensemble members.

The climate sensitivity metrics TCR & ECS decreased for EC-Earth3$_{\mathrm{p5}}$ to 2.1 and 4.0 K respectively, and therefore end up closer to the CMIP6 multi-model mean.

2.4 Downscaling with RACMO

Within the Dutch Climate Scenario project the KNMI regional climate model RACMO2v3 (hereafter referred to as RACMO) is used for the dynamical downscaling of the 16-member ensemble produced by the retuned EC-Earth3 model. The output from the RACMO ensemble is applied in the KNMI'23 scenario construction procedure. (Section 2.1). In addition, a number of reanalysis-based pseudo global warming (PGW) experiments (Section 2.4.7) is conducted with applications

in Chapters 5 and 7. In parallel, the sensitivity of summer drying to soil physics parameters is examined in Section 2.4.8 with application in Chapter 5.

2.4.1 CMIP6-compliant external forcings applied in RACMO

Of particular relevance for the entire scenario project is the specification of the external forcings in the RACMO simulations compliant with CMIP6.

Green-house gas and aerosol forcings

The treatment of green-house gases, including ozone, and aerosol forcings was directly ported from the CMIP6-version of EC-Earth3 into RACMO. This overhaul includes the data handling of external input files and the coupling with the radiation and cloud modules in the model physics. The latter was feasible because RACMO shares to a large degree its physics package with EC-Earth3.

The aerosol forcings consist of three contributions. Anthropologically induced aerosol optical properties are determined by application of the MACv2 Simple Plume model (Stevens et al., 2017) applied to CMIP6 reconstructed (Stevens et al., 2017) and future (Fiedler et al., 2019) emission scenarios. Background (or pre-industrial) tropospheric aerosol concentrations and associated aerosol optical properties are obtained from an off-line reanalysis driven TM5 simulation(Noije et al., 2014) forced with CMIP6 emissions for the year 1850. The background aerosol is fixed in time, apart from a seasonal cycle. Finally, aerosol optical depth coming from stratospheric aerosol is directly imported from CMIP6-dedicated datasets. The contribution related to major volcanic eruptions is part of the reconstructed stratospheric aerosol.

The total aerosol optical depth (AOD) is composed as the sum of the three contributions: anthropologically induced aerosol, tropospheric background aerosol, and stratospheric aerosol. Figure 3.35 shows the result of the annual mean total AOD at 550 nm, averaged over the NL-region, as used in the RACMO historical and scenario simulations.

Land-use change forcings

Reconstructed (up to 2015) and projected (from 2016 onward) land-use changes are derived from LUCAS-LUC compilations (Hoffmann et al., 2022) of cover fractions of Plant Functional Type (PFT) available at 0.1 degree resolution. The year 2015 in the LUCAS-LUC data set is tied to the satellite inferred LANDMATE2 compilation (Reinhart et al., 2022), which served as a starting point in specifying the (forward) evolution of projected changes and the (backward) evolution of reconstructed changes where the PFT cover fractions are inferred from the land-use cover fractions derived in the Land Use Harmonization 2 project (Hurtt et al., 2020).

After remapping to the RACMO domain, the PFTs are translated to the BATS-type classification underlying the set of vegetation parameters used by HTESSEL (Balsamo et al., 2009), the land surface module employed by both RACMO and EC-Earth3$_{\mathrm{p5}}$. This deviates from the approach taken in CMIP6-EC-Earth3 (Döscher et al., 2022) and EC-Earth3$_{\mathrm{p5}}$, where a single realization with EC-Earth3-Veg coupled to the dynamic vegetation model LPJ-Guess was used to translate the CMIP6 land-use change forcings directly into vegetation parameters required by HTESSEL at the resolution of EC-Earth3. These vegetation maps could also have been used in the RACMO scenario runs, however, since neither the discrepancy in resolution could be overcome by a simple disaggregation to the RACMO resolution, nor did it seem meaningful (at least not from the perspective of downscaling) to operate RACMO loaded with a coarse-resolution vegetation map, we decided to choose otherwise and impose land-use changes through LUCAS-LUC. This choice led to some unforeseen repercussions in the interpretation of the analyzed results as will be discussed later.

2.4.2 Lateral and sea-surface boundary conditions

Lateral boundary conditions are taken from EC-Earth3$_{p5}$ 6-hourly resolved multi-level atmospheric fields that were stored from the model year 1949 onward. In order to reduce the huge volume of EC-Earth3$_{p5}$ model output that we estimated to be needed for the purpose of downscaling we developed an alternative method to derive the lateral boundary conditions. Instead of following the conventional approach of nesting an RCM in a GCM in which multi-level fields on the 3D RCM-grid are derived from GCM model level data (91 levels in case of EC-Earth3) we inferred the required fields form an optimally determined set of 23 pressure levels (Reerink et al., 2023). By doing so we managed to achieve a relative reduction in data volume of about 75 %, which, expressed in absolute numbers, amounted to several Peta bytes.

The relaxation of prognostic variables in the lateral boundary zone follows the revised method introduced in Lenderink et al. (2003), in which the relaxation of the mass variables temperature, specific humidity and surface pressure is confined to the outermost 8-point zone, while the relaxation of the momentum variables is spread over the outermost 16 points employing a relaxation function which falls off two times slower as for the mass variables. Spectral nudging is not applied.

Sea surface boundary conditions include sea surface temperature and sea-ice extent. A slab ocean model (Attema and Lenderink, 2014) applied in a disc area centered around the North Sea is used to slightly adapt sea surface temperatures from EC-Earth3$_{p5}$ employing a Q-flux correction in order to better match the model representation of the sea surface energy balance.

2.4.3 RACMO model formulation

The package of physical parameterizations of RACMO2v3 is primarily adopted from IFS-ECMWF Cycle33r1 (ECMWF, 2009). The TKE-based vertical diffusion scheme describing air-surface energy and moisture exchanges and boundary-layer mixing processes, which was introduced in RACMO2v2 (Meijgaard et al., 2012), is retained without modifications apart from a bug-fix. New components compared to RACMO2v2 include the short wave radiation module SRTM in combination with the Mc-ICA to describe the coupling of cloud-radiative interactions, and the fresh water lake model FLake (Mironov et al., 2010). In addition, a few extensions in the radiation scheme, the prognostic cloud scheme, and the land surface model, were found required in order to cope with the various input data sets related to external CMIP6-related forcings. These were adopted from EC-Earth3 which used the formulation IFS-Cycle36r4 (ECMWF, 2010) as starting point.

The so-called "snow-accumulation issue", manifest in high-elevation grid cells in RACMO2v2 owing to erroneously high values of snow albedo once the snow mass exceeded a threshold value, which in turn led to even larger snow mass values, is resolved in the new version (Meijgaard, 2019).

2.4.4 RACMO simulations and output

The RACMO scenario simulations are carried out at 12 km horizontal resolution on a 40-level vertical mesh. The model domain is depicted in Figure 2.63 together with a map of the model resolved surface height. The main analysis region NL+RM is more or less located in the centre of the domain. Compared to the downscaling simulation in the previous scenario project the domain is considerably extended to the south and east to reduce the direct influence from the lateral boundaries, in particular the eastern boundary, where most of the outflow happens. Outflow is more difficult to handle by the boundary relaxation than inflow conditions. Also the option to perform further downscaling experiments based on RACMO output with the climate version of Harmonie required an extension of the domain to the south.

The downscaling simulations cover the period 1949-2014 for the historical experiment, 1949 serving as a spin-up year, followed by either the period 2015-2165 for the SSP5-8.5 experiment, or the period 2015-2120 for the SSP1-2.6 and SSP2-4.5 experiments. Model output is converted into NetCDF and organized in files per parameter per model year. The resulting archive contains

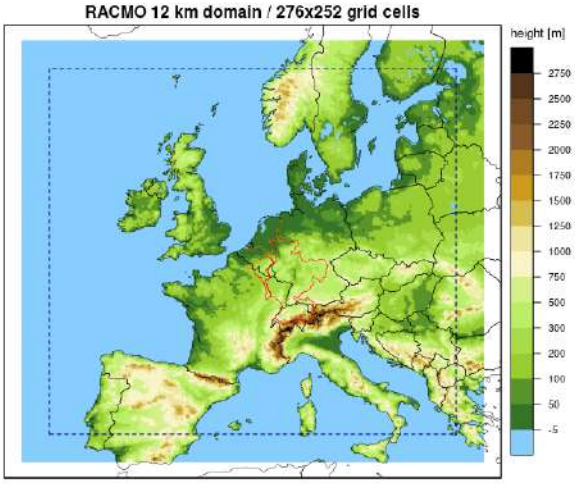

Figure 2.63: RACMO modelling domain displaying model surface height. The dotted line separates the 16-point wide lateral boundary zone from the interior domain where the model evolves freely. Land points enveloped by the red lines (Rhine- and Meuse-catchment) and orange line (Netherlands) indicate the NL+RM analysis region.

3-hourly resolved output (only precipitation is stored 1-hourly), and inferred from that daily and monthly output.

2.4.5 Features in RACMO land-use data forcings

After all RACMO simulations had been performed, a number of features, some of them unforeseen, in the land-use data and the changes therein, and their application in HTESSEL, the land surface scheme used in RACMO, became apparent. They make it difficult to interpret the calculated changes in precipitation or wind speed related properties from the RACMO output. Here we discuss a few of them in more detail.

Temporal inhomogeneity in reconstructed land-use data

The impact of an inhomogeneity identified in the reconstructed land-use data is best illustrated by Figure 2.64. This figure shows the difference in the RACMO-simulated wind speed between the period 2071–2100 and the reference period 1991–2020. In all seasons an area stretching from the northwest to the central part of the Netherlands shows up as behaving differently from the surrounding area. In winter, wind speed is projected to increase in the whole domain, but the increase is much stronger in the indicated area than elsewhere. Most notably, this area has very sharp edges, suggesting an artefact. In summer, the same region is distinguished by showing hardly any change, while the wind speed is projected to decline everywhere else.

Figure 2.65 shows time series of wind speed at the two points marked in Figure 2.64, corresponding to Eindhoven (outside the suspected area) and De Bilt (within this area). The De Bilt series show a clear inhomogeneity (upward jump) around 2005, which is absent in the Eindhoven series. Furthermore, the development after 2005 is different between the two locations, which is most evident in winter, when the wind speed stays constant in Eindhoven, but steadily increases in De Bilt.

In contrast to the wind speed, the surface pressure difference field between the two periods appears to be quite smooth (not shown), meaning that also the geo-wind (horizontal derivative of the surface pressure) is smooth. While the surface pressure is a model variable, surface wind is

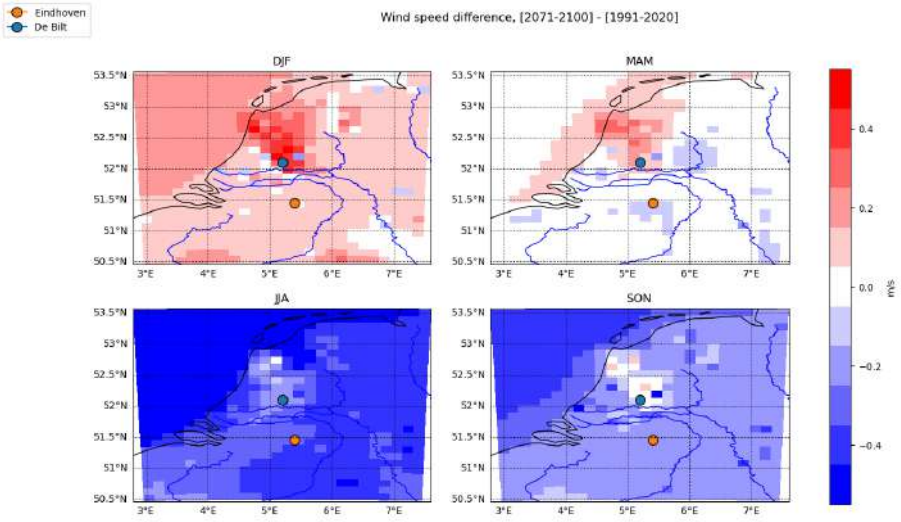

Figure 2.64: Change in wind speed between the periods 2071–2100 and 1991–2020 as simulated by RACMO in the SSP5-8.5 emission scenario. Shown is the mean over all 16 RACMO runs for each of the four seasons.

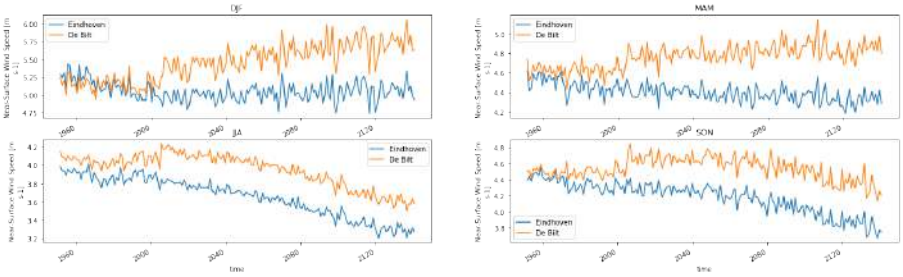

Figure 2.65: Time series of wind speed from RACMO (SSP5-8.5) at the two land points marked in Figure 2.64.

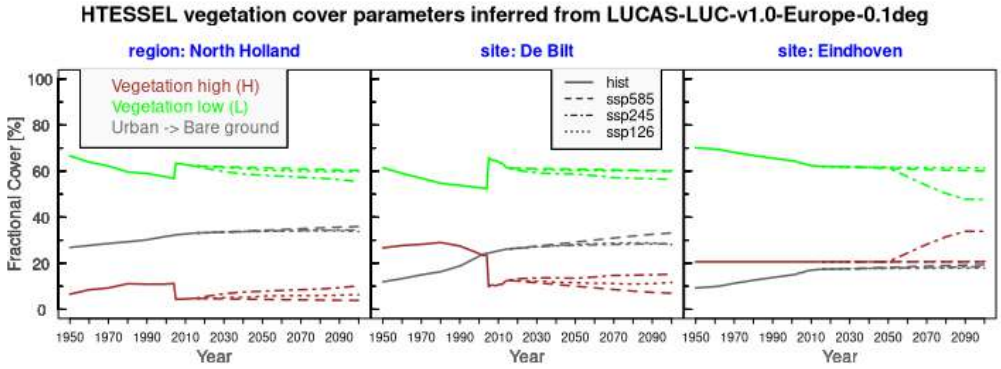

Figure 2.66: Cover fraction of HTESSEL low and high type vegetation at three sites/region in the Netherlands as used in the RACMO historical and scenario simulations.

diagnosed based on the surface roughness. Evidently, the strange change pattern of the surface wind must somehow be caused by the representation of the surface roughness in the model. It indeed turned out that there is an issue with the land-use change map used in the historical simulation up to 2014 (LUCAS-LUC historical; Hoffmann et al. (2022)). In the transition from 2004 to 2005, the land-use change map prescribes an abrupt drop in high vegetation coverage in the northwest-southeast oriented area, covering North Holland and De Bilt, accompanied by a similarly large rise in low vegetation coverage as shown in 2.66. The step-like replacement of prescribed high vegetation by low vegetation results in a sharp reduction of the surface roughness length in HTESSEL, and consequently a distinct increase in mean wind speed.

These distinct changes in vegetation coverage from 2004 to 2005 are inherited from the widely used land-use change database compiled within the Land-Use Harmonization 2 (LUH2) project (Hurtt et al., 2020) as is illustrated in Figure 2.67. In the grid cells covering North Holland and De Bilt there is a sudden rise in fraction of C3 and C4 crops (low vegetation type) at the expense of potentially forested secondary land (filled in LUCAS-LUC with high vegetation). Unlike suggested by the right panel of Figure 2.66, abrupt changes in land-use fractions are also seen for the grid cell representing Eindhoven, i.e. reductions in cover fraction of pasture, C3- and C4 crops, and a rise in potentially non-forested secondary land (right panel in Figure 2.67). However, in LUCAS-LUC these land-use types are all classified as low vegetation type, and therefore the changes according to LUH2 for Eindhoven hardly (if not at all) impact the local wind speed.

To complete this part of the subsection, we briefly mention that the inhomogeneity feature in the reconstructed land-use database also hampered a trend analysis of near-surface wind speed over recent decades across parts of the Netherlands (Luu et al., 2023).

Urban fraction treated as bare soil in HTESSEL

At the same time the inhomogeneity issue became evident, it was realized that the effect of a projected increase of urbanisation in the entire country until the end of the century was not properly captured in HTESSEL. The reason is that urban areas are not explicitly represented but treated as 'bare soil' with a corresponding low model roughness length of 0.013 m, which is lower than the value of any of the vegetation types. Consequently, in the model area-mean roughness decreases in the course of time, while urbanisation, when it replaces low vegetation, should lead to an increase. Typically, a value of 0.5 m could have been used for urban roughness length, which is the same value as tabulated for interrupted forest.

Projected afforestation in the SSP1-2.6 scenario

While projected land-use changes throughout Europe are quite modest in the high-end scenario (SSP5-8.5), apart from a steady urbanization rate, changes in the low-end scenarios (SSP1-1.9,

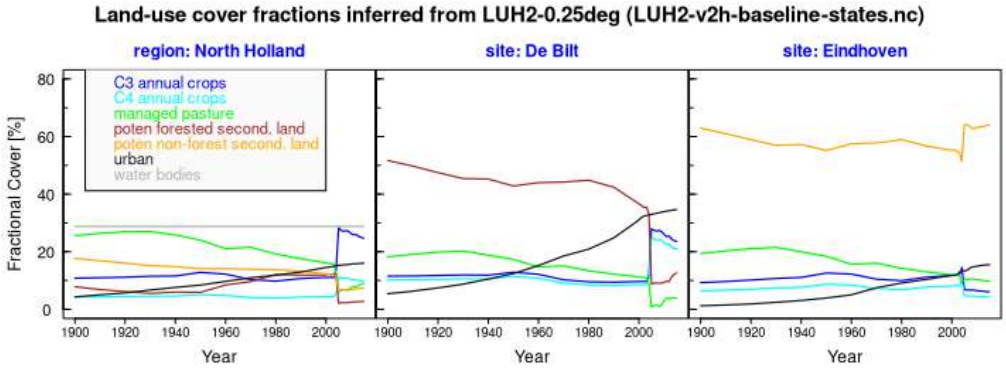

Figure 2.67: Land-use cover fractions until 2014 according to the LUH2 reconstruction for the same three regions/sites as in Figure 2.66

SSP1-2.6, and SSP2-4.5) are determined by projections of active afforestation in most European countries. One might argue the feasibility of the projected rates of afforestation, but that discussion is not at issue here. In the projections, these changes are introduced intentionally, and they are explicitly mentioned in the formulation of future scenarios in the Land-Use Harmonization 2 project (Hurtt et al., 2020) and accompanied by an all-tree-cover product describing projected forest cover change. These are then translated into PFT-fractions contained in the LUCAS-LUC scenario products, and from there, to fit our purpose, into HTESSEL vegetation parameters. To put it briefly, where and when forest change is projected according to LUH2, this will appear in RACMO as a region where low vegetation will be replaced by high vegetation. And this will have consequences for the rate of change of some meteorological parameters.

An example is a relatively short period of merely two decades of intense tree planting which in the SSP1-2.6 scenario is projected to be carried out in a 50x50 km^2 region located in the south of the province Groningen and the north of Drenthe. In the center of this region the corresponding increase of high vegetation coverage is in the order of 50% of the total coverage. Qualitatively, this impacts the RACMO simulations in the following way. Since, within the framework of the model, high vegetation is characterized by high roughness length, the mean local wind speed will decrease, while the exchange of momentum with the surface due to friction will increase, so will the amount of mixing in the boundary layer, and also its mean height. The increase in momentum flux implies a local deceleration of the atmospheric flow which combined with the increased mixing gives rise to more precipitation. The effect of these changes tends to spread in the prevailing upwind direction through dynamical interactions. A more detailed analysis of the effect of changes in vegetation type on precipitation is given in Maat et al. (2013) who found comparable results as described here from a reverse-kind of senstivity experiment in which they replaced the forest coverage over the Veluwe by grassland.

It is emphasized that the changes themselves are relatively small, in the order of 5% or less. However, because the land-use change forcing for a given SSP-scenario is exerted in all RACMO simulations in the same way the impacts on local meteorology including precipitation will emerge as a signal in the ensemble mean result as can be clearly seen in Figure 2.68. In fact, removing the land use change forcing in a single simulation will already show fairly well to what extent the precipitation response is determined by the land-use change. This is illustrated in Figure 2.69 which shows the relative change in precipitation obtained for a single member with and without the external land-use change applied. The land-use change itself is shown by the change in cover fraction with high vegetation. Evidently, leaving out the land-use change results in a spatially much smoother change in precipitation. This holds for all seasons.

The distinct precipitation changes are not seen for all areas where imposed increases in high vegetation cover are substantial, like in the extreme south of Limburg and adjacent regions in Belgium and Germany. The reason is that in these regions high vegetation is already present in

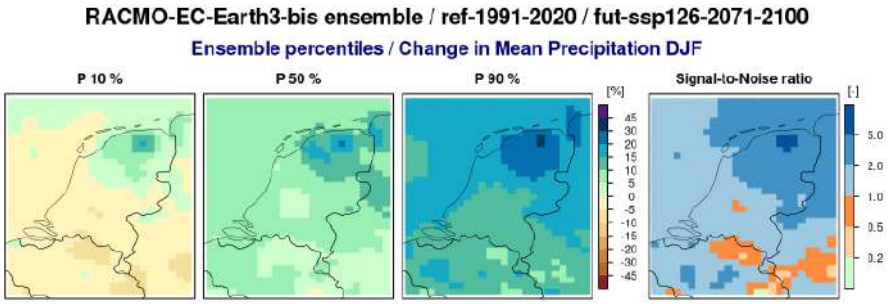

Figure 2.68: Relative change in DJF precipitation for the 10, 50, and 90% percentiles of the 16-member RACMO ensemble between future (2071-2100) under the SSP1-2.6 scenario and the reference period (1991-2100). Also shown is the normalized signal-to-noise ratio where the signal is obtained as the ensemble mean and the noise is a measure of the ensemble spread (Aalbers et al., 2018). Values larger than 1 indicate that the change signal is statistically significant.

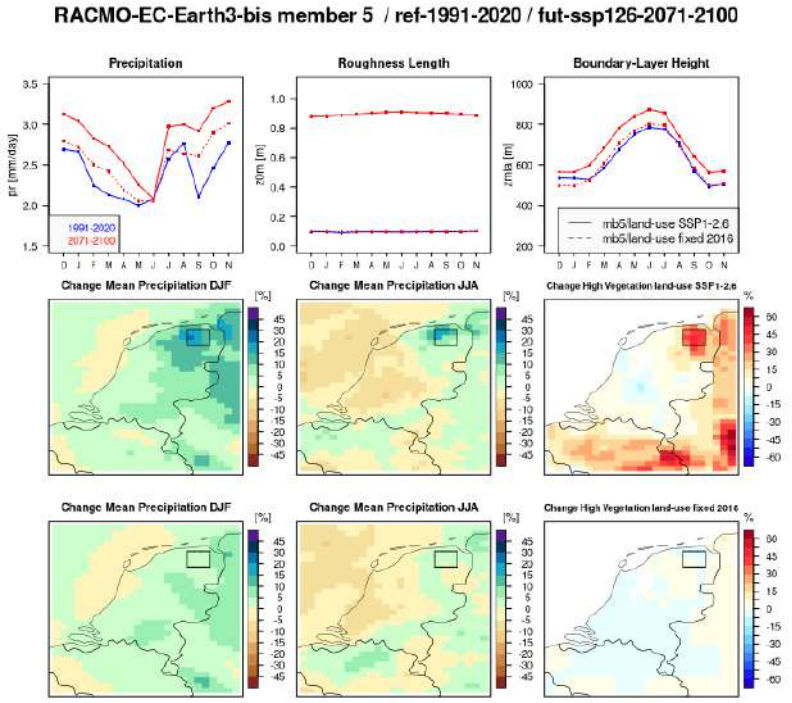

Figure 2.69: Changes in relative precipitation for RACMO member 5 (see Figure 2.68) for the winter and summer season for the default simulation (centre row) with projected land-use changes according to SSP1-2.6 imposed, and for a sensitivity simulation (bottom row) with land use of the future period (2070-2100) fixed to the year 2016. The center-right panel shows the map with the change in high vegetation imposed on the model following the land-use change projection according to SSP1-2.6. The bottom-right panel shows the same map with the difference between 2016 and the average over the reference period. The top row shows the annual cycle of precipitation, surface roughness length, and boundary-layer height for both the reference and the future period averaged over the rectangular region around the area with highest change in coverage of high vegetation.

the reference period. Because of that the relative changes in high vegetation and, correspondingly, in surface roughness length are much smaller, which in turn reduces the relative effect on precipitation.

A qualitatively similar impact of projected afforestation on the relative change in precipitation is derived from the RACMO simulation under the SSP2-4.5 scenario. Compared to the analysis shown in Figure 2.69 it is situated further to the west in an area centered in the south east of the province of Friesland. However, the corresponding increase in high vegetation cover is smaller and moreover projected to occur some decades later, after 2060. The associated impact on precipitation (not shown) is similar, but smaller, to what was found for the SSP1-2.6 scenario in Figure 2.68.

2.4.6 Comparing RACMO and EC-Earth precipitation changes in the SSP5-8.5 scenario

Spatial patterns of precipitation change across the NL+RM region and its surroundings derived from the RACMO and the forcing EC-Earth3$_{\text{p5}}$ ensembles under the SSP5-8.5 scenario show common features on the larger scales, but profound differences also emerge. Some of them can be related to small-scale resolved topography in RACMO, but, especially in the summer season, a robust difference across a larger region is seen that cannot be easily explained. Figure 2.70 shows the relative changes in DJF-precipitation under the SSP5-8.5 scenario according to EC-Earth3$_{\text{p5}}$ and the downscaling with RACMO for three ensemble percentiles. The large-scale features agree reasonably well with largest changes over the North Sea (in the NW-corner of the displayed area) and the southern Alps. Averaged over the NL+RM region the GCM and the RCM agree almost exactly over the mean change in all three percentiles, but, not unexpectedly, in RACMO much more spatial structure is apparent which in most cases is tied to contrasts in topography. This not only applies to the Alps, but also to the lower mountain ranges in Germany (e.g. Sauerland, Schwarzwald, Erzgebirge), Belgium (Ardennes), and the French and Swiss Jura. It is not entirely clear what causes these spatial features in DJF-precipitation response with larger positive values over the higher elevation mountain ridges in contrast to smaller positive, or even negative, values over the lower elevation surroundings. We speculate that in the vicinity of substantial topographic gradients any long-term change in atmospheric flow strength and direction will affect the precipitation. But also changes in humidity vertical structure may play a role, although it is not straightforward to explain why this affects precipitation that falls over the mountain range differently from what falls on the lee side of the mountains. While the DJF change signal in EC-Earth3$_{\text{p5}}$ is everywhere statistically significant, in RACMO there is an areal band along the Alpine mountain range where the signal is small and ranges between negative for P10 to slightly positive for P90.

The corresponding results for JJA are shown in Figure 2.71. Although there is, like for DJF, again agreement in the large-scale spatial structure with a negative response in both RACMO and EC-Earth3$_{\text{p5}}$ in the western part of the region, gradually passing into a positive response when moving to the east, there are also a number of substantial differences. In particular, regions with positive changes in EC-Earth3$_{\text{p5}}$ in the eastern part of the region have extended to the west in RACMO and now cover parts of the NL+RM region corresponding to subcatchments in Central Germany (e.g. the Main).

Averaged over the NL+RM region, this results in a considerably smaller negative response for RACMO compared to EC-Earth3$_{\text{p5}}$, in the order of 8 to 10 %, irrespective of the ensemble percentile. A similar difference between RCM- and GCM-response was also found in the large EURO-CORDEX RCM ensemble produced with forcings from CMIP5-GCMs (Coppola et al., 2021) where the RCM-response in JJA-precipitation in Central Europe for 2071-2100 (rcp8.5) compared to 1981-2010 shows slightly less drying than the response derived from the forcing GCMs. Also the transition zone across Europe separating areas with positive responses in JJA-precipitation from those with negative responses is situated further to the west/south-west in the RCM-ensemble compared to the forcing GCM-ensemble.

Finally, what stands out in Figure 2.71 are grid cells with large positive values along the Alpine mountain ridge very close to the southern edge of the Rhine catchment; some of the cells are just

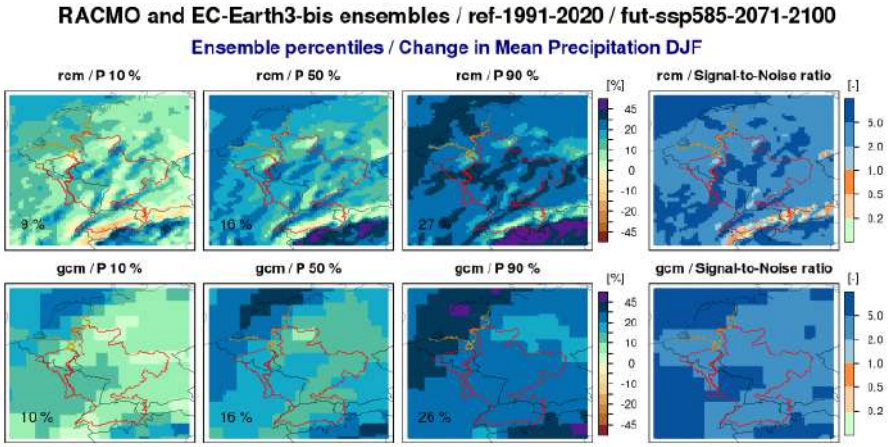

Figure 2.70: Relative change in DJF precipitation for the 10, 50, and 90 % percentiles of the 16-member RACMO ensemble (top row) and the EC-Earth3$_{\text{p5}}$ ensemble (bottom row) between future (2071-2100) under the SSP5-8.5 scenario and the reference period (1991-2100). The panels on the right hand side show the normalized signal-to-noise ratio where values larger (smaller) than 1 indicate that the change signal is statistically (not) significant. The area enveloped by the red lines (Rhine- and Meuse-catchment) and orange line (Netherlands) indicate the NL+RM analysis region. The numbers in the lower-left corner of the panels are the mean change values obtained by averaging the grid cell relative changes in the NL+RM region.

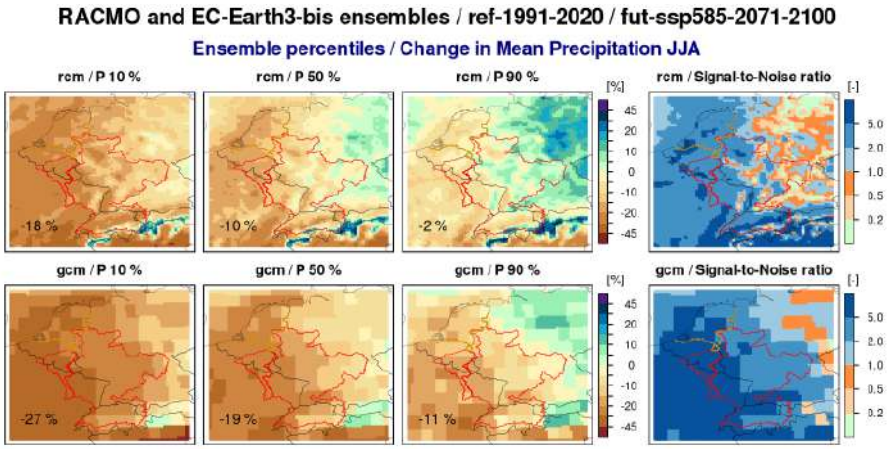

Figure 2.71: Like Figure 2.70 but for JJA

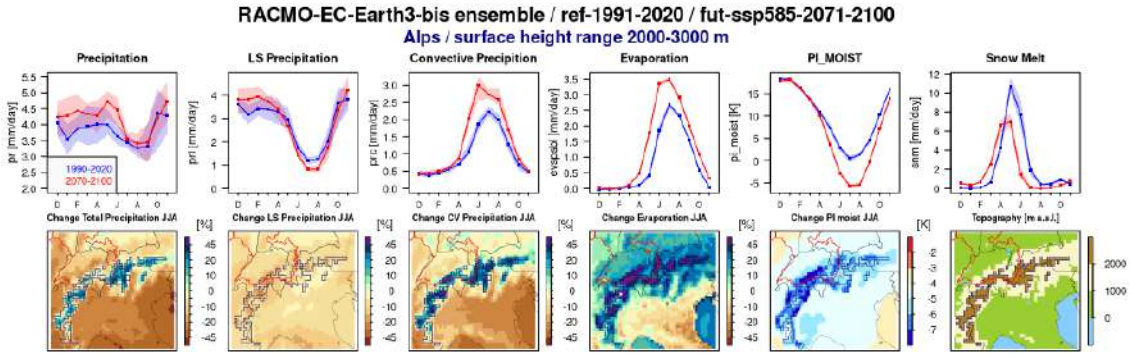

Figure 2.72: Annual cycle (top row) of total precipitation, large-scale (LS) and convective (CV) precipitation, evaporation, the potential instability (PI) index for moist convection, and snow melt, averaged over the subset of grid boxes with model surface height above 2000 m. (Note that the annual cycle along the horizontal axis starts with December.) The PI is calculated following Giorgi et al. (2016) as the difference in potential equivalent temperature between 500 hPa and the surface; the more negative the PI the higher the potential for moist convection to occur. Also shown (bottom row) are the relative change in total, LS and CV precipitation, evaporation, and the change in PI for the summer (JJA) season. Note: for the sake of comparison the changes in total, LS and CV precipitation, respectively, are calculated relative to the total precipitation in the reference period. The panel in the bottom-right panel contains the surface height map.

inside, but the majority of them are outside the catchment perimeter. This is in agreement with Giorgi et al. (2016) who analyzed that the majority of regional models projected an increase in summer precipitation at high elevations in the Alpine region unlike what was found in most of the forcing global models. They argue that this is largely due an increase in convective rainfall in the fine-scale regional models ($\sim$ 12 km) triggered by an increased potential for moist convection related to excess surface heating and moistening. This line of reasoning is illustrated in Figure 2.72 which clearly shows that in the summer season the reduction in large-scale precipitation at the highest elevations is more than compensated by the enhancement in convective precipitation. The spatial change patterns of convective rainfall and the potential for moist convection to occur expressed as the potential instability index (PI) (see figure caption for explanation of the PI) do correlate very well. It seems plausible that the shift in the timing of the snow melt peak from May/June in the reference period to April/May in the future period amplifies the increase in convective precipitation through an enhanced increase in surface temperature with elevation resulting in a higher potential for moist convection.

2.4.7 Pseudo-global warming (PGW) experiments

The results obtained with the 16-member RACMO ensemble driven by EC-Earth3$_{\text{p5}}$ as discussed so far in Section 2.4 are meant to be used in the resampling methodology introduced in Sections 2.1.8 and 2.1.9 where the resamples built from EC-Earth3$_{\text{p5}}$ are derived from changes in the selections of dry-trending (*dry11*) and wet-trending (*wet11*) models, respectively. The tacitly adopted presumption is that application of the resampling criterions result in EC-Earth3$_{\text{p5}}$ resamples that are more or less representative for the median of the underlying selection of CMIP6-models, irrespective of the parameter. While this holds for e.g. temperature and precipitation, this is not the case for (absolute) humidity; as extensively elaborated in Section 5.5 the increase in absolute humidity in EC-Earth3$_{\text{p5}}$ is much larger than found in the CMIP6-ensemble, in particular in summer and autumn, across most of the European domain. As concluded in Section 5.6, the consequence of this behaviour in EC-Earth3, the origin of which is not clear yet, is that scenarios of humidity changes and associated changes in precipitation extremes cannot be based on resamples derived from the EC-Earth3$_{\text{p5}}$ driven RACMO.

In order to overcome this setback, we have instead conducted and applied a series of RACMO-simulations in the framework of pseudo global warming (PGW) (Schär et al., 1996a; Brogli et al., 2019, 2021; Lenderink et al., 2022; Aalbers et al., 2023). In essence, a PGW-experiment consists of two simulations, a control simulation and a perturbed simulation. The control simulation typically is an evaluation experiment in which RACMO is downscaled from a re-analysis, here ERA5 (Hersbach et al., 2020). In the perturbed experiment, the lateral and sea surface boundary fields (temperature, humidity, momentum, surface pressure, sea surface temperature) taken from the reanalysis are modified by adding the mean climate change derived from a multi-member GCM or a multi-model set of GCMs, prior to downscaling. A more elaborate discussion of the implications of the PGW-approach, including pro's and cons compared to the conventional GCM-driven RCM-downscaling, is provided in Section 5.7.

Within the scenario project we have composed PGW-perturbations from three sets of multi-model ensembles, i.e. from all 33 CMIP6 models (*pgw-all33*), the dry-trending models (*pgw-dry11*), and the wet-trending models (*pgw-wet11*), as well ad from the 16-member EC-Earth3$_{\text{p5}}$ model (*pgw-ece3*), at various levels of global warming: +1.5, +2.0, +3.0, and +4.0 K. In this subsection we only looked at results obtained with *pgw-dry11*, *pgw-wet11*, and *pgw-ece3* at +3.0K global warming. Results obtained with *pgw-dry11/wet11/all33* are used in Chapter 5 discussing small-scale convective precipitation, while time series from the *pgw-dry11* simulations form one of the basis elements of the future weather case presented in Chapter 7.

At this stage we restrict the analysis to a direct comparison between the PGW-results and the EC-Earth3$_{\text{p5}}$ driven RACMO ensemble, with a focus on change in JJA-conditions across the NL+RM region, in order to examine how they mutually relate. In Figure 2.73 shows changes for precipitation, dew point temperature, and dew point depression derived from the various types of simulation. Evidently, the EC-Earth3$_{\text{p5}}$ driven RACMO ensemble (in this Figure built from the first four members, but that hardly makes a difference with the full ensemble) has the largest drying averaged over the NL+RM region, although the *pgw-dry11* change pattern shows as stronger gradient over Central Europe. On the other end, the *pgw-ece3* simulation results in a net wetting in most of the NL+RM region which is likely related to the high change in dew point temperature (a measure of absolute humidity). The change patterns of dew point temperature derived from RACMO-EC-Earth3$_{\text{p5}}$ and *pgw-ece3* are very similar, and, with exception of the Alpine region, considerably higher than derived from the other *pgw*-runs. This contrast is undoubtedly a signature of EC-Earth3$_{\text{p5}}$. A similar result is found for the change in dew point depression (the difference between air temperature and dew point temperature, which makes it a measure of relative humidity), though the spatial patterns of this variable show a stronger north-south gradient than the dew point temperature.

2.4.8 Sensitivity to soil physics parameters

Until this point, all RACMO-simulations have been carried out with the same model physics, referred to as the standard physics. Here we explore the possibility of generating a dryer summer climate by modifying the soil physics. In the standard physics, the soil module and parameter settings are the same as used in EC-Earth3$_{\text{p5}}$. Adjustments in the modified soil scheme were twofold: i) 25 % of the precipitation over land was directly rerouted as fast surface runoff, ii) the root depth distribution was made twice as shallow. Though these changes appear rather drastic, they are not entirely unrealistic, foremost, however, they were chosen such to yield a non-negligible impact on climate change without unacceptably deteriorating the climate itself. Altering the model physics implies that also the simulation of the control period had to be redone; first we conducted the *pgw-dry11-soilpar* experiment only (see Section 5.7), from which we learned that the future period is more affected by the modified soil parameters than the control period, resulting in a larger drying response signal (compare left- and center-bottom panels in Figs. 5.14, 5.15, 5.16, and 5.17). At a later stage, we also conducted the *pgw-wet11* and *pgw-ece3* experiments with the modified soil physics parameters; likewise we repeated 30-year time slices (ref: 1990-2020; fut: 2070-2100) of a sub-ensemble (members 1 to 4) of RACMO-EC-Earth3$_{\text{p5}}$ with modified soil physics.

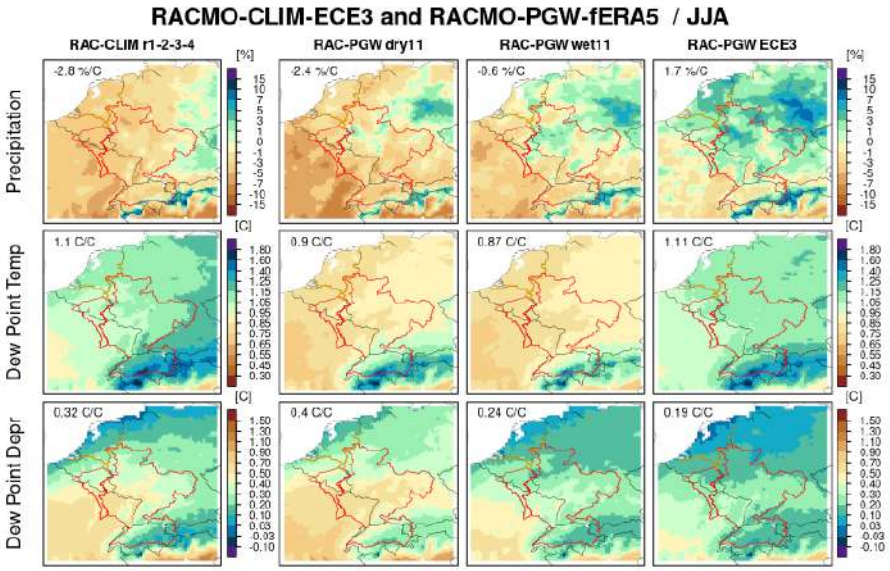

Figure 2.73: Change patterns for JJA of precipitation (top row), dew point temperature (middle row), and dew point depression (bottom row), for RACMO-EC-Earth3$_{\text{p5}}$ ensemble, members 1 to 4 (left column), and *pgw-dry11/wet11/ECE3* (three columns on the right). All values are scaled with the global temperature change with respect to the reference period 1991-2020. For the PGW-runs this is +3 K, for the climate run with future time slice 2071-2100 it is +3.8 K. For years from 2015 onward the SSP5-8.5 scenario is assumed. Meaning of numbers within the panels is according to Figure 2.70

Figure 2.74 summarizes the outcomes from the simulations with modified soil parameters for JJA-precipitation compared to the simulations with standard physics. The figure shows that in any case the modified soil physics results in a stronger drying, or drying instead of wetting for *pgw-ece3*. The largest effect is found for the *pgw-dry* experiment, while the smallest effect is seen for the ensemble mean of the few-member climate run. In resume, within the set of PGW-experiments, the larger the summer drying in the simulations with standard physics, the larger the drying impact of the modified soil physics. In that sense, the RACMO-EC-Earth3$_{\text{p5}}$ subsample seems positioned differently, as it shows the largest drying with standard physics combined with smallest additional drying with modified soil physics. This is likely due to the different nature of the experiments: while PGW-experiments are essentially probing thermodynamic sensitivity, a conventional RCM-GCM experiment is susceptible to changes in prevailing synoptical circulation as well.

2.4.9 RACMO Summary

The 16-member EC-Earth3$_{\text{p5}}$ ensemble is dynamically downscaled with RACMO2v3 at 12 km horizontal resolution in a domain centered around the NL+RM region. External forcings of greenhouse gas concentrations, aerosol fields, and land-use changes are compliant with CMIP6 reconstructions and projections. Where necessary, the model formulation was adapted to couple the externally forced parameters to the model physics, specifically the implementation of the SRTM module for short wave radiation, and small extensions to the prognostic cloud scheme. Some further modifications in the model formulation include the application of the lake model FLake, and an updated version of the slab ocean model. Lateral boundary conditions were inferred from EC-Earth3$_{\text{p5}}$ fields stored on pressure levels rather than model levels implying a huge reduction in forcing data volume.

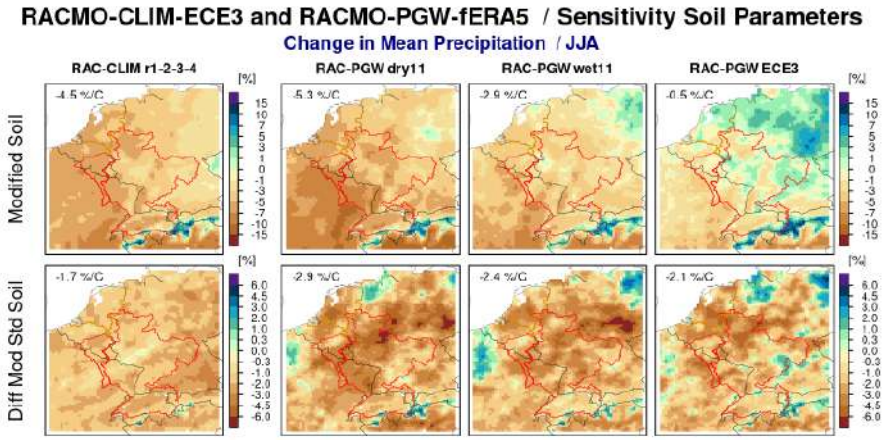

Figure 2.74: Patterns of precipitation change for JJA scaled with global warming (see caption Fig 2.73) derived from the experiments with modified soil physics (top row) and enhanced drying with respect to standard physics (bottom row). Precipitation changes in experiments with standard physics is according to top row in Fig 2.73. Meaning of numbers within the panels is according to Figure 2.70

High values of climate change in absolute humidity apparent in EC-Earth3$_{p5}$, a feature in which the model turns out to be an outlier compared to the rest of the CMIP6-models, seriously complicated the development of scenarios of rainfall extremes along the lines of resampling. We therefore resorted to the alternative approach of pseudo global warming (PGW) experiments which allowed us to quantify the change in rainfall extremes more directly in relation with the dry-trending and wet-trending CMIP6 selections. In addition, we explored the possibility of generating stronger trends of summer drying by modifying soil physics parameters. All experiments with modified soil physics lead to enhanced summer drying suggesting that part of the uncertainty in summer climate response is contained in the formulation of soil processes.

Analysis of the RACMO simulations revealed certain features that were found present in all members of the ensemble, and for that reason they will, inevitably, also show up in the resamples. Their origin could in some cases be identified as an impact, e.g. in changes in mean wind speed or precipitation, triggered by local or small-scale temporal changes in the reconstructed or projected land-used forcings. In other cases, typical features appear related to the model formulation, to the resolution, or an expression of both. Although we did not always succeed in providing a robust explanation for the seen model behaviour, knowledge or awareness of the potential origin may already help in interpreting the results.

2.5 KNMI'23 data products

2.5.1 Time series transformation

As an alternative to bias correction, a time-series of observations can be be transformed to obtain what these data would look like in future climate. This transformation can be designed to preserve a selected climate signal derived from the RACMO runs for the historical and the future climate. It was applied earlier to produce the KNMI'14 scenarios; see e.g. Bakker, 2015.

Bias correction of climate model simulations and time-series transformation (TT) each have their strengths and weaknesses, depending on purpose and specific circumstances:

- A time-series transformation starts from data with realistic dependencies in time and between different variables (e.g. the dependence between precipitation and humidity, or the distribution of the lengths of intervals without rain). Applying separate transformations for

different variables preserves these dependencies, which may be an advantage if they are not well represented in the model output. However, this may be a drawback if the dependencies are realistic in the simulations, in particular if they change over time: such changes cannot be represented by time-series transformation.

- Another factor is the simplicity of the mapping(s) involved: for example, if the climate signal is simple (e.g. a uniform increase in temperature) but the bias has a complicated form, time-series transformation may have the practical advantage that it is easier to estimate from data. But the opposite may also be encountered: the bias may be simple and the climate-change signal may be complicated (e.g. changes may be different in the normal range of values and in the tail range).

- Furthermore, bias-corrected model data are available at all model grid points, whereas transformed time-series are only available at measurement sites. Therefore, bias-corrected model data may be more useful if spatial averages over specific regions are required

- Bias-corrected model data for a grid point are representative for a surrounding area, depending on the effective resolution of the model (in part determined by the processes resolved in the model). A transformed time-series represents only the site of the measurement.

- Another difference is that observational time-series for a given location are naturally limited in volume (typically to a 30-year period), whereas a model may produce a much larger dataset (e.g. an ensemble) for a given climate. If this is the case, then bias-correction may produce more data for the user; on the other hand, a time-series transformation may be more accurately calibrated from the model data.

- It is emphasised that the uncertainty in the extreme quantiles has the same impact on time-series transformation as it has on bias correction.

Results of time-series transformation and specific issues with the transformation for particular variables are discussed below section 2.5.1.

For the transformation of a time-series of observations, the Quantile Delta Mapping can also be used, just as for bias-correction of RACMO output: in the calculation, the roles of the observations and of the RACMO-output for the future climate are switched.

This is illustrated in Figure 2.75. The solid arrows show the climate signal from RACMO for a few quantiles. This signal is added (dashed arrows) to the quantiles of the observations (black line), which results in the the dashed cumulative distribution of the transformed time-series of observations.

Note that this dashed distribution is identical to the dashed line in Figure 2.25. This shows that using Quantile Delta Mapping for transforming a time-series of observations results in a time-series having (at least approximately) the same quantiles as when used to bias-correct the model output for the future climate. However, the temporal ordering of the ranks of the values will be different.

Results of time-series transformation

In the figures below the climate signal in TT is compared with the signal as obtained from the RACMO resamples. Transformation of observed time series is only applied for The Netherlands, so in the figures only results for The Netherlands are shown. For the observations, the stations with daily precipitation measurements are used, supplemented with other meteorological parameters from the nearest station. Climate signals are only shown if the observed period (1991-2020) contains at least 20 years of data.

precipitation Figures 2.76 and 2.77 compare the signal in the transformed observed timeseries with the signal that comes directly from the RACMO runs. It shows that TT is able to reproduce the signal well, although small differences exist. Note the change from a drying trend in the 95%-percentile to a wetting trend in the 99%-percentile.

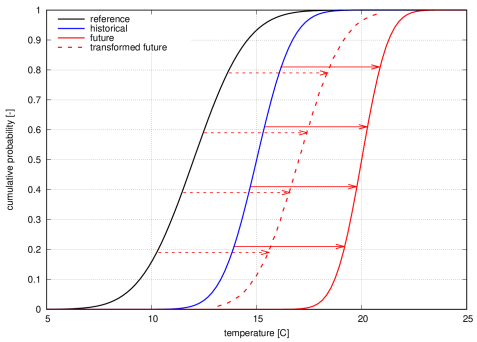

Figure 2.75: Explanation of timeseries transformation method. The solid arrow show the climate signal in the (unbiased) RACMO data, the dashed arrows have similar lengths but are applied to the observed (black) distribution. The dashed distribution is identical to the dashed line in Figure 2.25.

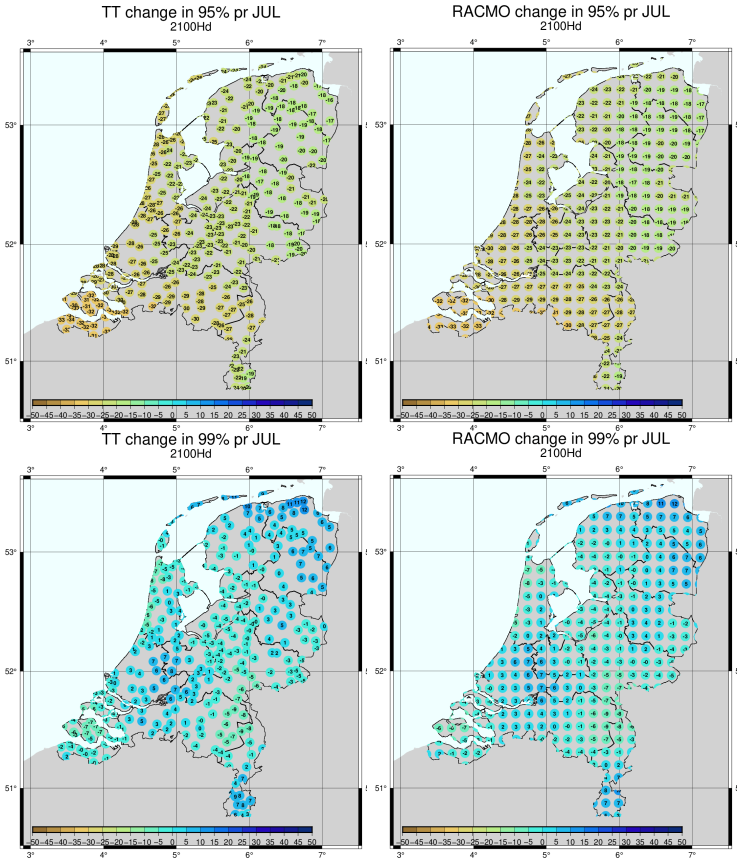

Figure 2.76: Change in the 95% (upper) and 99% (lower) percentiles of the precipitation in July for timeseries transformation (left) and RACMO (right) for the 2100Hd scenario.

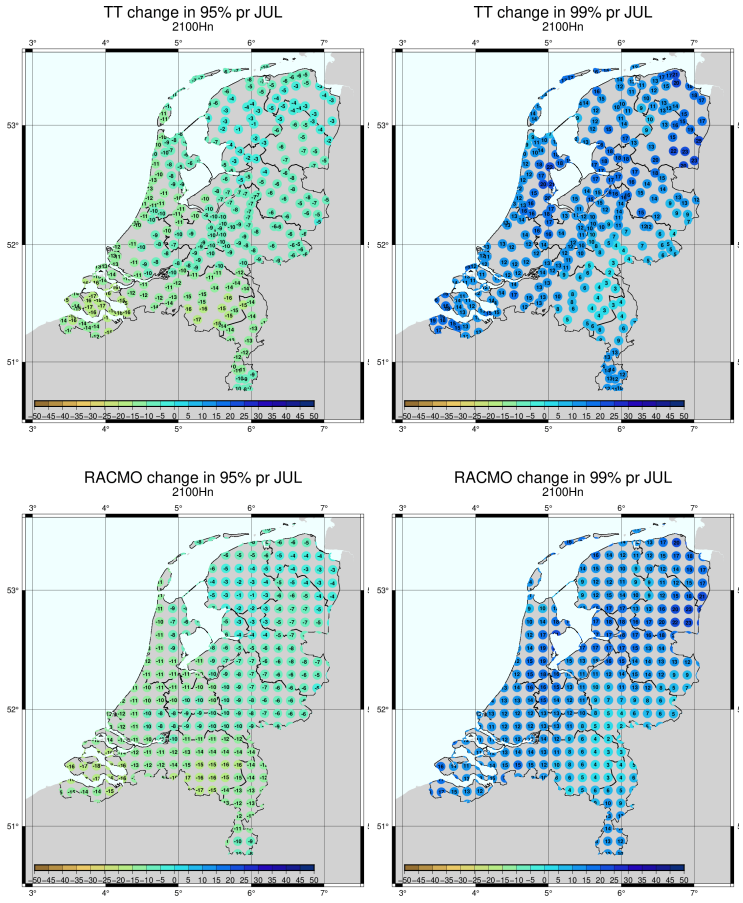

Figure 2.77: Change in the 95% (left) and 99% (right) percentiles of the precipitation in July for timeseries transformation (upper) and RACMO (lower) for the 2100Hn scenario.

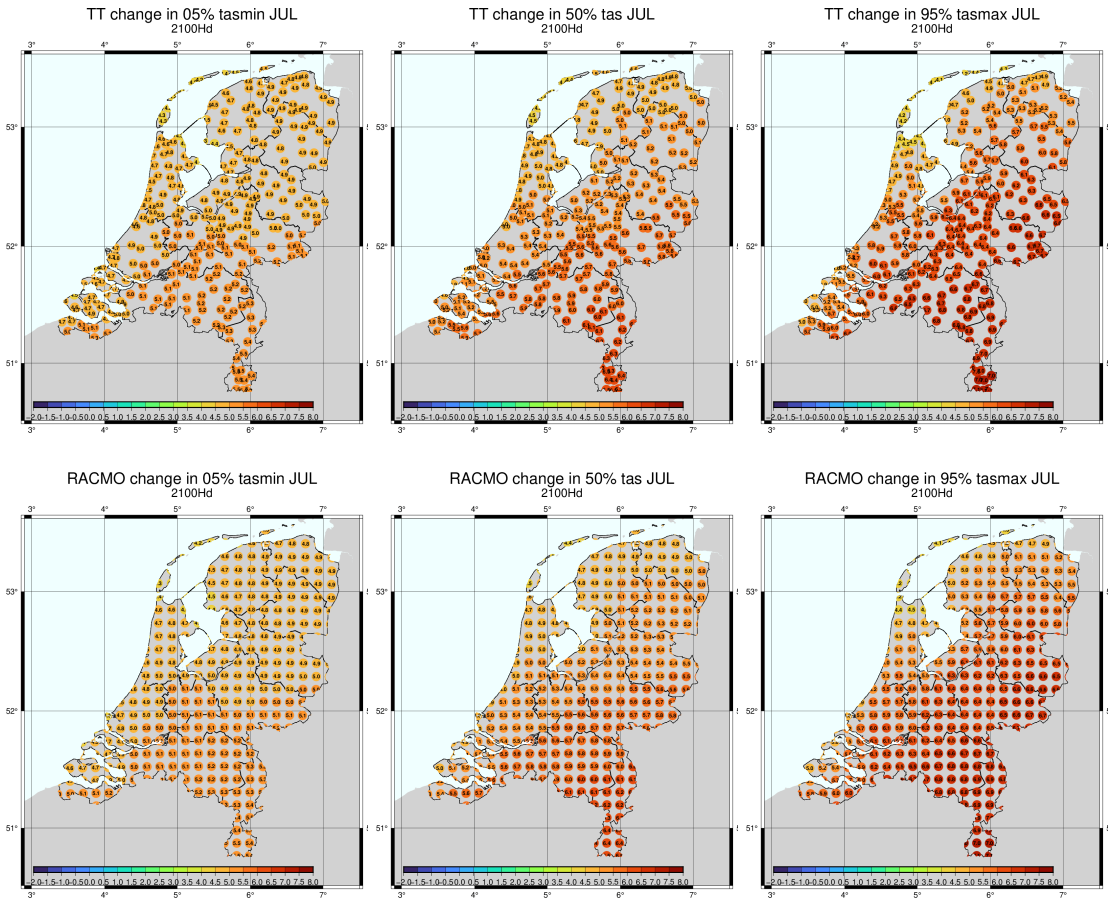

Figure 2.78: Change in the 5%-percentile of the minimum temperature (left), the 50%-percentile average temperature (middle) and 95%-percentile maximum temperature (right) in July for time-series transformation (upper) and RACMO (lower) for the 2100Hd scenario.

temperature The change in the 5%-percentile of the minimum temperature, the 50%-percentile average temperature and 95%-percentile maximum temperature in July are shown in Figure 2.78 for the 2100Hd scenario. Also here, TT reproduces the climate signal from RACMO well. Note the spatial difference in the warming: less along the coast and most in Limburg. Note also that the minimum temperature increases less than the average temperature, and the maximum temperature increases more than the average.

number of dry days Figure 2.79 shows the change in the number of dry days (defined as the number of days with less than 1mm of precipitation) according to TT and to BC. Also here the agreement is good.

duration of dry days Figure 2.80 shows the change in the number of consecutive dry days (defined as the number of days with less than 1mm of precipitation per day) according to TT and to BC. Here TT underestimates the change in the increase of consecutive dry day with approximately 50%. This indicates that the change in persistence is not fully captured by TT.

number of tropical days Figure 2.81 shows the number of tropical days (i.e., the maximum temperature exceeds 30°C) for the observations (left upper) and for BC (left lower). Also shown are the situations according to 2100Hn (middle column) and 2100Hd (right column). The number of tropical days for TT agrees well with the BC results.

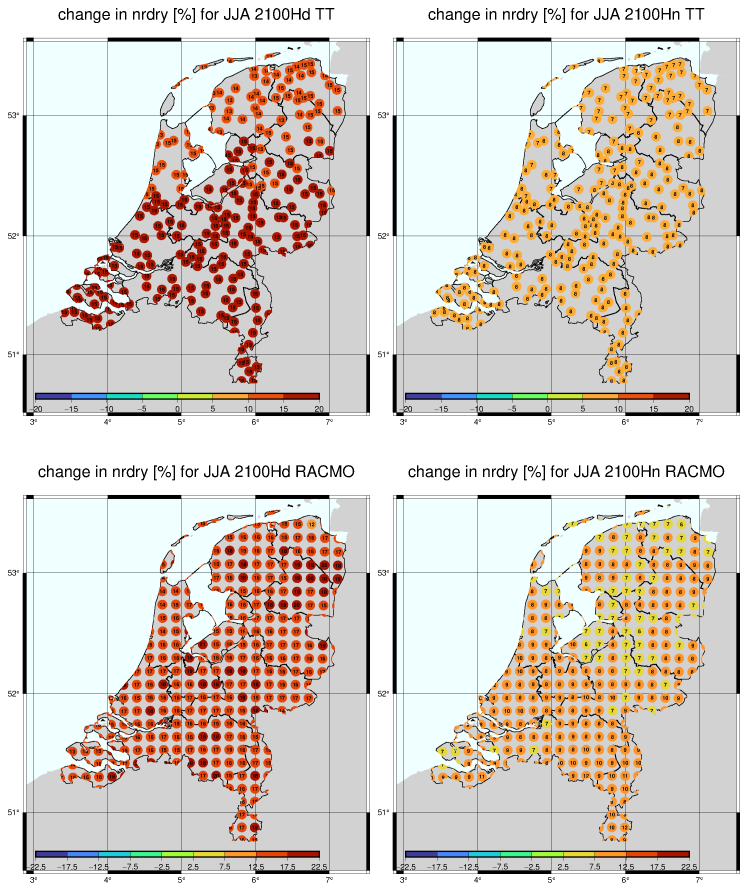

Figure 2.79: Change in the number of dry days (threshold 1mm) in JJA for timeseries transformation (upper) and RACMO (lower) for the 2100Hd (left) and 2100Hn (right) scenario.

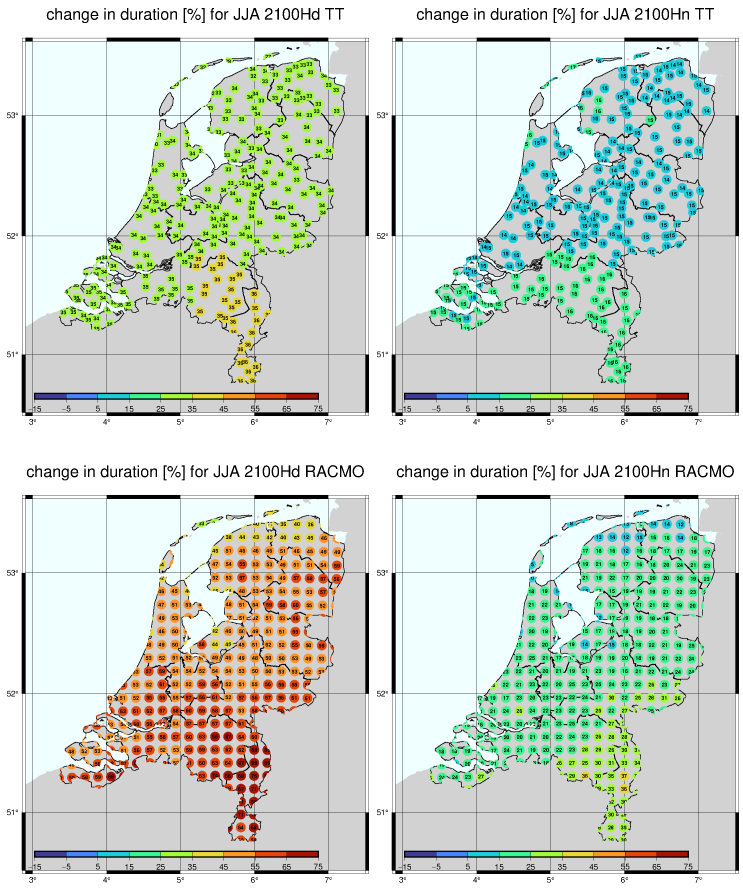

Figure 2.80: Change in the duration of dry days (threshold 1mm) in JJA for timeseries transformation (upper) and RACMO (lower) for the 2100Hd (left) and 2100Hn (right) scenario.

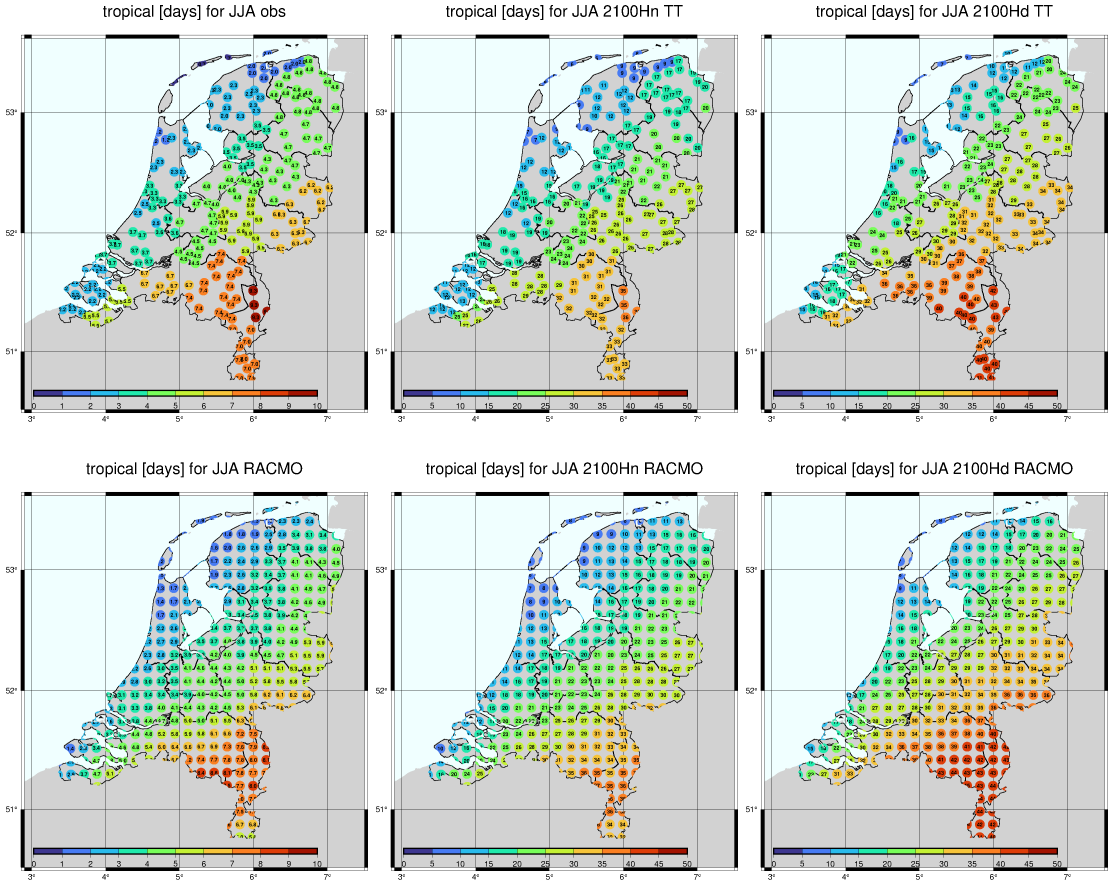

Figure 2.81: Number of tropical days according to observations (left), TT for 2100Hn (middle) and 2100Hd (right), and for the BC RACMO runs (lower row).

Chapter 3

Observed trends and scenarios per variable

3.1 Temperature

3.1.1 Introduction

Temperature is the primary variable affected by the enhanced greenhouse effect, and local or regional changes are usually highly correlated with the global-mean temperature change. This section describes the results of the CMIP6 as well as the RACMO runs for the Netherlands, focusing on the relation between global-mean and regional temperatures as well as the relation between mean and maximum temperatures. Results are mainly shown for SSP5-8.5, but due to the close connection with global-mean temperatures they can easily be scaled to other SSPs.

3.1.2 Observations

To describe observed changes of near surface temperature (i.e., the temperature at 2 m above ground, also known as 2-m-temperature), we use the monthly-mean ERA5 data (Hersbach et al., 2020). They are nearly indistinguishable from the observation-based E-OBS data (Cornes et al., 2018). Figure 3.1 shows the regression of the annual-mean ERA5 temperatures onto the observed global-mean temperature from the HadCRUT5 dataset (Morice et al., 2021). The regression gives local temperature change in degrees per degree of global-mean temperature change.

Over most of the region shown in Figure 3.1 the regression is larger than one, indicating that the local temperature rises faster than the global mean. Over the Netherlands, the acceleration of the temperature rise with respect to the global-mean approaches a factor of two, consistent with earlier results of Oldenborgh et al. (2009). The regression shows a clear sea-land gradient as land warms faster than water. This land effect explains a large part of the local warming acceleration.

In the Netherlands, temperature has risen by about 2°C since the beginning of the 20th century (Figure 3.2, left panel). However, the maximum temperatures (highest daily maximum, or TXx) have risen twice as much (Figure 3.2, right panel). At the beginning of the 20th century, annual-maximum temperatures lay around 30°C, and 1920 experienced the lowest maximum temperature with only 26.3°C. The last year in which the annual-maximum temperature in De Bilt did not exceed 30°C was 1993, with a maximum temperature of only 29°C. Presently, the mean annual-maximum temperature in De Bilt lies around 34°C. With 37.5°C, the highest temperature so far was reached in 2019.

3.1.3 Attribution

As the temperature in north-western Europe rises faster than the global-mean temperature (Figure 3.1), there must be processes at work that regionally reinforce the global-mean temperature

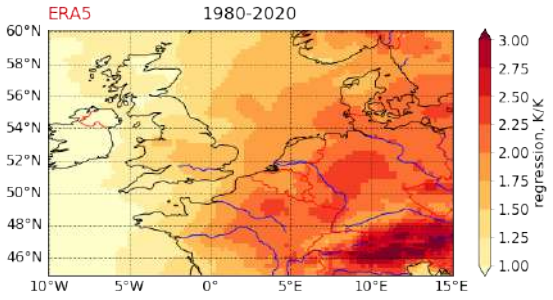

Figure 3.1: Regression of annual-mean temperature from ERA5 over Europe on global-mean temperature (HadCRUT5) during 1980-2020. The result is to be read as 'x degree local temperature change per degree of global-mean temperature change'.

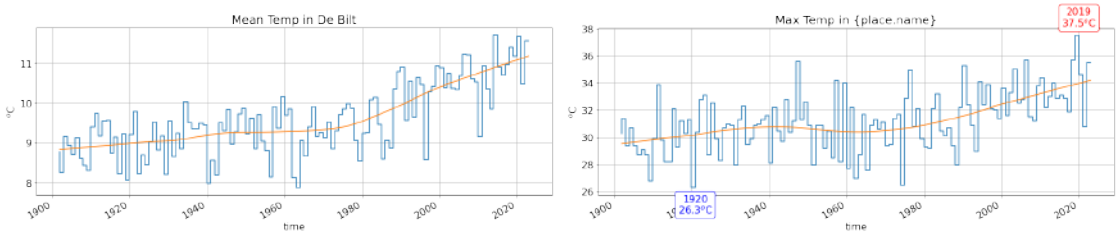

Figure 3.2: Temperature change in the Netherlands (De Bilt). Left: annual mean temperature, Right: annual-maximum temperature (highest daily maximum, or TXx). Data from KNMI daggegevens (2022). Annual values in blue, trend line in orange.

increase. One obvious candidate is the fact that north-western Europe is a land region (albeit at the margin of a continent), and land warms faster than the ocean (Figure 3.1; see also Sutton et al. (2007), Joshi et al. (2008), and Kleidon and Renner (2017)). A second effect is a change of circulation towards more (south-)westerly directions (Figure 3.3). The effect is largest in winter (Oldenborgh et al., 2009), when south-westerly winds bring relative warm air into western Europe. A third effect is the increase in sunshine duration since the 1980s (Figure 3.4). Cleaner air has led to less backscatter of shortwave radiation and to less clouds (Dong et al., 2022). Obviously, more sunshine leads to higher temperatures.

3.1.4 Projections

In this section the projected temperature change over the Netherlands is assessed from the RACMO runs (Section 2.1.8) that form the basis for the scenario tables (Chapter 10). The change is calculated according to the *matched warming* procedure (Section 2.1.1). Furthermore, the results are not shown separately for the two groups (dry-trending and wet-trending), since the temperature signal does not differ much between them (see Table 3.2 and scenario tables).

Local vs. global temperature response

As global-mean temperatures increase, so do the regional ones. Table 3.1 shows the global and regional (Netherlands-mean) temperature change in 2100 according to the *matched warming* procedure (see Section 2.1.1) with respect to the reference period. The regional warming in EC-Earth3$_{p5}$ is slightly higher than in CMIP6 (standard dataset), and it hardly exceeds the global-mean warming. The temperature evolution in the RACMO runs (last column) follows that of the driving EC-Earth3$_{p5}$ runs, with no extra warming due to local feedbacks other than already resolved in EC-Earth3$_{p5}$.

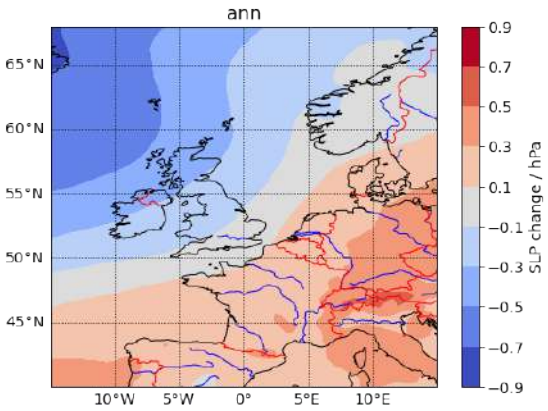

Figure 3.3: Change of annual-mean mean sea level pressure over north-western Europe between the 30-year reference period (1991–2020) and the preceding 30-year period (1961–1990) from ERA5.

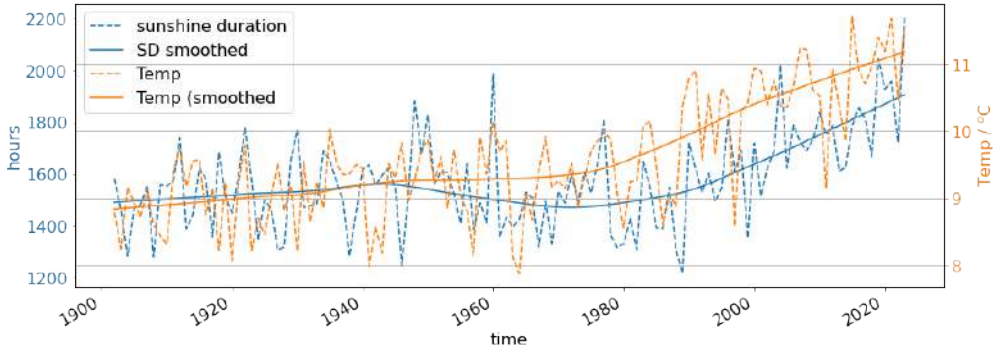

Figure 3.4: Annual sunshine duration (left axis) and annual-mean temperature (right axis) in De Bilt from KNMI daggegevens (2022). Annual values dashed, trend line continuous.

	CMIP6		EC-Earth3$_{p5}$		RACMO	
scen	glob	NL	glob	NL	glob	NL
SSP1-2.6	0.7	0.7	0.8	0.8	-	0.9
SSP2-4.5	1.8	1.6	1.9	2.0	-	2.1
SSP5-8.5	3.8	3.7	3.9	4.2	-	4.3

Table 3.1: Warming level at the time the global warming reaches the IPCC best estimates for 2100 (*matched warming*, see Section 2.1.1)) relative to the reference period for the standard dataset from CMIP6, for the EC-Earth3$_{p5}$ runs, and for RACMO. The columns denoted *glob* contains the global-mean warming, the columns denoted *NL* the warming averaged over the Netherlands. Obviously, there is no global-mean for the RACMO runs.

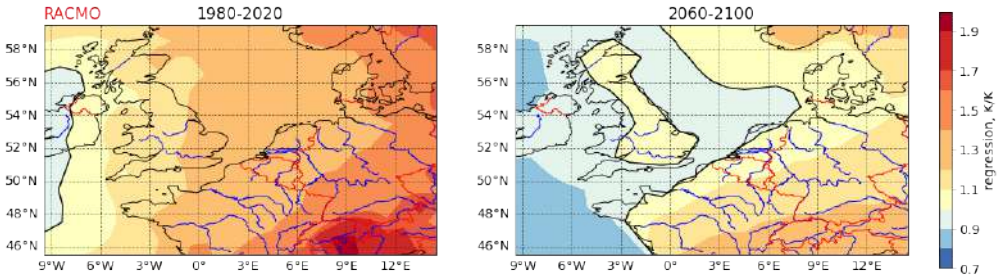

Figure 3.5: Regression of the annual-mean temperature over Europe from the RACMO runs on the global-mean temperature from the driving EC-Earth3 $_{p5}$ runs (SSP5-8.5) for the period 1980-2020 (left) and a future period of the same length (2060-2100; right). The line where local and global temperature rise are equal (regression equals unity) is added in black.

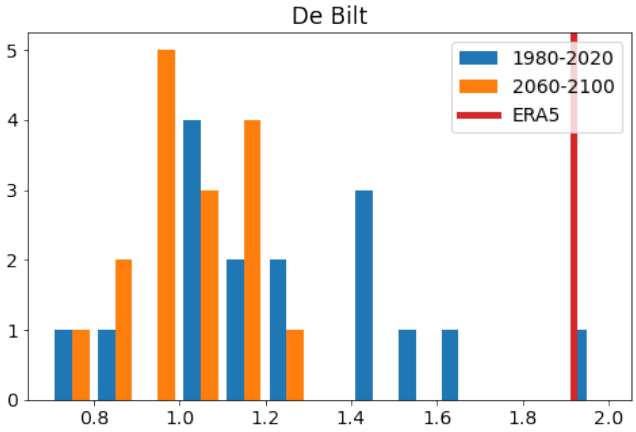

Figure 3.6: Distribution of the regression coefficients for De Bilt of the annual-mean temperature from the RACMO runs on the global-mean temperature from the driving EC-Earth3 $_{p5}$ runs (SSP5-8.5) for two periods. The corresponding value from ERA5 is marked in red.

The faster-than-global warming over the Netherlands in the RACMO runs is a continuation of the observed trend (Section 3.1.2). However, the magnitude of the regional enhancement (the regression on the global-mean temperature) in RACMO is smaller than in the observations, and it declines in the future. While in ERA5 (substitute for observations) the regression reaches values around 2 over the Netherlands (Figure 3.1), the modelled regression over the same period (left panel of Figure 3.5, note the different colour bar) only reaches values around 1.3, declining to even lower values (around 1.1) for the period 2060–2100 (right panel of Figure 3.5).

That the regression is higher for the observations than for the ensemble-mean of the RACMO runs is partly an averaging effect. Figure 3.6 shows the distribution of the regression coefficients for De Bilt. Only one of the sixteen RACMO members reaches a regression that equals that of ERA5 (marked in red) over the period 1980–2020. For two members the regression is even lower than one, while for most members it lies between 1 and 1.3. The high regression values found in ERA5 could be due to internal variability. For the future period, all RACMO members show lower regression values with much less spread.

If we use CMIP6 model output instead of RACMO, we obtain the same low regression coefficients. Obviously, some of the local effects that enhance the warming are missing, or are at least weaker, in the models than in the observations. Furthermore, they seem to become less effective

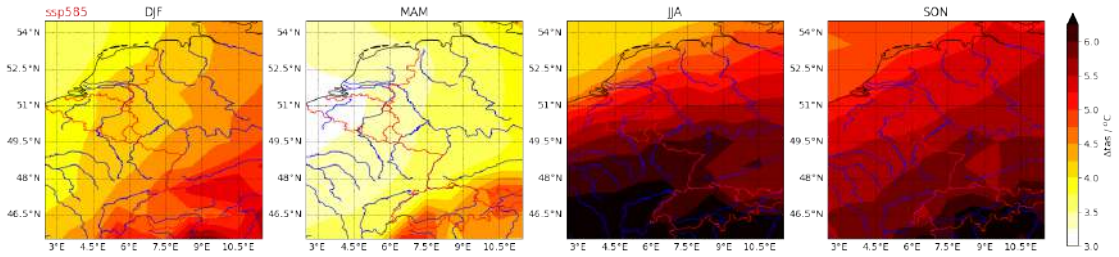

Figure 3.7: Seasonal-mean temperature increase (*matched warming*) over the Netherlands and the Rhine-Meuse catchment in SSP5-8.5 driven RACMO runs.

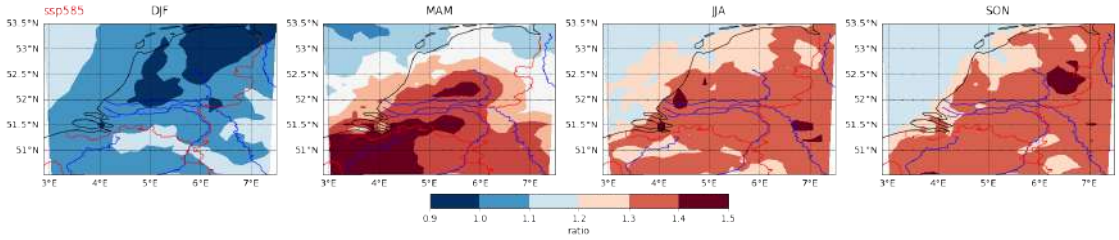

Figure 3.8: Ratio between the maximum and the mean temperature change between 2071–2100 and 1991–2020 (SSP5-8.5). The mean temperature change is calculated as the mean of the daily-mean temperature over the season and the respective period. The change of the maximum temperature is calculated from the mean over the two periods of the maximum of the daily-maximum temperatures over the season. This is done for all members of the RACMO ensemble separately. Plotted here is the maximum of the ratios from all members. In this way the results shown here can be directly compared to the ratio of the orange trend lines in Figure 3.2.

in the future. That models fail to reproduce the enhanced warming in Western Europe is known for long (e.g., Oldenborgh et al. (2009)), but the reasons are still unknown.

Seasonal temperature response

The temperature increase over the Netherlands has a clear sea-land gradient (Figure 3.7), with the coastal areas warming less than the regions towards the south-eastern part of the country. The gradient continues south-eastward beyond the Dutch border. The gradient is largest in summer, when the warming difference between the coast and the south-eastern part of the country reaches 1°C, and smallest during spring, when it is hardly visible. This warming gradient is directly linked to the similar gradient of the regression coefficient with the global-mean temperature (Figure 3.5).

Temperature extremes

Temperature extremes continue to grow faster than the mean temperature. Figure 3.8 shows the ratio between the change of the season-maximum temperature to the season-mean temperature for the four seasons between the future (2071–2100) and the reference period. The seasonal temperature mean in a period is simply the average over all daily-mean temperatures (TG) in the season within that period. For the maximum temperature we take the mean over the period of the seasonal-maximum of the daily-maximum temperatures (TXx). For each RACMO ensemble member, this is equivalent to what can be inferred from the observed trend lines in Figure 3.2. The ratio of the two changes (mean and max) is calculated for each of the RACMO ensemble members, and the maximum of these ratios is plotted in Figure 3.8.

In all seasons but winter the maximum temperatures increase more than the mean temperatures. In winter the mean temperature grows faster than the maximum temperature because

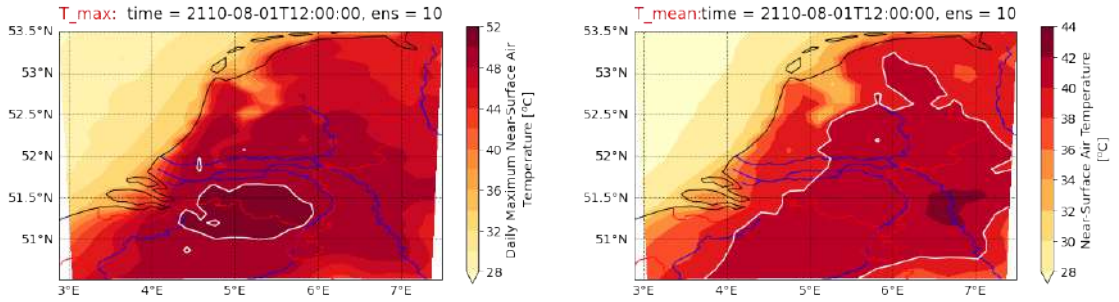

Figure 3.9: Temperature fields on the day with the highest maximum temperature in De Bilt in the RACMO ensemble for SSP5-8.5 (1 Aug 2110 in member 10). Left: maximum temperature, white contour at 50°C; right: daily-mean temperature, white contour at 40°C. Note the different scales.

winter warming comes mainly from the elimination of extremely cold days. Over most of the Netherlands, the projected ratio between the changes of maximum and mean warming is below 1.4 (Figure 3.8). This is smaller than the observed ratio of around two that can be inferred from the two orange trend lines in Figure 3.2. Higher trends for maximum than for mean temperatures are found over a large area in north-western Europe (Patterson, 2023). Note, however, that in Figure 3.8 the largest ratio of the 16 RACMO runs is shown. For a comparison with the single realisation of observations the median might be more appropriate, which is even lower. Reasons for models to underestimate the trend of temperature extremes are unknown (e.g., Patterson (2023), Min et al. (2013)).

While the ratio of maximum-to-mean change in the RACMO runs are lower than one would expect based on the observations, individual hot events can attain very high temperatures. Indeed, the highest temperature reached at the grid point representing De Bilt is 50.1°C on 1 August 2110 in ensemble member 10. The maximum and mean temperature fields for this day are shown in Figure 3.9. The daily-maximum temperatures on this day exceed 50°C in the southern parts of the Netherlands, with the daily-mean exceeding 40°C in nearly the whole country!

Adding climate sensitivity uncertainty

As shown in Figure 3.5, the local temperature is in pace with the global-mean temperature. This will not change with a different climate sensitivity. The local temperature will rise with roughly the same factor of the global-mean temperature as displayed in Figure 3.5. The KNMI'23 scenarios have been derived from the matched warming approach (see Chapter 2), thus eliminating the effect of the climate sensitivity from the beginning. The largest uncertainty for the local/regional changes are local feedbacks that are missing or are too weak in the models.

3.1.5 Summary and conclusion

For the different scenarios, Table 3.2 displays some key values of temperature change in the Netherlands from the full scenario tables (see Chapter 10). These values are based on the bias-corrected data (see Section 2.1.10). For all scenarios the annual-mean warming in the Netherlands is close to the global-mean one. Summer warming clearly exceeds warming in the winter, with the highest warming levels for the Dry scenarios in summer. In winter there is hardly any difference between the dry and wet scenario variants.

The overall picture arising from Table 3.2 reflects changes in other temperature-related parameters. They all scale well with the global-mean temperature change, indicating a robust mechanism connecting global- and regional-scale changes. For temperature itself the scaling factor is

[1] from the Dutch *nat* = wet

		Global	Netherlands					
		annual	annual		winter		summer	
Scenario	SSP		d	n	d	n	d	n
L	1-2.6	0.8	0.9	0.9	0.7	0.7	1.2	1.1
M	2-4.5	1.9	2.0	1.9	1.6	1.6	2.5	2.3
H	5-8.5	4.0	4.4	4.1	3.7	3.9	5.1	4.7

Table 3.2: Temperature increases (excerpt from the full scenario tables) for warming in 2100 with respect to the reference period (in °C). The values in the *Global* column are the IPCC best estimates for SSP1-2.6, SSP2-4.5 and SSP5-8.5 (see Table 2.1). The values for the Netherlands represent the average warming over the Netherlands for the whole year (annual), winter and summer for the dry- (*d*) and wet-trending (*n*)[1]scenario variants.

only slightly larger than one. Summarised, the scenario tables (Chapter 10) show that over the Netherlands

- the local/regional mean temperatures increase only slightly faster than the global-mean temperature
- the temperature change increases south-eastward away from the coast
- the changes of the mean daily-maximum and the daily-mean temperatures are comparable, but ...
- ... the maximum daily maximum temperature increases much faster and can exceed 50°C under SSP5-8.5 around 2100
- the temperature increase in summer and autumn is larger than in winter
- in summer, the Dry variants warm faster than the Wet variants, while ...
- ... the difference between the two variants is small in winter
- in winter the cold extremes warm faster than the warm extremes, and *vice versa* in summer.

In Section 3.1.2 we saw that the CMIP6 models fail to reproduce the observed accelerated regional warming compared to the global mean warming, as well as the much larger increase in hot extremes than average temperatures. These problems translate into the downscaled RACMO runs. As a result, the projected local warming at a global warming level of 1.5°C is at the lower bounds of values obtained by a linear extrapolation of the observations (Figure 8.1). These model problems raise the question how to value the main results of the scenarios as presented here, especially the finding that

- the mean warming over the Netherlands is roughly equal to the global-mean warming, and
- temperature extremes warm only modestly faster than the mean temperature.

It is hard to answer this question as long as the reason for the model-observation discrepancy is not clear. If the model deficiencies work through in the projections, the warming rates reported here are only a lower bound of the future temperature evolution. Future warming levels could be significantly higher than those reported here. On the other hand, known contributors to the locally enhanced temperature increase (reduced air pollution, changed wind directions, see Section 3.1.2) cannot go on forever. Clearly, continued research to find the reasons for the model deficiencies is needed.

3.2 Precipitation

3.2.1 Introduction

Rainfall can be distinguished into convective precipitation and large-scale precipitation. Convective precipitation is caused when the sun heats the air close to the ground, causing it to rise. It is typical for summer conditions and often accompanied by thunderstorms. Large-scale precipitation occurs when air masses that are advected by the large-scale (synoptic) circulation cool down when forced to rise near frontal systems - warm air over cold air - or over orography. This section deals with the large-scale precipitation, and the convective precipitation is the topic of Chapter 5.

A general characteristic of climate change or global warming is that warmer air can contain more moisture. A larger moisture content potentially means larger precipitation, since precipitation essentially is a release of atmospheric moisture. Another consequence of global warming is more evaporation from land- and water surfaces. All water that is evaporated to the atmosphere (a continuous process) should eventually precipitate out (which in contrast to evaporation is a discontinuous process), since it is a closed system. The rate of the atmospheric moisture increase with temperature is about 7% per °C . This is also known as the Clausius-Clapeyron (CC) moisture rate.

As a result of climate change we often see precipitation changes that are of the same order of magnitude as the CC rate. The actual precipitation response may be higher or lower than the CC rate for several reasons. Precipitation largely depends on (local) atmospheric motions and temperature differences in the atmosphere (both in horizontal and vertical directions), which depend in turn on the spatial and temporal scales relevant for individual precipitation events or systems. Due to global warming, local or regional precipitation may also (systematically) decrease. This is usually related to a change in the large-scale atmospheric circulation, e.g. when the prevailing wind direction changes from directions where the air originates from sea (with typically larger moisture contents because of relatively more evaporation from water surfaces) to directions where the air originates from land (with typically smaller moisture contents because of relatively less evaporation from land surfaces).

3.2.2 Observed precipitation and climate scenario projections for the Netherlands

Looking at the (long-term) trend in historical precipitation over the Netherlands, there are clear differences from season to season. Seasonal mean precipitation trends over the Netherlands are largest for winter and smallest for spring. The increase in mean precipitation between the early 1900s and present day is roughly 30% for winter, 20% for autumn, 10% for summer and 5 to 10% for spring (see Figure 3.10). The increase in annual mean precipitation of almost 20%, logically, lies in the middle of the seasonal trends (not shown in the figure).

This figure also presents the seasonal precipitation over the Netherlands in "2050" and "2100" (i.e. for the 30-year climates centred respectively around 2050 and 2100) for the four (main) KNMI'23 climate scenarios (i.e. Ld, Ln, Hd and Hn)[2]. For winter the increases in the climate scenarios are a continuation of the long-term historical trend. The largest increases are present in the Hn scenario, and the smallest ones in the Ld scenario. In spring and autumn the changes in the climate scenarios are relatively smaller and only partly a continuation of the long-term historical increase. For summer the changes in most climate scenarios are opposite to the increasing long-term historical trend. The decrease in summer precipitation is largest in the Hd scenario. The smallest *change*, effectively almost no change, occurs in Ln. The decrease in summer precipitation, in three of the four scenarios, takes already place in "2050". This means that a 'sign change' of the observed trend in summer precipitation should likely occur in the near future. Note that the

[2]Note that there are also additional KNMI'23 climate scenarios; the Md and Mn scenarios that correspond with the SSP2-4.5 emission scenario, and a single scenario 2033_L that correspond with the 1.5°C target in the 'Paris agreement'. For the latter no distinction between wet and and dry is made. Also for these additional climate scenarios precipitation response results are presented in the remainder of this section.

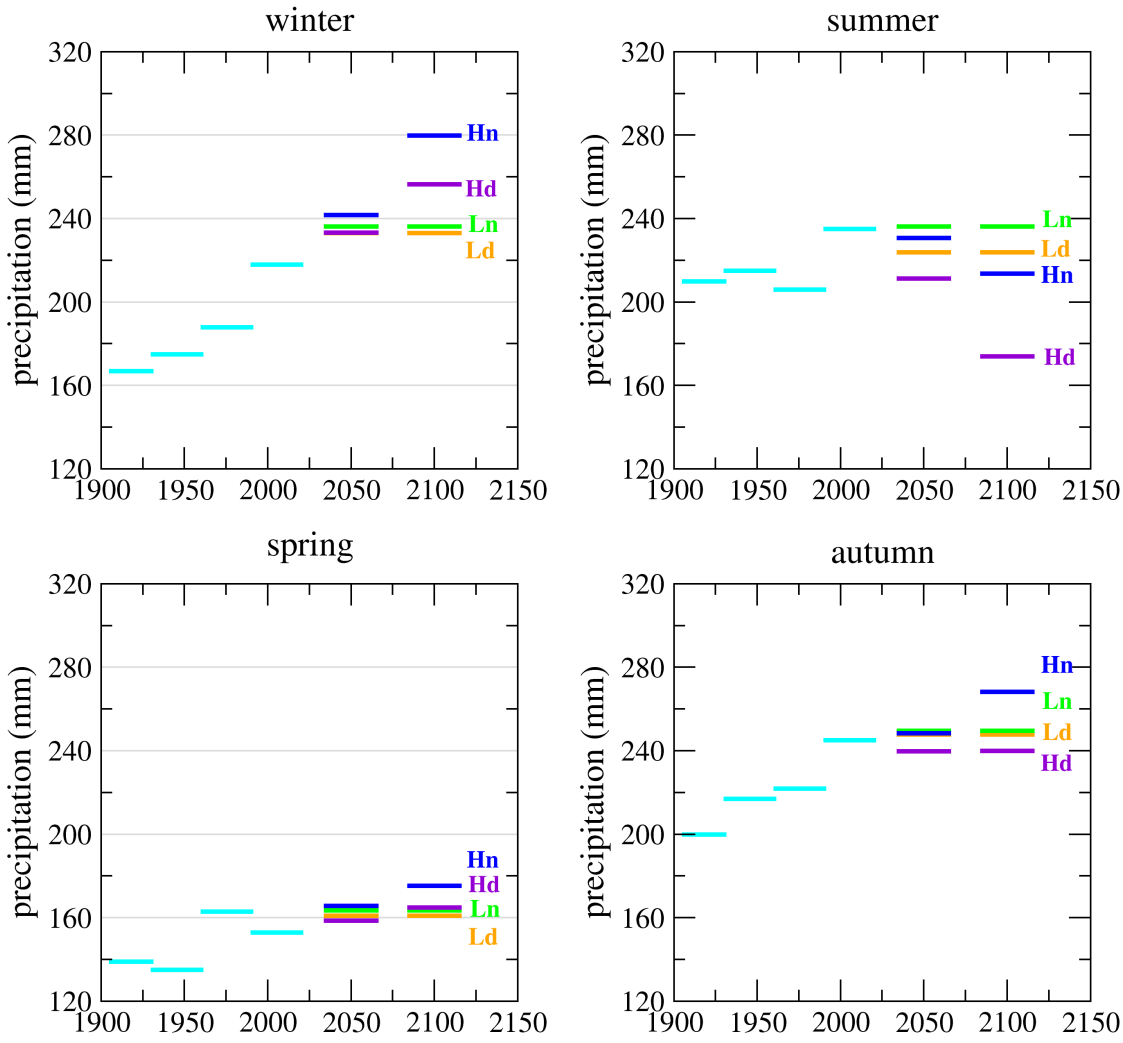

Figure 3.10: Seasonal mean precipitation for the Netherlands for historical 30-yr normal periods and for the four main KNMI'23 climate scenarios for 2050 and 2100.

term 'sign change' is used loosely here, since the long term historical increase (≈10%) is probably not significant (more precisely, not statistically different from zero). In theory it is therefore not allowed to call it a 'sign change', but from Figure 3.10 it is clear what is meant. This 'summer drying' in the KNMI'23 scenarios is a familiar feature that is, as in previous projections, projected in the current future simulations with global climate models for the Netherlands and surrounding area. Figure 3.11 (in the next subsection) shows that the trend in summer precipitation in the area covering the Netherlands and the river basins of the Rhine and the Meuse (denoted as NL+RM) becomes a decreasing trend at the latest around 2040 for the climate models that are part of the 'Wet trending group' of models and somewhat earlier for the models in the 'Dry trending group'. Note, that in the summer precipitation time series for the Netherlands (available at urlhttps://www.knmi.nl/klimaatdashboard) there may be already a first indication that the increase in mean summer precipitation slows down somewhat after 2000, although it is too early for a definitive conclusion.

3.2.3 Precipitation responses for the different SSP emission scenarios

In this subsection the precipitation response under different emission scenarios as a function of time is presented. It is generally accepted that the 'skilful scale' of climate models corresponds to a spatial scale of several model grid cells. In addition, precipitation at the scale of a model grid cell is known to have relatively large natural variability (compared to, e.g., temperature). Consequently, it is less meaningful to look at the precipitation response of the few grid cells only that cover the Netherlands in a coarse resolution global climate model. We therefore analyse the precipitation response over an area exceeding the Netherlands and consider the NL+RM area as being most relevant for many Dutch climate impact applications. The different figure panels of Figure 3.11 show the precipitation response for this area while distinguishing:

- Three greenhouse gas emission scenarios representing the IPCC Shared Socioeconomic Pathways (SSP): SSP1-2.6, SSP2-4.5 and SSP5-8.5,
- The four meteorological seasons, and the whole year (denoted as Annual),
- The group-averages of the 'Wet trending group' and the 'Dry trending group'.

The overall picture that emerges from Figure 3.11 is: i) the responses (whether positive or negative) 'increase' with time, ii) the responses are stronger for higher emission scenarios, and iii) for the Wet trending group positive responses are stronger (more positive), and negative trends are weaker (less negative), than for the Dry trending group. Consequently, for the Dry trending group negative responses are stronger (more negative), and positive responses are weaker (less positive), than for the Wet trending group. The latter is of course largely a consequence of the definition of the Wet and Dry trending groups (see Chapter 2).

3.2.4 Differences in area-mean precipitation responses between CMIP6, EC-Earth3 and RACMO

Before the precipitation response patterns for each of KNMI'23 climate scenarios, which are obtained from RACMO, are presented and discussed, we have a closer look at the differences in relevant area-mean precipitation responses between the different climate models used in the KNMI'23 climate scenario construction chain. The purpose of this comparison is two-fold: i) to show that the area-mean precipitation responses between the different model types can be different, including the size of such differences, and, ii) to show that the area-mean precipitation responses in the KNMI'23 climate scenarios (based on RACMO) are consistent between the different climate scenarios in terms of ΔGSAT rate.

The three main steps in the construction of the KNMI'23 climate scenarios, for which also three different types of climate models are used, are briefly summarised here because we want to compare the precipitation responses in each of these three steps. The first step involves the available set of 33 CMIP6 global climate models, and the distinction in a Wet - and Dry trending group of models. These CMIP6 model projections determine the 'resampling-criteria' used for resampling the time series of the simulations with EC-Earth3$_{\text{p5}}$, i.e. the re-tuned version of the global climate model EC-Earth3 (see Section 2.3) in the second step. In the third step the resampled time series from EC-Earth3$_{\text{p5}}$ are substituted with those of EC-Earth3$_{\text{p5}}$ downscaled with the regional climate model RACMO. For details see Chapter 2.

In addition to the above mentioned purpose, comparison of the responses in steps 1 and 2 shows how well the 'resampling criteria' are reproduced by the actual resampling. For precipitation the reproduction is in general not as close as for temperature, for which the correspondence is very good (not shown). Comparison of the responses in steps 2 and 3 (with step 3 being the 'end result' defining the climate scenarios) shows what is the effect of the dynamical downscaling with RACMO.

These three steps are performed for each of the (eight) distinct global mean temperature changes (ΔGSAT or dGSAT) resulting from different combinations of (three) SSPs and 30-yr future periods centred around 2050, 2100 and 2150 w.r.t. the historical reference period 1991-2020

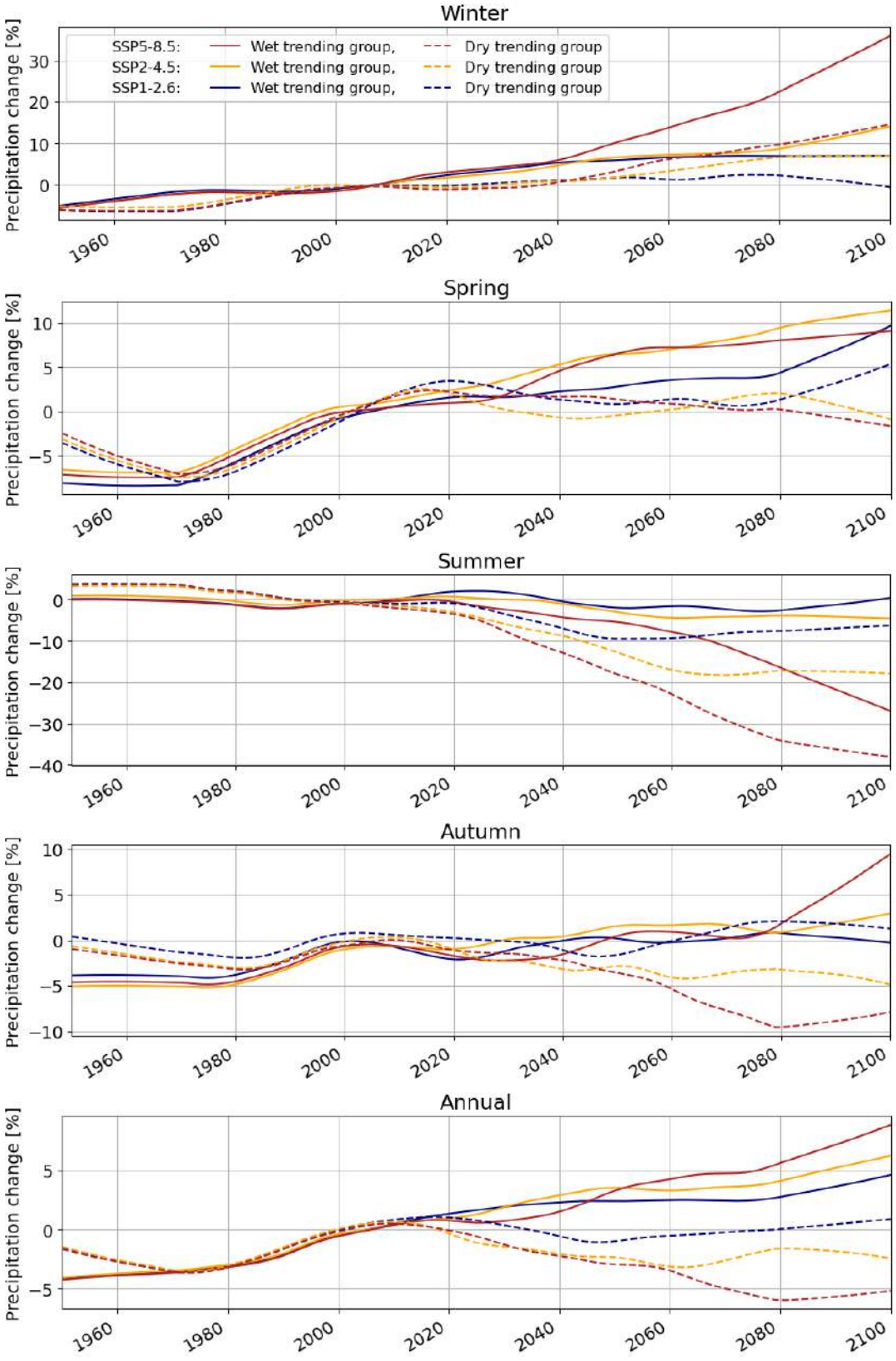

Figure 3.11: Seasonal and annual mean precipitation changes in the NL+RM area for three emission scenarios (SSP1-2.6, SSP2-4.5 and SSP5-8.5); average of the 'Wet trending group' (solid lines) and average of the 'Dry trending group' (dashed lines). Changes smoothed over time based on Valk (2020). All changes relative to the reference period 1991-2020.

Climate scenario name	ΔGSAT [°C]	Emission scenario	Future period
2033_L	0.6	SSP1-2.6	ΔGSAT = 1.5°C wrt pre-industrial
2050_Ld, 2050_Ln	0.8	SSP1-2.6	2050
2100_Ld, 2100_Ln	0.8	SSP1-2.6	2100
2150_Ld, 2150_Ln	0.8	SSP1-2.6	2150
2050_Md, 2050_Mn	1.1	SSP2-4.5	2050
2100_Md, 2100_Mn	1.9	SSP2-4.5	2100
2150_Md, 2150_Mn	2.1	SSP2-4.5	2150
2050_Hd, 2050_Hn	1.5	SSP5-8.5	2050
2100_Hd, 2100_Hn	4.0	SSP5-8.5	2100
2150_Hd, 2150_Hn	5.5	SSP5-8.5	2150

Table 3.3: Climate scenario names and corresponding global mean temperature changes (ΔGSAT) w.r.t. 1991-2020, emission scenario and future period (30-yr period centred at year). Note that 2050_Ld, 2100_Ld and 2150_Ld are identical climate scenarios, as well as 2050_Ln, 2100_Ln and 2150_Ln. 2033_L is a single scenario without Dry and Wet variants.

that serve as a basis for the climate scenarios (see Tabel 3.3). For the climate scenarios for 2050 and later there are two different scenario variants, the Dry and Wet variants (labelled respectively with a 'd' or a 'n' in the climate scenario name). For the 2033 climate scenario (with a ΔGSAT of 0.6°C, corresponding with the 1.5°C in the Paris agreement), no distinction between Dry and Wet variants is made. The most relevant (area-mean) precipitation statistics for each of the 15 distinct climate scenarios in the three steps (i.e. the three types of models) are presented and compared in Figures 3.12 to 3.15. Table 3.3 connects the global mean temperature changes, ΔGSAT, which are the basis for the climate scenarios (and which are plotted in these figures on the x-axis) with the KNMI'23 climate scenario names as well as the corresponding SSP scenario and future time period.

Figure 3.12 shows for each of the climate scenarios, ordered by ΔGSAT, the change in the seasonal and annual mean precipitation in the NL+RM area for: i) the change-value used as resampling criterion (based on the CMIP6 models, i.e. step 1, in blue), ii) the corresponding change-value in the EC-Earth3$_{p5}$ resampled series (from step 2, in orange) and iii) the corresponding change-value resulting from the RACMO downscaling (from step 3, in green). For each climate scenario 33 different resampling simulations were performed[3]. From these 33 resampling simulations a single one is finally selected (see for the selection procedure Section 2.2). The selected one is represented by the coloured bars for the EC-Earth3$_{p5}$ resampling (orange) and for the corresponding RACMO downscaling (green). The results from all 33 different resampling simulations are represented by 33 black dots in the coloured bars (note that each EC-Earth3$_{p5}$ resampling alternative has a corresponding downscaled RACMO alternative). The resampling criteria themselves (the blue bars, step 1) are the same for each of the 33 resampling simulations, and therefore no black dots are plotted. The goal of the selection procedure is to reduce the 'sampling noise' in each of the different the climate scenarios. For certain cases this sampling noise can be relatively large. An example is the relatively large spread of the black dots in the greens bars of the 'Spring - Dry' panel.

Although in general the differences between the precipitation response in the selected EC-Earth3$_{p5}$ resampling simulation and the corresponding resampling criterion in Figure 3.12, i.e. the differences between the orange and blue bars, are reasonably small, the differences between the RACMO and the EC-Earth3$_{p5}$ responses, i.e. the differences between the green and orange bars are sometimes systematically larger. The much larger spatial resolution of RACMO compared to EC-Earth3$_{p5}$ means a better representation of sea-land contrast and orography and a larger

[3]Only 11 different simulations for the climate scenarios with a ΔGSAT of 5.5°C (i.e. for 2150_Hd and 2150_Hn), see Section 2.2 for details.

resolving resolution of the dynamical and physical processes on the spatial scale relevant for the KNMI'23 climate scenarios (essentially the Netherlands and the Rhine and Meuse basins). The RACMO responses are thus more skilful, and therefore considered favourable, to the corresponding EC-Earth3$_{p5}$ responses.

A clear difference between RACMO and EC-Earth3$_{p5}$ is the systematic smaller reduction of summer precipitation in RACMO both in the Dry and Wet scenarios as presented in Figures 3.12 and 3.13. A reduced reduction of summer precipitation in RCMs compared to GCMs is also reported by Coppola et al. (2021) for the Central Europe region. Section 2.4.6 discusses this difference further.

The overall picture emerging from Figure 3.13 (for NL) and Figure 3.12 (for NL+RM) is that the differences between RACMO and EC-Earth3$_{p5}$ are comparable for NL and NL+RM. Apart from the already mentioned differences in the summer precipitation response, these differences are most pronounced in spring and autumn for the Dry scenarios (both for NL and NL+RM). They are possibly related to the differences in the summer precipitation response (e.g., due to a difference in the shift of the seasonality). Note that seasonal and annual mean precipitation for NL and NL+RM are both resampling criteria (step 1) for the EC-Earth3$_{p5}$ resampling (step 2).

Figure 3.14 presents the results for another important precipitation resampling criterion, namely the once per 10-yr annual 10-day maximum area-average (NL+RM) precipitation, abbreviated as pr10day10yr. As the response of this variable is a relevant proxy for changes in extreme river discharges in the Rhine and Meuse rivers, it is included as a resampling criterion. Figure 3.14 shows that the EC-Earth3$_{p5}$ resampling (orange bars) very well matches the resampling criteria (blue bars), and that there is little spread between the 33 EC-Earth3$_{p5}$ resampling alternatives (black dots in orange bars). The downscaled RACMO pr10day10yr responses (green bars) are, however, systematically smaller than those for EC-Earth3$_{p5}$ (orange bars), and the spread between (i.e. the uncertainty in) the 33 resampling alternatives for RACMO (black dots in green bars) is considerably larger than for the corresponding EC-Earth3$_{p5}$ resamples. No literature was found that systematically analysed differences between RCMs and their driving GCMs regarding the response in precipitation extremes such as pr10day10yr.

The pr10day10yr responses from RACMO (that define the climate scenarios) are systematically larger for the 'Wet' scenarios than for the 'Dry' scenarios. Further, the pr10day10yr responses are well consistent between the different climate scenarios; the responses increase systematically with the increase in global mean temperature (ΔGSAT), both in the 'Dry' and 'Wet' scenarios which is in accordance with the dependency of the pr10day10yr response with ΔGSAT in the resampling criteria. Thus, in the climate scenarios also changes in extreme precipitation like pr10day10yr and pr1day10yr 'largely scale' with ΔGSAT.

Apart from being a resampling criterion, pr10day10yr is used as one of the two variables whose response is used to select one of the 33 EC-Earth3$_{p5}$ resampling simulation alternatives that ultimately determines a climate scenario. In brief, the resampling simulation that is selected is the one for which the RACMO response in pr10day10yr (together with the RACMO response in pr1day10yr, see next paragraph) is closest to the center of gravity of both responses (from the 33 resampling alternatives).

The second variable used in the selection procedure is the once per 10-year *summer 1-day* maximum *NL-average* precipitation, abbreviated as pr1day10yr (thus, the same exceedance probability, but shorter precipitation duration, averaged over a smaller area, and events restricted to the summer season), presented in Figure 3.15. These two variables are chosen for the selection procedure because they are important (impact) variables, and their responses contain a relatively large 'sampling noise'. Selecting 'the middle one' with respect to these two variables from the 33 alternatives reduces this sampling noise and consequently optimises the consistency in the precipitation responses between the different climate scenarios, in particular for these two variables. For details about the resampling selection procedure see Section 2.2.

Pr1day10yr is not used explicitly as a resampling criterion. Therefore in Figure 3.15 there are also no CMIP6 based resampling criteria plotted, nor the EC-Earth3$_{p5}$ resampling results. Pr1day10yr is, however, a relevant variable for extreme summer precipitation over the Netherlands, and its downscaled RACMO response is also quite noisy as a result of sampling noise shown in the

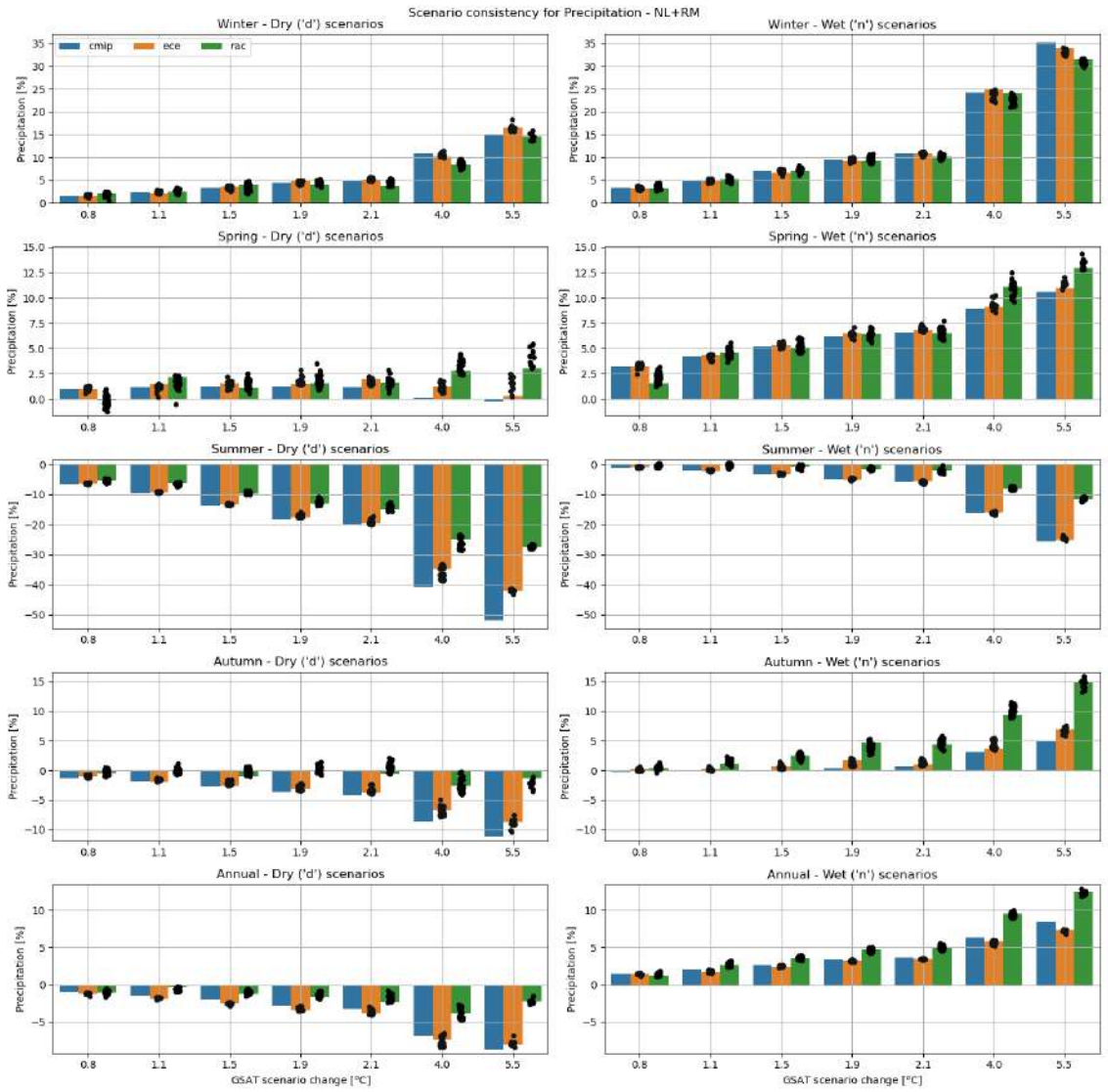

Figure 3.12: Consistency in seasonal and annual average precipitation responses in the area covering the Netherlands and the river basins of the Rhine and the Meuse (NL+RM) between the CMIP6 resampling criteria (blue bars), the EC-Earth3$_{\mathrm{p5}}$ resampling results (orange bars) and the RACMO downscaling of the EC-Earth3$_{\mathrm{p5}}$ resampling results (green bars) as a function of target global mean temperature change used for the different climate scenarios. Left panels for the 'Dry-scenario' variants and right panels for the 'Wet-scenario' variants. Dry/Wet variants respectively based on the Dry- and Wet trending groups of CMIP6 climate models (see main text). Note the different vertical scales in the different panels.

figure by the relatively large spread of the black dots. As for pr10day10yr, using pr1day10yr in the selection of one of the 33 resampling alternatives helps to reduce the sampling noise and thus to enhance consistency in the pr1day10yr response between the climate scenarios. Since pr1day10yr is not an explicit resampling criterion, its difference in the response between the Dry and Wet scenarios and the dependency of its response with ΔGSAT, similar to those for pr10day10yr, are intrinsic characteristics of the EC-Earth3$_{\mathrm{p5}}$ resamples downscaled with RACMO. In summary,

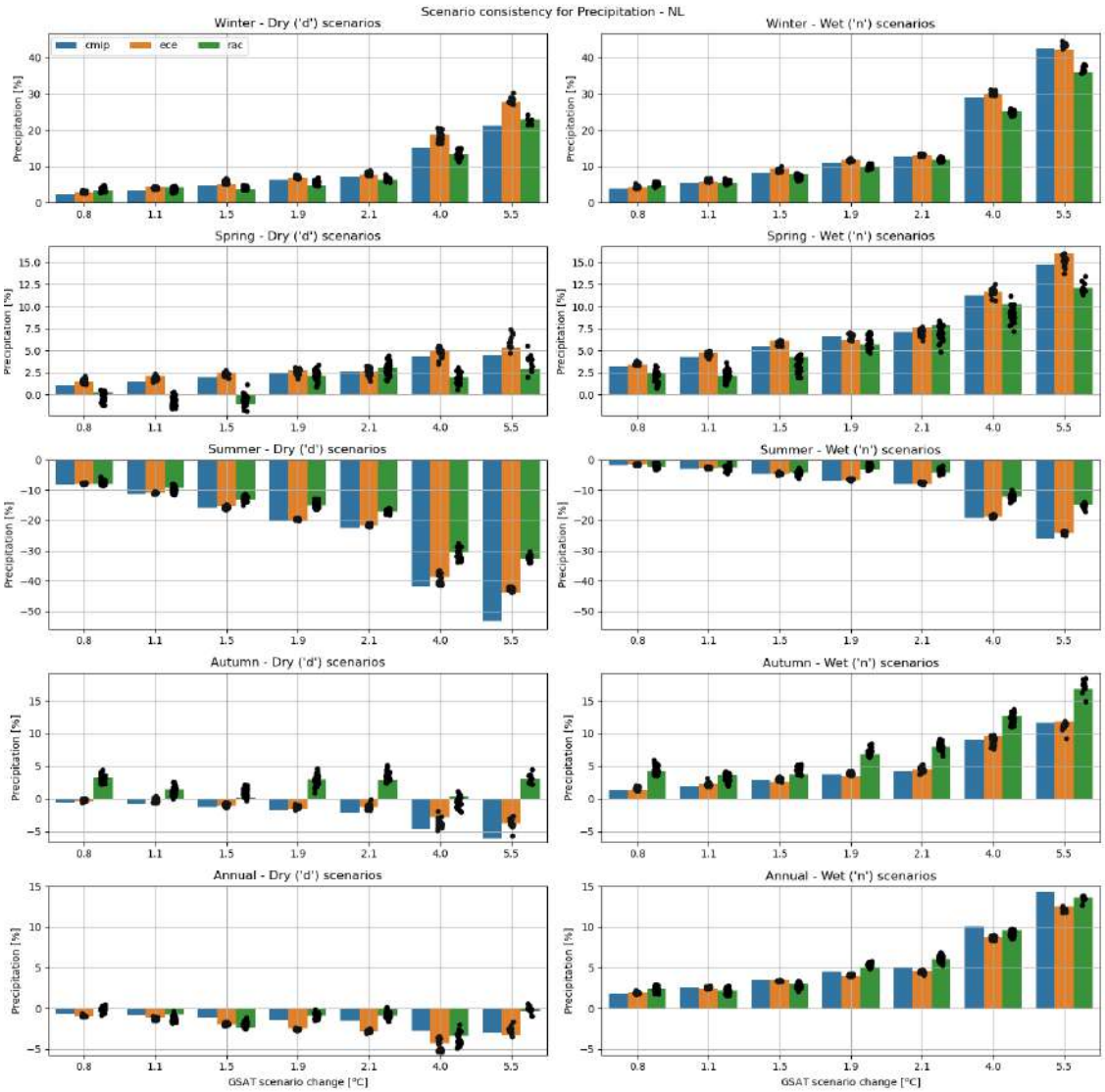

Figure 3.13: As Figure 3.12 but for the NL area (NL) rather than the NL+RM area.

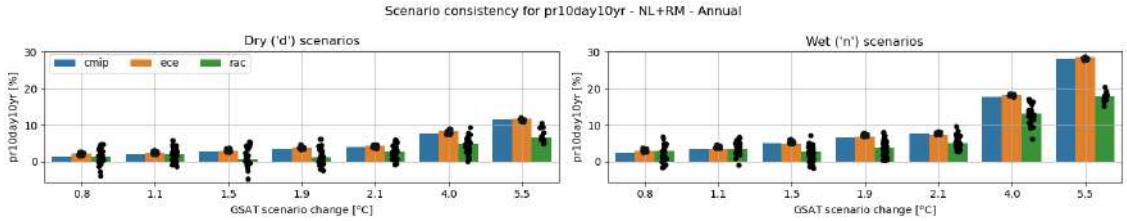

Figure 3.14: Similar to Figure 3.12 but for the once per 10-yr annual 10-day maximum area-average (NL+RM) precipitation (pr10day10yr) which is by definition an annual statistic.

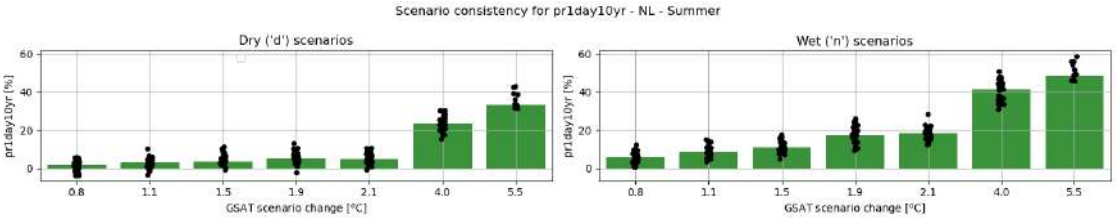

Figure 3.15: Similar to Figure 3.14 but for once per 10-yr summer (JJA) 1-day maximum NL-average precipitation. Since this variable is not a resampling criterion for the EC-Earth3 $_{p5}$ resampling, only its results for the RACMO based downscaling are presented.

also changes in extreme precipitation like pr10day10yr and pr1day10yr 'scale to a large extent' with ΔGSAT in the climate scenarios.

3.2.5 Onset and ending of summer drying

Figures 3.12 and 3.13 show a clear summer drying both for the Dry and Wet scenarios. The results for spring and autumn are however less robust. This is very likely related to differences in the time of the year when the summer drying starts and/or ends. Figure 3.16 shows for the 2085_Hd and 2085_Hn scenarios (with a ΔGSAT of 4.0°C) the change in the mean precipitation per calendar month. The first month after winter that has a negative precipitation change is regarded as the month that onsets the summer drying, and the last month after summer with a precipitation decrease marks the ending of the period of the summer drying. The figure shows that in all four panels the onset is earlier and the end is later in the Hd scenario compared to the Hn scenario. Both shifts are roughly one month, so the summer drying period lasts about two months longer in the Dry scenario compared to the Wet scenario. The fact that May may have a negative or positive change partly explains the difference in the response for the whole spring (MAM), same for the either decreasing or increasing response in September and the autumn (SON) response. In addition, there are also some differences between the RACMO and EC-Earth3 $_{p5}$ responses, e.g. a somewhat earlier ending in RACMO in the Hn scenario and a somewhat earlier start in RACMO in the Hd scenario. Although these latter differences seem subtle, all these differences together (between the months of onset and ending in respectively RACMO and EC-Earth3 $_{p5}$) contribute to the somewhat mixed results for spring and autumn in Figures 3.12 and 3.13, while the summer drying for the JJA months is very robust.

3.2.6 RACMO response patterns and atmospheric circulation change

In this subsection we look at the seasonal precipitation response in the full RACMO domain, together with the corresponding change in the atmospheric circulation (represented by the change in the MSLP (mean sea level pressure) pattern. For the four meteorological seasons Figure 3.17 presents both responses for the Hd and Hn climate scenarios. The first two rows are respectively for the Dry and Wet scenario variants for 2050, the third and forth rows are for 2100 and the last two rows for 2150. Both for MSLP and precipitation, and in all seasons, the amplitudes of both responses increase with ΔGSAT (i.e., from 2050 to 2100 to 2150).

In particular for winter and summer we will have a closer look at the relation between circulation and precipitation changes. For winter, the change in the MSLP field corresponds to an increase in the (at this latitude dominant) westerly circulation, which implies an increased transport of moist air from the Atlantic. This results in increased precipitation over most of the RACMO domain. The amplitudes of both responses correlate well; the responses are larger for the Wet scenarios than for the Dry scenarios (resp. the Hn and Hd scenarios), and larger for the scenarios with larger ΔGSAT.

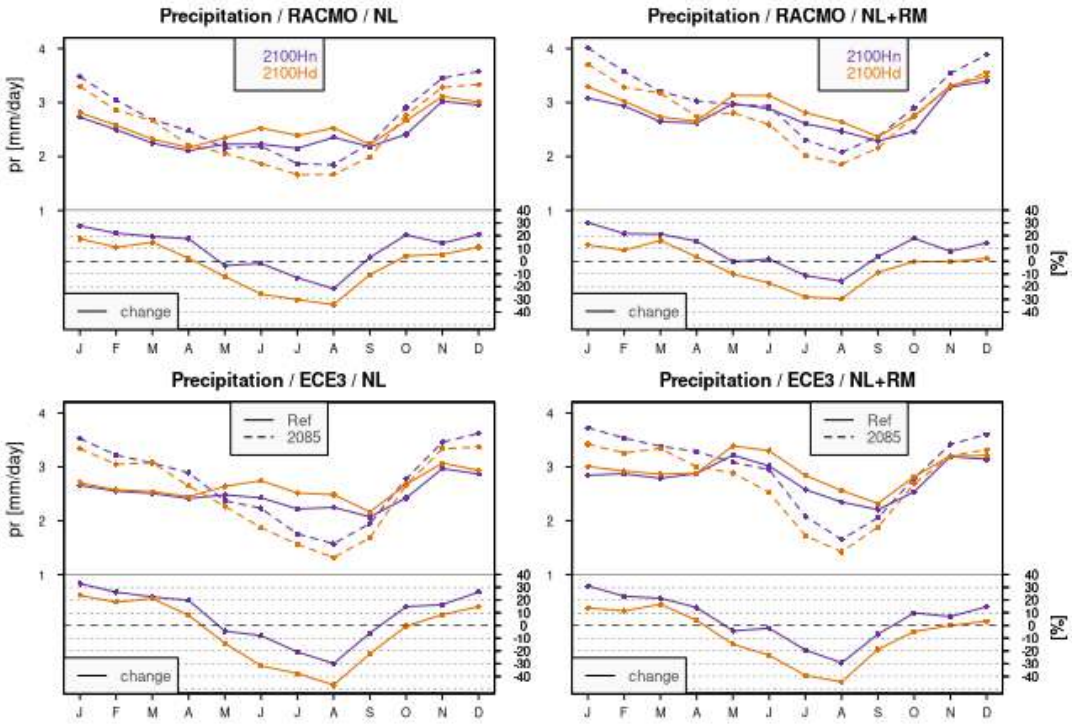

Figure 3.16: Monthly mean precipitation and changes therein for 2085_Hd and 2085_Hn for RACMO (top) and EC-Earth3$_{\text{p5}}$ (bottom) and for the NL and NL+RM regions (resp. left and right).

In summer, the circulation change represents an 'atmospheric blocking' situation for approximately the southern half of Europe (including the Netherlands), implying a decrease of the (dominant) westerly circulation with a subsequent precipitation decrease. Both types of scenarios have this precipitation decrease, with the largest precipitation reduction occurring in the scenario with the largest reduction of the westerly circulation / strongest blocking, being the Dry, or Hd, scenarios. Also in summer there is a clear correlation between the circulation and precipitation changes. As a result the circulation and precipitation changes are smaller (larger) in climate scenarios with less (more) warming.

Similar figures haven been made for the Md/Mn and the Ld/Ln climate scenarios. These figures (not shown) represent similar dependencies between the atmospheric circulation and precipitation responses in winter and summer. In summary we find stronger increases in westerlies with stronger precipitation increases in winter in the Wet scenarios compared to the Dry scenarios, and larger increases in atmospheric blocking (frequencies) with stronger precipitation decreases in summer in the Dry scenarios compared to the Wet scenarios.

3.2.7 High-res RACMO response patterns for seasonal mean precipitation

In this subsection the RACMO response patterns for seasonal and annual mean precipitation are given for the KNMI'23 climate scenarios. Figure 3.18 presents these change patterns for the Hd and Hn scenarios in 2050, 2100 and 2150. The panels in this figure are similar to those in Figure 3.17, but for a smaller domain around the Netherlands (and at the 12× 12km^2 RACMO resolution), so the (spatial) details of the precipitation response can be identified better. Similar figures for the 'M' and 'L' scenarios are presented respectively in Figures 3.19 and 3.20.

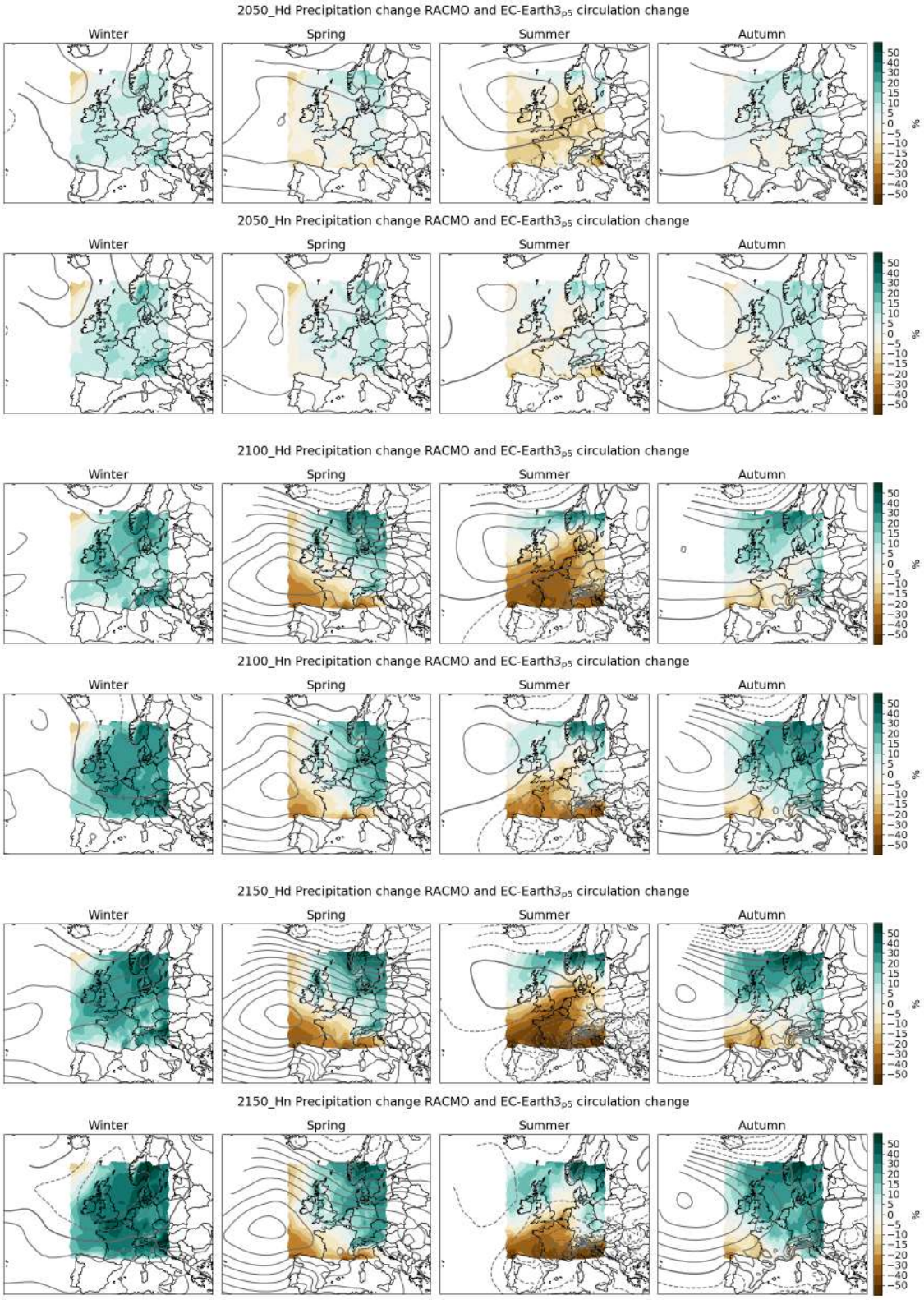

Figure 3.17: Changes in seasonal mean precipitation over Europe (full RACMO domain) and corresponding change in mean sea level pressure (MSLP) for the climate scenarios Hd and Hn for 2050, 2100 and 2150. MSLP change contour interval is 0.5 hPa (increases: solid contours; decreases: dashed contours). MSLP change for the larger spatial domain is obtained from the driving model EC-Earth3 $_{p5}$.

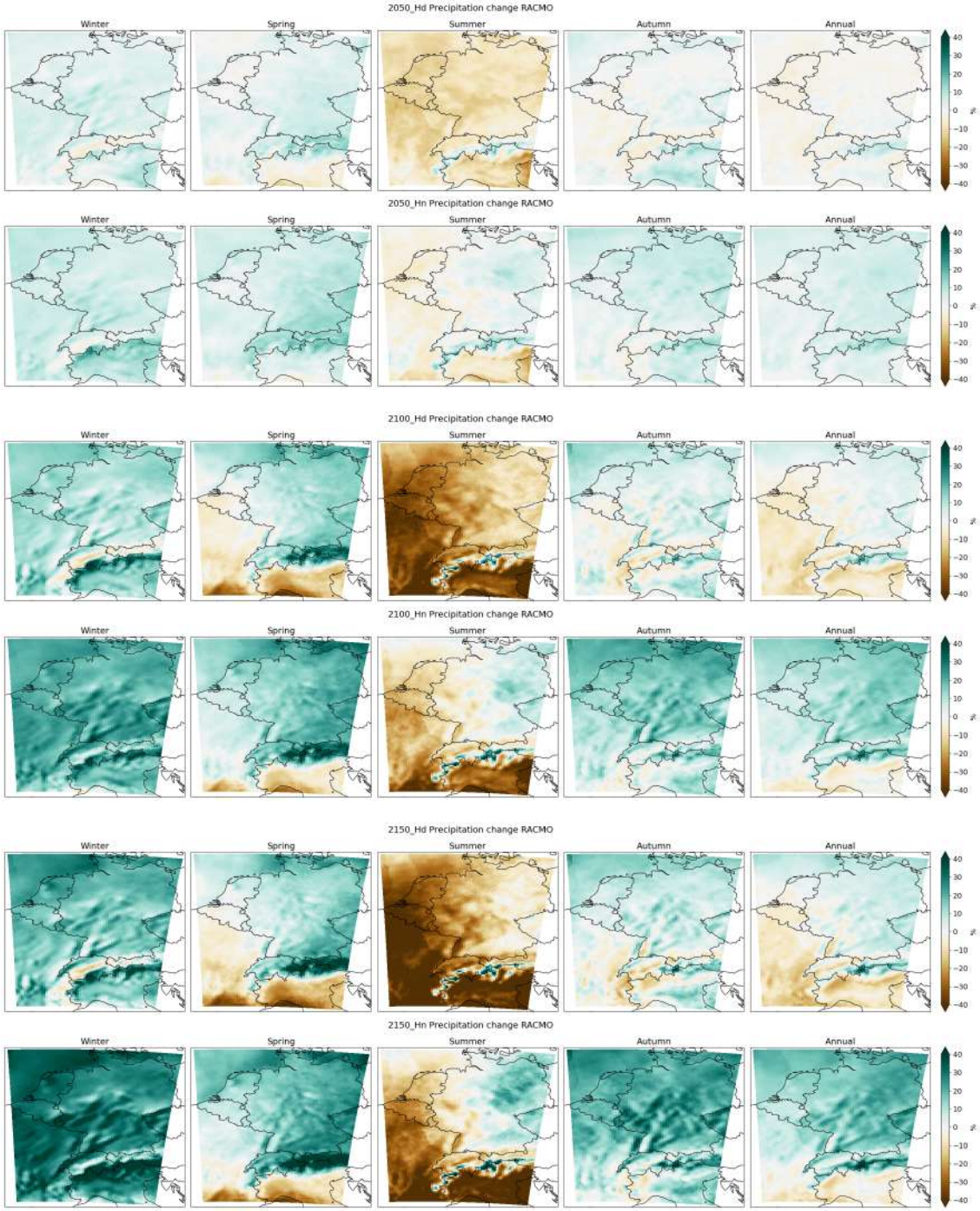

Figure 3.18: Changes in seasonal and annual mean precipitation over Europe (RACMO 12×12 km^2 grid) for the Hd and Hn scenarios in 2050, 2100 and 2150. These scenarios have a ΔGSAT of 1.5°C in 2050 (first and second row), of 4.0°C in 2100 (third and fourth row) and, of 5.5°C in 2150 (fifth and bottom row). The RACMO data in these panels are bias-corrected prior to calculating the changes, see section 2.1.10 for details.

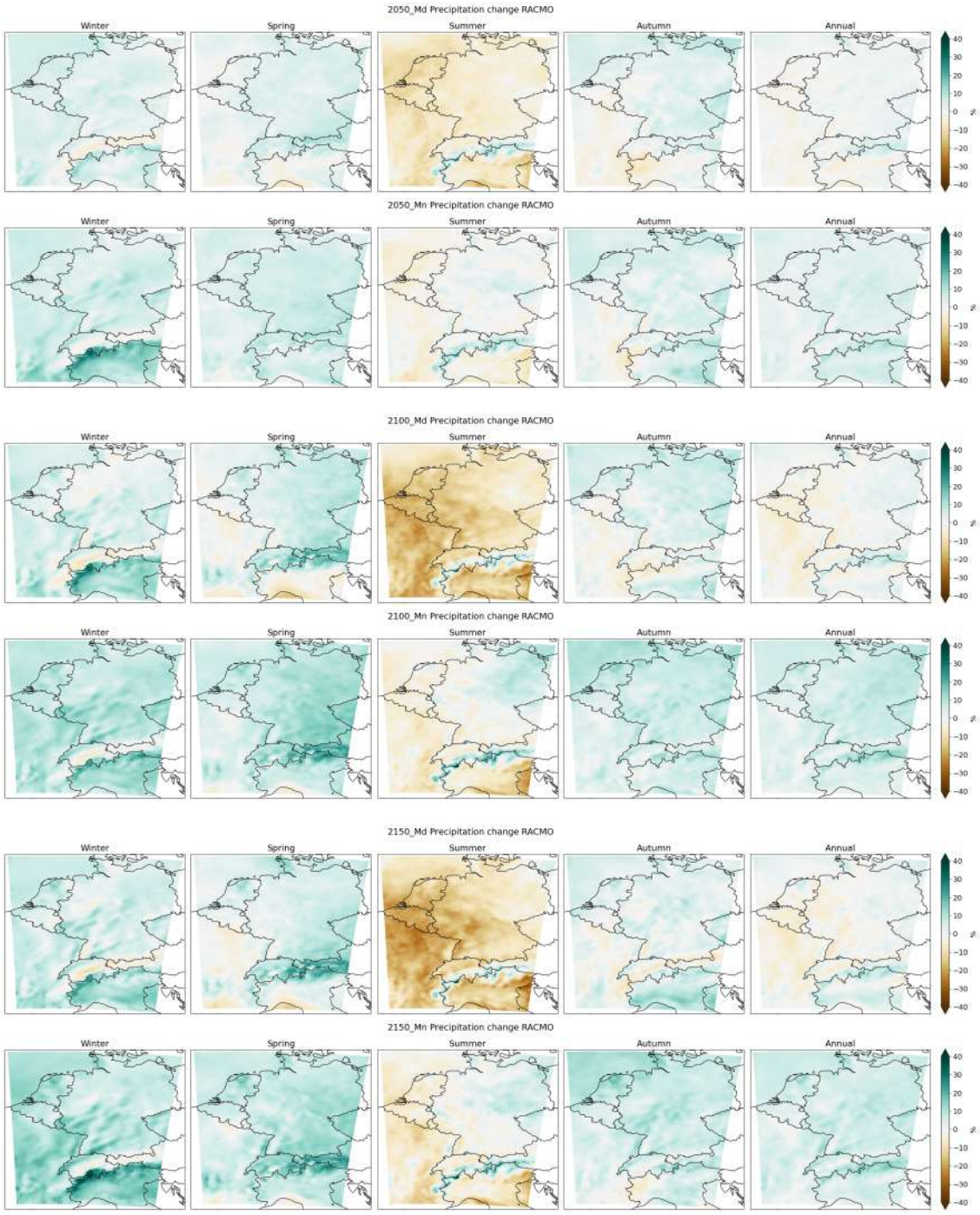

Figure 3.19: As Figure 3.18, but for the Md and Mn scenarios in 2050, 2100 and 2150. These scenarios have a ΔGSAT of 1.1°C in 2050 (first and second row), of 1.9°C in 2100 (third and fourth row) and, of 2.1°C in 2150 (fifth and bottom row). The RACMO data in these panels are bias-corrected prior to calculating the changes, see section 2.1.10 for details.

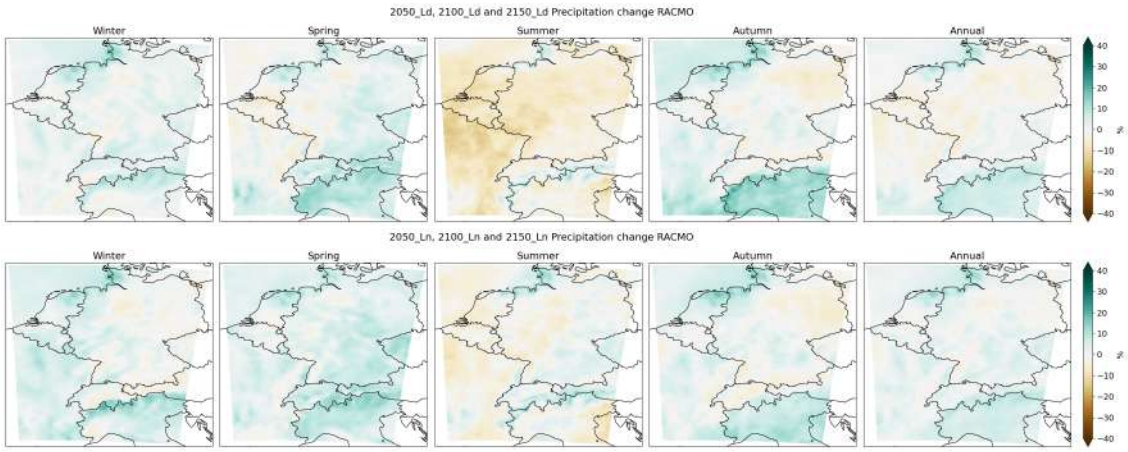

Figure 3.20: As Figure 3.18 but for the Ld and Ln scenarios in 2050, 2100 and 2150. The Ld and Ln scenarios for 2050, 2100, 2150 all have a ΔGSAT of 0.8°C, the Ld scenario is therefore identical for 2050, 2100 and 2150, same for the Ln scenario. The RACMO data in these panels are bias-corrected prior to calculating the changes, see section 2.1.10 for details.

In general the precipitation response patterns over the Netherlands are part of larger response patterns over the given domain (see also Figure 3.17). The response patterns are weaker and 'noisier' for the Ld and Ln scenarios than for the Md and Mn scenarios, which in turn are weaker and noisier than those for the Hd and Hn scenarios. Similarly, with the exception of the 'L' scenarios, the response patterns are weaker and 'noisier' for the scenarios for 2050 than for the scenarios for 2100, which in turn are weaker and noisier than those for 2150. Thus overall, the precipitation responses are weaker and noisier for the climate scenarios with lower warming. Furthermore, stronger/the strongest precipitation increases occur in winter in the Wet scenario variants, while stronger/the strongest precipitation decreases occur in summer in the Dry scenario variants. Rather than discussing all details we focus on the most characteristic features.

One of the most robust responses is the precipitation decrease in summer over the whole of the Netherlands (with the exception of the very North of the Netherlands in the Ld, Ln and 2033_L scenarios, which is discussed in more detail below). The summer precipitation response pattern has two components, an east-west gradient and a north-south gradient with in particular severe drying south of the Alps. The summer response is negative almost everywhere in the Dry scenarios, while for the Wet scenarios the response in the eastern part of the domain (and north of the Alps) is positive. As a result the Netherlands almost always lies in the drying part. Changes in winter precipitation are predominantly positive, and more positive for the Wet scenarios than for the Dry scenarios.

Another robust response that stands out is the opposite change in the Alpine region compared to the surrounding area, which is particularly apparent in winter and summer. In summer this seems to be related to increased convective precipitation at high altitudes in high-resolution climate models (RCMs) in contrast to the forcing global models (see Section 2.4.6 for a more elaborate discussion). Understanding the precipitation response anomaly in the Alps in winter seems more difficult. In winter it is somewhat less robust than in summer since it is only present as a sign change in the Dry scenario variants. In the Wet variants there is some weakening of the (overall positive) response, but no sign change. In Section 2.4.6 it is speculated that effects of changes in the atmospheric circulation in areas with strong topographic gradients and changes in the vertical humidity profile may play a role.

A further point worth mentioning is a relatively small but very robust effect present in every seasonal response pattern for the Ld and LH scenarios (figure 3.20). This effect involves an area that stretches from approximately the Northern part of the Netherlands (Groningen and Drenthe) to the northern part of Lower Saxony and Schleswig-Holstein in Germany. In this area

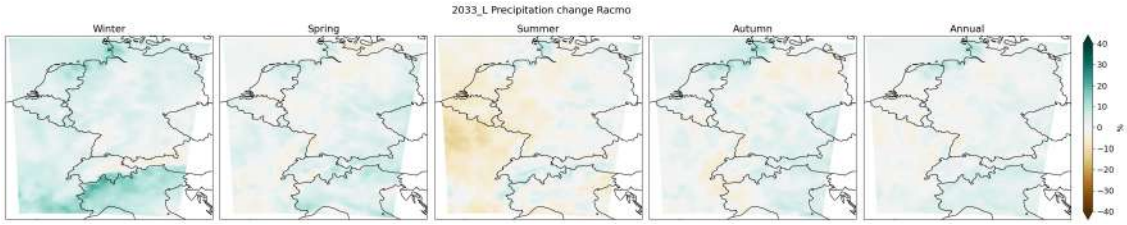

Figure 3.21: As Figure 3.18 but for the 2033_L scenario, corresponding with the 1.5°C target in the Paris agreement (and a ΔGSAT of 0.6°C wrt to the climate scenario reference period 1991-2020).

precipitation decreases less than in the surrounding area in summer, or it even slightly increases while surrounded by decreases, and increases somewhat more in the other seasons. A systematic change in the land use, and specifically the vegetation type, turns out to be the cause. Large scale afforestation is a relevant socio-economic change component under SSP1-2.6, including in this particular area. The afforestation in this, and other, areas is therefore 'automatically' included as a change in the vegetation type in the SSP1-2.6 (EC-Earth3$_{p5}$-)RACMO simulations (see Section 2.4.5. This apparently leads to a precipitation change 'anomaly' in afforestated areas that is persistent throughout the year.

Figure 3.21 presents the RACMO precipitation response patterns for the 2033_L scenario, i.e., the climate scenario that corresponds to the 1.5°C target in the Paris agreement. Since the 2033_L scenario is also based on SSP1-2.6 EC-Earth3$_{p5}$ and RACMO projections, the precipitation change patterns resemble those for the Ld and Ln scenarios. The 'afforestation effect' is also visible in this scenario.

In a number of climate scenarios the sign of the precipitation response changes within the Netherlands, in particular in the scenarios with lower warming, which are 'noisier' by definition. It is then useful to know whether such differences in the response are significant, more precisely, whether the changes themselves significantly differ from zero, and/or whether changes at two different nearby locations statistically differ from each other (whether or not these two changes differ in sign). In other words we want to rule out the possibility that (differences between) changes are due chance because of the natural variability in the climate system.

There exist several (parametric) statistical tests for this purpose, e.g., the well known t-test. But then every comparison (with zero or between locations) needs its own test, and with many (dependent) tests this also introduces the so-called 'multiple comparison problem'. We therefore derive and use an easy rule of thumb for the statistical significance of (local) changes in seasonal mean precipitation, and for differences between such changes for different locations. We make use of basic principles, such as the standard deviation (variance) of the data and the assumption that the seasonal mean precipitation is normally distributed. The details of deriving these rules of thumb numbers (limit values) are described in the Annex to this subsection (see Section 3.2.8). For a local change in seasonal mean precipitation to be statistically different from zero (i.e., no change), such a change should be larger than ±5% (fist rule of thumb), while for changes in seasonal mean precipitation at two different locations (second rule of thumb) the difference in the changes should be larger than ±7%. Note that these rule of thumb numbers specifically hold for seasonal and annual mean precipitation, and not for other variables or daily precipitation, and are an approximation to a real test. Still, both numbers correspond with an, often used, significance level of 5%, similar to the significance level of ordinary (parametric) tests.

Applying these rules of thumb to the differences in the local changes in seasonal mean precipitation within one scenario, we can conclude that the (small) areas with sign differences over the Netherlands for winter and summer in the scenarios (Figures 3.18 to 3.20) are not significantly different form zero and/or different from each other. Such differences should thus be interpreted with care since they are expected to occur due to fluctuations resulting form natural variability

in the climate system as simulated by the climate model. From a statistical point of view these differences are therefore meaningless.

In summary of this section, there is a clear 'wetting signal' over the RACMO domain in winter. This precipitation increase is more pronounced for the Wet scenarios than for the Dry scenarios. In summer there is a clear 'drying signal', which is most pronounced for the Dry scenarios, with decreases over the whole domain. In contrast, in the north-eastern part of the domain the Wet scenarios are not drying in summer but getting wetter. For spring, the change patterns are also more mixed. Generally it is becoming wetter in the northern part and getting dryer in the southern part, where the drying part is shifted more southward in the wet variants. For autumn, for the Wet scenarios the patterns look similar to those for winter (mostly precipitation increases) but with a somewhat smaller amplitude, for the Dry scenarios the change pattern looks quite mixed with relatively small spatial scales. Annually the response patterns are mixed as well, but with a more wetting tendency for the Wet scenarios (with the exception of the southern part of the domain), and a more drying tendency for the Dry scenarios (with the exception of the north eastern part of the domain). For the Netherlands the Wet and Dry scenarios are, in terms of change in annual mean precipitation, quite distinct, i.e., a wetter climate in the Wet scenarios and a drier climate in the Dry scenarios. Note that for the annual mean this is largely a consequence of how the Wet and Dry scenarios are constructed (see Chapter 2). The change patterns described above are quite similar for the scenarios with a different global warming level (see Table 3.3), with lager amplitudes of the patterns for larger ΔGSAT, and smaller amplitudes for smaller ΔGSAT. In other words, the seasonal and annual mean precipitation change patterns to a large extent scale with the global warming level.

In cases where the sign of the change is non-uniform over the Netherlands, the change is relatively small and likely not significantly different from the larger areas with an opposite response. This is related to the fact that the influence of natural variability (i.e., random noise) in the RACMO responses at the temporal and spatial scales considered here are a relevant part of the climate scenarios.

3.2.8 ANNEX: Rule of thumb for the significance of changes in seasonal mean precipitation

This subsection describes the rule for the significance of precipitation changes used in the previous subsection (Section 3.2.7). It is not essential for understanding the previous subsection, or this whole section on precipitation. It gives the background for and the derivation of the 'approximate significance limits' applied in that subsection.

The rule of thumb actually involves two (related) rules of thumb; one for identifying whether a change in seasonal mean precipitation differs statistically from zero, and another one for identifying whether two changes in seasonal mean precipitation (at different, nearby, locations) differ statistically from each other. They are derived from first statistical principles with the following assumptions: i) seasonal mean precipitation is normally distributed, ii) the variability of seasonal mean precipitation is approximately the same for all four meteorological seasons (winter, spring, summer and autumn), iii) the variability of seasonal mean precipitation in the future climate is in close approximation the same as for the current climate.

The starting point for the rules of thumb is a commonly used estimate of the (natural) variability (i.e., the uncertainty) of a quantity, namely its standard deviation, usually denoted as σ, of that quantity. For KNMI'14 standard deviations were determined from long observed station time series for the variable of interest. For 30-year mean seasonal precipitation, σ is as large as about 5% of the mean value (for all four meteorological seasons). To make this more explicit assume a 30-year seasonal mean precipitation of 200 mm (which is quite realistic for Dutch standards) with a corresponding standard deviation σ of 5%, which is often written as 200 ± 10 mm. Assuming now that the 30-year seasonal mean precipitation is normally distributed, the 95% confidence interval ($(\pm 2\sigma)$ for the 30-year seasonal mean precipitation ranges from $\sim$ 180 to 220 mm. This effectively means that the uncertainty in the 30-year seasonal mean precipitation is 40 mm (i.e., 20%), or four times σ). More precisely, this range corresponds to the 95% confidence range (based on the

normal assumption) and meaning that there is a probability of (only) 2.5% that the 'real' value lies below 180 mm, and also a 2.5% probability that it lies above 220 mm.

This σ of 5% can also be used to determine whether the 30-year means of two independent 30-year periods (e.g., those of the current and future climates) differ significantly, or, equivalently, whether the difference between the two climates significantly differs from zero. We use the estimate of σ of 5% for the 30-year seasonal mean precipitation for the current climate as well as for the future climate. Further, it should be taken into account that the climate responses in the climate scenarios are based on 30-year means from 240-year simulations (rather than on a 30-year mean from a single 30-year period) and therefore have a smaller σ than the 5% estimate (for a 30-year mean from a 30 year period). This reduces the σ of interest with a factor $1/\sqrt{8}$. To construct again a (standard) 95% confidence range (for no significant change from zero), the resulting reduced σ is multiplied by $\pm$ 1.96. Together this yields a factor of $\pm$ 0.98 ($\sqrt{2}/\sqrt{8} \times 1.96$) to get the proper 95% confidence interval from the initial σ of 5%. Because the simulated time series are eight times longer (240 yr) than the standard scenario period (30 yr), coincidentally a factor of almost 1 results, leading to an interval of $\sim$ -5 to +5% for which the response is not significantly different from zero, and thus statistically meaningless.

The initial σ of 5% for the (30-year) seasonal mean precipitation is a measure of the natural variability at the local spatial scale (a station or a RACMO grid cell). Above, for the first rule of thumb for differences between periods, we applied it to two different (independent) time periods, implicitly assuming equal locations. Similarly, a 95% confidence interval can be constructed for the difference between two changes at different (independent) locations, assuming equal time periods. This corresponds to a 'difference of a difference', which, by definition, has a σ (and consequently 95% confidence interval for no significant difference) that is $\sqrt{2}$ as large. This yields a not-significant difference interval of $\sim$ -7 to +7%. Hence spatial differences in seasonal mean precipitation changes should be at least $\sim$ 7% apart in order to denote them as significantly different changes (i.e., a statistical meaningful difference of changes). This is the second rule of thumb. A practical difficulty with applying it is, however, that the locations or grid cells should be sufficiently far apart to be independent. An objective distance for independence is difficult to give (also differs from variable to variable), but it is definitely not true for two neighbouring grid cells.

Note again that the ranges derived here depend on the estimate of σ for the '30-year seasonal mean precipitation' and assumptions (such as normality and independence). They should therefore be regarded as 'rule-of-thumb' numbers to get an idea of the significance of the responses, and differences in responses, of seasonal mean precipitation as presented in the figures in this subsection on precipitation. These specific ranges are thus neither applicable to changes in (or differences in changes in) precipitation extremes. nor to changes in other variables, since these typically have a different uncertainty (larger or smaller σ) than seasonal precipitation means. Finally, these rules of thumb are also introduced to enhance the awareness that not every response or difference in response is statistically meaningful, even though a change differs from zero, or two changes differ.

3.3 Wind and storm

3.3.1 Introduction

Wind has several impacts on society. Traditionally, the focus has been on strong winds as they cause various hazards. On land, the danger arises from falling trees and collapsing structures, on sea high waves threaten ships and marine structures like oil rigs or wind turbines, and along the coast wind driven water set-up can lead to flooding. With the growing importance of wind energy, also episodes with low winds start to become problematic. In KNMI'23 we therefore pay attention to both ends of the wind speed spectrum.

The hazards as described above are caused by the wind close to the ground. Usually the 10 m wind is considered, i.e., the wind at a height of 10 m above ground. However, wind turbines harness

the wind at hub height, which typically is 100 m over sea and a bit less over land. Therefore, we also pay attention to the 100 m wind and its projected change.

3.3.2 Observations

The longest reliable series of wind measurements is available from Schiphol airport and goes back to 1969. The annual-mean wind speed there exhibits a small increase until about 1990, when it started to decline by roughly 2%/decade. The decline took mainly place in winter (see Figure 3.22). Due to the large interannual variability, these trends are not statistically significant at the 95% level. The declining trend is confirmed by the (shorter) series from other land stations, but not from K13, a production platform on the North Sea at 3.22°E, 53.22°N (see Figure 3.22). A slight wind speed reduction over land is a common phenomenon and usually ascribed to increasing surface roughness (Vautard et al., 2010; Wever, 2012).

To get a spatial impression of the wind trends over the Netherlands and the surrounding area, we turn to the ERA5 reanalysis data (Hersbach et al., 2020). Over their common period, the reanalysed winds compare very well with the observed ones. As an example, Figure 3.23 shows the comparison between observed (KNMI uurgegevens, 2023) and ERA5 winds at three locations. The upper panel shows annual-mean winds speeds at three locations (two land, one sea). Observed and reanalysed speeds are close together, and their trends, if any, are indistinguishable. The lower panel shows a comparison between hourly wind speeds at station Schiphol, together with their difference. Also on hourly scale the two wind products are close together bis a mean bias over 2015 of 0.065 m/s. Therefore, we use the ERA5 winds as a surrogate of the observed winds in the remainder of this section.

Figure 3.24 shows the linear trends (regression on time) of the 10 m wind speed for winter and summer over the period 1950–2020. Note that this trend cannot be directly compared with those shown in Figure 3.22 for the observations as they are computed over a longer period of time. This longer period is shown here to show that even over a longer period the (linear) trends are small. The winter trend is positive, but non-significant at the 99% level, over most of north-western Europe. The summer trend is slightly negative, and even significant in a small region that includes the Netherlands. The trends of the mean wind speed at 100 m as well as the trends of the maximum hourly wind speeds show the same pattern and the same relative change of less than 2%/decade (not shown).

That the small wind speed trends of less than 2%/decade are not statistically significant is caused by the high inter-annual variability. For the annual-mean wind speed the standard deviation

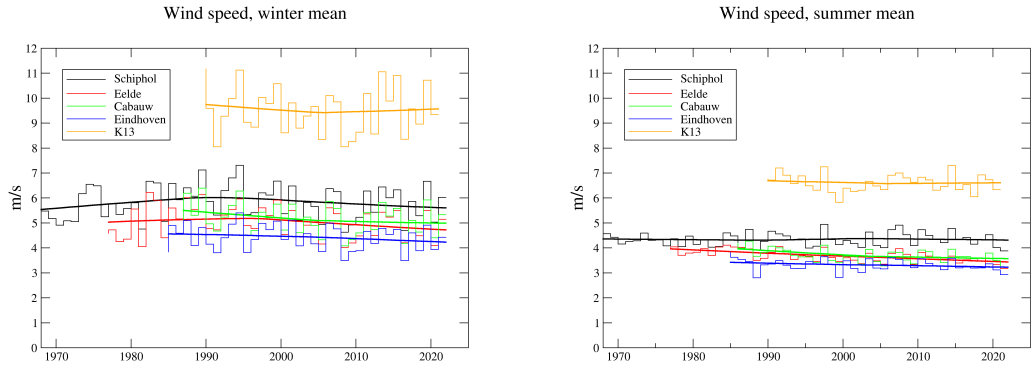

Figure 3.22: Observed seasonal-mean 10-m wind speeds for winter (DJF, left) and summer (JJA, right) at four land stations and one North Sea station (K13).

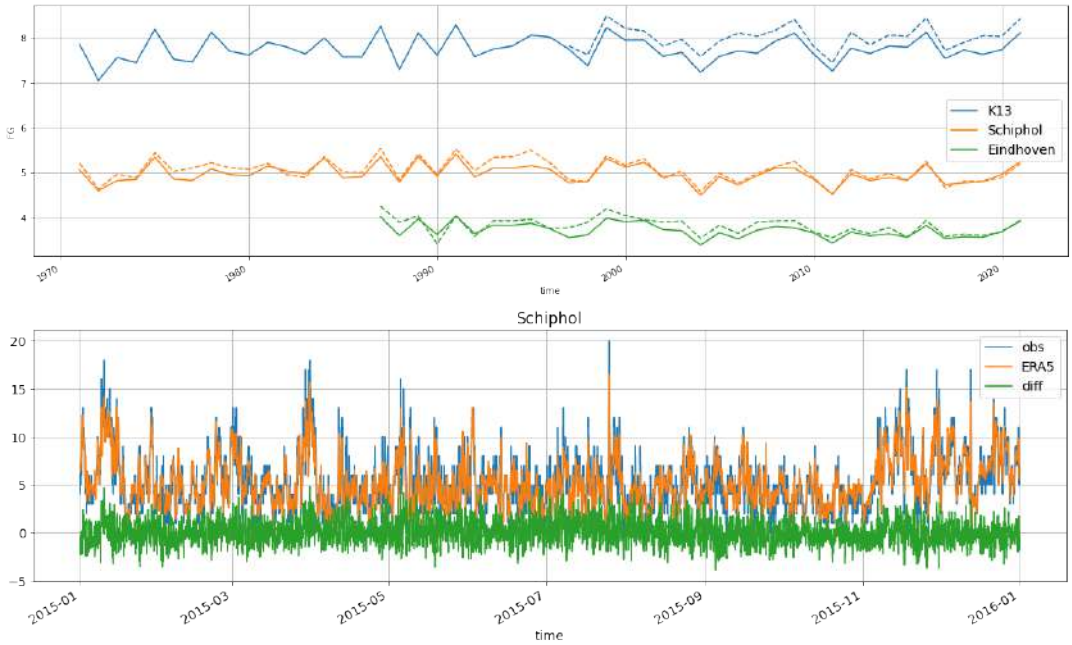

Figure 3.23: Comparison between observed (KNMI uurgegevens, 2023) and reanalysed (ERA5) wind speeds. Upper panel: Annual-means at two land and one sea station. Continuous line ERA5, dashed line observations. Lower panel: One year (2015) of hourly wind speeds and their difference at station Schiphol.

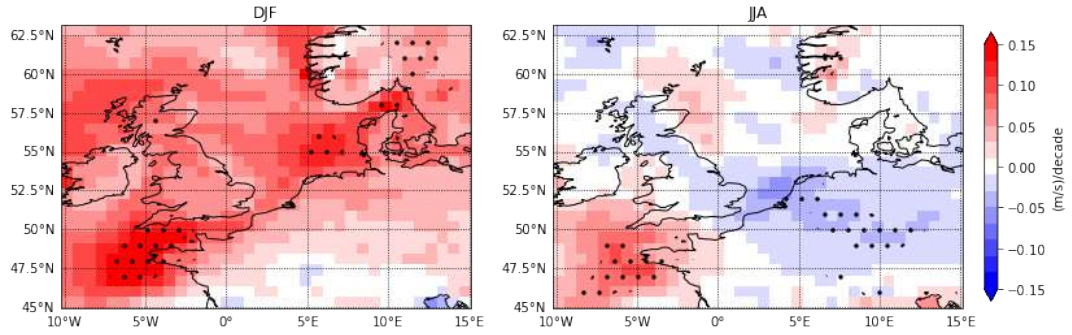

Figure 3.24: Linear trend (regression on time; in (m/s)/decade) of the mean 10-m wind speed in winter (DJF, left) and summer (JJA, right) from the ERA5 reanalysis (period 1950–2020). Grid points at which the change is statistically significant at the 99% level are marked by a black dot.

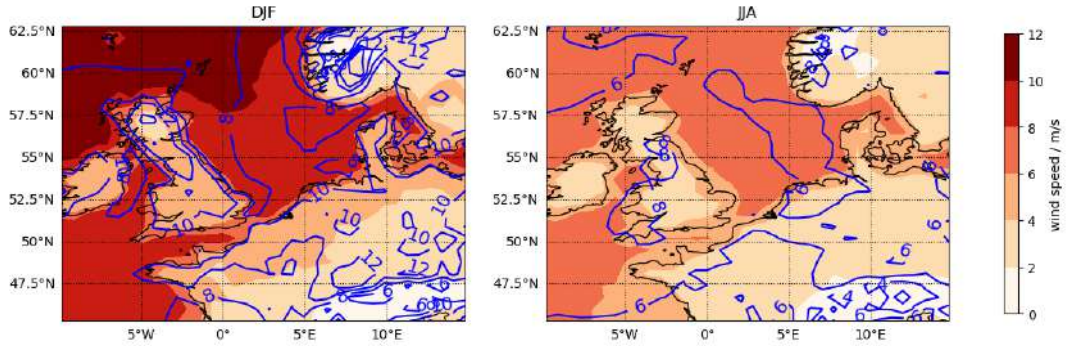

Figure 3.25: Mean (colours) and standard deviation (as percentage of the seasonal-mean) of seasonal-mean 10-m wind speed for winter (DJF, left) and summer (JJA, right) in ERA5.

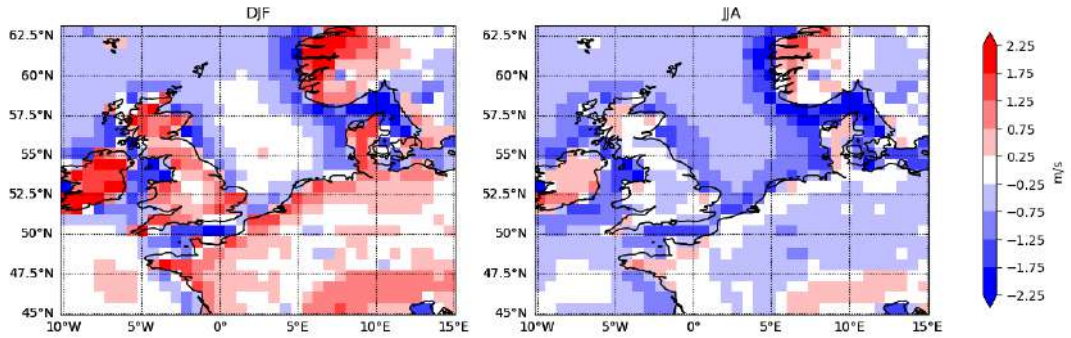

Figure 3.26: Difference of 10-m wind speed between the mean of CMIP6 and ERA5 during the historical period (1951-2014) for winter (left) and summer (right). Along the coastlines the result is unreliable because the interpolation from the different model grids to a common grid does not account for differences in land-sea mask.

is in the order of 4% of the mean, and for seasonal values even around 10%, with higher values over land than over sea (see Figure 3.25).

For ERA5 we have hourly data available, not only for near-surface wind speed, but also for a height of 100 m, and a measure of wind gusts at 10 m. It appears that these variables are highly correlated, with correlations generally exceeding 0.95. Correlations are higher in winter than in summer, and higher over sea than over land. The same high correlations are found for seasonal data. We therefore assume that the 100-m wind and wind gusts exhibit the same fractional changes as does the 10-m wind.

3.3.3 Model results

CMIP6

Wind data were available for only 28 of the 33 CMIP6 models of the standard set. They are marked in Table C.1. The CMIP6-related figures in this section are based on these 28 models plus the *r1i1p1f1* variants of EC-Earth3-AerChem, EC-Earth3-CC, EC-Earth3-Veg-LR, and IPSL-CM6A-LR-INCA.

Hahmann et al. (2022) have compared winds from CMIP6 and ERA5 with observations at a few measurement sites in the North Sea. They find a good agreement between the three sources. The good agreement between CMIP6 and ERA5 over sea is confirmed by Figure 3.26, which shows the difference between the CMIP6 models and ERA5. In winter the difference is close to zero over the North Sea and slightly positive over land. In summer it is negative nearly everywhere, with

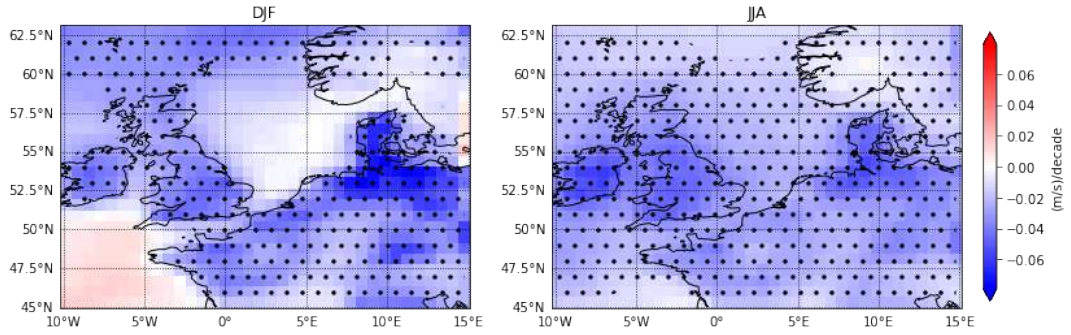

Figure 3.27: Linear trend of the mean CMIP6 10-m-wind speed over the period 1950-2020. This Figure should be compared to Figure 3.24, which shows the same quantity for ERA5. Stippling denotes grid boxes where the trend is statistically significant at the 99% level. Note, however, that taking the mean over 28 CMIP6 models removes much of the inter-annual variability, so that even a small trend becomes statistically significant.

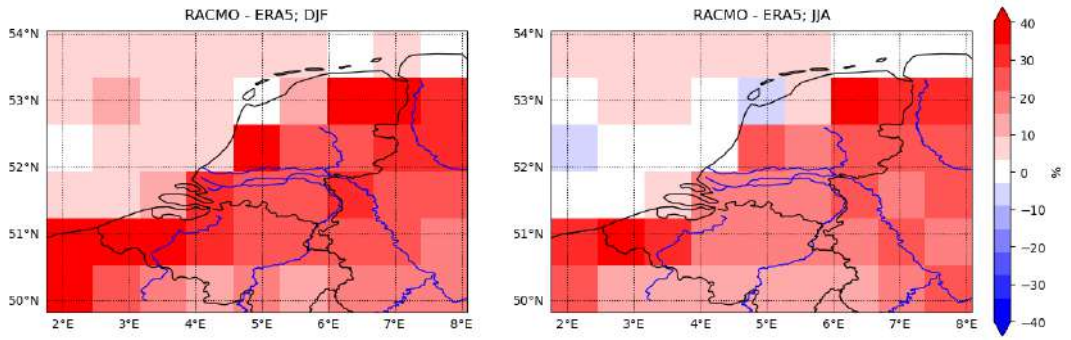

Figure 3.28: Relative difference over the reference period of 10-m-wind between the ensemble-mean RACMO output and ERA5 as a percentage of ERA5.

larger values over the North Sea than over land. However, as the spread of the mean wind speed between the CMIP6 models is large (order 1 m/s), the ERA5-mean lies always within the range of the CMIP6-means, albeit often near its ends.

The CMIP6 models agree with observations and with ERA5 in having a large inter-annual variability and only small trends. Trends are shown in Figure 3.27, which should be compared to Figure 3.24 for ERA5 trends. In both cases the trends are small, but the patterns differ, with CMIP6 trends being negative nearly everywhere. However, this is true for the mean over the 26 CMIP models considered. The patterns for individual models exhibit a large diversity, with some models showing nearly the same pattern as ERA5, and others showing a completely different one with increases over land. However, in all cases the trends are small, and ERA5 would be an indistinguishable member of the model ensemble.

RACMO

The RACMO ensemble shares basic features with the CMIP6 ensemble. The inter-annual variability is large, the linear trend over the historical period is negative, but small. However, unlike for the CMIP6 ensemble, the negative trend is largest in winter over the North Sea.

The relative difference between the RACMO-mean and the ERA5 10-m-wind speeds is shown in Figure 3.28. The RACMO wind speed is higher than the one from ERA5 nearly everywhere. The difference is small over sea (a few percent), but large over land. Besides the land-sea difference, the difference fields show no discernible patterns. Given that the pressure filed, the large-scale driver

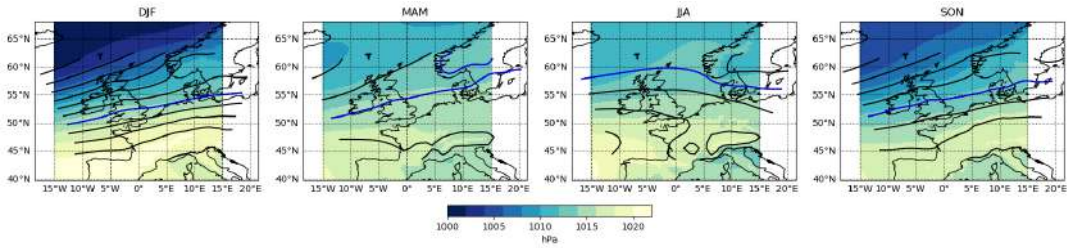

Figure 3.29: Seasonal-mean sea level pressure averaged over the reference period from ERA5 (colours) and RACMO (isolines, with the 1014 hPa line shown in blue as reference).

of the wind, is nearly identical between the two data sets (see Figure 3.29), this indicates that the employed surface roughnesses are different between the models, presumably due to differences in the land-use maps (see Section 2.4).

The wind speed difference is removed by the bias-correction (see Sections 2.1.10 and 3.3.5). That the difference over sea is small is an indication that the large-scale flow is similar in both products. This is confirmed by the comparison of respective sea level pressure fields (Figure 3.29). As long as the impact of time-varying roughness fields over land is small, climate-change induced changes of the large-scale flow will impact land and sea in the same way. Therefore, wind speed *changes* from RACMO can be used to describe the climate change signal.

The two RACMO subsamples (i.e., wet- and dry-trending) that are used to construct the KNMI'23 scenarios are indistinguishable as far as the wind is concerned (not shown). For both resampling periods (control and future, respectively), their seasonal-mean wind speeds over the wider North Sea area are identical. As a consequence, wind changes for the two sub-scenarios are identical, too.

Summary

All investigated data sets (ERA5, CMIP6, and RACMO) show some basic similarities. The wind over the wider North Sea region is very variable (large inter-annual variability) and exhibits only small trends. Due to the large variability, the trends differ between the data sets, and between the different members of the CMIP6 ensemble. In general, they are statistically insignificant. Together with the similarity of the pressure fields, which are not influenced by local effects, this indicates that the models are suited to detect a climate *change* signal.

3.3.4 Projections

The CMIP6-projected changes in wind speed are small. As an example, Figure 3.30 displays the multi-model mean wind speed change for winter and summer for SSP5-8.5. In the Netherlands and the neighbouring North Sea region the fractional changes hardly exceed 1% in winter. In summer the wind speed decreases by a few percent over land and up to 9% over the southern North Sea. Patterns for the annual-maximum wind speed are comparable, with fractional changes in the same range. In the other SSPs the changes are even smaller (not shown).

While the model-mean changes as shown in Figure 3.30 are small, the inter-model variability is large. The inter-model standard deviation (Figure 3.31) of the projected changes shows values around 0.25 m/s, which is larger than the mean change. The details of the change pattern are therefore uncertain, but changes are small.

A specific hazard for the Netherlands are storm surges. Apart from wind speed, also the direction of the wind is important. The highest danger comes form north-westerly winds which drive the water of the North Sea directly towards the Dutch coast. The projections show only small changes in the frequency of wind directions, with a small decline for northwesterly winds in winter, when the storm surge danger is highest. As projected changes of both wind speed and wind direction are small, no increased storm surge danger is foreseen. This conclusion is confirmed

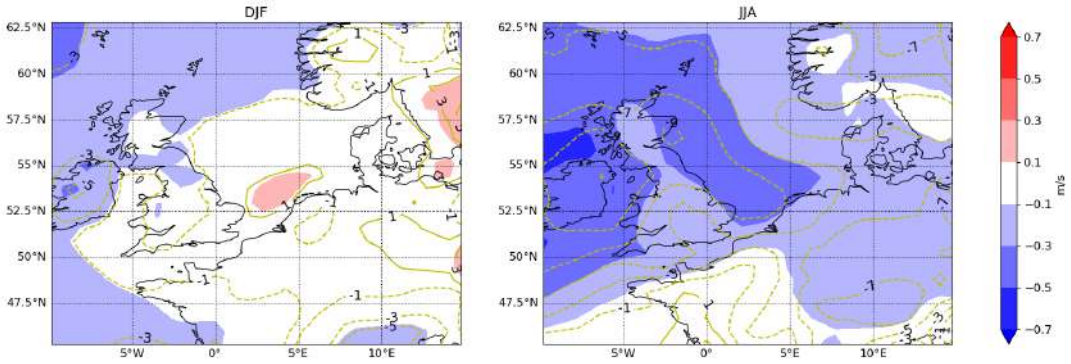

Figure 3.30: Change of mean wind speed between 2071–2100 and the reference period in winter (left) and summer (right). Shown is the multi-model mean of CMIP6 in SSP5-8.5. The colours indicate absolute values, the yellow lines percentages relative to the reference period. Contour interval is 2%, centred around zero.

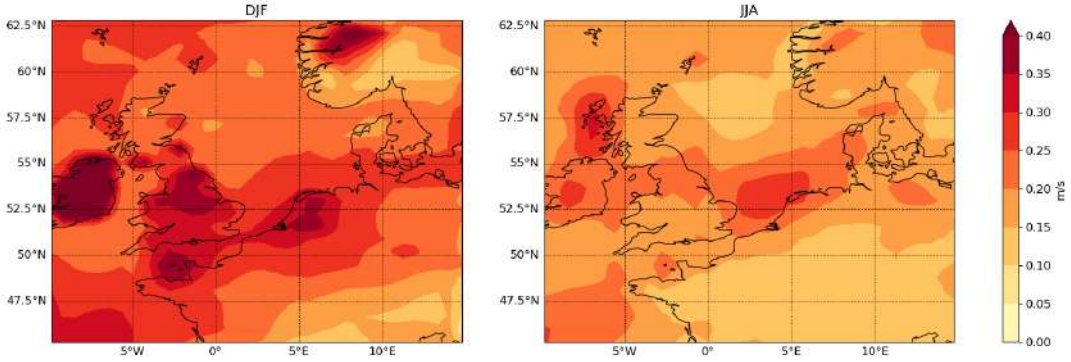

Figure 3.31: Inter-model standard deviation of the changes in mean wind speed between 2071–2100 and the reference period in winter (left) and summer (right). This figure should be compared with the mean changes as shown in figure 3.30.

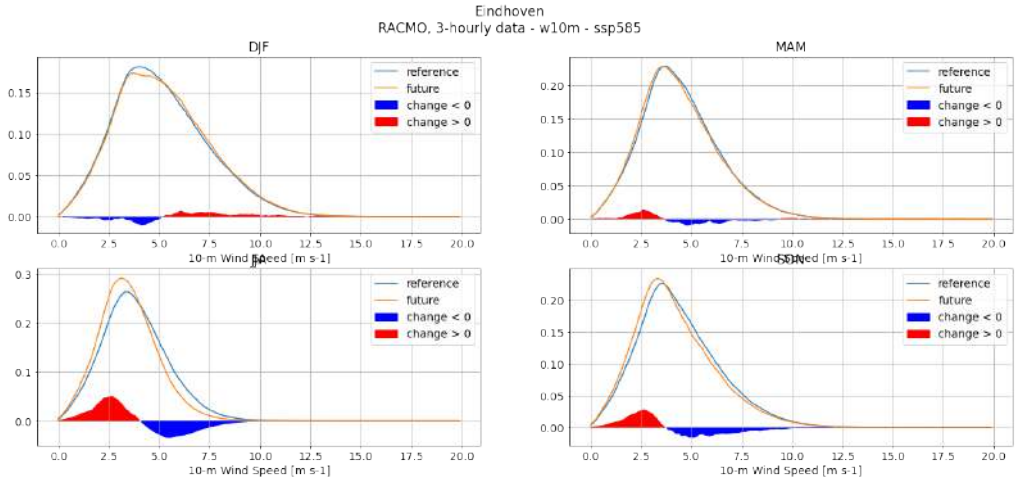

Figure 3.32: Frequency distributions of 3-hourly RACMO wind speeds at location Eindhoven. Presented are smoothed versions of the histograms, collected with a bin width of 0.1 m/s. The histograms are constructed from the output (not bias-corrected) of all 16 runs within the respective 30-year periods (reference (blue) and future (2071–2100; orange)). The smoothed difference of the histograms is indicated by the filled blue and red areas, with blue indicating a reduction in the number of 3-hourly winds in the respective bin in the future period, and red an increase. Note the different vertical scales.

by preliminary runs with the surge model WAQUA/DCSM5 (Gerritsen et al., 1995), driven by the RACMO winds, which indicate a slight decrease of the once-a-year return value along the Dutch coast.

The change in the wind speed distribution in Eindhoven[4] is shown in Figure 3.32. The largest changes are projected for summer and autumn with a clear shift towards lower wind speeds. In the other seasons changes are small. Most importantly, there is no discernible increase of high winds during winter. These findings are in accordance with the results shown above (Figure 3.30) regarding the mean wind speed.

The shift of the wind speed distribution towards lower wind speeds is reflected in the change of the length of periods with daily-mean wind speeds below a certain threshold, confirming earlier results of Van Nieuwenhuyse et al. (2023) and Vautard et al. (2018). Such periods are important for air quality (Van Nieuwenhuyse et al., 2023), which tends to deteriorate with reducing wind speed, and for wind power production. For a threshold of 3 m/s, Figure 3.33 shows the mean (left column) and their change (right column) of the longest period per year (upper row), and the mean number of days per year (lower row) with wind speed below that threshold. As the figure is based on bias-corrected output it is not reliable over sea (Section 2.1.10). Over land, the length of the longest calm period per year (upper row) changes by several days or roughly 20%, while the total number of calm days (lower row) increases by 10-20 days or roughly 10%. As can be expected from Figure 3.32, the changes mainly occur in summer and early autumn (not shown).

In accordance with the CMIP6 results, the KNMI'23 scenarios project only small changes in wind speed. In winter, the changes are not significant. This is good news for the safety of the Netherlands as it implies that on average the severity of storm surges will not increase. Of course, this statement excludes the impact of sea level rise (see Chapter 4). Furthermore, the large inter-annual variability in storm-severity known from the past will continue, and higher storm surges than seen in the recent past remain possible. For summer, a slight decrease of the mean wind speed is projected for all scenarios, but largest in SSP5-8.5. This might lead to reduced wind energy production, especially offshore.

[4]Eindhoven is used here instead of, as usual, De Bilt because the latter is contaminated by the artificial jump in surface roughness in the RACMO runs (see Section 2.4.5)

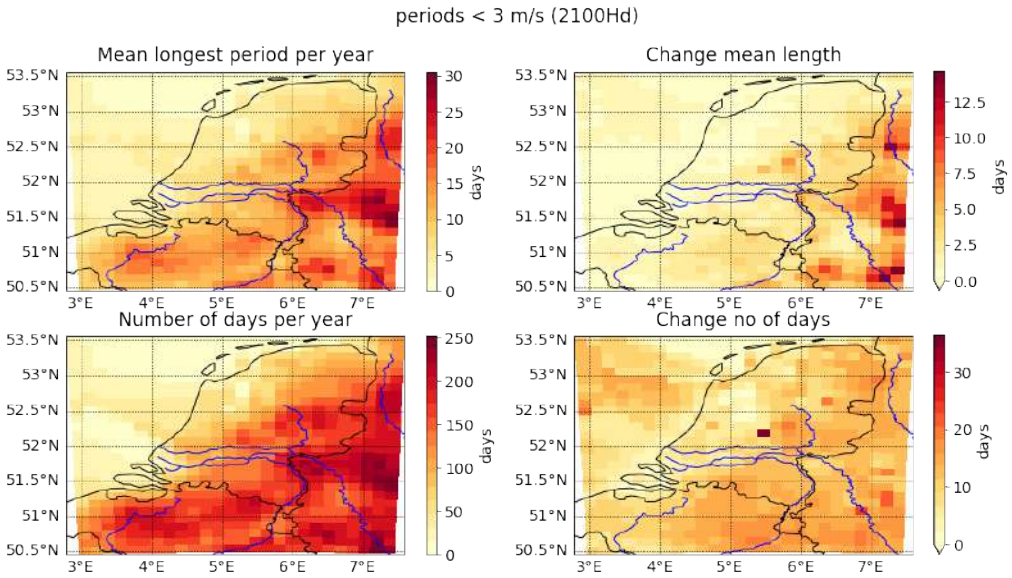

Figure 3.33: Periods with mean daily wind speed < 3 m/s. The left column shows values for the reference period, the right one the change for the future (2100) period. The upper row displays the mean of the longest period per year, the lower row the mean number of days per year. Means are taken over all ensemble members and the 30 years of the respective periods. Data are from the bias-corrected resampled RACMO runs for the high-emission scenario (Hd2100). Note the different colour scales.

3.3.5 Impact of the land-use changes in RACMO on wind

As detailed in Section 2.4.5, the land-use map used in the RACMO runs contains a step-wise change in 2004, as well as some strong assumptions about future land-use changes, especially extended urbanisation in the western parts of the Netherlands, and intensive afforestation in the northeast under SSP1-2.6 and SSP-4.5. The urbanisation is erroneously handled as 'bare soil' in RACMO, tending to lower the surface roughness and increase the wind speed, while the afforestation has the opposite effect. Therefore, the wind response in the RACMO runs is a superposition of changes induced by climate change, and changes induced by land-use changes, and it is difficult to disentangle them. However, sea points are unaffected by land-use changes. Trends at sea points can therefore act as proxies for climate-change induced trends at adjacent land points.

The effect of the jump in surface roughness from 2004 to 2005 can be removed by the bias correction (see Section 2.1.10) by treating the pre- and post-2004 periods separately. This is shown in Figure 3.34, which displays the development of the wind in Eelde (Groningen Airport; left) and De Bilt (right) in summer for SSP1-2.6/Ld. Eelde is strongly affected by the intense afforestation foreseen in SSP1-2.6, while the jump is clearly visible in De Bilt (orange and green lines). Also shown is the wind speed from ERA5 (blue), which, in accordance with Figure 3.28, is lower than the RACMO wind speed. The red lines show the bias-corrected wind speeds. The bias is indeed removed, and the jump in the De Bilt series has gone, but the impact of the afforestation on the Eelde time series is still there.

3.4 Solar radiation, clouds, fog and aerosols

3.4.1 Introduction

Clouds play a dominant role in the Earth's radiation balance. Dependent on their properties, in particular their height, they can have a heating and a cooling effect, with the latter prevailing on

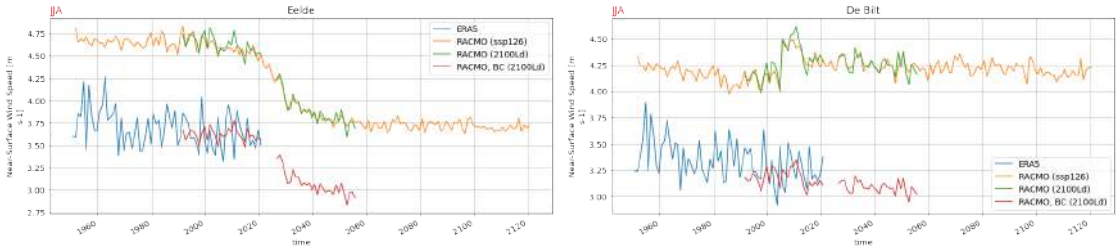

Figure 3.34: Time series of (modelled) wind in summer (JJA) in Eelde (Groningen) and De Bilt for SSP1-2.6/Ld. The blue curve is for ERA5, as a proxy for the observed wind. The orange and green lines are respectively the original and resampled RACMO outputs. As the RACMO curves are for the average of all realisations, their variability is lower than that of ERA5, which has only one realisation. The jump in 2004 and the large bias with respect to ERA5 are clearly visible. Finally, the red line is for the bias-corrected data. The jump is almost gone, and the mean values over the reference period now correspond to ERA5. The large drop in wind speed in the north of the Netherlands (Eelde) is due to the afforestation in SSP1 in that region and is unaffected by the bias correction.

a global scale. The response of clouds to a changing climate remains the most uncertain factor in climate projections, but the feedback is estimated to be positive with high confidence (Table 7.9 in IPCC, 2021b).

Aerosols are another important element in the radiation budget, both by directly scattering and absorption of radiation but also by indirectly affecting clouds and their properties. These aerosol–radiation and aerosol–cloud interactions constitute a global effective radiative forcing of -0.22 W m^{-2} and -0.84 W m^{-2} in 2019, respectively (Fig. 7.6 in IPCC, 2021b), i.e. these effects imply a cooling which partly offsets the warming by greenhouse gases.

In this section the effects of aerosols and clouds in western Europe and the Netherlands are analysed through observations and simulations of surface solar irradiance, also termed global radiation. In addition, a specific cloud type, namely fog, is studied in more detail because of its impact on safety, in particular related to transport. The formation of fog is governed by the meteorological conditions including temperature, humidity and wind speed, as well as by the abundance of aerosols, and these relations are highlighted.

3.4.2 Observed variability and trends (NL/NL+RM)

Solar radiation

In western and central Europe, the past decades, since about 1980, have been characterized by an increase in global radiation following a period with decreasing global radiation (Wild et al., 2021). This is also referred to as dimming and brightening. The general consensus is that the main drivers of these trends are aerosol pollutants, while clouds likely play an additional role, e.g., through indirect effects (Boers et al., 2017).

The increase in aerosol loads prior to 1980 followed by a decrease is also apparent in Figure 3.35. Peak aerosol optical depth (AOD) values in the Netherlands reached 0.35 around 1980, with temporarily even higher values due to stratospheric aerosol as a result of eruptions of El Chichón in 1982 and Pinatubo in 1991. By 2014 the AOD was back to 0.16. The scenarios SSP1-2.6 and SSP5-8.5 settle at values around 0.10 and 0.12, respectively, at the end of the century. Note that Figure 3.35 displays annual mean AOD values. The seasonal variation is considerable, with the highest values occuring in May–July and being about 30% higher.

Evaluation of simulated RACMO global radiation (also termed rsds = radiation surface downwelling shortwave) is performed with the third edition of the SARAH climate data record. SARAH-3 (Pfeifroth et al., 2023) was produced by the Satellite Application Facility on Climate Monitoring (CM SAF) from Meteosat geostationary satellite observations. It spans the years 1983 until 2020,

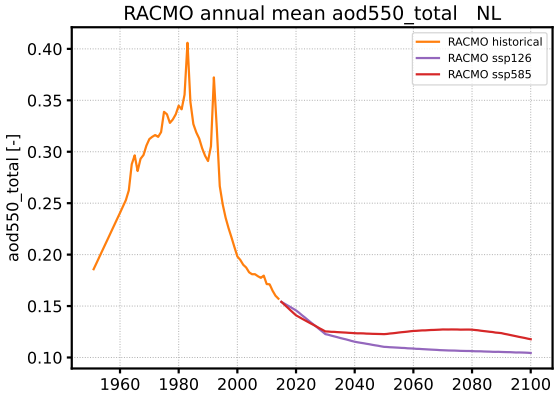

Figure 3.35: Annual mean total AOD at 550 nm, averaged over NL, as used for the RACMO historical and scenario simulations. The creation of the AOD input dataset and coupling with the radiation and cloud schemes in RACMO is described in Section 2.4.1.

and is augmented with a so-called interim climate data record into the present. Satellite rather than ground-based observations have been used for the current evaluation because they provide a complete and homogeneous coverage of the NL+RM region, while stations are unevenly distributed in space and time. Importantly, the SARAH data record has been thoroughly validated and shown to agree very well with surface stations (see validation documents in Pfeifroth et al. (2023) as well as evaluations of the previous SARAH edition in Pfeifroth et al. (2018)).

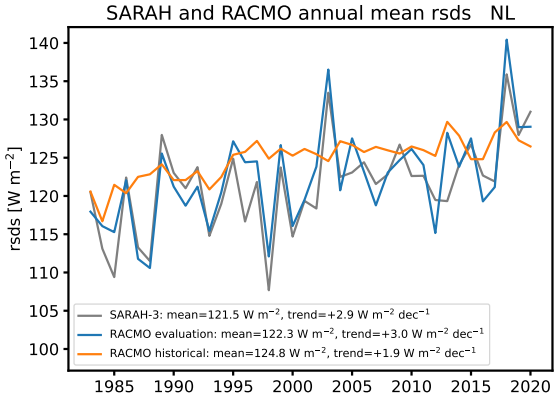

Figure 3.36: Annual mean global radiation for SARAH-3 and RACMO simulations for NL from 1983 to 2020. For RACMO both the evaluation run, driven by ERA5, and the mean of the 16 members of the historical ensemble simulation are shown. The RACMO evaluation run used input from SSP3-7.0 for the years 2015–2020. The historical RACMO runs were augmented by SSP2-4.5 simulations for the years 2015–2020.

The RACMO evaluation run, which is driven by ERA5, yields very similar annual mean global radiation in the Netherlands as SARAH-3 (Figure 3.36). The overall means differ less than one percent and year-to-year variations are consistent. Furthermore, the (strongly positive) trends are in agreement. The historical simulation curve shows little inter-annual variability because it is an average over the 16 ensemble members. On average, global radiation in the historical simulation is about 3% too high. Since the same aerosol input is used in the historical and evaluation runs (see Figure 3.35) the difference in global radiation between these runs must be largely related to clouds. The historical simulation yields a positive long-term trend, which can be explained by the

decrease in AOD. The trend is 35% smaller than in the observations and in the evaluation run, which suggests a contribution by clouds to the observed trend of about this magnitude.

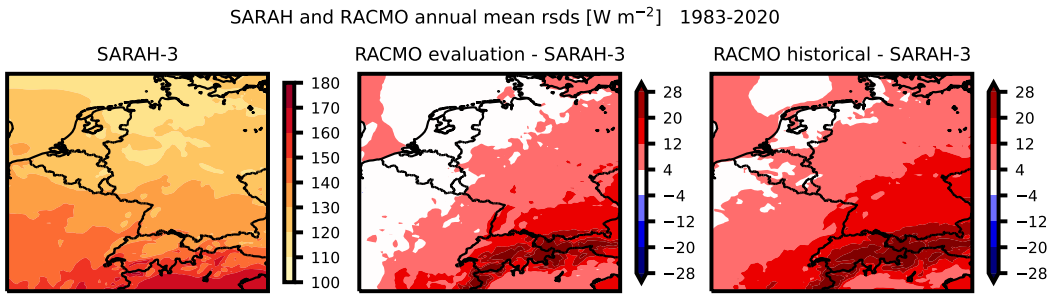

Figure 3.37: Multi-year (1983–2020) mean global radiation for SARAH-3 (left) and difference between RACMO simulations and SARAH-3 (middle and right).

While the RACMO global radiation simulations are very close to the observations in the Netherlands, they appear to have a positive bias further away from the coast (Figure 3.37). In southern Germany and eastern France the bias in both the historical and the evaluation runs amount to about 10% for the annual mean. Over the Alps even larger biases are found but there the satellite data has larger uncertainty due to the orography and snow cover complication the retrieval.

Fog

Fog refers to atmospheric conditions with condensed water in the near-surface atmosphere. The small water droplets suspended in the air reduce visibility. The observation of fog is quantified using observations of visibility. The observed light reduction between transmitter and receiver is translated into a measure in distance for which visibility classes are defined. The visibility class is reported hourly at the KNMI weather stations. The occurrence of fog is defined by the observations for which the visibility is smaller than 1 km. Dense fog is defined by a visibility smaller than 200 meter. Very dense fog is defined by visibility smaller than 50 meters. Weather warnings are issued in case of (very) dense fog.

Fog occurs in different types. The most common form of fog is radiation fog. Radiative cooling leads to saturation of humid air followed by condensation into small droplets. Advective fogs, mostly from the North Sea and large waters such as the IJsselmeer, result from saturated air masses which are transported over relatively cold water to the coast. Sometimes only the coastal area is affected by this sea fog while land-inward clear skies remain. Ground fog is typical for a Dutch summer morning with sheets of fog lingering over cold waters and grasslands. On new Year's Eve dense fog might form because of the enormous increase in the abundance of condensation nuclei from the fireworks. The available fog water is spread over more tiny droplets which strengthens the reduction in visibility, potentially even to less than 10 meters. These very dense fogs lead to dangerous traffic conditions.

As discussed above, air quality policies and technological development since the 1980s have led to significant improvements of the air quality in Europe and The Netherlands. This has been a key driver for visibility and fog occurrence (ref KNMI14). The number of fog hours per year in De Bilt is reduced by 50% in the last 40 years. Also the number of dense fog hours is reduced significantly in De Bilt over the 1955-2022 time period. (Figure 3.38). Similar trends in (dense) fog hours are observed in the long-term visibility records of De Kooij, Vlissingen, Eelde and Maastricht. In the table we provide the 1961-1990 and 1991-2020 climatologies for De Bilt and these other 4 stations (Table 3.4). Only for Eelde the number of dense fog hours is not decreased between both climatological periods.

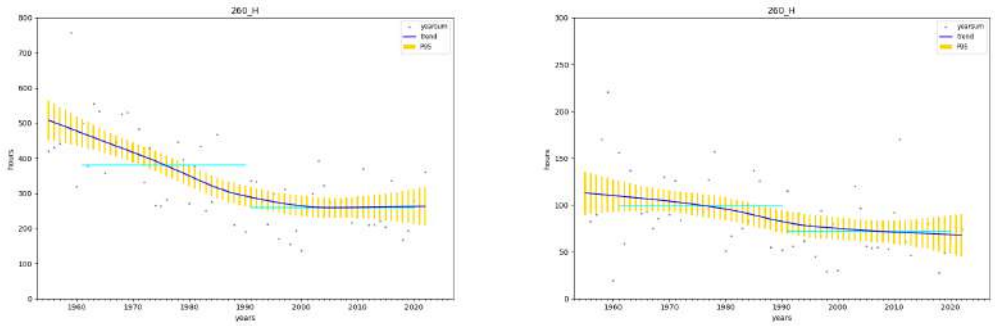

Figure 3.38: Fog hours (left) and dense fog hours (right) at De Bilt between 1955 and 2022.

in hours per year	De Kooy	De Bilt	Eelde	Vlissingen	Maastricht
Fog hours 1961-1990	304	380	455	235	296
Fog hours 1991-2020	188	259	311	144	162
Dense Fog 1961-1990	81	99	79	93	93
Dense Fog 1991-2020	55	72	84	52	58

Table 3.4: Fog hours climatologies for 1961-1990 and 1991-2020, respectively

A further reduction in (dense) fog hours due to further air quality improvements and changes in aerosol composition in the future has been discussed in (ref: Boers et al, 2015). The aerosol pathway in the Netherlands is one of decreasing aerosol concentration and of increasing hygroscopicity due to the continuous reductions in relatively insoluble organic components with respect to the rest of the aerosols including e.g. ammonium nitrates. Consequently, marginal further reductions in fog hours were projected for the rest of the 21st century (ref KNMI'14)

Potential changes in the meteorological conditions that are favourable for fog formation - light winds in a saturated stable shallow boundary layer - were not taken into account in the earlier projections for fog. Changes in the occurrence of such conditions might impact on the occurrence of fog hours in The Netherlands. Further, the ongoing urbanization and land use changes can be drivers on their own leading to more or less frequent occurrence of (prolonged periods of) fog. For example, a slight reduction in relative humidity might prevent fog formation in clean air masses that require supersaturation for fog formation. The Urban Heat Island (see city climate) might cause a local decrease in relative humidity associated with a higher local temperature that could prevent fog formation within the city, but not in the nearby meadows outside the city. Because fog formation and dissipation is based on a very subtle balance between temperature changes, relative humidity, wind speed and mixing processes, climate projections are inherently uncertain. Conditional for fog formation is however a low inversion layer with near-saturated air mass and light winds. The frequency of occurrence of these necessary conditions can be simulated with a climate model.

3.4.3 Projected regional response

Solar radiation

The projections of global radiation in the Netherlands according to simulations for four scenarios are shown in Figure 3.39. In general the low (SSP1-2.6) scenarios yield the larger increases, which is consistent with the lower AOD in Figure 3.35. However, in the high (SSP-5-8.5) dry scenario more frequent droughts and corresponding cloud-free episodes are simulated from June to September,

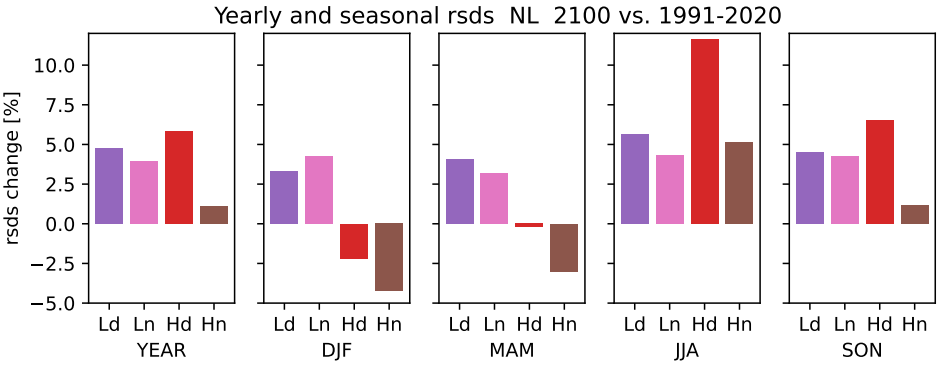

Figure 3.39: Relative change in annual and seasonal mean global radiation in 2100 versus 1991–2020. Four scenarios are shown for the NL region.

leading to sharp increases in global radiation in these months. As a result the high-dry scenario shows the largest increase on an annual basis.

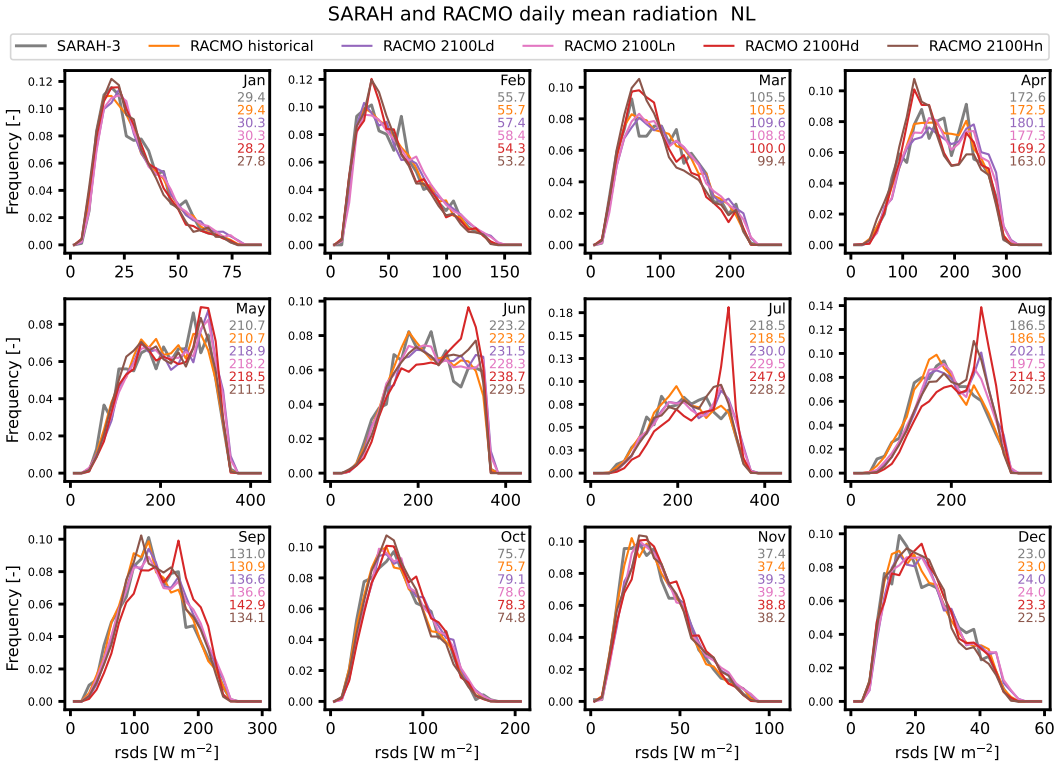

Figure 3.40: Frequency distributions of daily global radiation in NL on a monthly basis. The period is 1991–2020 for SARAH-3 and the RACMO historical simulations, and 2086–2115 ('2100') for the four future scenario simulations. Monthly mean values are indicated in the panels. Note that the simulations have been bias-corrected with respect to SARAH-3.

The changes per month are more clearly illustrated with frequency distributions of daily global radiation in Figure 3.40. The distributions of the historical simulations are very similar to the SARAH-3 observations, which is a result of the bias correction procedure. The high-dry scenario shows sharp peaks at high rsds values in the months June to September, corresponding to pre-

dominantly clear-sky conditions. These peaks are accompanied by a decrease in the number of days with low rsds, as is most apparent in July. The frequency distributions of the other scenarios remain closer to the historical runs. However, the low scenarios yield comparable global radiation increases in all months, leading on an annual basis to a similar increase as for the high-dry scenario (see Figure 3.39).

Fog

RACMO scenario simulations are used to provide projections for the number of potential fog hours in a changing climate. Favourable conditions for formation are analysed and classified as potential fog hours in case of a prolonged situation of at least 3 hours with a saturated shallow inversion layer and light winds. The probability of fog occurrence given these favourable meteorological conditions is derived from the relation between the observed fog hours and the RACMO historical simulation of the favourable meteorological conditions at individual stations for the historical time period. Projections of future fog hours are derived assuming that the probability of fog occurrence for given (favourable) conditions does not change in a future climate.

The RACMO model does not produce data on the number of hours with fog. As a proxy for the occurence of fog we use the ventilation:

$$v = h_{BL} u_{10m} \tag{3.1}$$

with h_{BL} the boundary layer height and u_{10m} the wind speed at 10 m. To map the ventilation to hours of fog model data, we compute the distribution of v computed from RACMO ERA5 data and visibility V_{max} from observational stations.

$$C(v, V_{max}) = P(v, V <= V_{max}) \tag{3.2}$$

The visibility data from the following observational stations are used:

235	De Kooy	269	Lelystad	344	Rotterdam
240	Schiphol	275	Deelen	348	Cabauw Mast
260	De Bilt	280	Eelde	350	Gilze-Rijen
265	Soesterberg	290	Twenthe	370	Eindhoven
267	Stavoren	310	Vlissingen	380	Maastricht

as well as the ventilation values on the RACMO grid points nearest to the location of these observational stations. Only data from 2003 to 2014 are used to compute the distribution in Equation 3.2 because in this period no major improvements in the air quality occurred. For each resampled RACMO member, i, the probability distribution of the ventilation $P_{vent,i}(v)$ is computed for the control and future periods. Assuming that the distribution in Equation 3.2 is the same in both periods, the probability of fog can be computed:

$$P_{fog,i}(V_{max}) = \int P_{vent,i}(v) C(v, V_{max}) dv \tag{3.3}$$

From this the number of hours of fog is given by

$$h_{fog,i} = h_p P_{fog,i}(V_{max}) \tag{3.4}$$

where h_p is the number of hours in the time period p with $p \in \{\text{ANN}, \text{DJF}, \text{MAM}, \text{JJA}, \text{SON}\}$. From these the ensemble mean and standard deviation are computed for both periods and the relative change in the mean from control to future. All the above distribution functions are implemented as one- or two-dimensional histograms with bins of 100 m^2/s in ventilation and 100 m in visibility.

3.5 Drought and evaporation

3.5.1 Introduction

Drought refers to sustained periods of below normal water availability (Tallaksen and Van Lanen, 2004). In meteorological context, we usually consider a precipitation deficit (i.e. lower than normal rainfall over a period of time) or a deficit in the climatological water balance (precipitation minus reference evapotranspiration, *PR - PET*). Through interactions with the land surface, meteorological drought then leads to below normal soil moisture (soil moisture or agricultural drought) and below normal groundwater, surface water and river discharge (hydrological drought) (Van Loon, 2015). Droughts impact society in many different ways, though generally these impacts are more closely related to soil moisture/hydrological drought than to the meteorological drought. Note that the intensity of soil moisture and hydrological droughts, and the magnitude of societal impacts, are location dependent and can be influenced by human behaviour. Therefore, and because these are meteorological scenarios, for the KNMI'23 climate scenarios we focus on changes in meteorological drought.

Many different indices exist to study drought occurrence and drought intensity. Historically KNMI has used the 'cumulatief doorlopend neerslagtekort' (*NT*) in its operations, which is defined as the difference between Makkink reference evapotranspiration and precipitation, accumulated from the 1st of April, with negative values set to zero. Recently, the Standardised Precipitation Index (*SPI*) (McKee et al., 1993) was added as a drought monitoring tool, and the Standardised Precipitation Evapotranspiration Index (*SPEI*) (Vicente-Serrano et al., 2010) was added as a variable on the climate dashboard to note if specific historical seasons were relatively dry or wet. For the development of the KNMI'23 climate scenarios we have used an index named 'water balance' (*WB*) which is similar to *NT* but with negative values for wet periods allowed (see Chapter/Section 2.1.8). We chose to focus on *WB* over *NT* because it is more symmetrical (applicable for both wet and dry spring/summer seasons), and because it can be computed using monthly data. In Section 2.1 we describe how *WB* is used in the resampling procedure. Here we analyse the scenario results in terms of this index. We have further analysed changes in drought based on *SPEI*, but do not include those results here as they are very much in line with the results for *WB*. The final discussion of the KNMI'23 results for drought is based on changes in *NT*, to align with the KNMI operations and thus this is the index our stakeholders are most familiar with.

It is important to note that all these indices for meteorological drought, including *WB* that was used in KNMI'23 scenario construction and both *WB* and *NT* discussed in this Section, make use of potential evapotranspiration. Potential evaporation is the amount of evapotranspiration that occurs if a sufficient water is available. It can be seen as the atmospheric demand for moisture from the surface. Actual evapotranspiration can differ from potential evapotranspiration, especially in times of drought when the surface is drier and might not be able to supply enough water. Reasons to use potential evapotranspiration in meteorological or climate applications, include, for example, the fact that actual evapotranspiration is complex to measure, varies significantly between locations (e.g. water surface, grass land or urban area), and its representation in climate models is strongly dependent on the complexity of the model's land component. At KNMI we use Makkink reference evapotranspiration as a measure of *PET*. Note that, the described changes in *WB* and *NT* are upper bounds of the actual changes in drought, due to the use of potential rather than actual evapotranspiration. For example, it is likely that the soil moisture response will not scale with these described changes during periods of significant drought (see e.g. Figure 8 of (Aalbers et al., 2023), which shows that future changes in soil moisture are larger for lower-intensity droughts than for higher-intensity droughts).

In this section we will discuss CMIP6-based projections of drought for the Netherlands and surroundings (NL and NL+RM regions), reflect on the success of the resampling procedure for drought specifically, the influence of dynamical downscaling, and discuss the KNMI'23 scenario values.

3.5.2 CMIP6 projections of regional change

Changes in seasonal mean values

The KNMI'23 standard set of CMIP6 models (33 models, Section 2.1.2) is used to determine the spread in the regional-mean climate change response. Figure 3.41 shows the model spread in projections of seasonal mean values for *PR* and *PET* for all SSPs and time horizons of the KNMI'23 scenarios. As an example, in the high emission scenario SSP5-8.5 in 2100, in the NL region *PR* is projected to increase by 15 mm (i.e. 8 %) in spring (March-April-May, MAM), though there is considerable model uncertainty for this value (80 % multi-model range: 15 ± 23 mm or 8 ± 14 %). In summer (June-July-August, JJA) the models project a decrease of *PR* of -52 ± 37 mm (or -30 ± 20 %). *PET* is projected to increase in both spring and summer, by 20 ± 10 mm and 52 ± 20 mm (11 and 16 ± 7 %) respectively in SSP5-8.5 in 2100. The increase in *PET* is due to increases in temperature and incoming solar radiation (not shown, see also Sections 3.1 and 3.4). Precipitation changes are discussed in detail in Section 3.2.

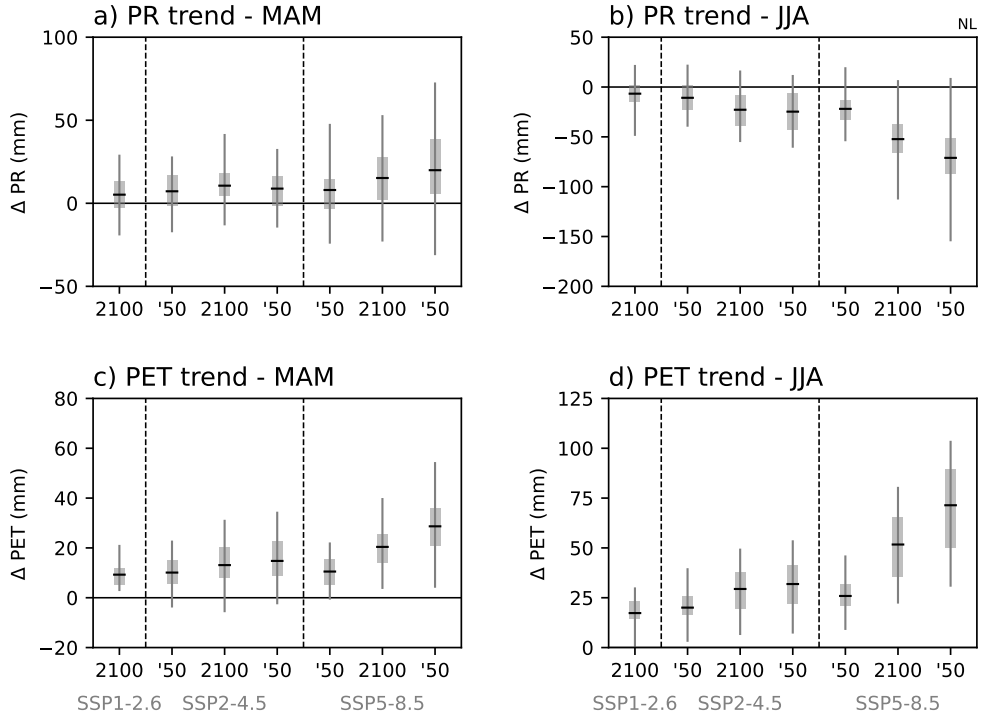

Figure 3.41: CMIP6 multi-model projection of **seasonal mean** regional climate change in the **NL region** for different SSP scenarios (SSP1-2.6, SSP2-4.5, SSP5-8.5) and time horizons (2050, 2100, 2150). Shown is the distribution of projected change in the standard set of 33 CMIP6 models (grey vertical line shows minimum and maximum, grey box shows 25th to 75th percentile), and their mean (black horizontal line). Variables shown: (a,b) precipitation (*PR*, mm), (c,d) Makkink reference evapotranspiration (*PET*, mm), in (a,c) March-April-May (MAM) and (b,d) June-July-August.

These projections of decreasing seasonal mean *PR* and increasing seasonal mean *PET* lead to a mean spring and summer climate that is drier in terms of the *WB*. For SSP-8.5 in 2100, the *WB* is projected to increase by 16 ± 16 mm in the period April to May and by 140 ± 60 mm in the period April to September (Figure 3.42). For reference, the September mean change of 140 mm is an increase of about 75 % of the climatological value of 180 mm, in May the increase is about 50 % of the climatological value of 30 mm.

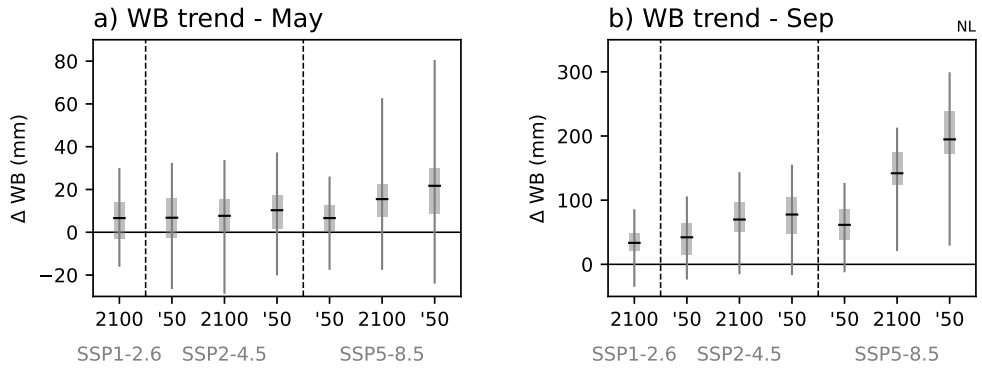

Figure 3.42: As Figure 3.41, but here for water balance (*WB*, mm). For (a) April to May, spring drought, and (b) April to September.

Changes in variability, i.e. dry and wet summers

The above described changes are the changes for the average spring or summer season. However, we are specifically interested in those seasons that are drier than the average season. The grey boxplots in Figure 3.43 additionally show the CMIP6 spread in relatively wet and dry seasons (defined by low/high percentile values for the season's value of *WB*), the middle grey boxplot 'mean' shows the same information as the boxplot for SSP5-8.5 2100 in Figure 3.42. There are weak signs of increasing variability in the spring season, i.e. the change towards higher values of *WB* (drying) is larger in dry springs than in wet springs. This is more obvious in the NL+RM region (Figure 3.44a) than in the NL region (Figure 3.43a). In summer there is no sign of increasing variability, the change in *WB* is similar for all percentiles investigated.

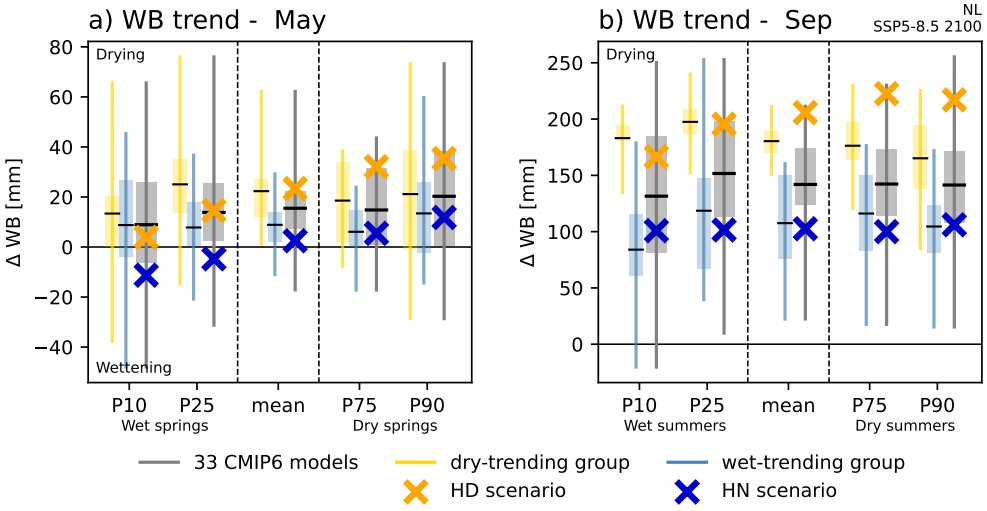

Figure 3.43: CMIP6 multi-model projection of regional climate change of the water balance (*WB*, mm), for average seasons ('mean') and for different 'extreme' seasons (i.e. wet or dry seasons) in grey boxplots. Similarly the CMIP6-based dry-trending and wet-trending groups are shown in yellow and blue boxplots, respectively. The EC-Earth3 $_{p5}$ resampled datasets, at the heart of the KNMI'23 scenario product, are shown in crosses (orange for the dry scenario, dark blue for the wet scenario). All for the NL region and the SSP5-8.5 2100 scenario, boxplots as in Figure 3.41. For (a) April to May, and (b) April to September.

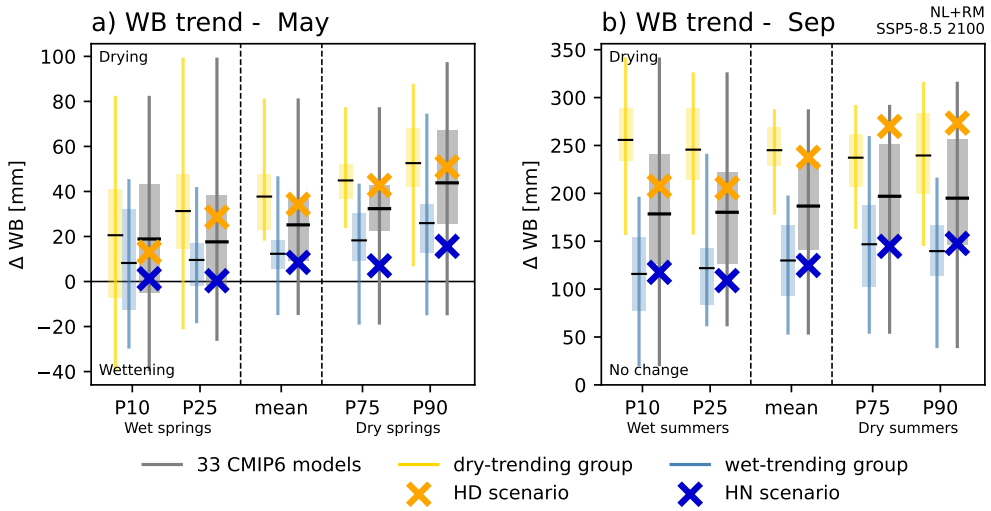

Figure 3.44: As Figure 3.43, but here for the NL+RM region.

Summary

Figures 3.41-3.44 show projections of regional climate change in CMIP6, specifically for drought-related variables/indices. Generally, there is a change towards a drier mean spring and summer climate. Though not immediately obvious, the changes in *PR*, *PET* and *WB* scale linearly with the global mean increase in temperature (ΔGSAT, not shown for *PET* and *WB*, for *PR* see Section 3.2.4). That means that changes are larger for scenarios with larger increases in the global mean temperature, e.g., the increase of *WB* September in 2100 is 33 mm in SSP1-2.6, 70 mm in SSP2-4.5 and 140 mm in SSP5-8.5 (CMIP6 matched-warming, multi-model means, Figure 3.42b). These difference are due to emission uncertainty, i.e., the unknown volume of future greenhouse gas emissions. The KNMI'23 scenarios have been developed for each of these SSP scenarios separately. Within an SSP scenario, and assuming the most likely value for climate sensitivity (Section 2.1.1), different CMIP6 models project different regional responses. This 'model uncertainty', related to model formulation, scientific understanding of regional climate change, and natural variability, is spanned through the use of two storylines (Section 2.1.5). In the next section we discuss changes in drought in these specific storylines.

3.5.3 KNMI'23 resampled datasets in relation to CMIP6 projections

Drought in CMIP6-based dry-trending and wet-trending groups

To capture part of the model uncertainty that exists between CMIP6 models the KNMI'23 scenarios provide two storylines: based on a group of dry-trending and a group of wet-trending models (Section 2.1.5). These groups have been defined such that they have largest difference in their *PR* response in summer, winter and year-total. Whether they also have large differences, i.e. span the model uncertainty, in *WB* is not immediately obvious. This depends on correlations between *PR* and *PET*, and on correlations between spring and summer.

The response for *WB* in the dry-trending and wet-trending groups, relative to the full CMIP6 distribution, is shown in Figures 3.43 and 3.44 (yellow and blue boxplots relative to grey boxplot). In September the two groups are well-separated and the group mean (horizontal black lines) fall approximately at the 75th and 25th percentile of the full CMIP6-distribution. This is the case for average summers ('mean' in the figures), but also for relatively wet and dry summers (defined by the percentile value of the May/September *WB*). In May the groups are also separated though less distinctively than in September. The group separation is less well-defined in the relatively wet and dry springs (e.g., P10 or P90 springs in the NL region, Figure 3.43a), though we note

that internal variability is likely to be rather large for these computed values and might be larger than model differences (the change in P10 springs computed over a 30 year period is based on just 3 seasons, and hence internal variability has a potentially large influence, see also Section 2.1.4).

More formally, Figure 3.45 shows the position of the group means within the full CMIP6 distribution for mean seasons. For *WB* these are approximately the P70 and P80 (dry-trending, May and September), and approximately P25 en P20(wet-trending, May and September), i.e. the two groups are well separated. If the resampling procedure is successful in reproducing these values, the resulting scenarios will be distinctive and will indeed span a substantial portion of the model uncertainty. To help/achieve the resampling goals for drought specifically, two *WB*-criteria for NL+RM are taken into account in the resampling procedure. Interestingly, the separation of the groups in *WB* is larger than the separation in the contributing variables *PR* and *PET* in individual months. This is likely due to temporally compounding effects in *WB*, through its accumulation from April onwards.

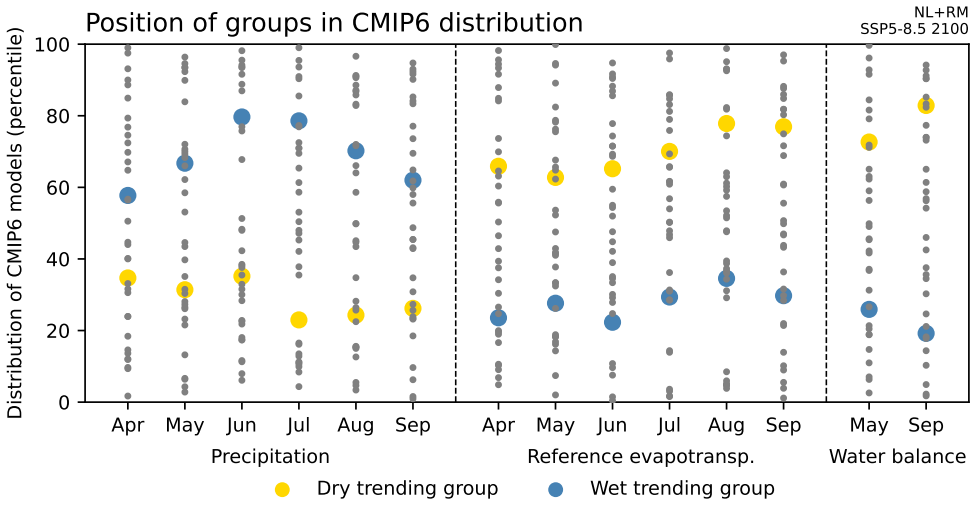

Figure 3.45: Percentile position of the means of the dry-trending and wet-trending group (yellow and blue, respectively) within the percentile-distribution of all 33 CMIP6 models (grey). A normal distribution is assumed to compute the percentiles. The X-axis shows different variables and months, the y-axis shows the distribution of CMIP6 models in percentiles.

Results of the resampling procedure

The resampling procedure applied in KNMI'23, designed to reconstruct the CMIP6 group responses with the EC-Earth3$_{p5}$ model to allow dynamical downscaling at a later stage, adds a step of complexity to the scenario procedure. The EC-Earth3$_{p5}$ model has a specific climate response, which, if it is very different from the group responses, complicates the reconstruction of these responses (Section 2.1.9). Here we analyse if this reconstruction has been successful for *WB* (i.e. we check if the resampling result is close to the applied resampling constraint), to judge how the scenarios map onto the uncertainty in the CMIP6 ensembles in terms of drought.

Orange and blue crosses in Figures 3.43 and 3.44 show the projection of *WB* in the resampled datasets for the SSP5-8.5 (H-scenario) in 2100. This extreme scenario is taken as an example as it has a large climate change response, and thus signal and noise are more easily separated, but also because this scenario has proven to be most challenging in the resampling procedure, due to relatively larger differences between the CMIP6-groups and EC-Earth3$_{p5}$. The resampling results should be compared to the mean of the CMIP6 group responses. In both May and September, the two resampled datasets have distinct responses that have overlap with their respective CMIP6-based group. In the NL+RM region, the resampled datasets almost exactly reproduce the group

mean response for average seasons (Figure 3.44, 'mean' column). In the NL region, the drying trend in the dry scenario in September is slightly larger in the resampled dataset than in the CMIP6-based group (Figure 3.43b). Also the response in the relatively dry and wet seasons (percentile columns in the figures) is relatively closely reproduced, though some differences can be noted. E.g. during relatively dry summers the projected drying trend is larger in the Dry resampled dataset than it is in the CMIP6-based dry-trending group (Figure 3.43b, P75 and P90), and the resampled datasets project an increase in *WB* variability in summer (larger drying trend in dry summers than in wet summers) that is not seen in the CMIP6-ensemble.

Summary

The KNMI'23 resampled datasets based on the EC-Earth3$_{p5}$ model reproduce the CMIP6 regional response in *WB* in the dry-trending and wet-trending relatively well. The resampling procedure successfully reconstructs the desired responses, despite quite large differences between the EC-Earth3$_{p5}$ model response and the dry-trending CMIP6 group (Figure 2.15). At this point in the scenario method and modelling chain, the sub-results are as desired and do indeed describe/capture a substantial part of the regional response uncertainty of the of drought in the NL/NL+RM region to climate change. It is important to note that these are indeed sub-results, the KNMI'23 scenario values are not based on these EC-Earth3$_{p5}$ resampled datasets but on their downscaled, bias-corrected RACMO equivalent. These final results are discussed in the next section.

3.5.4 KNMI'23 scenario results (bias-corrected RACMO)

RACMO specific added-value

Given the interest in detailed regional scenario data, the final KNMI'23 data are based on RACMO regional climate model simulations. The selected EC-Earth3$_{p5}$ resampled datasets, verified in the previous section, are replaced with RACMO resampled datasets (Section 2.4). Furthermore, RACMO model biases and differences between the observed climatology and the climatology in the resampled dataset (methodological) have been corrected (Section 2.1.10). In this section we show the final scenario results for the KNMI drought metric 'cumulatief doorlopend neerslagtekort' *NT*.

Before discussing these results some notes on the RACMO downscaling. Generally, RACMO is seen to add-value to the EC-Earth3$_{p5}$ simulations, higher spatial resolution allows finer simulation of the influence of, e.g., land-sea contrasts and orography. It should however be noted that a different regional climate model, would add-value in a slightly different manner. Regional climate models have their own model formulations and thus climate responses, similar to the different models and their responses in the CMIP6 ensemble. For drought specifically, RACMO reduces the magnitude of drying trends present in the EC-Earth3$_{p5}$ resamples, especially in summer. The RACMO trends are on the order of 20 % smaller than those in EC-Earth3$_{p5}$. Using existing analyses of the EURO-CORDEX ensemble (a multi-model regional downscaling experiment, based on GCMs from CMIP5) we know that RACMO is not an outlier in this case, regional models typically reduce the GCM-projected trends towards a drier European summer climate (Coppola et al., 2021) (e.g., smaller summer temperature trends, smaller precipitation decrease in summer, smaller solar radiation increase; their Figures 1b, 5b and 11). As such, we take the added-value of RACMO for drought-related variables as it is.

KNMI'23 scenarios of 'neerslagtekort' in the Netherlands

The resampling procedure selects and combines years, such that the climate change response in the EC-Earth3$_{p5}$ resampled datasets matches that of the CMIP6-based group constraints (Section 2.1.9). To achieve this, both the present-day resampled dataset and the future resampled dataset have specific characteristics. After applying RACMO downscaling and bias correction, the climatological characteristics of the present-day resample should match that of the observations in the reference period (1991-2020). Indeed, for *NT* the values of the median summer and the values for relatively dry summers (95th percentile, 5% driest years) match the observations

(Figure 3.46a). The figure further shows some well-known observed historic drought years (1976, 2018) close to or above the 95th percentile, and the maximum value in the present-day resampled dataset (sample size 240 years).

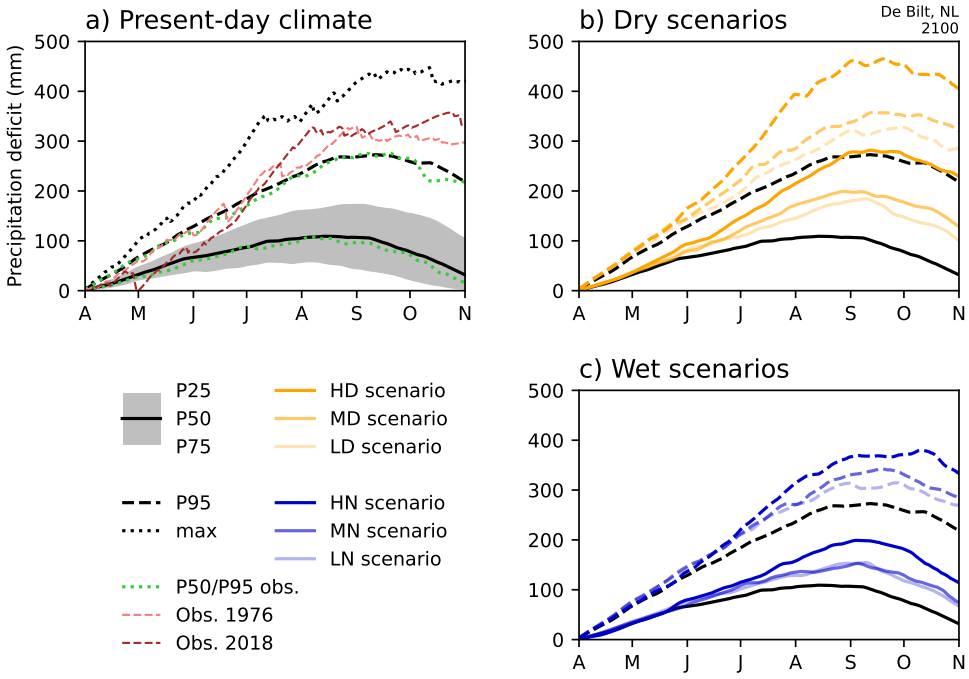

Figure 3.46: Time series of 'cumulatief doorlopend neerslagtekort' (*NT*, mm) in De Bilt, the Netherlands, based on bias-corrected RACMO data. (a) Present-day climate, representative of 1991-2020, solid line shows the median, grey shading shows the range from the 25th to 75th percentiles, dashed line shows the 95th percentile, dotted line shows the ensemble maximum. Dotted green and dashed red/pink lines show observational data, observational percentiles are computed over the period 1958-2022. (b,c) Scenario data for the dry (D, yellow colours) and wet (N, blue colours) scenarios, for all SSP-emission scenarios (H,M,L), and the present-day reference (black). Solid lines show the median in the scenario, dashed lines show the 95th percentile. To all lines, except the line for maximum and 1976/2018 summers in panel (a), a 7-day running mean has been applied.

In all scenarios future *NT* increases relative to the present-day values. Figure 3.46b,c shows the median and 95th percentile time series for all scenarios in 2100 (SSP1-2.6, SSP2-4.5, SSP5-8.5, or L-, M- and H-scenarios), the associated values at the 1st of June (taken as a representative date for spring drought) and at the 1st of September (taken as a representative date for summer drought) are shown in Tables 3.5 and 3.6. Generally, trends of *NT* are larger in the higher emission scenarios, and are larger in the Dry scenario versions. In SSP5-8.5 (H-scenario) the median value of *NT* at 1 Sept increases from 107 mm in the present-day to 197 and 268 mm in 2100 (Wet and Dry scenario, respectively), the 95th percentile of *NT* increases from 269 mm in present-day to 367 and 461 mm in 2100 (Wet and Dry, respectively). Note that in the most extreme scenario here (Hd) the future median summer is like the 95th percentile summer in the present-day climate.

In the present-day period there is no strong north-south gradient in the spatial pattern of climatological *NT* over the Netherlands (Figure 3.47a). The scenarios trends do have a gradient, with larger drying trends in the south of the Netherlands than in the north (Figure 3.47b-g). For example for the Hd-scenario in 2100, the increase in Leeuwarden is in the order of 150 mm (55 %), whereas the increase in Maastricht is in the order of 200 mm (70 %). Consequently, in the scenarios with substantial trends a climatological north-south gradient arises (Figure 3.48).

Scenario	Time horizon		P50 Dry	P50 Wet		P95 Dry	P95 Wet
	1991-2020	66			129		
L-scenario	2050		82	78		143	142
M-scenario	2050		83	73		157	151
H-scenario	2050		75	72		140	143
L-scenario	2100		82	78		143	142
M-scenario	2100		79	70		145	147
H-scenario	2100		94	80		165	137
L-scenario	2150		82	78		143	142
M-scenario	2150		75	67		162	144
H-scenario	2150		96	83		159	154

Table 3.5: Present-day and scenario values for 'cumulatief doorlopend neerslagtekort' (NT, mm) in De Bilt at 1 June (as in Figure 3.46) for all scenarios, based on bias-corrected RACMO data.

Scenario	Time horizon		P50 Dry	P50 Wet		P95 Dry	P95 Wet
	1991-2020	107			269		
L-scenario	2050		180	152		322	313
M-scenario	2050		161	134		329	310
H-scenario	2050		195	150		359	332
L-scenario	2100		180	152		322	313
M-scenario	2100		198	150		338	331
H-scenario	2100		268	197		461	367
L-scenario	2150		180	152		322	313
M-scenario	2150		199	153		361	318
H-scenario	2150		295	227		468	414

Table 3.6: As Table 3.5 but here for 1 September.

Discussion

The noted changes in NT show projected trends in drought for the April to September season. We have quantified changes in spring drought by investigating changes on 1 June and changes in summer drought by investigating changes on 1 September. These changes do not take into account possible changes in the seasonality of drought, through for example an earlier start of the drought season. Historically, KNMI starts the computation of NT on 1 April, but earlier starting dates are computationally of course also a possibility. Further research at KNMI will focus on this question and aim to analyse whether climate change will result in seasonal shifts in the start and/or end of the typical drought season, and whether this, e.g., impacts the intensity of summer drought.

Finally, as noted at the start of the introduction, the KNMI'23 scenarios provide information on changes in meteorological drought. Changes in for example soil moisture or river discharge that follow, are important, but not discussed here. Societal impacts more closely align with these variables.

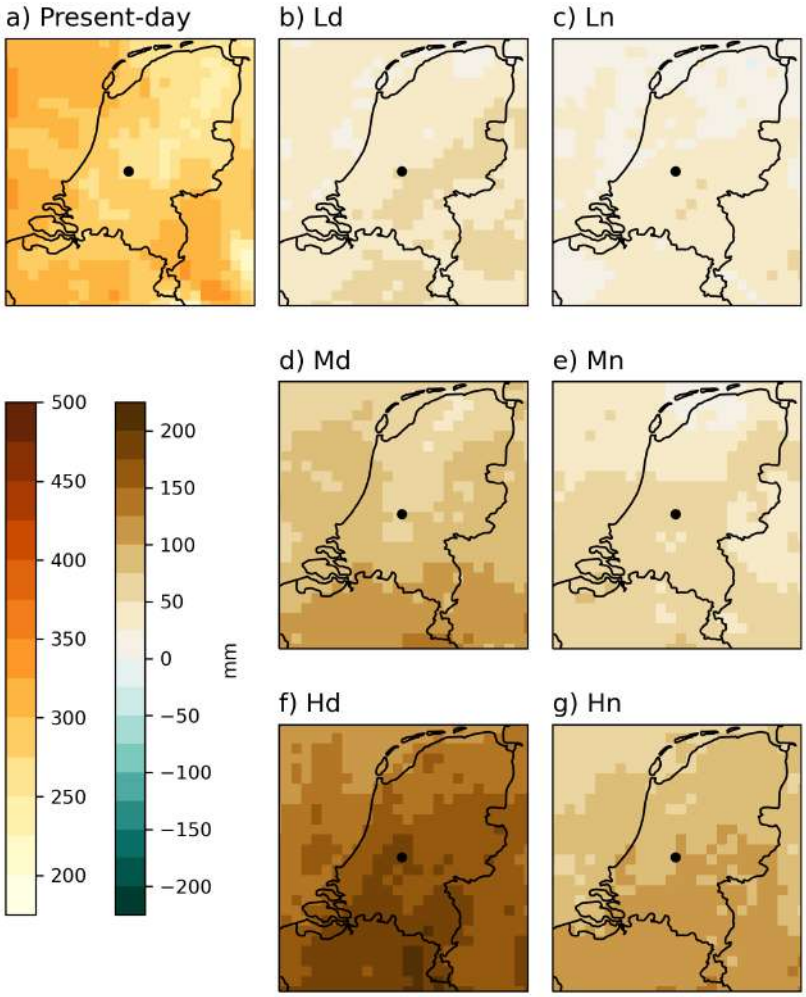

Figure 3.47: (a) Map showing the 95th percentile of the cumulatief doorlopend neerslagtekort' (NT, mm) on 1 September in the present-day climate (dashed black line in Figure 3.46a). (b-g) Projected change in 2100, per KNMI'23 scenario, of the 95th percentile NT (mm) on 1 September. A 7-day running mean has been applied to all data, black dot in the center shows location De Bilt (as in Figure 3.46).

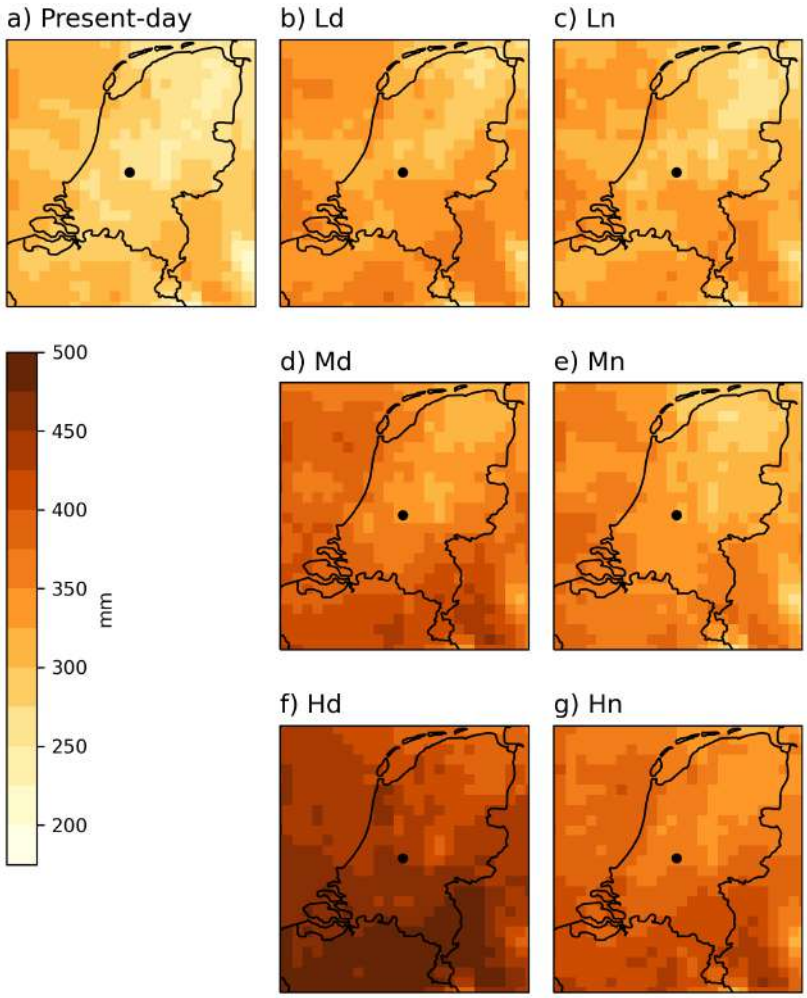

Figure 3.48: As Figure 3.47a, but here showing the absolute value of the 95th percentile NT (mm) on 1 September for all scenarios.

Chapter 4

Sea level rise

4.1 Introduction

The KNMI'23 scenarios of sea-level change along the Dutch coast are based on chapter 9 from the sixth assessment report (AR6) from the Intergovernmental Panel on Climate Change (IPCC) on the physics of climate change (Fox-Kemper et al., 2021). While the method of AR6 projections is constrained by the fact that it should work for all oceans in the world we adjust our scenarios to the Dutch coast. For the first time, these adjustments are informed by a closed sea-level budget based on recent advances in the field (Frederikse et al., 2016, 2020). Our goal is to develop scenarios that overlap with observations over the period 1993-2021, and seamlessly continue into the future. An additional requirement is that such a good connection between observation and scenarios not only holds for total sea level but also for each individual contributor (e.g., Antarctica, ocean-dynamic sea level...). This increases our confidence in the ability of models to also provide reliable century projections.

In contrast to sea level scenarios in KNMI'14, KNMI'23 scenarios no longer use global mean temperature change as driver, but they are directly conditioned on greenhouse-gas emission scenarios. This means that the uncertainty in temperature given an emission scenario is now also included in the uncertainty ranges that we provide. There are three reasons for us to include temperature uncertainties: 1) this approach is consistent with AR6; 2) by including more uncertainty it allows for risk-avoiding adaptation measures; 3) unlike atmospheric variables, oceans and ice sheets do not adjust quickly to temperature change. They adjust over a period of hundreds to thousands of years, making the response to a given temperature-change strongly time dependent. Adding temperature uncertainty given an emission scenario in the KNMI'23 scenarios is one reason why the uncertainty bands have become broader since KNMI'14. For KNMI'23 scenarios other than sea level the median of global temperature change in specific years is used, temperature uncertainties given an emission scenario are not included.

Another novelty with respect to KNMI'14 is that ocean-dynamic sea level is constrained by model selection using observations. Additionally, in KNMI'14 only the local vertical land motion due to recent mass loss from ice sheets, glaciers and land water storage were included. Those effect are called contemporary Gravitational, Rotational, and viscoelastic solid-Earth Deformation (GRD) (Gregory et al., 2019). In KNMI'23 we also include the local effects of Glacial Isostatic Adjustment (GIA), which is the vertical land motion due to the ice loss from the last glacial maximum about 20.000 years ago. Therefore KNMI'23 scenarios are more complete relative sea-level scenarios.

Furthermore, we include Low Likelihood High Impact (LLHI) scenarios. Those scenarios are either based on physical processes (mostly ice dynamics in ice sheets) not yet well-understood or difficult to quantify, or Structured Expert Judgement (SEJ), a different way to assess expert opinions. These LLHI scenarios are mostly conditioned on processes not yet observed in Antarctica, but physically plausible and, either observed in Greenland, or derived from geological evidence of

past changes. By conditioning these LLHI scenarios on specific processes these processes themselves can be interpreted as Early Warning Signals for an acceleration of sea-level rise associated with a transition from a standard scenario to a LLHI scenario.

4.2 Method

4.2.1 Sea-level budget

Since KNMI'14, the field of sea-level research has made important progress on closing the sea level budget on regional scale (Camargo et al., 2023), especially along the Northwest European shelf (Frederikse et al., 2016). In the sea level budget, the sum of the individual components contributing to the sea level rise (e.g. thermal expansion, glacier melt...) is compared with the observed sea level rise. When the sum of contributors is close to the observed sea-level change, we trust that we understand current sea-level rise. We develop two budgets for the recent period 1993-2021. One is based on satellite altimetry data averaged over a region close to the coast of the Netherlands (Fig. 4.1 a) and another one is based on the 6 tide gauges (Vlissingen, Hoek van Holland, IJmuiden, Den Helder, Harlingen, Delfzijl) distributed along the Dutch coast (Stolte et al., 2023). We use ice sheets, glaciers, and land water storage contributions from Frederikse et al. (2020). The direct influence of the nodal cycle is assumed to be in equilibrium with the astronomical forcing and is calculated as in Woodworth (2012). To compute the steric influence on sea level along the coast of the Netherlands we first compute ocean water density from quality-controlled ocean temperature and salinity data from the EN4.2.2 dataset (Good et al., 2013). The density is then integrated vertically from the ocean surface down to 500 m in the Bay of Biscay and from 500 m to 4000 m in the Norwegian Sea (Fig. 4.1 b). After testing a few different regression variables, this heuristic approach gave the best correspondence between the manometric adjustment in the North Sea for our coast and steric changes in the neighbouring eastern North Atlantic Ocean. This calculation is based on the assumption that because the North Sea is shallow, steric expansion there does not have a significant impact on sea level change but steric anomalies in the deep ocean propagate to the North Sea as a mass inflow. We then remove the global steric sea level from Frederikse et al. (2020) to obtain the regional steric anomaly. The separation between regional and global steric does not have an influence on total sea level but is performed to compare with climate models in which those two processes are computed separately. Once all known sources of sea level change above are computed, they are removed from the observed sea level. The effect of wind and inverse barometer on sea level are then computed from a multi-linear regression to zonal and meridional wind and pressure fields from the ERA5 reanalysis (Keizer et al., 2022). Since the budget from Frederikse et al. (2020) stops in 2018 we extrapolate ice sheets, glaciers, and land water storage up to 2021 using a linear fit to the last 10 years of the individual time series. This is possible because those terms are rather smooth and because at the inter-annual time scale, local sea-level change is mostly set by wind, the inverse barometer effect, and regional steric anomalies.

To estimate the influence of mass loss from land ice on regional sea-level we consider the fact that melt water from land ice will not distribute evenly over the oceans because decreasing mass of land ice affects the gravity-field of our planet and, as a result, the geoid, which is the surface an ocean in rest would possess. In addition, we also account for the elastic deformation of the solid earth and changes in the axis of rotation of the Earth induced by the change in mass distribution (Slangen et al., 2014). Those gravitation, rotation and viscoelastic deformation effects are referred to as GRD.

4.2.2 Sea-level scenarios

Contributions to sea-level change

Sea level scenarios are built by adding together all processes that provide a large contribution to decadal-to-century sea-level change along the coast of the Netherlands and are not part of

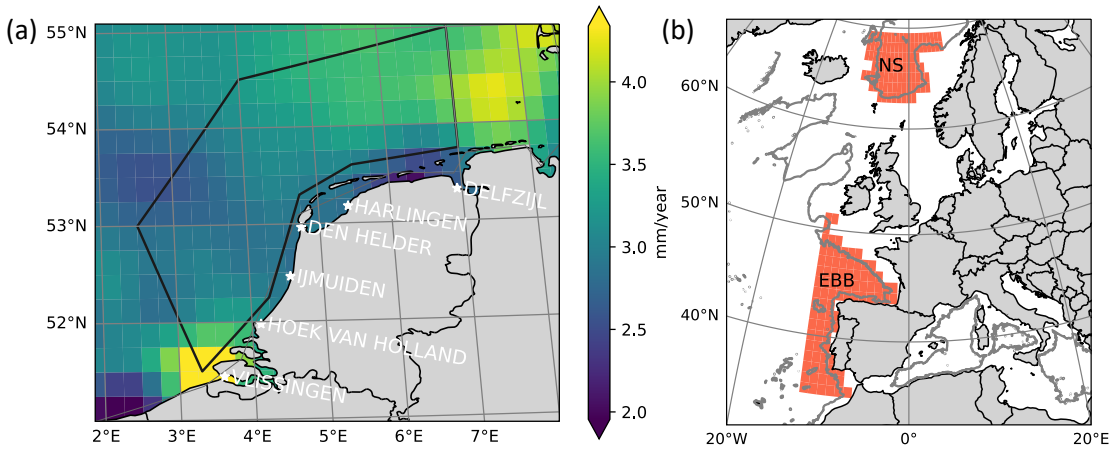

Figure 4.1: (a) Linear fit to the sea level from satellite altimetry over the period 1993-2021. The area over which we compute the spatial average sea level from satellite altimetry and climate models is represented with a black polygon. The locations and names of the 6 main tide gauges are indicated in white. (b) Regions of deep ocean used to compute steric sea level representative of sea-level change in the North Sea (EBB: Extended Bay of Biscay, NS: Norwegian Sea). The grey line shows the 2000m isobath.

natural sea-level variations that are unpredictable. Thus, the scenarios do not contain year-to-year variations induced by winds and fluctuating ocean currents. Below, we give an overview of the method and a more complete description can be found in the appendix 4.5:

1. *Oceans*: The contribution from oceans to sea-level rise is composed of global thermosteric sea-level due to the net ocean heat uptake caused by global warming, and of ocean dynamic sea-level (ODSL) associated with the change in ocean currents and the changed distribution of heat and salt across the oceans that is forced by global warming through changes in evaporation and precipitation, heat uptake, heat release, and winds. ODSL in CMIP6 models consists of regional steric anomalies and the direct effect of wind on sea level. We select models that produce a reasonable ODSL over the period 1993-2021 with a new method that we describe in the following section. The same models are used for the global thermosteric sea level. More information about the analysis of CMIP6 models is given in section 4.5.1.

2. *Glaciers*: Following AR6, this term is calculated with the same parametric fit as defined in AR5 but using 7 global glacier models from GlacierMIP2 (see 9.SM.4.5 from Fox-Kemper et al. (2021)).

3. *Antarctica*: For this contribution the dynamics and Surface Mass Balance (SMB) are separated. Ice dynamics is from van der Linden et al. (2023). This method uses subsurface warming from CMIP6 models around Antarctica to force Linear Response Functions (LRF) of ice sheet models from (Levermann et al., 2020). Basal melt sensitivity is calibrated to fit observations of ice discharge (Rignot et al., 2019). Here we select the calibration based on quadratic formulation of the basal melt in the Amundsen Sea region. The SMB is computed from GSAT in the same way as AR5.

4. *Greenland*: Since there was a minimal difference between AR6 and AR5 contribution but an important increase in complexity of the method we computed this contribution in the same way as AR5. The SMB and the ice dynamics are assessed separately. The SMB is computed from GSAT using a relation derived from a regional climate model (Fettweis et al., 2013) and the dynamics is assessed from ice sheet models.

5. *Land water storage*: As for AR5 we assume that this contribution is zero before 2006. From 2006 we fit a second order polynomial to rates in 2006 as estimated from AR5 to the AR6 values in 2100.

6. *Glacial Isostatic Adjustment (GIA)*: GIA models are still uncertain for the coast of the Netherlands (Vermeersen et al., 2018) but based on the sea level budget we choose to include GIA from the ICE-6G(VM5a) model (Peltier et al., 2015).

For the glaciers, the ice sheets and the land water storage the GRD effects are taken into account based on Slangen et al. (2014).

The change in Greenland surface mass balance (snow fall, melt and runoff) and in glaciers and small ice caps are driven by global mean surface air temperature (GSAT). We use the GSAT evolution from AR6 which are lower than the CMIP6 outputs because many CMIP6 models were assessed as having an Equilibrium Climate Sensitivity (ECS) above a reasonable range (see section 4.5.2).

To obtain the total sea level we use a Monte Carlo method to add the sea level contributors while propagating their uncertainty (Le Bars, 2018).

In the scenarios we consider the main sources of vertical land motion of the deep Pleistocene layer in the Netherlands on which the NAP is based. These are GIA and the elastic earth response related to the recent melting of land ice. Other sources of vertical land motion like gas extraction, water pumping, salt mining, soil oxidation, soil compaction are not considered. Gas extraction has a large effect on relative sea level in some places along the Dutch coast. Those effects are also filtered out of the tide gauge data that we use for comparison with our scenarios (Stolte et al., 2023).

Model selection for Ocean Dynamic Sea Level

For the first time we estimate a reasonable range of ODSL change for the period 1993-2021 from multiple lines of evidence and we select models that are able to simulate ODSL change within that range. We remove the wind effect from modelled ODSL because our period is relatively short and intrinsic variability of the wind can still have a large impact on sea level trends. To estimate the influence of wind on sea level we use a multi-linear regression of sea level on meridional and zonal wind and sea-level pressure. The multiple lines of evidence that we consider are shown in red in Fig. 4.2 and explained below:

1. Integration of steric sea-level in the top 2000m of the ocean in two regions: the extended Bay of Biscay (EBB) and the Norwegian Sea (NWS), and for two observational temperature and salinity products: EN4 and IAP (see section 4.2.1). In total, this gives 4 different estimates.

2. We remove the regional steric anomaly from the budget and assume that the budget must close. This provides an estimate for the tide gauge and the satellite altimetry budgets.

3. Ocean model reanalyses, that assimilate observations of temperature and salinity in a dynamical ocean model, also provide an estimate of ODSL. We use here the Simple Ocean Data Assimilation (SODA).

The total range in these estimates and their uncertainty is from -0.5 to 1.2 mm/yr. We exclude models for which the rate plus or minus one standard error does not overlap with the range of observational estimates (Fig. 4.2). Out of a total of 26 CMIP6 models, 12 models with too high rates and one model with too small rate were excluded, and 13 models featured trends that complied with the uncertainty range in the observations (Fig. 4.2). Out of those 13 models only 9 also have global steric sea-level data. Those are the 9 models on which our scenarios are based: ACCESS-ESM1-5, CNRM-CM6-1, CNRM-ESM2-1, EC-Earth3, INM-CM4-8, MPI-ESM1-2-LR, NorESM2-LM, NorESM2-MM, UKESM1-0-LL.

Many of the models excluded have an Equilibrium Climate Sensitivity (ECS) above the AR6 range but also models with a weaker ECS can be strongly biased. For instance, when a too large

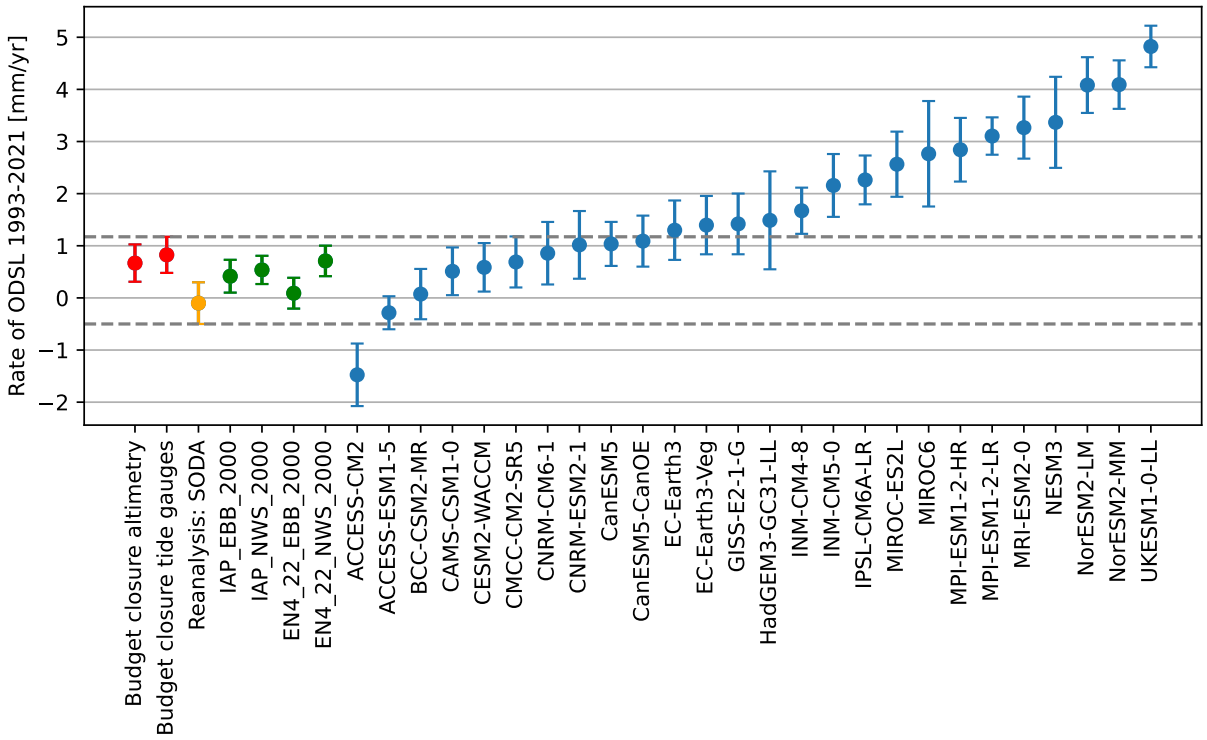

Figure 4.2: Rate of ODSL over the period 1993-2021 from multiple observational estimates (budget closure in red, reanalysis in yellow and regional steric sea level change in green) and from CMIP6 models (blue). The uncertainty ranges are ± one standard error in the fitting of a linear trend to the data with a least square method. The dashed horizontal grey lines show the minimum and maximum observational estimate.

decrease of the Atlantic Meridional Overturning Circulation is simulated, which is the major driver for an upward trend in ODSL for our coast (Katsman et al., 2008).

Comparison with other scenarios

The main differences between KNMI'23 and AR6 sea level scenarios are thus:

1. The scenarios start in 1995, instead of 2020 in AR6, so they can be compared with observations.
2. For ODSL we select CMIP6 models that have a realistic representation of ODSL over the period 1993-2021 based on multiple lines of evidence
3. While AR6 uses emulators to project GSAT and many sea level contributors: global thermal expansion, ice sheets, glaciers, here we only use emulated results for GSAT.
4. We consider relevant scientific findings published since the AR6 deadline for including scientific results (1-1-2021). This includes results from the Knowledge Program on Sea Level Rise funded by the Dutch Ministry of I&W and the Delta committee.

Compared to KNMI'14 described in de Vries et al. (2014) the main differences are:

1. The GSAT pathways used to drive some contributors to sea level in KNMI'14 diverged between the high and low scenarios already from the beginning of the scenarios and the high

temperature scenario was too high. By considering emission pathways instead of temperature pathways we do not have this problem in KNMI'23.

2. Because our scenarios are now driven by greenhouse gases emissions instead of temperature pathways, temperature uncertainty is included in the uncertainty in sea-level rise scenarios which increases the uncertainty ranges.

3. The global steric sea-level and ODSL changes were obtained from CMIP5 models and no selection was applied. In KNMI'23, CMIP6 models are used and a selection is applied for ODSL change.

4. In KNMI'14 the ODSL was computed from the spatial average over the whole North Sea. We now define a smaller region shown in Fig. 4.1.

5. In AR5 and KNMI'14 Antarctic dynamic was extrapolated from observations (Little et al., 2013b,a). We now use calibrated model estimates from (van der Linden et al., 2023).

For more information about the comparison of KNMI'14 scenarios with observations see section 4.4.4.

4.3 Results

4.3.1 Sea level observations

An important conclusion from AR6 that was given *high confidence* is: *"Global mean sea level rose faster in the 20th century than in any prior century over the last three millennia"*. This was confirmed again in more recent research by Walker et al. (2022) who used multiple sea level proxies. To check if this conclusion also applies to the coast of the Netherlands, we investigate the evolution of the rate of sea level rise over the last 2000 years from 3 independent observational products. For the long time scale we take the average rate from three sites from the study of Walker et al. (2022). Two sites in Scotland and one in Denmark, corrected for the long-term vertical land motion. Rates of sea level rise from 6 tide gauges along the Dutch coast corrected for wind and nodal cycle are from Keizer et al. (2022) and we additionally correct them for GIA using the ICE-6G model. Finally, the rate of sea level from satellite altimetry is computed as the weighted spatial average over the region shown in Fig. 4.1. The reasons for choosing this area are: (1) it seems that some tidal signals are not completely removed in the satellite data, so a large area is needed to average-out the tidal signal, and (2) the land-sea mask in the data is still rather coarse, putting sea over large parts of the land in coastal areas and over the IJsselmeer. We therefore select data further from the coast where the quality is higher.

In Fig. 4.3 (a) we see that the rate of sea level rise without GIA before the industrial revolution was close to 0 mm/yr and was followed by a sharp increase to reach an average rate between 2 and 3.5 mm/yr over the last 30 years. The acceleration of sea level rise along the Dutch coast that is observed by tide gauges during the 20th century (Steffelbauer et al., 2022; Keizer et al., 2022; Stolte et al., 2023) is the continuation of a process that started already in the 19th century.

4.3.2 Sea-level budget

Sea-level changes related to the ice sheets, glaciers and land water storage are shown in Fig. 4.4. Along the Dutch coast Greenland contributes less to sea level rise than Antarctica, even though Greenland mass loss at present is larger than Antarctic mass loss.

We present in Fig. 4.5 (left panel) the linear trend of each sea level contributors from the observed sea level budget and compare with the observed rate of sea-level rise (horizontal black line). The sum of sea level contributors is very close to the observations which suggests that we understand the reason for sea-level change over the period 1995-2021 along the Dutch coast. The larger contributor to sea level rise was the term called "ocean" in the histogram which includes

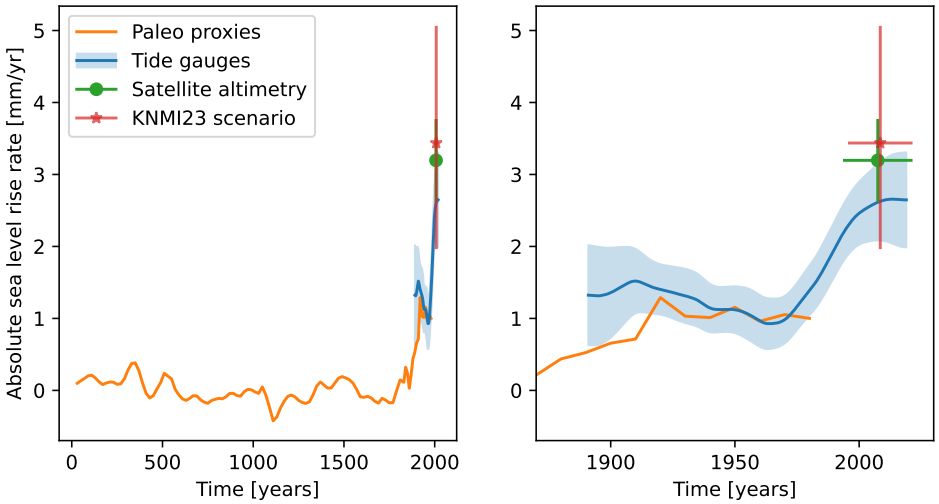

Figure 4.3: Regional rate of geocentric sea-level rise for the last 2000 years (a) and from 1870 to present (b). Paleo proxies are from the average of three sites, two in Scotland and one in Denmark (Walker et al., 2022). Estimates of rates and uncertainties for 6 tide gauges along the Dutch coast come from a GAM model and an advanced bootstrap method (Keizer et al., 2022). Rate from satellite altimetry is for the region shown in Fig. 4.1, vertical bars show ± 1 standard error. For KNMI'23 the results from the ssp245 emission scenario are shown. The vertical bars represent the 5th to 95th percentiles range. Horizontal bars for the satellite and KNMI'23 scenarios show the period over which the rates were computed with a linear least squares regression.

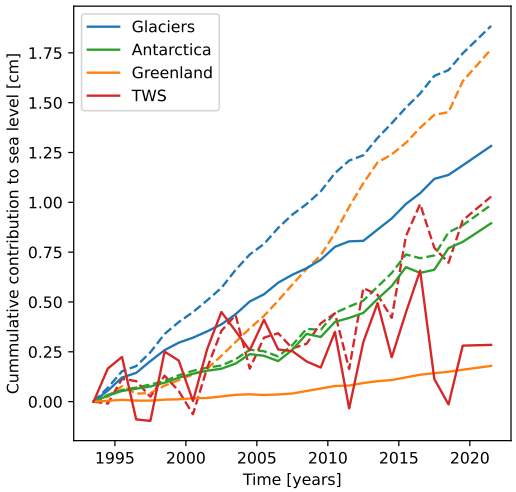

Figure 4.4: Global (solid) and local for the Dutch coast (dashed) cumulative contributions to sea-level rise since 1993 (TWS: Terrestrial Water Storage).

both global steric and ODSL effects. Then glaciers, Antarctica and GIA also played a large role. Other contributors: Greenland and land water had a relatively minor impact over this period.

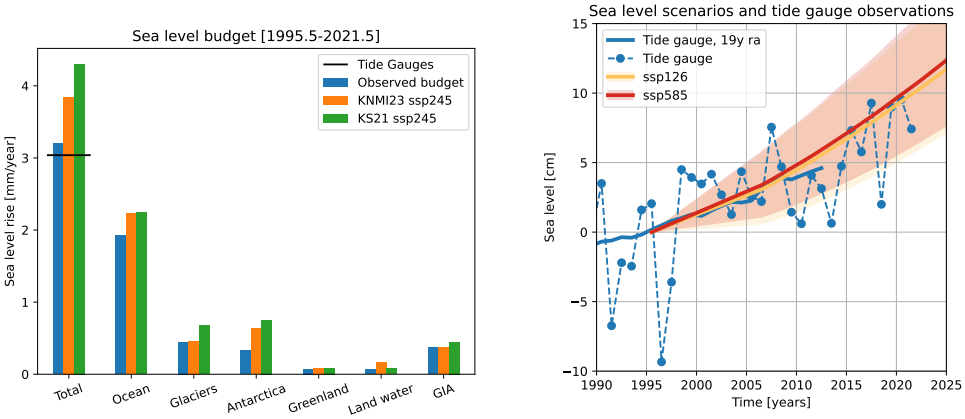

Figure 4.5: Left panel: Observed and modelled sea-level rate of rise for the Dutch coast over the period 1995-2021 decomposed in its various contributions. The label "KS21" stands for "Klimaatsignaal'21". The contribution called "ocean" is the sum of global steric sea-level and ODSL changes. Right panel: Time series of observed sea-level rise and KNMI'23 scenarios for the Dutch coast zoomed over the recent past and near future. Observations from tide gauges are shown as yearly averages (blue disks) and the 19-year running average (blue line).

4.3.3 Scenarios for the 21st century

For these scenarios we paid a lot of attention to obtain a smooth transition between observations and scenarios (Stolte et al., 2023). Scenarios are based on adding up individual sea level contributors so the first step was to understand why sea level rose over the past decades along the Dutch coast. Based on this budget we could improve sea level scenarios. While previous scenarios rose faster than observed sea level over the period 1995-2021, the trend in KNMI'23 is closer to the tide gauge observations. This is mainly the result of selecting models for ODSL as explained in section 4.2.2. The time series also show a good match between observed sea level smoothed with a 19-years running average and KNMI'23 (Fig. 4.5, right panel). The 19-year running average is a simple way to filter out the influence of the lunar nodal cycle, with a period of 18.6 years, and wind on sea level observations.

Sea-level change scenarios have been developed for three greenhouse gas emission scenarios: SSP1-2.6, SSP2-4.5 and SSP5-8.5. Projected changes in each component for the scenarios are displayed in Fig. 4.6 and the evolution of total sea level is shown in Fig. 4.7. For the target years 2050 and 2100 we show sea-level rise and rate for all three scenarios (Table 4.1).

4.3.4 Low-likelihood high impact scenarios

Despite including the latest knowledge from observations and state-of-the-art climate, glaciers and ice sheet models, the standard sea-level scenarios rely on assumptions that might not be appropriate for users who are risk averse or who would like to consider a broader range of possible futures (Haasnoot et al., 2015; Hinkel et al., 2019). Some physical mechanisms that are not yet included in standard models could accelerate the speed of sea level rise. These are for example the Marine Ice Cliff Instability (MICI) (DeConto and Pollard, 2016; DeConto et al., 2021) and more generally the influence of damage processes on the ice flow (Lhermitte et al., 2020). The effect of tides on grounding-line retreat (Ciracì et al., 2023) and the positive feedback between the ice sheets and the ocean and atmosphere (Bronselaer et al., 2018; Golledge et al., 2019). Additionally, current ice sheet models are considered to lack credibility by some glaciologists (Aschwanden et al.,

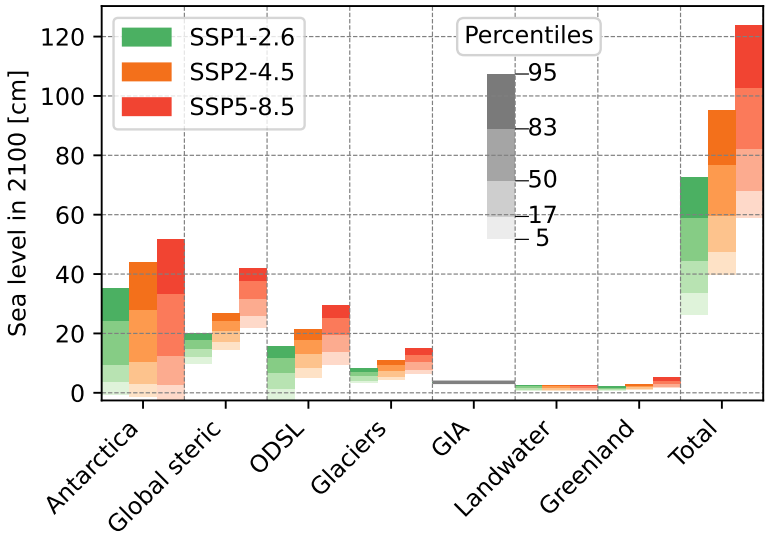

Figure 4.6: Drivers of sea-level rise along the Dutch coast in 2100 compared to 1995-2014.

2050			
	SSP1-2.6	SSP2-4.5	SSP5-8.5
Global steric	8 (5 to 10) cm	8 (6 to 11) cm	9 (6 to 12) cm
Ocean Dynamic Sea Level	7 (2 to 11) cm	7 (2 to 11) cm	8 (3 to 12) cm
Glaciers	3 (2 to 4) cm	3 (2 to 4) cm	3 (2 to 5) cm
Landwater	1 (1 to 1) cm	1 (1 to 1) cm	1 (1 to 1) cm
Greenland	1 (0 to 1) cm	1 (0 to 1) cm	1 (0 to 1) cm
Antarctica	3 (0 to 13) cm	3 (-1 to 14) cm	3 (-1 to 13) cm
GIA	2 (2 to 2) cm	2 (2 to 2) cm	2 (2 to 2) cm
Total	24 (16 to 34) cm	25 (17 to 36) cm	27 (19 to 38) cm
Rate total	5.9 (4.2 to 9.2) mm/yr	6.8 (5.0 to 10.8) mm/yr	8.2 (6.4 to 11.3) mm/yr
Rate (anomalies, rounded)	3.0 (1.0 to 6.0) mm/yr	4.0 (2.0 to 8.0) mm/yr	5.0 (4.0 to 8.0) mm/yr
2100			
Global steric	15 (10 to 20) cm	21 (14 to 27) cm	32 (22 to 42) cm
Ocean Dynamic Sea Level	7 (-2 to 16) cm	13 (5 to 21) cm	20 (9 to 30) cm
Glaciers	6 (3 to 8) cm	7 (4 to 11) cm	10 (6 to 15) cm
Landwater	2 (1 to 3) cm	2 (1 to 3) cm	2 (1 to 3) cm
Greenland	1 (1 to 2) cm	2 (1 to 3) cm	3 (2 to 5) cm
Antarctica	10 (-1 to 35) cm	10 (-1 to 44) cm	12 (-3 to 52) cm
GIA	4 (4 to 4) cm	4 (4 to 4) cm	4 (4 to 4) cm
Total	44 (26 to 73) cm	59 (40 to 95) cm	82 (59 to 124) cm
Rate total	1.5 (-0.6 to 6.4) mm/yr	6.6 (3.4 to 13.2) mm/yr	13.9 (8.9 to 26.1) mm/yr
Rate (anomalies, rounded)	-1.0 (-4.0 to 4.0) mm/yr	4.0 (0.0 to 10.0) mm/yr	11.0 (6.0 to 23.0) mm/yr

Table 4.1: Median and 5th to 95th percentile range of individual sea level contributions in 2050 and 2100 relative to 1995-2014 for the Dutch coast. The row "Rate total" is the rate of sea level independent of the reference period while the row "Rate (anomalies, rounded)" is the anomaly compared to the rate during the reference period which is 2.9 mm/yr. LLHI scenarios are not included in this table.

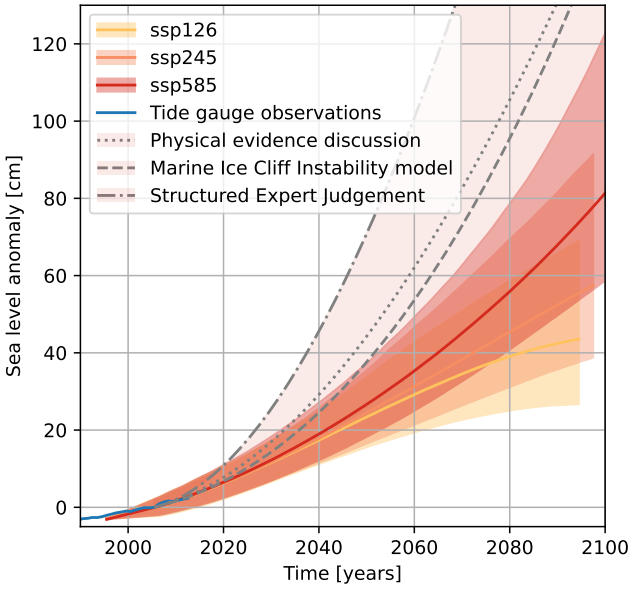

Figure 4.7: Sea-level scenarios at the Dutch coast for the SSP1-2.6, SSP2-4.5 and SSP5-8.5 emission scenarios compared to the reference period 1995-2014. The median and 5th to 95th percentile range are shown. Observed sea-level rise is the average of 6 tide gauge stations with a 19-year running average applied. Grey lines represent the low probability high impact scenarios (see section 4.3.4).

2021) and directly asking glaciologists about their estimate of future ice sheet mass loss results in higher numbers than provided by models (Bamber et al., 2019).

To include these insights into our scenarios we design three low-likelihood high impact (LLHI) scenarios shown in Fig. 4.7 and Fig. 4.8. 'Physical evidence discussion' is based on organising a discussion between climate scientists and sea level practitioners to estimate the largest physically plausible sea level rise for an RCP8.5 emission scenario (van de Wal et al., 2022). We make the assumption of perfect correlation between sea level contributors. For 'Marine Ice Cliff Instability model' we use the result the 83rd percentiles of an RCP8.5 emission scenario of a numerical model that includes the Marine Ice Cliff Instability physical mechanism for the Antarctic contribution (DeConto et al., 2021). Other contributions, e.g. thermal expansion, glaciers... , are from van de Wal et al. (2022). The 'Structured Expert Judgement' uses Antarctic and Greenland contributions obtained from the 95th percentile of a survey of the opinion of glaciologists (Bamber et al., 2019) other contributions are also from van de Wal et al. (2022). Additionally, to make the global contributions local, we compute vertical land motion and ocean dynamic sea level in the same way as the main scenarios and we use the same GRD method for the ice and land water storage. Since our LLHI scenarios are based on van de Wal et al. (2022) we only have heights for two future dates: 2100 and 2300. To obtain time series we add the constrain that scenarios should start from 0 in 2005 and start from the observed rates of sea level rise of 3 mm/yr (Stolte et al., 2023). These provide 4 constrains on the time series which we meet with a 3rd degree polynomial.

4.4 Discussion and Conclusions

4.4.1 New insights

Mass loss from the Greenland and Antarctic ice sheets is accelerating (Fox-Kemper et al., 2021; Otosaka et al., 2023). Compared to the period 1992-2001, mass loss from Greenland between 2009-2018 increased with a factor of 7; mass loss from Antarctica increased with a factor of 4. The ice sheets are expected to melt further this century. Future rate of mass loss will strongly depend on the amount of warming that is still to come (van der Linden et al., 2023; Goelzer et al., 2020). Mass loss on Greenland will be more and more determined by surface melt, while on Antarctica mass loss will depend on the amount of calving and basal melt caused by warm ocean water (Fox-Kemper et al., 2021). Due to GRD effects, Antarctic mass loss will contribute much more to sea-level rise for the Dutch coast than mass loss from Greenland. It is expected that if global warming exceeds 2 to 3°C the future of the Antarctic ice sheet becomes extremely uncertain due to the possible onset of various instability mechanisms on the ice sheet (DeConto et al., 2021). It is to be expected that floating ice shelves that act as buttresses and keep glacier flow towards the ocean on the Antarctic ice sheet relatively stable will start disappearing. When floating ice shelves disappear there is the possibility that ice cliffs arise that can collapse under their own weight, speeding up ice loss dramatically (Bassis et al., 2021). If Antarctica were to experience this type of Marine Ice Cliff Instability (MICI), it probably would start with the currently fast retreating Thwaites Glacier (Benn et al., 2022).

4.4.2 Sea-level rise up to year 2300

Sea-level rise will continue after 2100 (Fig. 4.8)). The method of the sea-level scenarios up to 2300 are described in section 4.5.3. The sea level scenarios from SSP1-2.6 and SSP5-8.5 diverge over time and from 2150 the uncertainty ranges don't overlap anymore. Sea-level rise stays below 2m in 2300 for the SSP1-2.6 scenario but could reach 6m for SSP5-8.5. This result highlights the importance of mitigation measures for keeping sea-level rise as long as possible contained within a range where adaptation is feasible and not too costly. Fig. 4.8) also shows a few different LLHI scenarios based on various assumptions. These scenarios should be interpreted as physically plausible and realistic but, based on present knowledge, highly uncertain and possibly unlikely. Our LLHI scenarios are based on SSP5-8.5 but we want to stress that for a more moderate emission

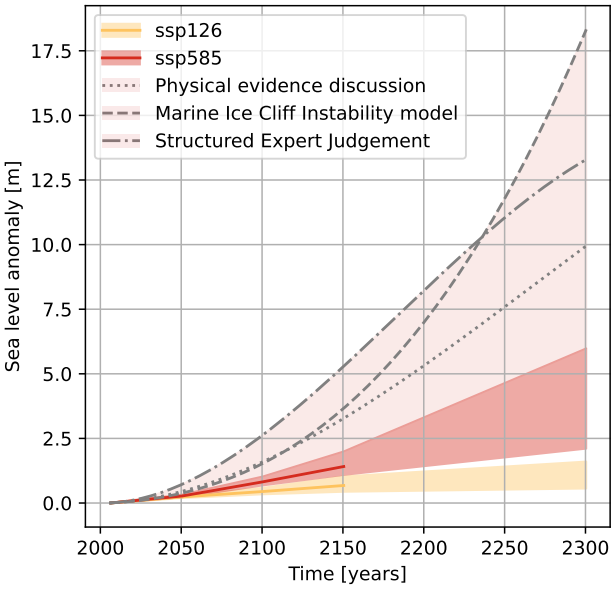

Figure 4.8: Projected future increase in sea-level at the Dutch coast until 2300 for the SSP1-2.6 and SSP5-8.5 emission scenarios. The median is only shown up to 2150, the 17th to 83rd percentile range are shown. Grey lines represent the LPHI scenarios.

scenario the processes giving rise to a LLHI scenario could also occur. In each case, even with no further temperature increase from now on, the fast retreat of the Thwaites glacier, the complete disappearance of its floating ice shelf and the onset of MICI remain realistic possibilities. Such a scenario is corroborated by geological evidence that in the Eemian (115.000-130.000 years ago), global mean temperature was ca. 1°C higher than pre-industrial values, so probably a little less warm than present, while sea-level was between 6-9 meter higher than present values.

4.4.3 Uncertainty in the time to reach a given sea-level rise

Instead of thinking about uncertainty in sea-level scenarios as an uncertainty in height for a given time we now think about an uncertainty in time when a given height will be reached (Slangen et al., 2022). We use the scenarios up to 2300 (Fig. 4.9). This provides different insights, for example while the height uncertainty at a given time is larger for an SSP5-8.5 scenario than for an SSP1-2.6, the time uncertainty to reach a given height is smaller for SSP5-8.5 compared to SSP1-2.6. For example the 17th-83th percentile uncertainty range to reach 0.5m sea-level rise under the SSP5-8.5 emission scenario is 2066-2083 while it is 2081-2229 for SSP1-2.6. The LLHI scenarios are also shown in Fig. 4.9.

4.4.4 Comparison between KNMI'14 sea level scenarios and observations

In the Netherlands sea level is monitored using 6 tide gauges distributed along the coast (Fig. 4.1 a). The monitoring report from 2019 (Baart et al., 2019) found that KNMI'14 scenarios show a larger sea level rise than observed from tide gauges up to 2017. In KNMI'23 we use data up to 2021. Since KNMI'14 did not include vertical land motion other than GRD we add a GIA contribution of 0.37 mm/yr in line with the sea-level budget. The two KNMI'14 scenarios are shown together with the yearly tide gauge data and the tide gauge data smoothed with a 19-year

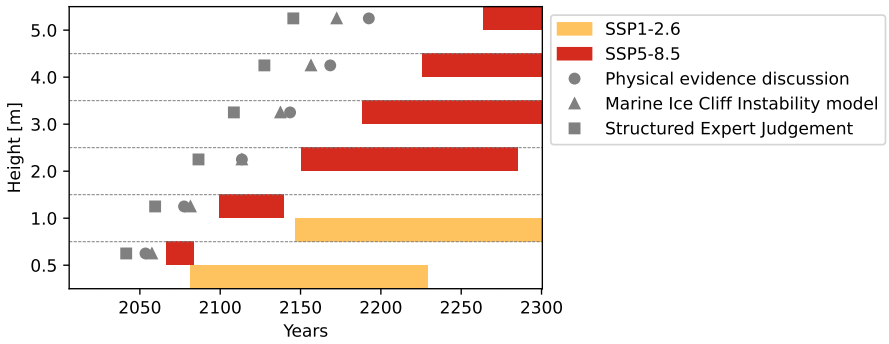

Figure 4.9: Projected time when sea level will reach a set of heights from 0.5m up to 5m along the Dutch coast for the SSP1-2.6 and SSP5-8.5 emission scenario. The scenarios up to 2300 are used. Grey markers represent the three LLHI scenarios.

running average in Fig. 4.10 (a). The 19-year running average is able to smooth the lunar nodal cycle which has a period of 18.6 years and a lot of the wind variability. Scenarios should be compared with this smoothed line because they do not include the interanual variability that is driven by local winds.

This comparison shows that observations are clearly lower than the high scenario in KNMI'14 and while they are still within the range of the low scenario: they are following the lower end of the range.

To understand the drivers of this discrepancy between the high scenario and observed sea level, we compare sea-level budgets for observations and scenarios (Fig. 4.10 b). The high scenarios overestimated two components the ocean and Greenland. This is because in that scenario the increase of GSAT was linearly interpolated between 2006 and 2050 values resulting in an overestimation of the increase at the beginning of the period. GSAT was used as a driving variable for Greenland melt, ocean thermal expansion and ODSL so those contributions were overestimated. This does not mean that the 2050 values from this scenario are also overestimated, just that the path that leads to those values is unrealistic. The scenarios of KNMI'14 were not made for short term monitoring.

This shortcoming has been repaired in KNMI'23. First, we don't base scenarios on a certain GSAT-increase (which was unrealistic in KNMI'14), but on an emission scenario. Second, we use model selection to ensure we only use models that show realistic trends over the satellite era (1993-2021). The discrepancy between observations and scenarios is much smaller now. Also, the KNMI'23 high and low scenarios diverge later in the century because greenhouse gas emissions only diverge later (Fig. 4.7).

4.4.5 Conclusions

1. There is increased evidence for sea level rise acceleration since KNMI'14, both globally and along the Dutch coast.

2. The expected values of the main projections remain stable since KNMI'14, indicating the robustness of our method for constructing sea-level scenarios.

3. The transition between observed sea level and scenarios is improved in KNMI'23 as a result of a better understanding of past sea-level changes.

4. The large uncertainty in ice sheet instability processes is explored by adding a few LLHI scenarios which indicate that sea-level rise of up to 2.5 meters in 2100 and 17.5 meters in 2300 along the Dutch coast cannot be ruled out.

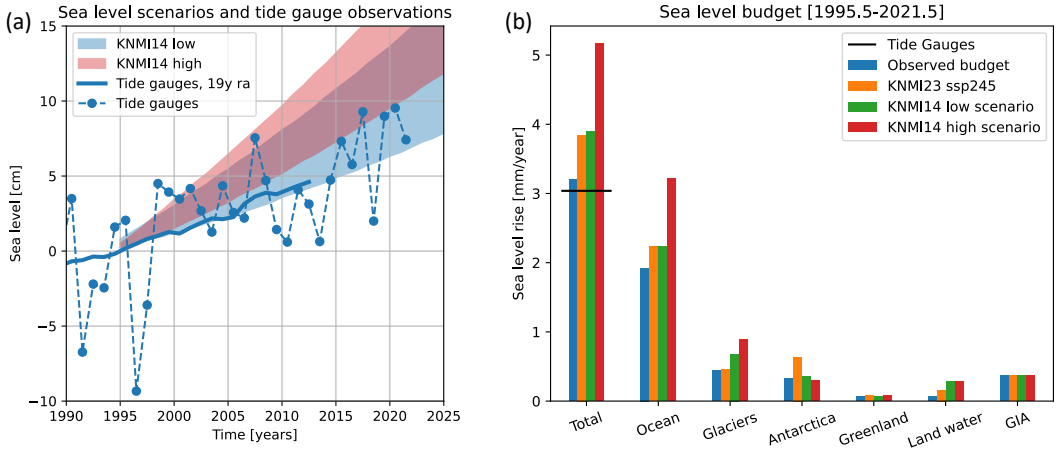

Figure 4.10: (a) KNMI'14 sea level scenarios compared to yearly averaged tide gauge data and tide gauge data smoothed with a 19-year running average. The reference period is 1986-2005. (b) Observed and modelled sea-level rate of rise for the Dutch coast over the period 1995-2021 decomposed in its various contributions. The contribution called "ocean" is the sum of global steric sea-level and ODSL changes.

4.5 Appendix: Complete method description

4.5.1 Computation of global thermosteric and ocean-dynamic sea level from CMIP6 models

Two contributors to sea level are directly available from the output of the models taking part in CMIP6. These are (1) the global-mean thermosteric sea-level change, often called thermal expansion, which is given by the CMIP variable *zostoga*, and (2) the spatially varying ocean-dynamic sea-level given by the variable *zos*. These two physical processes are separated in CMIP6 model outputs because, while *zos* is a model-variable, *zostoga* is not. This is because most climate models make the Boussinesq approximation and conserve volume rather than mass. In particular, they do not properly represent the expansion and contraction of the ocean water when its density changes. This is not a serious error and the global impact of changes in density can be computed offline, after the model simulation is completed, by integrating the global density changes (Greatbatch, 1994; Griffies and Greatbatch, 2012). Global-mean sea level is influenced by changes in both temperature (thermosteric) and salinity (halosteric). However, global-mean halosteric sea-level change is practically zero in the real ocean. Therefore global-mean steric sea-level changes are usually diagnosed using global-mean thermosteric sea-level change only. This eliminates the risk of including spurious global-mean halosteric sea-level changes (Gregory et al., 2019). Ocean dynamic sea level (ODSL) is "the local height of the sea surface above the geoid with the inverse barometer correction applied" (Gregory et al., 2019) and it is modelled directly by the climate models.

Besides running the climate models for the future with different greenhouse gas emission scenarios, each model also needs to run a long spin-up with stationary forcing, a historical experiment and a pre-industrial control (piControl) experiment. The historical experiment starts after the spin-up and covers the years 1850-2014 in CMIP6. It includes all known time-varying climate forcing for this period (e.g., anthropogenic, and volcanic aerosols and greenhouse gases, solar radiation). The future projections use the end of the historical simulations as initial conditions and run until 2100 except for a few models that run until year 2300. The piControl simulation branches out of the spin-up at the same time as the historical simulation and is at least as long

as the total duration of the historical and scenario simulations, so 250 or 450 years. Contrary to the historical simulation, piControl has no changes in the forcing.

We downloaded and post-processed the data from all available CMIP6 models. The downloading and post-processing of *zostoga* is relatively simple because since it is globally averaged it has only one dimension (e.g., time). Here are the two post-processing steps that we perform:

1. We combine the monthly data from all the models that use different time units and references into one file containing yearly averaged data using the same time variable for all models. This makes the data easy to share and analyze.

2. We use the piControl simulations of each model to remove the linear drift in the historical and future scenario simulations. This relies on the reasonable assumption that the drift is not sensitive to the external forcing (Hobbs et al., 2016). This step has a small impact on the ensemble mean projections (<1cm for *zostoga* in 2100) but it reduces the divergence between models.

The *zos* variable has three dimensions (time, latitude, longitude) which makes it more cumbersome to analyse. The first two steps of the post-processing are the same as for *zostoga*. Then, since all models discretise the ocean on different grids, the data needs to be regridded on a common grid to be able to analyse the models together. We choose a regular 1°x1° grid for that. The re-gridding is performed in a computationally efficient way by using the open-source library xESMF with a bilinear method for most models and a nearest-neighbour method for the few models for which the bilinear approach does not work. Additionally, the land/sea mask is also different between models. This creates some issues close to the coast or in almost enclosed seas like the Baltic and the Mediterranean seas where some models have outputs, but others have not. Two choices are possible for these areas, (1) spatial extrapolation of the available data to where there is no data, or (2) keep a different land/sea separation for each model. Method (2) is the usual choice (Church et al., 2013) but leads to awkward spatial discontinuities in maps of ensemble mean and standard deviation. Therefore, we chose option (1) here.

4.5.2 Sea level scenarios until 2100

To obtain estimates of total sea level change, each contributor is projected separately, and all contributors are then added together. The probabilistic sea level projection model is based on the "process-based" IPCC AR5 global projection framework Church et al., 2013. Note that AR5 used different frameworks for global and regional projections. We refer the reader to previous publications for a complete description of this framework: global probabilistic projections were described in Le Bars et al. (2017) and Le Bars (2018) while regional projections are described in Haasnoot et al. (2020). The main improvement between our approach and the one used in AR5 to make regional projections is that the dependencies between processes arising from a common dependence on GSAT are retained. This is important to have more accurate uncertainty estimates, as mentioned by Palmer et al. (2020) and Lambert et al. (2021). The trade-off for this higher accuracy is that it makes the model more complex. Some dependencies between sea-level contributors directly follow from their common dependence on GSAT but this is not the case for the dependence between GSAT and thermosteric sea level. Here we use a correlation factor of 0.4 between them (Le Bars, 2018).

In probabilistic projections based on CMIP5 a multiplication factor of 1.64 is sometimes applied to the GSAT and thermosteric sea level ensemble standard deviation to quantify the AR5 expert judgement that the model 5-95th percentiles range corresponds to the real-world likely range (a probability of 66% or more). Given that we use the temperature pathways from AR6 which are already corrected we do not apply the multiplication factor here.

Projections are obtained following a two-step process. First, global probabilistic sea level projections are computed using a Monte Carlo simulation to randomly sample each sea level contributor (X_x, see Table 1), with Surface Mass Balance (SMB) and dynamics (dyn) computed separately for the Greenland and Antarctic ice sheets:

$$X_{total}^{global} = X_{thermosteric} + X_{glaciers} + X_{Gsmb} + X_{Gdyn} + X_{Asmb} + X_{Adyn} + X_{LWS} \tag{4.1}$$

Symbol	Description
$X_{thermosteric}$	Global-mean thermosteric sea-level change
$X_{Glaciers}$	Glaciers and ice caps
X_{Gsmb}	Greenland SMB
X_{Gdyn}	Greenland dynamics (e.g. flow of ice into the ocean)
X_{Asmb}	Antarctic SMB
X_{Adyn}	Antarctic dynamics
X_{LWS}	Land water storage
X_{ODSL}	Ocean dynamic sea level
X_{GIA}	Glacial Isostatic Adjustment

To obtain regional sea level projections, each contributor is then multiplied by GRD patterns. These patterns (called F_x in the equation below) are the same as used in AR5 (Church et al., 2013; Slangen et al., 2014). Two more processes are also added: the ocean-dynamic sea-level changes, as diagnosed from the CMIP6 models (see section 4.5.1), and the vertical land motions which are assumed here to be solely composed of the Glacial Isostatic Adjustment (GIA):

$$\begin{aligned} X_{total}^{regional} = X_{thermosteric} + F_{glaciers}X_{glaciers} + F_{Gsmb}X_{Gsmb} + F_{Gdyn}X_{Gdyn} + \\ F_{Asmb}X_{Asmb} + F_{Adyn}X_{Adyn} + F_{LWS}X_{LWS} + X_{Odyn} + X_{GIA} \end{aligned} \tag{4.2}$$

Now we describe the models used for each contributor. The GSAT projections are taken from the AR6 "synthesis assessment" (4.3 in Lee et al. (2021)). They are based on the average of two methods: (1) CMIP6 projections constrained by observed past temperature and (2) an emulator based on two-layer energy balance model calibrated to have the Equilibrium Climate Sensitivity (ECS) and Transient Climate Response (TCR) assessed in AR6, chapter 7. These GSAT drive the Greenland and Antarctic SMB and glacier models.

For Greenland SMB (X_{Gsmb}), Greenland dynamics (X_{Gdyn}) and land water storage (X_{LWS}) the models are kept the same as in AR5. Greenland dynamics and land water storage contribution to sea level were assumed to be independent of temperature so the contributions do not change. However, the Greenland ice sheet contribution is temperature dependent. Therefore, as we update our temperature forcing from CMIP5 to AR6 these contributions also change compared to KNMI'14 and AR5.

Global-mean thermosteric sea level ($X_{thermosteric}$) and ODSL (X_{Odyn}) are computed from CMIP6 (section 4.5.1) with the selection process for ODSL (section 4.2.2). Only CMIP6 models that have data for both global-mean thermosteric sea level and ODSL are kept. The Antarctic dynamics is from van der Linden et al. (2023), using calibration from the quadratic formulation of basal melt in the Amundsen Sea region. For this method, all climate models and ice sheet models are considered equally probable except for CAS-ESM2-0 which we do not include in our projections because the subsurface ocean warming in this climate model is much higher than for other models. The Antarctic SMB is obtained from the same method as AR5 but with updated GSAT forcing. The glacier model is also updated according to AR6 (Fox-Kemper et al., 2021). The same parametric fit method as AR5 and KNMI'14 is used but the 7 GlacierMIP2 models are used instead of the 4 models used in AR5. The contribution from GIA is from the ICE-6G_C model (Peltier et al., 2015).

4.5.3 Sea level scenarios until 2300

The AR6 projections for year 2300 are published in Table 9.11 of AR6 (Fox-Kemper et al., 2021) for 2 scenarios SSP1-2.6 and SSP5-8.5; detailing the global mean budget in terms of thermal

expansion, Greenland, Antarctica, Glaciers and land storage for year 2300. For the LLHI High-end scenario the values for the assessment of MICI are included. In Table 9.A.7 the values for these scenarios are published for years 2050 and 2150. In AR6, assessments for 2300 values were based on a combined assessment of AR5/SROCC estimates, post-AR5/SROCC studies (Van Breedam et al., 2020), a reassessment of Aschwanden et al. (2019) for Greenland, and Structured Expert Judgment (Bamber et al., 2019). For Antarctica, the relevant post-AR5/SROCC studies are Bulthuis et al. (2019), Rodehacke et al. (2020), Lipscomb et al. (2021), complemented with LARMIP-2 estimates for mass loss in 2300 (Levermann et al., 2020), and a study including the Marine Ice Cliff Instability (DeConto et al., 2021). Final assessment of the projected ranges, combining all sources, comes from expert judgement of the lead authors in charge of the relevant sections of Chapter 9 in AR6.

Projections for 2150 are obtained by combining estimates of global mean thermal expansion from climate model simulations (FAIR) run till 2150 for the relevant SSPs, extending mass loss from glaciers and ice sheets by assuming constant rates of mass change between 2100 and 2150 and unchanged land water storage between 2100 and 2150. The ranges published in AR6 describe the likely range (17-83th percentiles). The AR6 projections are adjusted to the Dutch coast by taking into account the GRD effects. We use the AR5 GRD effects and assume that they do not change between 2100 and 2300. The ODSL contribution is assumed to stabilise after 2100 for SSP1-26 and continue to rise linearly for SSP5-85 and SSP5-85 LLHI.

4.6 Appendix: Data availability and reproducibility

4.6.1 Sea level budget

The EN.4.2.2 data were obtained from https://www.metoffice.gov.uk/hadobs/en4/ and are British Crown Copyright, Met Office, provided under a Non-Commercial Government Licence http://www.nationalarchives.gov.uk/doc/non-commercial-government-licence/version/2/.

4.6.2 Global thermosteric and ocean dynamic sea level from CMIP6

The synda library (https://prodiguer.github.io/synda/) was used to download CMIP6 data from the ESGF nodes. The code to prepare and analyze the data was written in Python and is available on GitHub under the open source GPLv3 license (https://github.com/dlebars/CMIP_SeaLevel), v1.0 was used for this work. The following open-source libraries were used: Xarray to read and write NetCDF files, xESMF (https://github.com/pangeo-data/xESMF) for the regridding, numpy and Pandas. The data file (*cmip6_zos_zostoga_v2.zip*) is available on Zenodo (10.5281/zenodo.5347691).

4.6.3 Sea level budget and projections

The code used for the sea level budget computation on which we base our bias correction was written in Python and is available on GitHub (https://github.com/dlebars/SLBudget). The code to compute the scenarios is also available on GitHub (https://github.com/dlebars/SLProj).

Chapter 5

Small-scale convective precipitation and convection permitting modeling

5.1 General overview

In this chapter changes in convective rainfall extremes are discussed. These extremes mainly occur in the summer season, roughly from May to September. However, in a warming climate rainfall also tends to become of a more convective nature in the other seasons, early spring, late autumn and even winter, which will also be covered here. By studying convective rainfall we specifically aim at relatively small-scale events, with spatial scales typically below a few hundred square km. But sometimes convective systems organise into larger so-called mesoscale convective systems, with scales up to the scale of small river catchments (like those affected by the summer flooding in 2021 in Limburg, Germany and Belgium). Convective events can also be embedded in large-scale rain structures – like in the flooding event mentioned above – so that a clear distinction between convective rain and large-scale rain is sometimes difficult to make. In winter embedded convection into large scale frontal systems could be come more frequent, which could also alter the precipitation response at larger scales. We therefore also provide some results on large scale winter precipitation change derived from the convection permitting models.

Future (convective) rainfall extremes are dependent on changes and processes at different scales: ranging from the continental scale (location of the jet stream and large-scale circulation) to the scale of low pressure systems and frontal zones, to the so-called mesoscale where the largest convective motions and cloud organisation occurs, up to even very fine scales of cloud droplets and their interactions (microphysics). Understanding and projecting future changes is therefore in essence related to a multi-scale problem where interactions at different spatial and temporal scales occur in a very complex manner. As such, there is no optimal modelling system that can provide the full answer, but we rely on output of different model types: global climate models (GCMs), regional climate models (RCMs) as well as so-called convection permitting climate models (CPMs).

In this chapter, results from different model types are combined using a simple framework to produce scenarios *consistent* with the *dry11* and *wet11* CMIP6 selection used in the main scenario construction methodology (see Chapter 2). However, these scenarios are not (fully) consistent with the generic table based on the resampling methodology for reasons discussed in this chapter. This is mostly related to the very strong increase in summer absolute humidity in the standard scenario runs, which is at the far upper end of the CMIP6 range. As part of this work we therefore performed an additional set of scenario runs with our regional climate model RACMO using a pseudo-global warming (PGW) approach. These runs can be considered as a credible alternative to the resampled scenario runs – yet, covering and focusing on different aspects and, in particular

displaying a more credible change in summer and autumn humidity values. They are used also to produce a heatwave future weather case as discussed in Chapter 7. Finally, we produce for each season tables for changes in hourly and daily extremes for local precipitation with return periods ranging from one year up to 1000 years.

Since we use different information sources from observations and models, and blend the information in a rather complex way, we provide here a general overview of the structure of this chapter, gradually zooming in on the scenario production. We start with an introduction on precipitation extremes with a focus on convective rainfall (Sec. 5.2). We continue by explaining how convective extremes are represented in climate models (Sec. 5.3), and discuss the limitations in common climate models in which convection is so-called parameterised. We also discuss the necessity of a new generation of climate models, convection permitting climate models (CPMs), and evaluate their behaviour in comparison to common convection parameterised models (Sec. 5.4). We further discuss from CMIP6 the changes to large-scale conditions – such as, absolute and relative humidity, circulation, and vertical stability – that could affect future precipitation extremes (Sec. 5.5). After this general part, we proceed more specifically with the scenario construction for small-scale rainfall extremes. We discuss the general setup (Sec. 5.6) and the available model streams with RACMO and the CPMs (Sec. 5.7 and Sec. 5.8). From these modelling streams we discuss the statistics used in the scenario construction (Sec. 5.9 and Sec. 5.10). Finally, this information is combined using a simple scaling approach to produce the scenario numbers (Sec. 5.11).

Besides the scenario tables for hourly and daily rainfall, we also looked more qualitatively to a number of other aspects of convective cloud systems. It should be noted that these aspects are still very uncertain given the present-day knowledge and modelling capacity. First, we looked at the scale of convective rain systems, and investigate potential increases in the size of convective systems. We also briefly looked at a number of other weather phenomena related to convective clouds: wind gusts, hail and lightning.

In this chapter we do not consider the influence of North Sea on coastal precipitation (Attema and Lenderink, 2014), as well as the influence of cities on extreme rainfall (Daniels et al., 2016). The CPM simulations are too short (with 10 years typically) to distinguish response patterns at such regional scales. Coastal precipitation changes also rely on detailed modelling of the North Sea, which is at present not modelled sufficiently in the CPMs.

5.2 Introduction rainfall types and processes

Rainfall can be distinguished into three main types: stratiform rain, convective rain and topographically enhanced rain (Poujol et al., 2020). All rain types involve an upward movement of air, yet the mechanism of the upward motions is different. In stratiform rain air is lifted in frontal zones, in convective rain air rises due to vertical instabilities of the atmosphere and in topographically enhanced rain air is lifted due to orography. When the air is moist enough – and as the air cools during upward motions due to the lower pressure and resulting (adiabatic) expansion – this leads to condensation of water vapour into cloud droplets and eventually rain when the cloud is deep enough.

Stratiform rain mostly occurs in frontal systems associated with low pressure systems. Fronts are large synoptic-scale structures at the interface between warm and cold air masses. Usually, a low pressure system is associated with a warm front, where cooler air masses are replaced by warm air, and a cold front with cooler air masses entering. Fronts usually span 500-1000 km (or more) in length and are approximately 100-200 km width. Since The Netherlands is a flat country topographic rain is generally not very important, although the influence of the hills in southern Limburg can be seen in the rainfall climatology.

In this chapter our focus is on convective rainfall, which is caused by vertical instabilities of the atmosphere. When the upper air is cold and the surface is warm the atmosphere can become unstable and warm surface air masses start to rise (and cooler air from aloft start to sink). This turbulent process is called convection. In clouds this mechanism is enhanced by latent heating. Latent heat is released when water vapour condenses into cloud droplets, and to a lesser extent

when rain or cloud droplets freeze into ice or snow. These processes causes the cloud air to become lighter – more buoyant – as compared the cloud environment and therefore result in further and stronger rising motions.

Outside and below a cloud the reverse processes may occur leading to strong downward motions. When rain falls outside or below a cloud it starts to evaporate in the unsaturated air. Evaporation leads to cooling, which induces downward motions. If this process is strong enough this leads to cold air masses moving downwards at substantial speed. The strength of these downward motions can be further enhanced by the weight of rain droplets. These cold downward air masses hit the surface and form so-called cold pools which start to spread horizontally. At the edge of cold pools often so-called gust fronts develop. These fronts can be associated with substantial wind gusts, potentially leading to severe damage. When a shower moves in, these cold pools can be often sensed well before the rainfall occurs; the wind starts to blow and the temperature drops by several degrees, in some cases by even 10 degrees or more.

Besides causing wind gusts, cold pools also play a crucial role in triggering of new convective cells and the organisation of smaller convective rain cells into bigger convective systems. At the cold pool gust front air moves upward, triggering new cells and converging moisture into new cloud systems. This process is particularly strong where different gust fronts collide. In the end, this mechanism leads to bigger and more organised convective systems (Lochbihler et al., 2021; Fuglestvedt and Haerter, 2020).

Convective rain dominates the extremes at smaller scales in the summer half year, roughly from May to September. But even outside this period convective rain may lead to high rainfall intensities. The warming of the atmosphere leads to more vertical instability due to enhanced latent heat release associated with higher humidity, also in the winter period, and therefore leads to more potential for convective rain systems (Chan et al., 2020; Berthou et al., 2022). Even more so, increases in convective rain could potentially give larger changes in winter precipitation than anticipated from common climate models (Kendon et al., 2020).

5.3 Convection in climate models

Common climate models have a rather simple prescription of convective processes. These models use a hydrostatic approximation of atmospheric motions. This allows them to run efficiently at computational grids of ∼10 km and coarser. The effective resolution of the resolved atmospheric phenomena is usually lower than the spacing of the numerical grid, typically 3-6 grid points wide. The common resolution of global climate models is at present 100-200 km, whereas regional climate model typically have a 10-25 km resolution. The RACMO runs used in the present scenarios have 12 km resolution. The coarseness of the grid, and the hydrostatic assumption applied, does not allow a realistic modelling of the atmospheric motions in a convective rain system.

Instead of resolving convective motions, these climate models typically use a simple prescription of the effect of convective processes in terms of resolved variables at larger scales. These prescriptions are called parametrizations. Convective parametrizations are usually based on simple physical concepts of the convective cloud processes – a simple cloud model – with a number of parameters that are usually estimated from very high resolution modelling, observations and tuning and evaluating the model in a weather prediction mode. This is a reasonable successful strategy, in many circumstances leading to good results in particular at larger spatial and temporal scales where rainfall is still dominated by the resolved atmospheric motions.

However, in climate models these convective parametrizations are one of the major sources of uncertainties (O'Gorman, 2012). This is in particular true in cases where the convective processes and the large-scale atmospheric flow interact, such as in the tropical convergence zone. It is also known that in humid conditions latent heat release can modify the large-scale atmospheric flow, leading to a positive feedback mechanism (Lenderink et al., 2017; Nie et al., 2018). There are many parametrizations for convection and uncertainty in the parameters, as well as structural uncertainty in how the simple model is formulated. A factor which is important in this respect is that these parametrizations are typically developed in weather prediction models from day-to-day

variability, and correlations between weather variables on the shorter time scales do not necessarily correspond well to the correlations found on climatic time scales. This implies that even though these parameterization may appear to work well in a weather context, there is no guarantee that they are reliable in a climate change context. Since parametrizations are developed to represent the *average* effect of the large-scale resolved variables on the convective processes they also do not sample individual clouds. *Convective* rain in a GCM therefore does not represent the intense rainfall in a typical convective system in the Netherlands. Therefore, results of these hydrostatic models tend to become less reliable going to smaller temporal and spatial scales.

In recent years, the advancement in computer power allows to run a new generation of climate models, running at grid-spacing between 2-5 km (Kendon et al., 2021). These models are called convection-permitting models (CPMs). In these models non-hydrostatic atmospheric dynamics and fine grid spacing allows a realistic representation of the larger scale convective dynamics. They still do not resolve small-scale convective processes, such as occurring at the interface between cloud and its environment – the reason why they are called convection-permitting instead of convection-resolving. Globally these models can only be run for a few years time due to their massive computational demands; typically they require 100 times more computational power than a typical RCM. At regional scales these models can now be run for longer periods, typically 10-30 years. This is still rather short to asses climate change effects on extreme convective rainfall, which can be partly solved by pooling information from larger areas.

Here, for the first time we can make use of the results of these innovative modelling systems. By comparison with observations, we show why they are a much more reliable source of future predictions of short duration convective rainfall extremes. To produce scenarios we analysed climate change signals from present-day and future simulations in an ensemble of seven CPM simulations.

5.4 Observations, evaluation models and scaling

Conventional parameterized regional climate models (RCMs) and the newest generation non-hydrostatic convection permitting climate models (CPMs) are evaluated against hourly rainfall measurement for the Netherlands. Data for the Netherlands (labelled NL) consists of the Automatic Weather Stations (AWS) at around 30-35 locations spread rather evenly over the Netherlands. We used data from 1991 to 2020. Data for the middle and southern France is from 34 stations located below 400 m height in the central and southern part of France. This data, labelled SFR-cent, has been analysed by MeteoFrance (Erwan Brisson) and appropriate derived statistics have been provided to KNMI (Geert Lenderink). We are in particular interested in southern France as its climate is characterised by higher temperatures and lower relative humidity, which could be representative for future climate conditions in the Netherlands. We note that this data excludes stations close to the Mediterranean Sea, which are affected by extremes mainly occurring in autumn, and very dry summers and which are considered not to be representative for our future climate.

Here we take the summer half year, May to October, to get stable statistics on convective extremes from the short simulations. The scenarios are however derived for the normal seasons, winter, spring, summer and autumn. The information in this section is not used directly in the scenarios production, but is provided here as background information to understand, interpreted and evaluate model behaviour in comparison with the observations.

5.4.1 Extreme hourly rainfall statistics

We first consider the plain rainfall statistics derived from the pooled observed precipitation data. Figure 5.1 shows the pooled fraction of exceedance for NL and SFR-cent. The most striking difference between the RCMs and the CPMs is the difference in inter-model spread. The CPMs are generally close to the observations for moderately strong extremes up to 30 mm hour^{-1}. For more rare extremes, there are more discrepancies between observations and models: one model

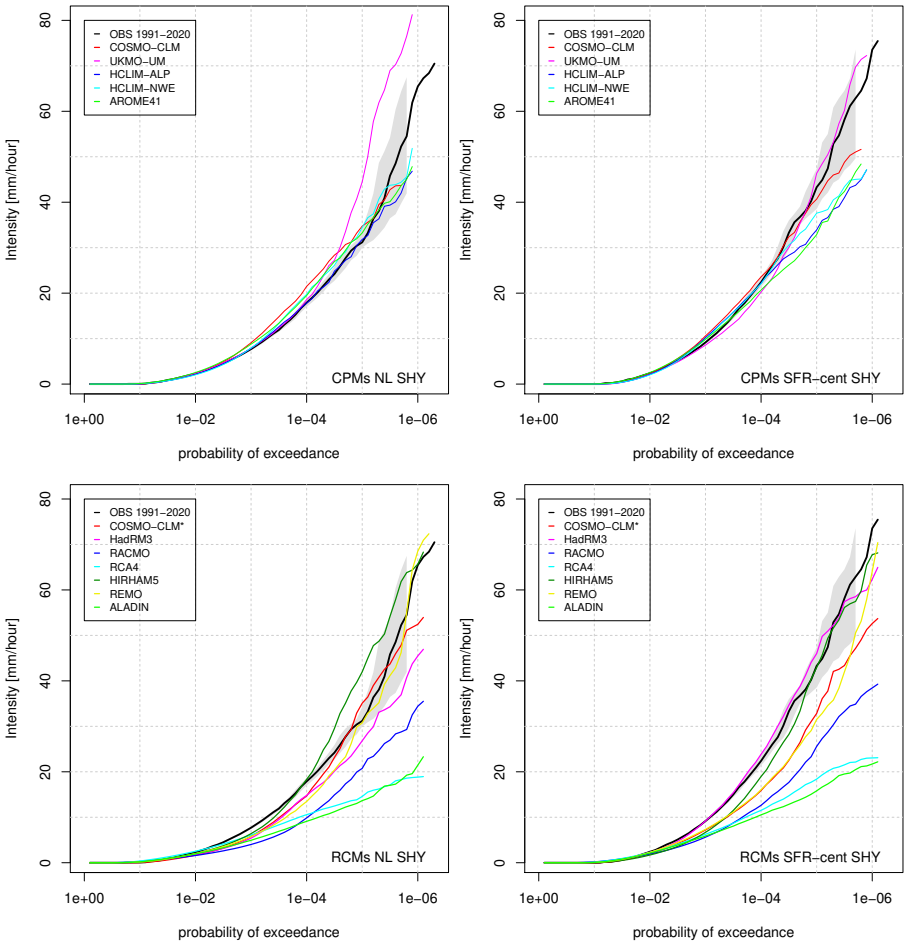

Figure 5.1: Probability of exceedance derived from the pooled data of all stations for the Netherlands and a selection of stations in the middle/southern part of France. Grey bands around the observations for 1991-2020 are 90% uncertainty ranges estimated from bootstrapping. Stations in the Netherlands (left-side plots) are the AWS stations (∼30 stations) providing hourly rainfall measurements. For France, we used stations with altitude below 400 m and located in middle and southern France, except stations close to the Mediterranean Sea (data source: Meteo France; Lenderink et al. 2023, in prep.).

over-predicts for the Netherlands, and the others under-predict for SFR-cent. Despite these small biases, some of them within the error band of observations, the CPM ensemble is clearly superior to the RCM model ensemble. Most of the RCMs strongly underestimate hourly rainfall extremes, and generally show much larger model spread.

5.4.2 Dew point temperature scaling

For hourly precipitation extremes, the most important cornerstone of the previous KNMI'14 scenarios is an analysis of scaling relations of rainfall extremes on the dew point temperature (Lenderink and Attema, 2015). In the previous scenarios these scaling relations were primarily used in a predictive context (using observed dependencies to predict future changes) whereas now they are more used to understand and evaluate model behaviour. Since the release of the previous generation scenarios in 2014, it has become clear that a straightforward direct application of observed dependencies from present-day climate variability to future changes is questionable (Fowler et al., 2021), although it appears to work in certain conditions (Lenderink et al., 2021a).

The aim of such a scaling analysis is essentially to determine how sensitive precipitation extremes are in the present-day climate to near surface absolute humidity. Dew point temperatures represent a simple measure of absolute humidity, with an increase of one degree equivalent to 6-7% more water vapor. To be more specific, the dew point temperature is the temperature at which an air parcel becomes saturated when cooled. In this analysis hourly rainfall data is paired to hourly dew point temperatures from 4 hours earlier (Lenderink and Meijgaard, 2008; Lenderink et al., 2011, 2017). For hours with rain this can be considered as a simple proxy of the atmospheric boundary layer (absolute) humidity in which the shower developed. The paired data is then classified according to the dew point temperature in bins of typically 2 degrees wide (usually taking overlapping bins with steps of 1 degree). For the data in each bin, percentiles of the rainfall distribution are then computed from only the hours with rain (wet conditional percentiles). Using data from the Netherlands – taking the data from 30-35 AWS stations within the Netherlands over the last 30 years as one data set – a very regular behavior is obtained for the highest percentiles representing the extremes of the data set. In the summer season they display a dependency of 13-14% increase per degree dew point, two times the expected Clausius-Clapeyron (CC) relation. In the following, this behavior is called 2CC scaling, whereas a dependency above the CC rate is is called super CC scaling.

For sub-hourly precipitation the same dependency of 2CC is found, even extending over a larger dew point temperature range (Fowler et al., 2021; Loriaux et al., 2013). For daily extremes, however, the dependency is lower, mostly following a CC relation. This suggests that on longer time scales rainfall is more dominated by constraints in moisture transport from larger scale atmospheric flow conditions (with no direct feedback from convective processes on the flow) forcing a CC dependency, whereas on shorter time scales dynamical feedback processes may give rise to super CC behavior due to enhancement of convective motions and cold pool related cloud organization processes (Fowler et al., 2021; Loriaux et al., 2013; Lenderink et al., 2017; Lochbihler et al., 2021; Haerter and Schlemmer, 2018). We note, that these processes and how they relate to super CC behavior are still not well understood (see aforementioned papers).

Figure 5.2 shows dew point temperature scaling results for the data of the Netherlands (NL, upper panels) and southern France (SFR-cent, lower panels). For both areas, the observations clearly show super-CC behaviour, in both areas close to the 2CC rate for the most extreme events (the 99 and 99.9th percentiles). In addition to the observations, we show results for the two KNMI regional climate models, the convection parameterized model RACMO (right) and the convection permitting model HCLIM (middle). Clearly, RACMO simulates too low hourly rainfall. Also, dew point temperature dependencies are less reliable, ranging from underestimations of the scaling rates in the low dew point temperature range to overestimations for the strongest extremes in NL for high dew point temperatures. For SFR-cent RACMO generally shows a scaling rate close to CC rate and fails to reproduce the 2CC rate in the observations (most clearly visible for the 99th percentile in blue).

HCLIM generally is much closer to the observations, satisfying the observational relation to a reasonable degree. While clearly being more reliable, HCLIM is not 'perfect' either. In general it tends to slightly overestimate the intensities – a consequence mostly of a underestimation of the frequency of rain which results in an overestimation of the percentiles conditional on rain occurrence (Schär et al., 2016). (We note that this overestimation is not found using percentiles derived from all hours including dry hours.) More importantly, it also appears that the high scaling rates in the observations for high dew points, in the range between 16-20 °C, are underpredicted in HCLIM for SFR-cent. This suggests that HCLIM has difficulties to keep a super CC behaviour for the drier conditions in SFR-cent. This behaviour is also found for one other HCLIM run for the period 2008-2019, although we note that the difference with scaling rates from the observations is still mostly within the statistical error margins.

We next consider dew point temperature scaling in an ensemble of RCM and CPM results (rather than for a single RCM and CPM). We now consider the 99th percentile, which is still *extreme* enough, while being not too much affected by statistical errors due to low sample size. Again, the most obvious difference between CPMs and RCMs is the difference in ensemble spread. While a few RCM results (in particular, the MetOffice RCM in pink) are still close to the observa-

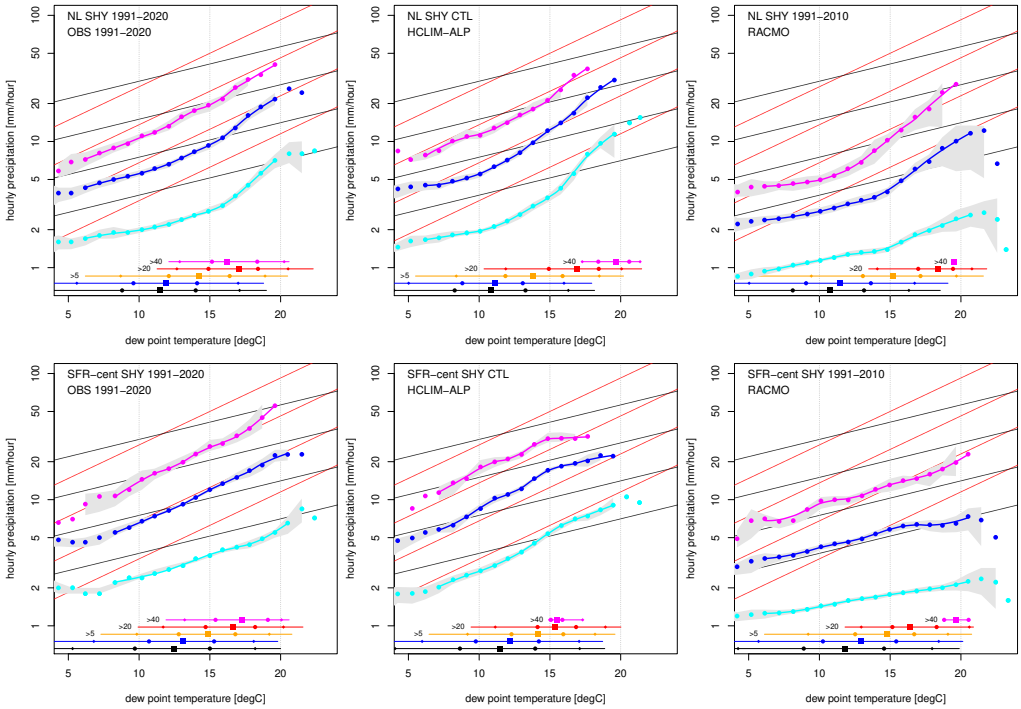

Figure 5.2: Scaling of hourly precipitation extremes on dew point temperature (T_d); upper panels for the Netherlands and lower panels for middle/southern France, with from left to right: observations, results for HCLIM (CPM) and RACMO results (RCM). Cyan, blue and magenta lines showing the 90, 99, and 99.9th percentile based on wet hours only. Dotted black and red lines show a dependency of 1 and 2 times the CC relation. Horizontal lines at the bottom show the T_d range for all hours (black), hours with rain (blue) and hours with rain exceeding 5 (orange), 20 (red) and 40 (magenta) mm, with the line showing the 1 to 99th percentile range and markers the 5, 25, 50 (square), 75, 95th percentiles. Grey bands are uncertainty estimates from a bootstrap procedure. Loess smoothed lines are plotted for a relevant T_d range (orange line, showing the 1-99th percentile range of T_d for hourly rain exceeding 5 mm), and uncertainty bands are plotted where more than 90% of the bootstrap samples contained sufficient data.

tions, as an ensemble they are clearly not reliable. In particular, selecting on rainfall events with low relative humidity, they generally fail to predict a realistic increase in rainfall extremes with dew point temperature, most strongly visible for SFR-cent (lower bottom in Fig. 5.3).

In addition to these scaling results, we also analysed absolute and relative humidity dependencies from a different angle. Instead of conditioning on dew point, we now take a complementary approach and condition the data according to the rainfall intensity. We take all hours, hours with rain, and hours with rain exceeding the 50, 90, 95, 99, 99.5, and 99.9th percentile of rain. As before, we use the same paired data with temperature as well as dew point temperature taken 4 hours prior to the precipitation. As expected, extreme rainfall events – as represented by the higher percentiles – occur on average at high(er) dew point temperatures (left panels in Fig. **??**). For wet events the average is around 12 °C dew point, increasing to around 16 °C on average for the most extreme events.

As a measure of relative humidity we use the dew point depression, the difference between the actual temperature and the dew point temperature. Each degree increase in dew point depression corresponds to a drop in relative humidity of typically 4-5 %. Generally more intense rainfall events occur on average with higher dew point depression (that is, lower relative humidity). This behaviour is seen for both NL and SFR-cent (middle and right panels in Fig. **??**). In general, the CPMs pick up this behaviour producing rainfall extremes at higher dew points and higher dew

point depression (lower relative humidity). However, while the RCMs are generally good at the dew point temperature dependency, they fail in representing the dew point depression dependency. In other words, most RCMs only produce high hourly rainfall extremes under high relative humidity. Only one model, the Metoffice HadRM3, appears to realistically reproduce the observed relations. We note that a similar result is also obtained from a scaling analysis by looking at the extreme rainfall intensities between low and high relative humidity (Lenderink et al. 2023, in prep.).

The erroneous sensitivity in RCMs to decreases in relative humidity may also affect the predicted decreases in mean summer precipitation. Because the contribution of extremes to mean precipitation is considerable in summer this could also imply that most RCMs – and likely GCMs as well since they typically use the same parameterizations – are too sensitive to decreases in relative humidity, for instance due to soil drying processes (Hohenegger et al., 2009).

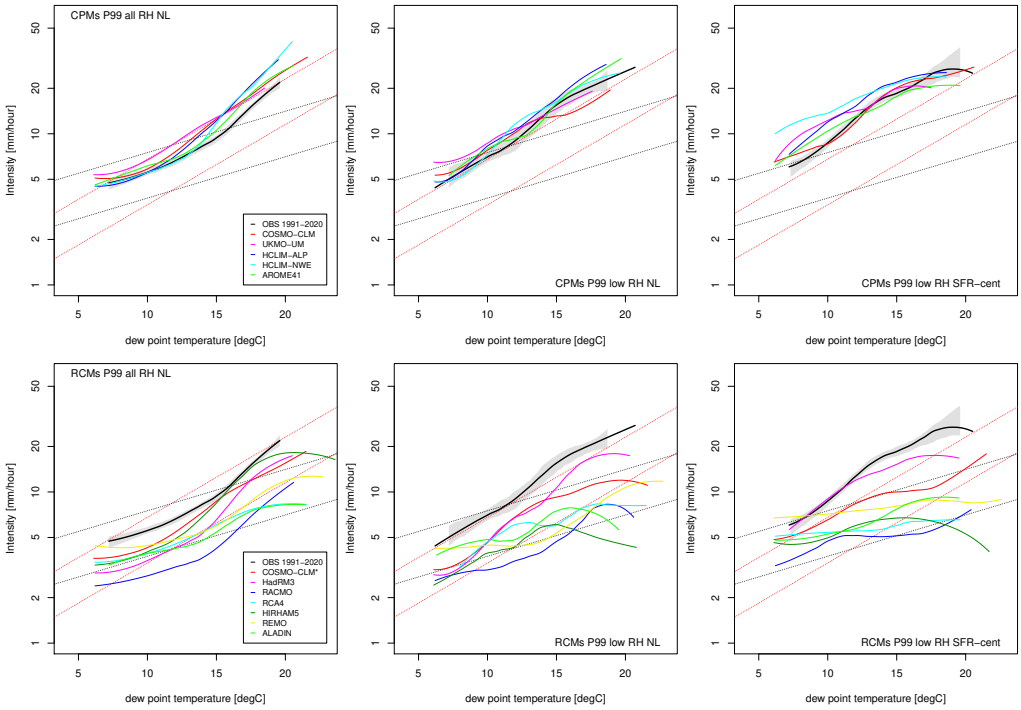

Figure 5.3: Comparing of scaling of the 99th percentile of hourly rainfall between observations and CPMs (upper panels) and observations and RCMs (lower panels). From left-to-right, the Netherlands and all relative humidity, the Netherlands only low relative humidity, and southern/middle France only low relative humidity. For low relative humidity a lower threshold of the dew point depression of 6 degrees is used.

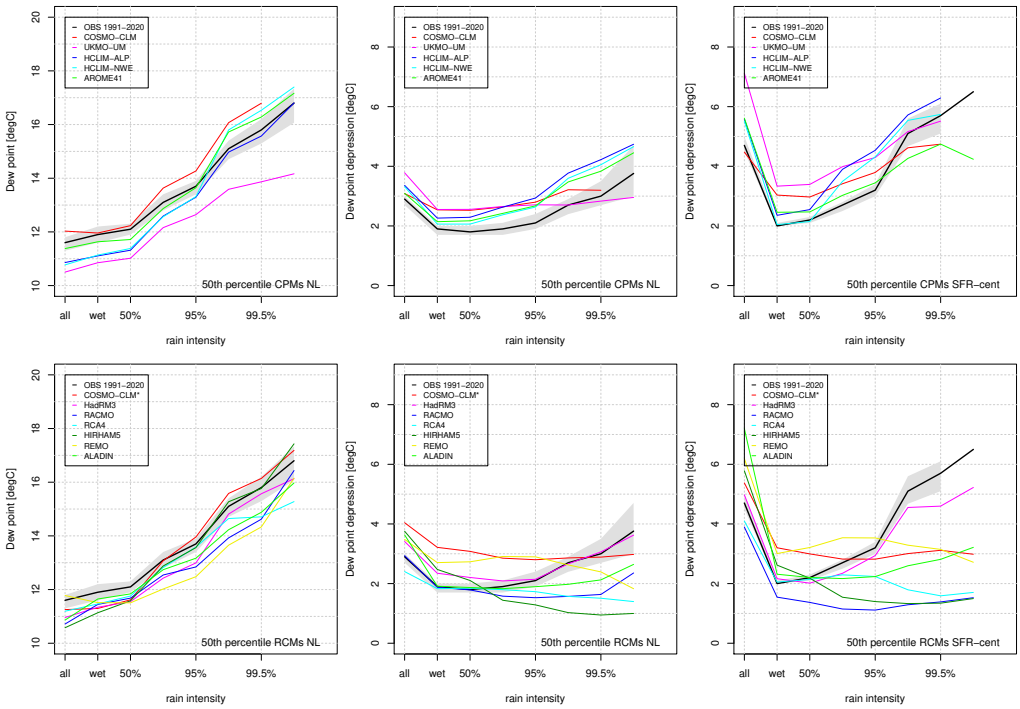

Figure 5.4: Median dew point temperature, T_d and median dew point depression, conditional on hourly rainfall intensity; for all hours (that is, climatology, including dry hours), wet hours, and those with hourly rainfall exceeding the conditional 50, 90, 95, 99, 99.5, and 99.9th percentiles. Upper panels show CPM results, lower panels show RCM results; from left to right, T_d for NL, dew point depression for NL, and dew point depression for SFR-cent. We use paired precipitation and T_d time series (T_d are 4 hours prior to rainfall).

5.5 CMIP6 changes in large-scale drivers

Future changes in atmospheric conditions at large scales affect future convective rainfall extremes at small scales. We discuss here a small number of these atmospheric variables; how they physically interact with or influence convective processes and how they change in the CMIP6 ensemble. We note that this is obviously a (large) simplification of reality, the *drivers* of changes of convective rainfall are not well known due to lack of physical understanding and complexity of the processes involved, imperfect models and insufficient model results. For instance, due to the sparseness of the CPM simulations we cannot fully disentangle the role of different atmospheric drivers. In the final method to produce the scenarios we will therefore only take the dew point temperature change (reflecting humidity change, taken from the wider sample of CMIP6 merged with information from the regional climate model simulations) and the rain frequency change (mostly set by large-scale circulation change) as input, but here we consider a number of other known drivers too: relative humidity and vertical stability.

We take the CMIP6 selection of 33 models as a benchmark, and consider the results at 4 degrees global warming from the SSP5-8.5 experiment. A high-end emission scenario is used here to get a relatively large signal-to-noise, so that we can estimate the change per degree global warming more reliably. Like in the main scenario structure, we look at changes in the selection of 11 dry trending models (*dry11*) the selection of 11 wet trending models (*wet11*) and all CMIP6 models (*all33*)[1]. Not for all CMIP6 models dew point temperature is available, and we only took the data of the models providing humidity values: 26 models total, and 8 dry and 10 wet models. Note that for simplicity we use the same abbreviations, *dry11*, *wet11*, and *all33* to refer to the subsets of CMIP6 simulations.

For practical and science reasons we cannot discuss all possible large-scale influences on convective rainfall extremes, but focus on the main thermodynamical drivers. For instance, we neglect changes in vertical wind shear which is known to affect mesoscale convective systems (Kahraman et al., 2021). We also focus on the seasonal mean changes that can be easily derived from CMIP6 model output, although the mean changes may not always reflect the changes at the time of the convective events (Attema et al., 2014). This is in particular true for dynamical aspects, since the changes in mean circulation are also composed of changes in the frequency of weather circulation patterns besides changes to the patterns themselves (Vries et al., 2022).

5.5.1 Absolute humidity: changes in dew point temperature

Rainfall extremes are expected to increase mainly because of future increases in absolute humidity of the air. The saturation humidity (the maximum absolute humidity before saturation occurs at a given temperature) of the air increases by 6-7% per degree (at near surface temperatures and pressure) following from the Clausius-Clapeyron (CC) relation, an *indisputable* physical law based on the thermodynamics of liquids and gasses. As the ratio between the absolute humidity and saturation humidity – a variable called relative humidity – is expected to show comparatively small changes with global warming because of constraints in the energy budget (Schneider et al., 2010) this implies also increases of the actual humidity of the air.

In winter with relative moist surface conditions (with no constraints on evaporation due to limited availability of soil moisture) relative humidity is expected to remain close to present-day conditions. However, in summer and over dry continental regions where available surface moisture limits evaporation, relative humidity is usually expected to decrease. At the same time, the temperature rise is also larger because of reduced evaporation. In most areas, the increased saturation humidity due to the temperature increase dominates the decrease due to relative humidity, so the actual humidity is usually increasing. For the Netherlands, situated next to the North Sea and close to the Atlantic ocean, decreases in relative humidity in summer are relatively modest.

[1]The CMIP6 model selection is based on the 4 degrees warming, and is based on yearly precipitation change, This has been done before the final selection used in the resampling procedure, and the selection of models is therefore not identical to those in Chapter 2; see section 5.11

Here, we avoid the complexity of the competing effects of increases in saturation humidity (following from the temperature increase) and decreases in relative humidity (following mostly from soil moisture feedback processes) on absolute humidity by using the dew point temperature T_d. The dew point temperature expresses absolute humidity in a temperature, and is defined as the temperature at which an air parcel becomes saturated when cooled. Per definition, and close to the surface, one degree rise in dew point temperature equals 6-7% more water vapour following from the CC relation. Increases in dew point temperature are often even be more evenly distributed over the continent than increases in temperature itself (Lenderink and Attema, 2015).

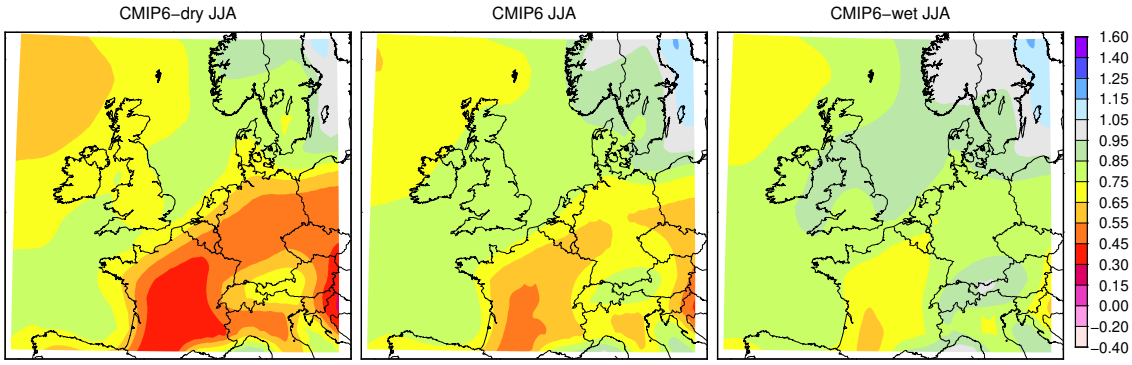

Figure 5.5: Changes in dew point normalised by global temperature change [°C/°C] in wet and dry selection of CMIP6 models.

For the Netherlands, the dew point temperature changes in CMIP6 in summer shows increases between ∼0.6 and 0.8 °C per degree of global warming, on average in the three sub-selections of CMIP6 models (Fig. 5.5). In terms of absolute humidity changes this equals to 4-6% increase per degree global warming. For more southern parts of Europe, the increases in dew point temperature are smaller, and the normalised dew point temperature change decreases (with respect to NL) to values below 0.5 °C per degree global warming, in the dry selection of models.

Considering the individual models as well as the other seasons, typical changes in dew point temperature for the Netherlands are between 0.6 and 1.0 °C per degree global warming (Fig. 5.6). There is some seasonality with in general the smallest values in spring (due to relative cold conditions over the western Atlantic ocean) and summer (due to soil drying mechanisms) and highest values in autumn and winter. In summer, models show considerable spread most likely related to soil drying feedback (see also Sec. 5.7). Model spread is in particular large for the central France point (close to Paris) with fractional dew point temperature changes between 0.2 and 1 (Fig. 5.6, lower panel).

It unfortunately also turned out that dew point temperature changes in EC-Earth3$_{\mathrm{p5}}$ are very high (pink points at right in Fig. 5.6). In winter and spring they are substantially higher than the CMIP6 *wet11* mean, but still largely within the CMIP6 envelope. However, for summer and autumn, the EC-Earth3$_{\mathrm{p5}}$ results are at the far upper end of the range, well beyond the *wet11* mean and typically two standard deviations above the CMIP6 mean response. Thus, it appears that EC-Earth3$_{\mathrm{p5}}$ is an outlier model in terms of absolute humidity changes in summer and autumn well beyond the most likely range estimated from CMIP6.

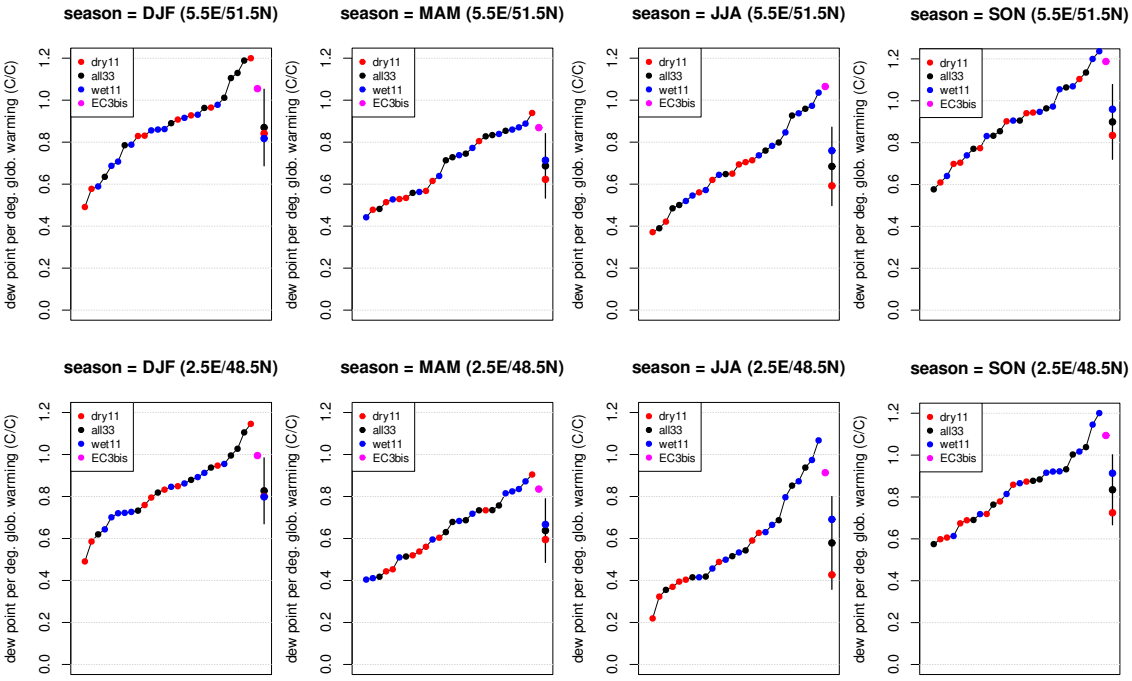

Figure 5.6: Changes in dew point temperature, T_d, normalised per degree global temperature change in all CMIP6 models. (matched warming at 4 degree global temperature rise). Shown is the distribution of all CMIP6 models providing humidity (26) with distinction in *dry11* (red) and *wet11* (blue) models. On the right of each panel, EC-Earth3 $_{\text{p5}}$ is shown (magenta) in comparison with the CMIP6 model mean, with the bar the mean $\pm$ one standard deviation, and red and blue dots the *dry11*and *wet11* mean values. Results are from latitude/longitude close to Eindhoven (upper panel) and Paris (lower panel)

5.5.2 Relative humidity: changes in dew point depression

Besides absolute humidity, changes to relative humidity could affect convective precipitation extremes as well. As discussed above, cold pools and downdrafts, which form when rain falls in unsaturated air, play an important role in the dynamics of convective rain systems. Stronger cold pools could develop with lower relative humidity as more evaporation of rain could occur (Lochbihler et al., 2021). Also lower relative humidity could be associated to larger convective inhibition leading to a stronger build up of instability before convection can be triggered (Lochbihler et al., 2021). This eventually could lead to more vigorous convection. Results from Section 5.4 also point at these mechanisms. In contrast, lower relative humidity in the cloud layer could also lead to stronger cloud erosion, leading to less deep cloud systems and smaller values of liquid water and ice loading (Fowler et al., 2021; Derbyshire et al., 2004). Also, in rather dry conditions, there may not be sufficient moisture for clouds to form; clouds form when rising air becomes saturated and the level at which this occurs is primarily dependent on the relative humidity.

Therefore, the influence of relative humidity changes on the occurrence of convective rainfall extremes is still rather uncertain; in conditions that are still relatively moist, convection may be enhanced when the relative humidity decreases, whereas in dryer conditions the reverse may be expected.

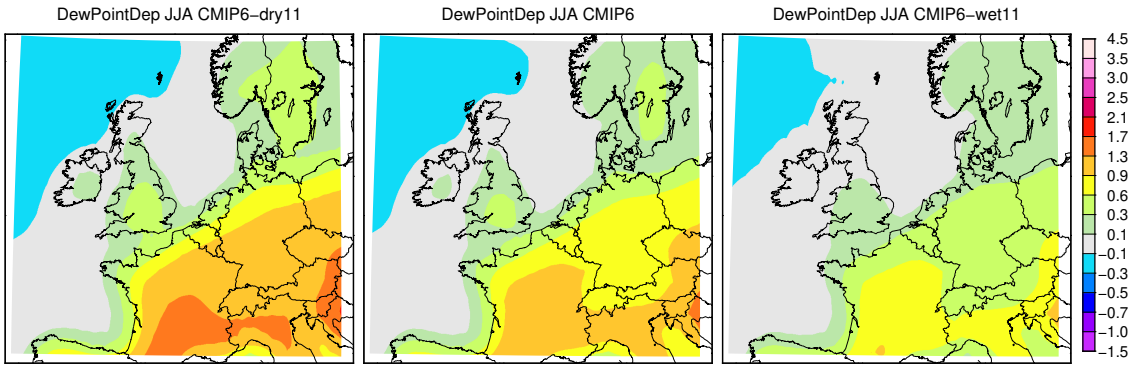

Figure 5.7: Summer changes in dew point depression normalized by global temperature change in *dry11*, *all33*, and *wet11* of CMIP6 models.

Changes in relative humidity are expressed here as a change in dew point depression (difference between the actual temperature and dew point temperature). Typically, an increase of one degree in dew point depression corresponds to 4-5% decrease in relative humidity. Again we consider here the fractional change normalised by the global temperature change.

In summer, we obtain the expected patterns in dew point depression change with small changes over the Atlantic and North sea (or even negative), whereas over the continent the dew point depression increases with warming (Fig. 5.7). Overall the pattern of changes is rather similar in the different selections of CMIP6 models. As expected, the pattern of lower relative humidity over the central and southern Europe is strongest in the *dry11* selection.

We proceed with the seasonal dependencies in the individual CMIP6 simulations for the Netherlands and central France as shown in Fig. 5.8. In winter there is a large model agreement on small changes in relative humidity in CMIP6 as anticipated over wet surfaces (Schneider et al., 2010). In spring, most of *dry11* models show a small decrease in relative humidity. In summer, this gets much more pronounced with on average a fractional increase in dew point depression of 0.5 °C, and somewhat larger in the *dry11* selection. Unsurprisingly, the response in central France is larger. In autumn the response decreases again. It is also interesting that the selection in *dry11* and *wet11* distinguishes the models rather well in summer and autumn (better than dew point temperature) with almost all *wet11* model on the left side and *dry11* models on the right side of the plot. This suggests that soil memory is a factor in explaining the separation between *dry11*

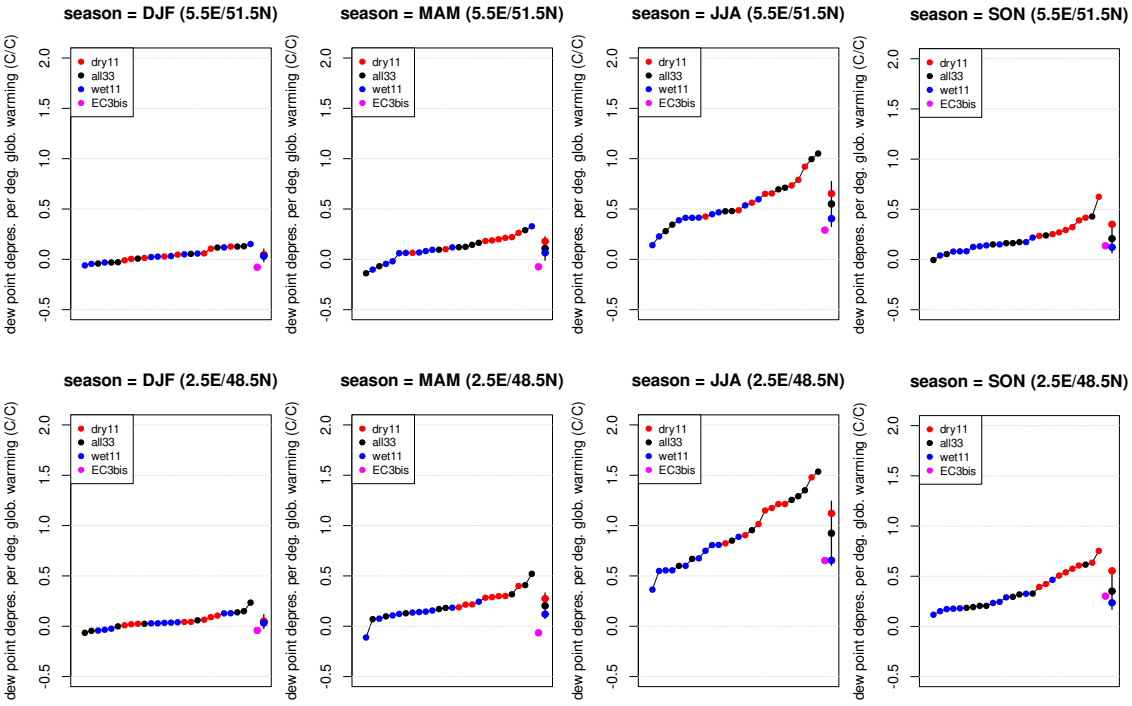

Figure 5.8: As Fig. 5.6, but now for dew point depression changes. Positive values denote decreases in relative humidity of order 4-5% per degree.

and *wet11*. This could directly result from the precipitation response, but also originate from the soil scheme and the feedback between the surface and precipitation and cloud processes.

5.5.3 Stability: temperature lapse rate change

Convective clouds develop in vertically *moist unstable* atmospheres, with relatively warm and moist surface layers and cold temperatures at higher altitudes. Latent heat release by condensation in clouds plays an important role here. This is measured by moist instability, a combination of the temperature difference between the surface layers and temperatures aloft – the temperature lapse rate measuring the stability in dry environments – and the temperature increase due to condensation of water vapour into clouds droplets. Here, we main look at the dry stability, since the moisture component is a nonlinear function of humidity which we cannot assess from seasonal mean data.

Future conditions over the Netherlands are characterised by more stable dry lapse rates. Yet, due to the higher absolute humidity of the air, latent heat release in clouds will also increase, potentially leading to stronger instabilities. The net effect of the stabilising lapse-rate changes and the destabilising effect of increase in latent heat release as measured by the moist stability is relatively small, but likely positive (that is, stronger instability) for the strongest and heaviest cloud systems as measured for instance by increases in the maximum values of convective available potential energy CAPE (Lenderink and Attema, 2015). This provides a mechanism for stronger updrafts in the most heavy showers.

The overall spatial pattern of changes in stability, in terms of temperature difference between the 300 hPa and 925 hPa pressure level, is shown in Fig. 5.9. In general, CMIP6 projects a rather robust pattern of enhanced warming at 300 hPa as compared to near the surface, mostly over the Atlantic ocean, extending to over Scandinavia. Over the Mediterranean the effect is reversed, most likely due to enhanced near surface warming which in turn is enhanced by the occurrence

of the heat low response (see below). We note that a similar pattern of lapse rate changes is also observed in re-analyses data from the past 70 years.

Zooming in on the Netherlands temperature change as a function of pressure shows enhanced warming with altitude, see Fig. 5.10 (left panel). However, to compute the dry stability change the change of pressure levels with warming should be accounted for; pressure levels move up in a warming atmosphere and cause a stabilisation of the atmosphere as moving down to the comparable height level causes additional warming (Lenderink et al., 2019b). Taking this pressure effect into account it shows that warming at high altitudes is approximately twice the surface warming (Fig. 5.10, right panel).

Therefore, in terms of the dry lapse rate the atmosphere stabilises considerably. This is however offset by enhanced latent heat release in cloud systems, in particular when the air is moist with dew point temperatures exceeding 15 °C. Also, these profiles represent the mean state of the atmosphere. Days with enhanced surface warming due to dryer soils and lower relative humidity (like those occurring in the seasonal means in southern Europe) can partly offset the enhanced warming aloft (Attema et al., 2014). It is therefore not straightforward how the mean dry lapse rate change will affect the most extreme rainfall events.

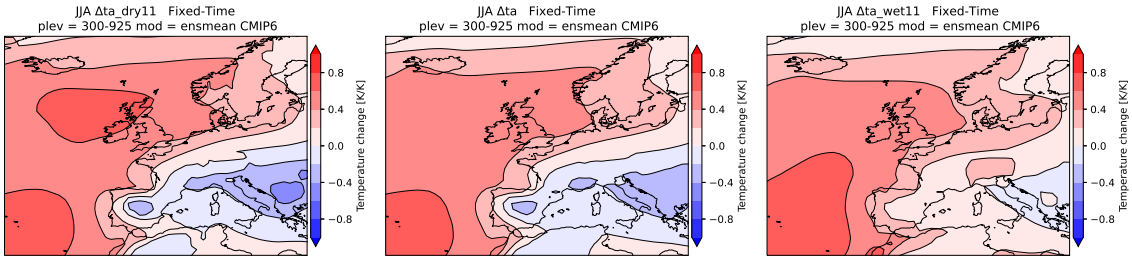

Figure 5.9: Changes in atmospheric dry stability (925 hPa temperature minus 300 hPa temperature) normalized by global temperature change in *wet11* and *dry11* selection of CMIP6 models.

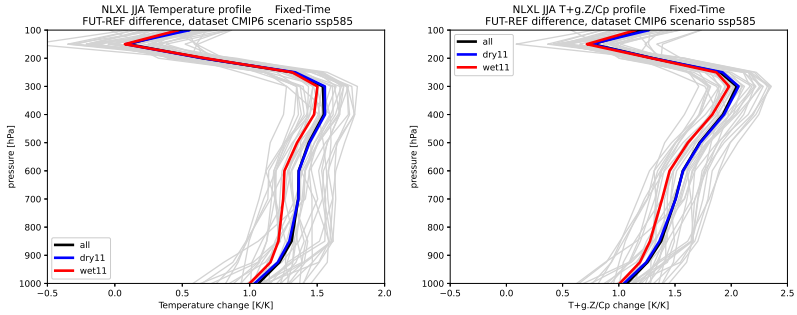

Figure 5.10: Summer changes in warming profile normalized by global temperature change in *wet11* and *dry11* selection of CMIP6 models averaged over a box enclosing the Netherlands. Left warming at constant pressure level, and right the warming taking the shift in pressure levels into account showing a larger stabilization (see main text).

5.5.4 Large-scale circulation changes

Finally, atmospheric large-scale circulation changes affect convective rain extremes in various ways. The heaviest convective extremes usually occur embedded in large-scale disturbances, typically with a frontal system moving in at the end of a warm period. These disturbances cause large-scale convergence of moisture and also destabilize the atmosphere, giving atmospheric conditions in which mesoscale or clustered convective systems can develop (Lenderink et al., 2017; Nie et al.,

2018). Reversely, the occurrence of high pressure systems typically cause more stable lapse rates and drying tendencies leading to low relative humidity. This will affect both the frequency of convective rain as well as its severity.

To account for large-scale circulation change, it would be best to distinguish between different circulation types. We did some analysis in the CPMs to investigate the response of rainfall extremes conditional on four large scale circulation clusters (Vries et al., 2022), but this turned out be rather inconclusive because of poor statistics (signal-to-noise) due to the short simulation length. There were some indications that the response of rainfall extremes in summer was relatively weak for westerly circulation types, which could be related to the stronger stabilisation of the atmosphere over the Atlantic, and relatively strong for northerly circulation types. However, these results are (far) too preliminary and uncertain to be used here. We therefore only consider the seasonal mean pressure response.

The *dry* and *wet* selections of CMIP6 models, in Figure 5.11, show very similar pressure response patterns, with a high pressure system building up west of the British Isles, and a low pressure response in the Mediterranean (see construction of generic scenarios). Most likely, this response pattern is related to the cold Atlantic temperatures and a heat low response over the Mediterranean. The response pattern in the *dry11* CMIP6 models is stronger than in the *wet11* selection. This implies that we will see a stronger reduction in rainfall frequency in summer in the *dry11* selection.

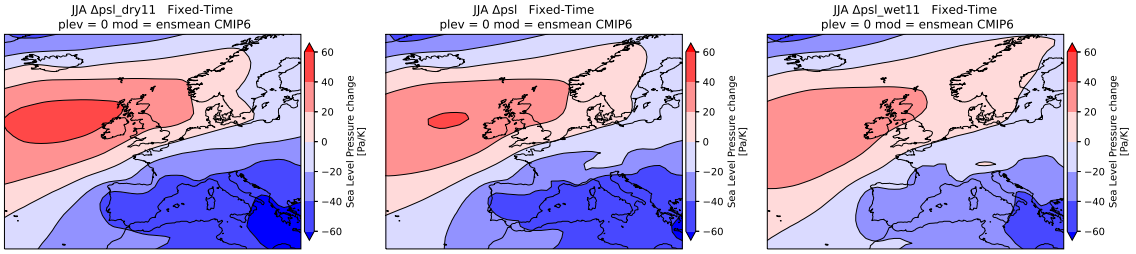

Figure 5.11: Changes in near surface pressure (normalised by global temperature change (in Pa/K) in *dry11*, *all33* and *wet11* selection of CMIP6 models. Results are obtained from SSP5-8.5 and 4 degrees global warming.

5.6 Overview scenario construction

Here, we provide a brief general overview of the scenario procedure: the available model results and the framework in which they are combined to produce the scenario numbers for extreme precipitation.

To start with, we will have a look at the output from the RACMO ensemble. As we will see, the new scenario runs are characterised by rather strong increases in daily rainfall extremes which could be traced back primarily to the very large (that is, the upper end results of the CMIP6 model range) dew point temperature increase originating from EC-Earth3$_{\text{p5}}$ (Fig 5.6). Therefore[2], we could not construct our extreme precipitation scenarios based on the humidity changes from the RACMO-EC-Earth3$_{\text{p5}}$ results. Instead we used an additional limited targeted set of simulations with RACMO using a pseudo warming (PGW) approach. These experiments also include modifications in the soil physics to improve the consistency with the CMIP6 range of projected changes in absolute and relative humidity.

The reliability of convective rainfall extremes in RACMO – and in general in parameterised regional climate models – is generally considered to be (rather) low for the reasons stated in the previous sections. In particular, this applies to changes in sub-daily rainfall extremes at local scales, but for summer it is also unclear how these limitations affect daily extremes at larger

[2]As discussed below this could not be improved significantly by resampling

scales due to the interaction between the convective rainfall processes and the resolved flow under humid conditions (Lenderink et al., 2017; Nie et al., 2018). In this respect, the CPM simulations are considered to be much more reliable. However, despite the improved physical description of convective processes in CPMs, the CPMs results are limited in terms of signal-to-noise and representativeness; they only cover a small range in large-scale change conditions (e.g. changes in SSTs and changes in frequency of high and low pressure systems, jet stream location) and only have a typical length of 10 years.

We also need to pool data from large areas because of the relatively short simulation length, thereby losing the ability to distinguish between regions. We therefore only provide change values representative for the whole of the Netherlands. This also means that the data we will use is from large area over western central Europe, which is different from the combined NL-Rhine catchment area.

Due to aforementioned limitations in data and knowledge and the need for combining different data sources in a simple framework, the main structure of the scenarios follows the procedure of previous KNMI climate scenarios (Lenderink and Attema, 2015). In this framework, changes in rainfall extremes are separated into two components: the change in the frequency of rain and the change in the intensity of rain. Changes in the intensity are in this separation conditional on the occurrence of rain. We further assume that the changes in intensity can be estimated from the (2m) dew point temperature change, since the dew point temperature is a measure of absolute humidity of the air. Changes in the intensity of rain per degree dew point temperature change are derived from the available CPM simulations, including additional evidence from the observed scaling relations discussed in Sec. 5.4. Changes in the dew point temperature are derived from a mix between the RACMO PGW experiments, the CMIP6 range as well as the CPM results. Changes in the frequency of rain also use a mix between the RACMO PGW experiment and the CPM results. Using the intensity as well as rain frequency change we transformed the present-day distribution of rainfall into a future distribution. From comparing the present-day distribution with the *futurized* distribution changes at different return levels are computed.

The procedure to account for intensity changes and frequency changes is improved from the past KNMI climate scenarios. In previous generation scenarios future rainfall time series were constructed by transforming an observed time series using a simple mapping, including leaving out or adding rain events. Changes are derived from the transformed time series, and this adds uncertainty due to the time series transformation program, including e.g. the uncertainty due to adding/removing wet events but also due to parametric choices in the method. Here, instead of constructing time series, we modified the full rainfall distribution itself. This rainfall distribution is computed from hourly and daily observations in the Netherlands, and fitted to a generalized Pareto distribution (GPD) in order to better describe the extremes. From the (transformed) distribution changes at different return levels are computed. In the past scenarios, the limited length of the transformed time series involves large fitting/extrapolation errors for events with return levels beyond 10 years. The new procedure allows to provide changes also for rarer events up to a return level of 1000 years, which could not be determined from the transformed time series used in the previous climate scenarios. We emphasise, however, there still is large inherent uncertainty on how the most extreme events change, which can only be solved by better understanding of the physical processes and longer model simulations.

5.7 RACMO runs

5.7.1 ECEARTH driven RACMO ensemble

We first analysed the present climate scenario runs with RACMO driven by EC-Earth3$_{\text{p5}}$ (hereafter shortly, RACMO-K23) in comparison to the climate scenario runs with RACMO performed for the KNMI'14 scenarios (RACMO-K14). Changes are computed for the future period 2071-2100 in comparison to the present-day period, 1991-2020. We looked at the high end RCP8.5/SSP5-8.5

scenario, reaching a 3.2 degrees global temperature rise compared to present in RACMO-K14 and 3.8 degrees in RACMO-K23.

The new scenario runs, RACMO-K23, display a very strong increase in precipitation extremes in summer. For instance, the increase of the 99th and 99.9th percentile (wet days only) of daily rainfall is 1.5 times higher (and even a bit more for the 99.9th percentile) in the new simulations when scaled with the global temperature rise as compared to the previous simulations, RACMO-K14 (Fig. 5.12). In particular, for the 99.9th percentile (approximately once every 20 years) the increase per degree global temperature rise is 11-12 %, translating in a 45 % increase at 4 degrees global warming (in agreement with the result of the 2100 Hn in the generic scenario table).

Most of the large increase in summertime daily rainfall extremes can be traced back to the very high increase in dew point temperature, which is approximately 40-50 % higher in the new scenario runs as compared to the runs used in the previous generation; see next section where we show the dew point temperature change in RACMO-K23 in comparison with the PGW runs (Fig. 5.14). When the local seasonal mean dew point temperature is used as the scaling variable, the sensitivity of the 99th percentiles is approximately the same for both ensembles (Fig. 5.13). However, for the most extreme events represented by the 99.9th percentile, the new RACMO simulations still have a stronger sensitivity to warming. For autumn results are similar with the new simulations producing approximately 50 % higher change in rainfall extremes (slightly less than for summer). For spring results of the two ensembles are much more similar, with no substantial differences between the two ensembles.

Because the high response of extremes in RACMO-K23 is related to the high dew point temperature response, and the change in dew point in these runs is very high in comparison to CMIP6, we conclude that the response in RACMO-K23 is a plausible upper boundary, but not a likely one. Since we aim to produce scenarios covering the central range of CMIP6, we investigated the possibility to improve with resampling. However, it turned out that this could not be solved by the resampling method. It turned out that resampling hardly affects absolute humidity changes in summer, which appears to concur with our finding below that we need to change the surface scheme physics to get substantial spread in dew point temperature change (see next section). Consequently, changes in absolute humidity in the resampled climate scenarios are high in comparison to CMIP6. (typical summer values in the resampling are dew point temperature increases at the same rate as the global temperature rise). In agreement, the response of rainfall extremes in the Hn scenario (high global temperature rise, wet variant) is also high, typically at the upper boundary of (or slightly above) the values derived here. In contrast, however, this is not the case for the Hd scenario scenario (high global temperature, dry variant). It appears that resampling can introduce a small bias in the summertime rainfall statistics; in order to obtain a mean precipitation decrease it favours to resample extreme rainfall days over a decrease in rainfall occurrence leading to a (somewhat) biased change in rainfall extremes and rainfall frequency change[3]. This bias offsets the high increase in humidity. So for the Hd scenario this leads to a more average result despite the high humidity increase in that scenario.

We can only speculate on the cause of the anomalous high dew point temperature changes in EC-Earth3$_{\text{p5}}$. It may well be related to the very warm response of Atlantic ocean, in particular in the summer and autumn. This response could be due to a large shortwave radiation increase in the runs over most parts of the North Atlantic ocean, but also to a shallow ocean mixed layer. At the same time the high pressure response west of Great Britain is relatively weak. This allows relative warm and moist air from the Atlantic ocean to enter the north and central part of Europe. While this is physically a plausible storyline, for summer (and autumn) we do not consider this as a likely scenario of changes in humidity and related changes in rainfall extremes. Therefore, we

[3]In most of the RCM and CPM results, the decrease in mean summer precipitation for The Netherlands is a consequence of the decrease in frequency of rain events; see e.g. Fig. 5.24 and 5.19. This has also been observed in the construction of the KNMI'06 scenarios. In the resampled results somewhat more than half of the summer response is due to the decrease in frequency of rain (0.1 mm threshold), which was also obtained in the scenarios of 2014. It appears likely that the resampling removes too many high intensity events from the rainfall distribution in order to obtain a realistic mean change, which is the results from the fact that rainfall is close to a Pareto distribution where extremes have a large influence of the means.

followed a different approach here using information from a different set of RACMO simulations using pseudo-global warming to provide a basis for our scenarios as detailed in the next section.

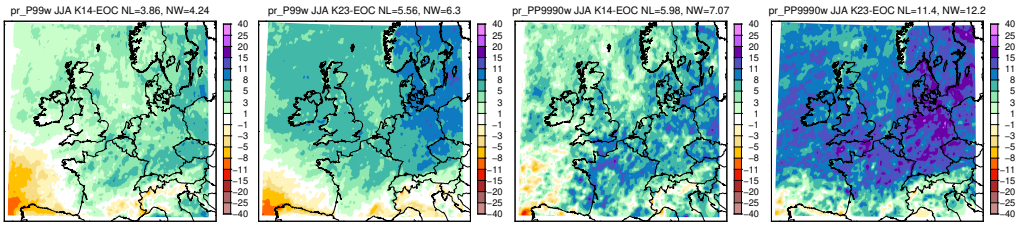

Figure 5.12: Relative change in precipitation extremes per degree global warming [%/°C]. Panel 1 and 2, the change in wet 99th percentile from RACMO-K14 and RACMO-K23, respectively. Panel 3 and 4, the wet 99.9th percentile. Averages across NL and a north western Europe (NW) are shown in header of each panel.

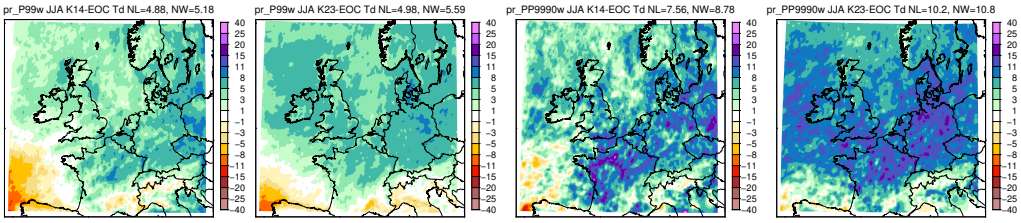

Figure 5.13: As previous figure but now the change per degree seasonal mean local 2m dew point temperature change.

5.7.2 Pseudo-global warming RACMO runs

For the reasons stated above, a set of so-called pseudo global warming (PGW) simulations with RACMO has been produced in addition to EC-Earth3$_{p5}$ driven runs. The PGW approach takes the mean change from a global climate model or a set of global climate models and imposes this as a mean perturbation at the boundaries, lateral as well as sea surface temperatures, of the regional model (Schär et al., 1996b). Typically, the control simulation now consists of a re-analysis based simulation (which is close to the historical observations in that period). This forces the control simulation close to reality with typically low biases as the large-scale forcing is essentially bias free given the quality of present-day reanalysis data. The future experiment now consists of the control experiment perturbed by the mean changes to circulation, temperature and humidity as derived from the CMIP6 ensemble. This is done on a monthly basis, with these fields interpolated smoothly in time.

The PGW approach is generally good at capturing the mean changes, such as the seasonal mean temperature and precipitation change (Brogli et al., 2019, 2021; Lenderink et al., 2022). It has also been applied successfully for simulations of future drought conditions over Europe based on the past summer of 2018 (Aalbers et al., 2023), and is applied for a heatwave case in these scenarios (Chapter 7). However, by construction the method neglects changes in the frequency of weather systems – as it basically repeats present-day weather under future conditions – and therefore does not capture all possible changes. Likewise, and partly as a consequence of this, the response could be biased. Some research showed that this is likely not a large effect, although we can not say for sure (Lenderink et al., 2022; Vries et al., 2022). A big advantage of the PGW approach is that by neglecting/reducing changes in weather variability it generally has a much better signal-to-noise ratio and potentially detects the greenhouse gas forced signal much better (Lenderink et al., 2022). Concluding, while the PGW method has pros and cons, results of PGW

experiments generally can be considered as plausible future scenarios, in particular if they are interpreted as scenarios for the forced changes.

With the PGW approach we performed a number of model experiments. With the standard RACMO model physics, we performed 3 experiments. First a control simulation for the period 1979 until 2021 has been produced using ERA5 boundary conditions. We then performed three simulations for future climate using the PGW approach. This gives three simulation pairs for present-day and future climate. Besides these, we also performed one simulation pair (control and future) using a modified soil physics scheme in order to obtain a dryer summer climate (see below). We thus arrive at 4 experiments:

- PGW-*all33*. The GCM mean change over *all33* models at 3 degrees global warming, standard RACMO physics
- PGW-*dry11*. The GCM mean change averaged across the selection of *dry11* models, standard RACMO physics
- PGW-*wet11*. The GCM mean change averaged across the selection of *wet11* models, standard RACMO physics
- PGW-*dry11-soil*. The GCM mean change from selection of *dry11* models, modified setup of the RACMO soil physics scheme.

The perturbations have been computed for the period in which the global mean temperature rise is 3 °C as compared to the reference period 1991-2020. In the PGW experiments greenhouse gas concentrations have set for the central future year from the SSP5-8.5 scenario. We did some experiments also with PGW approaches based on mean changes from different selections of dry and wet CMIP6 models, but results turned out to be rather insensitive to these choices. Only when PGW perturbations are derived from single (or perhaps few) GCM simulations, differences become substantial (Aalbers et al., 2023).

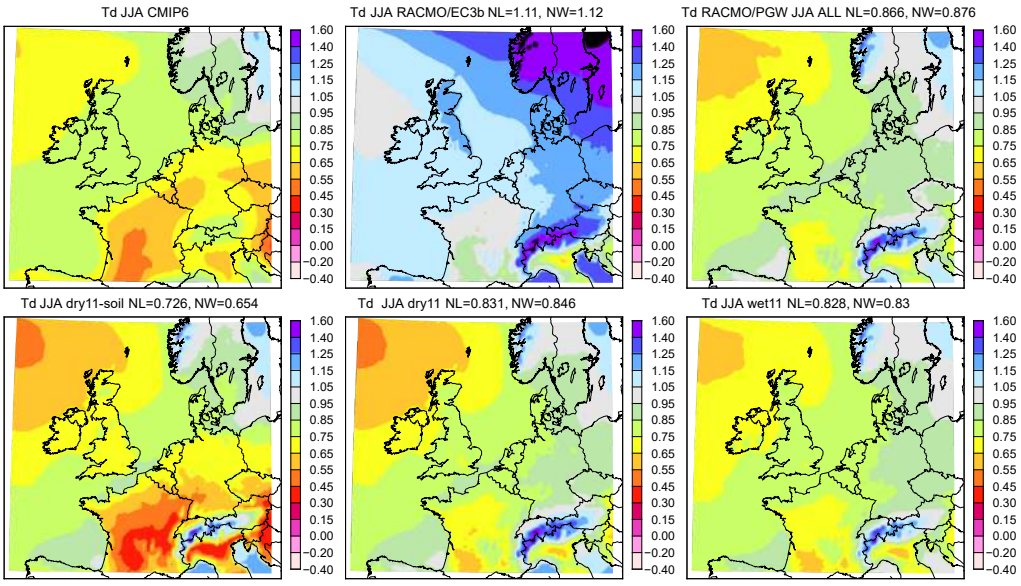

Figure 5.14: Summer (JJA) changes in dew point temperature (fraction of global temperature rise) in different set of simulations. Top panels from left to right: CMIP6 mean, middle: RACMO-ECE3bis, and right: RACMO-PGW with perturbation PGW-*all33*. Lower panels from left to right; RACMO-PGWs: PGW-*dry11-soil*, PGW-*dry11*, and PGW-*wet11*.

The dew point temperature from the PGW experiments using the standard RACMO model physics shows a change pattern much more similar to the CMIP6 pattern, although on average

still too wet – a clear improvement to the EC-Earth3$_{p5}$ driven simulations (Fig. 5.14). However, it was also found that the PGW perturbations derived from the different dry and wet CMIP6 subsets did not produce any substantial difference in changes in dew point temperature (Fig. 5.14, bottom row, middle and right panel). Apparently, differences in large-scale change from the lateral boundaries are insufficient to cause substantial spread in projected dew point temperature change, and differences between dry and wet selection are more related to physical processes within the domain rather than forced from the outside.

A known important source of inter model spread in summer is the soil scheme, since available soil water has a strong influence on evaporation, and therefore directly on temperature, absolute and relative humidity, which could also feed back on to cloud processes, radiation and rainfall. Therefore, and after some short tuning experiments where we modified a number of parameters in the soil scheme, we repeated the *dry11* PGW experiment with a different parameter setting in the soil scheme. We only performed this experiment for the *dry11* PGW perturbation (and control period as well) because we wanted to extend the projected range at the dry side; see results. In this experiment, we modified two (basic) soil parameters: i) we rerouted 25% of the rain directly in fast runoff, and ii) we halved the root depth. Since we modified the physics of the model, we also had to rerun the control period. It turned out that this experiment has a relatively small impact on the model climatology for the control period, but has substantial impact on the climate change response (Fig. 5.14, bottom row left panel).

The dew point temperature depression, as a measure of near surface relative humidity, shows the typical pattern over Europe with the increase in dew point depression in southern Europe corresponding to a decrease in relative humidity (typically one degree dew point depression is equivalent to a 4-5 % change in relative humidity). In this case, however, the difference between RACMO-K23 and the RACMO PGW runs is only marginal, and likewise the sensitivity to the PGW boundary condition. All runs have also lower changes (less drying) than the CMIP6 model mean. Relative humidity therefore appears primarily controlled by the RACMO physics, with only weak influences from the boundaries. Only the simulation with modified soil scheme shows a more strong drying pattern in southern Europe (compared to the *dry11* CMIP6 model mean in Fig. 5.7).

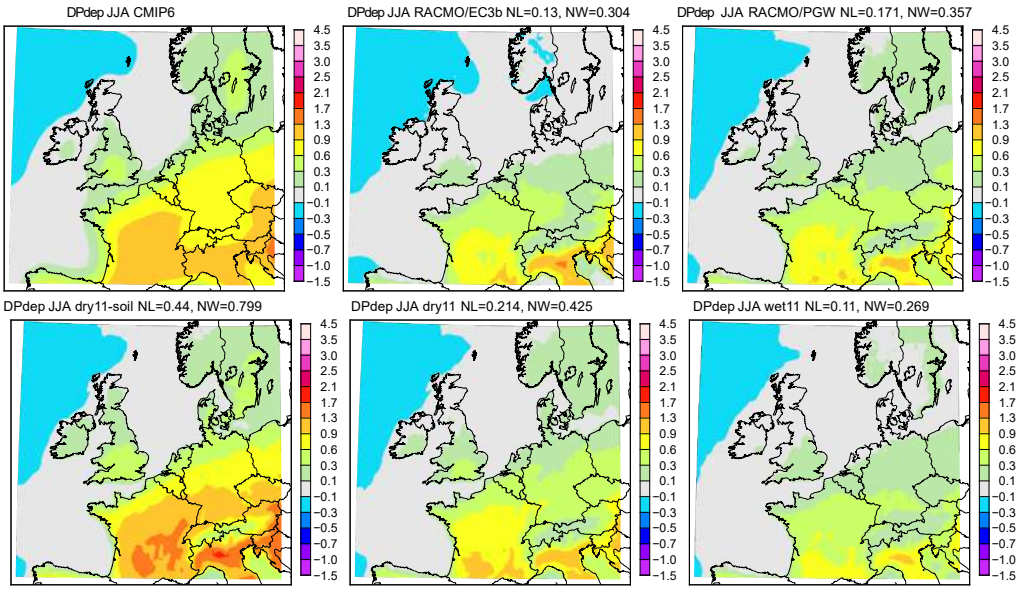

Figure 5.15: As previous figure, but now for dew point temperature depression (a measure of relative humidity)

The mean summer (JJA) precipitation change in the PGW experiment shows a very similar response pattern to the EC-Earth3$_{p5}$ RACMO ensemble, RACMO-K23. (Fig. 5.16), with over

larger areas very similar sensitivities to global warming (e.g. averages across NWEUR (north western Europe), -2.2 versus -2.9% per degree global warming). However, looking in detail to NL differences are more substantial (-1.2 versus -3.9% per degree). The latter difference is outside the range that can be forced from the *dry11* and *wet11* CMIP6 boundary conditions. It is also noted that the RACMO experiment projects smaller drying trends over the Netherlands and Germany, and greater increases in precipitation over southern Scandinavia. This could be due to systematic differences between regional climate models as compared to coarse resolution global models (Coppola et al., 2021). From further inspection, it looks like the PGW experiment is slightly biased towards a wet response in particular due to (slightly) higher response of rainfall extremes, which could be related to the mean stability change imposed. However, from these runs we could not quantify this effect, but in principle it can be quantified from an ensemble of PGW simulations as performed in Lenderink et al. (2022).

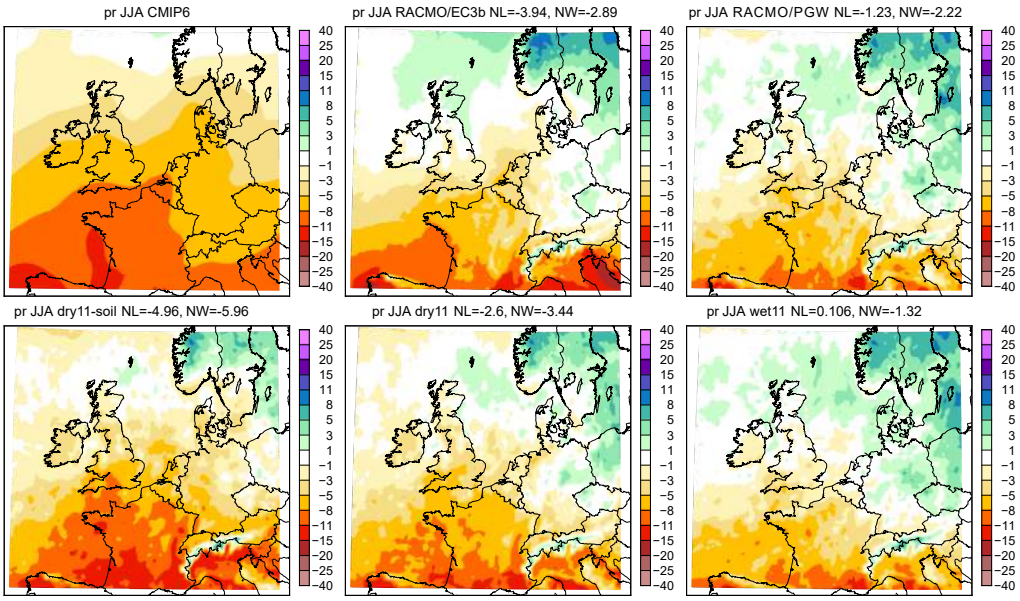

Figure 5.16: As previous figure, but now for precipitation change scaled by the global temperature rise [%/°C].

For completeness we also plotted the 2m temperature change. The PGW run captures the overall response pattern of CMIP6 (comparing top left and top right figure in Fig. 5.17). But RACMO evidently underestimates the increase in temperature over southern Europe. (From a correlation analysis between soil moisture, evaporation and temperature, we have indications that RACMO has a rather large buffering of soil wetness implying that soil moisture constraints on evaporation are generally rather weak in RACMO). The perturbed soil physics RACMO PGW run, however, leads to a much higher temperature response over southern Europe. Results for the 99th percentile of daily temperature (not shown here) display similar differences between the different PGW runs: the largest difference between the PGW-*dry11-soil* ($\sim$ 2 times global temperature) and PGW-*wet11* runs ($\sim$ 1.5 times global temperature), with the PGW-*dry11* sitting in the middle, suggesting that differences in temperature response are approximately equally explained by large-scale forcing and internal regional climate model physics; see also Chapter 7. Finally, RACMO-K23 has a very strong temperature response over northern Europe, which appears one of the main reasons for the high dew point temperature response (as over wet a surface the change in relative humidity is small; see response in dew point depression close to zero in Fig. 5.14).

In summary, the PGW runs show credible scenarios for future changes of many variables. By combining the uncertainty in large-scale conditions (represented by the *wet11* and *dry11* PGW perturbation derived from CMIP6) with modifications in the soil scheme a rather large range in

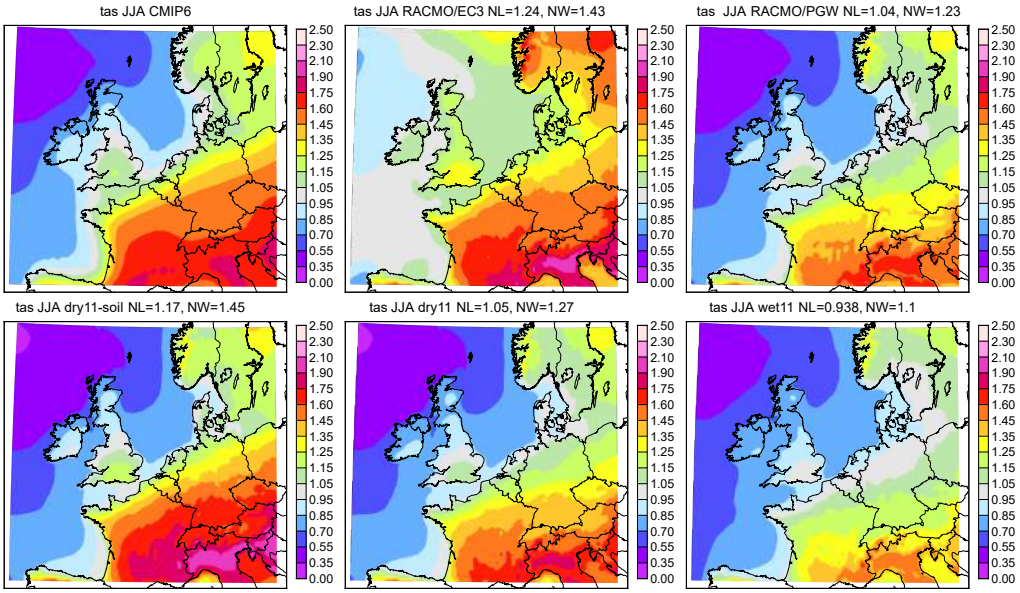

Figure 5.17: As previous figure, but now for temperature change

summer conditions can be constructed. For absolute humidity changes (dew point) this range is much larger than the range obtained by resampling, and is in much better agreement with the CMIP6 spread.

However, we also note that the large decrease in mean summer precipitation in the CMIP6 projections over the Netherlands is not captured in the PGW runs; the combined effect of soil scheme modifications and the *dry11* PGW perturbation only reaches a ∼20% decrease in the H*d* scenario for 2100 (when extrapolated to the 4 degrees global warming level of that scenario). This is where the range of the PGW runs falls short of the range produced by the resampling method, which appears to be more effective in reducing means summer precipitation reflecting the lower end of the CMIP6 response. It is beyond the scope of the work here to establish whether this is realistic or not. We noted e.g. that despite the fact that RACMO is a hydrostatic model, it still produces dynamical features mimicking organised convective systems (possibly related to the stronger than observed dew point temperature dependency for the most extreme events and high dew points in Fig. 5.2, top right figure). These convective systems could be response for a relatively wet future climate in comparison to the coarser resolution GCMs. Thus, the more muted response may well be related to systematic differences between the RCMs and the GCMs (Coppola et al., 2021). This could for instance be due to the better representation of convective rain processes in RCMs as compared to GCMs.

5.8 Available CPM simulations and preprocessing

In recent years results from a number of CPM climate simulations have become available, and these will be used here for the first time to produce scenarios for small-scale rainfall extremes for the Netherlands. Most of these runs have been performed as part of the European project EUCP. In this project a very large effort has been put on producing convective permitting model simulations for Europe. We analysed runs for western Europe, where the domain included (most of) the Netherlands. Some of the models have been run for two future periods, middle of the century as well as end of the century. From these model simulation we only took the end of the century period in order to have the largest signal to noise, noting that these simulations are rather short in time span (typically only 10 years). We note that we did not include both periods, since in that case the random fluctuations due to internal variability in the control period would be

counted twice (see also discussion in Lenderink and Attema (2015) of the regression to the mean which creates a spatial correlation in the response when the same control period is used).

	control	future	GCM	method	ΔT_{glob}	remarks
COSMO-MPI	96-05	90-99	MPI	GCM	3.7	rather wet/cold over GB
COSMO-PGW	00-09	92-01	MPI	PGW	3.7	
HCLIM-ECEARTH	95-05	89-99	ECEARTH	GCM	3.6	rather dry in summer
HCLIM-PGW	08-18	-	ECEARTH	PGW	1.5	
HCLIM-P2K	03-16[1]	-	Idealized	SUR	2.0	idealized setup, only 10 months
AROME-CM5	96-05	90-99	CM5	GCM	3.6	
UM-HadGEM	98-07	96-05	HadGEM	GCM	5.2	extreme summer: very dry

Table 5.1: Overview of CPM experiments. [1]only 10 separate months.

Six relatively long (∼10 year) simulations are available for analysis (Table 5.1). Four of these simulations use different GCM boundary conditions; they are characterized by rather large noise due to internal variability, but also include the most comprehensive set of changes. Two simulations use a pseudo global warming approach: *HCLIM-PGW* and *COSMO-PGW* applying changes in temperature, humidity and circulation. One run, *HCLIM-P2K* consisting of only 10 summer months selected on the occurrence of widespread convective rain in central Europw, has a very simple PGW approach based on vertical uniform warming and constant relative humidity and does not include any circulation change (Lenderink et al., 2019b). Thus, this run only captures humidity effects, and underestimates the stabilizing effects found in the GCMs shown in Fig. 5.10, and is therefore less representative for future conditions.

Since these runs are rather short in length, we have to pool data from large areas to obtain sufficient signal-to-noise. In this case the area over the Netherlands is too small to get reliable results. We consider mainly two domains: an area covering the Netherlands, Belgium and Luxembourg (Benelux), and a larger area north of the Alps, including large parts of Germany, the North of France, as well as the Benelux area. For this analysis region we only consider points with an altitude below 400 m height, so excluding the higher parts of southern Germany in order to exclude most of the orographic effects.

All of the CPM data have been regridded first to coarser grid, taking the mean, a sample value, as well as the max value of 5 by 5 grid points. The sample value is the middle point of the 5 by 5 grid square (for details see Lenderink et al., 2019b; Lenderink et al., 2021b). This is done for the hourly precipitation data. Here we only use the mean values over the 5 by 5 grid points, which is comparable to the resolution of RACMO (12x12 km^2). It turns out that not all CPMs provide reliable rainfall statistics at their grid scale. In particular, the UK Met Office model gives very high grid-point scale rainfall extremes. Also, in terms of dew point temperature scaling, the CPMs appear to converge better when averaging rainfall over 5 by 5 grid points.

Earlier analysis of hourly extremes in the runs performed by HCLIM have shown typical changes between one and two times the Clausius-Clapeyron relation, when scaled with the dew point temperature changes in summer (Lenderink et al., 2019b; Lenderink et al., 2021b). Analysis of other model results, however, also showed results consistent with the CC relation and no super CC behavior (Ban et al., 2020). Unfortunately, it is difficult to compare results as different studies (like the studies mentioned here) use different temperature definitions; local temperatures, regional temperature, local dew point temperatures as a well global mean temperatures have been used in various studies (Lenderink et al., 2018).

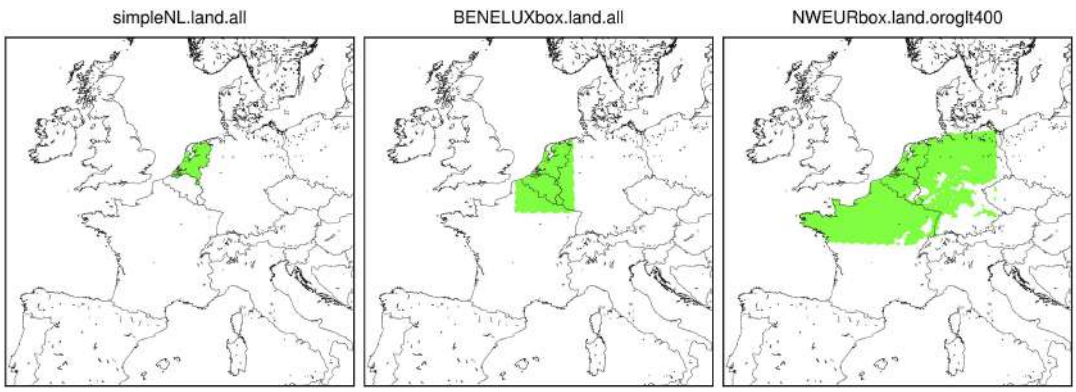

Figure 5.18: The three different analysis areas. Left is the NL area used to derive typical dew point temperature change. Middle and right are the Benelux and NWEUR area (selection below 400 m height) used to derive the rainfall extreme statistics. In general, the largest area (NWEUR) is chosen in order to increase signal-to-noise given the relatively short simulations available, yet we also inspect the results for the Benelux area to explore the representativeness of the NWEUR results for the Netherlands.

5.9 Drivers: dew point temperature and rain frequency changes

After setting the overall scene – the different modeling systems and their general outcomes – we here zoom in on the two drivers that are used in the scenario production: rain frequency changes and dew point temperature change. We first discus results from the RACMO (and partly CMIP6) and then continue with the CPM results.

5.9.1 RACMO runs and CMIP6

First, we have a closer look at the relation between mean precipitation change in summer and the change in wet-day frequency (threshold 0.1 mm day^{-1}). Earlier results obtained in the production of the KNMI scenarios in 2006 revealed that circulation change mainly affects mean precipitation through a change in rain frequency, while changes in the average intensity of rain are less affected by circulation change (Lenderink et al., 2007). We investigate whether the same relation hold for the new simulations, in which case mean precipitation change can be used as a simply proxy for the frequency change as well.

Mean precipitation and rain frequency change are shown for RACMO-K14, RACMO-K23, and PGW-*wet11* and PGW-*dry11-soil* in Fig. 5.19. The previous scenario ensemble, RACMO-K14, has the strongest drying pattern in south-western Europe, likely related to the stronger pressure response in those run (Vries et al., 2022). The new scenario runs, RACMO-K23, show a less pronounced drying signal and also stronger increases over southern Scandinavia. The PGW runs show overall a very similar change pattern in mean precipitation. For NL the PGW runs cover a mean precipitation decrease between 0 and 5 % per degree global temperature rise. For NL most of this change can indeed be attributed to a change in the frequency of rain (number of days with rain exceeding 0.1 mm). This also applies to the two ensembles as well. In general, mean precipitation change in summer is therefore primarily explained by a change in the frequency of rain, while the average intensity (average over all wet events) is unaltered. (Note, this is not a general property everywhere in the domain, but rather a property of the area close to NL.) The latter occurs through a shift of the rainfall distribution: while the intensity of weak events decreases the intensity of strong events increases. So, in a warming climate stronger events grow at the expense of weaker rainfall events (Lochbihler et al., 2019).

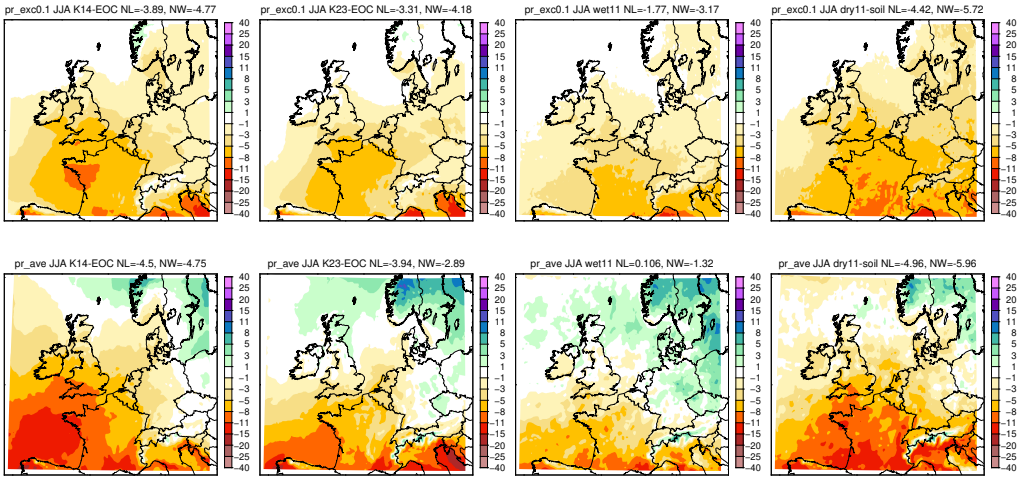

Figure 5.19: Summer (JJA) changes in frequency of rain (precipitation above 0.1 mm) (upper panels) in comparison to seasonal mean changes (lower panels). Results are scaled by the global temperature rise (% per degree). From left to right: RACMO-K14, RACMO-K23, and PGW-*wet11* and PGW-*dry11-soil*.

We compare mean dew point temperature change in the four seasons in CMIP6 with those derived in the PGW experiments. For the dry scenario, we use the CMIP6 *dry11* subset and compare the results to the PGW-*dry11-soil* experiment (Fig. 5.20), and for the wet scenario we compared the CMIP6 *wet11* subset to the PGW-*wet11* experiment (Fig. 5.21). Overall, the two PGW experiments faithfully reproduce the average of the dry11/wet11 CMIP6 models. However, in detail, the PGW runs for the dry scenario still have higher dew point temperature increase in comparison to the CMIP6 *dry11* selection in summer and autumn. Further experimenting with soil modifications in RACMO did not lead to further improvements in this respect. It could be that the relatively high future precipitation amounts in RACMO (weak precipitation decrease) prevent a drying out extending far into autumn, but it could also be related to non-parametric differences in the soil scheme (structural uncertainty).

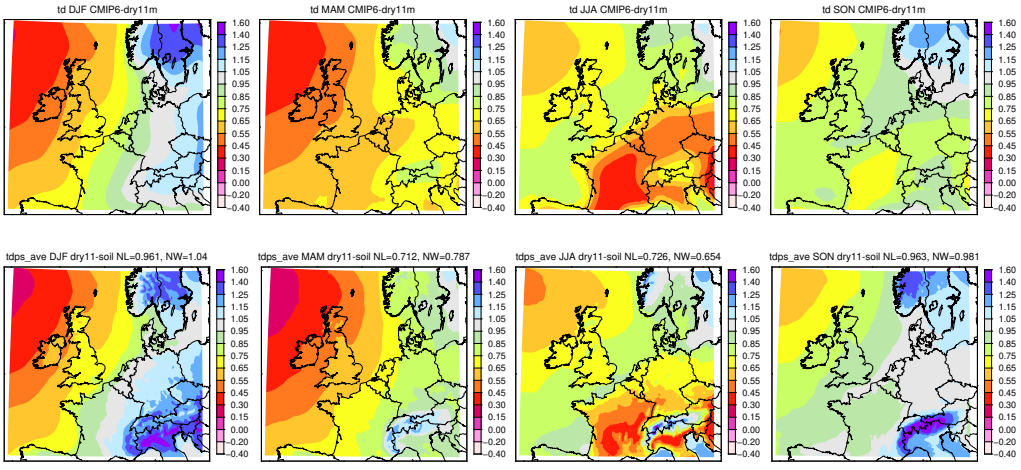

Figure 5.20: Changes in dew point temperature in the *dry11* subset of CMIP6 (upper panels, from left to right, DJF to SON) in comparison to the changes in PGW-*dry11-soil* (lower panels). Changes are given per degree global temperature rise. For the PGW experiment the averages over the subareas NL and NWEUR are given.

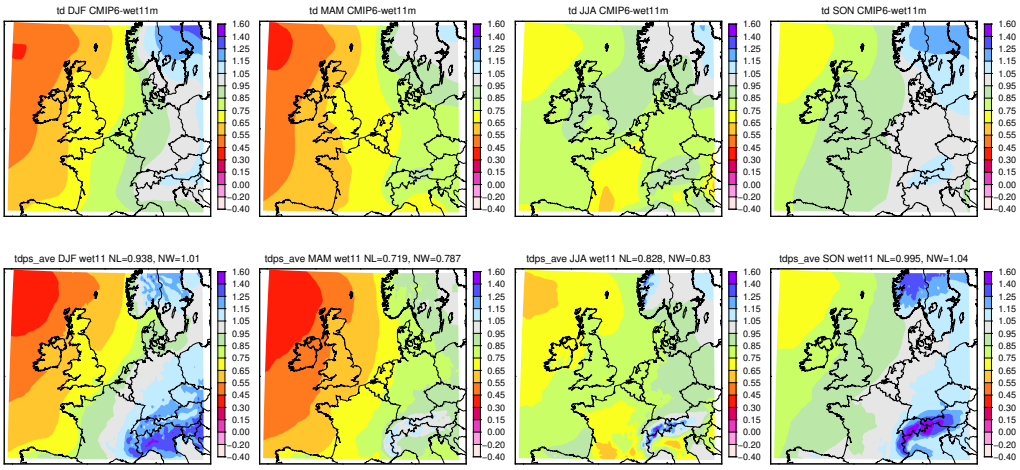

Figure 5.21: As previous figure, but now for the *wet11* subset of CMIP6 and the PGW-*wet11* experiment

Changes in the frequency of daily rainfall are shown in Fig. 5.22. Except for summer, and autumn for the dry scenario run, changes in the rain frequency are rather small. In summer, changes are between -1.8 and -4.4 % per degree global warming. If we take a mean precipitation change as a proxy for frequency change, the CMIP6 models suggest a stronger decrease. On average, they project a decrease in mean precipitation of 8-9 % per warming degree.

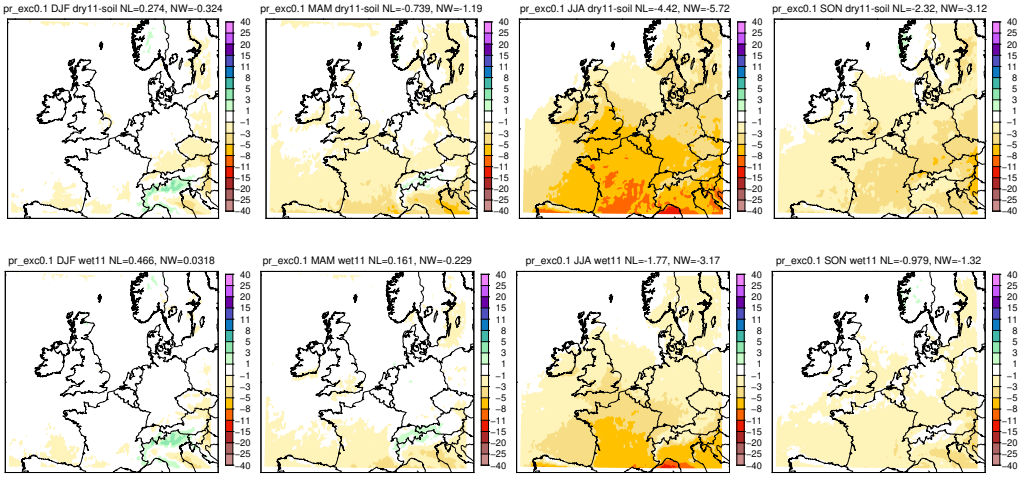

Figure 5.22: Seasonal changes in the frequency of rain in PGW-*dry11-soil* (upper panels) and PGW-*wet11* (lower panels). Shown are relative changes scaled with the global temperature change (% $^{\circ}C^{-1}$).

5.9.2 CPM runs

Next we consider the changes in dew point in the CPM simulations. We first investigate whether a seasonal mean change in dew point is sufficiently representative. For example, it could be that the changes on extreme rainfall days deviate substantially from the changes on average days. We therefore performed an analysis of changes in dew point conditional on different rainfall intensities classes. Here, we used a paired dew point rainfall time series (with dew point preceding the rainfall event) like in a scaling analysis (Section 5.4). For different intensity classes we computed the mean

dew point temperature change from the future period with respect to the control period; e.g. for all rainfall events, and those above the 90th (wet conditional) percentile.

We investigated the response for the Netherlands (area NL in Fig. 5.18) since this is the most representative for our climate, and considering the general spatial gradients with lower changes in more central and southern parts of Europe. In general, we find only small dependencies on the rainfall intensity. Only, in autumn there is a systematic decrease in dew point temperature changes with rainfall intensity. Most likely this is a seasonality effect, with the strongest extremes occurring early autumn, for which the drying response is still relatively large.

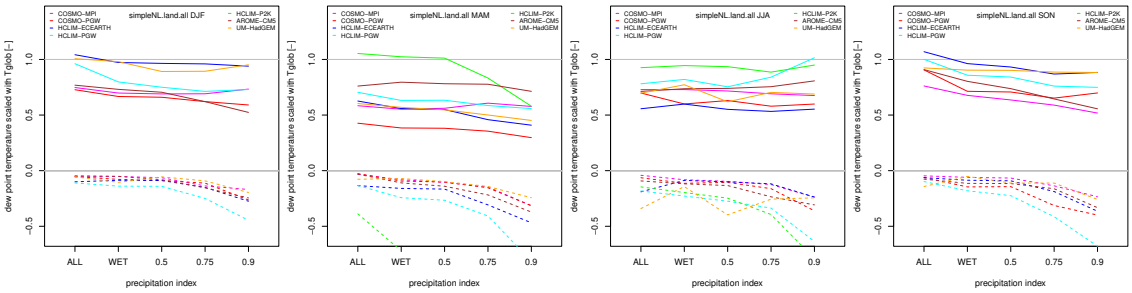

Figure 5.23: Change in dew point for NL conditional on a number of rainfall intensity classes: *ALL*, *WET* and hours with rain exceeding the 50,75, 90th percentile (wet conditional) of rain intensity. Plotted negative (dashed lines) give a measure of the spread in the response within the analysis domain (difference between 5 and 95 percentile over the area of the response). This is a measure of the spatially representativeness of the dew point temperature change. Note that *HCLIM-P2K* (green line) is not very reliable as the runs are very short, which reflected in the large spatial differences.

Given the small dependencies on intensity, and the overall model spread, we decided to use the most robust measure: the mean dew point temperature change. This is also easier as we do not have to distinguish between daily and hourly rainfall. In the previous scenarios, we took the dew point temperature change on wet days from RACMO (Lenderink and Attema, 2015). But, the CPMs results here do not provide strong evidence that this is needed. (Even more, taking dew point change conditional on rainfall in RACMO may also introduce biases due to erroneous dependency of rainfall to relative humidity, for example because the extremes in RACMO mostly occur at high relative humidity).

Typical change in dew point temperature per degree global warming in the CPMs are: for DJF 0.7-1; for MAM 0.5-0.8, for JJA, 0.6-0.8, and for SON, 0.7-1.0. These ranges correspond very well with the typical CMIP6 based results for the Eindhoven location (Fig. 5.6, upper panels). Therefore, in terms of humidity changes the CPM simulations fit well within envelope of the CMIP6 projections.

Second, we briefly looked at the changes in mean precipitation in summer versus changes in the frequency of rain. For this analysis we took the mean over the Netherlands, and found typical decreases of 4 to 8 % decrease of mean precipitation per degree global warming. Mean precipitation from the *HCLIM-P2K* only represents thermodynamic changes (without circulation and relative humidity change) and are considered less realistic. Two models fall outside of this band, with *UM-HadGEM* simulating much larger changes, and *AROME-CM5* simulating much smaller changes. We note that the response in mean precipitation in the CPMs is generally stronger than in the RACMO results. The cause of this behavior is not established, but we note here that most of the CPMs do show a dry bias in summer, possibly related to soil processes. This is also observed in the HCLIM runs used for the future weather heatwave case discussed in Chapter 7. One possible reason is that soil schemes have not yet been optimally adapted to the higher rainfall intensities in the CPMs, resulting in too much rapid runoff (Berthou et al., 2020). The drying response in *UM-HadGEM* is very strong, and is accompanied with very high temperature changes over

Europe, in central part of Europe more than 10 °C. These aspects still need further investigation, but are outside the scope of this work.

In summer, for all model simulations, except the surrogate warming *HCLIM-P2K*, mean precipitation change is close to change in frequency of daily rain. Again, this confirms that decrease in mean rainfall is mostly originating for a frequency changes, and that the mean intensity over all rainfall events is basically unchanged. The frequency of hourly events increases slightly more on average, which corresponds to a stronger increase in intensity at the hourly time scale as compared to daily.

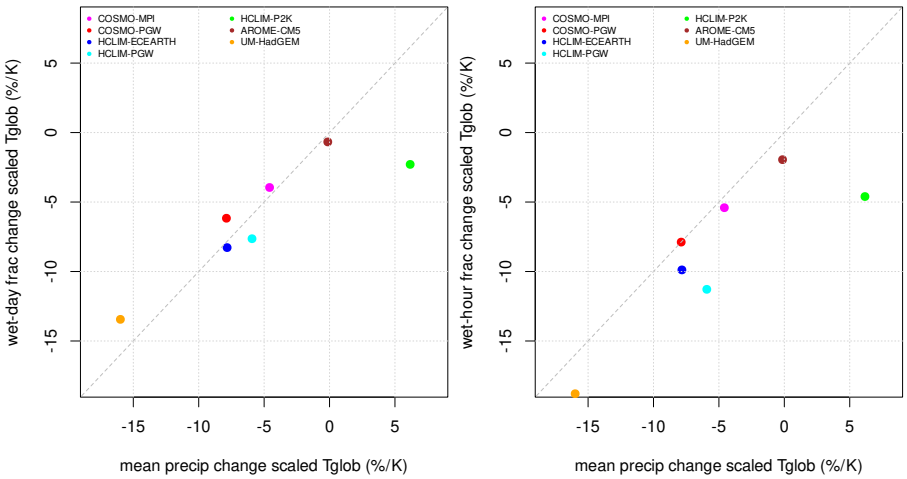

Figure 5.24: Changes in frequency of rain events against changes in mean precipitation in summer JJA for the NL area. Lefts shows changes in frequency of daily rainfall, and right the frequency of hourly rainfall. In general, frequency changes are larger for hourly rainfall (corresponding also to a larger (positive) change in the intensity of rainfall. Note that *HCLIM-P2K* (green dot) is not very reliable as the runs are very short and the experiment is idealized.

5.10 Sensitivity of rainfall extremes to dew point temperature

We now use the CPM simulations to establish relations between the rise in dew point temperature and increases in rainfall intensity. These are called rainfall intensity sensitivities. Besides looking at the sensitivity to dew point temperature, we also considered a more simple sensitivity to global temperature to establish the robustness of the results. We emphasize here that the rainfall intensity sensitivities are established using expert judgement where we try to match multiple constraints ("lines of evidence") from different modeling streams as well as observations. Inevitably, in this process, there is some degree of subjectivity involved.

Hourly and daily precipitation data have been pooled for the analysis regions (Fig. 5.18). For each separate month, changes in hourly and daily extremes are derived by computing the changes from the pooled distribution as a function of probability of exceedance (or more precisely the fraction of exceedance obtained by assigning each hourly grid point value the same probability). We here took the conditional probability, taking only the data with precipitation above 0.1 mm (hourly or daily). Thus the relative intensity change as a function of probability of exceedance is computed (by dividing future by the control period).The response is now scaled by the monthly mean dew point temperature change or global temperature change. We used an exponential scaling here to account for the fact that absolute humidity is approximately an exponential function of dew point temperature; although we note that differences with a linear scaling are generally rather small as compared to the overall uncertainty. This gives us a rainfall intensity sensitivity to dew

point temperature (or global temperature). We also performed the analysis by taking a more representative dew point temperature change derived from day/hours with heavy rain as done in Lenderink et al., 2021b, but this gave approximately similar results and the advantage of a better connection to the extremes was offset by more noise due to a smaller sample size.

The rainfall intensity sensitivity derived for each separate month is then averaged for the months in a season. So, the summer JJA season consists of the average sensitivity across June, July and August. The averaging is done by a geometric mean to avoid a large effect from outliers, noting that a geometric mean is better suited (that is, less risk of biased result) for noisy data dealing with relative changes. We also performed that same procedure, but now for the data pooled over a season directly. For summer this gives very similar results (not shown). However, in particular for the transitional seasons, spring and autumn, this gives less reliable results as in those cases the extremes are usually dominated by only one month, in particular for the hourly extremes (May for spring, and September for autumn). Thus our averaging takes into account the seasonality of hourly extremes.

Since we are dealing with only short simulations, we have to pool data from large areas in order to obtain sufficient signal-to-noise. The basis of our scenarios is therefore the largest analysis region: NWEUR, where we only considered the grid point with altitude below 400 m (Fig. 5.18, right panel). Statistics over high altitudes appear to be different from those at lower altitudes and are therefore left out (Lenderink et al., 2019a). In addition, the NL+ area used for generic scenario is too small and contain too many high altitude grid points. We therefore aimed for a large area North of the Alps, motivating out choice for NWEUR. However, we also note that potentially there are regional differences within this area, which we cannot establish given this data set. In particular, for spring and autumn, regional differences may occur due to the influence of the North Sea. Also the presence of a high pressure system in summer over the British Isles could cause regional differences. Therefore, as an indication, we also looked at the results pooled over the BENELUX area (Fig. 5.18, middle panel)

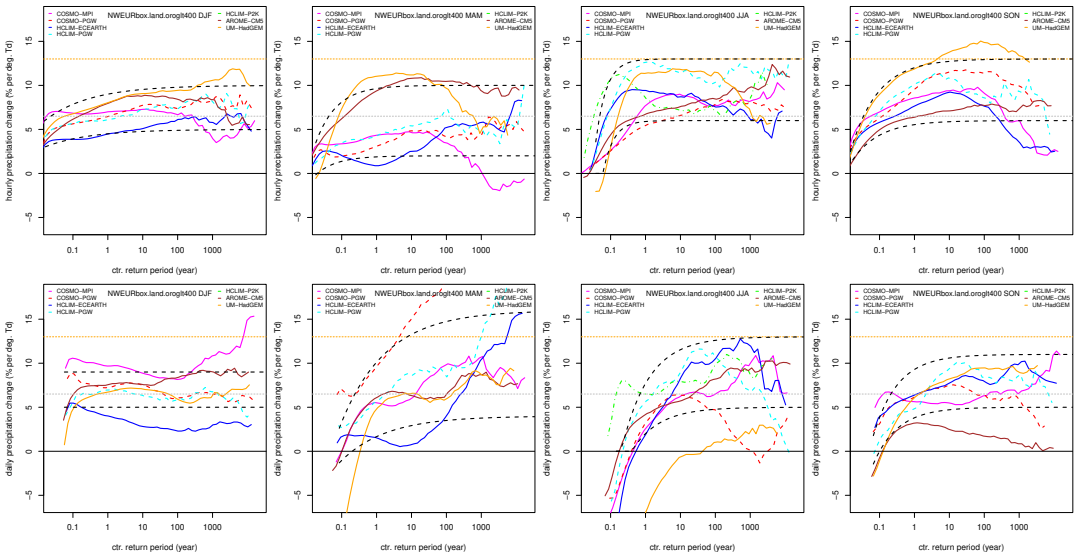

Figure 5.25: Dependencies of hourly (top) and daily (bottom) precipitation extremes on the global temperature rise T_d. Results are shown for pooled data over the NWEUR region.

Besides computing the sensitivity to dew point temperature, we also simply scaled the precipitation response with global temperature rise. This procedure is much simpler and gives equally good results as dew point temperature scaling for the runs analysed here; the ensemble spread is approximately equal, and in a few cases even smaller than when dew point temperature is used (e.g. daily extremes in spring). However, the downside is that it cannot correct for systematic

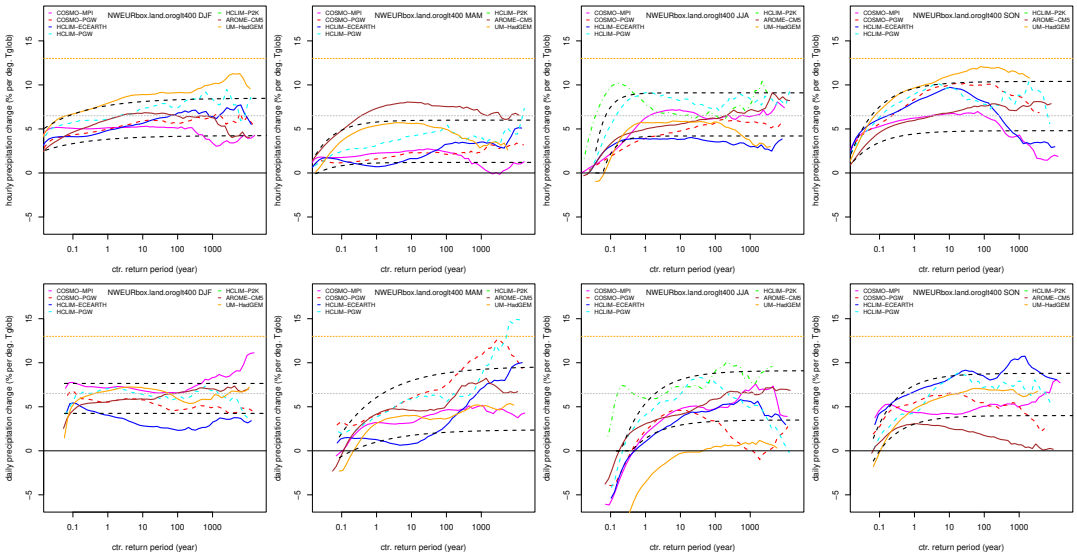

Figure 5.26: Dependencies of hourly (top) and daily (bottom) precipitation extremes on the global temperature rise T_{glob}. Results are shown for pooled data over the NWEUR region.

differences in dew point temperature change per degree global warming between the CPMs and the range we want to cover in the scenarios (range in dew point suggested by CMIP6 results). That this could be important is shown by the differences between the two RACMO ensembles, with the higher response in the new scenario runs (RACMO-K23) largely *explained* by the higher dew point temperature response. We also note here the close similarity in observed long-term variations in hourly rainfall extremes and dew point temperature variations (Lenderink and Attema, 2015). This suggests that taking dew point temperature change as a basis for the long term change is a physically justified approach.

Results for the NWEUR region are shown in Fig. 5.25 for dew point temperature and Fig. 5.26 for global mean temperature. Before discussing the CPM results in more detail, we first explain the method of "fitting" an upper and lower bound of the precipitation intensity sensitivity to these results.

Fitting of the precipitation intensity sensitivities has been done *by eye*, adjusting the parameters of the fits until the upper and lower curves reasonably represent the spread of the CPM ensemble. Given the sparseness of the data and presence of considerable random noise, but also the expert judgement that not all simulations are equally probable or consistent with the scenario assumptions, we do not think that a more objective method is appropriate. As an example, the *UM-HadGEM* simulation shows a very strong drying response in summer over central Europe with temperatures rising 10 degree and more, and very strong reductions in rainfall frequency and amounts (50 % and more). Although, this may be a plausible result, it is far outside the average of the CMIP6 based *dry11* scenario we are trying approach. We therefore gave this simulation less weight for the summer season. Also, there are a few simulations using a PGW approach that may be considered less realistic in the sense that the mean circulation and stability change imposed affects all extremes in a similar way (in particular, the uniform warming experiment *HCLIM-P2K*).

We used a simple formula as function of return period, t_{rp}, to estimate plausible ranges. The return period is based on rainfall frequency of the control period. This formula reads as:

$$\alpha(t_{rp}) = a_o f(t_{rp}) \tag{5.1}$$

with

$$f(t_{rp}) = 1 - \exp\left(-z_e \log 10(t_{rp}/t_o)\right) \tag{5.2}$$

and $z_e = 1/\log 10(t_e)$. Here t_o is the return period where f becomes zero and t_e and e-folding time scale. This formula gives approximately a gradual convergence to a constant intensity increase with a e-folding time scale. Obviously, the dependency on return period is an assumption, but in general it appears to fit the data rather well.

The parameters are fitted *by eye* to the band of model outcomes. The resulting upper and lower bounds are given in each plot by the two black dashed lines. A central estimate is also obtained by the average between upper and lower estimate. For completeness we provide the *fitting* coefficients in Table 5.2. We note also that in some cases the data hints at a stronger increase for very long return levels (and weaker for short return periods), but this is considered to lie within the upper and lower bounds of the fits. Examples of such behaviour are visible for spring daily extremes in Fig. 5.26 and daily extremes in summer for smaller Benelux region in Figs. 5.27, 5.28, yet we note that the data is far too limited to be able to make a statistical significant statement on this.

Fitting also took into account the sensitivity to global temperature rise (instead of dew point temperature). This was not done independently, but instead we used a constant factor between the two sensitivities. The proportionality factor is the typical ratio between dew point temperature rise and global temperature rise in the CPM ensemble. For instance, for summer it is 0.7 – the typical rise in dew point shown in Fig. 5.23 – implying that a 10 % sensitivity to dew point temperature corresponds to a 7 % sensitivity to the global temperature. The factors for the other seasons are in the caption of table 5.2.

Results for the NWEUR region are shown in Fig. 5.25 for dew point temperature and Fig. 5.26 for global mean temperature. For hourly rainfall we typically find sensitivities to the dew point temperature between 5% and 13% per degree. In spring, values appear lower, whereas in summer and autumn the values are higher (between one and two times the CC rate). Sensitivities to global temperature are as expected lower, since the dew point temperature rise is generally lower. They generally spread around the CC rate, with again lower values in spring. The sensitivity is surprisingly similar in winter and summer – despite the fact that rainfall is more convective in summer and we expect higher response for convective rain – as higher sensitivities to dew point temperature are partly compensated by lower changes in dew point temperature in summer. In spring and autumn such compensation does not occur leading to lower sensitivities to global warming in spring and higher in autumn. In general, the model spread is similar to the spread obtained with dew point temperature, except for spring where results with global temperature show less spread. Given these good results using simply global temperature as a scaling variable, we constructed the *dry11* based scenario in such a way that the results are very similar to a scenario constructed using global temperature as a scaling variable (see next section).

For daily precipitation we typically find sensitivities of a few percent below those for hourly extremes. The exception is spring, for which we typically find equal or even larger sensitivities. Also the data hint at a disproportional increase for the most extreme events, at return levels of 100 years and beyond. These are not captured in the functional dependency on return period of the fit. Results are qualitatively similar to Fig. 9 in Ban et al. (2020) with respect to the differences between seasons and differences between hourly and daily.

Results for the Benelux reveal (much) more spread (Fig. 5.27 and 5.28). It is obvious that we start to see the limitations of the short simulations. Interesting, the spread obtained with the global temperature appears smaller than with dew point temperature change, but it is also difficult to compare due to differences in the range plotted (y axis). To make a more fair comparison one should compare the relative spread in the ensemble compared to the fitted upper and lower band. Nevertheless, in general there is no strong evidence that the sensitivities for the Benelux area are different from those derived for the larger NWEUR area.

	hourly					daily				
	a_o		t_o		t_e	a_o		t_o		t_e
DJF	5	10	0.001	0.001	20	5	9	0.0001	0.0001	1
MAM	2	10	0.02	0.01	4	4	16	0.2	0.05	20
JJA	6	13	0.06	0.03	2	5	13	0.4	0.2	6
SON	6	13	0.01	0.01	6	5	11	0.1	0.05	5

Table 5.2: Used coefficients for upper and lower estimates of precipitation intensity sensitivity to dew point temperature change. For a_o and t_o upper and lower estimates are given, and the e-folding time scale t_e is the same for both estimates. Scaling coefficients for the sensitivity to global temperature rise are the same for t_o and t_e. The scaling coefficient a_o is multiplied by the following factors: for DJF 0.85, for MAM 0.6, for JJA 0.7 and for SON 0.8. This is close to the typical dew point temperature change per degree global warming in the CPM results for NL, see Fig. 5.23.

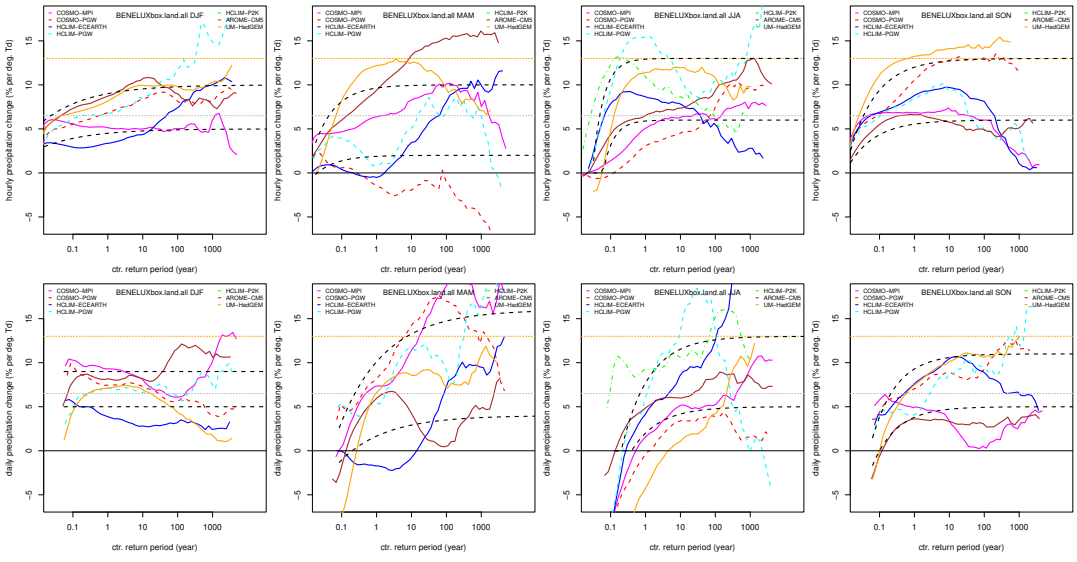

Figure 5.27: Dependencies of hourly (top) and daily (bottom) precipitation extremes on the global temperature rise T_d. Results are shown for pooled data over the BENELUX region.

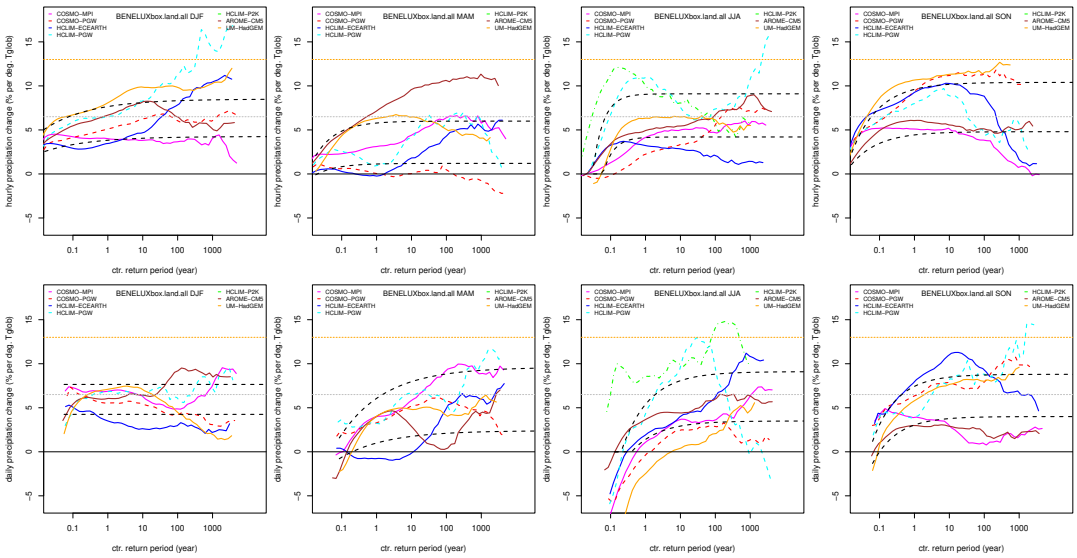

Figure 5.28: Dependencies of hourly (top) and daily (bottom) precipitation extremes on the global temperature rise T_{glob}. Results are shown for pooled data over the BENELUX region.

5.11 Scenarios for hourly and daily rainfall extremes

Here, we assemble all information to construct scenarios for small scale hourly and daily rainfall extremes. This is done by a simple transformation of the observed distribution of rainfall using a rain frequency change, Δf_w, and an intensity change ΔI_p. The latter is derived from the sensitivity of rainfall extremes to the dew point temperature rise multiplied by the dew point temperature change. This procedure is very simple and is similar to the one used in the previous set of climate scenarios (Lenderink and Attema, 2015). We note that although other variables, like stability change as well as *relative* humidity change, could be important as well, with the available CPM simulations we cannot quantify their effects.

The intensity sensitivity has been established already in the previous section (Sec. 5.10). Specific choices for the dew point temperature change as well as the frequency change are made here based on the background information provided in section 5.9.

Like in the main scenarios, we construct our scenarios for rainfall extremes on the two CMIP6 based classes given by the selection of *dry11* and *wet11* models[4]. We name these scenarios SLPXd and SLPXn. The last character n refers to the Dutch word "nat" (wet) and d to "droog" (dry), and "X" refers to the level of global warming. We only distinguish here on global warming since all parameters scale with the global temperature rise. Thus, at 4 degrees global warming the scenarios are labelled as SLP4d and SLP4n.

For summer and to a lesser degree autumn, the dry scenario, SLPXd is characterised by relatively small dew point increases and relatively high decreases in rain frequency as compared to the wet scenario, SLPXn. For spring, the two scenarios are the same for spring, but differ for winter with SLPXn having a stronger increase in dew point temperature. We already note that SLPXd is mostly consistent with a simple scaling of the CPM results directly with the global temperature rise, whereas SLPXn extrapolates the response of rainfall extremes towards generally higher humidity change values and therefore gives stronger responses in rainfall extremes.

5.11.1 Method

To start with we first define a number of things. First, the probability of exceedance is given by:

$$F(p) \equiv Pr(P \geq p) \tag{5.3}$$

The conditional distribution based on only wet *events* – either hourly or daily rainfall amounts – above a certain rainfall threshold p_o can written as:

$$F_c(p) \equiv Pr(P \geq p \mid P > p_o) \tag{5.4}$$

It can be easily derived and understood that these two distributions are related through

$$F(p) = f_w F_c(p) \tag{5.5}$$

where f_w is the fraction of events above the precipitation threshold p_o.

We first determine these for the reference climate period, which will be based on observations for the Netherlands (see below). As illustrated by a simple schematic in Figure 5.29, we construct a future probability of exceedance distribution $\hat{F}(p)$ (future is denoted by a $\hat{}$) by combining intensity changes ΔI_p and a frequency changes Δf_w as follows:

$$\hat{F}(p) = f_w(1 + \Delta f_w)\ \hat{F}_c(p) \tag{5.6}$$

[4]The selection is based on dry and wet model at 4 degrees global warming and SSP5-8.5 scenario, which differs slightly from the final set used in the generic scenarios. We used here: *dry11* MPI-ESM1-2-LR, NorESM2-MM, UKESM1-0-LL, ACCESS-ESM1-5, HadGEM3-GC31-LL, MRI-ESM2-0, NESM3, AWI-CM-1-1-MR, GISS-E2-1-G, BCC-CSM2-MR, KACE-1-0-G; and *wet11* CESM2, FGOALS-g3, ACCESS-CM2, CIESM, EC-Earth3-Veg, FGOALS-f3-L, CNRM-CM6-1-HR, CNRM-ESM2-1, CNRM-CM6-1, CanESM5-CanOE, CanESM5. Yet, the influence on the outcome is very likely marginal.

with

$$\hat{F}_c(p) = F_c(\hat{p}), \text{ and } \hat{p} = \frac{p}{1 + \Delta I_p} \tag{5.7}$$

The first equation accounts for the changes in the frequency of wet events, whereas the second equation causes an intensification of the events by a fraction $1 + \Delta I_p$. Coding of the last term is done by multiplying each p value from the observed present-day distribution by $1 + \Delta I_p$, and then interpolating the distribution back to the original p values. This can be understood by rewriting the last equation to $\hat{F}_c(p^*) = F_c(p)$, with $p^* = p(1 + \Delta I_p)$.

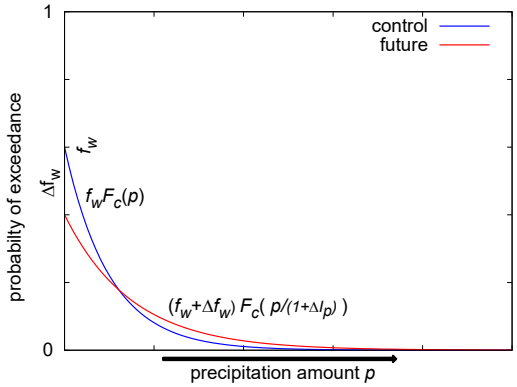

Figure 5.29: A simple schematic of the applied transformation to compute the scenarios taking both intensity as well as frequency change into account. The future distribution (red) is constructed from the present distribution (blue) by a multiplication in the y-direction with the frequency change, and a multiplication in the x-direction with the intensity change. We note that for a typical summer situation with decreases in rain frequency and increases in intensity this leads to a decrease of low rainfall amounts, yet an increase in high amounts with a transition at intermediate intensities.

Observed distributions are shown in Figure 5.30. For the hourly rainfall we used the 30 NL AWS stations, period 1991-2020, and for the daily observations the P13 observational data set. Data is pooled, sorted, and the probability of exceedance for rainfall amount belonging to i-th in the sorted time series is computed from a simple formula:

$$F(p_i) = 1 - \frac{i - 0.5}{n} \tag{5.8}$$

where i is the index number of the sorted time series, and n the total length of the time series. We note that 1-$F(p_i)$ is a commonly used formulate for a percentile computation. A return period in years is computed from:

$$t_{rp} = \frac{1}{F(p_i)\ n_{yr}} \tag{5.9}$$

where n_{yr} is the number of hours/days in a year. Since we compute these statistics per season, this is mostly the numbers of hours or days within the season (i.e. 90 days and 2160 hours).

A GPD distribution is fitted to all events with a return period above 1 year. It is shown that this fits the observed distribution quite well, with only relatively small deviations at very rare return levels of 100 years and beyond. This was necessarily because transforming the raw distribution resulted in some noise for the changes occurring at very long return periods.

As a sanity check and to illustrate how the method treats intensity changes combined with frequency changes, we plotted the changes at different return levels, for hourly and daily precipitation for summer. We assumed a 30% constant (i.e. not dependent on return level) increase in rainfall intensity and computed the changes for different values of frequency change in the range between -40 and +10 % (Fig. 5.31). As expected, with no frequency change the model gives the

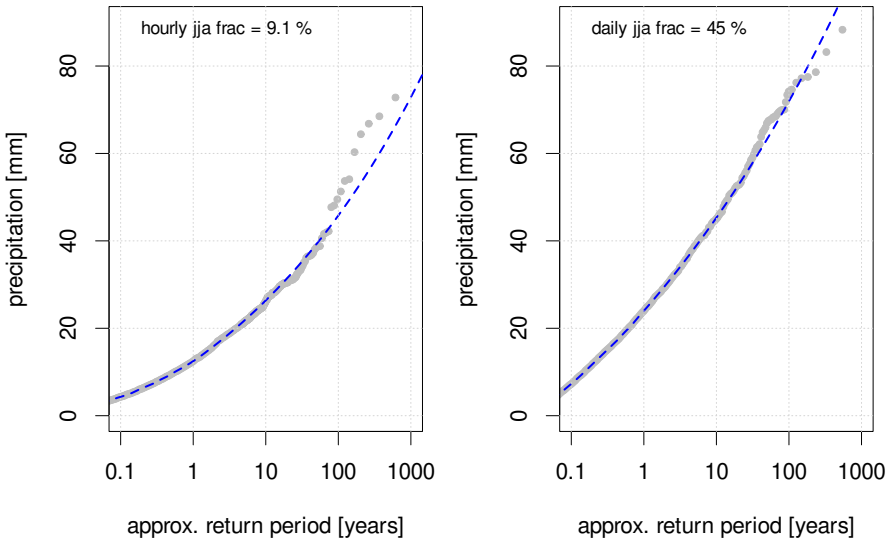

Figure 5.30: Fitted distributions

same 30 % increase at all return levels. For decreasing rainfall frequency the response becomes smaller. The response for the most frequent events(return level of 0.1 and 1 year) is most strongly affected by the frequency decrease, whereas the most rare events (return level 1000 years) are much less affected by the frequency decrease – a property that can be understood from the approximate exponential tail of the rainfall distribution. We also note that for return levels of one year and beyond the results for daily and hourly extremes is very similar, showing the underlying distribution is not very important as long as it shares the same exponential behaviour.

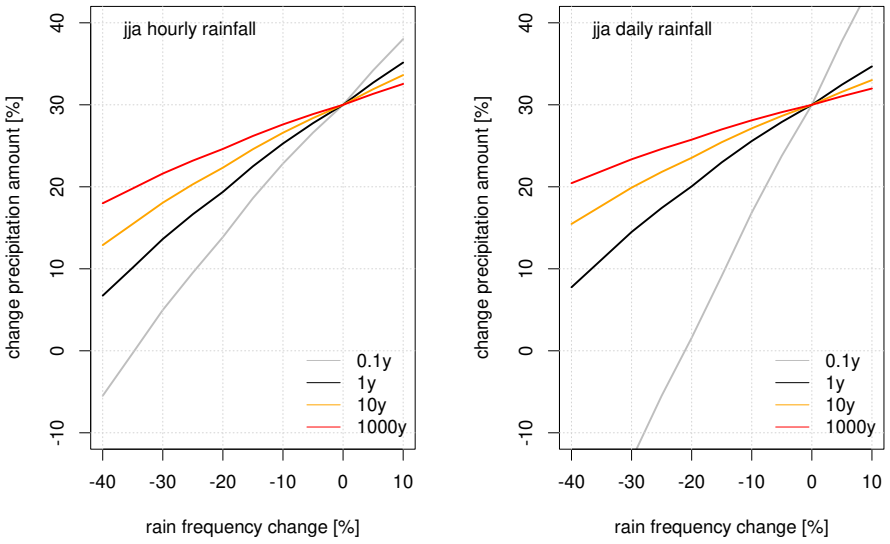

Figure 5.31: An example of how rain frequency change affect the changes in rainfall extremes at different return levels. We assume here an intensity change of 30%. Results are shown for hourly and daily rainfall, and are derived from the fits to the observed data in the previous figure.

5.11.2 Specific choice steering variables: dew point and frequency change

In all our scenarios we assume that the change in dew point temperature as well as frequency change scales linearly with the global temperature change. This neglects possible nonlinear effects, such as in changes in stability of the atmosphere and due to soil drying feedback processes. (Lenderink and Attema, 2015; Aalbers et al., 2018). While this is obviously a simplification, there is simply insufficient data to make a more informed decision on this. This also neglects that the change in frequency is a fractional change for which exponential inter/extrapolation would be better, but the influence would be small (compared to the uncertainty) so we choose the linear interpolation for simplicity (i.e. rounded numbers).

We base our choices primarily on the PGW experiments, PGW-*dry11-soil* for the dry scenario and PGW-*wet11* for the wet scenario. But, we made small adjustments to the PGW results motivated by expert judgement taking into account the results from CMIP6 and the CPMs. Summarized these are:

- DJF. The change in dew point temperature in the PGW experiments is rather high compared to the CPMs, as well as the CMIP6 models. Therefore, we adjusted the value to 0.8 for the dry scenario.
- MAM. The two PGW experiments gave almost no distinction, whereas the range in CMIP6 in the CPMs and CMIP6 is rather large. We therefore accounted by adjusting 0.1 for the dry and wet scenario.
- JJA. We slightly increased the range derived from the PGW experiments, rounding to the outer 0.05 value. We neglected the low values of 0.5-0.6 as suggested by the CPMs/CMIP6 since we think these are too low, and may be associated with too strong drying out of the soil in many models. For instance, most CPMs suffer from a dry summer bias with too low relative humidity (Lenderink et al., in prep).
- SON. Like in winter, the PGW runs are biased as compared to the CPMs and CMIP6 results, and do not cover the dryer range. We therefore adjusted the dry scenario.

Frequency changes are less important as they mostly influence the lower return periods, and have little impacts on the extremes. Typical errors of 5% frequency change lead to errors in the change of rainfall extremes at return level of 10 year of 2-3% (Fig. 5.31). This means that we do not need very precise estimates here. We give here the numbers for the scenarios at the 4 degrees global warming level, SLP4d and SLP4n. For these scenarios we used for winter and spring no frequency change. For summer we used -25% for SLP4d, and -10% for SLP4n, and for autumn -10% for the dry and no change for the wet scenario. These numbers are primarily based on the PGW runs. But we made a few small ($\sim$5%) changes to the PGW results in order to increase the spread between the scenarios and to account for the CPM results. The largest two are: the change for the dry scenario is adjusted from -20% derived from the PGW-*dry11-soil* experiment to -25% to account for the larger values in the CPMs, and in autumn the change is adjusted from -4% to 0% in the wet scenario to increase the spread between the two scenarios.

	CMIP6	CPMs	RACMO PGW		Scenario	
	range[1]	range[2]	dry11-soil	wet11	SLPXd	SLPXn
DJF	0.7 - 1.1 (1.1)	0.7 - 1.0	0.95		0.8	0.95
MAM	0.5 - 0.9 (0.9)	0.5 - 0.8	0.71		0.6	0.8
JJA	0.5 - 0.9 (1.1)	0.6 - 0.8	0.73	0.83	0.7	0.85
SON	0.7 - 1.1 (1.2)	0.7 - 1.0	0.98		0.8	1.0

Table 5.3: Changes in dew point temperature per degree global warming for the scenarios. Results are given for the typical range in GCM and in the CPMs, the results from the two PGW experiments, and in the last columns the choices made for the two scenarios. Where differences between the two PGW experiments are small (< 0.03) we only provide the average. [1]the typical range is derived from standard deviation in Fig. 5.6, and between brackets is the EC-Earth3$_{\text{p5}}$ result (rounded to 0.1). [2]approximate estimate from Fig. 5.27. Scenario values derived for the Hn/Hd scenario using the resampling procedure are: DJF, 0.98/1.0; MAM, 0.93/0.9; JJA, 0.98/1.08; SON, 1.15/1.18. Typically they are close to the values from the unresampled runs, with only marginal differences between the dry and wet resamples.

5.11.3 Results scenarios 4 degrees global warming

Final changes values for the two scenarios for a global warming level of 4 °C, SLP4d and SLP4n are shown in Fig. 5.32 for daily rainfall and Fig. 5.33 for hourly rainfall. A global warming level of 4 °C with respect to the control period (1991-2020) is reached in 2100 in the SSP5-8.5 emission scenario. Each plot contains a central esimate (sold black line) and a uncertainty band (dashed lines), and percentage changes are also given.

These *uncertainty* values given by the upper, lower and central estimate should not be interpreted in a strict likelyhood sense with the center value representing the most likely change, and the upper and lower bounds having low probability. They rather give a plausible upper and lower bound of estimated changes as derived from the model results, with the central value in the middle. Additional information – not used here as it is too preliminary to use – may *bias* the best estimate towards the upper or the lower bound. For instance, although CPMs are a big improvement as compared to common regional climate models, their strength and weaknesses have not been fully assessed yet. For instance, there are indications that CPMs still do not resolve the cloud turbulent processes sufficiently to reproduce the cloud updraft strength and cloud clustering processes realistically (Purr et al., 2019; Prein et al., 2021). In addition, CPMs appear to underestimate the scaling relation for very high dew points, and also generally underestimate differences in hourly extreme precipitation between the Netherlands and the warmer climate in central southern France (Lenderink et al 2023, in draft). Therefore, the best estimate for hourly precipitation changes in summer may well be at the upper end of range given, or reversely in other cases at the lower bound.

We showed earlier that the rainfall sensitivities derived from simple scaling with the global temperature were as robust as those derived from dew point temperature scaling (Sect. 5.10). In some cases scaling with global temperature even seems to produce slightly better results (e.g. spring, daily extremes). This could happen for instance because the sensitivity to dew point could be correlated with relative humidity change. A larger decrease in relative humidity could be associated with a relatively weak increase in stability since lower relative humidity is likely associated with stronger surface warming. This could enhance extreme precipitation as compared to the case with a stronger stabilisation. The dry scenario SLPXd has been constructed in such a way that the results are similar to the results obtained when the intensity change is derived from rainfall sensitivity to global temperature. Results for the change in daily extremes, comparing the two methodologies, are shown in Fig. 5.34.

Typical changes – here the median estimate – for daily extremes are surprisingly constant throughout the year, at 4 degrees global warming for the 100 year return value 22-26% in SLPXd and 29-35 in SLPXn. This is the result from a compensating effects of the rainfall intensity sensitivity and the fractional increase in dew point. One interesting point is the high upper range

for spring, suggesting the possibility of large organised convective systems in spring causing large changes at the daily time scale. We also note that the change in winter is typically 7% per degree global warming, with upper bound of 9% per degree. This is substantially higher than the typical 5% per degree increase in RACMO. There are indications that this difference between the CPMs and RCMs in winter is systematic, with the CPMs producing substantially larger changes (Kendon et al., 2020).

Changes in hourly extremes are generally rather similar to those at the daily timescale. In winter and summer they are almost identical for large return periods, although we note that changes for yearly events are typically larger in summer because of a lower influence of frequency changes (Fig. 5.31). In spring changes at the hourly time scale are lower and in autumn higher than the change at the daily time scale. Qualitatively, these difference are the same as in Ban et al. (2020).

		dry		wet		all		
		K14	**K23**	K14	**K23**	K14	**K23**	K23-1000y
1hr	1yr	22-45	**5-26**	25-51	**17-46**	22-51	**5-46**	12-49
1day	10yr	6-45	**5-26**	6-45	**12-41**	6-45	**5-41**	10-49

Table 5.4: A comparison of changes values (%) between KNMI-14 (K14) and the present scenarios (K23). Since the KNMI14 was computed at a global warming level of 3.5 °C and the present scenarios at 4 °C, we multiplied all values from KNMI'14 by 1.14. Scenarios are given for the dry and wet branch, and "all" is the total range spanned by the two branches. The full range at a 1000 year return level is provided in the last column.

Finally, we compared the changes in summer (JJA) to the values provided in the previous scenario set issued in 2014 (Table 5.4). Values of the KNMI'14 scenarios have been scaled to 4 degrees global warming to make them comparable to the changes derived here – a factor 1.14 to move up from 3.5 degrees to 4 degrees global warming. In general, the change values are comparable to the previous scenarios, although they are generally slightly lower. For hourly extremes the lower bound estimate is considerably lower, 5 % versus 22 % in KNMI'14. This is partly caused by the lower change in dew point temperature in the SLPXd scenario as compared to KNMI'14 W_H scenario. In addition, in the present scenarios we much better accounted for rain frequency changes, which also leads to smaller increases (Fig. 5.31).

In addition to the changes values in summer, we also provided changes for the other seasons too. For these seasons we can not compare directly to previous results. For daily extremes in winter we may compare to the changes in 10-day sums as in general there are only small changes in the frequency of rain events, and changes in 10 days extremes do not differ much from the change for daily extremes. Typically, these give values between 20% for the dry variants and 30% for the wet variant, which is within the range given here. Yet, the new scenarios suggest the possibility of higher changes up to almost 40 % for daily extremes in winter.

Finally, we provide the scenario values for 4 degrees global warming in Table 5.5-5.8, representative for the H scenario for 2100. By good approximation the scenario values for other global warming levels can be estimated by linear inter- or extrapolation using global warming. We note that this is not exact as the relation of intensity with dew point temperature is somewhat non-linear, but the errors are generally small in relation to the overall uncertainty. Exact values for other warming levels can be found at the end of this Chapter.

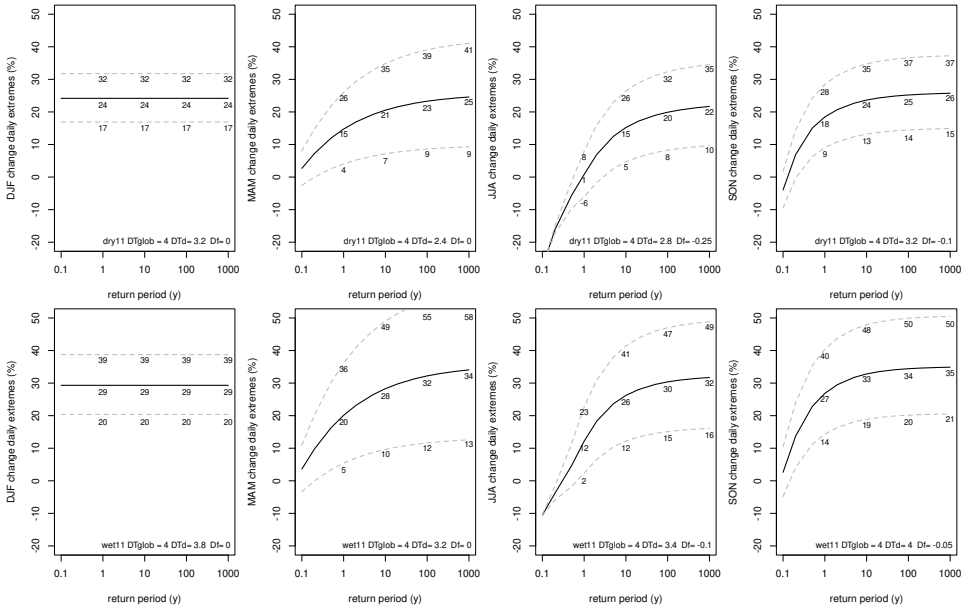

Figure 5.32: Scenarios for daily rainfall extremes for a global temperature rise of 4 °C. Upper panel shows the results for the dry scenario, and lower panel for the wet scenario. From left to right, results for DJF, MAM, JJA and SON.

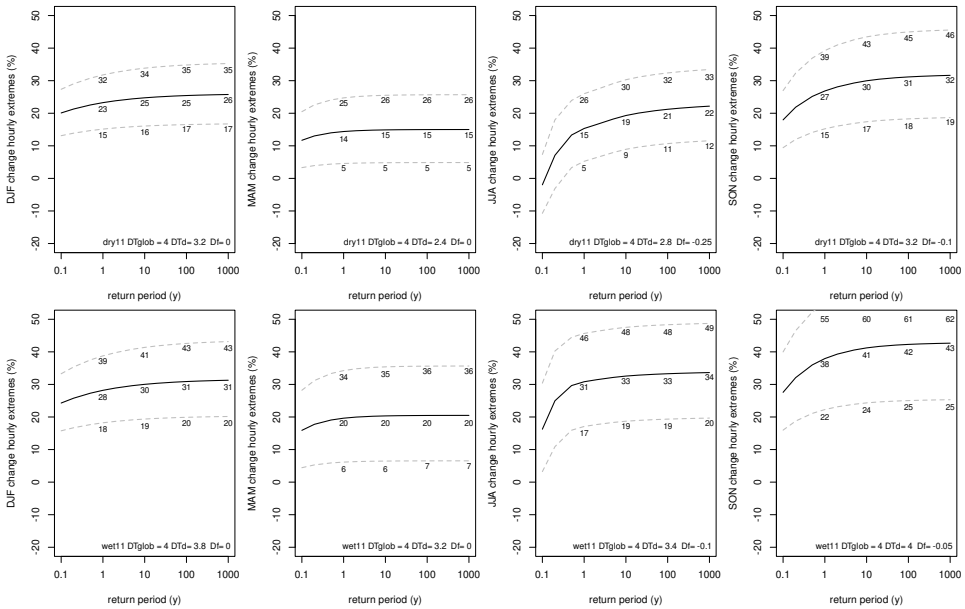

Figure 5.33: Scenarios for hourly rainfall extremes for a global temperature rise of 4 °C(similar to previous figure).

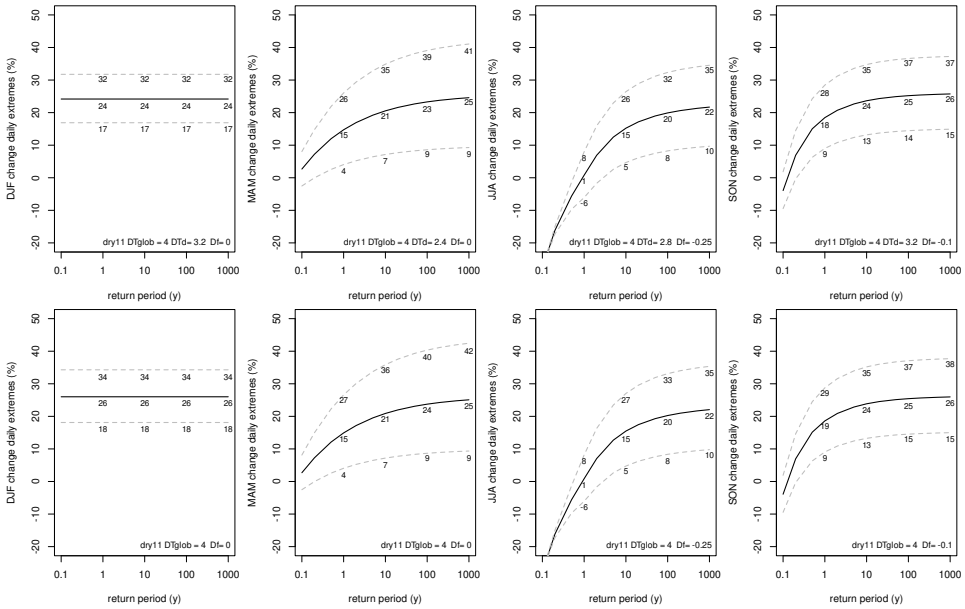

Figure 5.34: Comparison for the dry scenario SLP4d of daily extremes between two methods. Upper panel, based on scaling with dew point temperature (standard method), lower panel results obtained from direct scaling on the global temperature rise (alternative method). For the dry scenario both methods give almost identical results (except winter where there are some small differences).

	DJF (%)				MAM (%)				JJA (%)				SON (%)			
	pres.	future			pres.	future			pres.	future			pres.	future		
0.1	7	17	24	32	5	-3	3	8	8	-28	-28	-28	8	-9	-4	2
1	19	17	24	32	16	4	15	26	26	-6	1	8	23	9	18	28
10	30	17	24	32	31	7	21	35	48	5	15	26	42	13	24	35
100	39	17	24	32	51	9	23	39	76	8	20	32	69	14	25	37
1000	46	17	24	32	79	9	25	41	111	10	22	35	105	15	26	37

Table 5.5: relative changes for daily rainfall extremes based on the dry11 scenario at 4 °C global temperature rise.

	DJF (%)				MAM (%)				JJA (%)				SON (%)			
	pres.	future			pres.	future			pres.	future			pres.	future		
0.1	7	20	29	39	5	-3	4	11	8	-11	-11	-10	8	-5	3	10
1	19	20	29	39	16	5	20	36	26	2	12	23	23	14	27	40
10	30	20	29	39	31	10	28	49	48	12	26	41	42	19	33	48
100	39	20	29	39	51	12	32	55	76	15	30	47	69	20	34	50
1000	46	20	29	39	79	13	34	58	111	16	32	49	105	21	35	50

Table 5.6: relative changes for daily rainfall extremes based on the wet11 scenario at 4 °C global temperature rise.

	DJF (%)				MAM (%)				JJA (%)				SON (%)			
	pres.	future			pres.	future			pres.	future			pres.	future		
0.1	2	13	20	27	2	3	12	20	4	-11	-2	7	3	9	18	27
1	5	15	23	32	6	5	14	25	13	5	15	26	7	15	27	39
10	8	16	25	34	13	5	15	26	26	9	19	30	13	17	30	43
100	12	17	25	35	25	5	15	26	46	11	21	32	21	18	31	45
1000	18	17	26	35	44	5	15	26	73	12	22	33	31	19	32	46

Table 5.7: relative changes for hourly rainfall extremes based on the dry11 scenario at 4 °C global temperature rise.

	DJF (%)				MAM (%)				JJA (%)				SON (%)			
	pres.	future			pres.	future			pres.	future			pres.	future		
0.1	2	16	24	33	2	4	16	28	4	3	16	30	3	16	28	40
1	5	18	28	39	6	6	20	34	13	17	31	46	7	22	38	55
10	8	19	30	41	13	6	20	35	26	19	33	48	13	24	41	60
100	12	20	31	43	25	7	20	36	46	19	33	48	21	25	42	61
1000	18	20	31	43	44	7	20	36	73	20	34	49	31	25	43	62

Table 5.8: relative changes for hourly rainfall extremes based on the wet11 scenario at 4 °C global temperature rise.

5.12 Spatial characteristics of summertime rain showers

5.12.1 Summary and key points

In the previous sections we mostly ignored the spatial structure of precipitating systems. In this subsection we retain this information and examine how *spatial characteristics* such as the size of intense summertime rain showers may change in a future warmer climate. Precipitation cells are detected in hourly CPM data for May-October as contiguous areas with an hourly accumulation of at least 4 mm. In observations of De Bilt about 30% of the total rain in JJA falls at these intensities. Properties of the rain cells such as peak intensity, size and total volume, are then analysed. The characteristic life time of the showers is left for future research. Our main findings are: (i) There is a robust decrease in the number of cells, up to 10% per degree global warming. Reductions occur predominantly in JJA for cells with peak intensities below 15-20 mm/hr. Higher-intensity cells increase in frequency. (ii) Cell size and total precipitation volume show a consistent trend towards higher values. Equivalently we see percentiles of the intensity, area and total volume robustly increase, though with values that generally do not exceed Clausius Clapeyron (after scaling by global temperature increase). (iii) Finally, cells with high local peak intensities (P90 and above) in the future are generally also larger in size, and result in larger total precipitation amounts. Thus, the most extreme rain cells in the future climate will not only have more impact at the local scale (due higher peak intensities) but also influence larger areas. Key-figures: 5.35, 5.38-5.39, 5.41-5.42.

5.12.2 Introduction

As has been discussed in detail in earlier sections, local convective activity and precipitation rates are influenced by many factors. Many of these change in a warming world. We use regional climate models to inform us about and if possible to understand these changes. To analyse precipitation at a sub-daily time scale we make use of convection permitting regional climate models (CPMs) which are better suited than coarser resolution RCMs (Coppola et al., 2020; Ban et al., 2021; Pichelli et al., 2021; Lenderink et al., 2021b; Lucas-Picher et al., 2021). Some further motivation of why we use CPMs in the study of (extreme) precipitation is given by two examples.

Example 1. The event of 19 June 2013 Figure 5.35 shows an example of particularly intense shower development on a warm summer day in the CPM HCLIM38-AROME (HCLIM38 from here). In fact, this case resulted in the highest one-hour precipitation amount near the Netherlands in an 11-year long climate integration. This particular climate integration was obtained using reanalysis data from ERA-Interim at the domain boundaries for the period 2008-2018. In the 'real' world (as opposed to the 'model' world of HCLIM38) also a lot of precipitation fell on 19 and 20 June 2013 (e.g., more than 90 mm was reported in Heino). Because the HCLIM38 simulation was a climate run forced by reanalysis and not a weather forecast, there is no exact correspondence to observations, but the large-scale characteristics (e.g., weather type, typical temperature distribution) agree with the observed state. The event was triggered on a very warm summer day near a region with a strong temperature gradient. Over a southwest to northeast oriented confluence line (see arrows of the wind gust field) convection starts in the early afternoon. From 15:00 UTC onward the convection gets increasingly organised and expands strongly in size and produces a locally very intense downpour. The gust field shows signs of rapidly developing cold pools. In the south west of the shown domain a second large system develops. The time evolution of a few aggregated statistics of the precipitation and gust field are shown in Fig. 5.36, in which one can clearly see expansion in the size and the total precipitation volume as the shower develops. The highest intensities are seen prior to the time when the showers have their largest size. The next day another large system developed over the domain (Fig. 5.36).

As already stated, the case was selected because it gave rise to the highest one-hour precipitation amounts. Nevertheless, we consider the life cycle, spatial structure, typical time of occurrence and precipitation intensities reached in the CPM simulation to be quite realistic. Analysis of cases

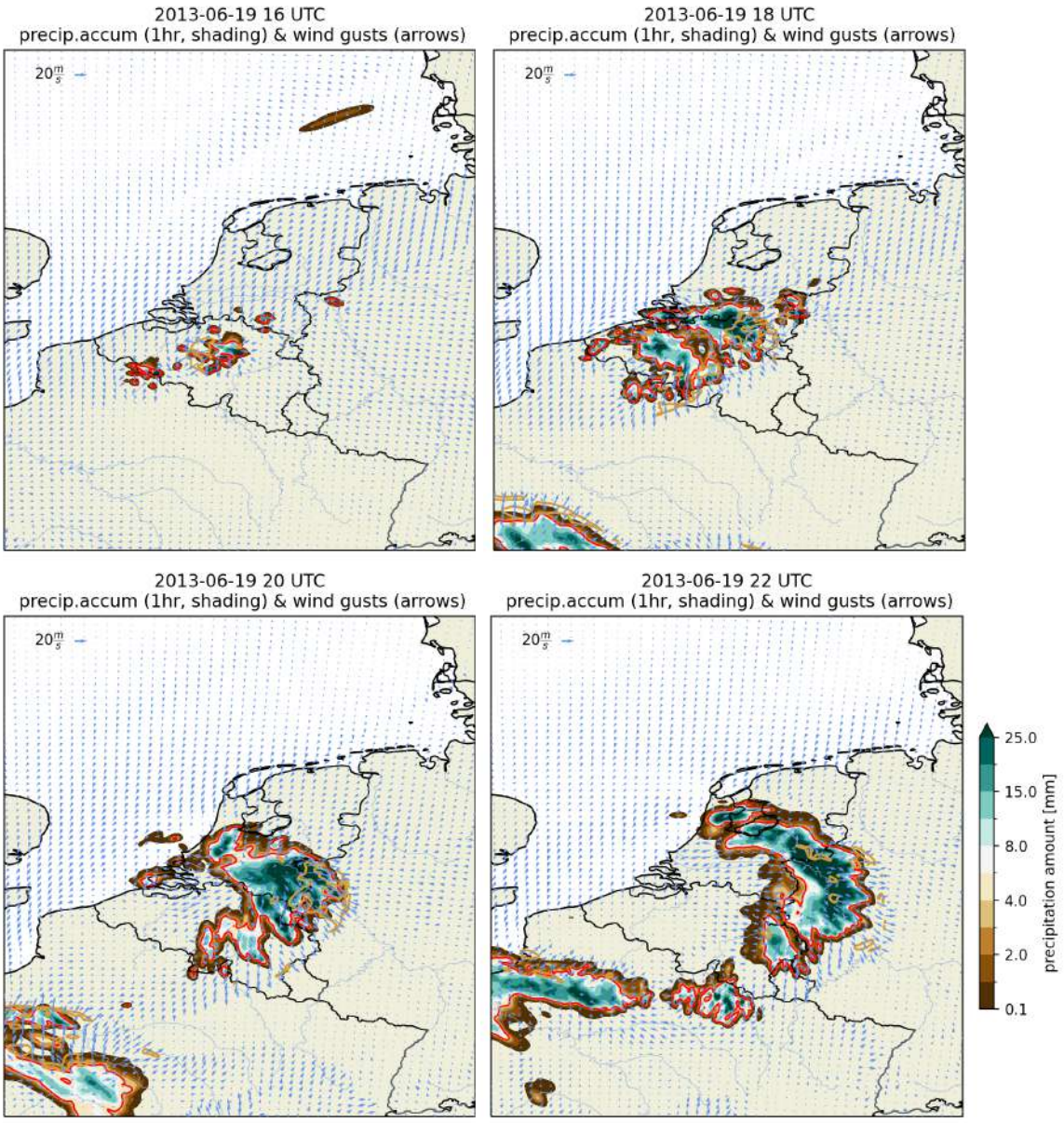

Figure 5.35: Development of intense convective showers on a warm summer day in HCLIM38, taken from the CTL simulation on the NWE domain (Tbl 5.21). Shading shows the hourly precipitation amount (timestamp marks the half hour point). Red contours show the 4 mm/hour threshold used in the rain cell analysis. Arrows show the wind gust field at the end of the shown hour.

like these gives us confidence that CPMs are capable of resolving the type of extreme (convective) events that are relevant for society.

Example 2. Hourly precipitation and diurnal cycle As already stated, RCMs that operate at lower resolution than the CPMs have difficulties in resolving the precipitation statistics at sub daily time scales, especially at smaller spatial scales and at higher intensities. This is illustrated with an example taken from Belusic et al. (2020b). Figure 5.37 (left panel) shows the probability to find hourly maximum precipitation values over the Netherlands above a certain threshold, in radar data (black), and in a CPM (HCLIM38, blue) and RCM (RACMO2, light blue) simulation.

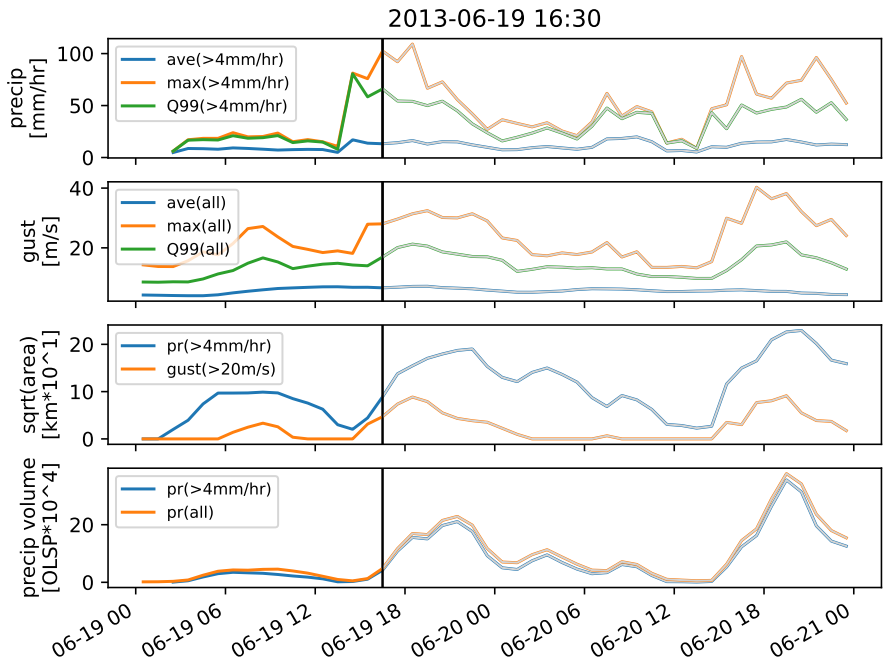

Figure 5.36: Statistics for the case of Fig. 5.35. Top panel shows the average, maximum and 99th percentile of precipitation for all grids where the 4 mm/hr threshold is exceeded (this threshold is used in the main text to diagnose cells). The vertical line indicates the time used in the title, corresponding to the top-right panel of Fig. 5.35. Second row: average, maximum and 99th percentile of wind gusts. Third row: linear size (i.e., the square root of the area) of the precipitation exceeding 4 mm/hr and gusts exceeding 20 m/s. Fourth row: total precipitation volume, as measured in Olympic Swimming Pools (2,500 m^3).

Input here are high-resolution gridded radar data of the period 1999-2009 and data of the same period for the CPM and RCM. Both HCLIM38 and RACMO2 simulations were forced by ERA-Interim reanalysis (period 1999-2009). The spatial resolution of the radar data is comparable to that of HCLIM38 and in this comparison all model data has been put on the same (fine scale) radar grid by using a nearest neighbour remapping. Confidence intervals (shaded bands) were estimated using bootstrapping with yearly blocks.

While the CPM follows the radar data rather closely over almost the entire range of probabilities, the RCM falls short and does not reach the low-probability high-intensity events. Of course, by choosing the spatial maximum over a domain (the Netherlands) this particular example zooms in on small-scale precipitation extremes. One can argue that it is unfair to compare the models at this resolution, since the RCM will never be able to generate the fine spatial scales and associated amplitudes. However, if the data of the radar and the CPM are first coarse-grained to the resolution of the RCM, there still remains a big difference between RCM and CPM (not shown). When aggregating the data to country-level (average hourly values over the whole of the Netherlands), however, much of the 'added value' of the CPM disappears (Suppl. Fig. 5.49 left panel).

The remaining panels in Fig. 5.37 show a high percentile (middle) and the average (right) as a function of the hour of the day. Again we see that the CPM is much better than the RCM in simulating the diurnal cycle in the amplitude of the most intense local-scale showers, while again this added value disappears at the spatial scale of the country (Suppl. Fig. 5.49). The winter months produce similar differences, albeit with lower maximum intensities. Therefore, also in winter shortlived localised precipitation extremes are better reproduced with the CPM, while at country level RCM and CPM are comparable.

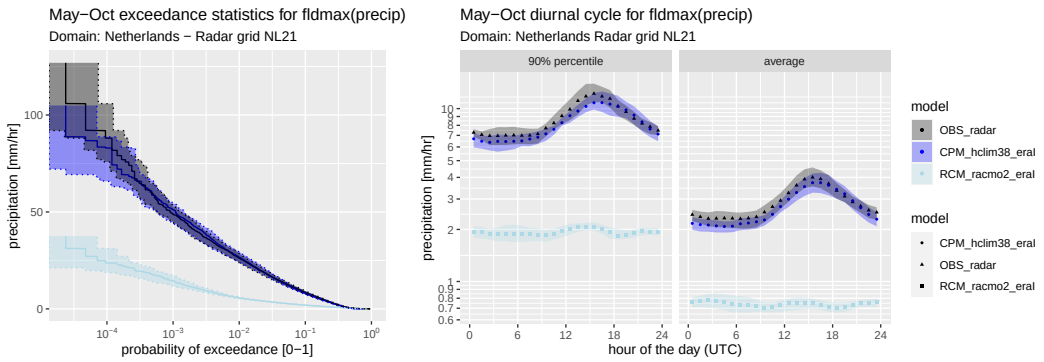

Figure 5.37: Left: probability exceedance for hourly precipitation maxima over the Netherlands. Middle and right panel: 90%-percentile and average of spatial maximum precipitation, for each hour of the day. Shading shows 95% confidence estimates, obtained by bootstrapping.

5.12.3 Data and methods

We focus on precipitation occurring during the "convective" summer half year (May to October). Hourly precipitation fields taken from the CPMs are analysed with the tracking software CELLTRACK (Lochbihler et al., 2017; Moseley et al., 2013). Data is taken from a number of different CPMs (see Table 5.21). Using CELLTRACK we detect rain cells above a certain threshold. These cells are then analysed for specific properties such as cell-average precipitation (mm/hr), local peak intensity (mm/hr), cell size (km) and area (km^2) and cell total precipitation amount. The duration of convective showers is left to future research. Although the life-cycle of convective rain showers is a relevant aspect (see e.g., Fig. 5.35 where the largest events typically last more than a single hour and increase their size quite strongly over time), this metric depends rather sensitively on how the tracking software deals with the process of merging and splitting of rain cells.

Detection threshold Diagnosing rain cells starts by choosing a detection threshold. Higher thresholds will reduce the number of cells and lead to smaller cell areas. Because this chapter is tailored to high precipitation amounts the relatively high threshold of 4 mm/hr is chosen. This avoids the number of cells to become very large and the statistics to be dominated by cells with low intensities. In the case study shown in Fig. 5.35 the 4 mm/hr threshold is indicated (red contours). During the event many small-sized cells merge into one big system. In De Bilt about 30% of the summer rain in JJA falls as precipitation with intensities above 4mm/hr (see supplementary figure 5.50). In the winter (DJF) this reduces to less than 5%. Once a threshold has been chosen, precipitation objects (i.e. cells) are found by finding spatially distinct contiguous areas above this threshold in space. Precipitation features below the threshold are discarded.

Aggregation and region representative for the Netherlands The outcome of the tracking analysis is a set of rain-cell centers (locations of the the weighted center of mass of the precipitation), along with a number of properties. A further spatial aggregation step is necessary to infer statistically robust information. Suppl. Fig. 5.51 shows the average number of cells per summer month in one of the KNMI HCLIM38 simulations (simulation HIST, Tbl. 5.21), where masking has been used for regions that exceed 400 m altitude. The dashed area is the region that we consider representative for the Netherlands and below we only use cells that have a cell-center within this box and that is below 400 m elevation. This box is identical to the "NWEURbox" used in earlier sections (Fig. 5.18). While there are interesting spatial differences in the figure, over the target region the cell-density is reasonably homogeneous.

Probability of exceedance and return period In the results we often display the frequency or the pooled fraction of exceedance, which is simply the exceedance probability of the spatially and temporally pooled data over the entire target region. Assuming that all cells could have occurred anywhere within the region, the exceedance frequency can be converted easily to an empirical estimate of the return period for a given area (i.e., the average time between two events in say a box of 50x50km) by multiplying it by an area-factor. This area-factor is the ratio of area of the target box by the total area of the domain from which data is pooled. Note that this approach assumes that cells are independent. The case study (Fig. 5.35) shows that this is generally not the case and that there are correlations in space and time. Therefore the estimated return periods are a lower bound to the true return period.

Natural variability and uncertainty estimation The CPM simulations have a length of about 10 years. Signal to noise ratios are largest if future and historic runs are separated far in time. In the KNMI CPM simulations we carefully selected certain members of a 16-member EC-Earth/RACMO ensemble for downscaling with HCLIM38. In an attempt to minimise regression to the mean effects in the future response, these members were chosen because (for the selected periods) they were closest to the ensemble average in properties like the large-scale circulation and mean precipitation climate. Nevertheless, natural variability in variables like precipitation remains notoriously high (even in a stationary climate differences of 10% in climatological quantities like the 30-year mean precipitation are not uncommon). Therefore, to provide some estimate of the uncertainty in the statistics, a simple bootstrapping method is used, which is based on resampling data in year blocks (basically creating n surrogate time series of the same length as the original series, by sampling years with replacement). In the multi-model part of the study instead of bootstrapping we use the ensemble spread to measure uncertainty.

5.12.4 Results

This section describes the main findings on the spatial characteristics and future changes of rain cells above 4 mm/hr in the target domain and below 400m altitude. First we discuss the HCLIM38 KNMI simulations. Thereafter more CPMs are included and summary statistics are presented.

Results: one CPM (HCLIM38 KNMI simulations)

Below, we focus on the differences between the end-of-century (EOC) run (2090-2099) and the historic reference run (1996-2005) of HCLIM38.

Cell number In HCLIM38 the total number of tracked cells decreases substantially, between 15-20% (see numbers in the legend in the left panel of Fig. 5.38). The reduction occurs mostly in JJA (not shown) and for cells with peak cell intensities smaller than 15-20 mm/hr (the dotted line shows the ratio of the absolute exceedance frequencies). The number of cells with high intensities thus increases, in line with the previous sections which were based on Eulerian approaches.

Cell intensity There is a systematic shift towards higher intensities in the warmer climate: the relative exceedance frequency increases at all intensities (dashed lines in the left panel of Figure 5.38). As said, above 15-20 mm/hr even the absolute frequency of cells increases (dotted lines). When expressed as a ratio the increase is substantial. For example, a cell peak intensity of 50 mm/hr and above is found three times as often in the future. This has as a consequence that despite the substantial decrease in the total number of cells (see point above), the return periods for high peak intensities reduce substantially, or, equivalently that the peak intensity at a given return period increases. This is made explicit in the right panel. For example, in the historical simulation an intensity of 60 mm/hour had a return period of 40 years (for an area of 50x50 km^2 within the domain), but this reduces to less than 10 years in the end-of-century future simulation. Similar results are obtained for cell-average precipitation (but shifted to lower values).

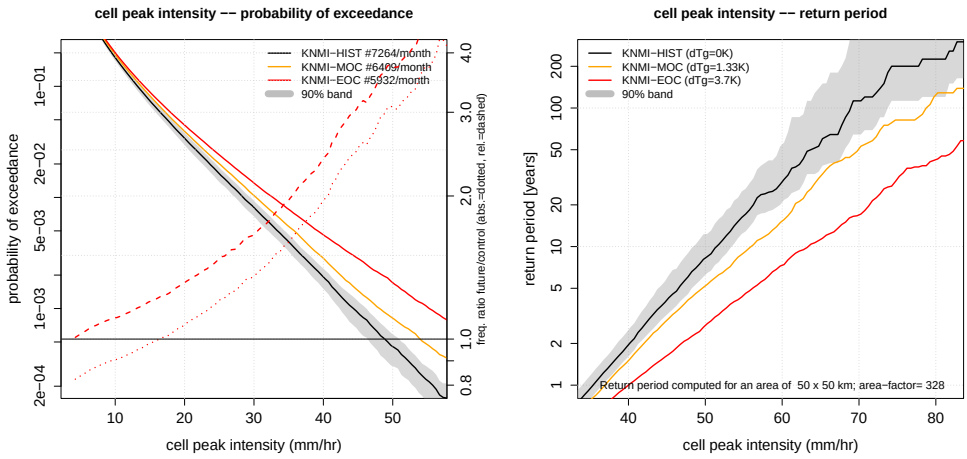

Figure 5.38: (left) Probability of exceedance for cell peak intensity. The dashed line shows the ratio of the *relative* exceedance frequencies (end-of-century to present-day), the dotted line the ratio of the *absolute* exceedance frequencies. (right) Return periods for a domain of 50x50 km, assuming all cells could occur anywhere in the target region. Only return periods over 1 year are shown. Shading shows 90% confidence estimate obtained via bootstrapping.

Cell size Cell size is computed as the square root of the cell area, disregarding any information about the shape of the cells. Figure 5.39 shows that there is a small but systematic shift towards bigger cells. Once cells are formed (keep in mind that all cells exceed the threshold of 4 mm/hr), they have a tendency to be larger in the future climate. Only cells with sizes exceeding 30 km increase in number (dotted line in the left panel of Fig. 5.39). These changes are reflected in the local return period estimates (right panel); there is a clear reduction of the return period at a given intensity, or, equivalently, an increase in the size at a given return period.

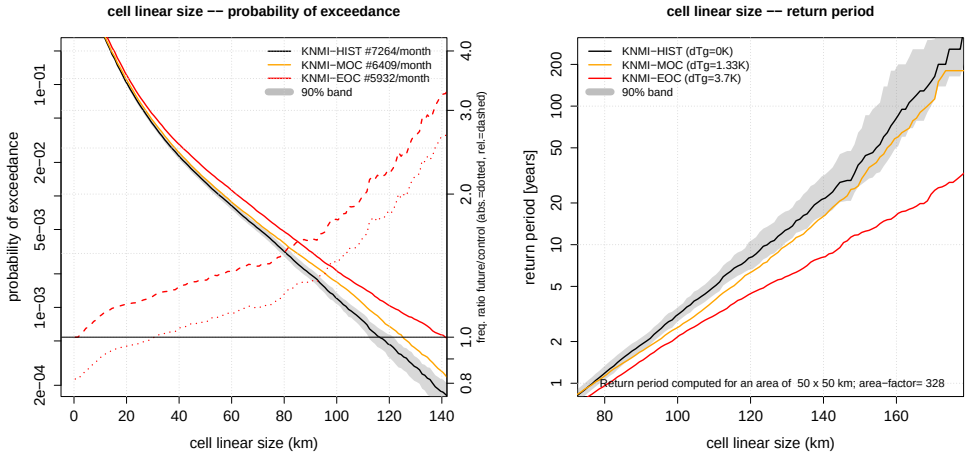

Figure 5.39: As Fig.5.38 but for cell size (computed as the square root of the cell-area).

Cell intensity as a function of cell size Intensity and cell size are related. To examine this relation in the CPM data Figure 5.40 shows intensity percentiles conditional to cell size. To construct the conditional percentiles all cells within a given size-range (a bin-size of 20 km is used

in the x-direction) are pooled prior to computing the intensity percentiles. To guarantee that the percentiles are reasonably well sampled we required there to be at least $10/(1-q)$ cells falling in the category (q denotes the quantile, say $q = 0.90$ for P90). For example, for the P99 percentile to be shown in the figure, at least 1000 cells were required. This has as a result that not all percentiles can be shown at all sizes simply because there were too few of those cells available. A small but systematic shift towards higher intensity values can be seen in the figure. Lower percentiles remain largely unaffected because of the lower bound on the threshold. Below the P99 percentile, the changes do not exceed the CC-rate, shown here as the grey band (Note that the KNMI-EOC run has $dTglob = 3.7K$). For the highest percentiles the CC-rate is reached. Cell average precipitation (right panel) again behaves more modestly. Weak increases appear from the 99th percentile upwards. Because cell-size is explicitly known from the value at the x-ordinate, the implied changes in precipitation volume can be inferred by multiplying the average precipitation percentile with the square of the cell-size (Suppl. Fig. 5.52).

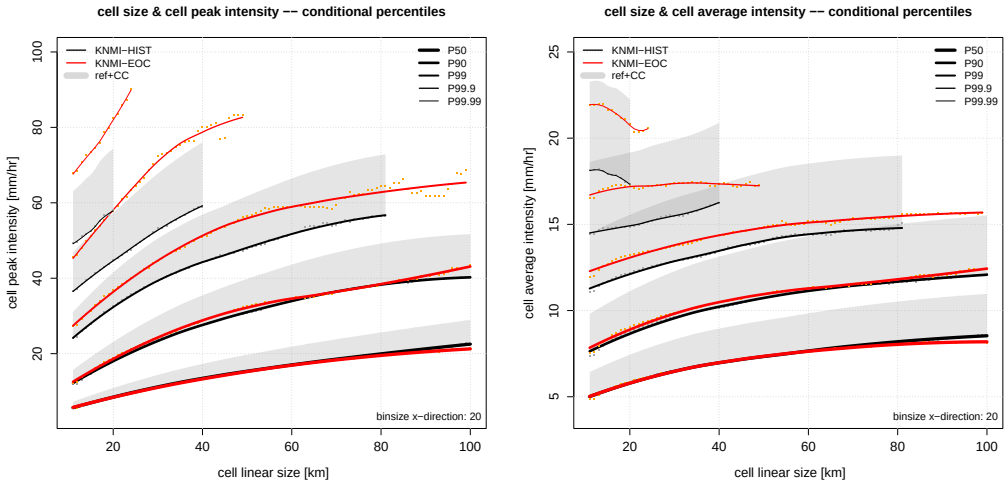

Figure 5.40: (left) Percentiles of peak intensity conditional to size, in the HIST and EOC simulations of HCLIM38. The tiny dots show the actual data points, the lines have been obtained by a simple Loess filter through the data. The grey bands shows scaled HIST values with 0-7% per degree warming and a global warming level equal to that of KNMI-EOC (+3.7K). (right) Same but for average intensity.

Cell total precipitation volume To get a feeling for the sheer amount of water produced by even modestly sized showers, cell total precipitation volume (area times precipitation amount) is the final metric that will be discussed. We express the volume in units of Olympic Swimming Pools (1 OSP=2,500 m^3 of water). A simple calculation shows that to cover an area of 1 km^2 with 1 mm of water one requires 0.4 OSP. With the same reasoning 1 mm of rain falling in one grid-cell of HCLIM38 (2.5x2.5 km^2) is equivalent to 2.5 OSP. Thus the minimal rain cell that meets our criteria (i.e., one grid box and 4 mm/hr) produces ten Olympic Swimming Pools of water. A more reasonably sized cell with an average intensity of 4 mm/hr and covering 100 grid cells (25x25 km^2) produces 1000 Olympic Swimming Pools water equivalent. One issue with a volumetric metric like total precipitation volume is that it combines information of both cell-average intensity and cell-size (or cell area). A high total volume can be reached by various types of showers ranging from a small-area high-intensity shower to a large-area weak-intensity one, and everything in between. Because the future response is different at different intensity and size, without constraining either of them, the future changes are bound to be difficult to interpret. From Fig. 5.40 we saw that the largest changes in cell-average precipitation occur for small-sized cells. To avoid the signal to be mixed up weak-intensity but larger cells, we limited the maximal allowed cell area to be less than 25x25 km^2 (arbitrary shape). This implies that most of the future change is due to the change

in the cell-average precipitation. The result (Suppl. Fig. 5.53) is in line with previous findings, showing a shift towards higher values Although the changes may seem not very large they still imply a reduction of the return period of a 3000 OSP rain dump from 40 to 20 years (right panel).

Results: Multi-model analysis

Rain cells were also detected for the other CPMs. Rather than showing the same figures again for all different models, we provide a number of summary statistics. These summary statistics focus on the future changes scaled by the global temperature increase of the underlying GCMs. The scaling is done because the models differ in their applied warming level. In this analysis we include only cells with a cell area less than 100x100 km^2. Cells can be of any shape, as long as their total area does not exceed this value. It needs to be remarked that especially the number of detected cells varies considerably between the simulations. Note also that inherently to applied methodology (i.e., detection of contiguous cells above a threshold) many statistics will show a near zero-change at the lowest percentiles. This happens because the smallest cell that is detected has a size of 1 grid box and an amplitude equal to the detection threshold. Shifts towards lower intensities will thus express themselves partly as decreases in detected cell-frequency.

Frequency and intensity changes Figure 5.41 shows the multi-model statistics for cell intensity. A robust picture emerges in which there are absolute decreases in cell frequencies between -10-0% per degree warming under RCP85 (excluding MOHC-MOC which shows stronger decreases). This frequency reduction occurs mostly for cells with peak intensities below 20 mm/hour. Model spread arises from both natural variability (two times 10 years is simply too short for extreme events), differences in model physics and differences in large-scale circulation response. The systematic shift towards higher intensities is even more clear when comparing the relative frequencies (right panels). Results for cell area and volume are quite similar and show systematic relative frequency changes towards higher values (Fig. 5.54). Thus there will be relatively more cells that may have high impact because of their peak intensity, their size, or their total precipitation volume.

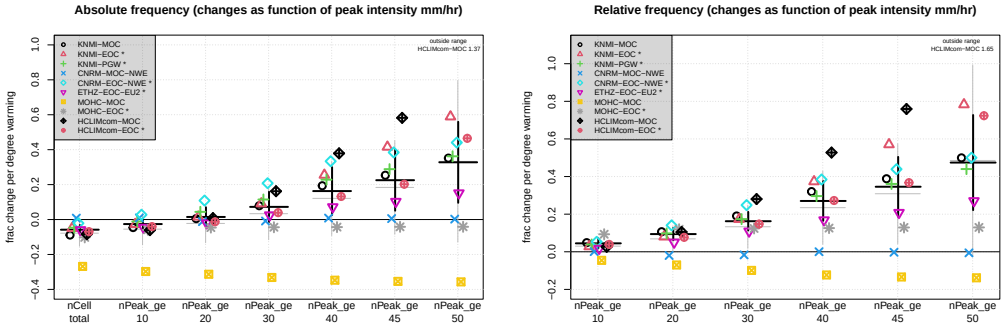

Figure 5.41: Multi-model summary statistics (I): Absolute (left) and Relative (right) change per degree warming of frequency for cell peak intensity. The black horizontal lines denote the multi-model mean of the models with the largest signal-to-noise ratio (* in legend), the vertical lines ± one ensemble standard deviation. Grey thin horizontal lines indicate multi-model mean of all models).

Percentile changes An alternative but equivalent description of the future changes can be given in terms of the changes of the percentiles of intensity, area or precipitation volume (Suppl. Fig. 5.55). In essence this is a description of the change of intensity at a given return period, while the frequency viewpoint describes the change of return period of a variable to exceed a given level. For

peak intensity (top-left), the percentile changes are all positive (consistent with the relative frequency changes), but the ensemble-mean remains under the 7% per degree increase. The highest percentile shown here (P99.9) increases with about 5% per degree warming. Note that there is quite a bit of scatter in these results but that the outliers are generally the runs with the smallest signal-to-noise ratio (the ones that do not carry a star in the legend). For total cell precipitation volume (Suppl. Fig. 5.55) top-right panel) fractional changes reach Clausius-Clapeyron scaling values at the higher percentiles. Note that the highest percentile shown here is influenced by the choice to limit the maximal included area. Without the size restriction the flattening does not occur. Size and area percentiles (second row) are both positive and almost independent of percentile value chosen. Also here, the highest percentile is influenced by the area limit.

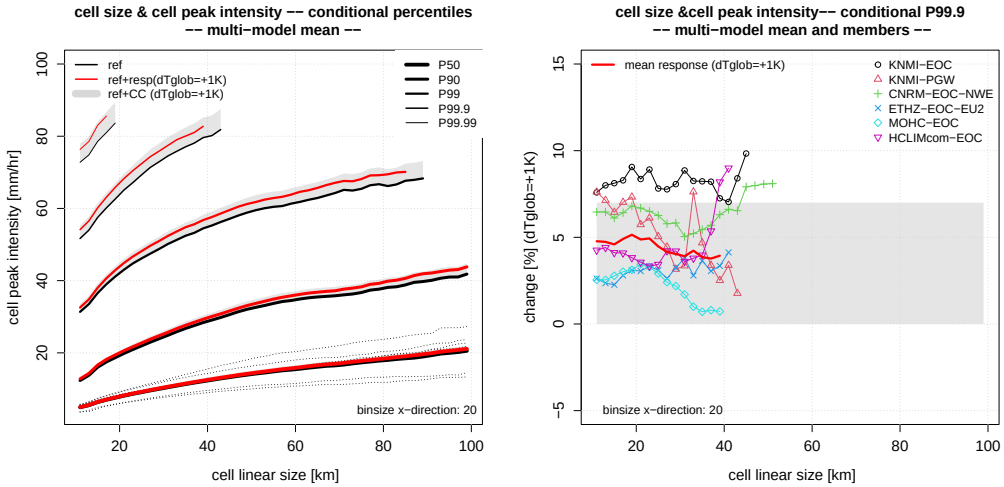

Figure 5.42: Multi-model summary statistics (II): Intensity changes conditional to cell size. (left) Multi-model mean values for control climate (black) and a +1K warmer climate (red), obtained by adding the scaled response to the control simulation. The grey bands shows the 0-7% CC-rate. (right) Individual model contributions to the P99.9 changes.

Cell intensities as a function of cell size Similar to Fig. 5.40 intensity percentiles conditional to cell-size were constructed for the other CPMs. However, because they have different global warming levels, for each contributing model the scaled response is added to the control simulation, instead of using the raw future data. The left panel of Figure 5.42 shows the multi-model mean result for peak intensity. For this statistic we included only the CPMs with the highest signal-to-noise ratio. The resulting figure is quite similar Fig. 5.40, but the lines are shifted in the vertical, because of differences in for example mean state. For the lowest percentile (P50) we illustrate this by showing the individual model contributions (thin lines). The grey band shows the 0-7%/K CC-scaling rate, which is generally not exceeded by the multi-model mean, not even at the highest percentile. The right panel Figure shows the scaled response of the individual ensemble members for P99.9. This graph confirms that KNMI-EOC was indeed the CPM with the strongest increase at that percentile (even beyond CC-rate). Similar figures with smaller values are obtained for cell-average precipitation (not shown).

Conditional percentiles for cells above P90 peak intensity Finally, cell intensity, size, area and total cell precipitation volume are related (see discussion around Fig. 5.40 and the previous point). To make this more explicit we computed changes in conditional percentiles for subsets of present-day and future cells that exceed the P90 value of the peak intensity (estimated for each climate separately). This gives an impression of how the cell structures differ between present-day

and future cells of high intensity. The peak intensity of P90 and above were already discussed (Figure 5.55 top-left panel) and change with at least 4%/K. The conditional percentiles of the other cell properties show that average intensities also increase (but less than the peak intensity, as expected), and almost independently of the conditional percentile chosen (Figure 5.43). Total precipitation volume changes in contrast increase more strongly than the peak intensities. Since we saw that the conditional percentiles of the cell-average intensity could not cause this, it must be the combination of average intensity and area. The conditional area percentiles are indeed higher than those of the average intensity (bottom-right). Thus, cells that exceed the P90 levels of the future not only have more intense peaks but are also larger in size.

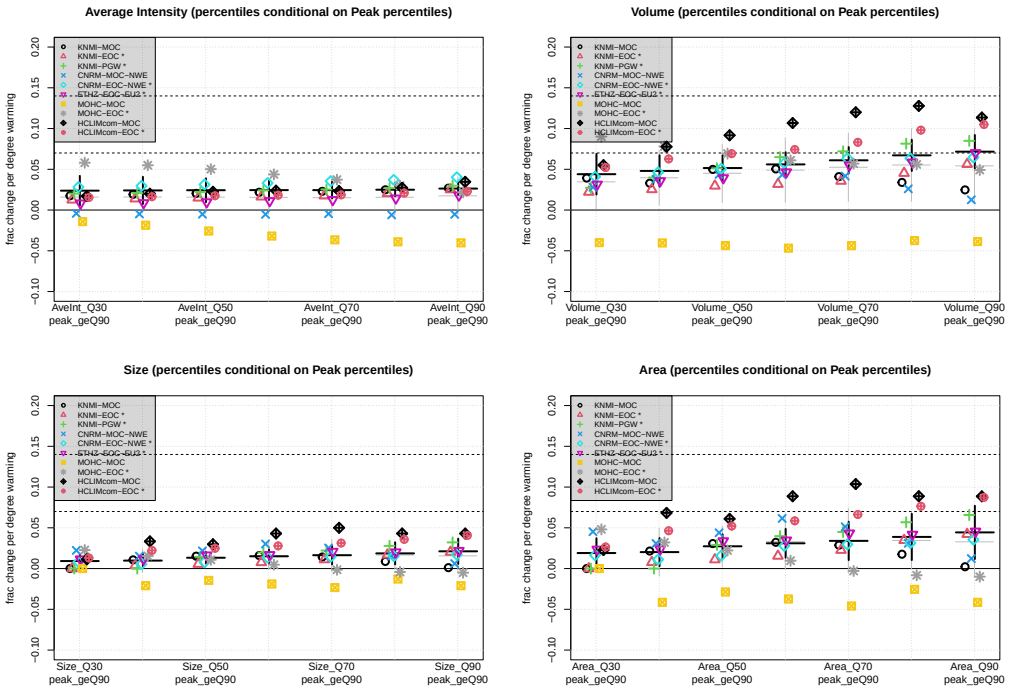

Figure 5.43: Multi-model summary statistics (III): Changes in the conditional percentiles for peak intensities exceeding P90 (note that P90 is computed for present-day and future separately.). Horizontal dashed lines are drawn at 7 and 14 % per degree warming. Other conventions as in Fig. 5.41.

5.13 Windgusts, hail, and lightning

5.13.1 Summary from IPCC report

The occurrence of severe convective storms and the associated severe events, including convective windgust, hail, and lightning, is affected by environmental conditions of the atmosphere, such as CAPE and vertical wind shear. The uncertainty of future changes, however, arises from the changes in the balance between these environmental conditions.

Future projections of severe convective storms are usually studied either by analysing the environmental conditions simulated by climate models, or by a time-slice approach with higher-resolution convection-permitting models by comparing simulations downscaled with climate model results under historical conditions and those under hypothesized future conditions (Kendon et al., 2017).Up to now, individual studies using convection-permitting models gave projections of extreme events associated with severe convective storms in local regions only, and it is not generally possible to obtain global or general views of projected changes of severe convective storms. Prein et al. (2017) investigated future projections of North American mesoscale convective system (MCS) simulations and showed an increase in MCS frequency and an increase in total MCS precipitation amount by the combined effect of increases in maximum precipitation rates associated with MCSs and increases in their size. Rasmussen et al. (2020) investigated future changes in the diurnal cycle of precipitation by capturing organized and propagating convection and showed that weak-to-moderate convection will decrease, and strong convection will increase in frequency in the future.

5.13.2 Hail

Hailstorms are dangerous and costly phenomena that are expected to change in response to a warming climate. As a result of anthropogenic warming, it is generally anticipated that low-level moisture and convective instability will increase, raising hailstorm likelihood and enabling the formation of larger hailstones; the melting height will rise, enhancing hail melt and increasing the average size of surviving hailstones; and vertical wind shear will decrease overall, albeit with limited influence on the overall hailstorm activity, owing to a predominance of other factors. Given geographic differences and offsetting interactions in these projected environmental changes, there is spatial heterogeneity in hailstorm responses. Observations and modelling lead to the general expectation that hailstorm frequency and hail size will increase in most regions of Europe. However, these projected changes show marked spatial and temporal variability. Owing to a dearth of long-term observations, as well as incomplete process understanding and limited number of convection-permitting modelling studies, current and future climate change effects on hailstorms remain highly uncertain.

5.13.3 Additive regression models to an ensemble of 14 regional climate simulations

Rädler et al. (2019) showed that the frequency of damaging convective weather events including lightning, hail and severe wind gusts will likely increase over Europe until the end of this century. They applied a set of additive regression models to an ensemble of 14 regional climate simulations and found that convective instability will increase as a result of rising humidity near the earth's surface. Even though a slight decrease in thunderstorm occurrence in southwestern and south-eastern Europe is projected, the frequency of severe weather will increase throughout Europe, in particular for very large hail. It might be expected that Arctic amplification would lead to a weaker jet stream and, thus lower vertical wind shear, but they find instead that the jet changes little or even increases in situations with convective instability.

Using historic weather data and reports, the European Severe Storms Laboratory (ESSL) in Germany developed a model to predict the likelihood of thunderstorms and related severe hazards across Europe over a 6-hour period on the basis of atmospheric conditions. They applied their

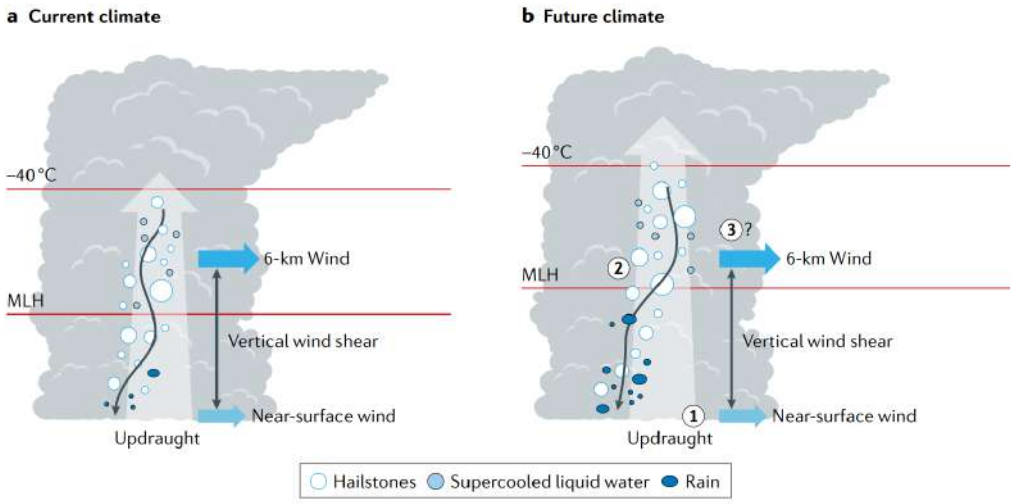

Figure 5.44: Hail- relevant atmospheric phenomena in current and future climates. The expected changes in hail- relevant atmospheric phenomena between the current (panel a) and future (panel b) climates. The numbers in panel b correspond to the following changes: (1) increased low- level moisture leads to increased convective instability and updraught strength; (2) an increase in the melting level height (MLH) leads to enhanced melting of hailstones and a shift in the distribution of hailstone sizes towards larger hailstones; and (3) changes in vertical wind shear may affect storm structure and hailstone trajectories, but are generally overshadowed by instability changes. Figure reproduced from Raupach et al. (2021)

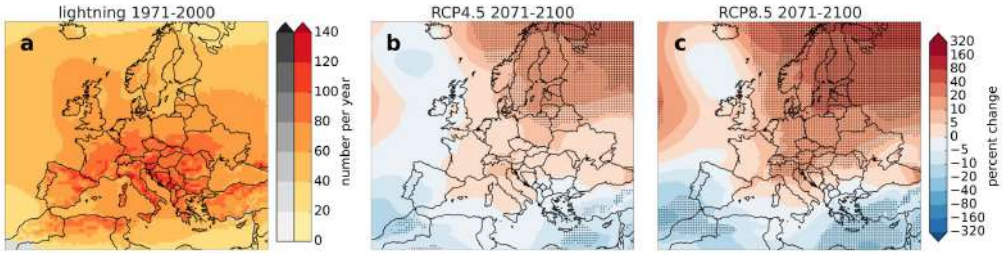

Figure 5.45: Simulated annual 6-hourly periods with lightning in a the historical period (1971–2000) and percentage of change at the end of the century (2071–2100) in the b RCP4.5 and c RCP8.5 scenarios. Trends in b, c are called (very) robust where the change is larger than (twice) the initial standard deviation of the model ensemble. (Very) robust changes are indicated by (large) black dots. Areas where models already diverge greatly for the historical period are displayed in gray. Figure reproduced from Rädler et al. (2019).

model to an ensemble of 14 regional climate models to assess future changes in the frequency of thunderstorm-linked hazards across Europe. Their results cover two carbon emissions scenarios: In one, emissions peak in 2040, whereas in the other, emissions continue to rise. The results show a strong increase in lightning frequency – the number of 6-hour periods with lightning – across
5700 northern and eastern Europe. They predict a smaller increase across western- and central Europe, whereas southwestern and southeastern Europe are likely to see decreases in lightning frequency. Changes are largest in the continuing emissions scenario, with 20% increases in lightning frequency projected in northern and eastern Europe by 2071–2100. For the Netherlands more neutral to a slight increase can be seen from such predictions. Large hail and frequency of convective windgusts

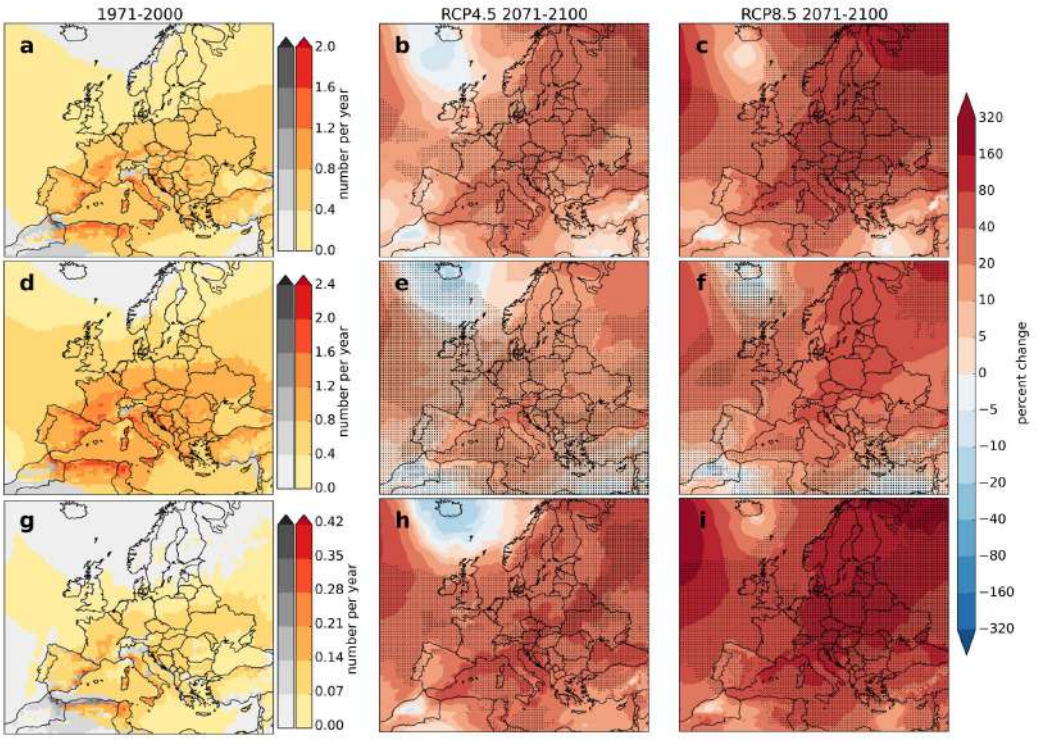

Figure 5.46: As previous figure, but for a–c hail $\geq$ 2 cm, d–f wind gusts $\geq$ 25 m/s, and g–i hail $\geq$ 5 cm. Figure reproduced from Rädler et al. (2019))

of more than 25 meters per second are also predicted to increase, at a larger rate than lightning occurrences.

5.13.4 Summary for the Netherlands

Heavy showers are more common in a warmer climate in all seasons, and generally the heaviest showers increase the most, especially for the day extremes. Information about thunderstorms, hail and gusts of wind is still very limited. Recent research that takes better account of underlying physical processes often gives a more uncertain picture than previous studies based on statistical relationships (Kahraman et al., 2022). Due to the increase in water vapor and the expected stronger vertical movements, the largest hail grains are likely to become larger. In addition, due to warming, the height of the freezing level rises, causing smaller hail grains to melt more often before they reach earth. Gusts of wind and convective wind gusts during showers can become stronger due to more evaporation of precipitation. Whether lightning will occur more often in the Netherlands is uncertain.

5.14 Winter precipitation change in the CPMs

In winter the upper estimate of the changes in rainfall extremes is generally somewhat lower than in the other seasons, as expected because of the lower occurrence of convective rain. However, the changes are substantially higher than those derived from RACMO. Typical changes in RACMO are 4-5 % per degree global warming. From the CPMs we find typically 6-7 % per degree global warming. While the changes here are derived for local extremes (that is, representing ∼10x10 km^2), the higher sensitivity appears to extend to larger scales too. In particular, we are also interested in the Rhine catchment rainfall extremes as the RACMO results appear to be so much lower than the CC prediction (typically on 2-3% increases per degree warming).

We briefly studied the response derived from the two PGW experiment. These runs are in particular useful as they have a high signal-to-noise ratio because most of the natural variability has been filtered out by the approach (Lenderink et al., 2022). The sensitivity derived for Rhine catchment 1-day and 10-day precipitation appears to be close to 7% per degree global warming (Fig. 5.47). The RACMO PGW experiment forced by CMIP6 mean changes gives a sensitivity of only 4% per degree, substantially lower than then CPM results. The long ensemble typically gives less of an response, typically around 3 % per degree.

The higher sensitivity in the CPMs could be due to the PGW approach itself, due to the perturbations used in the PGW approach, but also due to a systematic higher response in the CPMs as compare to RACMO. To investigate further, we also plotted responses for a number of sub regions, The Netherlands, middle part of the Rhine, the high part in Switzerland, as well as the full Rhine catchment above Lobith (Fig. 5.48). From this figure it appears that for RACMO a response of 3-4% per degree is typical for the lower parts, and a response approaching zero for the Swiss part. For COSMO and HCLIM the response is typically 7% per degree for the lower parts, and 4-7 % per degree for the higher parts. In particular, the CPMs therefore affect changes in the rainfall for the higher parts.

We cannot rule out here that the higher response in the two CPMs is due to the specifics of the PGW experiment. Still, it is quite interesting to see how they tell a different and more extreme story of possible changes in Rhine catchment precipitation. For a risk averse user, and if safety is an issue, it could be worthwhile to take these higher responses of winter rainfall extremes into account.

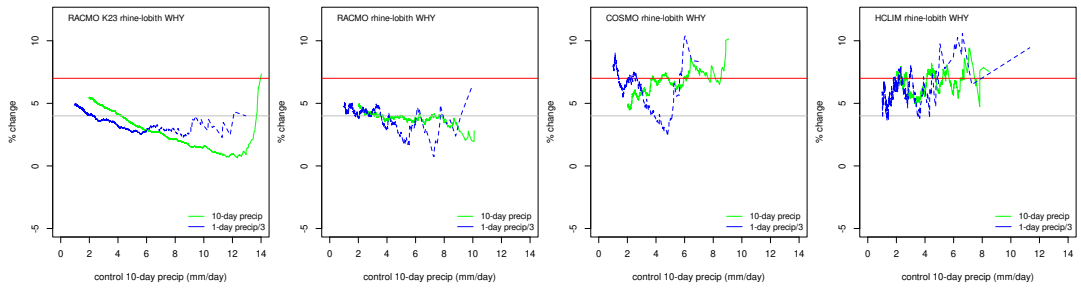

Figure 5.47: Response in changes in winter half year 1-day and 10-day Rhine catchment mean (upstream of Lobith) rainfall per degree global warming (1-day precipitation has been divided by 3 on the x-axis to make it fit). A response of 4% (grey) and 7% (red) per degree global warming is given the two coloured straight lines. Left to right are, RACMO EC-Earth3$_{\text{p5}}$ experiment, RACMO PGW experiment (mean change from all CMIP6 models), COSMO PGW experiment, and HCLIM PGW experiment. We note that the PGW method is used here since that method filters most of the internal variability in winter (Lenderink et al., 2022).

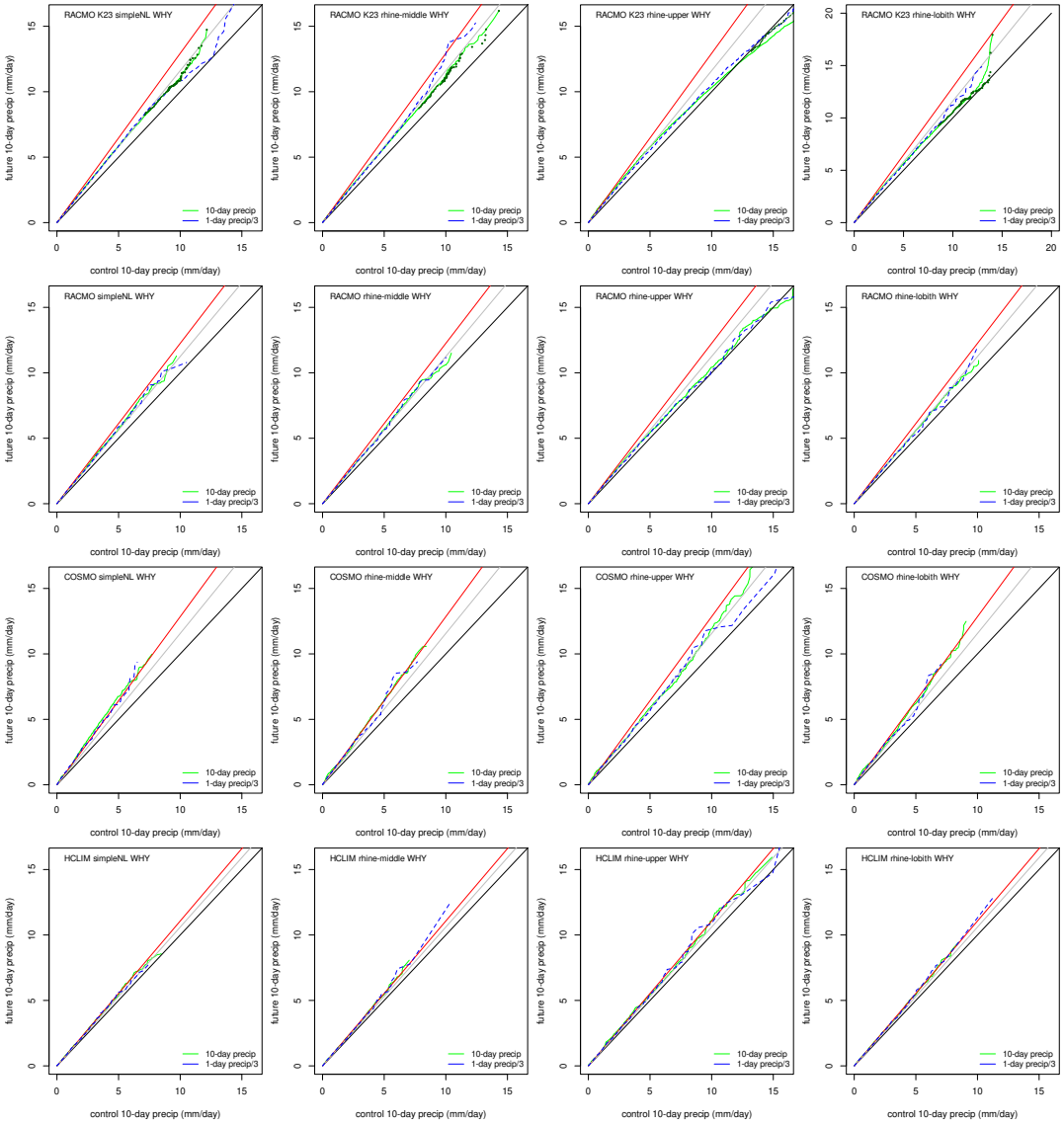

Figure 5.48: Changes in winter half year 1-day and 10-day Rhine catchment mean (upstream of Lobith) rainfall, comparing control period with future in a quantile-quantile plot (1-day precipitation has been divided by 3 to make it fit). A response of 4% (grey) and 7% (red) per degree global warming is given the two coloured straight line. Left to right are precipitation averaged across the Netherlands, lower German part of the Rhine, the high Swiss part of the Rhine, and Rhine catchment upstream Lobith. For top to bottom are RACMO EC-Earth3 $_{\text{p5}}$ scenario (2071-2100 compared to 1991-2020, 3.8 degrees global warming), RACMO PGW experiment (3 degrees global warming), COSMO PGW experiment (3.7 degrees global warming) and HCLIM PGW experiment (1.5 degree global warming).

5.15 Concluding remarks

- **Advances in modeling: convection permitting climate models**. The new generation convection permitting climate models (CPMs) display much more realistic behavior for local (sub-)daily rainfall extremes from convective showers, such as i) much better present-day extreme statistics, ii) much more realistic dependencies on absolute and relative humidity, and iii) much better model agreement. These improvements result from explicitly resolving the largest dynamic structures of convective clouds, in contrast to the statistical prescriptions (called parameterizations) used in common regional climate models (RCMs, such as RACMO) or global climate models (GCMs, such as ECEARTH).

- **Limited availability of CPM results**. Due to the very high computational demands of CPMs – approximately 100 times larger than RCMs when run on a comparable domain – century long simulations over large domains cannot be performed. Typical simulations with CPMs are still 10 years on domains limited to 2000 by 2000 km^2 (with some exceptions of larger domains or longer simulations). For the Netherlands only a limited set of simulations is available, covering only a small part of the possible changes in large-scale conditions.

- **Scenario construction by scaling**. Because the sparseness of the CPM results, we use a simple scaling technique to produce the scenarios. In short, we assume that changes in the rainfall distribution are separable into a frequency change and intensity change. The intensity change is scaled with the dew point temperature rise, and the sensitivity to dew point temperature is derived from the CPM results. Dew point temperature change as well as frequency change is derived primarily from the coarser resolution model results (RACMO/CMIP6).

- **Advances in scenario method**. The scenario method is basically the same as in the previous KNMI'14 climate scenarios (Lenderink and Attema, 2015). However, the present procedure accounts much better for frequency changes and is much more precise in establishing changes in very rare events. Previously changes were derived from a transformed precipitation time series of limited length; now they are derived from a transformed fitted GPD distribution. Therefore, we can compute changes up to a return time of 1000 years. We note however that changes for such large return values remain inherently uncertain. We basically assume here that processes affecting the very extreme events are similar to those affecting the more moderate extreme events (a typical assumption made in many studies; e.g. in climate attribution studies).

- **New information from CPMs in comparison to previous scenarios**. The sensitivity of rainfall intensity to dew point temperature changes has now been derived from the CPM climate runs. At the time of the production of the KNMI'14 scenario, comparable CPM results were not available. The sensitivity to dew point was derived using expert judgement informed by observed relations as well as a very limited set of 1-day case studies with a CPM. Despite the lack of proper CPM modeling results the chosen sensitivities do not differ substantially from the values derived here. In general, therefore the changes in hourly and daily rainfall extremes for the present scenarios are rather similar to the changes given in the previous generation climate scenario (summer).

- **Uncertainty in scenarios**. For each scenario – set by the global temperature rise and the wet or dry sub-selection – the changes in hourly and daily rainfall extremes are given as a upper, lower and central estimate. These bounds are based on the upper and lower end of the sensitives derived from the CPMs. In this process subjective choices have been made, e.g. concerning the region considered to be representative, the weighting of *outlier* model results (an excessively dry model or an simplified model experimental setup) and the assumed functional dependency on return period. More model experiment are definitely needed to further establish these sensitivities. Therefore, we do not assign a probability to the three estimates, and the central estimate is not necessary the most likely. It may also

be that there is a (stronger) systematic dependence on return period, for instance, with the upper bound becoming more likely for the most extreme events (some hints can be found in the data for daily extremes in summer and hourly in winter, but this cannot be reliably assessed with the data).

- **Seasonal dependency** Despite that summer is characterised by the highest frequency of convective showers – and expecting the sensitivity of convective extremes to warming to be strongest because of the positive feedback from latent heating – the (percentage) changes in rainfall extremes do not generally peak in summer. In contrast, changes are generally rather evenly distributed throughout the year. Partly the high sensitivity to dew point in summer is offset by a lower dew point temperature rise and a decrease in rain frequency. The largest possible changes are in spring (for daily: up to 56% at 4 degrees global warming) and autumn (for hourly: up to 62% at 4 degrees warming). In a more extreme drying scenario in summer, such as for example in a simulation by the UK MetOffice model, with a stronger decrease in mean summer precipitation and lower humidity increases, this effect could be even stronger with a future shift of the rainfall extremes from the summer season to spring and autumn (Chan et al., 2020).

- **Convective organisation**. Analysis of a rain cell tracking scheme showed that in general the models project increases in the rain cell size. In the future, the distribution of rain cells shifts to bigger cells. While small cells decrease in number with warming, the biggest cells increase in number.

- **Influence of model physics on summer climate**. In this chapter we also performed a number of RACMO experiments using a pseudo-global warming approach. This approach has also been used to construct the 2019 heat wave in a future warmer climate (Chapter 7). Here, we were mostly interested in a realistic spread in absolute and relative humidity change in comparison with CMIP6. It turned out that it was necessary to modify the physics of RACMO (soil scheme) in order to achieve this goal. In particular, for absolute humidity the EC-Earth3 $_{p5}$ ensemble revealed an anomalously high response (far upper end of CMIP6 range) and resampling did not lead to substantial improvements. Also, for other variables, such as relative humidity, temperature and precipitation, the physics modification in RACMO appear to have a large influence (as large as, or larger than, the difference related to subset of dry11 and wet11 CMIP6 boundaries). This suggests that a considerable part (typically 50 %) of the uncertainty in summer climate response is governed by the soil physics, and how it interacts with clouds, radiation and precipitation. In future scenarios the influence of uncertainty in model physics should therefore be account for in order to span a more realistic range in future summer conditions.

- **PGW experiments versus resampling**. Besides absolute humidity change, the PGW experiments also showed in other aspects a somewhat different view on climate change as compared to the (resampled) EC-Earth3 $_{p5}$ RACMO ensemble, with i) stronger warming at cold days in winter (1.5-2 times global warming), weaker mean warming in summer (slightly below global warming level), and yet stronger warming on hot days (1.5-2 global warming; see also Chapter 7). Decreases in relative humidity in summer are effectively enhanced by the soil modifications, apparently somewhat outside the resampling range ($\sim$1.8 degrees dew point depression increase suggesting -8%, versus -5% change in relative humidity at 4 degrees global warming).

- **Winter large-scale precipitation in CPMs**. The CPMs provide some early indications that changes in large-scale winter precipitation can be larger than anticipated. This is visible for hourly and daily extremes at local scales derived here. Yet, even at 10-day time scales and aggregated over the Rhine catchment area typically changes are between 5-7 % per degree global warming. This would yield a plausible upper change in 10-day extremes over the Rhine catchment area of close to 30% with a warming level of 4 °C. This is substantially

higher than the number derived from RACMO. Yet, we also acknowledge that these are very preliminary results that need to be confirmed by new simulation and analyses.

5.16 Scenario tables

5.16.1 Relative changes at 1 degrees global warming

	DJF (%)				MAM (%)				JJA (%)				SON (%)			
	pres.	future			pres.	future			pres.	future			pres.	future		
0.1	7	4	6	7	5	-1	1	2	8	-6	-6	-6	8	-2	0	1
1	19	4	6	7	16	1	3	6	26	-1	1	3	23	2	5	7
10	30	4	6	7	31	2	5	8	48	2	4	7	42	3	6	8
100	39	4	6	7	51	2	5	9	76	2	5	8	69	4	6	8
1000	46	4	6	7	79	2	6	9	111	3	5	8	105	4	6	8

Table 5.9: relative changes for daily rainfall extremes based on the dry11 scenario at 1 °C global temperature rise.

	DJF (%)				MAM (%)				JJA (%)				SON (%)			
	pres.	future			pres.	future			pres.	future			pres.	future		
0.1	7	4	6	8	5	-1	1	3	8	-2	-2	-2	8	-1	1	3
1	19	4	6	8	16	1	5	8	26	1	3	5	23	4	6	9
10	30	4	6	8	31	2	6	10	48	3	6	9	42	4	7	10
100	39	4	6	8	51	3	7	12	76	3	7	10	69	5	8	11
1000	46	4	6	8	79	3	8	12	111	4	7	10	105	5	8	11

Table 5.10: relative changes for daily rainfall extremes based on the wet11 scenario at 1 °C global temperature rise.

	DJF (%)				MAM (%)				JJA (%)				SON (%)			
	pres.	future			pres.	future			pres.	future			pres.	future		
0.1	2	3	5	6	2	1	3	5	4	-1	1	4	3	3	5	7
1	5	4	5	7	6	1	3	6	13	2	4	7	7	4	6	9
10	8	4	6	8	13	1	4	6	26	3	5	7	13	4	7	10
100	12	4	6	8	25	1	4	6	46	3	5	8	21	4	7	10
1000	18	4	6	8	44	1	4	6	73	3	5	8	31	4	7	10

Table 5.11: relative changes for hourly rainfall extremes based on the dry11 scenario at 1 °C global temperature rise.

	DJF (%)				MAM (%)				JJA (%)				SON (%)			
	pres.	future			pres.	future			pres.	future			pres.	future		
0.1	2	4	5	7	2	1	4	6	4	1	4	7	3	4	6	9
1	5	4	6	8	6	2	5	8	13	4	7	9	7	5	8	12
10	8	4	6	9	13	2	5	8	26	4	7	10	13	6	9	12
100	12	4	7	9	25	2	5	8	46	4	7	10	21	6	9	13
1000	18	4	7	9	44	2	5	8	73	4	7	10	31	6	9	13

Table 5.12: relative changes for hourly rainfall extremes based on the wet11 scenario at 1 °C global temperature rise.

5.16.2 Relative changes at 2 degrees global warming

	DJF (%)				MAM (%)				JJA (%)				SON (%)			
	pres.	future			pres.	future			pres.	future			pres.	future		
0.1	7	8	11	15	5	-1	1	4	8	-14	-13	-13	8	-4	-2	1
1	19	8	11	15	16	2	7	12	26	-2	1	5	23	5	9	14
10	30	8	11	15	31	4	10	16	48	3	8	13	42	6	11	16
100	39	8	11	15	51	4	11	18	76	4	10	15	69	7	12	17
1000	46	8	11	15	79	5	12	19	111	5	10	16	105	7	12	17

Table 5.13: relative changes for daily rainfall extremes based on the dry11 scenario at 2 °C global temperature rise.

	DJF (%)				MAM (%)				JJA (%)				SON (%)			
	pres.	future			pres.	future			pres.	future			pres.	future		
0.1	7	10	14	18	5	-2	2	5	8	-5	-5	-5	8	-2	2	6
1	19	10	14	18	16	3	10	17	26	1	6	11	23	7	13	19
10	30	10	14	18	31	5	13	22	48	6	12	19	42	9	15	22
100	39	10	14	18	51	6	15	25	76	7	14	21	69	10	16	23
1000	46	10	14	18	79	6	16	26	111	8	15	22	105	10	16	23

Table 5.14: relative changes for daily rainfall extremes based on the wet11 scenario at 2 °C global temperature rise.

	DJF (%)				MAM (%)				JJA (%)				SON (%)			
	pres.	future			pres.	future			pres.	future			pres.	future		
0.1	2	6	10	13	2	2	6	10	4	-4	0	5	3	5	9	13
1	5	7	11	15	6	2	7	12	13	3	8	13	7	7	13	18
10	8	8	12	16	13	2	7	12	26	5	10	14	13	8	14	20
100	12	8	12	16	25	2	7	12	46	5	10	15	21	9	15	20
1000	18	8	12	16	44	2	7	12	73	6	11	16	31	9	15	21

Table 5.15: relative changes for hourly rainfall extremes based on the dry11 scenario at 2 °C global temperature rise.

	DJF (%)				MAM (%)				JJA (%)				SON (%)			
	pres.	future			pres.	future			pres.	future			pres.	future		
0.1	2	8	11	15	2	2	8	13	4	2	8	15	3	8	13	19
1	5	9	13	18	6	3	9	16	13	8	15	21	7	11	18	25
10	8	9	14	19	13	3	10	16	26	9	15	22	13	12	19	27
100	12	10	14	19	25	3	10	16	46	9	16	22	21	12	19	27
1000	18	10	15	20	44	3	10	16	73	9	16	22	31	12	20	27

Table 5.16: relative changes for hourly rainfall extremes based on the wet11 scenario at 2 °C global temperature rise.

5.16.3 Absolute values at 4 degrees global warming

	DJF				MAM				JJA				SON			
	pres.	future			pres.	future			pres.	future			pres.	future		
0.1	7	9	9	10	5	5	5	6	8	6	6	6	8	7	8	8
1	19	22	23	25	16	17	18	20	26	24	26	28	23	25	27	29
10	30	36	38	40	31	33	37	41	48	51	56	61	42	48	53	57
100	39	46	49	52	51	55	63	71	76	83	92	101	69	79	87	94
1000	46	53	57	60	79	86	99	112	111	122	135	149	105	120	131	144

Table 5.17: Absolute values for daily rainfall extremes based on the dry11 scenario at 4 °C global temperature rise.

	DJF				MAM				JJA				SON			
	pres.	future			pres.	future			pres.	future			pres.	future		
0.1	7	9	9	10	5	5	5	6	8	7	7	7	8	7	8	9
1	19	23	24	26	16	17	19	22	26	26	29	31	23	26	29	32
10	30	37	39	42	31	34	39	46	48	54	61	69	42	51	56	63
100	39	47	51	55	51	57	67	79	76	88	100	112	69	83	93	104
1000	46	55	59	63	79	89	106	125	111	129	146	165	105	126	141	157

Table 5.18: Absolute values for daily rainfall extremes based on the wet11 scenario at 4 °C global temperature rise.

	DJF				MAM				JJA				SON			
	pres.	future			pres.	future			pres.	future			pres.	future		
0.1	2	3	3	3	2	2	3	3	4	4	4	5	3	3	4	4
1	5	5	6	6	6	6	7	8	13	13	15	16	7	8	9	10
10	8	9	10	11	13	14	15	17	26	29	31	34	13	16	17	19
100	12	14	15	16	25	26	29	31	46	51	55	61	21	25	28	31
1000	18	21	22	24	44	46	51	55	73	81	89	97	31	37	41	45

Table 5.19: Absolute values for hourly rainfall extremes based on the dry11 scenario at 4 °C global temperature rise.

	DJF				MAM				JJA				SON			
	pres.	future			pres.	future			pres.	future			pres.	future		
0.1	2	3	3	3	2	2	3	3	4	4	5	6	3	4	4	4
1	5	6	6	7	6	7	7	8	13	15	16	18	7	9	10	11
10	8	9	10	11	13	14	16	18	26	31	35	39	13	17	19	22
100	12	15	16	17	25	27	30	34	46	55	61	68	21	27	30	34
1000	18	21	23	26	44	47	53	60	73	87	97	108	31	39	44	50

Table 5.20: Absolute values for hourly rainfall extremes based on the wet11 scenario at 4 °C global temperature rise.

5.17 Appendix: Other supplementary information

Institute	Model	Simulations (rcp85 based)	Extra info
GCM forced			
CNRM	AROME41	HIST (1996-2005), MOC (2041-2050), EOC (2090-2099)	NWE-domain
KNMI	HCLIM38	HIST (1996-2005), MOC (2041-2050), EOC (2090-2099)	EC-Earth+RACMO
MOHC	HadREM3	HIST (1998-2007), MOC (2040-2049), EOC (2096-2105)	REU2-domain cutout
PGW			
ETHZ	COSMO	CTL (2000-2009), PGW (dTglob=+3.7K)	EU2-domain cutout
KNMI	HCLIM38	CTL (2008-2018), PGW (dTglob=+1.5K)	ERA-Interim+RACMO
Not used			
CNRM	AROME41	HIST (1996-2005), MOC (2041-2050), EOC (2090-2099)	ALP3-domain
ETHZ	COSMO	HIST (1996-2005), MOC (2041-2050), EOC (2090-2099)	ALP3-domain
HCLIMcom	HCLIM38	HIST (1996-2005), MOC (2041-2050), EOC (2090-2099)	ALP3-domain

Table 5.21: CPM simulations available for the cell-tracking analysis. In the table 'MOC' stands for middle-of-the-century, 'EOC' for end-of-century. Some simulations listed as 'not-used' were discarded because their domain did not cover a substantial fraction of the target area.

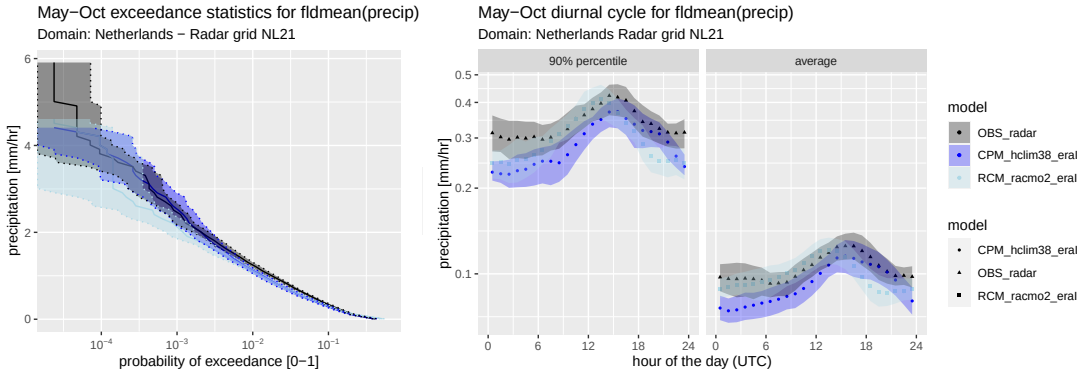

Figure 5.49: As in Figure 5.37 but for hourly spatial averages.

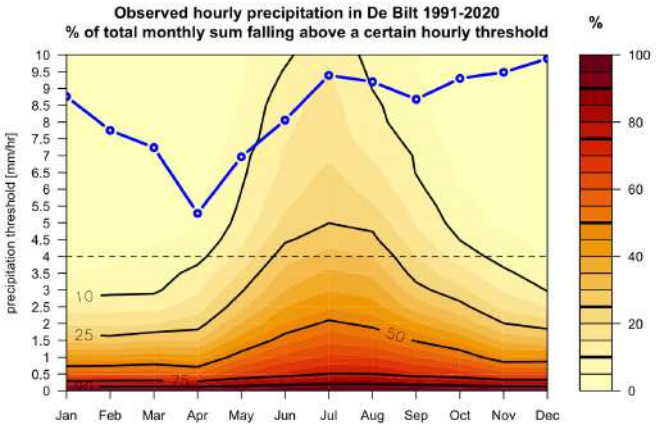

Figure 5.50: Observed precipitation in De Bilt (Netherlands). Shading shows percentage of total monthly precipitation falling in hourly amounts above a certain threshold (y-axis). The horizontal black line denotes the 4mm/hr threshold used in this study. The blue line with markers shows the monthly percentage of the total annual precipitation (using the same scale as the y-axis on the left, but with different units [%]).

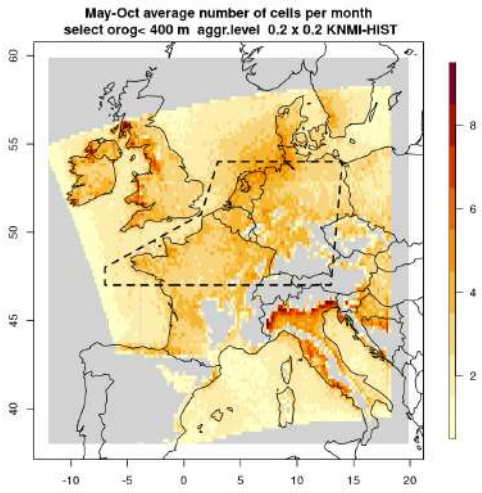

Figure 5.51: Number of cells in the HCLIM simulation KNMI-HIST. The dashed box is referred to as the NWEbox. Cells are used that have a center of (precipitation) mass within this box and below an altitude of 400m.

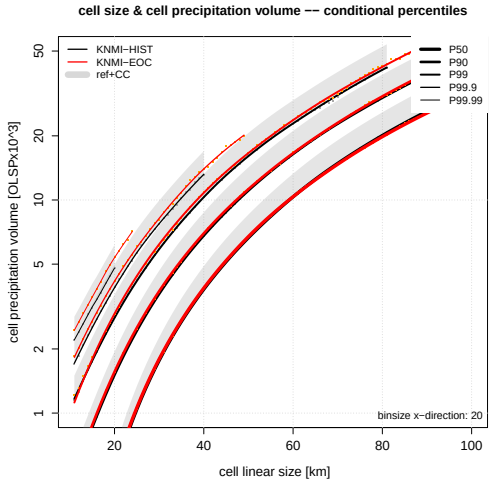

Figure 5.52: As in Fig. 5.40 but for cell total precipitation volume.

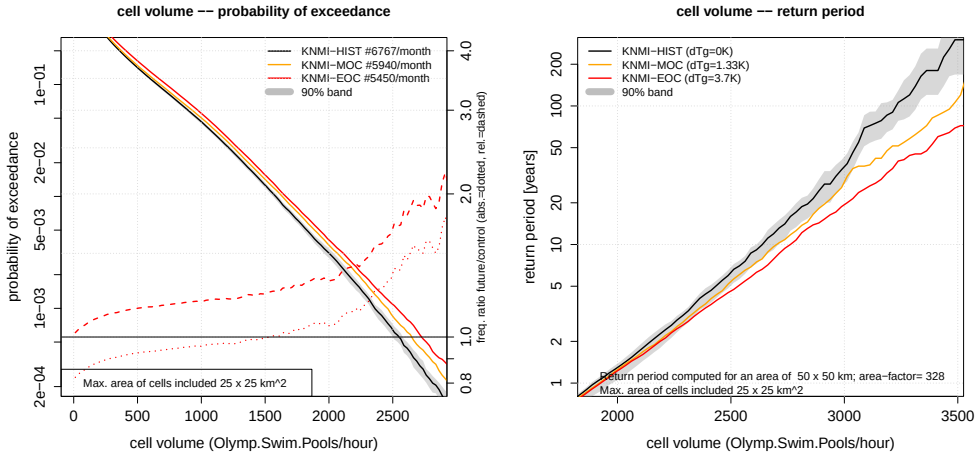

Figure 5.53: As Fig.5.38 but for cell volume. Top row: maxima cell area included 25x25 km^2. Tracking threshold used: 4mm/hr.

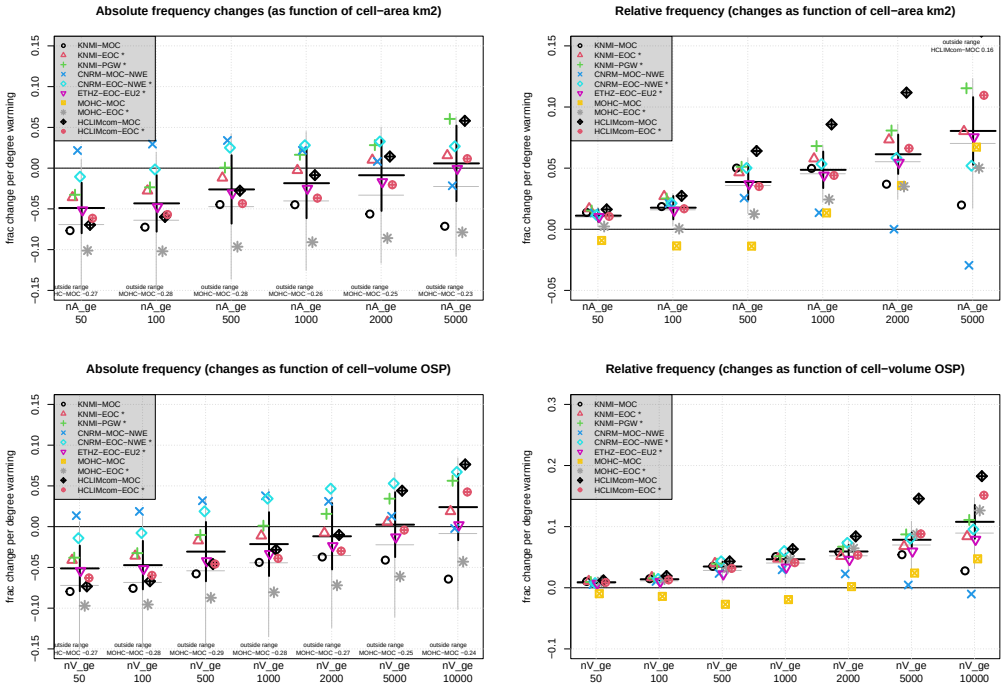

Figure 5.54: Multi-model summary statistics. Frequency change per degree global temperature increase for: (top row) cell area; (bottom row) cell total precipitation volume. Other conventions as in Fig. 5.41.

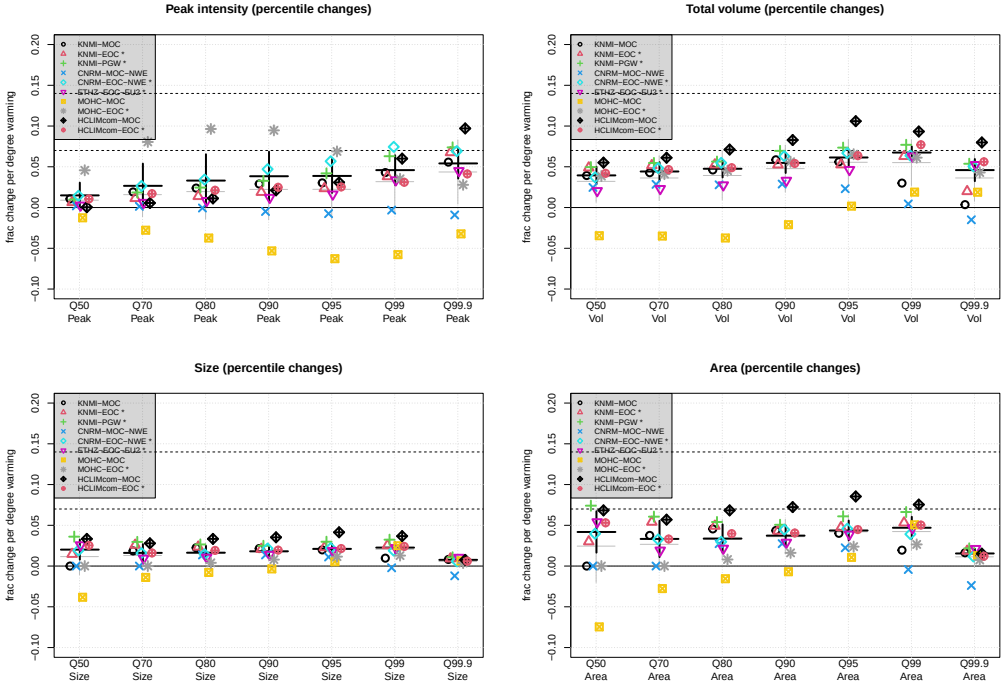

Figure 5.55: Multi-model summary statistics. Percentile changes per degree global temperature increase. Horizontal dashed lines are drawn at 7 and 14 % per degree warming. Other conventions as in Fig. 5.41.

Chapter 6

Climate change in cities

6.1 Introduction

Cities as centres of economic activity are main contributors to climate change. The observed trend in urbanisation worldwide reflects the attraction this activity has on the populace. The continuation of this trend in the future is explored in the shared socioeconomic pathways. SSP's define the baseline worlds that might occur without climate policy. These pathways lead to future emissions and warming levels. SSP's with associated representative concentration pathways RCP's are the drivers of the greenhouse gas concentrations that are prescribed to the CMIP climate projections.

As the urbanisation trend results in an increasing fraction of the world's population living in cities, cities are more and more becoming a focus for climate change impacts and adaptation measures. Cities and climate change are thus related through both cause and effect. In addition, it is a well known fact that cities through the way they are built modify the local energy and water balance and thus affect the local and regional weather and climate.

To study urban climate change and its impact in the framework of the KNMI climate scenario's the full range of scales from global to local must be bridged. This can only be achieved through downscaling using a chain of models. At the time of preparation of this document the highest resolution of data available came from the mesoscale climate model HCLIM that was used to downscale information from the RACMO regional climate model, provided from the EU-CORDEX regional downscaling experiment based on RCP8.5 runs of CMIP5. HCLIM provided results for a historic period 1995-2005, a mid-century period 2040-2050 and an end-century period 2090-2100. HCLIM contains a town energy balance module (Masson, 2000) that models the modification of the local climate by cities. This urban effect is not represented by the larger scales of the global and regional models.

At the resolution of the HCLIM model, that has a grid point distance of 2.5 km, the representation of the climate in the city is still coarse. Even Amsterdam, the most populated city, is only covered by 35 grid boxes. To study the city climate at the scale of streets and blocks that are relevant to impacts and adaption measures further downscaling with micrometeorological models or with parameterisations derived from these micrometeorological models or observation studies is required.

In this chapter the results of the HCLIM model are analysed for the additional information over the regional model it provides, in particular with respect to the question whether the modification by the city of the regional climate and the contrast between the climate of the city and its surroundings, e.g. the urban heat island, are themselves sensitive to climate change. In addition pertinent literature is evaluated with respect to the possibility of further downscaling of these results.

6.2 Observing and modelling of the city climate

The study of the effect of urban areas on the local climate can be dated back to the work of Howard (1833) in the early 19th century. His measurements at positions in the city of London and its surroundings indicated the existence of an urban heat island. That the urban climate is still very much an active area of research indicates that, while conceptually the causes of the urban-rural contrast are well understood as a result of differences in the energy and water balance, in practice the observation and modelling of the urban climate remains a challenge. Because the urban climate depends on urban form, urban fabric, siting and regional climate, results of a study at a particular site, for instance with respect to the daily and seasonal variation of the urban heat island, may not easily transfer to other sites, or be generalised. This is often acerbated by incomplete descriptions of the experiments and conceptually different definitions of the temperatures evaluated, e.g. the surface urban heat island (SUHI) as observed by satellites and the canopy urban heat islands (CUHI) observed in-situ (Stewart, 2011).

Lately micro-meteorological models have been employed to model the urban climate in detail. To isolate the impacts of urban form and fabric from geography on urban heat and human thermal comfort Nice et al. (2022) constructed a set of 9814 idealised scenarios spanning the urban parameter space, from which detailed heat risk maps for Australian cities were derived. Validation proved this method can indeed isolate form and fabric from geography and regional climate and may thus be a candidate for the downscaling of the regional climate to city scale.

Stewart et al. (2021) studied the diurnal evolution of the urban heat island to explain differences observed in the timing of the maximum urban heat island in different climate conditions relative to the idealised case of Oke (1982). Oke constructed the idealised case for clear calm summer weather conditions in a moderate climate and found reduced afternoon cooling leading to relatively warm nights in the city, but no great difference in midday temperatures. Stewart et al. found that thermal inertia plays an important role. In general urban temperatures will be higher than rural temperatures, but low thermal inertia of the rural landscape, as in the case of dry soils, may result in rapid warming and higher rural temperatures midday. Another result of this study is the importance of distinguishing surface temperatures from the air temperature when calculating impacts and the proper identification of the horizontal and vertical surfaces that contribute to the impact, for instance their contribution to the radiant temperature when calculating a thermal comfort index.

If, as these two examples indicate, it is indeed possible to isolate direct effects of urban form and fabric from the underlying climate it should be possible to study and treat them separately, in particular when evaluating adaptation measures in the current context. Unless of course climate change forces structural changes in the environment, such as changes in vegetation and/or drying of the soil that is not countered by active watermanagement.

A partial alternative to expensive micro-meteorological modelling would be to employ parameterisations derived from observations. An example is given by Theeuwes et al. (2017) who demonstrate through dimensional analysis that, at least for several Western European cities, the daily maximum of the CUHI can be diagnosed from the local climate, given by the daily mean incoming radiation S, diurnal temperature range DTR and windspeed U and the urban form and fabric given by the sky view factor SVF and vegetation fraction f_{veg}:

$$UHI_{max} = (2 - SVF - f_{veg}) * \sqrt[4]{\frac{DTR * S}{U}} \tag{6.1}$$

Within the bounds of applicability of this diagnostic relation ($0 < f_{veg} < 0.4$; $0.2 < SVF < 0.9$) the RMSE of UHI_{max} voor cities in the Netherlands and surrounding countries is smaller than 1^{o}C. The maximum UHI_{max} for the investigated cities is of the order of 7^{o}C.

This relation where applicable also provides an indication of the development of the urban heat island under climate change. The trend in the observed diurnal temperature range is much smaller than the trend in the minimum and maximum temperature.

Figure 6.1a shows the evolution of the diurnal temperature range from 1900 onward. This diurnal temperature range is strongly correlated to the incoming radiation and the variation thereof

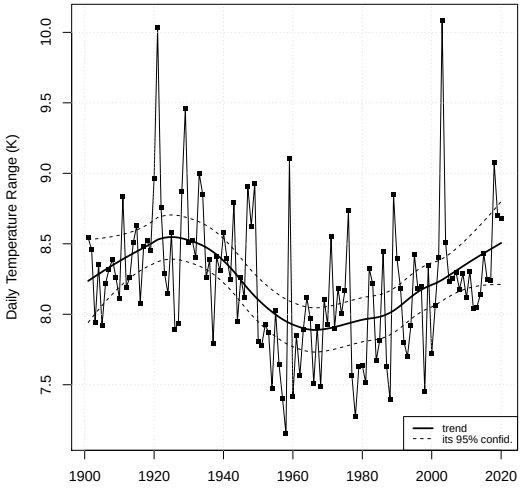

(a) Historical variation of the diurnal temperature range at De Bilt

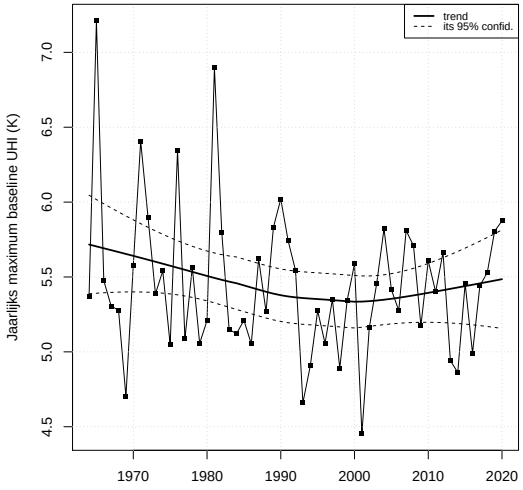

(b) Regional background value of UHI at De Bilt

Figure 6.1: Variations and trends in diurnal temperature range and the meteorological factor in UHI_{max}

due to aerosol concentrations (dimming and brightening effects.) The absence of a consistent trend indicates that the climate change effect on the urban heat island is probably small. For the period where simultaneous observations of temperature, radiation en windspeed are available the absence of a consistent trend outside the range of year to year variation this finding is supported, see figure 6.1b. As will be discussed below on the basis of local downscaling with the HCLIM model this probably also holds for the future.

The diagnostic relation has limitations. Because it is based on a selection of observations it does not account for days with unfavourable conditions such as fog and rain. Because it focusses on the instantaneous UHI and not its history it necessarily neglects processes such anthropogenic heat and heat storage. Moreover, the diagnostic is local and must be supplemented by the underlying spatial variation of the landscape and climate when studying the total effect of climate change on the city and future weather.

Figure 6.2 shows the spatial differentiation of temperatures in the surroundings of Amsterdam for a summer and a winter day in 2017. These maps were calculated by the UrbClim model and are available through the Copernicus Climate Change Service C3S. The spatial distribution of temperature is influenced by the proximity of large water surfaces and by large scale weather, that provides cooling in the city from the environment, and advects plumes of city heat to the rural landscape.

How climate change affects the urban heat island is an important question in relation to impacts and adaptation, but not the only one. Cities modify the local atmospheric boundary layer through changes in the energy and water balance and through this the weather over the city and in its surroundings. In particular this can change the local precipitation climate. Daniels et al. (2016) have determined this urban effect by analysis of daily precipitation amounts from the voluntary observation network of the Netherlands. They found an average increase of 7% due to the influence of cities. This effect was strongest in the summer months, and in particular in situations of low wind. This indicates that cities contribute through the initiation and modification of convective showers. Urban heat and aerosols may be a cause. Because of its proximity to the area studied the

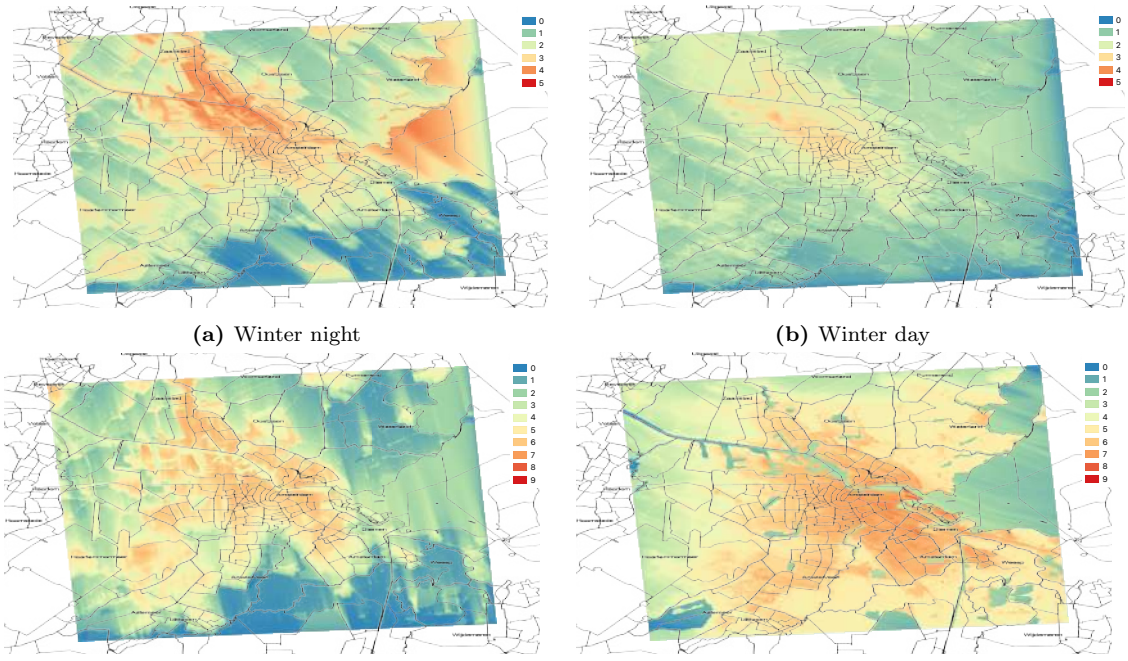

(a) Winter night **(b)** Winter day

(c) Summer night **(d)** Summer day

Figure 6.2: UrbClim simulations of Amsterdam surface temperatures

North Sea cannot be ruled out as a contributor to the observed effect. However, when accounting for this contribution, Daniels et al. still find an urban effect.

As official rain gauges are situated outside of cities these results can not be directly applied to the precipitation in the city itself. In an alternative study Overeem (2014) used hourly sums of precipitation from the KNMI climatological radar data set, calibrated by the rain gauge network. He finds an average 3.5% difference in precipitation between urban and rural pixels. This increase in precipitation is particularly noticeable north of city of Rotterdam and over the city of Amsterdam. However, the uncertainty in the determination of the urban-rural contrast is larger than the observed effect, which therefore may not be significant. A further analysis of 15 and 60 minute precipitation sums for increasing thresholds indicates that for the extreme levels of precipitation that are relevant for urban watermanagement rural and urban environments can not be distinguished. Intuitively this can be explained as a result of extreme precipitation events resulting from the organisation of convective events on scales that are larger than the limited dimensions of Dutch cities.

6.3 Downscaling with Harmonie Climate HCLIM

The operational convection permitting weather model Harmonie has been adapted for the downscaling of regional climate models by the international HCLIM project. A description of the model is given in chapter 7. It is important to note that the model uses a town energy balance module TEB (Masson, 2000) to represent the effect of urban areas. It currently uses a grid point spacing of 2.5 km. The smallest scales that can be confidently modeled on this grid are of the order of 10km. As Dutch cities are relatively small, care should be taken when making a detailed interpretation of the model results at intra-city scales.

This also implies that care should be taken when interpreting the the output of HCLIM directly in terms of impacts and their trends, in particular when these impacts are related to the exceedance of thresholds and trends are related to changes in extremes. Wouters et al. (2017) show that dynamical downscaling is only a first step in the modelling of trends in impact indicators, in their

case a heat stress indicator. Schwingshackl et al. (2021) discuss how the heat stress indicator chosen should be application specific, and how the trends of these indicators in a warming climate may vary considerably. While the KNMI'23 scenarios intend to be general, and in a sense application agnostic, it is of course true that their true value will only be realised through further analysis of climate change impacts and the evaluation of adaptation measures. This further analysis naturally should focus even more on the urban context, as the additional urban heat implies that critical thresholds will be more readily exceeded and urban density implies that the exposure is greater and health effects, excess mortality and production losses will be more significant and trends in these will be greater than those in global mean temperature.

HCLIM has been used to downscale results from the EU-CORDEX runs of the ECEARTH-RACMO model chain for the RCP8.5 scenarios from CMIP5. As this is a computationally intensive process calculations were limited to three 10 year periods for the historic climate 1995-2005, mid-century 2040-2050 and end-century 2090-2100. Results were extracted for the location of the 40 largest Dutch cities and the sites of the automatic weather stations of KNMI, airports and North Sea platforms.

To verify the HCLIM results a comparison was made between the history run of the model and observations for the same period at the automatic weather station of KNMI in De Bilt. Figure 6.3 gives the results for the mean per decade (10 day period) as a scatterplot and marginal distributions. As this shows there is a good correspondence between the HCLIM historical run and observations but also quite some spread, in particular for the warm and cold extremes. This is more clearly shown by overlaying the marginal distributions of the daily mean temperature, the daily maximum temperature in summer, and the daily minimum temperature in winter (figure 6.4). The model has a cold bias, in particular in the maximum temperatures, for instance resulting in 24 modeled tropical days while 46 were observed. This cold bias in not a simple shift in temperature, as is indicated by 51 icedays modeled where 83 were observed. Climate and climate change indicators related to extremes therefore can not be inferred from the model output without proper calibration, e.g. quantile mapping. This is a topic for later study.

The focus here lies on the contrast between urban and rural areas and the effect climate change possible has on this. To evaluate this effect in the context of the model a comparison is made between forecasts at the position of the automatic weather station at De Bilt, considered to be in a rural setting, and a point in the centre of Utrecht, the fourth largest city in the Netherlands, at 5 km from De Bilt. Figure 6.5 shows the median temperature difference between these two points for the summer months as a function of the time of day (blue line indicates the history run). There is a distinguishable urban heat island effect. It has a diurnal variation that conforms to the variation reported in literature for a moderate sea climate, but its amplitude is less than 1°C. This is considerably less than the canopy heat island reported in literature, but more consistent with the findings of Dirksen et al. (2020) who analysed the daily mean temperature from crowdsourced observations at a scale of 1x1 km. At the still rather large scales represented in the model the urban temperature should not be seen as a canopy temperature. It is more a temperature that is representative of the overall energetic effect of the urban boundary layer on the atmosphere. Additional dynamical and/or statistical downscaling is needed to calculate the canopy heat island.

6.4 Evolution of the future climate

Figure 6.5 shows for Utrecht and for Amsterdam, by comparison of the diurnal variation of the UHI in the historical, mid-century and end-century climate, that the urban effect does not change much due to climate change. Of course, in the context of the model and at the scales represented. It was argued above, based on historical observations, that the canopy urban heat island, when modeled using the empirical relation derived by Theeuwes et al., has not changed greatly, apart from the dimming and brightening of the incoming radiation due to historical changes in air quality. Figure (climate change utrecht), graphing aspects of climate change for Utrecht, shows that, while there are significant changes in the overall temperature, the daily range of temperatures does not seem to be affected by climate change. This is consistent with the UHI in the model being constant and

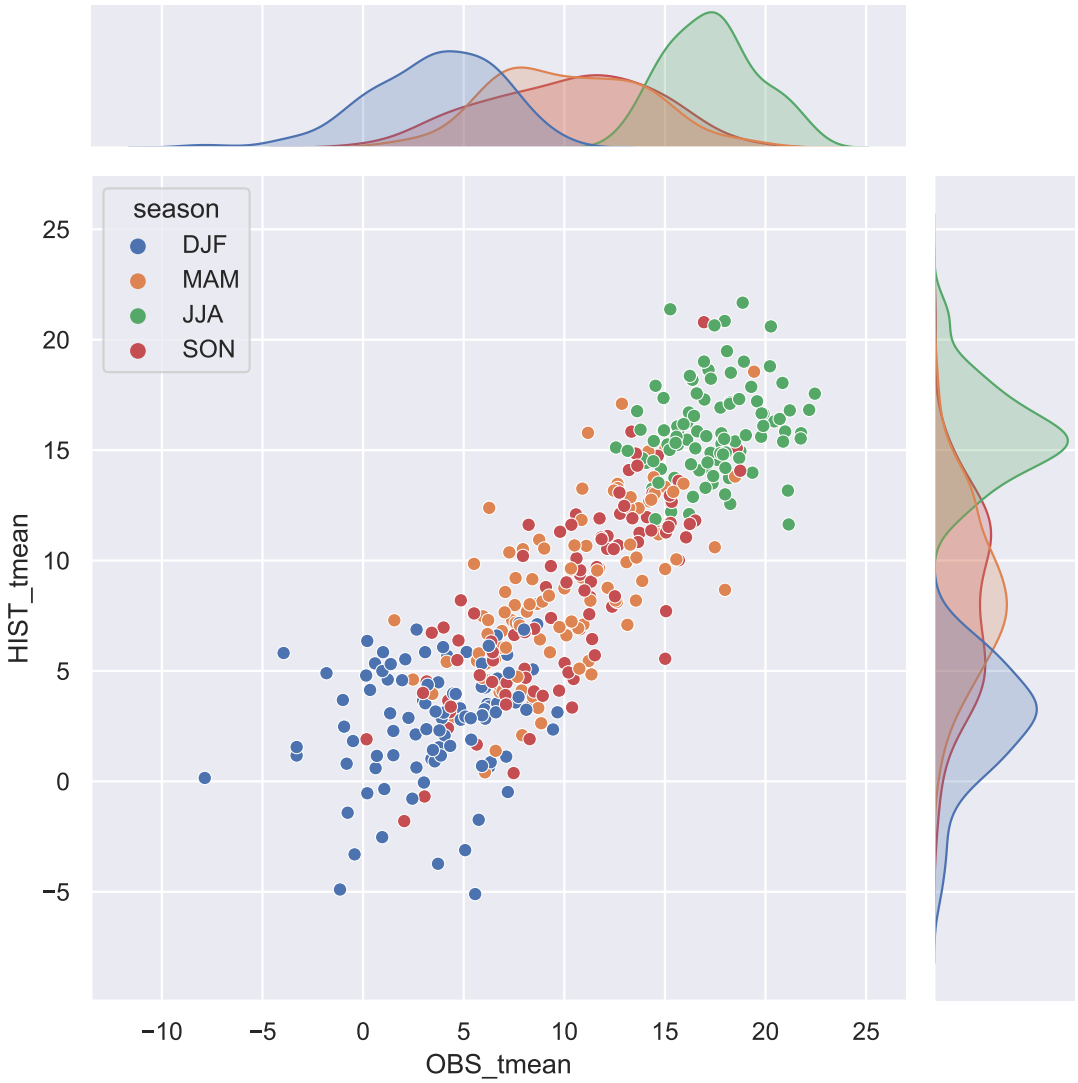

Figure 6.3: Scatterplot and marginal distributions of decadal mean temperature, comparing the historical run vs. observations at De Bilt

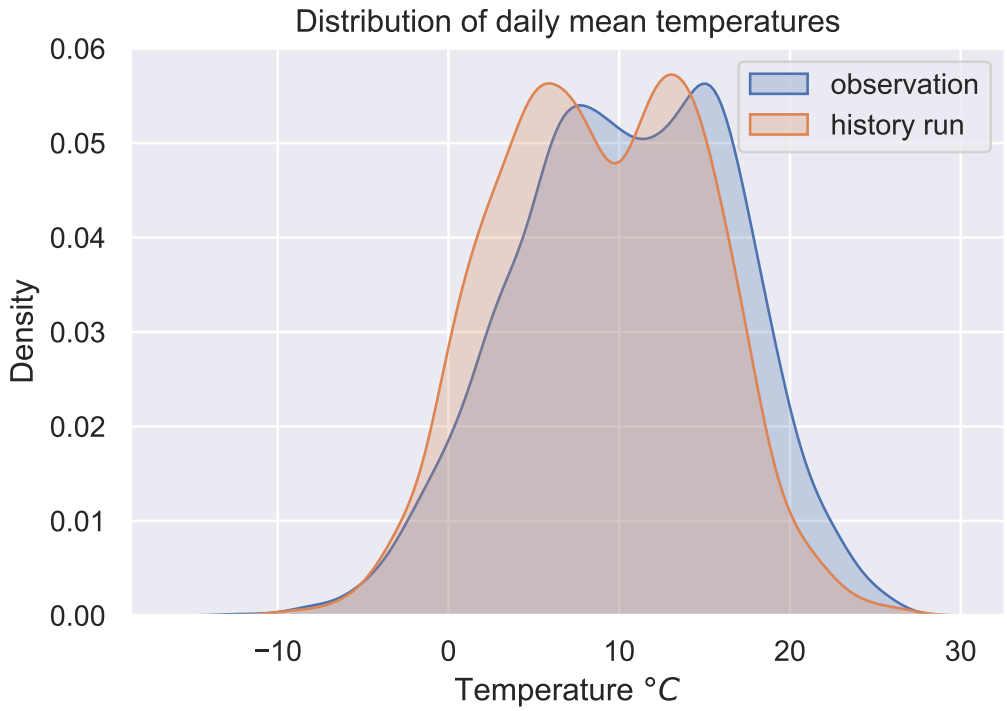

(a) daily mean

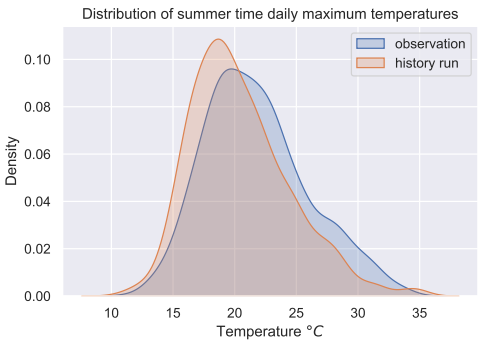

(b) summer time daily maximum

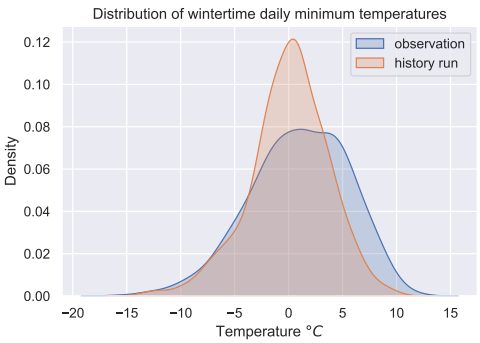

(c) winter time daily minimum

Figure 6.4: Comparion of observed and modelled marginal distributions of daily mean, maximum and minimum temperatures

(a) UHI Utrecht

(b) UHI Amsterdam

Figure 6.5: Urban heat islands of Utrecht and Amsterdam in the current and projected future climate

indicates that this may similarly be true for the CUHI at intra-city scales. This is an important finding as it supports the separation of the local urban effects from climate change effects. These urban effects and climate adaptation measures may be studied in the current climate and results from detailed observation studies and micrometeorological models may be superposed on regional climate projections. This would be an alternative to further dynamical downscaling. However, this would not account for structural changes in the rural environment due to climate change, such as changes in roughness or the drying of soils, that are not now included in the downscaling model, but might affect the UHI and its diurnal variation (Stewart et al., 2021).

Dutch cities are small relative to the scales in HCLIM, the high resolution climate model, and they are all similar in composition. Given that the total climate change may be seen as the superposition of urban effects and regional climate change the local differences in temperature between cities can be attributed to differences in the regional climate in which they are set. Figures 6.7 and 6.8 compare the climate projections for Den Haag, a coastal city, to those for Maastricht, an inland city. The graphs show both the median monthly climate as a line and the year to year spread as a coloured band. Clearly all temperatures increase, in particular in the second half of the century, and these increases exceed the variability. The proximity of the North Sea somewhat mitigates the heat for coastal cities. For inland cities maximum temperatures over 40^{o}C are not unlikely at the end of the century, accounting also for the cold bias of the model. It must be said that the coastal effect depends on the accuracy of the modelling of sea surface temperatures, but these have not been independently verified.

Sea surface temperatures and the proximity of the coast will also contribute to the precipitation climate. As the graphs show the monthly precipitation sums are highly variable, but the median monthly precipitation shows a change in the precipitation climate that has been described in other chapters of this report (3.2; 5). Wintertime precipitation increases, but there is a drying in spring and summer. For coastal stations there is a marked increase of precipitation in autumn but also a marked increase in variability. This effect reduces with the distance to the coast.

The effect of the North Sea has been indicated as a possible complicating factor in the analysis of the effect of urban areas on the precipitation climate of the city and its nearby surroundings in the observation study of Daniels et al. (2016) They found an increase in precipitation under the influence of cities in particular for the summer months under low wind conditions. They assumed this could be attributed to the urban heat affecting the boundary layer development over the city. Given that the Netherlands is a densely populated country with a large number of urban areas in close proximity to each other, it is expected that local and remote urban effects can be difficult to disentangle in a model such as HCLIM, resolving scales comparable to the average city size. Moreover, as Overeem (2014) found in his analysis of hourly sums of calibrated radar observations, the variability of precipitation sums at the radarpixel scale obfuscates the analysis of urban-rural differences. In particular contrasts in extreme precipitation amounts can

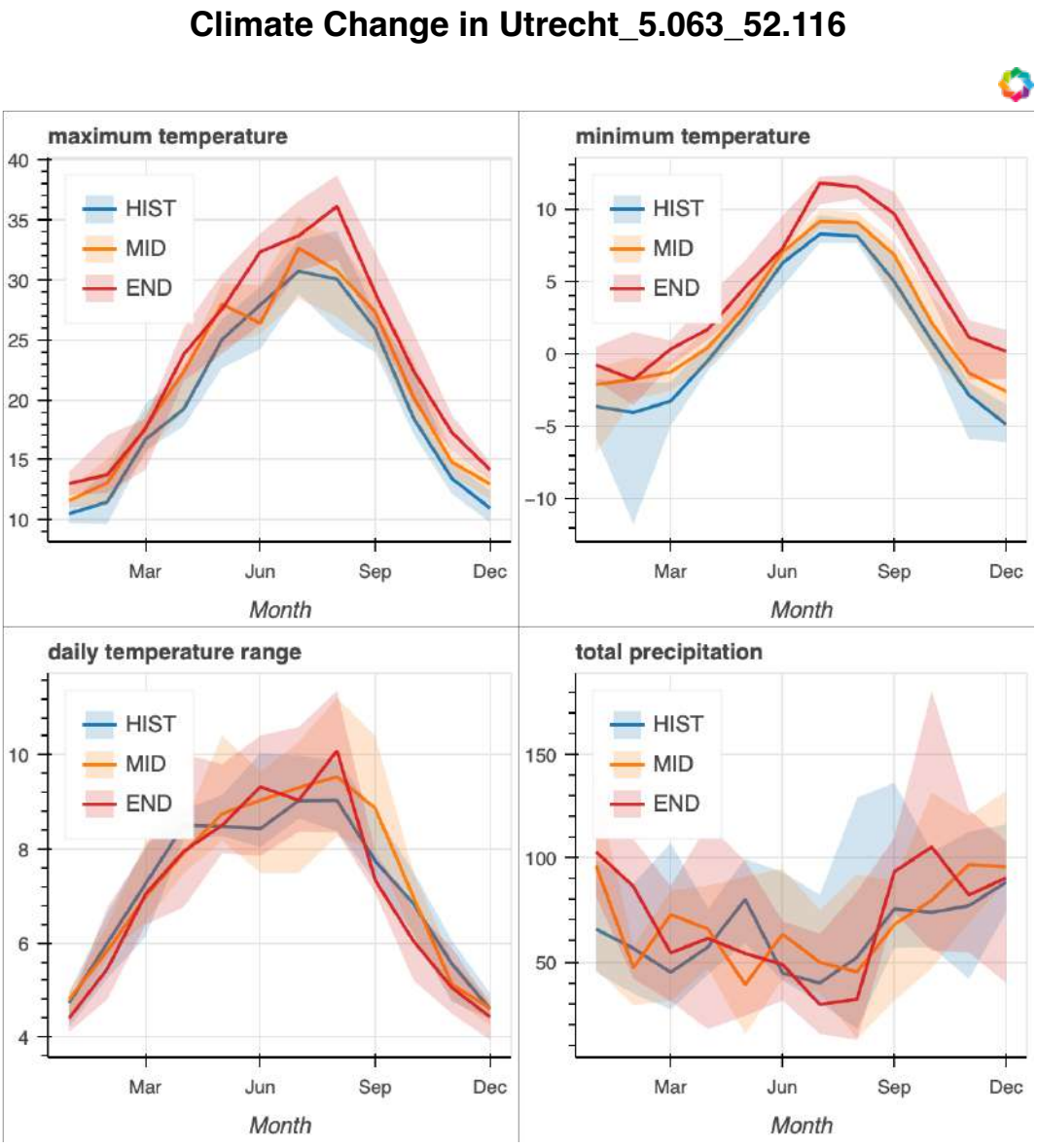

Figure 6.6: Climate change in Utrecht

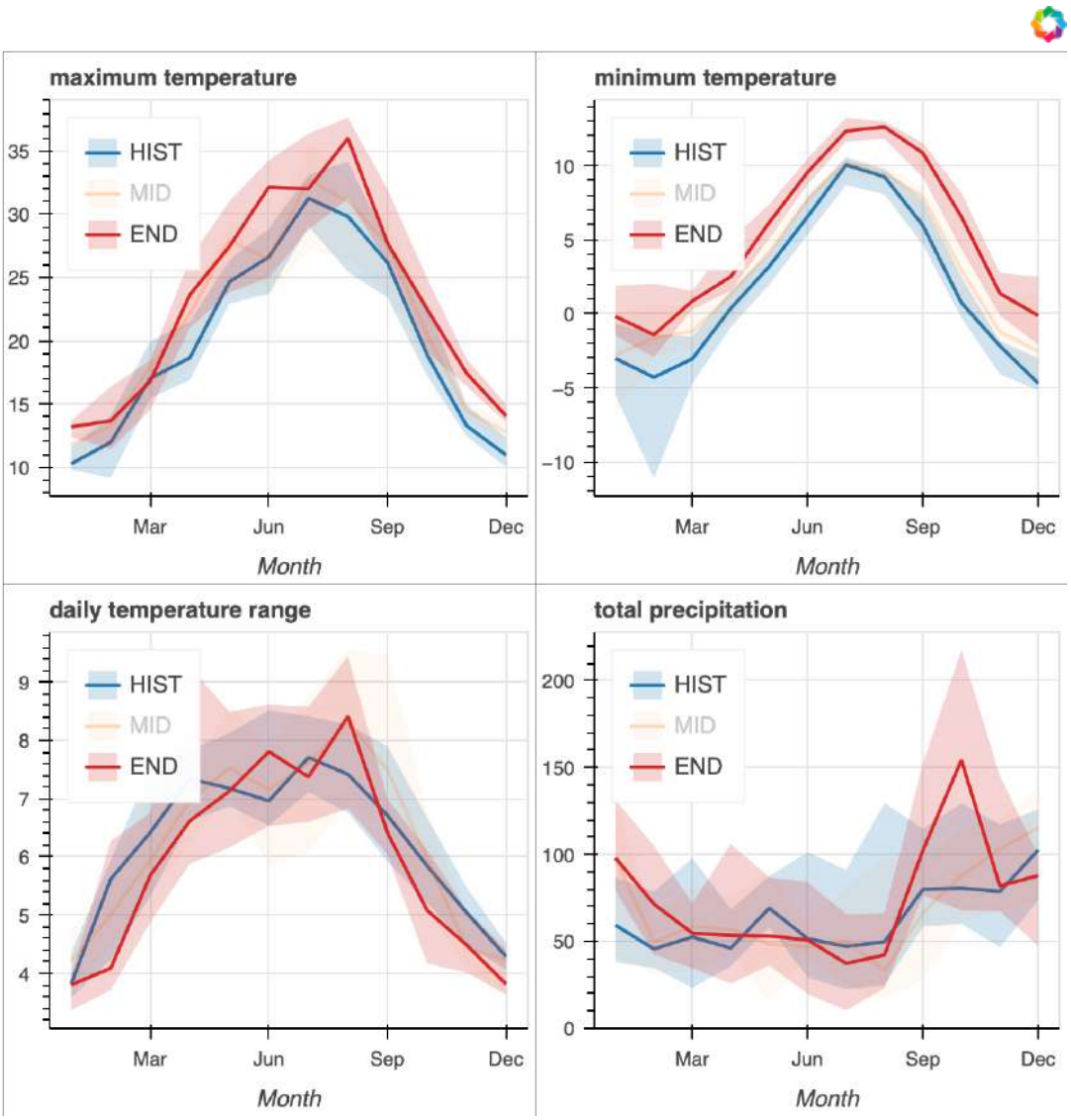

Figure 6.7: Climate change in The Hague

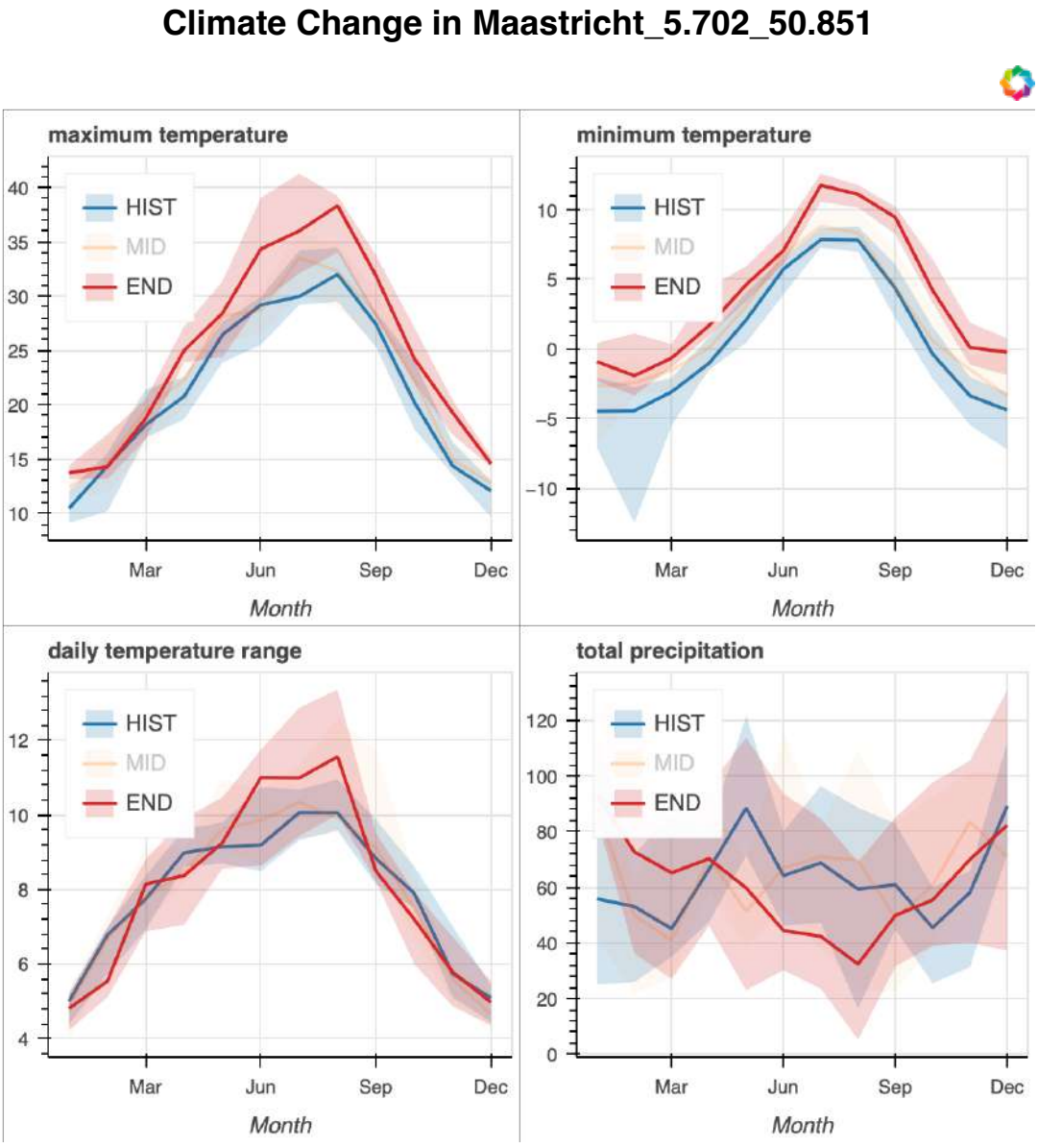

Figure 6.8: Climate change in Maastricht

not be determined significantly. Intuitively this may be explained as a result of the fact that the largest precipitation events, e.g. mesoscale convective complexes and squall lines, result from the organisation and advection of convection on scales much larger than the limited size of Dutch cities. The analysis of urban effects on precipitation will require modelling with a higher, possibly hectometric resolution, but may eventually not be of added value to the analysis of the impact of extreme precipitation events in urban areas.

6.5 Keypoints

Models such as HCLIM introduce the effect of urban areas on the regional climate but are still too coarse to confidently attribute temperature and precipitation effects to aspects of the city morphology. It can be argued, on the basis of historic observations and model studies, that the total local climate change in cities is a superposition of regional climate change and the modification of the local climate by urban form and fabric, where this modification is not in itself affected by climate change. Separation of the two then is the way forward. This requires further development of models such as HCLIM to run at higher resolutions to properly model the effect of the city on the regional climate. This development is underway in the WCRP-CORDEX flagship pilot study URB-RCC. Parallel to this the development of statistical downscaling, using detailed observations in and above the city, dynamical downscaling using micro-meteorological models and probably a combination of the two will allow detailed assessment of changes in the urban canopy, and links to impact models and adaptation measures. Again developments are underway, e.g. in the context of the ERC urbisphere project.

Chapter 7

Future Weather: revisiting the hottest days on record in the Netherlands

7.1 Summary and key-points

Summertime heatwaves are extreme meteorological events with a large societal impact (heat stress, tropical nights, increased mortality, etc). They can be characterised by their intensity, duration and spatial extent, which all are expected to increase in a warming world (along with frequency increases). The implication is that past summers that are in our minds as having been very exceptional, will become increasingly normal. In addition, new heat extremes at levels not experienced ever before, will make their appearance. In "Future Weather" we illustrate how these changes could play out for the heatwave that produced the hottest day to date in the Netherlands (40.7°C, Gilze-Rijen 25 July 2019). This is done using a chain of regional climate models in combination with the Pseudo Global Warming (PGW) approach. Our results indicate that if the 2019 July heatwave would occur in a world that is +2K warmer than today: (i) temperatures would reach values between 42.5-45°C in many places; (ii) the heat-wave intensity sum (cumulative "hittegolfgetal") would double; (iii) the time to "cool off" in between heatwaves would reduce, to a level where the total number of days spent in heatwaves roughly equals the number of cool days (Tx<25°C); (iv) the area where the 40°C threshold is passed will increase strongly; (v) the heatwave will last longer as a simple consequence of the higher temperatures (i.e., an earlier start and a later end). Further persistence increases could occur if the large-scale circulation changes are supportive, but the PGW-methodology is inconclusive on this aspect; (vi) the highest temperatures typically increase 1.5-2 times faster than the global mean, with higher values becoming more likely in scenarios with a stronger future drying. (vii) At even stronger warming levels (+4K above present-day) maximum temperatures could reach up to 50°C in urban areas and the summer of 2019 would become a nearly-continuous heatwave, interrupted by only few days with maximum temperatures below 25 degrees. (viii) Finally, during heatwaves the cities are 'islands of heat' where daily maximum temperatures and the night-time minima are typically 1-5°C higher than in nearby more rural areas. A first impression of these differences is obtained from new experimental simulations obtained at ultra-high resolution (500-150m). Key figures: Figs. 7.8 and 7.12-7.13.

7.2 Introduction

Historic weather and climate extremes are important (benchmark) events. Especially if their impact on society was large, they might trigger government policy action. Their story lines also tend to stick in the people's minds for a long time. For these and other reasons they can be quite

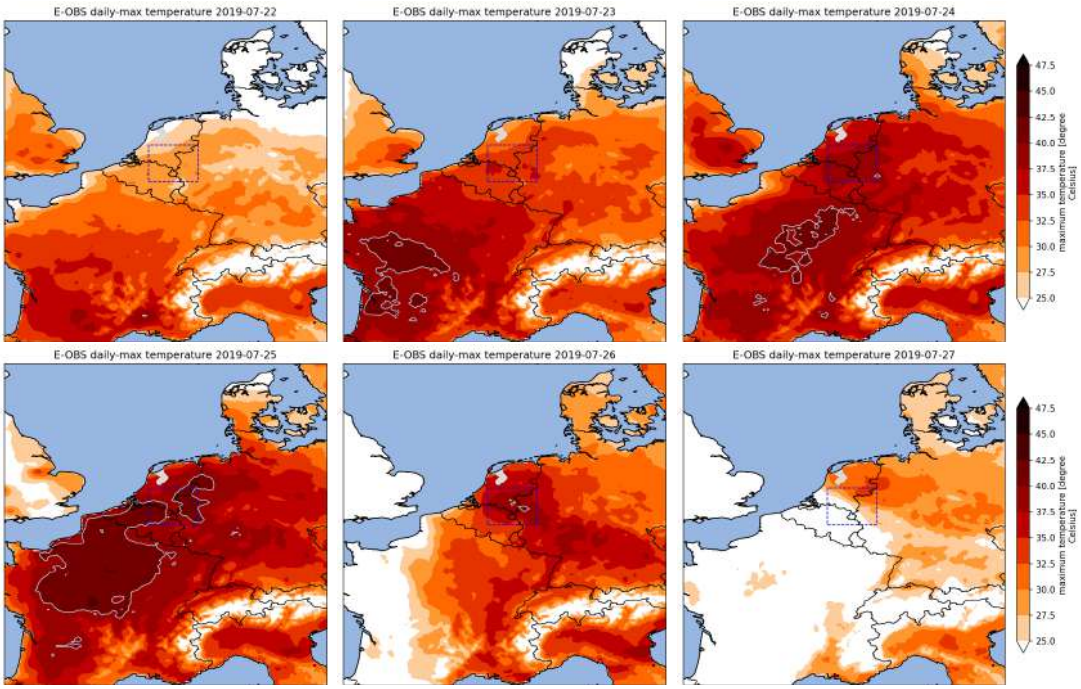

Figure 7.1: The heatwave of 22-27 July 2019 in observations of daily maximum temperature. The 40°C isotherm is shown by a light contour. Temperatures below 25°C are masked out white. The dashed box is the primary region analysed in this chapter. Data: 0.1 degree resolution E-OBS v26.0 (Cornes et al., 2018).

useful as a communication and illustration tool. In "Future Weather" we revisit such historic high-impact cases and transform them in a dynamically consistent way to a future, warmer climate. In the KNMI'14 scenarios for example, we described an extreme rainfall event and showed how it could become both more intense and more spatially extensive in a warmer climate. In the current chapter, we take the example of the record breaking heatwave of July 2019. During this heatwave the 40 degree Celsius barrier was broken in the Netherlands for the first time ever.

Setting the stage It is 24 July 2019. After a couple of already rather warm days with temperatures reaching over 25 degrees, the heatwave that has been in the Dutch news for the past few days is nearing its climax. On a gentle south to southeasterly breeze extremely warm and dry air arrives in the Netherlands in an abundance of sunshine. In France temperatures have been hitting 40°C in many places since the 23rd (Fig. 7.1). A month earlier, at the end of June, large parts of Europe already suffered from a rather intense heatwave. World Weather Attribution was very quick to investigate the case and soon concluded that heatwaves in Europe not only occur more frequently due to human-induced climate change, but also that they are now more intense (Oldenborgh et al., 2019). They had not anticipated a second intense heatwave to hit the same region in such short time. Weather forecasters state that the 75-year old all-time Dutch record of Warnsveld (38.6°C, 23 August 1944) might be 'broken' today (the 24th of July). This indeed happens. Eindhoven registers 39.3°C, implying a new temperature record. Nobody quite expected the record to be set again the next day, although weather forecasts hinted on it. But on the 25th the heat intensified and the 40°C temperature threshold was passed at various locations in the Netherlands, with a new temperature maximum of 40.7°C in Gilze-Rijen. Meteorologists were flabbergasted. The long-standing temperature record was not simply broken by a marginal amount, it was outright "shattered" by more than 2 degrees. The heatwave lasted two more days but the new record was not broken a third time. On the 27th winds changed direction and rain

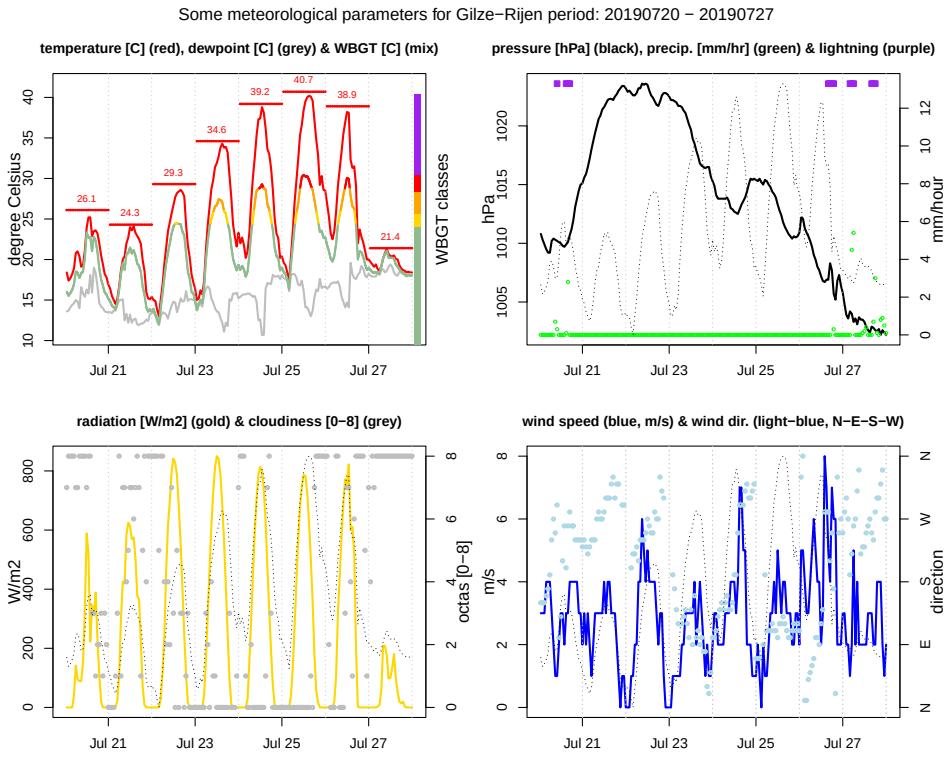

Figure 7.2: Hourly evolution of some meteorological parameters for Gilze-Rijen during the heatwave of July 2019. Top-left panel: 2m-temperature, dew-point temperature and Wet Bulb Globe Temperature (WBGT, degree C). The coloring of WBGT is based on the risk-levels described here (used: region II). Note that the hourly temperature snapshot data 'misses' the maximum temperature of 40.7°C on the 25th (horizontal line segments). For reference the 2m-temperature is also shown in the other panels (the thin dotted line). The top-right panel also shows if lightning was observed (purple). Data: KNMI.

showers appeared marking the end of the heatwave. Barely a month later, however, another – less intense – heatwave passed over the Netherlands (23-28 August 2019). After the record dry year of 2018, summer 2019 wrote history by its extremely high temperatures. Temperatures that would have been virtually impossible in most places without global warming (Vautard et al., 2020).

Heat intensity The hourly time series of a number of meteorological parameters as measured for the synops-station of Gilze-Rijen is shown in Fig. 7.2. The top-left panel shows 2m-temperature (red) and dewpoint (grey) and the wet-bulb globe temperature (WBGT, see the color scale on the RHS of the upper left panel). The latter takes into account aspects like humidity and radiation and aims to quantify how people that are outdoors experience heat (Liljegren et al., 2008). For example, a moderately warm but humid day (i.e. with high relative humidity) may feel as hot as a warmer day with lower relative humidity. WBGT is not (yet) officially used in forecasting in the Netherlands. In the US however, an impact scale is used by the National Weather Service to inform people on the risks of intense heat (see e.g., NWS). When applying this risk-scale to Gilze-Rijen the WBGT reaches the upper limits of level-4 ("High Threat"), remaining just short of the most severe "Extreme Threat" level-5 in which a strong recommendation is made to limit or delay all outdoor (work) activity until lower WBGT values are reached. Other variables were typical for intense heatwaves: abundant sunshine, low cloudiness (bottom left), no precipitation (except at the end of the period), high pressure nearby and not too strong winds. Note that in the afternoon of the 24th the wind speed increased markedly in Gilze-Rijen while turning towards

colder directions, thereby possibly preventing the 40-degree barrier to be reached already on that day. This change of the wind was less prominent on the 25th.

Record shattering The heatwave lasted from 22-27 July 2019 according to the official Dutch heat-wave definition (based on the maximum temperature in De Bilt: 5 days above 25°C of which 3 above 30°C). Heat records were broken and even 'shattered' by several degrees during that week in many other locations (Fig. 7.16). While for many locations in Western Europe the year 2019 still ranks as number one when measured in terms of the absolute temperature maximum, parts of Belgium and the UK have set new records over the past three years (Fig. 7.17). Following countless other record-breaking events across the world, scientists have started to investigate shattering probabilities more systematically. While in a steady climate the probability of breaking records – let alone shattering by several degrees – reduces over time, in a warming world it stays non-zero (Rahmstorf and Coumou, 2011; Fischer et al., 2021), or even increases with time if the warming rate increases. For Gaussian distributions this behaviour can be demonstrated analytically, but generally one needs large ensembles to determine the probability of such events (Sterl et al., 2008; Fischer et al., 2021; Vries and Vries, 2022).

Extremes are warming (much) faster than average As the climate warms the temperature distribution not only shifts, it also changes shape (see e.g. Holmes et al. (2016) and Wiel and Bintanja (2021)). Due to a variety of mechanisms and feedbacks (e.g., the lagged warming rate of the ocean, circulation change, enhanced drying of soil moisture) both the warm summer and the cold winter days in our region warm more rapidly than the global mean, and more rapidly than the local average summer and winter temperature (Oldenborgh et al., 2009; Haarsma et al., 2009; Coumou et al., 2018). For example in de Bilt the temperature increase of the warmest day of the year has been at least 2.5 times the global temperature increase (Fig. 7.18a). While climate models tend to underestimate this factor, they do confirm that the extremes warm considerably faster than average. Oldenborgh et al. (2019) argue that another relevant parameter is Tg3x, the maximum three-day daily-mean temperature. It is often possible to 'escape' one day of intense heat by going indoors, but when the heat lasts longer its consequences become more pronounced (Oldenborgh, 2019). Also the trend in Tg3x exceeds that of global mean temperature (Fig. 7.18b).

Outlook – Summer 2019 in a warmer world Given the previous considerations on the changes in extreme temperatures, it is of interest to find out how the intense 2019 heatwave would look in a warmer world. Regional climate models offer the unique possibility to examine this question, because by using them we can re-simulate historically occurred extreme weather conditions, using reanalysis at the lateral boundaries. Here we use a chain of hydrostatic and non-hydrostatic regional climate models from intermediate (12km) to very high (150m) spatial resolution to investigate the heatwave of July 2019, and to transform it to a warmer world. Below we first describe the methodology in some detail.

7.3 Data and Methods

The methodology that we use to 'futurize' historic weather, is known as the Pseudo Global Warming (PGW) approach (Schär et al., 1996a). In this approach, the large-scale day-to-day weather variability is taken from reanalyses such as ERA5, but a perturbation – referred to as the *delta field* – is added to simulate the mean effect of a warmer climate on that particular weather situation. This delta field is typically derived from the mean climate response shown by future projections such as CMIP6 assuming a certain warming level and associated greenhouse gas concentrations. These three-dimensional delta fields, derived for temperature, humidity, wind and surface pressure, are added at the lateral boundaries and in the interior at initialisation time. During the simulation the regional model is 'free' to adapt to these conditions in the interior.

The large-scale weather systems of the future simulation are similar to those occurring in the control simulation, but are modified by the addition of the small-amplitude delta field. The

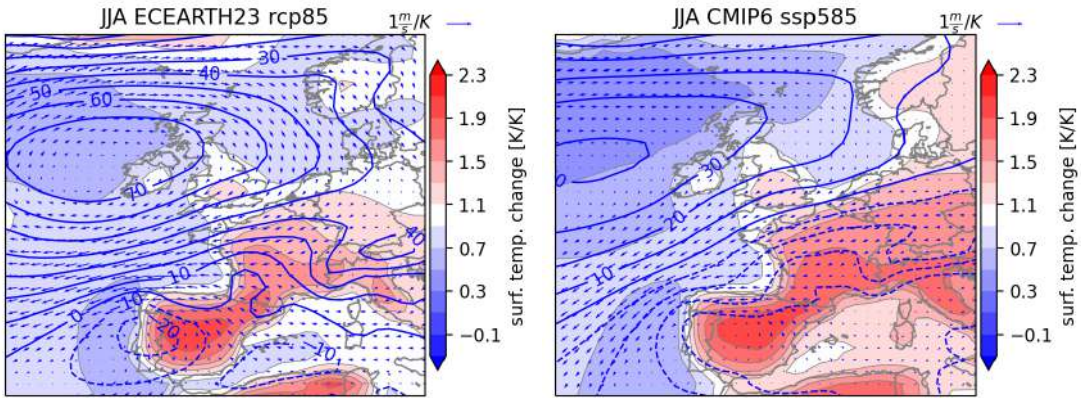

Figure 7.3: Large-scale future changes in summer (JJA) per degree warming for two of the sets of delta fields that were added to ERA5 at the lateral boundaries of RACMO2. Shading shows surface temperature change (K/K). Blue/red colors imply an increase that is weaker/stronger than the global temperature increase. Contours show changes in mean sea-level pressure (Pa/K) and arrows the changes in 850hPa wind (m/s/K). (left) ECEarth2.3, RCP8.5 derived from difference 2071-2100 minus 1991-2020 and scaled by the global temperature increase (3.12K). (right) CMIP6 'all-33', derived from matched warming at 4 degrees and rescaled afterward.

'futurized' weather systems experience the same state of other important factors such as sea surface temperature. By this we mean that if the summer of 2019 was anomalous in the CTL climate because of its sea surface temperature, it will still be anomalous in the future climate. This similarity makes that PGW simulations have a (very) high signal-to-noise ratio (Lenderink et al., 2019b; Brogli et al., 2019; Lenderink et al., 2021b). The approach has limitations because future changes in the large-scale variability are not included (Vries et al., 2022), but these are unimportant for the application at hand.

Available simulations

Many PGW simulations have been performed at KNMI over the past years. The regional climate model RACMO2 (Meijgaard et al., 2008, 2012) is used as the main modelling tool for creating the primary PGW output, using (transformed) ERA5 or ERA-Interim reanalysis as boundary and initial conditions. High-resolution dynamical downscaling of the RACMO2 output is then performed in a second step. The PGW delta fields were derived for various combinations of GCMs, and for various warming levels and emission scenarios. They fall into two groups:

1. Single-GCM-based delta fields for the RCP8.5 scenario (CMIP5): PGW delta fields were derived from EC-Earth2.3, HadGem2 and MPI-ESM based ensemble simulations. In this way three simulations for the period 1979-2020 were generated for a +2K warming scenario. To examine initial condition uncertainty, for each set an 11-member ensemble was created for the period 2018-2020, by starting new simulations at 5-day intervals from 1 January. A range of warming scenarios varying from +1.5 to +3K is used. First results are discussed in Aalbers et al. (2023).

2. CMIP6-based delta fields for the SSP5-8.5 scenario: PGW delta fields were created for the period 1979-2021 using either the ensemble mean over all available CMIP6 models (labelled "all-33"), or the "dry-11" and "wet-11" subsets, that generated the largest and smallest decrease in annual total precipitation in 2100 over the Netherlands. The delta fields are constructed for different global warming levels (+1.5, +2, +3, +4K) using matched-warming.

In total 115 RACMO2 PGW simulations were analysed. These form the core of our PGW-ensemble. The delta fields are determined per calendar month and linearly interpolated in time

when added to the boundary conditions at given time. There are (small but) noticeable differences between different sets of delta fields. Figure 7.3 illustrates some of these differences for two of the available sets for summer (JJA), showing surface temperature (shading), mean sea-level pressure (contours) and 850 hPa wind (arrows). The patterns are qualitatively similar but differ in amplitude. Prominent features are the enhanced warming over land and towards the Mediterranean, and a lagged warming of sea water, especially the North Atlantic, with an associated high-pressure response above Ireland (Haarsma et al., 2009). Especially the circulation changes are weaker in the second group. A primary reason is that it is based on averaging over "all-33" CMIP6 models while those of the first group are based on a single GCM. The "dry-11" subset differs slightly from "all-33" (a more eastward extension of the high, and slightly stronger circulation response), while the "wet-11" subset is cooler with less circulation response (Fig. 7.19). In addition to the circulation changes, the delta fields also indicate an increase in the (vertical) stability of the atmosphere. This increased stability comes with accompanying reductions in cloud cover and near-surface relative humidity, and an increase in shortwave radiation.

One final set of two simulations was performed (CTL and PGW+3K, using CMIP6 dry-11 for the delta fields) in which the surface scheme of RACMO2 was modified in such a way that evapotranspiration from plants is limited (both in CTL and PGW+3K). Evaporation is a cooling term in the heat budget and if it is reduced, the temperature increases more strongly at daytime, especially during the heatwave when there is abundant sunshine. This special RACMO2 simulation with modified surface parameters simulates what could happen in a scenario with strongly reduced soil moisture. It stands out from the other simulations by having among others higher temperatures already in the control climate.

High-resolution dynamical downscaling with HCLIM

To examine the spatial pattern of the heatwave in more detail a subset of these simulations has been further downscaled with HCLIM-AROME (Belusic et al., 2020b). HCLIM-AROME (HCLIM from here) is the climate version of Harmonie-AROME (Bengtsson et al., 2017) used at KNMI for NWP. HCLIM simulations have been used in various recent projects such as CORDEX-FPS and EUCP. Much of the recent literature on CPMs focuses on (extreme) precipitation (Coppola et al., 2020; Ban et al., 2021; Pichelli et al., 2021), but gradually more parameters are being studied, including temperature extremes (Lucas-Picher et al., 2021; Sangelantoni et al., 2023). Given the RACMO2 output from a PGW-simulation, the dynamical downscaling with HCLIM is implemented using a direct nesting approach at 1-hourly frequency. Because running HCLIM is computationally demanding, only a small subset of the RACMO2 simulations have actually been downscaled:

1. HCLIM38 simulations (PGW+1.5K, RCP8.5): Using a combination of ERA-Interim (2008-2017) and ERA5 (2018-2020) as boundary and initial conditions. The delta field was based on a warming level of +1.5K, derived from EC-Earth2.3. Nominal resolution of HCLIM38: 2.5km. A description of HCLIM38 can be found in (Belusic et al., 2020b). The 13 years of HCLIM38 data provide a context for the shorter simulations obtained with HCLIM43. The simulations were carried out as part of the EUCP project.

2. HCLIM43 simulations (PGW+2K, SSP5-8.5): Using ERA5 as boundary and initial conditions. The delta was based on the CMIP6 "dry-11" subset. Initially runs were started at 1 January 2019 to allow for enough spinup time. As motivated in more detail below, a second simulation was started at 1 July. Nominal resolution of HCLIM43 for these runs was similar to HCLIM38: 2.5km. At time of writing, HCLIM43 is still under development. The main code is shared with Harmonie Cy43 that is used in NWP (Bengtsson et al., 2017), but there are differences in the turbulence, convection and cloud scheme (Rooy et al., 2022) as well as the microphysics (Contreras Osorio et al., 2022) and the applied surface physiographical database notably in the surface/soil scheme.

3. Short ultra-high resolution HCLIM43 simulations (PGW+2K, SSP5-8.5): These were nested within the 2.5km resolution HCLIM43 simulations started on 1 July. These highest resolution runs (500m-150m horizontal resolution) were initiated a few days prior to the start of the heatwave (i.e., on 19 July 2023) and run on a smaller domain.

Target region

Despite being constrained by the reanalyses data, the regional climate model simulations will differ from the observations even in their control climate. Some of these differences occur due to small-scale (random) processes, that can be removed to some extent by averaging over a larger area. For this reason we take as our primary area of interest a region that is substantially larger than a single model grid box. The selected region encompasses the middle and south of the Netherlands and a small area outside the Netherlands (4.7-7E, 50.5-52.2N, SENL, "South-East Netherlands", see dashed boxes in Fig. 7.1). The SENL region experienced the highest temperatures in the Netherlands during the 2019 July heatwave. Time series of daily mean and maximum temperature will be compared to gridded E-OBS (Cornes et al., 2018) and geographical maps will be displayed for a larger region to put results into context.

7.4 Results

The following sections describe our main results. We start with an analysis of the time evolution of mean and maximum temperature in the target region (SENL) as obtained with the PGW ensemble. We then create a set of Future Weather (FW) time-series for various warming levels and discuss its impact in terms of measures of cumulative heat-wave intensity ('hittegolfgetal') and duration. Thereafter we discuss the spatial pattern and extent of the warming by looking at the high-resolution HCLIM simulations. A final section is added in which we have a brief look at differences between rural and urbanized areas. For this we will use the new set of HCLIM simulations at ultra-high spatial resolution (500-150m).

7.4.1 Heatwave Intensity and Duration

Control simulation (current climate) Figure 7.4 shows the evolution of 3-day running mean temperature in the SENL region from end of June to the beginning of September in the available RACMO2 PGW simulations. The black line indicates the observations, as taken from E-OBS. Color coding is used to indicate the global temperature rise associated with the delta-fields. Grey lines indicate the control (CTL) or reference runs (dTglob=0), i.e, the runs that are forced with un-modified ERA5 boundary conditions. The three warm periods in the summer of 2019 are clearly visible. There is some scatter in the RACMO2 CTL simulations (grey) but generally they remain close to the observations during this entire period. The spread results from differences in the simulation domain (not all runs were run on exactly the same domain), and from initial-condition uncertainty (Aalbers et al., 2023). The 'special' RACMO2 simulation with modified surface parameters that limit evaporation is indicated in the right panel. It has a positive bias in the 3-day mean temperature during the hottest days of the period, especially the July heatwave.

Future climate The future PGW simulations (orange/red colored lines) are warmer than their corresponding CTL simulation on most of the days. During the July heatwave the highest values are almost always reached by the simulations with the highest global temperature increase (+4K). It simply gets hotter and hotter. The special +3K PGW simulation in which the surface scheme of RACMO2 was modified, however, reaches the highest maxima of all (right panel). The PGW simulations at different warming levels overlap to some extent. For a particular warming level differences occur due to initial-condition sensitivity, but more importantly due to differences in the imposed delta fields. The spread demonstrates that creating an ensemble is essential if one aims to apply the PGW-approach in case studies. Although the SENL region is quite large and a

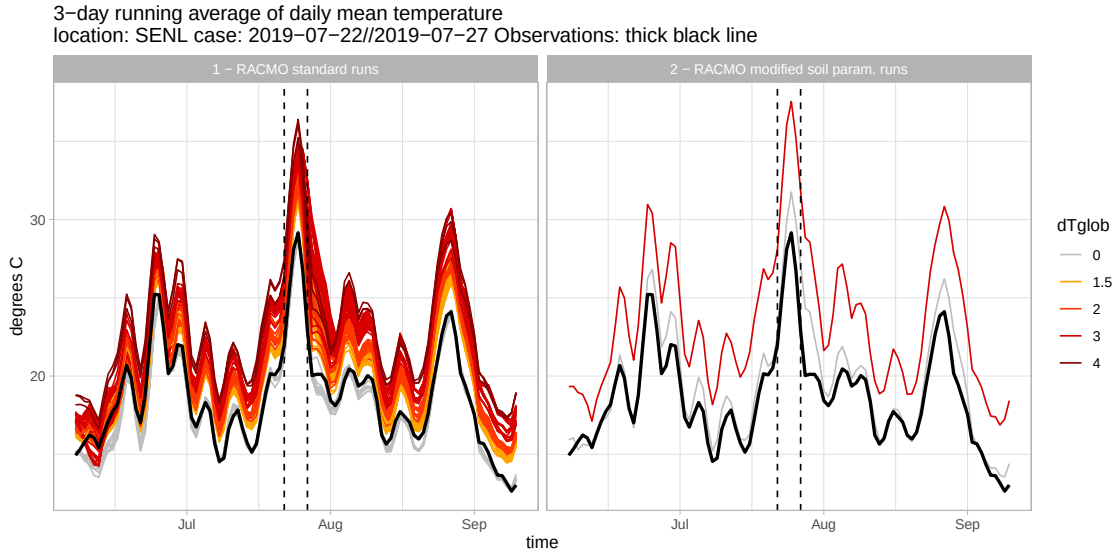

Figure 7.4: Three-day average temperature in SENL derived from the available RACMO2 simulations. The right panel describes the two RACMO simulations (ref and PGW+3K) with modified soil/surface parameters. In both panels, the thick black line denotes the observations.

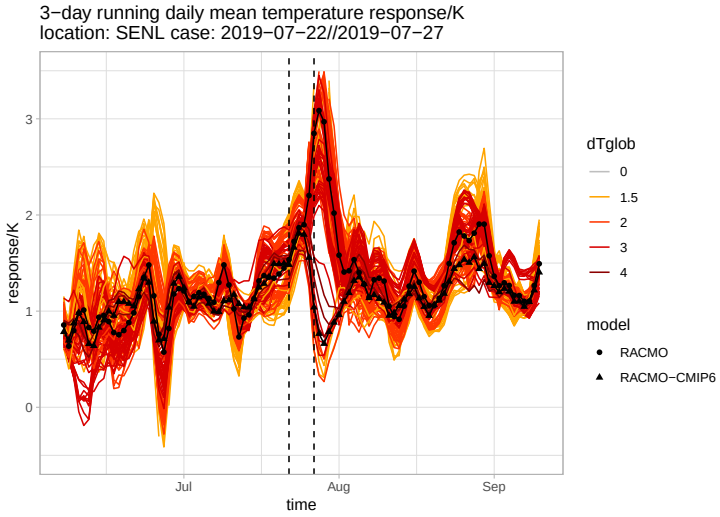

Figure 7.5: Scaled response of 3-day average temperature. The ensemble average scaled response of the PGW simulations derived by adding CMIP6-based delta fields is denoted as "RACMO-CMIP6" (triangles). The ensemble average of the remaining PGW simulations is labelled "RACMO" (circles).

heatwave is usually steered by the large-scale circulation conditions, the actual temperature field is sensitive to small differences in the large-scale forcing and local feedbacks (Sousa et al., 2018, 2020; Suarez-Gutierrez et al., 2020). Especially the end of the July heatwave is 'uncertain' in this perspective, as the small differences in circulation have a large impact.

Temperature Response Factor (TRF) Figure 7.5 shows the evolution of the 3-day running scaled PGW response. This scaled response, which we will refer to as the temperature response

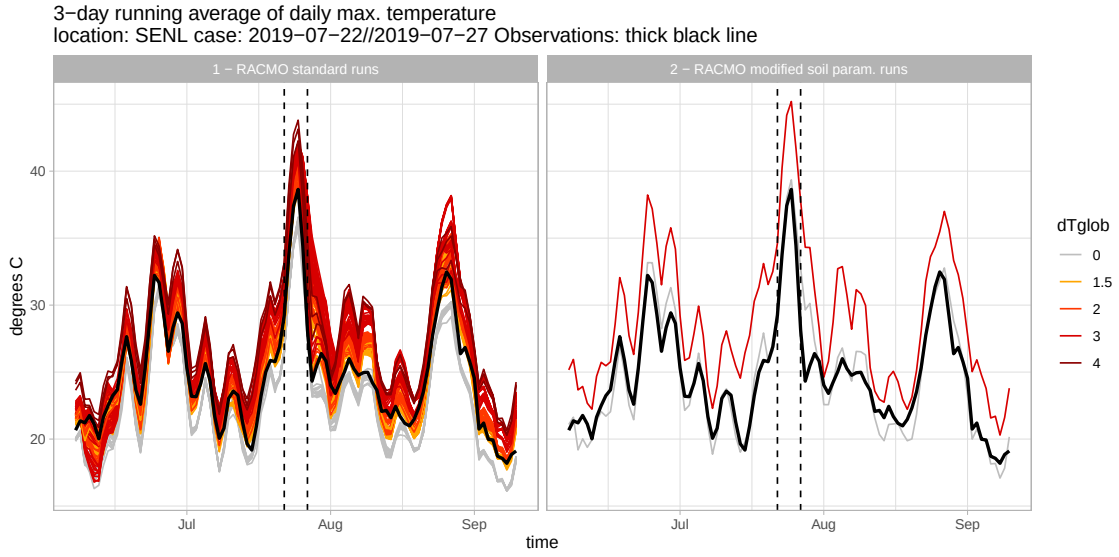

Figure 7.6: As in Fig. 7.4 but for three-day running average of maximum temperature.

factor (TRF) is computed as the difference between the 3-day running temperature averages of the PGW and CTL simulation, divided by the global temperature increase. By applying the scaling we can see how similar/different the response is apart from an overall factor (i.e., global temperature increase). A couple of observations are made. First, simulations with the largest TRF during the heatwave(s) are not necessarily those with the largest global temperature increase showing that initial condition uncertainty and the sensitivity to the delta field is substantial. Second, the ensemble of TRF reveals almost "dichotomous" behaviour in what might happen at the end of the July heatwave. Part of the ensemble shows a (very) large TRF. This response is seen mostly in the PGW experiments with delta fields derived from the single GCMs (first group of PGW experiments described in section 7.3). The large-scale circulation adjustment imposed by this set of PGW experiments adds an easterly component to the wind (Fig. 7.3). Since the end of the heatwave was caused by cooler air approaching from the west (Fig. 7.1) it is not too great a surprise that the added easterly wind component delays the end of the heatwave. The second group does not show this behaviour. The underlying delta fields of these simulations were smaller in terms of their circulation change component. In fact these are the PGW simulations of the second category described in section 7.3) and their average response is labelled "RACMO-CMIP6" in the figure. Finally, the RACMO2 simulation with modified surface scheme does not fall outside the ensemble and has for this reason not been plotted separately. Apparently, the constrained evaporation does not lead to an increased TRF. However, we need to keep in mind here that evaporation was constrained both in the CTL and in the PGW simulation. If evaporation would be unconstrained in the current climate, but limited in the future climate for example due to overall drier soil moisture conditions, this would lead to an amplified response.

Maximum temperature A similar analysis has been carried out for 3-day running maximum temperature (Fig. 7.6). The agreement between observations and the CTL simulations (grey lines) is less satisfying than with the 3-day average temperature: RACMO2 is systematically up to two degrees too cold in its maximum temperatures. Only the RACMO2 simulation with modified surface scheme attains approximately the correct temperature maxima in the CTL (right panel), at the cost of being too warm in the daily mean temperature. This +3K run with modified surface scheme again produces the highest temperature maxima. Similar to the 3-day mean temperature, the spread in temperature maxima is largest at the end of the July heatwave.

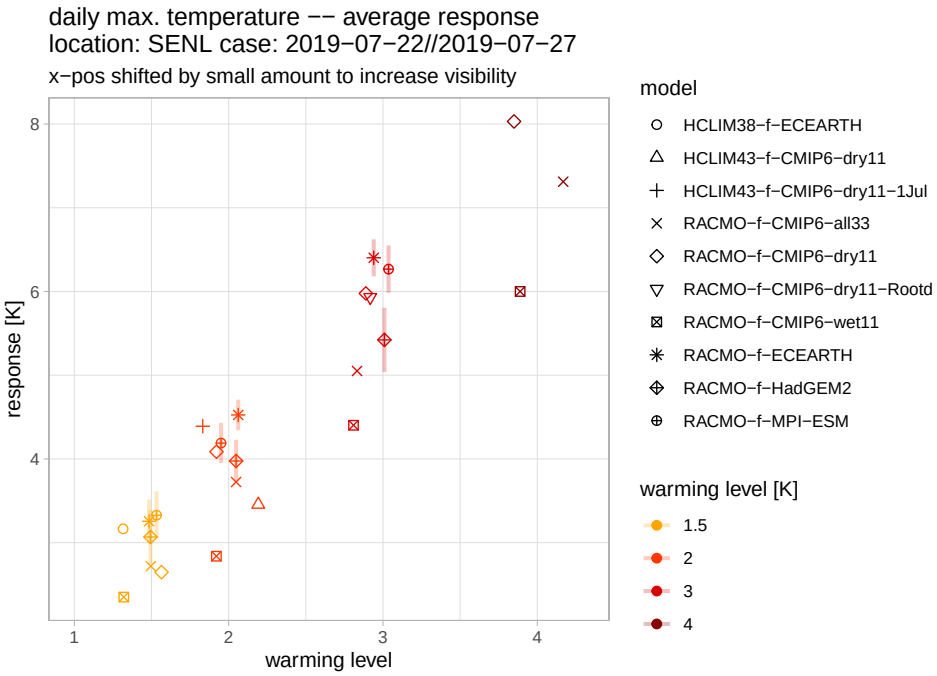

Figure 7.7: Scatter plot of response in maximum temperature averaged over the July heatwave, as a function of warming level. In the legend, the final three simulations are run as an initial-condition ensemble (11 members per warming level). Their spread ($\pm 1.64\sigma$) is indicated by the vertical line segments. Note that most models do not have experiments for all warming levels.

Sensitivity to initial-conditions and choice of delta field Figure 7.7 shows the average response in maximum temperature over the period of the July heatwave for the various PGW ensemble members. Here we also included the standard (i.e., 2.5km resolution) HCLIM PGW simulations. Note that not all models shown in the legend have simulations with all warming levels and also that each point has been shifted by a small random amount around the warming level (on the horizontal axis) to improve visibility. Initial-condition uncertainty is generally small compared to the impact of the different delta fields (see the vertical line segments). Furthermore, at all warming levels the smallest response is seen in the simulations labelled CMIP6-wet11 (TRF around 1.5). The CMIP-dry11 subset warms significantly more (TRF around 2). Two further remarks: The run with modified surface scheme (RACMO-f-CMIP6-dry11-Rootd, +3K) has a similar response as the standard run at that warming level (RACMO-f-CMIP6-dry11). And finally, from the two +2K HCLIM43 runs shown in the figure, the late-start run (HCLIM43-f-CMIP6-dry11-1Jul) has a larger response than the default run (HCLIM43-f-CMIP6-dry11).

Transforming the observations to a warmer climate To obtain an actual "Future Weather" (FW) analogue time series, many approaches are possible. The simplest is to add the unscaled PGW-response to the observations. A second approach is to transform each observed temperature with the average TRF corresponding to that temperature. This method is related to delta-quantile mapping. Here we use a third method, in which the ensemble of time-dependent TRF factors is used as a measure of the overall instantaneous uncertainty. The temperature of the FW analogue at a particular time t and warming level Δ_{Tg} is then given by the simple formula $T_{FW}(t) = T_{obs}(t) + \Delta_{Tg} \cdot TRF(t)$. Given that we have only a few simulations with HCLIM, here we included only the RACMO simulations.

Figure 7.8 shows the result for a +2K warming level. The shading represents the 5-95% range implied by the ensemble TRF. The ensemble gives a peak in 3-day running maximum temperature

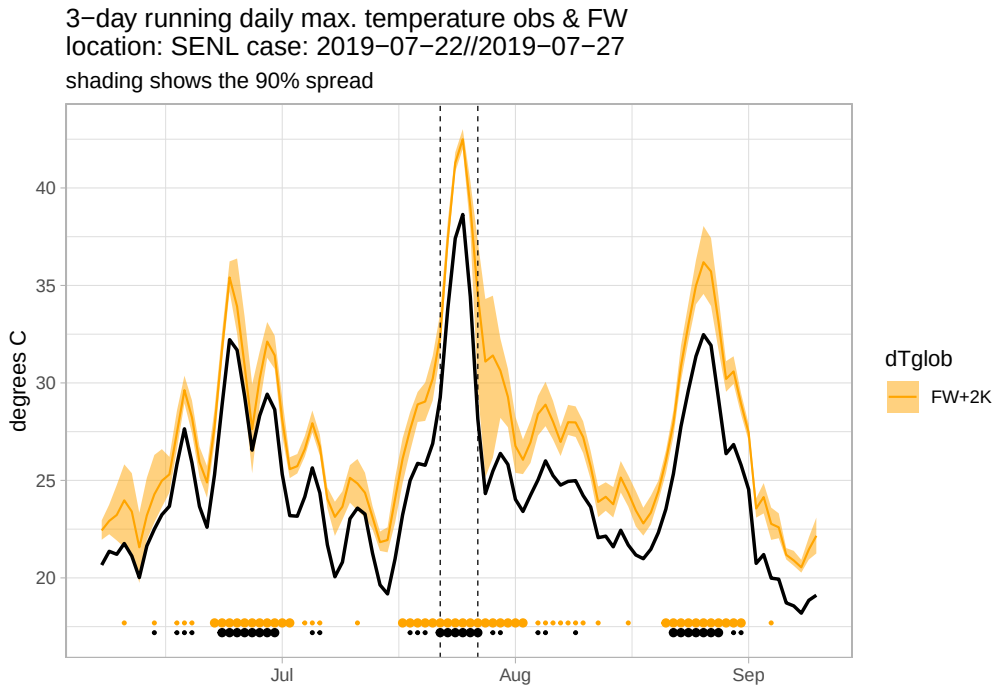

Figure 7.8: Transforming 3-day maximum temperature to a +2K warmer world following $T_{FW}(t) = T_{obs}(t) + \Delta_{Tg} \cdot TRF(t)$ with Δ_{Tg} the warming level, using all available RACMO2 simulations. The band denotes 5-95% range of the TRF at each day. The large and small dots near the bottom of the figure indicate heat-wave and "potential" heat-wave days (days with max temp above 25°C) respectively.

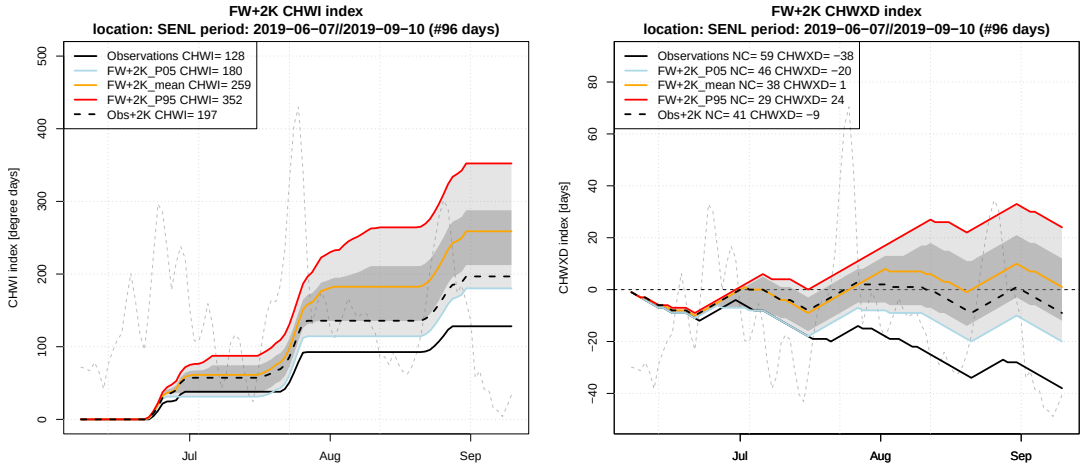

Figure 7.9: Cumulative heatwave intensity (left) and duration (right) indices for a +2K warming scenario. The light shaded area represents the 5-95% envelope, the dark shaded area the 5-95 range obtained from resampling. The numbers in the legend gives the value of the indices at the end of the period ("NC" is number of cool-off days). The grey dotted line in the background is the 3-day maximum temperature.

averaged over the target region (SENL) of around 42.5°C, with surprisingly little spread. This implies that if the historic July 2019 heatwave would occur in a 2 degree warmer world, it would produce 3-day temperature maxima between 40 and 45 degrees in large areas. The duration of the July heatwave increases strongly from 6 days to 17 days (see the big dots near the bottom of the figure). There is a large spread in the FW estimate toward the end of the July heatwave.

Cumulative measures of heat-wave intensity and duration The FW analogues can be used to compute cumulative indices for heat-wave intensity and duration over the entire summer season. A cumulative heat-wave intensity (CHWI) index is calculated as the cumulative temperature excess above 25°C during heatwaves that meet the standard criterion for a regional heatwave (5 days above 25°C of which 3 above 30°C). This measure is also used to rank the total impact of historic national heatwaves at the KNMI website ("hittegolfgetal"). To measure duration two metrics are used. The first is simply the total (cumulative) number of heat-wave days (CHWD). While this metric tracks the heat-wave days, it does not discriminate between days that are *not* part of heatwaves. We think it is justified to separate "potential" heat-wave days (any other day with daily maximum temperature above 25 °C) from true "cool-off" days (maximum temperature below 25°C). The cumulative heat-wave excess duration index (CHWXD) takes this into account and is defined as follows: A day that is part of a heatwave gets a value of +1, a regular summer day (Tx above 25°C) that is not part of a heatwave, gets a value 0, and days with Tx below 25°C a value of -1. The CHWXD increases linearly during heatwaves, it decreases on cool days and remains constant for isolated summer or even tropical days. Therefore a positive value x of CHWXD at the end of the season implies that there were x more heat-wave days than cool days.

The intensity and duration indices are shown in Figure 7.9 for the 2019 observations and the +2K FW analog. The start and end date are taken the same as in the previous figures. Two shaded bands are shown. The light shading is obtained by using at each day the 5-95% range of the TRF and adding these to the observations (i.e. using the band values in Fig. 7.8 as time-series). This band therefore describes the envelope spanned by the most 'optimistic' – in the sense of the least warming, using the lowest TRF at all days – and most 'pessimistic' time series that

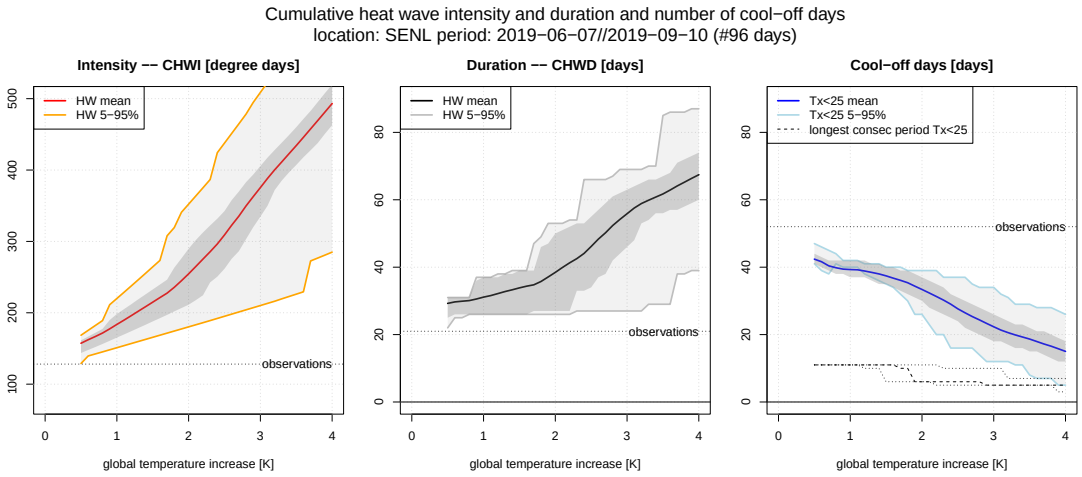

Figure 7.10: Cumulative changes of the summer of 2019 for a range of Future-Weather scenarios. Left: cumulative heat-wave intensity; Middle: cumulative number of days spent in heatwaves; Right: number of cool days with daily max temperature below 25C.

can be constructed. We show the envelope because even the most optimistic scenario produces significant changes. Dark shading is the 5-95% range from a 1000 member bootstrap ensemble[1].

The three periods with temperatures above 30 degrees are visible as three 'ramps' in the graphs (Fig. 7.9). In the observations (black line) the cumulative intensity index reaches a value of 128 at the end of the period. A +2K warming level increases this number by at least 40% (P05 lower bound, the most 'optimistic' scenario), but on average more than a factor 2. Simply adding a constant of +2K to the observations – equivalent to taking TRF=1 at all times – produces values towards the lower limit of the shown range (dashed line).

Time to "cool off" in between heatwaves shortens. This is most clearly seen in the duration (right panel in Fig. 7.9). Despite the hot summer, there were still 38 cool days more than heat-wave days in the observations. In other words, there is an excess of cool days. Historically this used to be the standard of course, with heatwaves being quite exceptional. However, under +2K warming the expected value of the cool-day excess reduces to values near zero, implying that there will be as many heat-wave days as cool days. As one moves up further in the grey band, the downslope periods (i.e., cool days) are being replaced increasingly by horizontal sections (warm or hot, but not yet classifying as a heatwave) and up-slope sections (heatwaves).

Warming levels beyond +2K Not surprisingly the intensity of heatwaves increases further in scenarios with stronger warming. If 2019 would happen under a +4K warming level, the expected intensity almost quadruples and the duration excess is around +50 (suppl. Fig. 7.20). It is needless to say, but having 50 more heat-wave days than cool days in a summer season would quite literally leave very little time to recover in between the heatwaves. In the most pessimistic scenario the summer of 2019 would become a near-continuous heatwave.

Figure 7.10 summarises how this plays out for intermediate warming levels. The left panel shows the end of season cumulative heat-wave intensity as a function of the warming level, the middle panel the total number of days spent in heatwaves and the right panel the number of cool days, including the longest length of such a period (thin lines). Dark grey shading indicates the 90% range of the previously discussed bootstrap ensemble, the thick lines and light grey shading

[1]The bootstrap ensemble was created by randomly drawing at each time instant a TRF value in between the 90% range of available TRF values (at that time) assuming a uniform distribution. For each of these synthetic runs the cumulative heatwave intensity and excess duration indices were computed and the shading simply represents the 90% range of these (cumulative) values at each day.

the envelope of most optimistic and pessimistic scenario. As expected, there is a continuous increase in the intensity and duration and a decrease in number of cool days. The increase is not completely linear due to the specific meteorological conditions in 2019, with especially the duration increasing more rapidly beyond +2K. Furthermore, note that the width of the envelope (i.e., the uncertainty) increases with warming level because it is computed from the spread of the TRF multiplied by the warming level. Finally note that these results are specific to the summer 2019. If other years are 'futurized' in the same way, the same tendencies will show up, but the actual numbers will be different.

7.4.2 Heatwave Area and Spatial Pattern

In addition to changes in intensity and duration also the spatial scale of the heatwave will get progressively larger as the world warms. In this section we have a closer look at the size and the spatial structure of the warming pattern during the 2019 heatwave. For this we use the HCLIM simulations. We have already showed (Fig. 7.7) that in terms of the scaled temperature response factor (TRF), HCLIM has a similar response as RACMO2. Below, we use the output of one specific HCLIM43 simulation, namely the "late-start" one that was initiated on 1 July 2019 and that uses as boundary forcing the PGW+2K RACMO2 output from the CMIP6-based "dry-11" subset. The control simulations of HCLIM43 were also started on the same day.

Soil moisture and bias The reason for using the "late-start" HCLIM43 runs and not one of the other available simulations, is that these runs had the smallest bias in their control simulations. HCLIM is quite sensitive to soil-moisture drying in spring and early summer during conditions that favour evaporation (e.g., abundant sunshine, and anomalously high temperatures). The most likely explanation for the drying is an overestimation of the latent heat fluxes which might be related to details of physiography-related parameters like LAI (leaf-area index). If the soil-moisture is below average and a heatwave happens to come by, HCLIM has a tendency to produce too high maximum temperatures. The physical reason is similar to what we saw in the RACMO2 simulation with modified surface scheme: (strongly) reduced soil moisture reduces evaporative cooling and thereby promotes higher temperatures. In the late-start HCLIM43 simulations the soil-moisture state is closer to neutral/climatology, and the bias in the maximum temperature during the heatwave is small.

Spatial pattern and impact area Figure 7.11 shows the time evolution and spatial patterns of the HCLIM43 simulation at standard resolution (2.5km). Unlike RACMO2 (which was generally too cold in maximum temperature) HCLIM43 attains maximum temperatures close to the observed values over the SENL region (top-left panel). Over the SENL region, the mean bias over the period from 14-31 July with respect to E-OBS is small (-0.04 K). It is subtracted from both CTL and PGW simulations using the same value for the entire domain. This seems appropriate for a region around the Netherlands[2]. With 3-day maximum temperatures above 42.5°C in the PGW+2K simulation, the associated TRF exceeds the value of two (top-middle panel). Averaged over the 6 days of the heatwave the TRF was above 1.5 almost everywhere in the Netherlands, except for the very North (top-right panel). The heat arrived from the south (Fig. 7.1) and the highest TRF values are also found in the southern provinces and across the border with Belgium. There are spatial differences in the response pattern (top-right), but more research is required to examine their robustness. The second and third row show the spatial pattern of the 3 warmest days (24-26 July). In the PGW run (right panels) a substantial area appears where 3-day temperature maxima are above 40°C. This increase in the area impacted by heatwaves remains hidden in the time-series analysis for a specific region. As the climate warms, future heatwaves will not only become more intense and last longer, they will also cover increasingly larger areas, thereby posing threats to ever larger numbers of people and their environment.

[2]A closer inspection of the patterns of OBS and CTL shows that the bias is not constant throughout the domain. Especially the UK is too cold and Northern Italy south of the Alps too warm. For the region around and south of the Netherlands, however, the constant-bias assumption seems acceptable.

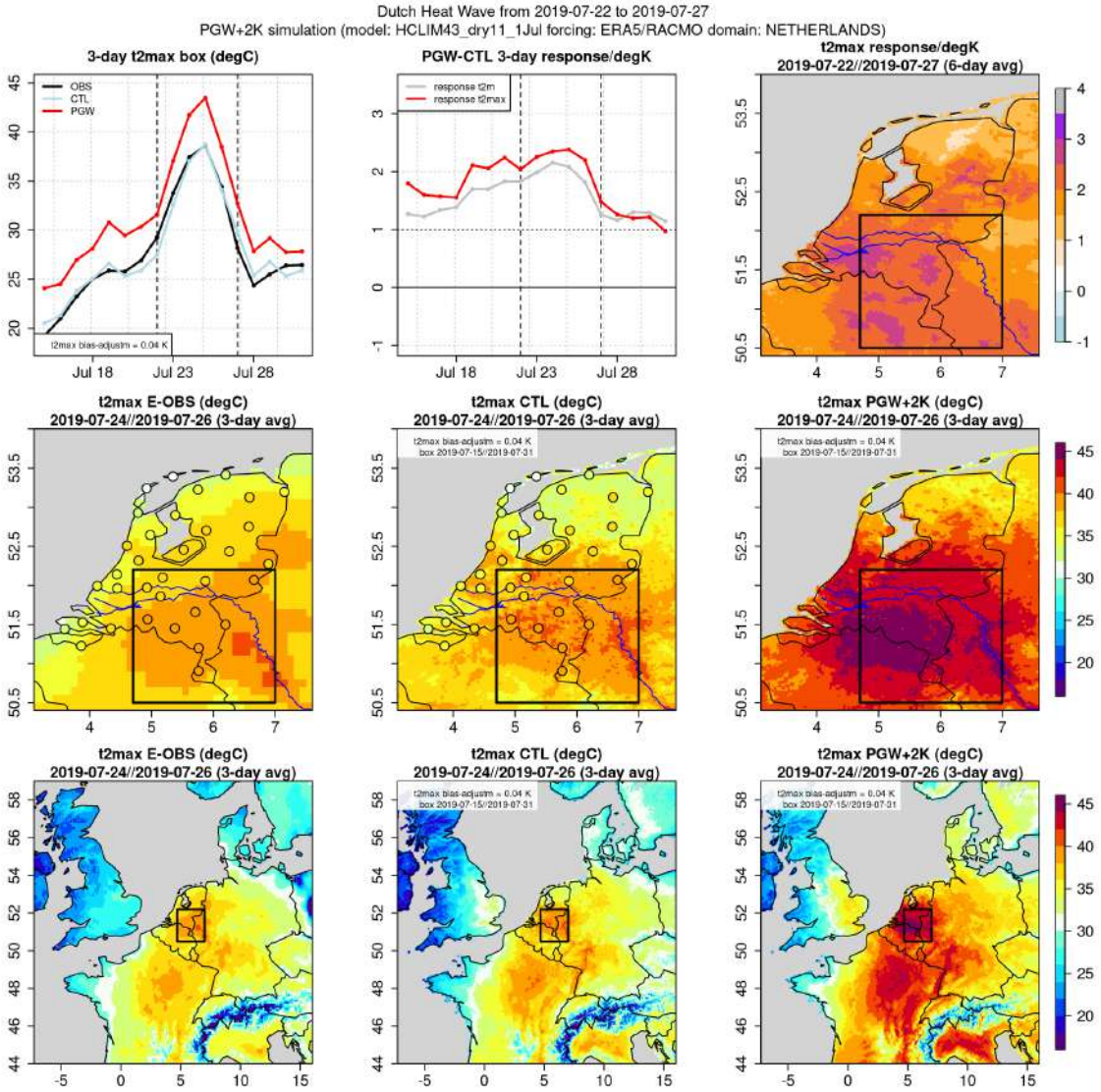

Figure 7.11: Maximum temperature in observations from E-OBS, and the HCLIM43 CTL and PGW simulations. The top-left panel shows the evolution of 3-day maximum temperature in SENL. Top-middle panel shows the scaled warming factor, top-right panel the average TRF for each grid box. The maps on the second and third row show the 24-26 July average daily maximum temperature in OBS, CTL and PGW. Small colored circles show the corresponding values from the meteorological stations in the Netherlands.

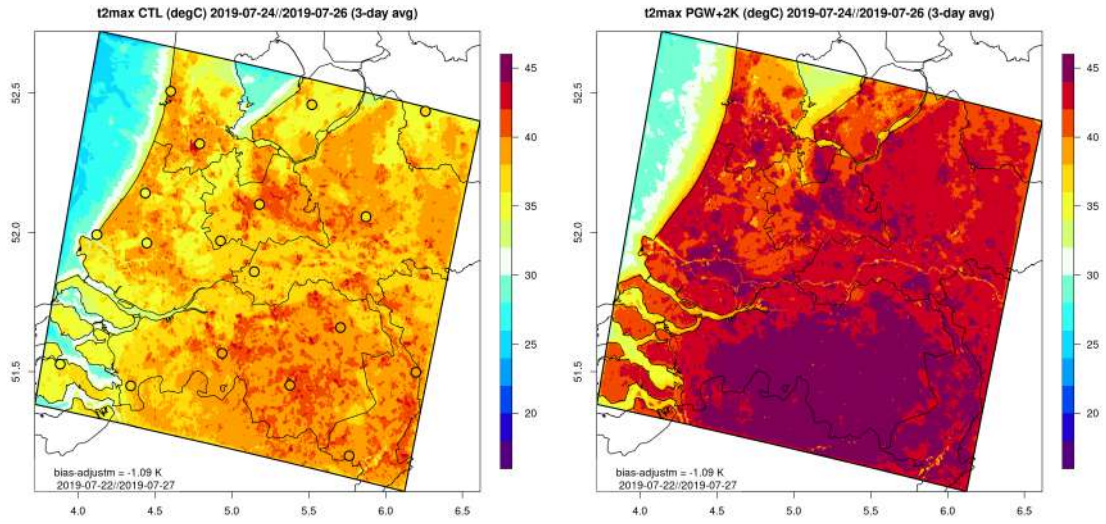

Figure 7.12: Daily maximum temperature during the three hottest days of the July heatwave in the 150m resolution simulation. A mean bias adjustment has been carried out with respect to the synops stations (colored circles). Left: CTL simulation. Right: PGW+2K simulation. The shading values are unbounded from below and above. The black line is the simulation domain boundary.

7.4.3 Effects of urbanization

At the scale of Western Europe, the spatial patterns of E-OBS and HCLIM43 look quite similar (bottom row in Fig. 7.11). However, at a smaller scale HCLIM43 displays much more spatial inhomogeneity (middle row). The darkest spots (i.e., highest temperatures) typically occur in regions with a high degree of urbanization. At 2.5km spatial resolution regional climate modelling with HCLIM is clearly starting to resolve city effects. Contrast this to the E-OBS gridded data set. E-OBS is generated by spatially interpolating data from the meteorological stations (circles in the maps) to a 0.1 degree gridded product. The meteorological stations are typically positioned outside the main cities, at locations that are representative for the immediate area. As a result, the cities do not really show up in E-OBS. On the other hand, it is well known that cities experience higher maxima than the rural areas around it. HCLIM starts to resolve city-effects at 2.5km resolution, but at even higher spatial resolution, the difference between rural and urban areas becomes much more visible. In this final section before conclusions, we examine this in some detail.

Ultra-high resolution simulations For this chapter on "Future Weather" we created a new set of PGW simulations in which HCLIM43 is run at a resolution "of the future" (500-150m) i.e., much higher than normal (2.5km). Although it may become feasible to create long climate integrations at these resolutions within a decade, at present it is only possible to run on small domains and for short time windows. In terms of model settings, an important difference is that at the highest resolution (150m) the shallow-convection parameterisation was switched off (Rooy et al., 2022). On a small domain it is even more essential to provide the right boundary conditions. As we have discussed before, HCLIM in standard setup tends to respond too strongly to warm and/or sunny meteorological conditions periods in spring and early summer. Most likely culprit is too much evaporation, probably related to details in the physiography. If the soil-moisture state is below-average at the start of the heatwave, a positive bias in maximum temperature will develop. For this reason we use as boundary conditions for the ultra-high resolution runs the output from the HCLIM43 standard runs that were started on 1 July 2019 (i.e., after the first warm period in June). This "late-start" simulation had substantially smaller temperature biases in July than the run that was started in January, but also a stronger temperature response over the SENL

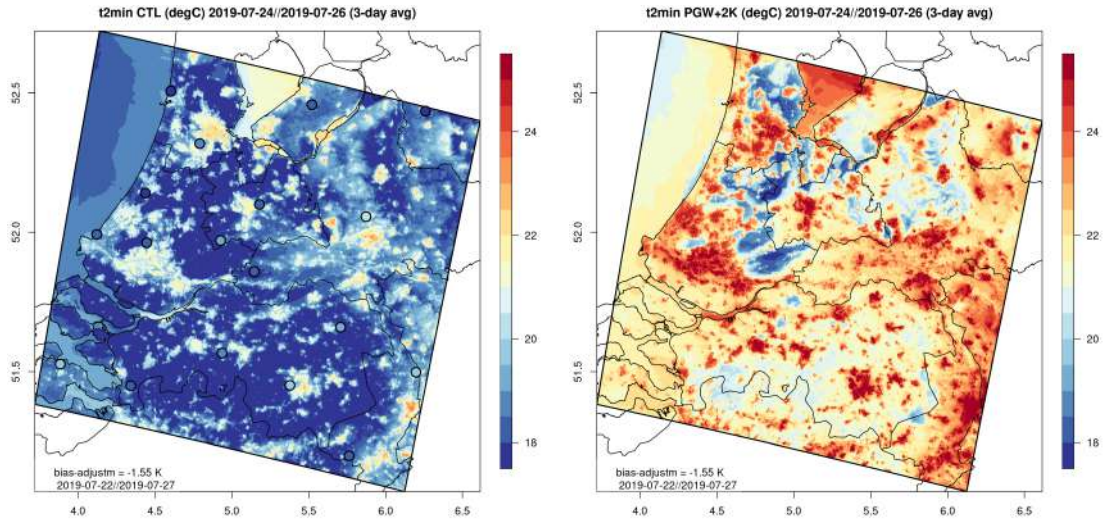

Figure 7.13: Daily minimum temperature during the three hottest days of the July heatwave in the 150m resolution simulation. A mean bias adjustment has been carried out with respect to the synops stations (colored circles). Left: CTL simulation. Right: PGW+2K simulation. The shading values are unbounded from below and above.

region than the standard run (Fig. 7.7). The scientific reason underlying the stronger response remains to be investigated. Note also that a bias adjustment is still needed, as the ultra-high resolution run tends to become too warm already in the current climate. We compute a single value for the bias using a simple extension of the nearest-neighbour procedure. For each of the main Dutch meteorological stations within the simulation domain, all (land) model grid within a radius of 0.025 degree are used. Their average difference with respect to that synoptic station is used as the model-bias for that location. The average over all local biases is then subtracted from the entire field. Why this bias develops (e.g., soil-moisture conditions, a lack of clouds and/or too much radiation) are to be investigated. Therefore, and as a disclaimer to what follows, we emphasise that the ultra-high resolution simulations discussed below are an experimental product and that our knowledge of the behaviour of HCLIM in this configuration is limited. The output is used to illustrate the typical differences between cities and rural areas, but not to provide actual quantitative numbers.

Cities – Islands of heat The first image we show is of the daily maximum temperature averaged over the three hottest days of the heatwave in the CTL simulation at 150m resolution (Figure 7.12 (left)). Qualitatively it is similar to the 2.5km run, but the imprint of the underlying land types is much stronger. Temperatures are 1-5 degrees warmer in urban and industrialised areas, locally even more, especially where bone-dry and dark concrete prevails (e.g., Schiphol airport). Sandy areas like the Veluwe and Utrechtse Heuvelrug are also clearly visible. Polders, lakes and rivers are substantially cooler.

The right panel shows the PGW +2K result. Similar to Fig. 7.11 a large area experiences maxima above 45°C. The response pattern appears to display less spatial inhomogeneity than the CTL or PGW pattern itself (supplem. Fig. 7.22). This would imply that the cities do not have a systematically stronger response than neighbouring more rural areas. Although undoubtedly this would be a relief to many people living in the cities, more research is required to examine whether this finding is robust. However, it will still be much warmer in the urbanised regions than outside it, implying that the direct heat stress will also be much higher. Note further that in this +2K warming scenario no changes in land use or surface types are included. All cities are assumed to preserve their size. Undoubtedly this also is a crude approximation. If cities expand, so will the

'red' spots on the maps. Current research in high-resolution climate modelling addresses questions like to what extent implementation of "green roofs" could help cities to prevent from overheating.

During the evening and early hours of the night cities remain much warmer than the rural areas especially during heatwaves. Abundant sunshine has warmed up buildings, concrete etc, and it takes a while for this heat to escape. At night finally the cities cool down, but still remain much warmer. Figure 7.13 shows the 6-day average minimum temperature. Now the cities light up even more than during the day. Excessively hot nights are related to substantially increasing mortality rates, much more than average daily or maximum temperature, as they interrupt the normal physiology of sleep (He et al., 2022). Rural areas like the Veluwe that were also hot during the day typically cool off rapidly at night. In the PGW simulation, only few cooler places remain.

7.5 Discussion

We have discussed how the intense heatwave of July 2019 could look if it were to occur in a warmer climate using regional climate modelling and the PGW approach. Here we reflect on a couple of points.

PGW method An important ingredient of the PGW-approach is the addition of the small-amplitude, slowly varying three-dimensional delta field to the boundaries of the regional climate model. This delta field describes the average future response of (ensembles of) GCM simulations such as (subsets of) CMIP6. In the interior the regional model adapts to the modified boundary conditions. By doing this, the main thermodynamic response is included. The result is a "futurization" of historic weather. Although the time-correlations between the control and PGW simulation are quite high for temperature (generally above 0.9), an ensemble approach is strongly recommended when futurizing single events. Recently an alternative to PGW has been proposed. In Sanchez-Benitez et al. (2022) a GCM is (spectrally) nudged to the observed ERA5 circulation. In their future scenarios also strong increases in temperature of the July 2019 heatwave are seen. Their conclusion is that temperatures around 50°C can not be excluded if a globally +4K warmer world experienced the same meteorological conditions. Our results point in the same direction.

Intensity, duration and spatial extent We focused on three defining characteristics of heatwaves: intensity, duration and spatial extent. All three will change (along with increases in frequency). While the quantitative details will vary from case to case, and from year to year, some aspects of the worked out example of 2019 we believe are quite robust. The intensity increases more strongly than the imposed level of global warming. For every degree of global warming the modelled maximum temperature typically increases by 1.5-2 degrees. According to the PGW experiments undertaken, there seems to be no real "flattening off" of this rate for global warming levels up to +4K (Fig. 7.7). Ensemble spread is caused by initial-condition uncertainty and by differences in the applied delta field. Systematically higher temperature responses were found if the delta field was derived from the 'dry-11' CMIP6 subset; these simulations warmed significantly more than those based on the 'wet-11' subset (e.g., Fig. 7.7). Heatwave duration increases to first order simply as a direct consequence of the higher temperatures (i.e., an earlier start and a later end). Further persistence changes could occur if the large-scale conditions are supportive, as we saw in several of the members of the PGW ensemble. However, the PGW approach is not well suited to give definite answers to the question of the changes in the duration, because the large-scale variability is fixed (and equal to the historic conditions). The areal extent – computed as the average area where the 40°C threshold is exceeded – also increases strongly. Finally we discussed differences between cities and more rural areas, by looking at experimental simulations at ultra-high spatial resolution. Already in the current climate the temperatures are substantially higher in the major cities, especially during heatwaves. This difference will remain in a warmer climate, implying that (large) cities will be the first to face extremely high temperatures, both during daytime and during the nights.

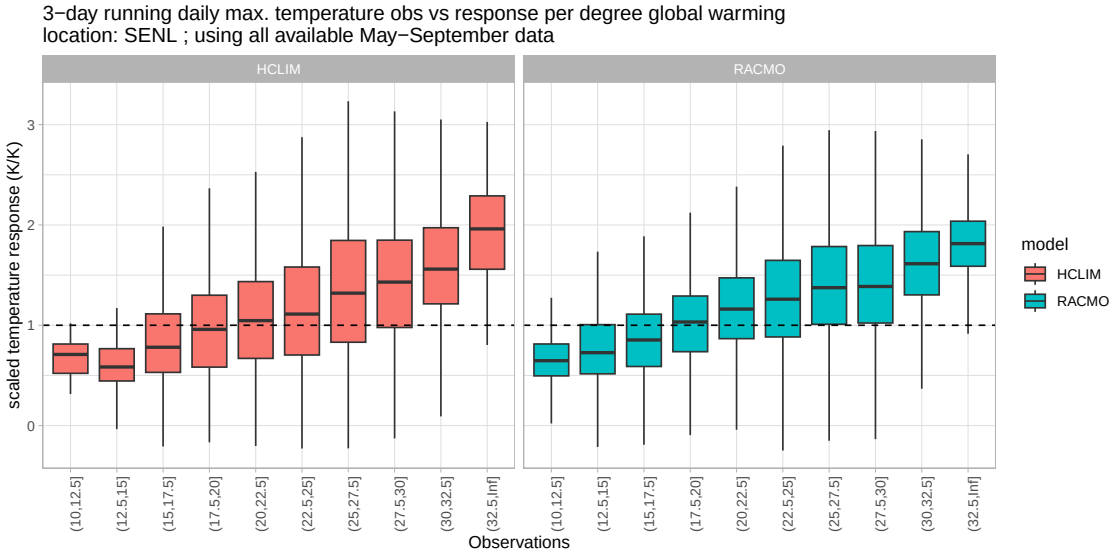

Figure 7.14: Scaled 3-day maximum temperature response (K/K) binned for observed temperature classes during May-September. A value of one at the y-axis indicates a scaling similar to the change in global temperature. The boxes range from 25% to 75% of the data. The thin lines (whiskers) extend maximally 1.5 times the IQR (interquartile range).

Representativeness of the future July 2019 heatwave for other hot days With its record-shattering temperatures the July 2019 summer heatwave was clearly exceptional in the current climate. Are there general lessons we can learn from its "futurization"? Can the conclusions be applied to other future heatwaves? First of all, it is important to state there is a large natural variability in heatwave frequency, intensity and duration. Some will last only a couple of days, some longer, some are hotter than others and 2019 was exceptionally hot. Therefore, *not* all future heatwaves will reach the same intensities as the 'futurized' July 2019. One of the important factors was the TRF, the temperature response scaled by the increase in global temperature. During most of the summer of 2019, the TRF was above unity and (generally) larger on days with high temperature. To check the representativity of the July 2019 case for other hot days we compute the scaled response using all available data from all years (many RACMO2 simulations were obtained for 2018-2020, but a number of them for 1979-2021). In Figure 7.14 we used all available May-September data from all available years to construct boxplots of the TRF of 3-day maximum temperature, binned by the observed temperature in the SENL target region (Results for 3-day mean temperature are in Fig. 7.21). The HCLIM simulations at 2.5 km resolution are also included. The TRF increases with temperature and is generally largest at the warmest days. The agreement between RACMO2 and HCLIM is quite good. The coldest days have a TRF below unity. This is not really unsurprising since these cold days occur typically when the wind is blowing from the west or north, which is the region where the warming lags behind (Fig. 7.3). For the majority of the warmest observed temperatures, however, the TRF is above 1.5, and thus quite similar to what we saw for the July 2019 heatwave. Based on these results over all years we are confident that heatwaves will get progressively warmer at a rate that considerably faster than the rise in global temperature, with implied longer duration and thus a larger impact.

Would the present-day 2019 summer still qualify as exceptional in a warmer climate? The answer to this question depends in part on the amount of global warming. A first-order estimate can be derived easily from the PGW simulations. This is done by creating 'futurized' time series of all historically available years (we use 1951-2021) and by comparing these to the historic series. To obtain the future series here we simply added the median of the scaling factors

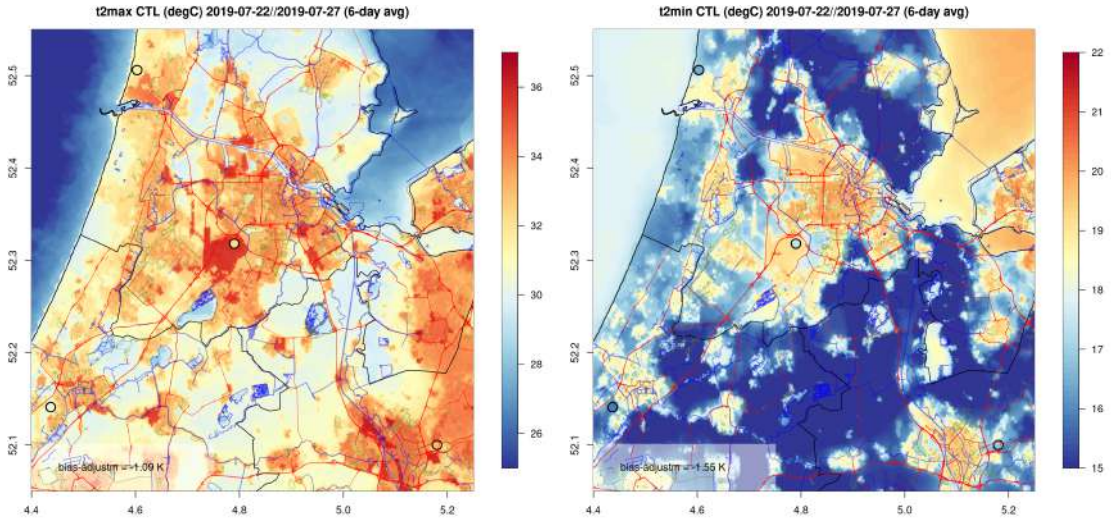

Figure 7.15: 6-day average of daily maximum temperature (left) and minimum temperature (right) during the heatwave in the 150m resolution simulation. Zoomed in on the Amsterdam area (Utrecht is in the south-east corner). Selected OpenStreetmap polygon features have been added (red lines: primary roads and motorways; blue: lakes, rivers, canals; green: parks and forests).

(horizontal lines in Fig. 7.14) to the observed daily time series [Note this is subtly different from the earlier approach used to obtain Fig. 7.8.]. We can then compute statistics like heatwave intensity, duration, and cumulative heatwavenumber ('hittegolfgetal') like before. We describe a few key results. In terms of the total summed heatwavenumber (CHWN) the summer of 2019 as it occurred ranked second after 2018, out of the 71 summers (1951-2021). In the +2K warmer climate, the 2018 summer as it occurred would no longer appear in the Top-10 in terms of CHWN, and 2019 would be lower still. In terms of maximum temperature, the year 2019 as it occurred would still rank in the top-10% in the +2K warmer climate. At a +4K warming level even the summer 2018 as it occurred would drop out of the Top-40 in terms of CHWN and also the maximum temperatures of 2019 would no longer be exceptional. Thus, as the warming of the world continues summers like 2018 and 2019 that are in our minds of having been quite exceptional will become increasingly normal.

Through the looking glass Because of its unprecedented level of spatial detail it is tempting to zoom further into the ultra-high resolution simulation. As a final illustration of just how rich the temperature field is, we created maps of the area around Amsterdam and overlaid it with some line and polygon features from OpenStreetMap (Fig. 7.15). In the maxima one can see the strong contrasts persisting right down into the towns and cities. Big canals like the "Noordzee-kanaal" are visible. Note also how Schiphol airport (the large red region in the center of the figure) and other industrial estates are generally warmer than the city center during the day. At night however the cities hold their heat much longer. With a 6-day average minimum temperature above 20°C occurring in parts of the larger cities, most of the nights there would qualify as 'tropical' (a 'tropical night' requires a minimum temperature above 20°C).

Final remark The PGW approach and the results in this chapter can not give a definite answer to the question of the (changed) probability of getting a July-2019-like heatwave in the future as it unfolds. Weather is not known for repeating itself – at least not in detail – and therefore an exact replay of 2019 is very unlikely. Nevertheless, we believe that "What-if" scenarios are meaningful as they can quantify the changes of events that historically were of very high impact.

Supplemental figures to this chapter

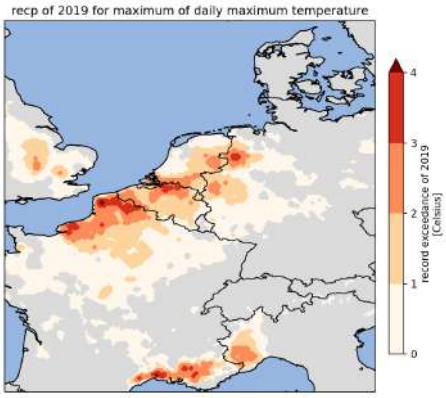

Figure 7.16: The amount of record exceedance in 2-meter maximum temperature (Txx) that occurred in 2019. Note: not all record exceedances occurred during the 22-27 July heatwave. Data: EOBS 0.1 resolution gridded data, 1920-2022.

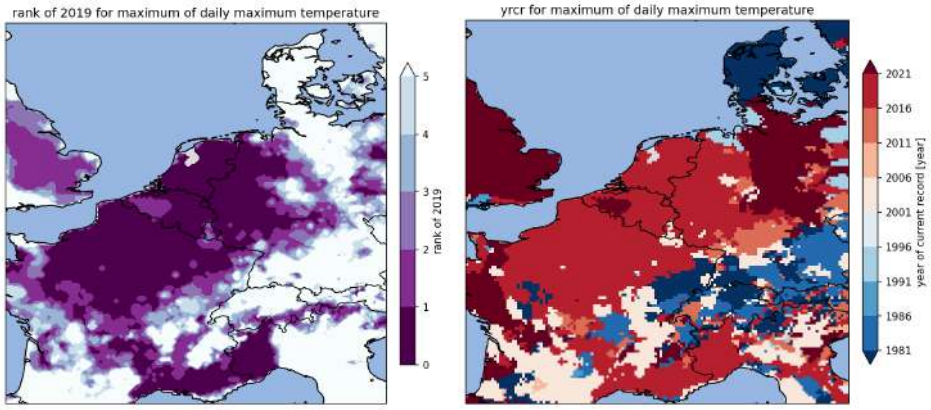

Figure 7.17: (left) Rank of the year 2019. (right) Year of the current maximum temperature.

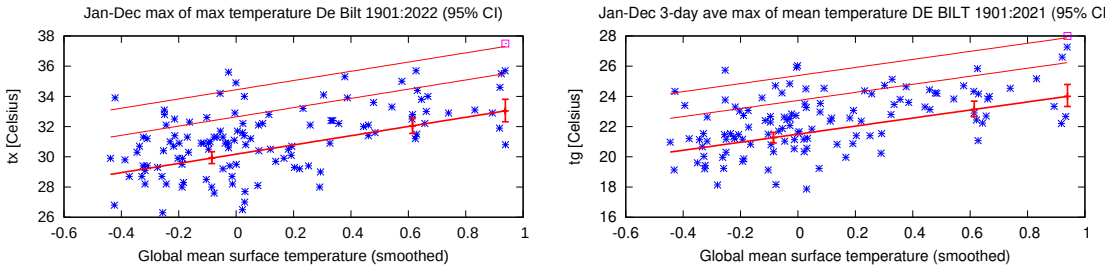

Figure 7.18: (left) Change of annual maximum of daily maximum temperature in De Bilt as a function of global temperature. The year 2019 is shown by the square in the top-right corner. (right) Same but for 3-day average temperature (data: climate explorer).

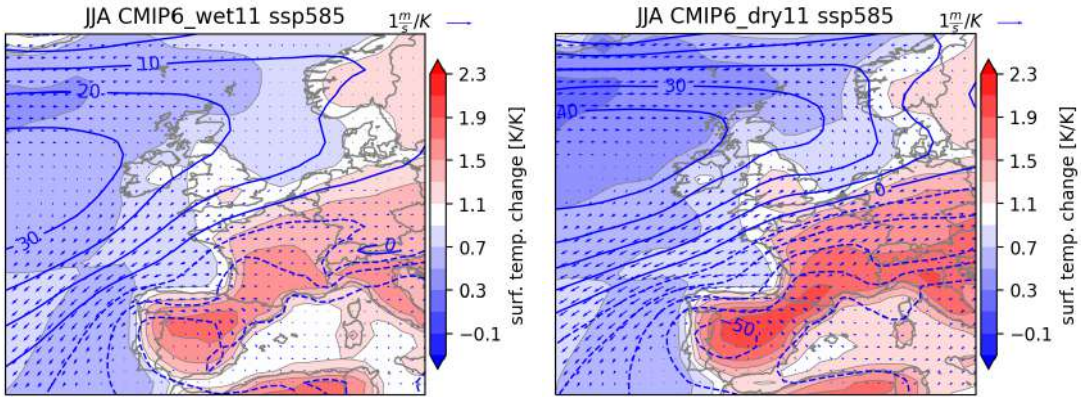

Figure 7.19: As in Fig. 7.3 but obtained for the "wet-11" (left) and "dry-11" (right) subset.

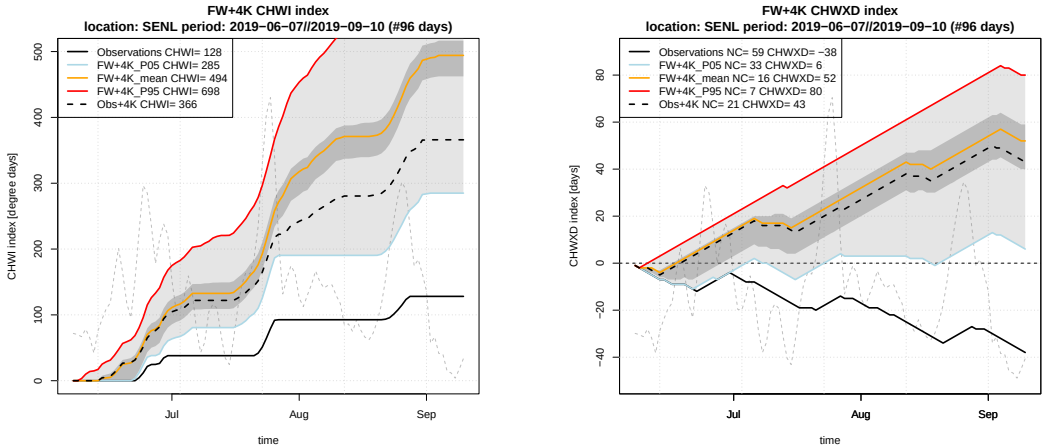

Figure 7.20: Cumulative heatwave intensity and duration indices for a +4K warming scenario. The different lines represent different subset of the RACMO runs and the grey shaded region represents the 5-95 range. The grey dotted line in the background is the 3-day maximum temperature.

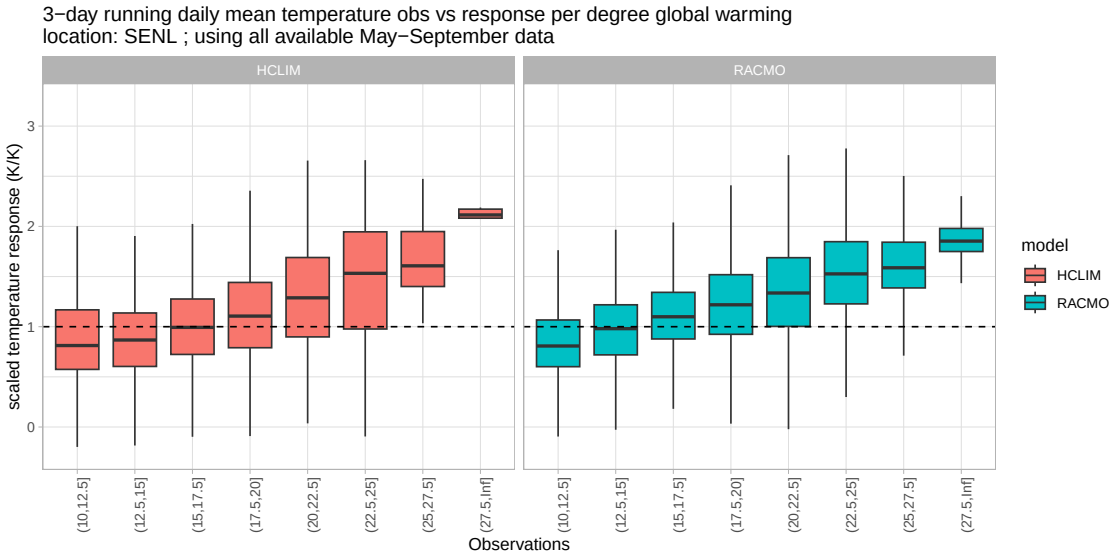

Figure 7.21: As in Fig. 7.14 but for 3-day mean temperature.

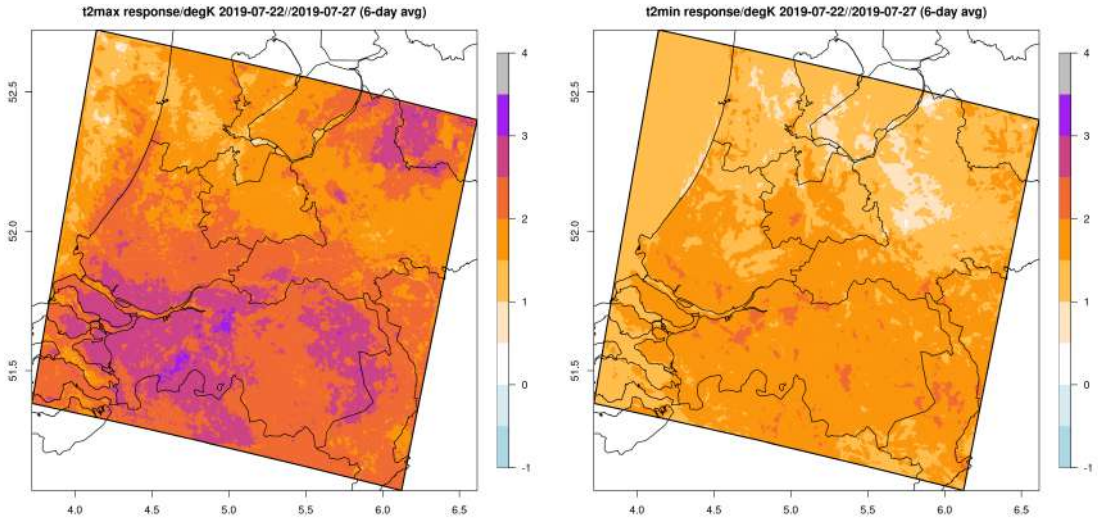

Figure 7.22: Average temperature response factor per degree warming (K/K) during the heatwave in the 150m resolution simulations. Left: maximum temperature. Right: minimum temperature.

Chapter 8

Storyline 1.5 degrees of global warming

8.1 Introduction

The primary goal of the Paris Agreement is to limit global warming to well below 2°C, preferably to 1.5°C, compared to pre-industrial (1850–1900) levels. The 1.5-degree goal has been confirmed during the 2021 COP26 meeting in Glasgow. The KNMI'23 climate scenarios are based on emissions following SSP1-2.6 or SSP5-8.5. In both cases global warming exceeds the internationally endorsed goal of 1.5 degrees.

Our *Paris scenario* for a global warming level of 1.5°C is obtained by the same procedure as used for the main scenarios, but with a warming target of 0.6°C above the temperature in the reference period. The latter figure results from the fact that according to the HadCRUT5 data set (Morice et al., 2021) the reference period is already 0.9°C warmer than the pre-industrial period.

However, the *current* climate (i.e., around the year 2020) is already about 1.2°C warmer than the pre-industrial one (WMO, 2022). This is so close to the 1.5-degree limit that a first impression of the climate in the Netherlands in a 1.5 degrees warmer world can be obtained by simply extrapolating past observed trends to the time global warming would reach 1.5°C . Doing so directly relates the "Paris climate" to the currently experienced one. Note that this approach assumes that the observed trend in the Netherlands is fully due to climate change, neglecting the effects of internal variability. As precipitation changes over short periods are dominated by internal variability, the extrapolation is only done for temperature.

8.2 Extrapolation of temperature observations

The current global warming of 1.2°C since the pre-industrial (1850-1900) period (WMO, 2022) is only 0.3°C away from the 1.5-degree goal. The left panel of Figure 8.1 shows time series of the observed temperature in De Bilt (KNMI daggegevens, 2022), together with the global mean temperature (from HadCRUT5, Morice et al. (2021)). If the present rate of warming continues, the 1.5°C limit is reached around 2033 (black dot). A linear regression of the two temperatures is shown in the right panel of Figure 8.1. Extrapolating the regression to a global warming of 1.5°C gives an annual-mean temperature in De Bilt of 11.4 ± 0.3°C (black square and two dots), corresponding to a warming of 0.9 ± 0.3°C (95% confidence interval) with respect to the reference (1991–2020) climate of 10.5°C. Compared to the *current* (2022) trend line value of 11.1°C, the increase is 0.3 ± 0.3°C. Thus a global-mean temperature increase of 0.3°C implies a warming over the Netherlands of between 0.0 and 0.6°C above the *current* temperature.

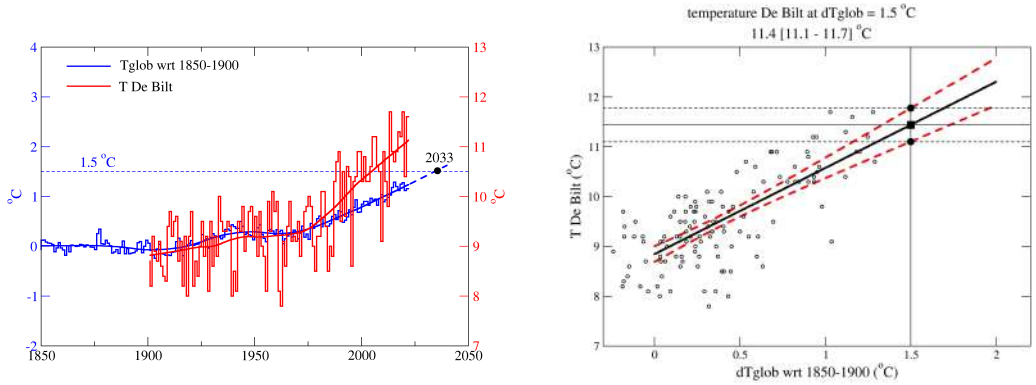

Figure 8.1: *Left:* Annual global-mean temperature anomaly with respect to the pre-industrial period 1850-1900 (blue, left y-axis), and annual-mean temperature in De Bilt (red, right y-axis) for the period 1901-2022. Using data from the 1991-2020 period, the global-mean temperature is linearly extrapolated to 1.5°C, which is reached in 2033 (black dot). *Right:* Linear regression of the two temperature series (thick black line) and 95% confidence interval (red dashed lines).

8.3 Model results

To compare the speed of warming as estimated from the extrapolation with that of the CMIP6 model results, we determine the year in which the models reach the 1.5-degree target (Figure 8.2). The distributions get narrower with higher emission scenario as the warming is faster, and the impact of internal variability on the mean temperature is lower. However, the means from the three emission scenarios are close together as the cumulative greenhouse gas emissions and thus their concentrations do not differ much between the three scenarios (IPCC, 2021a) for the near future.

Depending on the emission scenario, the models reach the 1.5-degree limit of global-mean warming on average between 2025 and 2032, which is earlier than the estimate of 2033 based on the extrapolation of past observed trends (Figures 8.1 and 8.3). This is because over the past thirty years the models warm faster than the observations. This can be seen from the dotted lines in Figure 8.3. They denote the linear trends over that period, extended to the period 1960–2050.

8.4 The 1.5-degree scenario

Based on the short investigation above, we expect the 1.5-degree global warming limit to be reached shortly after 2030, with an extra warming in the Netherlands of 0.6–1.2°C relative to the reference period (and 0.0–0.6°C relative to the trend-line level for 2020). How this extra warming translates into other variables is shown in Table 8.1. This table is obtained using the general method described in Chapter 2, but without the splitting into wet- and dry-trending scenarios. Within the short time horizon until 2033 natural variability is so large that our set of dry-/wet-trending CMIP6 models does not give a meaningful separation. We apply the method to the RACMO runs driven by SSP1-2.6-driven EC-Earth3$_{p5}$ runs at a warming level of 0.6°C above the level of the reference period, which is equivalent to 1.5°C above the pre-industrial level. The full table will be published on the KNMI'23 website.

The table shows that the local warming obtained from the scenario procedure is at the lower end of the range that is estimated from the extrapolation of the observations, which is 0.9 ± 0.3°C for the annual mean (Section 8.2). The reason is that the models (both CMIP6 and RACMO) fail to reproduce the observed rapid warming in Western Europe. This is a long-standing model problem already noted by Oldenborgh et al. (2009). If the underestimation of the local/regional

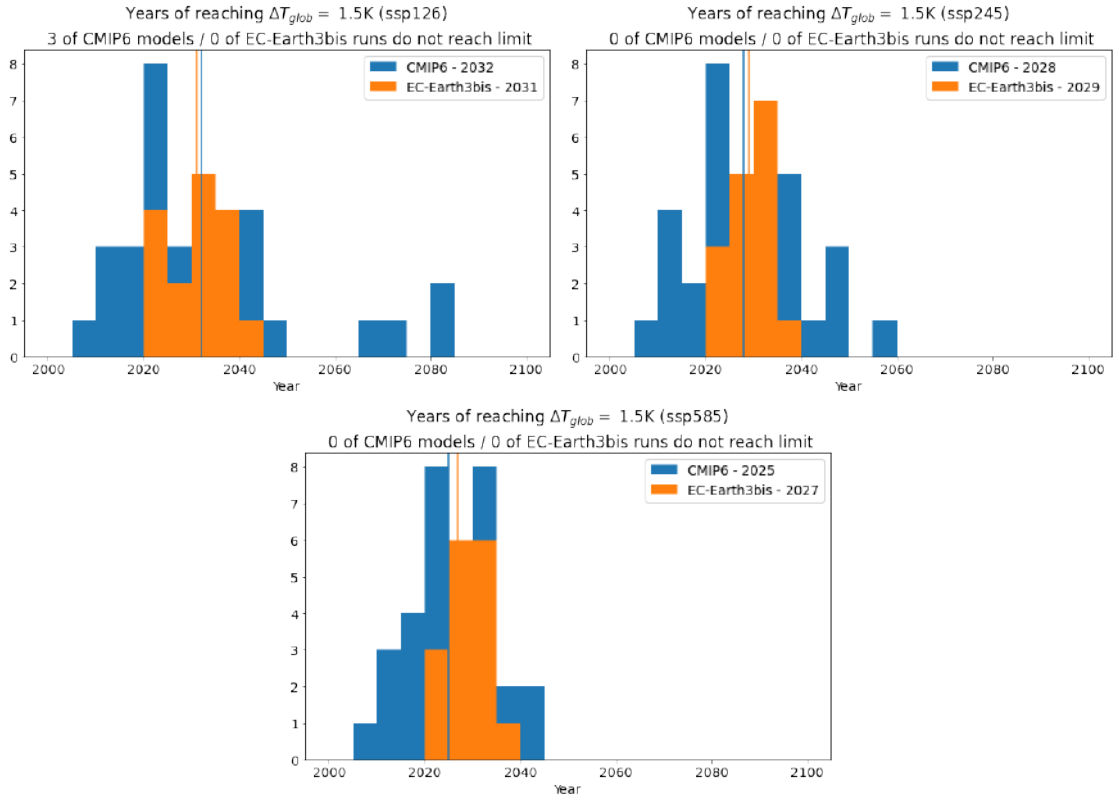

Figure 8.2: Histograms of years in which models reach $\Delta T_{\text{glob}} = 1.5°\text{C}$ above the pre-industrial level for the three SSPs considered. The vertical lines denote their means. These years are also displayed in the legend. Blue: CMIP6 models, orange: EC-Earth3 $_{\text{p5}}$ ensemble.

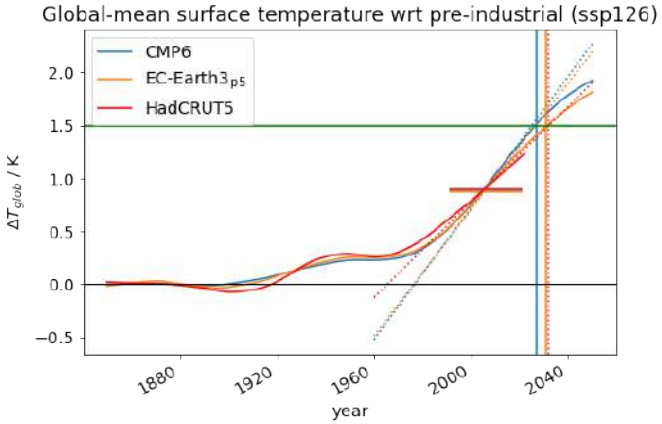

Figure 8.3: Trend of the global-mean temperature change since the pre-industrial period (1850–1900). *Blue*: mean of CMIP6 models, *orange*: mean of the EC-Earth3 $_{\text{p5}}$ runs, *red*: observations (HadCRUT5). The averages over the reference period are indicated by the horizontal lines. For the HadCRUT5 data the linear trend as determined over the reference period is shown as the dotted line and extrapolated to a longer period. The vertical lines mark the years in which the respective time series cross the 1.5-degree line (green). Note that we here show the year in which the model-mean crosses the 1.5°C line, not the mean of the years as in Figure 8.2. Due to the skewness of the distribution, these two years differ.

	annual	DJF	JJA
ΔT/°C	0.7	0.4	0.8
Δp/%	1.5	4.8	-2.7

Table 8.1: Changes wrt the reference period (1991-2020) in temperature and precipitation averaged over the Netherlands (annual, winter and summer) in the 1.5-degree scenario. The full table can be found in Chapter 10.

warming persists in the models, the warming levels in Table 8.1 are a lower bound of the actual warming levels. The projected precipitation changes in the 1.5-degree scenario are small.

8.5 Summary and conclusions

Based on a linear extrapolation of the observed global-mean temperature during the period 1991-2020, the Paris limit of 1.5-degree warming will be reached in 2033. The CMIP6 models warm faster and reach that warming a few years earlier. Extrapolating observed past trends from 2020 to 2033 suggests an additional warming in the Netherlands of 0.0–0.6°C as compared to the current (2020) level, or 0.6–1.2°C with respect to the reference period. This is twice as high as the range obtained from the model-based procedure that is described in Chapter 2 and used for the general KNMI'23 scenarios.

Chapter 9

Climate scenarios for the Caribbean Islands

9.1 Summary and key-points

This chapter discusses climate scenarios for the Caribbean islands of Bonaire, St. Eustatius and Saba (referred to as BES islands). Five variables are considered: temperature, precipitation, wind, sea level rise (SLR) and tropical cyclones (TCs). For all variables except TCs, we use a framework that is similar to the one used in the scenarios for the Netherlands. This includes a distinction between low (SSP1-2.6), medium (SSP2-4.5) and high (SSP5-8.5) emission pathways. For the generic variables (temperature, precipitation and wind) a further subdivision into a wet and dry trend scenario is made. Alternative methods are used for TCs. The main findings are:

Temperature: Warming continues in the high emission scenarios (Hd, Hn), reaching values up to +3.3K (above current climatology) in 2100. In the low emission scenarios (Ld, Ln) the warming plateaus at +0.8K around 2050, remaining approximately constant thereafter.

Precipitation: Strong reductions of more than 40% in 2100 in Hd; much smaller reductions in the wet scenario (Hn) and in all low emission scenarios. In Ln even a small increase occurs over St. Eustatius and Saba.

Wind: Small increases of a few percent (max. increase in annual wind speed over Bonaire under Hd in 2100 is around 10%).

Sea level rise: Present-day rates of SLR are on the order of 3-4 mm/yr. These rates increase in all scenarios, resulting in an expected (median) increase of sea level at the coast of Bonaire of 48 cm under SSP1-2.6 and 81 cm in SSP5-8.5 in 2100. There is a large uncertainty around these values. Implications of a partial collapse of the Greenland and Antarctic ice sheet are discussed.

Tropical cyclones: Increasing sea surface temperature (SST) tends to make TCs more powerful and wetter. Projected increases in upper-level wind shear may counteract this. Using synthetic storm risk modelling we estimated TC return periods. In the current climate, these are approximately twice as high for Bonaire as for the other islands. Future projections under SSP5-8.5 indicate minor changes up to 2050.

Note of caution: There is a discrepancy between observed and modelled historic trends, with the latter producing a systematic change towards El Niño like conditions (less precipitation, more wind, fewer TCs) and the former tending towards La Niña like conditions. Natural variability cannot be ruled out completely at this stage. However, there is a possibility that the models exhibit a systematic bias that, when corrected for, tends to shift the BES scenarios in the direction of La Niña, implying less drying and more TCs.

9.2 Introduction

The Caribbean islands of Bonaire, St. Eustatius and Saba (collectively referred to as the BES islands) are municipalities of the Netherlands. This report provides an analysis of the past, current and future climate of the BES islands. We also develop a set of climate scenarios for the region for temperature and precipitation, wind, sea-level rise and tropical cyclones. For the analysis of the past and present climate, our analysis relies on observational and reanalysis data. For the projected climate scenarios we use output from Global Climate Models (GCMs), except for tropical cyclones (TCs). There we adopt a comprehensive approach involving both a synthetic TC model and output from high-resolution regional climate models. Note that the BES scenarios are not as extensive as those developed for the European part of the Netherlands (hereafter referred to as the Netherlands). A brief overview of the methodology used for each variable is now given.

Precipitation, temperature and wind For these parameters, we focus on mean changes. We follow the approach used for the Netherlands as closely as possible while accounting for the specific conditions and limitations of the BES islands. To give one example, for the BES islands it makes more sense to make scenarios for a dry and wet season rather than for the classic summer and winter seasons. For temperature and precipitation, we use CMIP6 model output which is downscaled to obtain regional projections. However, unlike the Netherlands, statistical downscaling techniques are used for the BES islands instead of dynamical downscaling. This is the primary distinction between the two approaches. For wind, we also rely on CMIP6 model output. However, because some of the models did not provide daily wind data (only monthly), the statistical downscaling is not carried out.

Sea level rise To gain insight into the historical and future changes in sea level rise within the Caribbean region, we conducted an analysis of satellite-observed historic trends and projected trends from CMIP6 climate models following a low, medium, or high emission scenario. In addition to these, also much more extreme scenarios are outlined that could occur as a result of a collapse of the ice sheets of Greenland and Antarctica.

Tropical Cyclones Different approaches are employed to assess tropical cyclones (TCs), locally known as hurricanes, and their associated risk. The reason for this is twofold. Firstly, GCMs possess a too-coarse resolution, typically around 1.0°, to adequately resolve the TC's intensity, size and track. This limitation is particularly problematic for the most intense TCs which often have the greatest impact and inflict the highest damages. Secondly, GCM simulations generally cover climate conditions over 30 to 100-year periods, resulting in a relatively small sample size for calculating TC return periods, particularly for low-probability events with a high return period. As an alternative approach to assess TC risk, synthetic models have been utilized, as previously done in the "KNMI Klimaatsignaal'21" report (refer to Sect. 9.6.5).

In addition to employing synthetic modelling for TC risk assessment, we conducted detailed simulations of historical TCs using high-resolution regional dynamical downscaling. Adopting a storyline approach, we assessed the models' ability to simulate the major hurricane Irma (2017) under current climate conditions, and studied its potential changes in a warmer climate. To derive estimates of future changes in wind speed and precipitation associated with TCs, we employed targeted climate-change experiments using the Pseudo Global Warming (PGW) approach. These experiments allow for the projection of potential alterations in TC characteristics in response to a warmer climate.

This chapter continues with a summary of relevant findings from the latest IPCC report for the Caribbean. This is followed by the construction and discussion of the KNMI BES scenarios.

9.3 Summary of IPCC: observed and projected changes in the Caribbean

The IPCC AR6 WG I report (IPCC, 2021b) provides valuable insights into observed and projected climate change in the Caribbean region, which are summarized below. The summary is mainly based on the information provided in chapter 11 (Weather and climate extremes in a changing climate), Chapter 12 (Climate change information for regional impact and for risk assessment), and the Atlas. While much of this information also applies to the BES islands, additional details can be found in The State of the Caribbean Climate (Climate Studies Group Mona (Eds.), 2020) and Climate Trends and Projections for the Organisation of Eastern Caribbean States (OECS) Region (Van Meerbeeck, C., 2020).

- The Caribbean region has experienced significant warming (1901-2010), with trends of 0.19 °C (0.28 °C) per decade in daily maximum (minimum) temperatures (1961–2010) (*high confidence*). There is a significant increase in the intensity and frequency of hot extremes and a significant decrease in the intensity and frequency of cold extremes (*high confidence*).

- It is very likely that the Caribbean will continue to warm in the coming decades, although at a slightly lower rate than the global mean (*high confidence*). Climate models project a robust increase in the intensity and frequency of hot extremes, along with a robust decrease in the intensity and frequency of cold extremes (*high confidence*).

- While there is no significant long-term trend in precipitation over the period 1901-2012 in the Caribbean, significant interdecadal variability has been observed. From 1950 to 2016, a heterogeneous but prevalent drying trend has been identified in the region (*medium confidence*). Climate models project a reduction in precipitation over the Caribbean (*high confidence*), particularly during June to August by end of 21st century. The projected changes in consecutive dry days show inconsistent trends (*low confidence*), but there is an expected increase in the severity of agricultural and ecological droughts (*medium confidence*).

- It is *likely* that the global proportion of major tropical cyclone occurrences has increased over the last four decades, and this change cannot be attributed solely to internal variability (*medium confidence*). In the Caribbean, fewer but more intense TCs are expected (*medium confidence*), accompanied by higher rain rates (*very high confidence*). The intensity of TCs is anticipated to increase due to higher sea surface temperatures, although this could be inhibited by increases in vertical wind shear in the region.

- Sea level rise is *very likely* to continue in the Caribbean, exacerbating coastal inundation in conjunction with storm surges and waves. Shoreline retreat is projected for sandy coasts (*high confidence*). Additionally, there is *high confidence* in the intensification and duration of marine heatwaves.

9.4 BES scenarios for temperature, precipitation and wind

In this section, we construct and discuss the BES scenarios for the generic variables of temperature, precipitation and wind. The scenarios are developed for Bonaire separately and for St. Eustatius and Saba together. Here the focus is on the mean changes. Sect. 9.4.1 discusses the data, Sect. 9.4.2 the methods. This is followed by observed and projected changes (Sect. 9.4.3 and 9.4.4). In Sect. 9.4.6 we describe in more detail how the scenario results obtained for the specific islands are embedded within the much larger Caribbean region, and what the underlying large-scale drivers are. We believe this information is crucial as it might inform us how the difference between observed and modelled historic trends may influence the future projections and scenarios.

9.4.1 Data

To conduct statistical downscaling of (future) climate projections, it is essential to have access to long-term time series of accurate measurements from weather stations. However, for the BES islands, such comprehensive time series are not available. Consequently, we have used alternative datasets. For temperature and wind we use ERA5 reanalysis data (Hersbach et al., 2020). For precipitation, the best available datasets are based on weather station measurements on neighbouring islands. As a proxy for Bonaire we take precipitation data from Curaçao, while for St. Eustatius and Saba, we employ data from St. Martin. These datasets were obtained from the Global Surface Summary of the Day (GSSD). These observations have daily values with only a small number of missing data (2.6% and 1.4% for Curaçao and St. Martin, respectively). The quality of these observations was tested by comparing them to GPCP data.

To develop the BES scenarios we use daily data for precipitation and temperature. Daily data is necessary to be able to apply statistical downscaling. Out of the 33 CMIP6 models used for the Netherlands, only 29 provide daily data for precipitation and temperature. Therefore, for the BES scenarios, four models are excluded (CanESM5-CanOE, CIESM, FGOALS-f3-L and GISS-E2-1-G). For wind, we use monthly data as daily data was not available for a subset of the 29 GCMs. Furthermore, the wind scenarios (except for hurricanes) are based on model wind speed at 925 hPa rather than near-surface wind (usually at 10 m height). The 925 hPa wind is less noisy than near-surface wind, and while the climatologies will differ, we expect the trends to be quite similar. The limitation of using monthly instead of daily data is not too great a concern here since our focus is on changes in the mean wind. Extreme daily winds are primarily associated with hurricanes, which are not resolved by CMIP6 models anyway. Due to the smaller number of monthly values, statistical downscaling is not suitable. Therefore, we use the "raw" monthly CMIP6 output to derive BES scenarios for the mean wind.

The future projections and climate scenarios are derived from historical GCM simulations (reference period 1991-2020) and GCM simulations for different socio-economic pathways (SSPs) for the period from 2015 to 2100. The results presented in the general public report are based on computations derived from the forcing scenarios SSP1-2.6 and SSP5-8.5. Here we also include the forcing scenario SSP2-4.5.

9.4.2 Methodology

For the BES islands, six scenarios (four for the general public report) are provided for each of the target years, 2050 and 2100. The methodology can be summarized in the following steps:

1. **Selection of global temperature increase**: The change in global temperature (dT_{glob}) for each forcing scenario and target year is selected based on the best estimate provided by IPCC AR6.

2. **Matched warming method**: The corresponding thirty-year period is selected for each CMIP6 model that reaches the dT_{glob}.

3. **Definition of model groups**: Two groups of models are defined based on the changes in annual, dry season, and wet season precipitation in the BES region by the end of the century under the SSP5-8.5 scenario.

4. **Statistical downscaling**: The CMIP6 models in each group undergo statistical downscaling using the Quantile Delta Mapping method. This process is applied to precipitation and temperature variables.

5. **Calculation of projected change**: The projected variables for the target years 2050 and 2100 are computed as a function of global warming using a smooth function to reduce the noise introduced by natural variability.

Steps 1 and 2. Global temperature increase selection and Matched warming method

Steps 1 and 2 described in the previous section are applied globally. Therefore, both methods and results are in accordance with the Netherlands' scenarios. To provide a more detailed explanation of these steps, we refer the reader to Section 2.1.1.

Step 3. Groups of models definition

The third step of the methodology is similar to that used for the Netherlands but adapted for the Caribbean region. Due to the smaller size of Bonaire, St. Eustatius, and Saba (with a maximum area of 288 km^2), the masking method used for the Netherlands to obtain the 1-dimensional time series is not suitable. Instead we take the area-mean of the entire Caribbean region (defined as the region located between $10°N$ to $25°N$ and $85°W$ to $60°W$). The sensitivity of this choice was examined by using different-sized areas based on regions used in other studies such as Giannini et al. (2000), Herrera and Ault (2017), and Martinez et al. (2019), and it yielded similar results.

Once the time series for the BES region have been computed, we divide the 29 CMIP6 models into two groups, each consisting of ten models. The division is based on the future change in annual-mean, wet-season, and dry-season precipitation in the BES region. Specifically, we separate the ten wettest models and the ten driest models. The exact number of models in each group does not significantly affect the results. Precipitation is chosen as the primary selection criterion due to its relevance for people living in the Caribbean. Furthermore, studies like Giannini et al. (2000), Giannini et al. (2001a), and Rodriguez-Vera et al. (2019) demonstrate that precipitation in the Caribbean is sensitive to various configurations of global tropical atmospheric dynamics, such as El Niño or La Niña circulation, see Sect 9.4.6 for a more detailed explanation of El Niño / La Niña and how they affect precipitation in the Caribbean). Therefore, using precipitation as the central variable for the Caribbean ensures physically self-consistent scenarios. This approach closely resembles the one used for the Netherlands' scenarios, with the only difference being the seasons considered (wet/dry/annual instead of JJA/DJF/annual).

The selection of model groups was conducted once, specifically for SSP5-8.5 and the target year 2100, and subsequently applied to all other SSPs (SSP1-2.6, SSP2-4.5, and SSP5-8.5) and target years (2050, 2100). This single-time model-grouping method, as opposed to creating wet/dry groups for each target year and SSP, reduces the noise introduced by internal variability and provides a better representation of the climate change signal in the projections.

The division of the 29 CMIP6 models into two groups, based on the change in annual, wet and dry seasons' precipitation in the BES region under the SSP5-8.5 at the end of the century, leads to two scenarios for each SSP and target year.

Figure 9.1 illustrates the spread of the precipitation change (top) and temperature change (bottom) for the target year 2100 and the forcing scenario SSP5-8.5. The results are presented for the dry (red), wet (blue) and whole group of models (white). The upper panel demonstrates that the division into groups based on precipitation remains consistent across different seasons of the year. The lower panel shows that, for the entire year, models with larger decreases in precipitation also exhibit weaker increases in temperature, and vice versa. The driving factors behind this positive correlation between temperature and precipitation are discussed in Sect. 9.4.4.

It is important to note that the spread of models captured by the wet and dry groups is larger for precipitation compared to temperature. This discrepancy arises from the selection procedure employed. The wet and dry groups were specifically designed to encompass a significant portion of the CMIP6 model spread in precipitation response, while no such constraints were imposed on temperature. Therefore, if temperature and precipitation changes were uncorrelated, basic statistical principles would suggest that both wet and dry groups would yield a temperature response close to the ensemble mean. However, due to the positive correlation between precipitation and temperature response, this is not the case. Nevertheless, it is evident that for a given SSP, the wet and dry groups do not encompass the full range of model variability for temperature change. This behaviour is also observed in the generic scenarios for the Netherlands (as depicted in Fig. 2.14), where the spread captured by the ensemble mean of the groups is much smaller for temperature

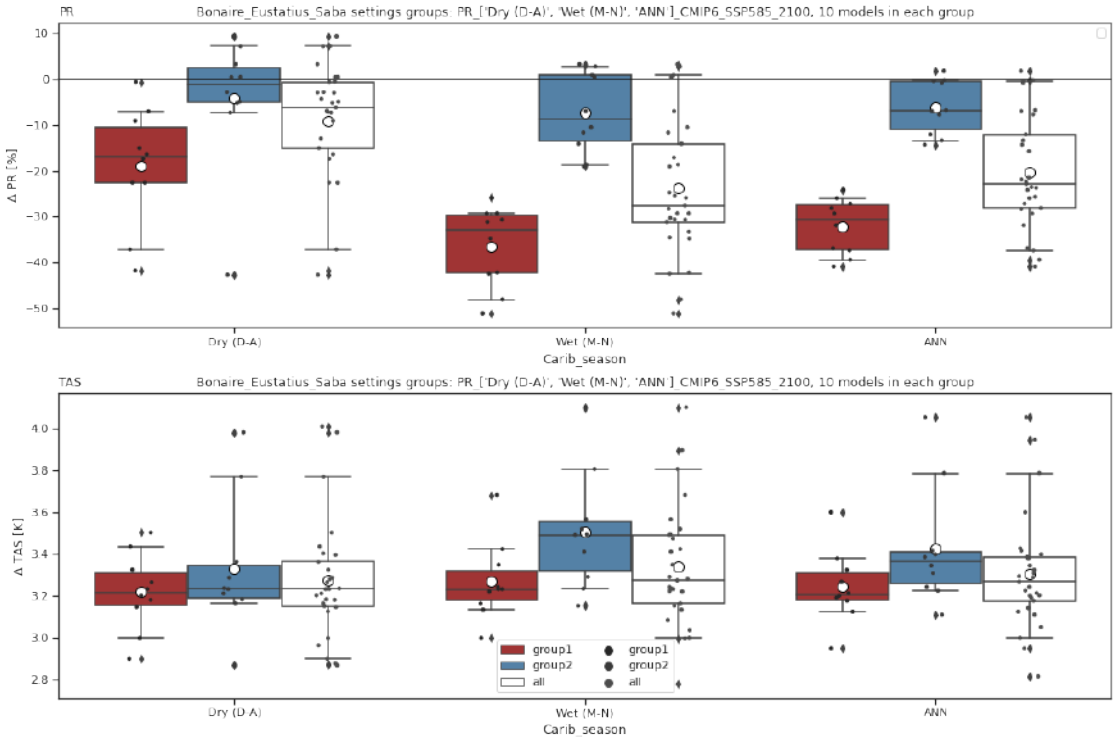

Figure 9.1: Spread of projected change in precipitation (upper panel) and temperature (lower panel) for the dry season (December to April), wet season (May to November) and annual period. Results are shown for the dry group of models (red), wet group of models (blue) and the entire set of models (white).

Variable:	Data set:
Temperature Bonaire	ERA5 Bonaire
Temperature St. Eustatius	ERA5 St. Eustatius
Precipitation Bonaire	GSSD station data Curaçao
Precipitation St. Eustatius	GSSD station data St. Martin

Table 9.1: Variables that are statistically downscaled, and the data set used for the BES islands.

compared to precipitation. Fortunately, for the BES islands, the model spread in the temperature response is considerably narrower compared to the Netherlands.

Step 4. Statistical downscaling

The fourth step of the methodology involves the downscaling of CMIP6 precipitation and temperature time series for the BES scenarios. Due to time and resource limitations, statistical downscaling is used instead of dynamical downscaling, and resampling is not applied. Note that for the wind scenarios, downscaling is *not* used; instead, the projected change is based on the raw CMIP6 output, as explained in Sect. 9.4.1. The time series from the nearest grid point to the islands of Bonaire and St. Eustatius in CMIP6 models are selected in order to differentiate between the two islands.

For temperature and precipitation, the method used for the statistical downscaling is the bias correction technique called Quantile Delta Mapping (QDM). Specifically, we use the univariate QDM approach. Several studies (Dieng et al., 2022; Cannon et al., 2015) consider this approach suitable for correcting climate model output, particularly for precipitation. It is also employed by other meteorological institutes, such as MeteoSwiss Feigenwinter et al., 2018. In the case of the Netherlands' scenarios, QDM is used to correct RACMO climatology biases (Section 2.1.10). QDM is a bias correction method that implicitly includes downscaling when the observed data set has a higher spatial resolution than the model grid. By comparing historical simulations with observations, QDM corrects systematic distributional biases in climate model outputs. Hence, it requires the availability of observations. For temperature, ERA5 reanalysis data is used, while GSSD station data is employed for precipitation. To bias correct temperature, both the ERA5 data set and CMIP6 models, the time series from the nearest grid point to the islands of Bonaire and St. Eustatius are selected as input for statistical downscaling. It is worth highlighting that the resolution of ERA5 data is inadequate to differentiate both Bonaire and St. Eustatius as discrete land areas within the ocean grid cells. Consequently, in the data set, these islands are represented by ocean grid points rather than land points. However, this does not affect the simulated absolute change in temperature during the present century due to the strong global warming signal in climate projections. This has been validated for the island of Curaçao, where accurate station data and ERA5 reanalysis are available. For precipitation, station data from neighbouring islands is used. Consequently, the CMIP6 models are downscaled to the locations of the airports of Curaçao and St. Martin, which serve as proxies for Bonaire and St. Eustatius, respectively. For each model, the nearest grid point to the station is selected. The nearest grid point method is also employed in Feigenwinter et al., 2018. Thus, the different scenarios for Bonaire and St. Eustatius / Saba originate from different input time series in the QDM, namely different CMIP6 time series from distinct grid points and different observed time series from various stations (for precipitation) or grid points (for temperature). Table 9.1 shows a summary of the above.

The QDM corrects systematic biases in the quantiles of a model. It achieves this by comparing quantiles of the present period's simulations with those derived from the observations (Feigenwinter et al., 2018; Cannon et al., 2015). For correcting the future projections, QDM assumes that the bias in each quantile in the future period is the same as in the present period. Therefore, the quantile trends are subtracted from the projected simulations, and the same quantile-dependent functions are applied. Finally, the quantile-dependent trends are added back to the corrected projected simulations. Consequently, QDM corrects the future projections while preserving the

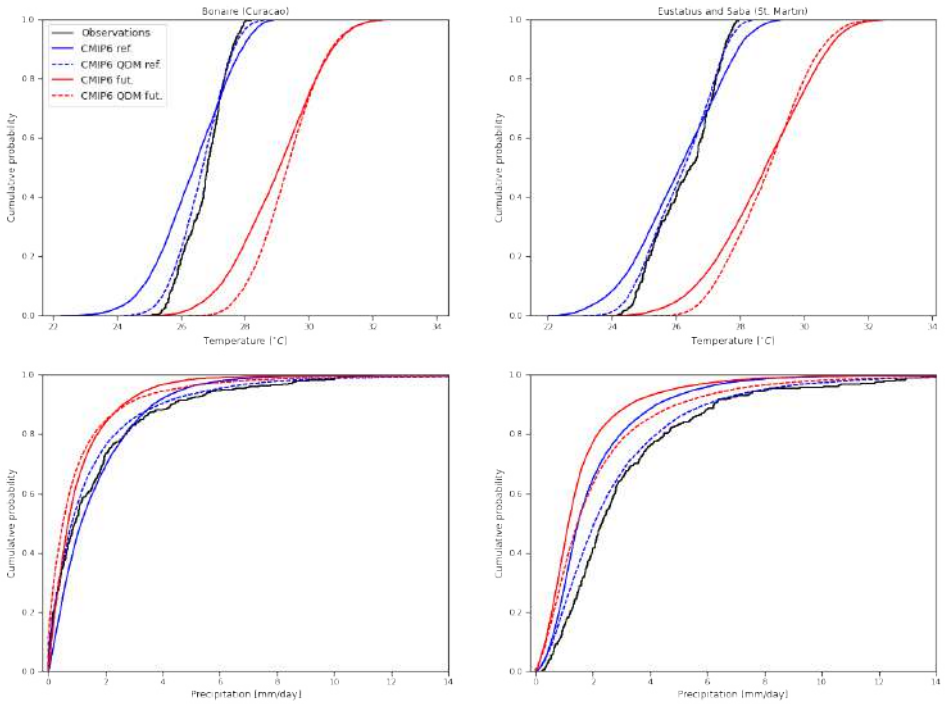

Figure 9.2: Cumulative distribution functions (CDFs) of temperature (upper panels) and precipitation (lower panels). The left panels show results for Bonaire (proxy: Curaçao), and the right panels for St. Eustatius and Saba (proxy: St. Martin). Black lines denote observations, blue lines CMIP6 model output (1991-2020) and red lines the future projections (matched warming, SSP5-8.5, 2100). Full lines show the raw (pre-QDM) CDF, dashed lines the corrected (post-QDM) CDF.

trend in each quantile (Cannon et al., 2015). Note that QDM does not preserve the mean trend itself. For a more comprehensive discussion of QDM, readers are referred to Section 2.1.10.

For the BES scenarios, we compute the transformation functions using 39 equally spaced quantiles ranging from 0 to 1. The QDM method is applied separately to each variable, island, and month. The period used to define the quantile-dependent functions aligns with the reference period (1991-2020). The transformation function is applied to the simulated time series using a moving window of thirty years. This approach ensures that the transformation function is consistently applied to thirty-year periods, which better represents extreme values. Considering that the projected time series exhibit a trend driven by global warming, analyzing longer periods result in the extremes at the start and the end of the time series being less represented in the higher and lower quantiles. Hence, it is important for the period used to define and apply the transformation functions to have the same length. For temperature, the adjustment parameters in the transformation function are additive, while for precipitation they are multiplicative.

Figure 9.2 presents the cumulative distribution functions (CDFs) of the variables for observations (black line), the reference period simulations (blue), and the future period simulations (with matched warming, red) for both raw (continuous) and corrected (dashed) time series. Comparing the corrected (dashed lines) with non-corrected (continuous lines) simulations provides a better understanding of the QDM explanation provided earlier. The CDFs for temperature (upper panels in Fig. 9.2) exhibit a resemblance to a normal distribution, while the precipitation CDFs (lower panels) resemble an exponential distribution.

Step 5. Calculation of projected change

The final step in producing the BES scenarios involves computing the projected change of the variables. To accomplish this, we express the projected variable as a function of global temperature increase for the three SSPs. Subsequently, we fit a third-order polynomial function to describe the relationship between the projected variable and warming. Since we assume that there is no climate change signal at 0 warming level, we force the polynomial function through the origin. Importantly, the fitted function incorporates the three SSPs, implying that we assume the regional climate change response is independent of the speed of global warming.

From the fitted function, we select the projected change of the variable for each target dT_{glob}. This approach is similar to the one employed in the scenarios for the Netherlands to choose the resampling criteria (Section 2.1.8). The primary advantage of this method is its ability to reduce noise introduced by internal variability, thereby enabling a more accurate capture of the climate signal in the final results.

9.4.3 Observed local trends

Temperature and precipitation trends from observations have been previously discussed in the "Klimaatsignaal'21" report. Here, we only summarise the main conclusions. In Bonaire, the temperature has shown an increase at a rate of approximately 0.15 $°C$ per decade since 1980. In Saba and St. Eustatius, the rate of temperature increase is larger, at around 0.23 $°C$ per decade. No significant trend in precipitation was identified, which is consistent with other studies and climate reports such as Van Meerbeeck, C. (2020), Herrera and Ault (2017), and Climate Studies Group Mona (Eds.) (2020). The "Klimaatsignaal'21" report did not discuss trends in the mean wind. A brief inspection of ERA5 reanalysis data reveals a small decrease in mean wind speed over the islands of Bonaire and St. Eustatius. This decrease is likely associated with the observed strengthening of the Walker circulation during the last few decades (Seager et al., 2019; Coats and Karnauskas, 2017; Bayr et al., 2014). The impact of the Walker circulation on past and future wind and precipitation in the Caribbean will be further discussed in Section 9.4.4.

9.4.4 Projected local trends

The projected changes in annual mean temperature and precipitation for the islands of Bonaire and St. Eustatius / Saba are depicted in Figure 9.3. The statistically downscaled CMIP6 time series are shown for temperature on both islands, while precipitation is represented for Bonaire (proxy: Curaçao) and for St. Eustatius / Saba (proxy: St. Martin). Under the SSP1-2.6 forcing, the mean projected temperature change for both islands remains under $1°C$ by 2100. Under SSP5-8.5 the temperature increases continuously throughout the century and is much stronger, around $3.5°C$ for the multi-model mean in 2100. The range of projected temperature change (90%-model spread, which includes interannual variability) across models is around $\pm 1°C$.

For precipitation, the low and high-emission scenarios also produce quite different results. In the low emission scenario (SSP1-2.6) the ensemble-mean change is only small despite the warming, while the SSP5-8.5 scenario projects strong reductions for all islands. The precipitation projections show large variations, caused by both interannual variability and model spread. For Bonaire precipitation reductions may range from very little change to a strong decrease of around 40% in SSP5-8.5. For St. Eustatius and Saba, the maximal reductions are somewhat smaller.

Figure 9.4 displays the projected changes in the mean wind speed for Bonaire and St. Eustatius / Saba, based on the CMIP6 models (not statistically downscaled). For SSP1-2.6, no significant changes in wind speed are projected. Under the high emission scenario SSP5-8.5 a slight increase of +3% for the multimodel mean is simulated for St. Eustatius and Saba, while Bonaire shows a stronger increase of up to +7% for the multimodel mean by 2100. The interannual and model spread is on the order of ±5% for both islands and forcing scenarios.

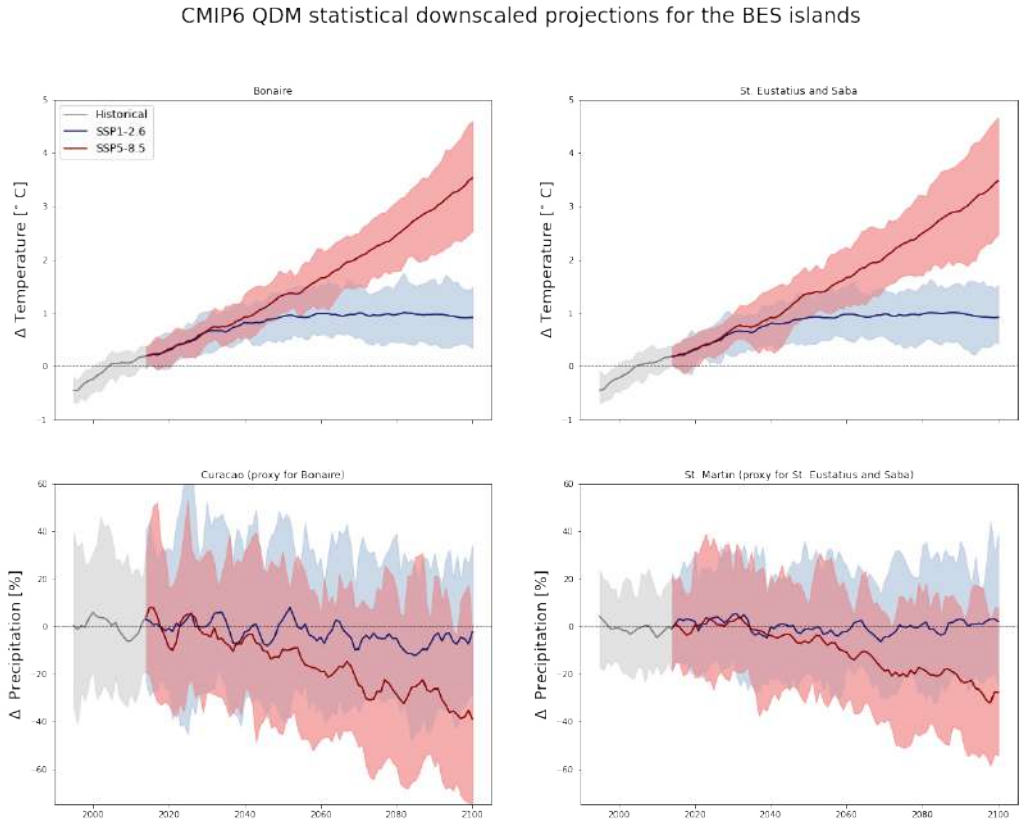

Figure 9.3: Projected changes in annual-mean temperature (upper panel) and precipitation (lower panel) for Bonaire (left) and St. Eustatius / Saba (right). The time series shown are the 29 CMIP6 models statistically downscaled and forced by the SSP1-2.6 (blue) and SSP5-8.5 (red). The historical period is shown in grey. The thick lines show the multimodel mean while the shaded regions show the 90% spread.

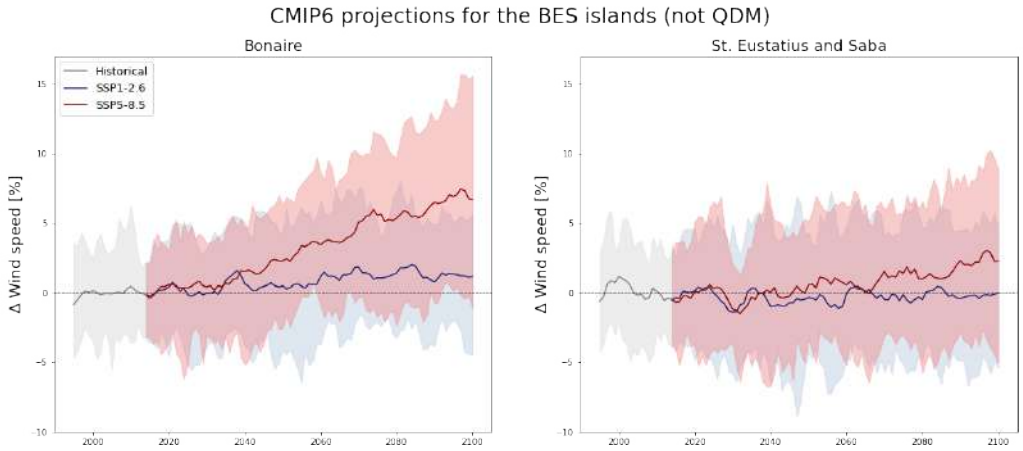

Figure 9.4: Projected change in wind speed for Bonaire and St. Eustatius / Saba. The time series shown are for the 29 CMIP6 models (not statistically downscaled) forced by the SSP1-2.6 (blue) and SSP5-8.5 (red). The historical period is shown in grey. The thick lines show the multimodel mean, while the shaded regions show the 90% spread.

Climate Scenarios for Bonaire – Temperature & Precipitation

Season	Variable	Indicator	1991-2020 observations	2050 ssp126 dry trend	2050 ssp126 wet trend	2050 ssp245K dry trend	2050 ssp245K wet trend	2050 ssp585K dry trend	2050 ssp585K wet trend	2100 ssp126K dry trend	2100 ssp126K wet trend	2100 ssp245K dry trend	2100 ssp245K wet trend	2100 ssp585K dry trend	2100 ssp585K wet trend
Annual	Temperature	average	28.5 °C	0.8 °C	0.8 °C	0.9 °C	1.0 °C	1.2 °C	1.3 °C	0.7 °C	0.7 °C	1.5 °C	1.6 °C	3.0 °C	3.3 °C
		year-to-year variations	0.3 °C	-0.0 °C	0.0 °C	-0.0 °C	0.0 °C	0.0 °C	0.1 °C	-0.0 °C	0.0 °C	0.0 °C	0.1 °C	0.1 °C	0.2 °C
	Precipitation	average amount	514.1 mm	-8.2%	-0.3%	-10.3%	-0.7%	-14.9%	-1.8%	-7.1%	-0.1%	-19.7%	-3.2%	-47.5%	-11.1%
		year-to-year variations	197.5 mm	-2.2%	4.7%	-3.4%	5.3%	-6.5%	6.1%	-1.6%	4.4%	-10.1%	6.4%	-29.0%	6.1%
Dry_season	Temperature	average	27.8 °C	0.8 °C	0.8 °C	0.9 °C	1.0 °C	1.2 °C	1.3 °C	0.7 °C	0.7 °C	1.5 °C	1.6 °C	2.9 °C	3.2 °C
	Precipitation	average amount	168.53 mm	-12.3%	-3.2%	-14.8%	-3.8%	-19.7%	-4.9%	-11.0%	-2.9%	-24.4%	-5.9%	-47.8%	-7.0%
Wet_season	Temperature	average	28.9 °C	0.8 °C	0.8 °C	0.9 °C	1.0 °C	1.3 °C	1.3 °C	0.7 °C	0.7 °C	1.6 °C	1.7 °C	3.1 °C	3.4 °C
	Precipitation	average amount	345.57 mm	-6.3%	1.5%	-8.3%	1.2%	-12.7%	0.1%	-5.4%	1.6%	-17.7%	-1.5%	-47.9%	-12.3%

Climate Scenarios for Bonaire –Wind (at 925 hPa)

Season	Variable	Indicator	1991-2020 observations	2050 ssp126 dry trend	2050 ssp126 wet trend	2050 ssp245K dry trend	2050 ssp245K wet trend	2050 ssp585K dry trend	2050 ssp585K wet trend	2100 ssp126K dry trend	2100 ssp126K wet trend	2100 ssp245K dry trend	2100 ssp245K wet trend	2100 ssp585K dry trend	2100 ssp585K wet trend
Annual	Wind	average wind speed	7.8m/s	1.8%	0.5%	2.3%	0.7%	3.4%	1.0%	1.6%	0.4%	4.5%	1.4%	10.8%	3.6%
		year-to-year variations	0.6m/s	-1.6%	0.6%	-2.4%	0.5%	-4.4%	0.3%	-1.2%	0.6%	-6.7%	0.0%	-17.3%	-1.6%
Dry_season	Wind	average	8.0m/s	1.1%	0.4%	1.4%	0.6%	2.0%	0.9%	0.9%	0.4%	2.8%	1.2%	7.1%	3.0%
Wet_season	Wind	average	7.6m/s	2.5%	0.6%	3.2%	0.9%	4.6%	1.3%	2.2%	0.5%	6.0%	1.8%	13.9%	4.6%

Figure 9.5: Climate scenarios for the island of Bonaire. The variables are evaluated for the entire year (annual) as well as for the dry season (December–April) and wet season (May–November). Interannual variability is calculated on a yearly basis.

Climate Scenarios for St. Eustatius and Saba – Temperature & Precipitation

Season	Variable	Indicator	1991-2020 observations	2050 ssp126 dry trend	2050 ssp126 wet trend	2050 ssp245K dry trend	2050 ssp245K wet trend	2050 ssp585K dry trend	2050 ssp585K wet trend	2100 ssp126K dry trend	2100 ssp126K wet trend	2100 ssp245K dry trend	2100 ssp245K wet trend	2100 ssp585K dry trend	2100 ssp585K wet trend
Annual	Temperature	average	27.8 °C	0.8 °C	0.8 °C	0.9 °C	1.0 °C	1.3 °C	1.3 °C	0.7 °C	0.7 °C	1.5 °C	1.6 °C	3.0 °C	3.2 °C
		year-to-year variations	0.2 °C	0.0 °C	0.0 °C	0.0 °C	0.0 °C	0.0 °C	0.1 °C	0.0 °C	0.0 °C	0.0 °C	0.1 °C	0.1 °C	0.2 °C
	Precipitation	average amount	1033.6 mm	-5.5%	2.6%	-7.4%	2.6%	-11.5%	1.9%	-4.7%	2.6%	-16.2%	0.7%	-43.6%	-8.3%
		year-to-year variations	254.3 mm	-0.9%	12.7%	-1.7%	14.0%	-4.0%	15.3%	-0.5%	11.9%	-6.7%	15.2%	-21.1%	5.4%
Dry_season	Temperature	average	26.8 °C	0.8 °C	0.8 °C	0.9 °C	0.9 °C	1.2 °C	1.3 °C	0.7 °C	0.7 °C	1.5 °C	1.6 °C	3.0 °C	3.2 °C
	Precipitation	average amount	303.7 mm	-3.3%	-3.4%	-4.6%	-4.0%	-7.8%	-5.1%	-2.7%	-3.1%	-11.5%	-6.0%	-34.1%	-9.4%
Wet_season	Temperature	average	28.5 °C	0.8 °C	0.8 °C	1.0 °C	1.0 °C	1.3 °C	1.3 °C	0.7 °C	0.7 °C	1.6 °C	1.6 °C	3.0 °C	3.3 °C
	Precipitation	average amount	729.9 mm	-6.8%	4.4%	-8.9%	4.6%	-13.5%	4.1%	-5.8%	4.3%	-18.7%	2.9%	-48.4%	-7.4%

Climate Scenarios for St. Eustatius and Saba – Wind (at 925 hPa)

Season	Variable	Indicator	1991-2020 observations	2050 ssp126 dry trend	2050 ssp126 wet trend	2050 ssp245K dry trend	2050 ssp245K wet trend	2050 ssp585K dry trend	2050 ssp585K wet trend	2100 ssp126K dry trend	2100 ssp126K wet trend	2100 ssp245K dry trend	2100 ssp245K wet trend	2100 ssp585K dry trend	2100 ssp585K wet trend
Annual	Wind	average wind speed	7.0m/s	0.0%	-0.0%	0.1%	0.0%	0.5%	0.2%	-0.0%	-0.0%	1.0%	0.4%	4.0%	1.7%
		year-to-year variations	0.6m/s	-2.6%	-1.6%	-3.3%	-1.8%	-4.8%	-2.1%	-2.3%	-1.5%	-6.3%	-2.2%	-12.2%	-1.2%
Dry_season	Wind	average	7.1m/s	0.3%	-0.8%	0.5%	-0.8%	0.9%	-0.6%	0.2%	-0.7%	1.4%	-0.4%	4.6%	1.9%
Wet_season	Wind	average	6.9m/s	-0.0%	0.6%	0.1%	0.7%	0.5%	0.9%	-0.1%	0.5%	1.0%	1.1%	4.1%	1.7%

Figure 9.6: Climate scenarios for the islands of St. Eustatius and Saba. The variables are evaluated for the entire year (annual) as well as for the dry season (December–April) and wet season (May–November). Interannual variability is calculated on a yearly basis.

9.4.5 Scenario tables for the BES islands

As discussed in the previous section, the projections for the BES islands give quite broad ranges of possible future values. This is a result of both model spread and interannual variability. In the final step, we now derive climate scenarios for the target years of 2050 and 2100. Using methods described before, for each emission pathway and target year, a dry- and a wet-trending scenario is created, using the 30-year periods around these target years. The final results assume the form of tables of mean changes and estimates of interannual variability (Figs. 9.5-9.6). Scenario values are produced for the annual mean, the dry (December–April) and the wet (May–November) season.

A few key results are now discussed. The warming continues in both the dry and the wet high emission scenarios (Hd, Hn respectively), reaching values up to +3.3K (above current climatology) in 2100. In the low emission scenarios (Ld, Ln) the warming plateaus at +0.8K around 2050, remaining approximately constant thereafter. The largest differences in temperature are therefore caused by the emission path. For precipitation, strong reductions of more than 40% in 2100 are seen only in Hd (high-dry); much smaller reductions are found in the wet scenario (Hn) and in all low-emission scenarios. In Ln even a small increase occurs over St. Eustatius / Saba. Therefore, in contrast to the temperature, for precipitation, we do see that the wet and dry scenarios are very different. Finally, for wind speed, the changes are generally modest. The maximal increase in annual wind speed occurring over Bonaire under Hd in 2100 is around 10%.

It is important to note that although CMIP6 models project a small but systematic increase in wind speed throughout the current century, observed trends have indicated a decrease in wind speed. Also, for precipitation, the models seem to be showing a stronger drying trend than the observations. These differences may be linked because wind and precipitation are related through the Walker circulation which could change in the future. In the next section, we explore the drivers underlying the future changes in more detail.

9.4.6 Large-scale drivers of Caribbean climate change

To gain insight into the drivers of climate change in the Caribbean region, it is essential to examine the spatial patterns of projected temperature and precipitation changes beyond the scale of individual islands. Figs. 9.7–9.8 show the ensemble-mean projected change for the dry and wet groups at the end of the century under SSP5-8.5. This scenario was selected due to its higher signal-to-noise ratio, enabling the identification of distinct atmospheric processes. One of the most striking aspects in Fig. 9.7 is the spatial extent of the mean precipitation change pattern. Numerous regions exhibit decreases in precipitation, while others display substantial increases. Across most of the Caribbean, robust reductions in precipitation are observed. Notably, the largest absolute reduction occurs during the wet season for both groups. As indicated in Fig. 9.3, a more pronounced drying trend is observed in Bonaire compared to St. Eustatius. For temperature, whereas warming occurs across all regions, a large-scale pattern is clearly visible.

Examining the spatial patterns of projected temperature and precipitation gives rise to two questions. Firstly, what processes drive the drying in the Caribbean region? And secondly, what causes the differences between the wet/dry patterns? To address these questions, it is important to have a general understanding of the current climate in the Caribbean.

In the present climate, the El Niño Southern Oscillation (ENSO) serves as the dominant driver of interannual variability in precipitation across the Caribbean (Giannini et al., 2000; Giannini et al., 2001a; Rodriguez-Vera et al., 2019). El Niño, the warm phase of ENSO, is characterized by anomalously warm sea surface temperatures (SSTs) over the central and eastern equatorial Pacific, which in turn drive the eastward migration or weakening of the Walker circulation. This shift leads to subsidence, intensification of trade winds, and moisture divergence in the Caribbean region, resulting in drier conditions. Conversely, during La Niña, the opposite pattern unfolds. Cold SST anomalies in the equatorial eastern Pacific drive the westward migration or intensification of the Walker circulation. As a result, the Caribbean experiences enhanced upward motion, weakened trade winds, and moisture convergence, leading to increased precipitation.

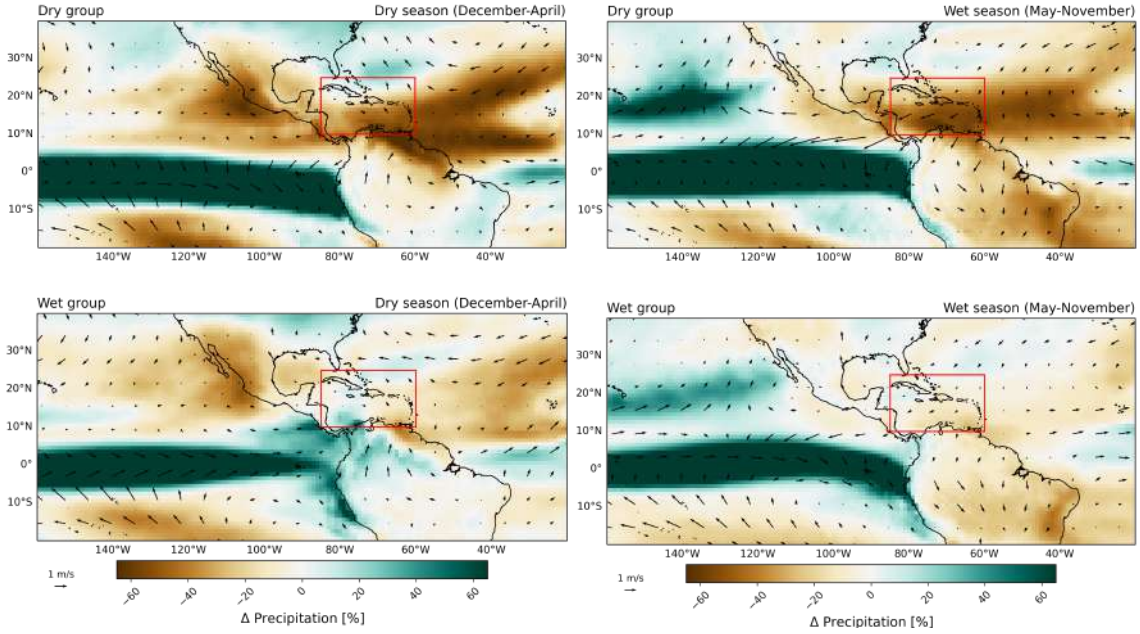

Figure 9.7: Projected relative precipitation change (colors, in %) and absolute wind change at 925 hPa (vectors, in m/s) for the dry (upper panels) and wet (lower panels) groups of models under SSP5-8.5 in 2100 (matched warming). The figures display changes for the dry season (December–April) in the left panels and the wet season (May–November) in the right panels. The data presented depicts the multimodel mean of the 10 CMIP6 models in each group (The groups are calculated for SSP5-8.5 in 2100). The figures show the raw (i.e., not downscaled) multimodel mean of the 10 CMIP6 models in each group.

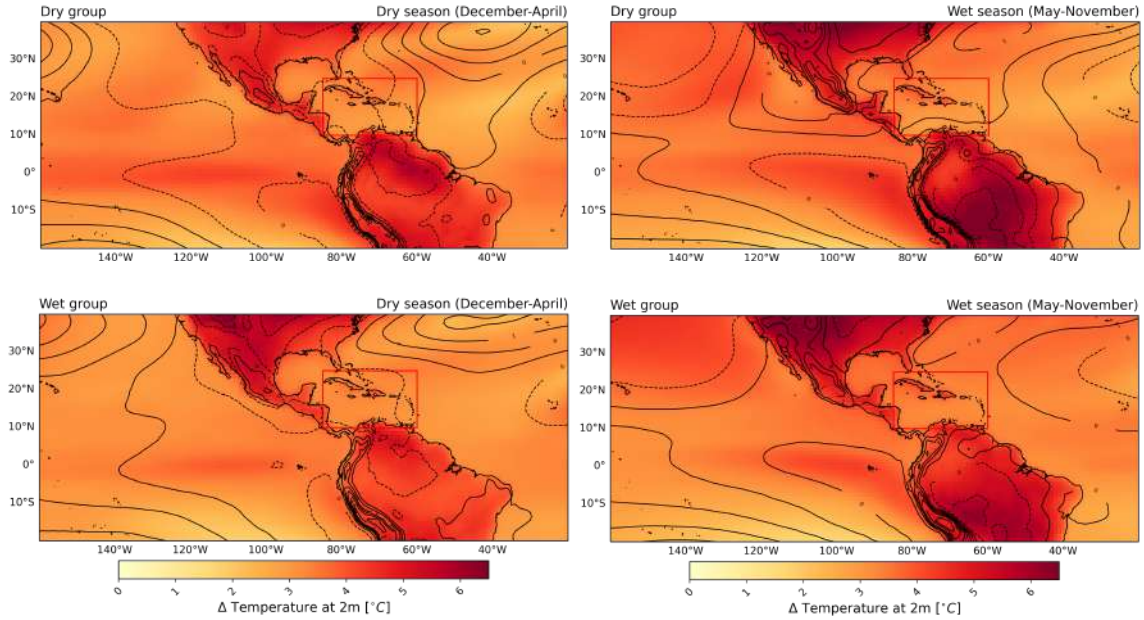

Figure 9.8: Projected change in 2m-temperature (colors, in $°C$) and sea level pressure (contours, in hPa) for the dry (upper panels) and wet (lower panels) groups of models under SSP5-8.5 in 2100 (matched warming). Positive sea level pressure changes are represented by continuous lines, negative changes are dashed. Changes are shown for the dry (December–April) and wet (May–November) seasons in the left and right panels, respectively. The figures show the raw (i.e., not downscaled) multimodel mean of the 10 CMIP6 models in each group. The red box indicates the Caribbean region.

A dominant El Niño-like circulation (or eastward migration of the Walker circulation) has been identified in CMIP6 models due to global warming (Fredriksen et al., 2020; Seager et al., 2019; Wills et al., 2022). Consequently, the projected drying in the Caribbean at the end of the century might be driven by the El Niño-like circulation. The signature of this circulation pattern can be observed in Figure 9.8 for all models and seasons, where stronger warming over the central east equatorial Pacific is evident. However, differences exist between the wet and dry groups of models. In Fig. 9.8 a stronger east equatorial Pacific warming can be seen for the dry group. Additionally, Fig. 9.7 shows that the increase in precipitation for the dry group is confined to the Intertropical Convergence Zone (ITCZ) region (a broad band along the Equator), whereas for the wet group, precipitation increase extends further east. These differences suggest that the dry group is characterised by stronger El Niño-like dynamics compared to the wet group.

When looking at the projected wind change (vectors in Fig. 9.7), the hypothesis stated in the previous sentence is confirmed. The dry group of models simulates a strong east equatorial Pacific warming, which drives a robust eastward migration of the Walker circulation, indicative of intense El Niño-like dynamics. As a result, the downward branch of the Walker circulation is situated over the Caribbean region, leading to moisture divergence and strong trade winds. Both of these factors are associated with dry conditions. Conversely, the wet group of models is characterized by a weaker warming in the equatorial east Pacific, resulting in a milder eastward migration of the Walker circulation. Consequently, subsidence, trade winds, and moisture divergence are weaker in the wet models, leading to wetter conditions.

The positive correlation between temperature and precipitation in the Caribbean, as derived from Fig. 9.1, can also be explained by the ENSO-like dynamics. As discussed earlier, the strength of the east equatorial Pacific warming is directly linked to the intensity of the zonal migration of the Walker circulation and subsequent wind patterns. Strong surface winds result in increased sensible

and latent heat loss from the sea, leading to cooler SSTs. Therefore, the eastward migration of the Walker circulation, driven by warm east equatorial Pacific SSTs, enhances trade winds in the Caribbean. These intensified trade winds contribute to both a decrease in precipitation and a decrease in temperature, thereby establishing a positive correlation between temperature and precipitation. Consequently, the wet group exhibit warmer temperatures and weaker winds (Tbls. 9.5 and 9.6) compared to the dry group. This ENSO-tropical Atlantic SST teleconnection has been previously investigated (Giannini et al., 2001b; Enfield and Mayer, 1997).

The mechanisms we have explained align with the findings of Brotons et al. (2023), where an investigation of the drivers of the Caribbean drying in CMIP6 models was conducted. Through the examination of the projected circulation changes and carrying out a moisture budget analysis, they found that the eastern and central Pacific warming, resembling an El Niño/Pacific Decadal Oscillation (PDO) pattern, emerged as the main driver of the Caribbean drying, particularly during the wet season. During the dry season, the advection of dry air from outside the Caribbean region appeared to be the dominant mechanism contributing to the drying trend. Furthermore, we concluded that the drying may also be influenced by the weakening of the Atlantic Meridional Overturning Circulation (AMOC), which results in the southward migration of the ITCZ, as well as land-sea temperature gradients that induce divergent flow over the Caribbean, ultimately enhancing dry conditions.

In summary, the dominant circulation change in the CMIP6 models resembles an El Niño-like pattern, characterized by a pronounced warming in the east equatorial Pacific. This warming drives the eastward migration of the Walker circulation, leading to subsidence, moisture divergence, and trade winds in the Caribbean. These changes result in reduced precipitation and a relative cooling or weaker warming of SSTs in the region. The dry models exhibit a stronger manifestation of this mechanism, with greater increases in trade winds, decreases in precipitation, and weaker warming compared to the wet models.

9.4.7 Discussion

The method used to develop the BES islands scenarios for the generic variables (temperature, precipitation and wind) offers several advantages and disadvantages. One obvious advantage is that the scenarios are based on a comprehensive set of global climate models (CMIP6 models), that allow for the incorporation of a large part of the uncertainty in the climate response. However, it is important to acknowledge that, in the end, the scenarios are only as good as the CMIP6 models that are included. The CMIP6 models have inherent known limitations and suffer from systematic biases that may have an impact on the reliability of the scenarios.

The most important of these biases relate to the Walker circulation response and the El Niño / La Niña discussion from the previous section. Despite the importance of equatorial Pacific SSTs in modulating Earth's climate and Caribbean precipitation, several studies indicate that CMIP6 models (as well as previous versions) fail to capture the recent warming trend in this region. Observations over the past few decades have shown a La Niña tendency, while CMIP6 models exhibit an El Niño tendency due to climate change (Bayr et al., 2014; Seager et al., 2019; Coats and Karnauskas, 2017; Kohyama et al., 2017). The discrepancy between observed and modelled equatorial Pacific SST trends has concerned the scientific community, and the drivers behind this mismatch remain a subject of ongoing debate. While some studies argue that these opposite trends are driven by internal variability (Bayr et al., 2014; Kociuba and Power, 2015), many others suggest that biases in climate models are the main cause (Seager et al., 2019). If the latter is true, the reliability of CMIP6 climate projections, including these climate scenarios, becomes questionable, even when using bias correction methods (which will be discussed further in Section 9.4.7). Therefore, it is crucial to approach the BES scenarios with caution, as CMIP6 models may exhibit an El Niño tendency and thereby potentially overestimate the drying and the increase in wind speed in the region. Incidentally, this bias may also have an impact on another hazard in the region, tropical cyclones. During El Niño like conditions tropical cyclone activity is generally suppressed. The potential bias in the equatorial Pacific warming trend poses a challenge to accurately represent future climate conditions in the region. While the QDM method employed

in this study helps in partially correcting the biases by comparing present and future simulations with observations, it does not fully address biases in trends.

In addition to the biases associated with CMIP6 models and their possible consequences for the scenarios, a major limitation encountered during the development of these scenarios is the lack of sufficiently long and accurate observational data sets for the Caribbean region. Despite extensive efforts to use various observational products, none of them provided the required quality for the BES islands. Furthermore, the absence of high-resolution gridded data sets specific to the Caribbean region, similar to the European Climate Observation System (EOBS) for Europe (Cornes et al., 2018), has limited the end product of these scenarios by not being able to provide gridded downscaled projections, but only 1-dimensional time series projections. Access to improved observational data sets would significantly enhance the quality and reliability of these scenarios. It is important to acknowledge that the current results represent the best achievable outcomes given the available resources and data limitations. However, the scenarios can be further improved with more accurate and comprehensive observations.

9.5 Sea level rise

9.5.1 Data

The sea level record from the tide gauge of Puerto Rico was downloaded from the Permanent Service for Mean Sea Level (PSMSL). Monthly sea level from satellite altimetry was downloaded from the Copernicus Marine Data Store. Globally averaged sea level from satellite altimetry was downloaded from AVISO. Tide gauge observations are relative sea level, they represent sea level compared to the earth's surface. On the other hand, observations from satellite altimetry are geocentric sea level. However, the global sea level from satellite altimetry is corrected for the effect of Glacial Isostatic Adjustment (WCRP, 2018).

9.5.2 Observed trends

There are no tide gauge data from the BES islands in the PSMSL database. However, there is a long, mostly uninterrupted, tide gauge record from Magueyes Island, Puerto Rico, extending back to 1955 (Figure 9.9 (a)). A long-term sea level rise is clear. We also see a fast sea level rise between 1955-1985, a plateau between 1985-2005 and a continued rise after 2005. This plateau could be due to natural climate variability in wind or local steric effects, but it could also be due to some missing data. There are 13 months of missing data between 1979 and 1982 out of a total of 36 missing months over the full-time series. We also compare tide gauge sea level observations to the satellite altimetry observations close to the tide gauge location. Over the period 1993 to 2021, the overlapping period between satellite altimetry and tide gauge observation, there is a very good agreement between the two measurements, even though the two methods do not measure exactly the same thing (see Section 9.5.1). The trend over the overlapping period is a little smaller in satellite altimetry measurement, with 3.2 $\pm$ 0.5 mm/yr, than at the tide gauge, with 3.8 $\pm$ 0.5 mm/yr. This difference could be due to vertical land motion. Some local subsidence at the tide gauge location would increase the sea level trend measured there, but would not have an effect on satellite measurements. The long-term linear trend from 1955 to 2022 is 2.0 $\pm$ 0.2 mm/yr, which indicates that sea level rise has accelerated in this region. Overall, we see that tide gauge and altimetry data are in good agreement for Puerto Rico which indicates that satellite altimetry provides useful results for the BES islands as well.

We now turn to the analysis of satellite altimetry measurements at the BES islands. Yearly time series are shown in Figure 9.9 (b). Sea levels can vary by up to 4 cm from one year to the next. The linear trend over the full period is 3.7 $\pm$ 0.3 mm/yr at Bonaire and 3.0 $\pm$ 0.4 at St. Eustatius / Saba, which is close to the global sea level rise of 3.4 $\pm$ 0.4 mm/yr.

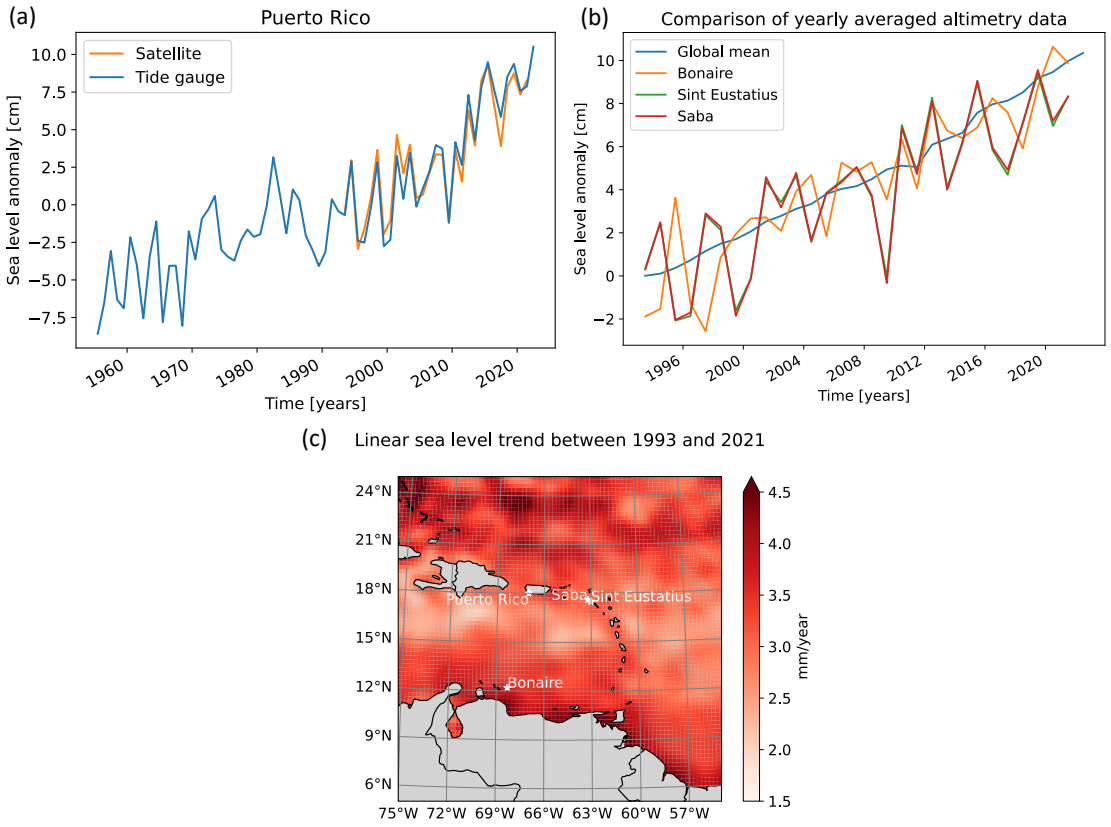

Figure 9.9: (a) Yearly averaged observed sea level at Puerto Rico from tide gauge and satellite altimetry. (b) Yearly averaged sea level for the BES islands and globally averaged from satellite altimetry. (c) Map of linear sea level trend in mm/yr for the Caribbean.

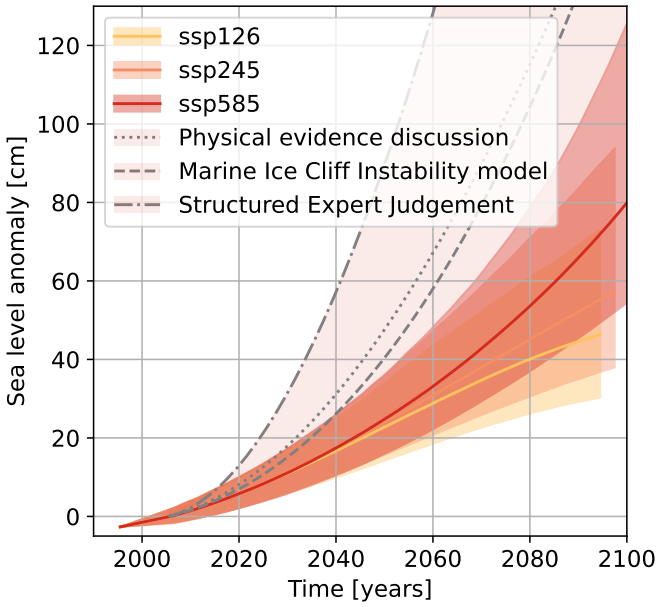

Figure 9.10: Sea-level scenarios at Bonaire for the SSP1-2.6, SSP2-4.5 and SSP5-8.5 emission scenarios compared to the reference period 1995-2014. The median and 5th to 95th percentile range are shown. Grey lines represent the low probability high impact scenarios (see chapter 4).

9.5.3 Projections

Sea level scenarios for Bonaire are shown in Figure 9.10. The median sea level in 2100 for the emission scenarios SSP1-2.6, SSP2-4.5 and SSP5-8.5 are 48, 59 and 81 cm respectively. The local sea level at Bonaire is expected to rise a little faster than the global mean while at St. Eustatius and Saba it is expected to be very close to the global mean. The numbers for 2050 and 2100 for Bonaire can be found in table 9.2 and for St. Eustatius / Saba in table 9.3.

We also define three low probability high impact scenarios for the BES islands shown in Fig 9.10 to highlight that multiple lines of evidence point to a small probability (less than 5% for the SSP5-8.5 emission scenario) of a collapse of the ice sheets of Greenland and Antarctica which could result in more than 150 cm sea level rise this century (see chapter 4).

9.6 Hurricanes

9.6.1 Introduction

Tropical cyclones (TCs), locally known as hurricanes in the Atlantic Ocean, are arguably one of the most impactful meteorological phenomenon in the Caribbean. TCs either form directly over the warm ocean waters in the Caribbean region or pass through it after having been formed further eastward over the open Atlantic Ocean, and being transported by (easterly) trade winds. TCs can have substantial impacts in coastal regions when they approach land and/or make landfall through their high wind speeds, large storm surges and high precipitation totals. These primary hazards, in turn, can trigger other hazards such as inland flooding and landslides in mountainous terrains. Without implementation of risk mitigation measures, it is expected that the societal impact of landfalling TCs will increase in the future, primarily driven by a combination of increasing storminess, sea level rise and coastal population numbers. It is therefore crucial to better understand TC characteristics and probabilities under future climate change.

To understand how the TC frequency may change, we need to study the environmental conditions under which TCs form and how these conditions change towards the future. This is discussed

2050			
	SSP1-2.6	SSP2-4.5	SSP5-8.5
Global steric	8 (5 to 10) cm	8 (6 to 11) cm	9 (6 to 12) cm
Ocean Dynamic Sea Level	4 (-2 to 10) cm	4 (-2 to 9) cm	3 (-4 to 9) cm
Glaciers	3 (2 to 5) cm	4 (2 to 5) cm	4 (3 to 6) cm
Landwater	1 (1 to 2) cm	1 (1 to 2) cm	1 (1 to 2) cm
Greenland	2 (2 to 3) cm	3 (2 to 4) cm	3 (2 to 4) cm
Antarctica	4 (0 to 14) cm	4 (-1 to 15) cm	4 (-1 to 14) cm
GIA	1 (1 to 1) cm	1 (1 to 1) cm	1 (1 to 1) cm
Total	23 (14 to 34) cm	24 (16 to 36) cm	25 (16 to 37) cm
Rate total	6.1 (4.4 to 9.6) mm/yr	6.8 (5.2 to 11.1) mm/yr	7.9 (5.9 to 11.3) mm/yr
Rate (anomalies, rounded)	2.0 (1.0 to 6.0) mm/yr	3.0 (2.0 to 7.0) mm/yr	4.0 (2.0 to 8.0) mm/yr
2100			
Global steric	15 (10 to 20) cm	21 (14 to 27) cm	32 (22 to 42) cm
Ocean Dynamic Sea Level	5 (-1 to 10) cm	5 (-2 to 12) cm	5 (-4 to 13) cm
Glaciers	7 (4 to 11) cm	10 (6 to 14) cm	13 (8 to 19) cm
Landwater	2 (1 to 4) cm	2 (1 to 4) cm	2 (1 to 4) cm
Greenland	6 (4 to 10) cm	8 (5 to 14) cm	13 (7 to 23) cm
Antarctica	11 (0 to 38) cm	11 (-1 to 48) cm	14 (-2 to 56) cm
GIA	1 (1 to 1) cm	1 (1 to 1) cm	1 (1 to 1) cm
Total	48 (31 to 78) cm	59 (39 to 98) cm	81 (55 to 127) cm
Rate total	3.0 (1.8 to 8.2) mm/yr	6.5 (3.5 to 13.6) mm/yr	14.6 (9.2 to 27.9) mm/yr
Rate (anomalies, rounded)	-1.0 (-2.0 to 4.0) mm/yr	3.0 (-0.0 to 10.0) mm/yr	11.0 (5.0 to 24.0) mm/yr

Table 9.2: Median and 5th to 95th percentile range of individual sea level contributions in 2050 and 2100 relative to 1995-2014 for Bonaire. The row "Rate total" is the rate of sea level independent of the reference period while the row "Rate (anomalies, rounded)" is the anomaly compared to the rate during the reference period which is 3.7 mm/yr. LLHI scenarios are not included in this table.

2050			
	SSP1-2.6	SSP2-4.5	SSP5-8.5
Global steric	8 (5 to 10) cm	8 (6 to 11) cm	9 (6 to 12) cm
Ocean Dynamic Sea Level	2 (-3 to 6) cm	1 (-4 to 6) cm	0 (-6 to 5) cm
Glaciers	3 (2 to 5) cm	4 (2 to 5) cm	5 (3 to 6) cm
Landwater	1 (1 to 2) cm	1 (1 to 2) cm	1 (1 to 2) cm
Greenland	2 (1 to 3) cm	2 (1 to 4) cm	3 (2 to 4) cm
Antarctica	4 (0 to 14) cm	4 (-1 to 16) cm	4 (-1 to 14) cm
GIA	1 (1 to 1) cm	1 (1 to 1) cm	1 (1 to 1) cm
Total	21 (13 to 32) cm	22 (13 to 34) cm	23 (14 to 34) cm
Rate total	5.8 (4.2 to 9.6) mm/yr	6.4 (4.6 to 11.0) mm/yr	7.5 (5.2 to 11.2) mm/yr
Rate (anomalies, rounded)	3.0 (1.0 to 7.0) mm/yr	3.0 (2.0 to 8.0) mm/yr	4.0 (2.0 to 8.0) mm/yr
2100			
Global steric	15 (10 to 20) cm	21 (14 to 27) cm	32 (22 to 42) cm
Ocean Dynamic Sea Level	3 (-2 to 7) cm	3 (-3 to 9) cm	0 (-10 to 10) cm
Glaciers	7 (4 to 11) cm	10 (6 to 14) cm	14 (9 to 21) cm
Landwater	3 (1 to 4) cm	3 (1 to 4) cm	3 (1 to 4) cm
Greenland	6 (3 to 9) cm	7 (4 to 12) cm	13 (7 to 24) cm
Antarctica	11 (0 to 40) cm	12 (-1 to 50) cm	14 (-3 to 58) cm
GIA	1 (1 to 1) cm	1 (1 to 1) cm	1 (1 to 1) cm
Total	46 (29 to 76) cm	57 (37 to 97) cm	78 (50 to 126) cm
Rate total	3.3 (1.7 to 8.7) mm/yr	7.2 (4.5 to 14.4) mm/yr	14.9 (8.8 to 28.8) mm/yr
Rate (anomalies, rounded)	0.0 (-1.0 to 6.0) mm/yr	4.0 (2.0 to 11.0) mm/yr	12.0 (6.0 to 26.0) mm/yr

Table 9.3: Median and 5th to 95th percentile range of individual sea level contributions in 2050 and 2100 relative to 1995-2014 for St. Eustatius and Saba. The row "Rate total" is the rate of sea level independent of the reference period while the row "Rate (anomalies, rounded)" is the anomaly compared to the rate during the reference period which is 3.0 mm/yr. LLHI scenarios are not included in this table.

in Section 9.6.2. Understanding how TC intensity and the probability (the reciprocal of which being a return period) of experiencing a certain TC (i.e., a Category-5 TC) in a certain location might change, requires a more detailed representation of TCs in the climate model data. It is, however, challenging to obtain such a representation from general circulation models (GCMs) alone. The reason for this is twofold. First, the spatial resolution of GCMs (0.25-1.0°) is insufficient to adequately resolve TC intensity gradients, size and track, particularly for the most intense TCs (Bloemendaal et al., 2022). Second, GCM simulations typically cover 30- to 100-year periods of historical and future climate, resulting in a relatively small sample of TCs. As a result, GCMs provide insufficient (both in time and space) data to make robust claims on changes in TC intensity and return periods. High-resolution regional dynamical downscaling is an alternative approach to study (the impacts of) TCs in a warming climate. This method uses the environmental conditions from GCMs within a fixed region (such as the Caribbean), but is run at a far higher spatial resolution to capture the small-scale dynamics typically underrepresented by GCMs. This way, we can analyse the TC structure and intensity of historical events under a future warming scenario. In Section 9.6.3, we explain this approach in more detail, and demonstrate its usage on a case study of Hurricane Irma (2017) under a set of targeted climate change-experiments. For these so-called pseudo-global warming (PGW) runs we deduce information on changes in precipitation and wind speed. Lastly, to provide insights into TC risk and how this changes under climate change, we need a large (preferably hundreds to thousands of years) data set of TC activity, with accurate TC intensity representation. PGW simulations, however, cannot be used for such studies: PGW simulations are designed to study a historical event under a different climate scenario, and cannot simulate new TCs that show unprecedented behavior, independent of that observed in the input data set (Bloemendaal et al., 2022). To overcome these limitations, we use synthetic modeling to create a new TC data set. In the approach described in this report, we extract TC characteristics from historical data and GCMs, and statistically resample and model these to generate a new synthetic TC dataset, spanning thousands of years. This approach is described in Section 9.6.5.

9.6.2 Future changes derived from environmental parameters

There is no general consensus as to how (and with which magnitude) TC characteristics are going to change under climate change (Knutson et al., 2020). Two important aspects are changes in TC frequency and changes in TC intensity. The main 'engine' that fuels a TC is high sea water temperatures (SSTs). TCs require SSTs exceeding 26.5° C to develop and further intensify. As such, it directly follows that – keeping all other environmental factors unchanged – increasing SSTs will expand the region where TCs occur, particularly in a poleward direction. Additionally, it is projected that these increasing SSTs may cause an earlier start of the Atlantic Hurricane Season, which currently runs from 1 June till 30 November (Truchelut et al., 2022). Furthermore, SSTs can also provide more energy to TCs through increased evaporation and latent-heat release, hereby making future TCs bigger, "wetter" (i.e., more rain) and probably also more intense (see e.g., Oldenborgh et al. (2017)). Lastly, extremely warm ocean waters (around 30° C) can also ignite TC rapid intensification; a process in which a TC intensifies at least 30 knots over a 24-hr period (Bhatia et al., 2022). Besides changes in SSTs, there are also other environmental factors contributing to TC development and intensification. Vertical wind shear is a key ingredient that could limit initial TC development; high levels of vertical wind shear can cause a developing tropical disturbance to be blown apart. In addition, mid-level relative humidity and vertical stability also play a role. While SST increases in all climate change scenarios, changes in the other large-scale environmental parameters are more variable and may even produce opposing tendencies for TC formation and intensification (Vecchi and Soden, 2007; Nolan et al., 2007).

Quantifying the impact of TCs requires detailed information on the wind and pressure gradients of a TC. Simulating such complex evolutions of a TC requires an atmospheric model with high spatial resolution. Most general circulation models (GCMs) that are nowadays used in CMIP5 and CMIP6 lack this level of spatial detail. Accordingly, "TC-like" disturbances and storms do develop in GCMs, but they lack specific characteristics and their intensities are often underestimated. They also do not reach the wind and precipitation intensities seen in the observations. Only in a few

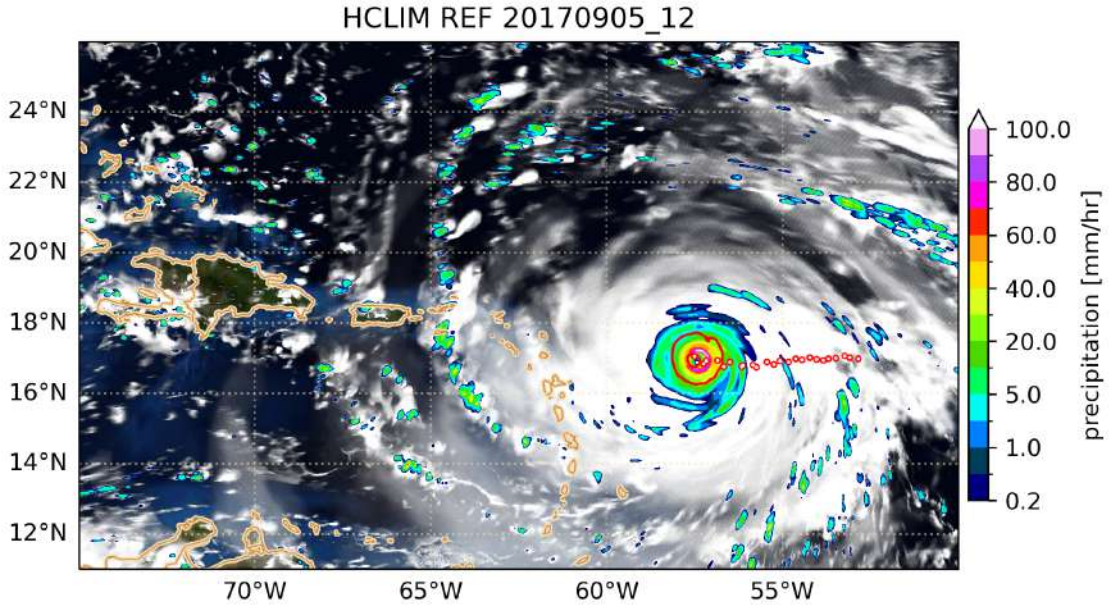

Figure 9.11: Hurricane Irma approaching the Caribbean (date: September 5, 12UTC) in the reference simulation (HCLIM38). White colors show the total cloud cover, shading the hourly precipitation. The track history (Irma entered the domain from the east) is indicated by the red dots. Coastlines are indicated by a sandlike color. The 12-Bft wind-speed isolines near the TC-center are added as red contours.

dedicated coordinated experiments (HighRes-MIP and PRIMAVERA) the spatial resolution of the GCMs is increased to levels where TC start to be more realistic. However, even in such high-resolution model intercomparison projects, the most intense TCs still tend to be underestimated (Roberts et al., 2020).

To overcome the shortcomings imposed by GCMs, we can use environmental TC indicators based on (large-scale) parameters that, contrary to the TCs themselves,*are* well-simulated by the GCMs. One of these environmental TC indicators is the Genesis Potential Index (GPI), first described in Emanuel and Nolan (2004) and later extended (see e.g., Camargo et al. (2007), Wang and Murakami (2020), and Gilford (2021)). The GPI gives an indication of the potential for a TC to form given the environmental conditions. The GPI computation requires various environmental parameters such as SST, 600hPa relative humidity, the magnitude of the vertical wind shear between 200 and 850hPa, absolute vorticity at 850hPa and the so-called "maximum potential intensity" (MPI; in hPa), which integrates information from SST and the moisture and temperature profiles. The GPI has been used to explain spatial and temporal variability of TC-occurrence in the current climate and, by changing the environmental data, can also provide indications of the expected future changes. As it is based on large-scale environmental conditions the GPI does not require the underlying global circulation models to resolve the TCs. In the supplementary material (Figs. 9.18) we have computed the GPI for the Caribbean region using ERA5 reanalysis data. Clearly visible is that while there are important source regions outside the Caribbean (left panel) the Caribbean is a region where TCs can reach high maximum wind speeds (right panel). Using metrics like GPI there is now growing consensus that the combined result of the competing mechanisms will be that TC intensity will increase towards the future, while at the same time overall TC frequency will (slightly) decrease. This also implies that the fraction of the most intense TCs will increase (Knutson et al., 2020). There is also general consensus that TCs will become wetter under future warming scenarios.

9.6.3 Dynamical downscaling of hurricanes

High-resolution dynamical downscaling with a regional climate model is an alternative approach to study TCs and their changes in a warming climate. We use a set of present-day and future regional climate model simulations for the Caribbean for the period 1979-2020, obtained with RACMO2.3 (RACMO from here) (Meijgaard et al., 2012). The RACMO2.3 simulations were conducted at a horizontal resolution of 12 km. A subset of years was further downscaled to 4 km resolution with HCLIM38-AROME (HCLIM from here) (Belusic et al., 2020a).

Methodology

Pseudo Global Warming approach The future simulations were created using the Pseudo Global Warming (PGW) approach (Schär et al., 1996a). In a PGW experiment first a reference simulation is generated using ERA5 reanalyses at the lateral boundaries (and as initial conditions). A future simulation is then produced by adding a slowly varying "delta-change" signal to the original (high-frequent) ERA5 lateral boundary data. Within the simulation domain the model is free to adapt to the modified boundary conditions. The RACMO simulations cover the period 1979-2020 (June-November only, to match the duration of the Atlantic hurricane season). Due to computational limitations, only a subset of these seasons has been downscaled with HCLIM, namely those hurricane seasons during which a major landfalling TC occurred in the region (1980, 1988, 1995, 1996, 1998, 2004, 2005, 2007, 2008, 2017 and 2020). The simulations were partly created for the EUCP project (EUCP, 2022a,b).

PGW and TP2 simulations We create two sets of future simulations. The first was obtained by adding a uniform 2K warming perturbation to the initial condition and the lateral and surface boundaries. Relative humidity is kept constant. Without this constraint the temperature increase would lead to a strong reduction in the relative humidity. This setup is referred to as TP2. The TP2 setup is not used for HCLIM, except for the 2017 season. In the second experiment (labelled PGW) the delta field was derived from CMIP5 ensemble projections for the RCP8.5 scenario. The delta fields (of temperature, pressure, horizontal wind components and humidity) comprise of end-of-century (2071-2100, RCP8.5) minus present-day (1976-2005) ensemble-mean projected changes derived from a subset of 19 CMIP5 GCMs. The mean surface warming in this simulation is about 3.4K. These simulations therefore have a stronger warming level than the TP2 runs but also include the projected changes in the large-scale circulation (notably the vertical wind shear) and vertical stability (Suppl. Figure 9.19). More details on the simulation setup and initial results can be found in the EUCP deliverable reports (EUCP, 2022a,b).

Cyclone tracking TCs were diagnosed in all experiments with the tracking software CELLTRACK (Lochbihler et al., 2017) using similar criteria as Gutmann et al. (2018). Potential cyclone 'cells' were diagnosed in each simulation as regions where the mean sea level pressure (MSLP) falls below 990 hPa, and that have a local pressure minimum below 980 hPa and a maximum wind speed of at least 15 m/s. These potential TC cells can form a track (in time) if they overlap in space. We only keep the track if it lasts at least three hours and if at least once during its lifetime the maximum wind speed exceeds 25 m/s. The track center (eye of the storm) is defined as the location of the MSLP minimum. The requirements differ slightly from Gutmann et al. (2018) who used an initial MSLP threshold of 27 hPa below climatology. As we have (in case of the HCLIM simulations) only 11 hurricane seasons, we used a fixed pressure threshold. For the RACMO simulations both setups gave similar results. In the final aggregation we retained only those cyclone tracks from all tracks that have a wind speed maximum above Tropical Storm (TS) criterium (wind speed above 34 knots). For these tracks we also record nearby precipitation (searching in a radius of 500 km around the center). In the comparison only those TC hours are retained that occurred in the same space-time window in both simulations (maximal time separation 48 hours). Statistics are based on these 'matched TC hours', where we used all hours rather than a single value per cyclone.

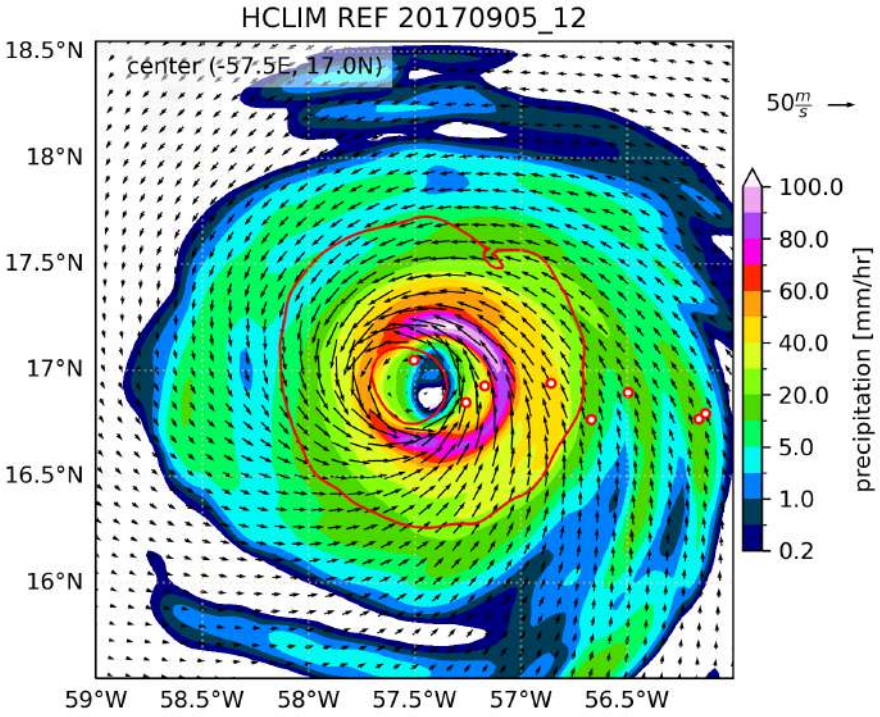

Figure 9.12: Close-up of Hurricane Irma shown in Fig. 9.11. Arrows indicate the wind vectors, other conventions as in Fig. 9.11.

Bias correction for wind speed As we will discuss later maximum wind speeds in HCLIM were over-estimated in the case of Hurricane Irma (2017). This happened for more TCs passing over the region. Therefore it seems appropriate to apply a bias correction to the hourly tracked output of wind speed. A simple quantile bias correction is used. First, we compute quantiles of present-day observed and modelled wind maxima distributions to derive quantile-specific correction factors. Subsequently, we apply these correction factors to the quantiles of the future set. We use a multiplicative approach with $N_q = 39$ quantiles. An additive approach gives similar results, and as long as N_q is not too small, results are not very sensitive to the exact value. Taking $N_q = 39$ is similar to what has been used elsewhere in this chapter. As the IBTrACS observations are rounded to 5 knots precision, an arbitrary random number between -2.5 and 2.5 knots is added to each observation. Supplementary Figure 9.20 (left panel) compares the observed and modelled distributions by means of a quantile-quantile plot (qq-plot) between observed and modelled maximum wind speeds. Deviations from the diagonal indicate the presence of a bias. Clearly the HCLIM control simulation develops a positive bias at about 50 m/s, roughly the start of the Cat. 3 intensity. At higher wind speeds the bias remains pretty constant. The bias correction method efficiently removes the bias (thick black line). The same approach was used to bias-correct the RACMO wind speed data (right panel Fig. 9.20). RACMO has a negative bias at very high wind speed. Note that maps of wind speed are shown as raw model output (e.g., Figure 9.12-9.13).

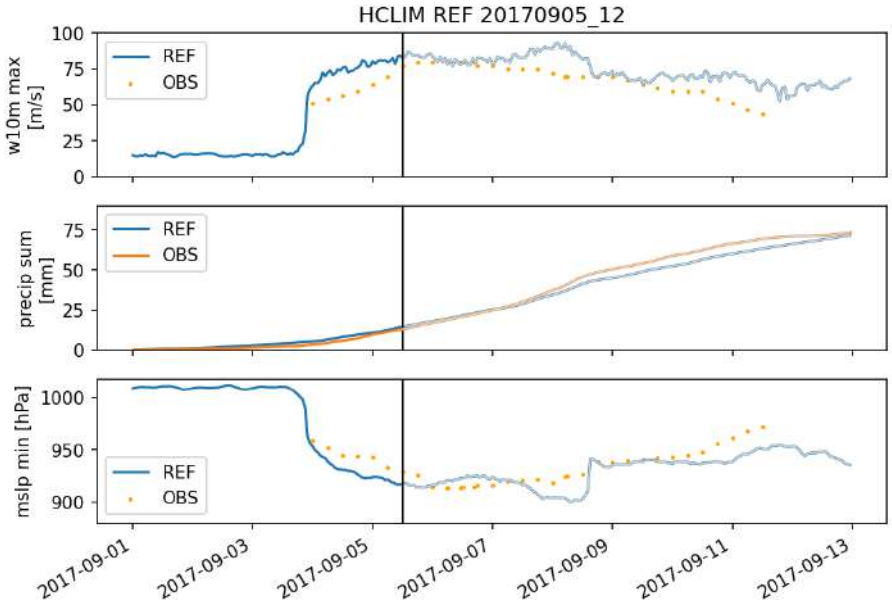

Figure 9.13: Statistics of maximum wind speed (top), cumulative precipitation (middle) and minimum sea-level pressure (bottom) over the domain shown in Fig. 9.11, between 1 and 13 September 2017. The vertical line marks the date shown in Fig. 9.11. The MSLP jump between 8 and 9 September is caused by Hurricane Irma exiting the domain and the next TC entering it.

9.6.4 Results of downscaling: Irma (2017), wind and precipitation extremes

This section describes the main results of the downscaling exercise. We start with a brief description of how Hurricane Irma (2017) materialised in HCLIM simulations. This is followed by a statistical analysis of future changes in wind speed maxima and precipitation intensities.

Case study: Hurricane Irma (2017)

Figure 9.11 shows a snapshot of Hurricane Irma (2017) as the storm approached the Caribbean in HCLIM. A close-up of the wind and precipitation field is shown in Fig. 9.12 while Fig. 9.13 gives the evolution of some basic statistics (aggregated over the domain of Fig. 9.11). Compared to IBTrACS (Knapp et al., 2010) the maximum wind speeds in HCLIM were higher (Fig. 9.13 top panel), along with lower than observed mean level pressure (bottom panel). Differences could arise for several reasons and we mention a few. Firstly, track differences: the modelled Hurricane Irma was further away from nearby land than in historical observations from IBTrACS (Knapp et al., 2010). As land interactions typically weaken a TC, this could give a reason why the modelled Hurricane Irma was more intense. These track deviations typically occur in such models, even if the regional model is constrained by the reanalysis at the boundaries. In EUCP (2022a) multiple regional climate models were seen to all result in slightly different tracks (and intensities), not unlike ensemble forecasts created with a numerical weather prediction model. Secondly, HCLIM is an atmosphere-only model and not coupled to an ocean model. Therefore there is no feedback from the TC on the near-surface ocean temperatures, which could constrain TC intensification. Thirdly, model wind speed drag relations may not be completely adequate at very high wind speeds. Finally, observations are not without uncertainty (Knapp et al., 2010; Mayers and Ruf, 2020; Knaff et al., 2021). In IBTrACS 3-hourly maximum wind speeds are rounded to 5 knots precision (about 2.5 m/s).

Despite these and possibly more limitations, HCLIM is clearly able to resolve the TC and many details of its core structure. There is proper eye formation, with an almost dry interior and low wind speeds (which is also observed in reality). Around the center there is a distinct region, called the eyewall, where the highest wind speeds and precipitation intensities typically occur. Large outwards spiralling cloud bands (white to transparent regions in the maps) demonstrate that a large area is influenced in some way or another by the passing by of Hurricane Irma. The TC's accumulated precipitation within the domain is quite close to observational estimates taken from GPM3-IMERG (middle panel in Figure 9.13). The observed structure of the precipitation pattern has a larger spatial scale than HCLIM (not shown).

Hurricane Irma in a warmer climate Hurricane Irma entered the domain via the eastern boundary and is therefore also present in the future simulations. Since the future track of Irma deviates from the track in the reference simulations, it is not very meaningful to show maps of differences. Maximum wind speeds and precipitation intensities increase in the warmer climate scenario, with largest changes in wind speeds found in TP2. These changes are quantified in the next section. Generally we see that the correspondence between the future and present-day TCs is best for those TCs that entered the domain already in a mature state (EUCP, 2022a). The correspondence is much less if the storms develop *in situ* (inside the domain). Note also that the PGW approach does not at all guarantee that the future TC 'survives' the modification process that occurs at the boundaries. Indeed, some of the storms did collapse in the future experiments upon entering the simulation region. Inside the region we also observe the development of new storms that were absent in historical observations. This happened particularly in the TP2 simulations, where many new, predominantly short-lived TCs developed. The next section compares the present-day and future simulations statistically.

Future changes in wind speed and precipitation

The main Atlantic TC genesis/development regions lie outside (to the east and north of) the simulation domain. As such, changes in TC frequency and intensity induced by changes in processes occurring these regions cannot be diagnosed using the PGW approach. For that reason we focus our discussion mostly on changes in TCs occurring *both* in the present-day and in the future climate PGW simulations (i.e. a present-day and future-climate Hurricane Irma). Furthermore, storms that develop within the simulation region but do not have a clear track are discarded.

Wind speed maxima Figure 9.14 (left panel) shows qq-plots for current climate (black) and the future (red) in HCLIM using the bias-corrected wind speed data. The observed distribution again is used on the x-axis. The displacement of the red line with respect to the diagonal shows that HCLIM projects the most intense TCs (above Cat. 3) to get substantially stronger in the warmer climate. The increases are (surprisingly) close to the changes projected from the large-scale Maximum Potential Intensity indicator in Fig. 9.18 and are also in line with IPCC statements that the most intense TCs might get intenser in a warmer climate. A word of caution is in place, as the future changes in HCLIM are largest for those values where the model showed a positive bias. Whether response and bias are correlated is a subject of future research. Note also that we have not provided an uncertainty estimate. A simple resampling method (selecting hours with replacement) almost certainly underestimates the real uncertainty. The results presented here should therefore be used primarily in a qualitative way.

The right panel in Fig. 9.14 shows the distributions and their differences, obtained using the bias-corrected data and a kernel density approach (smoothing bin-width 10 m/s). Dots show the observed distribution. Each density function is normalized, their difference therefore shows only relative shifts. As the qq-plot already hinted at, the distribution shows a systematic increase in the relative frequency of hours with very high wind speeds. The RACMO results are qualitatively similar (not shown) but changes in the PGW experiment are smaller than in HCLIM. In TP2, where the large-scale circulation adjustments are not made, the differences are larger, despite the

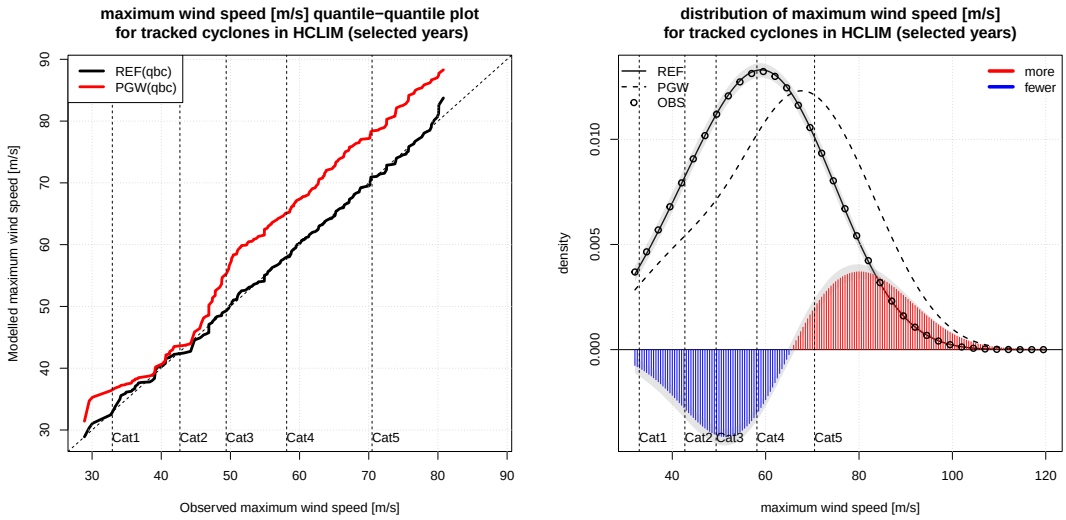

Figure 9.14: Left: quantile-quantile plot for hourly TC wind maxima (observations versus model). Bias-corrected wind speeds are used. Right: Kernel density estimates and future changes (binwidth 10 m/s). Hurricane categories are indicated by vertical lines.

global temperature increase being less than in PGW. Using all available years instead of only the selected 11 years, does not make a big difference.

Precipitation maxima For precipitation intensities we use the same approach as for maximum wind speeds. Bias correction is not used and the Fig. 9.15 should therefore be seen mainly as qualitative, indicating the direction of change. Note that in the qq-plot in the left panel, the Reference simulation is used as x-coordinate. Changes clearly point to higher maximum precipitation intensities. The increases are approximately 7% per degree global warming (Clausius-Clapeyron scaling rate). In the frequency perspective (right panel) this becomes clear as a systematic shift of the entire distribution towards higher values. The results for RACMO are very similar (not shown), where it is interesting to note that the TP2 precipitation changes are smaller than in PGW, oppositely to the wind speed differences which were larger in TP2 than in PGW.

9.6.5 Synthetic modelling of hurricanes: estimating return periods

As we demonstrated previously, downscaling and PGW methods can be used to simulate (historical) TCs in climate models and under various climate scenarios. Such efforts, however, do not provide information on the *probability* of a certain TC intensity in a certain location. This information is crucial for the design of TC risk mitigation efforts such as building codes or dyke/levee designs. Instead, scientists often use so-called synthetic models to obtain such information. Synthetic models are capable of overcoming the limitations imposed by the GCMs discussed in 9.6.1. In such models, TC characteristics (frequency, track, intensity, and other parameters of interest) are first extracted from either observational data or GCMs. This dataset of characteristics is representative for the same time period and/or climate scenario as the original input data. Next, this new dataset serve as input for a statistical (i.e., using statistical relationships) or dynamical (i.e., using physical relationships, see for instance Lee et al. (2018)) synthetic model. This synthetic model then resamples and models the TC characteristics to create a new dataset spanning many thousands of years, with the new dataset matching the overall statistics (mean, standard deviation) as were found in the original input dataset. This way, we can create a much larger dataset than the original observational or GCM dataset, and this larger dataset can then be used to support robust

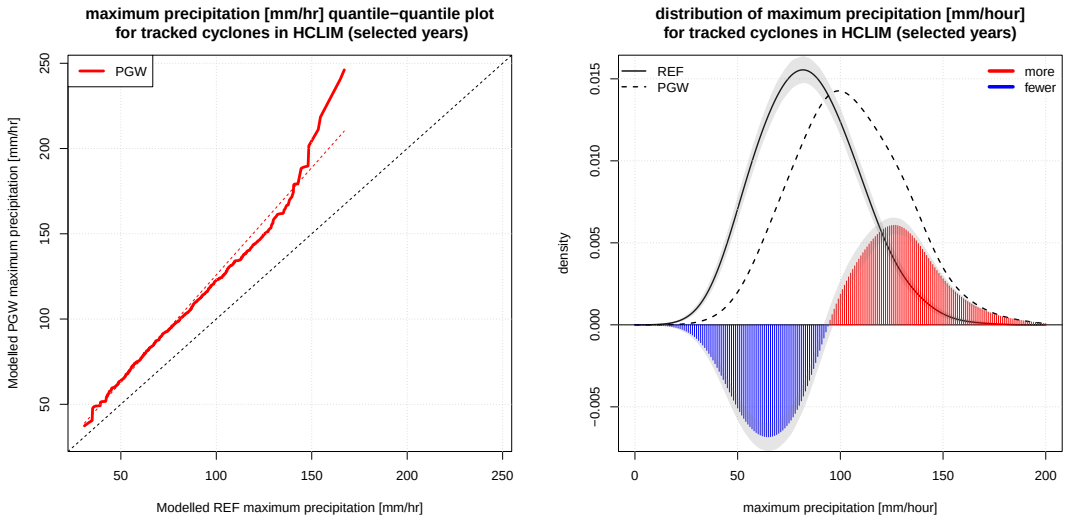

Figure 9.15: As in Fig. 9.14 but for TC-related maximum precipitation intensities. Left: qq-plot. The dashed red line shows the 7%/K global warming CC scaling applied to the Reference simulation. Right: Kernel density estimates (using 10 mm/hr as binwidth).

estimations of return periods exceeding the temporal length of the original dataset. This way, we can for instance say something about the 1-in-100 or 1-in-1,000 year TC, or what the return period for a Category-5 TC in a certain location would be. One such synthetic model is the STORM model (Bloemendaal et al., 2020). The Synthetic Tropical cyclOne geneRation Model (STORM) is a global-scale, fully statistical synthetic model that can be used to generate 10,000 years of synthetic TC activity from 30-40 years of climate simulations. We will not discuss STORM in detail here, but refer readers to Bloemendaal et al. (2020) for more information on the model. The STORM synthetic TC datasets were generated for two time periods/climate conditions, namely the historical climate (1980 - 2017, we will refer to this as the "baseline climate dataset") and the near-future climate (2015 - 2050 under SSP5-8.5, we will refer to this as the "future-climate dataset"). The baseline climate dataset was generated using input information (TC frequency, intensity, and track) from historical observations taken from the International Best-Track Archive for Climate Stewardship, in short IBTrACS (Knapp et al., 2010). The future-climate datasets were generated using information on relative changes in TC characteristics (frequency, intensity, track) from four GCMs, and consecutively applying these changes to the TC statistics extracted from IBTrACS (Bloemendaal et al., 2022). This yields one baseline climate STORM dataset and four future-climate STORM datasets.

Table 9.17 and Figure 9.16 show the return period of a certain TC intensity (given as Category on the Saffir-Simpson Hurricane Wind Scale) within 250 km of the islands. From these results, we can deduce that the return periods on Bonaire are approximately twice as high as on St. Eustatius and Saba. Similarly, the chances of a certain TC to occur on St. Eustatius and Saba is approximately double compared to Bonaire. This can be explained by the location of the islands compared to the typical direction of movement of tropical cyclones in the Atlantic basin. In the Atlantic basin, TCs, and predominantly intense TCs, form from tropical disturbances that move from the African coast into the Atlantic Ocean (the so-called Cabo Verde Hurricanes). Subsequently, under the influence of the trade winds, the TCs move in west-northwesterly direction in the direction of and over the Caribbean Sea. This increases the chances of a TCs approaching St. Eustatius and Saba, as these islands are located further north in the Caribbean, compared to Bonaire.

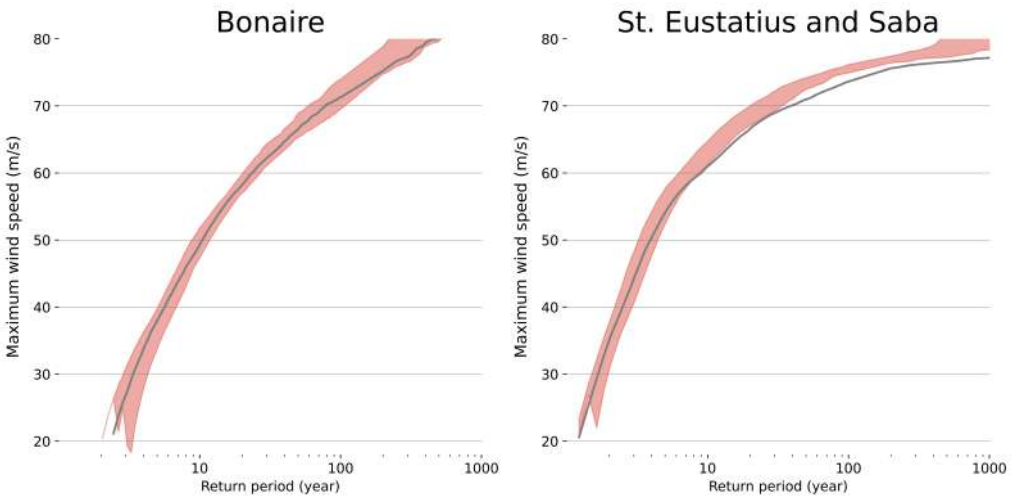

Figure 9.16: Return periods of various tropical cyclone wind speeds for the baseline climate (solid line) and the range of future climate simulations (shaded area) within 250 km from the islands.

Category	Period	Bonaire	St. Eustatius & Saba
1	1980 – 2017	4	2
	2015 – 2050	3 – 5	2
2	1980 – 2017	6	3
	2015 – 2050	6 – 8	2 – 3
3	1980 – 2017	10	4
	2015 – 2050	9 – 12	3 – 4
4	1980 – 2017	20	7
	2015 – 2050	17 – 22	5 – 7
5	1980 – 2017	78	39
	2015 – 2050	59 – 110	20 – 34

Figure 9.17: Return periods of tropical cyclones within 250 km of the islands.

Projections

When we assess the effects of climate change (2015 - 2050 period), we see little changes in return periods over the next decades. This is because the change in the total number of TCs over the Caribbean Sea is relatively low compared to the baseline climate. For St. Eustatius and Saba, we see a robust change in return periods for a Category-5 TC.

9.6.6 Discussion

In the previous sections multiple approaches were used to investigate future changes in tropical cyclones: dynamical downscaling using a storyline PGW approach (Sect. 9.6.3-9.6.4) and synthetic TC-modelling using STORM (Sect. 9.6.5). In Sect. 9.6.2 we discussed the effects that environmental changes could have on TC. We conclude this section with a few final remarks.

First, we restate that the chosen approach of dynamical downscaling in combination with the PGW framework can not diagnose changes that occur outside the domain. The approach relies on the historic (ERA5) climatology of TCs or TC-like disturbances entering the simulation domain, or those that develop spontaneously within the domain. Important genesis areas outside the domain might see future changes that could either hamper or favour TC initiation. The statistical analysis focused on the (changes of) TCs that appear near-simultaneously in both present-day and future simulations. The results are in general agreement with IPCC statements that the strongest TC might strengthen further and that they will get wetter (i.e., more precipitation). Under a scenario in which vertical shear and stability do not change (i.e., in the TP2 simulations) the future changes in TC-related wind speeds will probably be larger than in scenarios in which they do change (i.e., as in the PGW simulations). This connects to the discussion in Sect. 9.4.7, where it was shown that the CMIP6 model show a systematic El-Niño like response towards the future, while observations are currently not showing this. Therefore, in some ways, we can regard the TP2 simulations as an alternative scenario in which this El-Niño TC-suppressing state is absent.

Secondly, the preceding downscaling results were obtained using one RCM/CPM combination. The results qualitatively point in the same direction but differ quantitatively. Adding more models would undoubtedly increase the model spread. We are confident that the precipitation increases are a robust feature (see for example EUCP (2022a) where more CPMs were compared in different ways). For wind speed, we are more cautious, especially in the light of the positive bias of HCLIM at very high wind speeds. In RACMO where the highest wind speeds show a negative bias, the response was still positive but smaller. More research is clearly needed here.

If a TC hits an island, it will often be – almost regardless the exact details of its intensity – an impactful event. Therefore, one could argue that the *absolute* frequency change is the most important parameter from the impact point of view. This is the question that has been addressed using the approach of synthetic TC modelling. Tbl. 9.17 shows that according to this approach the future frequency changes up to 2050 will be not be very large. Also here a word of caution is in place, because the changes derived in STORM inevitably rely also on the future projections by GCMs that might be systematically biased.

One of the impacts associated with TCs are storm surges. Whether or not a high storm surge occurs during a TC, depends sensitively on the TC-track and the details of the local bathymetry, such as the slope and depth of the coastal sea (see also the Klimaatsignaal report). In Dullaart et al. (2023) the Caribbean RACMO simulations were analysed and used to derive the storm surges associated with two historic TCs: Maria (2017) and Dorian (2019). Especially for Dorian, the increase in surge height found in a warmer climate was substantial. Note that the projected increases in sea level still have to be included. This implies that without sufficient adaptation measures, critical water heights can be expected to occur more frequently in the future, perhaps even for TCs that in the current climate (and at the current height of mean sea level) would impose no threat. In combination with the projected increases in TC-related rainfall coastal erosion is enhanced, which for a low-lying island like Bonaire could erode away the land to live on.

To conclude, we briefly reflect on the question of whether the downscaling exercise with HCLIM and RACMO can also teach us something about the *absolute* frequency changes mentioned earlier.

We discussed that if the large-scale changes in vertical wind shear and stability turn out to be similar to the end-of-century CMIP5 projections (Fig. 9.19 left panel), TC formation could be limited in the western part of the Caribbean (Fig. 9.18 bottom left panel). In the PGW simulations the total number of tracked TC hours is indeed lower than in the reference simulations. If, on the other hand, the large-scale circulation and stability remain more or less unaltered (as in TP2), the higher temperatures potentially make the area better suitable for TC genesis and development. In the RACMO TP2 simulations this clearly occurs and many, sometimes short-lived, TCs are additionally formed in the interior of the domain. This implies that under these conditions the total absolute frequency of TC activity could increase quite significantly. Investigating the sensitivity of the TC genesis and development on the large-scale conditions is a subject of current and future research.

Acknowledgments The GPM3-IMERG data were kindly provided by the NASA Goddard Space Flight Center's and PPS, which develop and compute the GPM3-IMERG as a contribution to GPM and archived at the NASA GES DISC.

Supplementary figures for this chapter

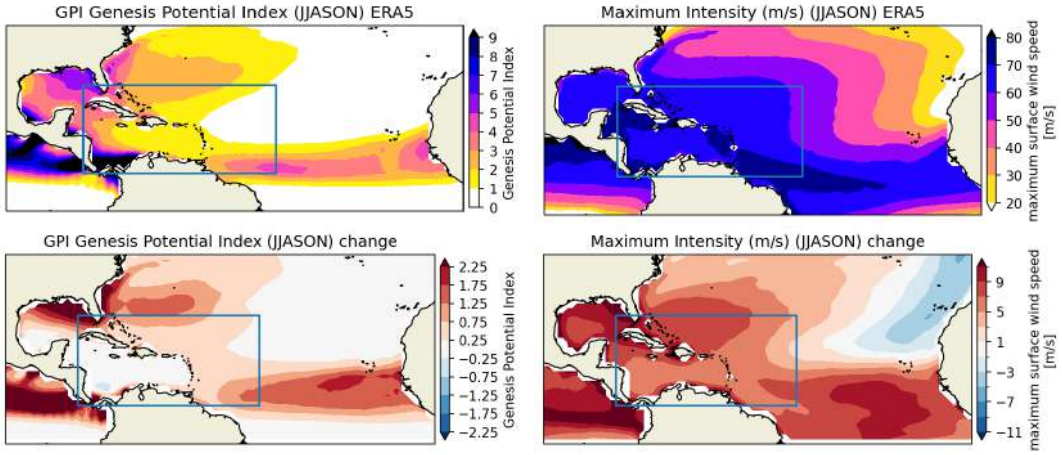

Figure 9.18: Top: TC genesis potential index (GPI, left) and Maximum potential intensity (right) in the current climate, derived using monthly ERA5 data for the period 1979-2020. Bottom: Future changes to GPI and Maximum potential intensity, derived by adding the PGW perturbation to the monthly ERA5 data for the period 1979-2020. The rectangle denotes the approximate region for the regional climate model simulations with RACMO2.3.

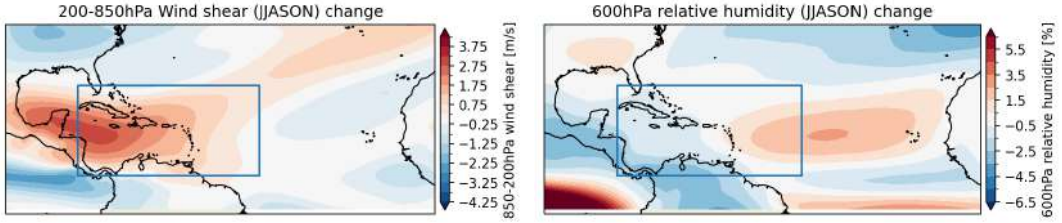

Figure 9.19: Future change in vertical wind shear and mid tropospheric relative humidity derived from the PGW perturbations.

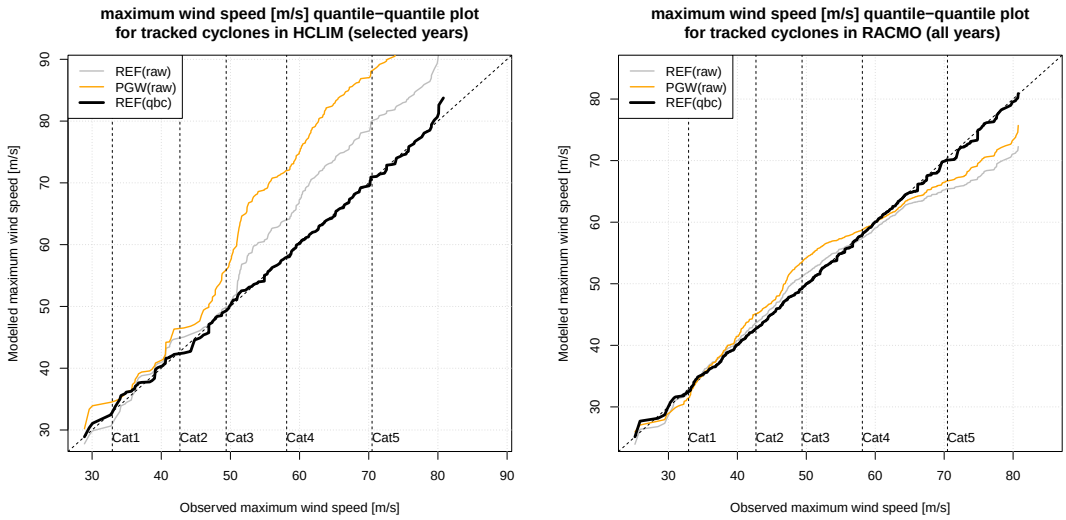

Figure 9.20: Left: Quantile-quantile plot (qq-plot) of observed hourly wind maxima from IBTrACS and modelled hourly wind maxima in the control and future simulations of HCLIM. Only 'matched' cyclones were used. The grey/orange lines give the raw, non bias-corrected qq-plot for the control/PGW simulations, the thick black line the bias-corrected qq-plot for the control simulations. Saffir-Simpson Hurricane categories are indicated by vertical lines. Right: As left panel but for RACMO, and using all available years (1979-2020).

Chapter 10

Dissimination of KNMI'23 scenarios

We have prepared a range of products, for different audiences and different applications. This chapter gives a short overview of these products, and their link to the methods or analyses described in this report.

10.1 Public report

A public report summarising the scenario data and interpretation of them has been prepared in both Dutch and English. The public report focuses on the High and Low emission scenarios (SSP5-8.5, SSP1-2.6, referred to as 'H' and 'L'), readers interested in the Middle emission scenario (SSP2-4.5, 'M') are directed to the website. In this section we provide a short overview of the content of the public report, and point the reader towards the relevant sections in this scientific report.

At the core of the public report sits a table showcasing calculated changes for a wide range of meteorological indices, averaged for the Netherlands as a whole. A copy of this table is included here (Figure 10.1). The data in this table, plus additionally more indices and the data for the M scenarios have also been made available on the website. All changes noted in the table have been computed using the bias-corrected resampled RACMO data (see Section 2.1).

Next, two summarising figures, or infographics are included in the public report (reproduced as Figures 10.2 and 10.3 here). The first shows a graphical summary of the position of the different scenarios along two axes (emission uncertainty axis, and regional response uncertainty axis: wet-dry), and scenario results for five key meteorological indices, listed below. For each of these indices the changes in 2100 are shown as a stacked bar, with a discrete scale from 1 to 6. The largest change in the scenarios considered (Ld, Ln, Md, Mn, Hd, Hn) has been set to six blocks, the other scenarios are scaled linearly. For example, the largest change in annual mean temperature is found in the Hd scenario, 4.4 ° C, this will be six blocks. Changes in other scenarios scale linearly, i.e. 0.66 ° C per block: e.g. 0.9 ° C in Ld and Ln are equivalent to one block, and 2.0 ° C change in Md becomes two blocks. Data was taken from the general scenario table (Figure 10.1).

- **Temperature** - We consider the change in annual mean and summer temperatures, both result in the same distribution of blocks.
- **Winter precipitation** - Percentage change in winter mean precipitation.
- **Summer convective rainfall** - Percentage change of hourly precipitation extremes with an average return time of 100 years.

Seizoen	Variabele	Indicator	Klimaat 1991-2020 = referentie-periode	2050 (2036-2065)				2100 (2086-2115)			
				Ld	Ln	Hd	Hn	Ld	Ln	Hd	Hn
	Wereldwijde temperatuurstijging ten opzichte van 1991-2020			+0,8°C	+0,8°C	+1,5°C	+1,5°C	+0,8°C	+0,8°C	+4,0°C	+4,0°C
	Wereldwijde temperatuurstijging ten opzichte van 1850-1900			+1,7°C	+1,7°C	+2,4°C	+2,4°C	+1,7°C	+1,7°C	+4,9°C	+4,9°C
Jaar	Zeespiegel bij Nederlandse kust	gemiddelde niveau	0 cm [1]	+24 (16 tot 34) cm	+24 (16 tot 34) cm	+27 (19 tot 38) cm	+27 (19 tot 38) cm	+44 (26 tot 73) cm	+44 (26 tot 73) cm	+82 (59 tot 124) cm	+82 (59 tot 124) cm
		tempo van verandering	3 mm/jaar [1]	+3 (1 tot 6) mm/jaar	+3 (1 tot 6) mm/jaar	+5 (4 tot 8) mm/jaar	+5 (4 tot 8) mm/jaar	-1 (-4 tot 4) mm/jaar	-1 (-4 tot 4) mm/jaar	+11 (6 tot 23) mm/jaar	+11 (6 tot 23) mm/jaar
	Temperatuur	gemiddelde	10,5°C	+0,9°C	+0,9°C	+1,6°C	+1,5°C	+0,9°C	+0,9°C	+4,4°C	+4,1°C
	Neerslag	hoeveelheid	851 mm	0%	+3%	-2%	+3%	0%	+3%	-3%	+8%
	Zonnestraling	gemiddelde	120 W/m²	+5,8 W/m²	+4,8 W/m²	+5,4 W/m²	+2,5 W/m²	+5,8 W/m²	+4,8 W/m²	+7,1 W/m²	+1,3 W/m²
	Vochtigheid	gemiddelde relatieve vochtigheid [2]	82%	-1%	-1%	-1%	0%	-1%	-1%	-1%	+1%
	Verdamping	potentiële verdamping (Makkink)	603 mm	+7%	+6%	+9%	+6%	+7%	+6%	+17%	+11%
	Wind	gemiddelde windsnelheid	4,8 m/s	-0,1 m/s	-0,1 m/s	0,0 m/s	0,0 m/s	-0,1 m/s	-0,1 m/s	-0,1 m/s	-0,1 m/s
Winter	Temperatuur	gemiddelde	3,9°C	+0,7°C	+0,7°C	+1,2°C	+1,3°C	+0,7°C	+0,7°C	+3,7°C	+3,9°C
		gemiddelde dagmaximum	6,3°C	+0,7°C	+0,7°C	+1,1°C	+1,2°C	+0,7°C	+0,7°C	+3,5°C	+3,6°C
		gemiddelde dagminimum	1,4°C	+0,7°C	+0,7°C	+1,2°C	+1,4°C	+0,7°C	+0,7°C	+4,0°C	+4,2°C
	Neerslag	hoeveelheid	218 mm	+4%	+5%	+4%	+7%	+4%	+5%	+14%	+24%
		aantal natte dagen (≥ 0,1 mm)	57 dagen	0,0 dagen	0,0 dagen	0,0 dagen	+0,6 dagen	0,0 dagen	0,0 dagen	0,0 dagen	+1,1 dagen
		aantal dagen ≥ 10 mm	5,4 dagen	+0,4 dagen	+0,5 dagen	+0,5 dagen	+0,8 dagen	+0,4 dagen	+0,5 dagen	+1,6 dagen	+2,5 dagen
		10-daagse neerslagsom die eens in de 10 jaar wordt overschreden	109 mm [3]	-2%	+2%	0%	+2%	-2%	+2%	+8%	+15%
	Zonnestraling	gemiddelde	34 W/m²	+1,2 W/m²	+1,5 W/m²	+0,8 W/m²	+0,4 W/m²	+1,2 W/m²	+1,5 W/m²	-0,7 W/m²	-1,5 W/m²
	Vochtigheid	gemiddelde relatieve vochtigheid [2]	87%	0%	0%	+1%	+1%	0%	0%	+1%	+2%
	Wind	gemiddelde windsnelheid	5,6 m/s	-0,1 m/s	-0,1 m/s	0,0 m/s	+0,1 m/s	-0,1 m/s	-0,1 m/s	+0,1 m/s	+0,2 m/s
		aantal dagen met windrichting tussen noord en west	13 dagen	+0,1 dagen	-0,8 dagen	0,0 dagen	+0,1 dagen	+0,1 dagen	-0,8 dagen	-1,7 dagen	-1,0 dagen

Seizoen	Variabele	Indicator	Klimaat 1991-2020 = referentie-periode	2050 (2036-2065)				2100 (2086-2115)			
				Ld	Ln	Hd	Hn	Ld	Ln	Hd	Hn
Lente	Temperatuur	gemiddelde	9,6°C	+0,8°C	+0,7°C	+1,3°C	+1,1°C	+0,8°C	+0,7°C	+3,6°C	+3,3°C
		gemiddelde dagmaximum	13,7°C	+0,9°C	+0,8°C	+1,2°C	+1,0°C	+0,9°C	+0,8°C	+3,3°C	+2,9°C
		gemiddelde dagminimum	5,5°C	+0,7°C	+0,7°C	+1,4°C	+1,3°C	+0,7°C	+0,7°C	+3,9°C	+3,7°C
	Neerslag	hoeveelheid	153 mm	+1%	+3%	0%	+4%	+1%	+3%	+4%	+10%
	Zonnestraling	gemiddelde	161 W/m²	+6,6 W/m²	+5,2 W/m²	+3,2 W/m²	+0,8 W/m²	+6,6 W/m²	+5,2 W/m²	-0,2 W/m²	-4,8 W/m²
	Vochtigheid	gemiddelde relatieve vochtigheid [2]	78%	-1%	-1%	0%	0%	-1%	-1%	+1%	+2%
	Verdamping	potentiële verdamping (Makkink)	190 mm	+6%	+5%	+6%	+4%	+6%	+5%	+10%	+6%
	Droogte	maximaal neerslagtekort april en mei	76 mm	+11%	+6%	+15%	+5%	+11%	+6%	+21%	+8%
	Wind	gemiddelde windsnelheid	4,7 m/s	-0,1 m/s	-0,1 m/s	0,0 m/s	0,0 m/s	-0,1 m/s	-0,1 m/s	+0,1 m/s	0,0 m/s
Zomer	Temperatuur	gemiddelde	17,3°C	+1,2°C	+1,1°C	+2,1°C	+1,7°C	+1,2°C	+1,1°C	+5,1°C	+4,7°C
		gemiddelde dagmaximum	21,7°C	+1,4°C	+1,2°C	+2,2°C	+1,7°C	+1,4°C	+1,2°C	+5,4°C	+4,7°C
		gemiddelde dagminimum	12,9°C	+1,0°C	+1,0°C	+1,9°C	+1,8°C	+1,0°C	+1,0°C	+5,0°C	+4,9°C
	Neerslag	hoeveelheid	235 mm	-8%	-2%	-13%	-5%	-8%	-2%	-29%	-12%
		1-daagse neerslagsom die eens in de 10 jaar wordt overschreden [4]	63 mm [3]	+4 (1 tot 6)%	+5 (2 tot 7)%	+6 (2 tot 9)%	+9 (5 tot 14)%	+4 (1 tot 6)%	+5 (2 tot 7)%	+15 (5 tot 26)%	+26 (12 tot 41)%
		uurlijkse neerslag die eens per jaar wordt overschreden [4]	16 mm [3]	+4 (2 tot 6)%	+6 (3 tot 8)%	+6 (2 tot 9)%	+11 (6 tot 16)%	+4 (2 tot 6)%	+6 (3 tot 8)%	+15 (5 tot 26)%	+31 (17 tot 46)%
	Zonnestraling	gemiddelde	206 W/m²	+12 W/m²	+9,1 W/m²	+14 W/m²	+7,4 W/m²	+12 W/m²	+9,1 W/m²	+24 W/m²	+11 W/m²
	Vochtigheid	gemiddelde relatieve vochtigheid [2]	77%	-2%	-1%	-2%	-1%	-2%	-1%	-4%	-1%
	Verdamping	potentiële verdamping (Makkink)	286 mm	+8%	+6%	+11%	+7%	+8%	+6%	+22%	+14%
	Droogte	maximaal neerslagtekort april t/m september	160 mm	+22%	+13%	+35%	+15%	+22%	+13%	+79%	+37%
		maximaal neerslagtekort april t/m september dat eens in de 10 jaar wordt overschreden	265 mm	+16%	+9%	+30%	+16%	+16%	+9%	+63%	+30%
	Wind	gemiddelde windsnelheid	4,2 m/s	-0,1 m/s	-0,1 m/s	-0,1 m/s	-0,1 m/s	-0,1 m/s	-0,1 m/s	-0,2 m/s	-0,2 m/s
Herfst	Temperatuur	gemiddelde	11,2°C	+1,0°C	+0,9°C	+1,8°C	+1,6°C	+1,0°C	+0,9°C	+5,0°C	+4,8°C
		gemiddelde dagmaximum	14,5°C	+1,1°C	+1,1°C	+1,9°C	+1,6°C	+1,1°C	+1,1°C	+5,1°C	+4,6°C
		gemiddelde dagminimum	7,8°C	+0,9°C	+0,9°C	+1,8°C	+1,7°C	+0,9°C	+0,9°C	+5,1°C	+5,1°C
	Neerslag	hoeveelheid	245 mm	+4%	+5%	+1%	+4%	+4%	+5%	+1%	+13%
	Zonnestraling	gemiddelde	77 W/m²	+3,7 W/m²	+3,5 W/m²	+3,7 W/m²	+1,4 W/m²	+3,7 W/m²	+3,5 W/m²	+5,4 W/m²	+1,0 W/m²
	Vochtigheid	gemiddelde relatieve vochtigheid [2]	85%	-1%	0%	-1%	0%	-1%	0%	-1%	0%
	Wind	gemiddelde windsnelheid	4,7 m/s	-0,1 m/s	-0,1 m/s	-0,1 m/s	0,0 m/s	-0,1 m/s	-0,1 m/s	-0,2 m/s	-0,1 m/s

Figure 10.1: KNMI'23 scenario table values for the mean climate change in the Netherlands around 2050 and 2100. High (H) and Low (L) emission scenarios included, wet (n) and dry (d) storylines. Reproduced from the KNMI'23 public report.

- **Meteorological drought** - The average number of blocks based on two indices: the Apr-Sep maximum precipitation deficit, and the 1-in-10 year Apr-Sep maximum precipitation deficit. With precipitation deficit defined as the NT in section 3.5.
- **Sea level rise** - The average sea level rise along the Dutch shore, in cm relative to 1995-2014.

Following a similar method, the second figure (Figure 10.3) shows some main results regarding the change in extremes. The figure shows the Low and High emission scenarios, but does not distinguish between wet and dry, the blocks show the average number of blocks between the wet and dry scenario variants. Here the block-towers represent:

- Return time of summers in which a maximum temperature of 40 ° C is reached in De Bilt.
- Percentage change of the annual highest 10-day precipitation event, with an average return time of 10 years.
- Percentage change of the annual highest hourly precipitation event, with an average return time of 100 years.
- Percentage change of the 1-in-10 year Apr-Sep maximum precipitation deficit.
- The average sea level rise along the Dutch shore, in cm relative to 1995-2014.

The public report then has several pages that discuss the trends and projections for different variables separately. The information reflects the content of Chapter 3 of this scientific report (for temperature, precipitation, drought, solar radiation, wind, and fog). Additionally, for temperature the future weather case (Chapter 7) and climate change in cities (Chapter 6) are discussed, and for precipitation the special product for convective rainfall extremes (Chapter 5) is described. The information for sea level rise is derived from Chapter 4 here. Finally, a near-term projection is given for temperature change in the Netherlands for a global warming level of 1.5 ° C above pre-industrial, as in the Paris agreement. This information is constructed following the same method as the general scenarios (Chapter 2.1), using the Low emission scenario and a 2033 time horizon.

The public report chapter on climate change in the Caribbean Netherlands (BES islands) is based on the information in Chapter 9, both for the meteorological information and the sea level rise information.

Several practical examples, or impact cases, are provided to show what the described climate changes would mean for Dutch society, water management, nature etc. These have been prepared with stakeholders and experts outside KNMI. The impact cases are not discussed in this scientific report.

The public report ends with two pages that discuss similarities and differences between KNMI'23 and the previous version of the national climate scenario's KNMI'14, based on Chapter 11.2, and background information, for example on SSP scenarios, natural variability and climate sensitivity. This last information is based on general scientific knowledge, and is discussed throughout this scientific report (starting in Chapter).

10.2 Website

The KNMI website will have a part dedicated to the KNMI'23 climate scenarios. Here the different reports can be downloaded, as well as an A4 summary and Frequently Asked Questions (FAQs). Additional products for communication with the general public include a video animation on the climate scenarios, a video showing scenario use in practise, and a podcast.

The final part of the website will be a data portal, from which users can select and download (subsets of) the main scenario table (Figure 10.1) and users can download the RACMO data based on which the table values were computed (resampled, bias-corrected RACMO data). To facilitate the user, we have regridded the RACMO data on a regular latitude-longitude grid of 12 km horizontal resolution. Also a single dataset for the reference period (1991-2020) is provided,

rather than a reference dataset for each scenario and time horizon separately (developed in the resampling procedure, Chapter 2). Finally, for data of the future period, we have shifted the time axis such that it aligns with the time horizon of interest (this was shifted in the matched-warming procedure, Chapter 2). These modification can lead to minor differences (maximum 2 %) in scenario table values if these were to be re-calculated.

Figure 10.2: Graphical depiction of the KNMI'23 climate scenarios for the Netherlands. Reproduced from the KNMI'23 public report.

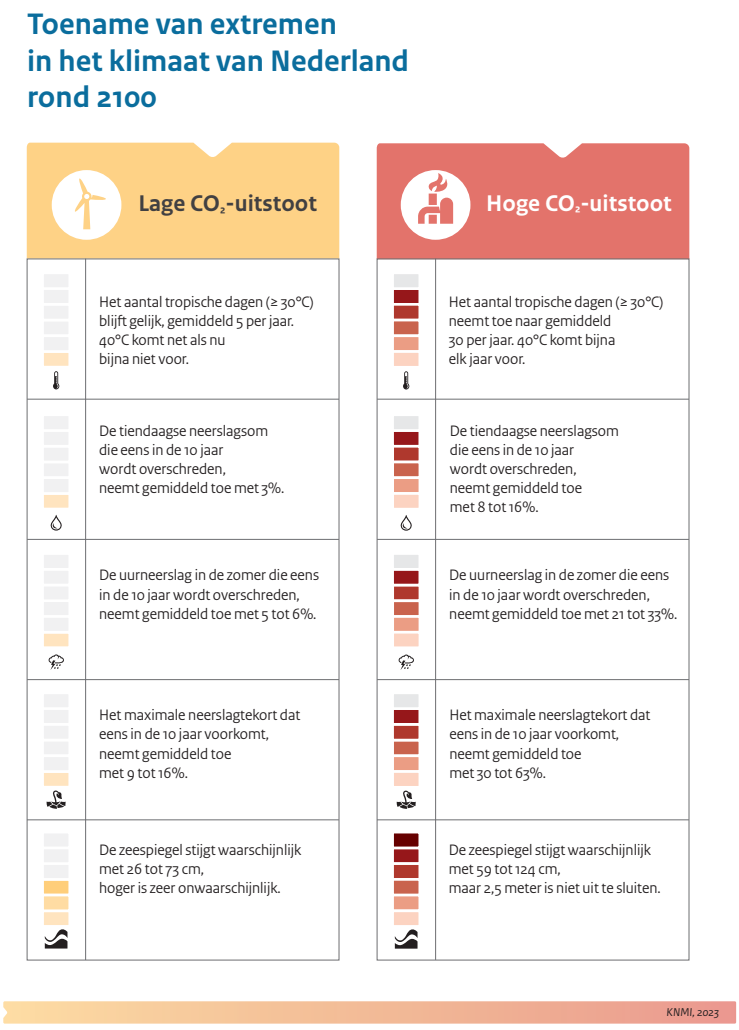

Figure 10.3: Graphical depiction of the change in extremes in the KNMI'23 climate scenarios. Reproduced from the KNMI'23 public report.

Chapter 11

Guidance for use

Although there is a separate user report, not all relevant information for users of the KNMI'23 scenarios could be included in this user report (ref. . . . .). Therefore, some more general information on the use of climate scenarios and some more in depth information on certain subjects is included in this chapter (partly based on earlier reports from tailoring studies (Bessembinder et al., 2015); (Bessembinder et al., 2018); (**PRIMAVERA**). Much more guidance to users can be supplied, however, often tailoring is required (11.1.4).

11.1 Using climate scenarios for different purposes

When using climate scenarios it is important to keep in mind the aim of your study. Below some guidelines are given for using climate scenarios for different purposes.

11.1.1 Which scenarios to use for impact, adaptation and vulnerability studies?

The KNMI'23 climate scenarios are chosen in such a way that they span a considerable part of the possible futures. IPCC does not give probabilities for the underlying shared socio-economic pathways (SSP's). This would require knowledge about which socio-economic developments are more probable than others. As a consequence, KNMI does not provide probabilities for the individual KNMI'23 scenarios as well, although we can state that it is most probable that the future climate in the Netherlands will be somewhere in between the KNMI'23 scenarios.

In most cases it is better to ask which climate scenario is most relevant for the user, and not which one is most probable. Most users are more interested in extremes, which are by definition rare and therefore less likely. The relevant time horizon is not the same for all users. For example, in the case of adaptation of a sewerage system in urban areas, often the climate scenario with the largest increase in extreme hourly rainfall is used, since water excess and flooded streets may have a very high impact in urban areas. Depending on the underground the sewerage system will have a shorter (peat, clay) or longer (sand) life time, and different time horizons will be used.

Given the objective of most impact, adaptation and vulnerability studies, it would be useful to use a complete set of climate scenarios. By comparing the results of the various climate scenarios one can determine how robust various adaptation measures are. Measures that work well for all scenarios are often of interest to policy makers. Due to for example the time available or financial resources not all climate scenarios are used in impact and adaptation studies. In these cases it is advisable to cover as much as possible the range of the most relevant climate variable.

For policy making, in general a choice is made for one climate scenario as the basis for the policies. The choice for one (or several) climate scenarios can be affected by, inter alia:

- What is accepted by society (e.g. because of the costs now and in the future, or potential for behavioural change)?;

- What are the possible impacts/risks of climate change?;
- What are the possibilities to adjust a 'wrong choice' related to climate adaptation measures with later policies?;
- What are the costs incurred in vain if the climate changes less than previously assumed, or what are the additional costs if climate change is stronger than previously assumed?
- How fast can further adaptation measures be implemented (e.g. raising of sea dikes takes more time and money than supplying extra sand to the beach to protect the coast)?;
- Which SSP-scenarios are assumed more likely by the user (e.g., if one assumes that the world will develop according to the IPCC SPSS 5-8.5 scenario, then a strong increase in temperature can also be considered more likely)?;
- Which scenarios are most relevant (e.g. industries that use surface water as cooling water, are likely to be more interested the scenarios with strong increases in (summer) temperatures, since these pose the largest risks of a shortage of cooling water)?.

As can be seen, the choice for one or more climate scenarios for policy making depends also on many factors that are not related directly to climate science. To explore the potential impact of climate change one can also look at potential tipping points, situations in which the current management or policy is no longer tenable (Kwadijk et al., 2010). In a second stage, one can then determine when these tipping points will be reached under the various climate scenarios.

11.1.2 What time horizon to use?

To make a choice on the time horizon or time horizons to use in a climate change impact study, check for the following aspects:

- Life cycle of the adaptation measure/structure: when you construct something that has to last for a long time, take this into account and take a longer time horizon. E.g. the pipes of sewerage systems stay in the ground for 40-80 years (in the Netherlands). Also at the end of their life cycle they should be able to drain the water of intense precipitation events (expected to increase in most of Europe). The same is true for bridges and tunnels before they are replaced or adapted. Therefore, the time horizon to take into account is the starting time of construction plus the expected life time (for a new sewerage system somewhere between 2050 and 2100);
- How fast can you adapt to changes: some adaptation measures take a lot of time and money before they are implemented (e.g. increasing dike height along coasts or rivers), whereas other adaptation measures may be implemented fast and/or cost relatively little money (e.g. take an alternative route in case of very local flooding of a road or tunnel). Sometimes it depends also on the life cycle how fast adaptation measures can be taken. When a structure is close to the end of its life cycle, the replacement can be anticipated and combined with adaptation.

11.1.3 How to deal with uncertainties?

In discussions on climate change inevitably the uncertainties on the future climate are discussed. Uncertainties can be due to imperfect knowledge about the climate system[1] or the socio-economic

[1] In this report this is also called 'Uncertainty in the climate response' or 'scientific uncertainty' (See paragraph 1.2.2), including uncertainty about 'climate sensitivity'. In other literature this is often referred to as 'model uncertainty'.

system causing the emission of greenhouse gasses[2] and/or it can be due to intrinsic variability in the climate system, the natural variability[3].

In discussions on climate change inevitably the uncertainties on the future climate are discussed. Uncertainties can be due to imperfect knowledge about the climate system or the socio-economic system causing the emission of greenhouse gasses and/or it can be due to intrinsic variability in the climate system, the natural variability. At global level many natural variations are leveled out. E.g. a relatively warm year in some regions is generally combined with a relatively cold year in other regions. At continental scale or smaller regions, the natural variations are larger (e.g. at the scale of Europe or the Netherlands). Natural variations, the intrinsic variability of the climate system, are different for each variable and each time step. For example, natural variations are larger for precipitation than for temperature, larger for extremes than for the mean, larger for single locations than area averages, and for the Netherlands compared to Europe. Generally, taking into account uncertainties will improve decision making. Uncertainty due to natural variability cannot be reduced, but it can be quantified with statistics. Uncertainties due to imperfect knowledge about the climate system or the socio-economic system can be reduced by doing more research to better understand the climate and societal systems. In the meantime, climate scenarios can be used (no probability assigned to the scenarios!) to study the effect of known uncertainties and the implications for impacts and adaptation options. The current KNMI'23 scenario's are constructed in such a way that the axis L to H represents the uncertainties in socio-economic developments, and the axis n-d represents the uncertainties in the climate system.

The KNMI scenarios cover a broad range of outcomes of the possible future climate, but do not cover all possible outcomes and uncertainties. It is therefore useful to look at the aim of your study as described before in paragraph 11.1.1. For example, if you would like to cover a large part of the uncertainties, it could be useful to use additional climate scenarios. If your system is vulnerable to extremes, it might be useful to look at tipping points or additional extreme scenarios (11.1.4).

11.1.4 Additional tailoring

The generic KNMI'23 scenarios provide a comprehensive package of information (in reports and online) and products such as time series and use cases. They are targeted to a diverse group of policy advisors, engineers and scientists preparing the Netherlands for future climate change. To develop products that meet their requirements, several stakeholder workshops were held and a user board was set up. However, not all user requests could be included in the development of the scenarios. The diversity of the requests was simply too large to do so. For specific users and applications, KNMI will be able to provide further details based on the KNMI'23 scenarios. The developed products such as transformed time series and bias-corrected time series offer a good basis for further tailoring. For example, KNMI will be able to provide more information on compound extremes, multi-day precipitation totals, and rainfall duration and statistics. Additional climate scenarios can also be developed on request, e.g., exploring a wider range of possible future climates, including extreme but plausible (low probability/high impact) situations. These extreme scenarios may be useful for stress tests, or when attempting to determine at what point in time particular adaptation strategies will no longer be adequate. Finally, KNMI will support sectors with follow-up work, which includes providing advice on good practices in scenario use.

11.2 Difference between KNMI'23 and the previous KNMI'14 scenarios

The basis for the KNMI'14 climate scenarios (Lenderink et al., 2014) was the IPCC assessment report from 2013 (IPCC, 2013). The KNMI'23 climate scenarios are based on the most recent

[2] In this report this is also called 'uncertainty in future anthropogenic forcings' or 'policy uncertainty' (See paragraph 1.2.1). In other literature this is often referred to as 'scenario uncertainty'.

[3] See paragraph 1.2.3

scientific insights of the 2021 IPCC report (IPCC, 2021b) and the most up-to-date and intricate climate models and data. Differences between KNMI'14 and KNMI'23 are also due to some methodological changes in the development of the climate scenarios. The main changes in the KNMI'23 scenarios compared to the 2014 scenarios are:

- The KNMI'23 scenarios are directly linked to the IPCC emission scenarios and thus to climate policy.
- The scenarios look further into the future: up to 2150. For sea level up to 2300.
- The changes are given relative to the most recent reference period for the climate in the Netherlands: 1991-2020.
- The scenarios indicate a stronger increase in drought.
- For sea level rise, knowledge of the contribution of Antarctica has improved; we also provide estimates for the highest possible sea level in the future.
- The increase in extreme summer showers is better substantiated. The increase in the most extreme showers remains high, the increase in less extreme showers, which occur a few times a year, is less than in the KNMI'14 scenarios.
- The scenarios provide additional information about high temperatures.
- Climate scenarios for the Rhine and Meuse river basins are added to the KNMI'23 scenarios: the amount of precipitation in the regions upstream in the Rhine and Meuse is important for river discharges in the Netherlands and, therefore, for calculating (the probability) of both high and low river discharges.
- More information for spring and autumn in the KNMI'23 scenarios: the KNMI'14 scenarios emphasized summer and winter.
- The scenarios also describe future climate change on the BES islands.

Partly because of the drought problems of recent years, users of the climate scenarios indicated that dealing with water scarcity is one of the most important challenges for the future. That is why, in the KNMI'23 climate scenarios, it was decided not only to divide the scenarios into high emissions (H) and low emissions (L), but also to calculate two variants (d and n) in which the degree of desiccation in the summer and the increase in precipitation in the winter differs. This resulted in scenarios with a decrease in annual precipitation (d) and scenarios with an increase in annual precipitation (n).

In the KNMI'14 climate scenarios, we used two other variants, based on changes in airflow patterns. These changes in airflow patterns indirectly influence the amount of rainfall in the seasons. In KNMI'14 (as in KNMI'06), a change in airflow patterns in summer (leading to dryer summers) was combined with a change in airflow patterns in winter (leading to stronger increase of rainfall). In the KNMI'14 climate scenarios, annual precipitation therefore increases in all scenarios. New analyses for KNMI'23 showed that there is no direct link between the changes in airflow patterns between summer and winter. Therefore, other combinations of changes in rainfall in the various seasons could be made, which are more relevant for water management [4]. Due to the choice of dry and wet variants, the temperature change in the low and high emission scenarios has a smaller bandwidth than in 2014.

Table 11.1 shows the main differences between the two sets of climate scenarios.

[4]This choice was made in consultation with users from especially the water management sector.

Table 11.1: Main differences between the KNMI'14 and KNMI'23 scenarios.

	KNMI'14	**KNMI'23**
Greenhouse gas emissions (socio-economic scenarios)	Based on moderate and high emissions: RCP4.5 and RCP8.5	Direct coupling with low and high emissions: SSP1-2.6 (belonging to the Paris Climate Agreement) and SSP5-8.5
Annual average temperature	Bandwidth greater around 2050	By including the Paris Agreement, in 2100 less warming in the low-emission scenario
Annual average precipitation	Increase in all scenarios	Increase or decrease
Extreme precipitation per hour/day	First estimates based on observations and climate models	Better substantiated with high-resolution climate models
Sea level rise	Does not take into account possible extreme sea level rise	Additional estimates for the highest possible sea level rise (low probability, high impact)
BES islands	-	Made for the first time
Reference period	1981-2010	1991-2020
Time horizons	2030 - 2050 - 2085	2033 (1,5°C) - 2050 - 2100 - 2150 - 2300 (for sea level rise)
Basic information for impact studies	Only transformed time series	Transformed and bias corrected time series

To compare the climate scenarios, table 11.2 shows the range of the values in the scenarios for the year 2050 for a number of variables. Table 11.3 shows the changes for 2100. In order to be able to compare the KNMI'14 values from around 2085 with the KNMI'23 scenario values for around 2100, the data of 2085 have been extrapolated to the year 2100 in line with the global temperature increase between 2085-2100 in the IPCC AR5 report. The table shows absolute values of the variables, that means that for KNMI'14 the changes calculated for 2050 and 2100 are added to the values in the reference period 1981-2010. For KNMI'23 the changes are added to the reference period 1991-2020. Note that not only climate change causes a difference between the two reference periods, but also natural variability may play a role. For temperature observations and scenario's for De Bilt are taken, since these were used in KNMI'14, for precipitation averages for the Netherlands.

11.3 Scenarios in neighbouring countries

Most countries in Europe produce national or regionalised climate scenarios or projections for their own country, often using the same basic information (regional climate model projections) from large European projects such as CMIP and EURO-CORDEX, but all with their own methods and timing to construct climate scenarios. Therefore, comparison of these national sets of climate scenarios is not straightforward. Table 11.4 gives some characteristics of the various sets of climate scenarios from our neighbouring countries and countries sharing the river basins of Rhine and Meuse. Table 11.5 presents an overview of the links to regional climate scenarios of various European countries.

Table 11.2: Range KNMI'14 and KNMI'23 scenarios for 2050.

	Reference period 1981-2010	**Reference period 1991-2020**	**KNMI'14**	**KNMI'23**
Sea level, rate of change (mm/year)	2,0	3,0	3,0-9,5	4,0-11,0
Average temperature (year) (°C)	10,1	10,5	11,1- 12,4	11,3-12,1
Average temperature in winter (°C)	3,4	3,9	4,5-6,1	4,5-5,2
Coldest day of the winter (°C)	-5,9	-5,6	-3,9 to -0,8	-4,3 to -3,6
Average temperature in summer (°C)	17,0	17,4	18,0-19,3	18,4-19,5
Warmest day of the summer (°C)	24,7	25,5	26,1-28,0	27,0-28,5
Average yearly precipitation (mm)	851	851	872-898	834-877
Average precipitation in winter (mm)	211	218	217-247	227-233
Average precipitation in summer (mm)	224	235	195-227	204-230
Once every ten years day extreme summer (mm)	44	63	45-54	64-72
Average highest rainfall deficit apr-sep (mm)	144	160	145-187	181-216

Table 11.3: Range KNMI'14 and KNMI'23 scenarios for 2100.

	Reference period 1981-2010	**Reference period 1991-2020**	**KNMI'14**	**KNMI'23**
Sea level, rate of change (mm/year)	2,0	3,0	3 to 15	-1 to 26
Average temperature (year) (°C)	10,1	10,5	11,5-14,4	11,3-14,8
Average temperature in winter (°C)	3,4	3,9	4,8-8,2	4,5-7,8
Coldest day of the winter (°C)	-5,9	-5,0	-2,9 to 2,7	-4,4 to -0,7
Average temperature in summer (°C)	17,0	17,4	18,3-21,3	18,4-22,6
Warmest day of the summer (°C)	24,7	25,2	26,9-30,4	26,7-32,1
Average yearly precipitation (mm)	851	851	898-921	825-919
Average precipitation in winter (mm)	211	218	221-285	227-270
Average precipitation in summer (mm)	224	235	167-226	167-230
Once every ten years day extreme summer (mm)	44	63	45-65	65-89
Average highest rainfall deficit during the growing season (mm)	144	160	145-228	181-286

Table 11.4: Characteristics of climate scenarios of neighbouring countries and countries connected by Rhine and Meuse.

Country	Year of publication of most recent climate scenarios	Used models	Socio-economic scenarios	Reference period	Time horizons	Display
Belgium	2020	ALARO	RCP 2.6, RCP 4.5 and RCP 8.5	1961-1990	2050, 2085	Range per RCP
Germany (DWD)	2018	DWD Referenz-Ensembles	RCP 2.6, 4.5 and 8.5	1971-2000	Each ten years from 2031-2100	Per climate model or the 15,50 and 85 percentile of the ensemble
Germany (GERIC-S/Helmholtz	2015	EURO-CORDEX	RCP 4.5 and 8.5 and ENSEMBLES A1B	1971-2000	Each ten years from 2031-2100	Percentiles
Switzerland	2018	EURO-CORDEX	RCP 2.6, 4.5 and 8.5	1981-2010	2035, 2060, 2085	Range per RCP
France	2020	Multi-models	RCP 2.6, 4.5 and 8.5	1976-2005	2035, 2055, 2085	Per climate model or different percentiles of the ensemble

Table 11.5: Overview of national climate scenarios of different European countries (links August 2023)

Country	Website	Year
Belgium	www.meteo.be/resources/misc/climate_report/KlimaatRapport-2020.pdf	2020
Germany	www.dwd.de/DE/klimaumwelt/klimaatlas/klimaatlas_node www.regionaler-klimaatlas.de www.climate-service-center.de www.meeresspiegel-monitor.de	2018 2016 2015
Denmark	www.dmi.dk/klima-atlas/data-i-klimaatlas	2020
Finland	www.ilmasto-opas.fi/tag/ilmasto	2015
France	www.drias-climat.fr	2020
Ireland	www.met.ie/epa-climate-projections-2020	2020
Norway	www.klimaservicesenter.no/climateprojections	2017
Austria	www.bmk.gv.at/themen/klima_umwelt/klimaschutz/anpassungsstrategie/publikationen/oeks15	2015
Portugal	www.portaldoclima.pt/	2016
Spain	www.aemet.es/es/serviciosclimaticos/cambio_climat	2017
United Kingdom	www.metoffice.gov.uk/research/approach/collaboration/ukcp/index	2018
Sweden	www.smhi.se/en/climate/future-climate/advanced-climate-change-scenario-service/met/sverige/medeltemperatur/rcp45/2071-2100/year/anom	2021

Bibliography

Aalbers, E. E. et al. (2023). "The 2018 west-central European drought projected in a warmer climate: How much drier can it get?" In: *Natural Hazards and Earth System Sciences (NHESS)* 23 (5), pp. 1921–1946. DOI: 10.5194/nhess-23-1921-2023.

Aalbers, E. E. et al. (2018). "Local-scale changes in mean and heavy precipitation in Western Europe, climate change or internal variability?" In: *Climate Dynamics* 50.11-12, pp. 4745–4766. ISSN: 14320894. DOI: 10.1007/s00382-017-3901-9.

Andrews, T. et al. (2012). "Forcing, feedbacks and climate sensitivity in CMIP5 coupled atmosphere-ocean climate models". In: *Geophysical Research Letters* 39.9. DOI: https://doi.org/10.1029/2012GL051607.

Aschwanden, A. et al. (June 2019). "Contribution of the Greenland Ice Sheet to sea level over the next millennium". en. In: *Science Advances* 5.6, eaav9396. ISSN: 2375-2548. DOI: 10.1126/sciadv.aav9396.

Aschwanden, A. et al. (Dec. 2021). "Brief communication: A roadmap towards credible projections of ice sheet contribution to sea level". In: *The Cryosphere* 15.12. Publisher: Copernicus GmbH, pp. 5705–5715. ISSN: 1994-0416. DOI: 10.5194/tc-15-5705-2021.

Attema, J. and G. Lenderink (2014). "The influence of the North Sea on coastal precipitation in the Netherlands in the present-day and future climate". In: *Climate Dynamics* 42, pp. 505–519. DOI: 10.1007/s00382-013-1665-4.

Attema, J. J., J. M. Loriaux, and G. Lenderink (Jan. 2014). "Extreme precipitation response to climate perturbations in an atmospheric mesoscale model". In: *Environmental Research Letters* 9.1, p. 014003. ISSN: 1748-9326. DOI: 10.1088/1748-9326/9/1/014003.

Baart, F. et al. (2019). *Zeespiegelmonitor 2018: De stand van zaken rond de zeespiegelstijging langs de Nederlandse kust.* Tech. rep.

Bakker, A. (2015). *Time series transformation tool version 3.1.* Technical report TR-349. KNMI.

Balsamo, G. et al. (2009). "A revised hydrology for the ECMWF model: verification from field site to terrestrial water storage and impact in the Integrated Forecast System." In: *Journal of Hydrometeorology* 10.3, pp. 623–643. DOI: 10.1175/2008JHM1068.1.

Bamber, J. L. et al. (June 2019). "Ice sheet contributions to future sea-level rise from structured expert judgment". In: *Proceedings of the National Academy of Sciences* 116.23, pp. 11195–11200. ISSN: 0027-8424, 1091-6490. DOI: 10.1073/pnas.1817205116.

Ban, N. et al. (2021). "The first multi-model ensemble of regional climate simulations at kilometer-scale resolution, part I: evaluation of precipitation". In: *Climate Dynamics* 57.1-2, pp. 275–302. ISSN: 14320894. DOI: 10.1007/s00382-021-05708-w.

Ban, N. et al. (July 2020). "Analysis of Alpine precipitation extremes using generalized extreme value theory in convection-resolving climate simulations". In: *Climate Dynamics* 55.1-2, pp. 61–75. ISSN: 0930-7575, 1432-0894. DOI: 10.1007/s00382-018-4339-4.

Bassis, J. N. et al. (June 2021). "Transition to marine ice cliff instability controlled by ice thickness gradients and velocity". en. In: *Science* 372.6548. Publisher: American Association for the Advancement of Science Section: Report, pp. 1342–1344. ISSN: 0036-8075, 1095-9203. DOI: 10.1126/science.abf6271.

Bayr, T. et al. (2014). "The eastward shift of the Walker Circulation in response to global warming and its relationship to ENSO variability". In: *Climate dynamics* 43.9, pp. 2747–2763.

Belusic, D., H. de Vries, and et al. (2020a). "HCLIM38: A flexible regional climate model applicable for different climate zones from coarse to convection permitting scales". In: *Geosci. Model Dev.* 13, pp. 1311–1333. DOI: https://doi.org/10.5194/gmd-13-1311-2020.

Belusic, D. et al. (Mar. 2020b). "HCLIM38: a flexible regional climate model applicable for different climate zones from coarse to convection-permitting scales". In: *Geoscientific Model Development* 13.3, pp. 1311–1333. ISSN: 1991-9603. DOI: 10.5194/gmd-13-1311-2020.

Bengtsson, L., U. Andrae, and et al. (May 2017). "The HARMONIE-AROME model configuration in the ALADIN-HIRLAM NWP system". In: *Monthly Weather Review* 145 (5), pp. 1919–1935. ISSN: 15200493. DOI: 10.1175/MWR-D-16-0417.1.

Benn, D. I. et al. (June 2022). "Rapid fragmentation of Thwaites Eastern Ice Shelf". English. In: *The Cryosphere* 16.6. Publisher: Copernicus GmbH, pp. 2545–2564. ISSN: 1994-0416. DOI: 10.5194/tc-16-2545-2022.

Berthou, S. et al. (2020). "Pan-European climate at convection-permitting scale: a model inter-comparison study". In: *Climate Dynamics* 55.1-2, pp. 35–59. ISSN: 14320894. DOI: 10.1007/s00382-018-4114-6.

Berthou, S. et al. (Nov. 2022). "Convection in future winter storms over Northern Europe". In: *Environmental Research Letters* 17.11, p. 114055. ISSN: 1748-9326. DOI: 10.1088/1748-9326/aca03a.

Bessembinder, J., L. Bouwer, and R. Scheele (2018). "Climate and climate change: protocol for use and generation of statistics on rainfall extremes. CEDR TRANSNATIONAL ROAD RESEARCH PROGRAMME". In.

Bessembinder, J. et al. (2015). "Guideline on the use of data for the current and future climate for road infrastructure, Part A1 of the ROADAPT guidelines". In.

Bessembinder, J., B. Overbeek, and G. Verver (2014). "Inventarisatie van gebruikerswensen voor klimaatinformatie - KNMI". In: *KNMI*.

Bhatia, K. et al. (2022). "A potential explanation for the global increase in tropical cyclone rapid intensification". In: *Nature Communications* 13.1. DOI: 10.1038/s41467-022-34321-6.

Bloemendaal, N. et al. (Feb. 2020). "Generation of a global synthetic tropical cyclone hazard dataset using STORM". In: *Scientific Data* 7.1. DOI: 10.1038/s41597-020-0381-2.

Bloemendaal, N. et al. (2022). "A globally consistent local-scale assessment of future tropical cyclone risk". In: *Science Advances* 8.17, eabm8438. DOI: 10.1126/sciadv.abm8438. eprint: https://www.science.org/doi/pdf/10.1126/sciadv.abm8438.

Boers, R., T. Brandsma, and A. P. Siebesma (2017). "Impact of aerosols and clouds on decadal trends in the all-sky solar radiation over the Netherlands (1966–2015)". In: *Atmospheric Chemistry and Physics* 17, pp. 8081–8100. DOI: 10.5194/acp-17-8081-2017.

Brogli, R. et al. (2019). "The role of Hadley circulation and lapse-rate changes for the future European summer climate". In: *Journal of Climate* 32.2, pp. 385–404. ISSN: 08948755. DOI: 10.1175/JCLI-D-18-0431.1.

Brogli, R. et al. (Nov. 2021). "Future summer warming pattern under climate change is affected by lapse-rate changes". In: *Weather and Climate Dynamics* 2.4, pp. 1093–1110. ISSN: 2698-4016. DOI: 10.5194/wcd-2-1093-2021.

Bronselaer, B. et al. (Dec. 2018). "Change in future climate due to Antarctic meltwater". In: *Nature* 564.7734, pp. 53–58. ISSN: 0028-0836, 1476-4687. DOI: 10.1038/s41586-018-0712-z.

Brotons, M. et al. (2023). "Drivers of Caribbean precipitation change due to global warming. Analyses and emergent constraint of CMIP6 simulations". In: *Climate Dynamics* (in review), NA.

Bruggeman, W. et al. (2015). "Deltascenario's voor 2050 en 2100 - Nadere uitwerking 2012-2013". In: *PBL*.

Buiteveld, H. and M. Eberle (2005). *Hydrological Modelling in the River Rhine Basin: Daily HBV model for the Rhine basin / project leaders: Hendrik Buiteveld ... Project execution: Mailin Eberle*. Bericht / Bfg, Bundesanstalt für Gewässerkunde dl. 3. BfG.

Bulthuis, K. et al. (Apr. 2019). "Uncertainty quantification of the multi-centennial response of the Antarctic ice sheet to climate change". en. In: *The Cryosphere* 13.4, pp. 1349–1380. ISSN: 1994-0424. DOI: 10.5194/tc-13-1349-2019.

Camargo, C. M. L. et al. (Jan. 2023). "Regionalizing the sea-level budget with machine learning techniques". English. In: *Ocean Science* 19.1. Publisher: Copernicus GmbH, pp. 17–41. ISSN: 1812-0784. DOI: 10.5194/os-19-17-2023.

Camargo, S. J. et al. (2007). "Tropical cyclone genesis potential index in climate models". In: *Tellus A: Dynamic Meteorology and Oceanography* 59.4, p. 428. ISSN: 1600-0870. DOI: 10.1111/j.1600-0870.2007.00238.x.

Cannon, A. J., S. R. Sobie, and T. Q. Murdock (2015). "Bias correction of GCM precipitation by quantile mapping: how well do methods preserve changes in quantiles and extremes?" In: *Journal of Climate* 28.17, pp. 6938–6959.

Casanueva, A. et al. (2020). "Testing bias adjustment methods for regional climate change applications under observational uncertainty and resolution mismatch". In: *Atmospheric Science Letters* 21.7, e978.

Chan, S. C. et al. (Aug. 2020). "Europe-wide precipitation projections at convection permitting scale with the Unified Model". In: *Climate Dynamics* 55.3-4, pp. 409–428. ISSN: 0930-7575. DOI: 10.1007/s00382-020-05192-8.

Chen, D. et al. (2021). "Climate Change 2021 (IPCC AR6 WG I): The Physical Science Basis; Chapter 1: Framing, Context, and Methods". In: *Climate Change 2021: The Physical Science Basis. Contribution of Working Group I to the Sixth Assessment Report of the Intergovernmental Panel on Climate Change*. Ed. by V. Masson-Delmotte et al. Cambridge, United Kingdom and New York, NY, USA: Cambridge University Press, pp. 147–286. DOI: 10.1017/9781009157896.003.

Church, J. A. et al. (2013). *Sea Level Change. In: Climate Change 2013: The Physical Science Basis. Contribution of Working Group I to the Fifth Assessment Report of the Intergovernmental Panel on Climate Change [Stocker, T.F., D. Qin, G.-K. Plattner, M. Tignor, S.K. Allen, J. Boschung, A. Nauels, Y. Xia, V. Bex and P.M. Midgley (eds.)]* Tech. rep. Cambridge University Press, Cambridge, United Kingdom and New York, NY, USA.

Ciracì, E. et al. (May 2023). "Melt rates in the kilometer-size grounding zone of Petermann Glacier, Greenland, before and during a retreat". In: *Proceedings of the National Academy of Sciences* 120.20. Publisher: Proceedings of the National Academy of Sciences, e2220924120. DOI: 10.1073/pnas.2220924120.

Climate Studies Group Mona (Eds.) (2020). *The State of the Caribbean Climate*. URL: https://www.caribank.org/publications-and-resources/resource-library/publications/state-caribbean-climate (visited on 10/08/2022).

CMIP6 CMOR Tables (2023). *CMOR tables Github*. available at: https://github.com/PCMDI/cmip6-cmor-tables. last access: 1 May 2023.

CMOR3 conventions (2023). *CMOR tables Github*. available at: https://cmor.llnl.gov/. last access: 1 May 2023.

Coats, S. and K. Karnauskas (2017). "Are simulated and observed twentieth century tropical Pacific sea surface temperature trends significant relative to internal variability?" In: *Geophysical Research Letters* 44.19, pp. 9928–9937.

Contreras Osorio, S. et al. (Dec. 2022). "Impact of the Microphysics in HARMONIE-AROME on Fog". In: *Atmosphere* 13.1212, p. 2127. ISSN: 2073-4433. DOI: 10.3390/atmos13122127.

Coppola, E. et al. (July 2020). "A first-of-its-kind multi-model convection permitting ensemble for investigating convective phenomena over Europe and the Mediterranean". In: *Climate Dynamics* 55.1-2, pp. 3–34. ISSN: 0930-7575, 1432-0894. DOI: 10.1007/s00382-018-4521-8.

Coppola, E. et al. (2021). "Assessment of the European Climate Projections as Simulated by the Large EURO-CORDEX Regional and Global Climate Model Ensemble". In: *Journal of Geophysical Research: Atmospheres* 126.4, e2019JD032356. DOI: https://doi.org/10.1029/2019JD032356.

Cornes, R. C. et al. (2018). "An Ensemble Version of the E-OBS Temperature and Precipitation Data Sets". In: *Journal of Geophysical Research: Atmospheres* 123.17, pp. 9391–9409. DOI: https://doi.org/10.1029/2017JD028200.

Coumou, D. et al. (Sept. 2018). "The influence of Arctic amplification on mid-latitude summer circulation". In: *Nature Communications*. ISSN: 2198-6061. DOI: 10.1038/s41467-018-05256-8.

Daniels, E. E. et al. (2016). "Observed urban effects on precipitation along the Dutch West coast". In: *Int. J. Climatol* 36.4, pp. 2111–2119. ISSN: 0899-8418. DOI: https://doi.org/10.1002/joc.4458.

de Vries, H., C. Katsman, and S. Drijfhout (Nov. 2014). "Constructing scenarios of regional sea level change using global temperature pathways". In: *Environmental Research Letters* 9.11, p. 115007. ISSN: 1748-9326. DOI: 10.1088/1748-9326/9/11/115007.

DeConto, R. M. and D. Pollard (Mar. 2016). "Contribution of Antarctica to past and future sea-level rise". In: *Nature* 531.7596. Number: 7596 Publisher: Nature Publishing Group, pp. 591–597. ISSN: 1476-4687. DOI: 10.1038/nature17145.

DeConto, R. M. et al. (May 2021). "The Paris Climate Agreement and future sea-level rise from Antarctica". In: *Nature* 593.7857. Number: 7857 Publisher: Nature Publishing Group, pp. 83–89. ISSN: 1476-4687. DOI: 10.1038/s41586-021-03427-0.

Derbyshire, S. et al. (Oct. 2004). "Sensitivity of moist convection to environmental humidity". In: *Quarterly Journal of the Royal Meteorological Society* 130.604, pp. 3055–3079. ISSN: 00359009. DOI: 10.1256/qj.03.130.

Dieng, D. et al. (2022). "Multivariate bias-correction of high-resolution regional climate change simulations for West Africa: performance and climate change implications". In: *Journal of Geophysical Research: Atmospheres* 127.5, e2021JD034836.

Dirksen, M. et al. (Oct. 1, 2020). "Downscaling daily air-temperature measurements in the Netherlands". In: *Theoretical and Applied Climatology* 142.1, pp. 751–767.

ES-DOC/EC-Earth3 (2023). *ES-DOC, EC-Earth-Consortium, the EC-Earth3 model description*. available at: https://explore.es-doc.org/cmip6/models/ec-earth-consortium/ec-earth3. last access: 1 May 2023.

Dong, B., R. T. Sutton, and L. J. Wilcox (2022). "Decadal trends in surface solar radiation and cloud cover over the North Atlantic sector during the last four decades: drivers and physical processes". In: *Climate Dynamics* 60.7-8, pp. 2533–2546. DOI: 10.1007/s00382-022-06438-3.

Döscher, R. et al. (2022). "The EC-Earth3 Earth system model for the Coupled Model Intercomparison Project 6". In: *Geoscientific Model Development* 15.7, pp. 2973–3020. DOI: 10.5194/gmd-15-2973-2022.

Dullaart, J. et al. (2023). "Improving our understanding of future tropical cyclone intensities in the Caribbean using a high-resolution regional climate model". In: *submitted*.

ECMWF (2009). *IFS Documentation CY33R1 - Part IV: Physical Processes*. available at: https://www.ecmwf.int/en/elibrary/74344-ifs-documentation-cy33r1-part-iv-physical-processes/. DOI: 10.21957/8o7vwlbdr.

— (2010). *IFS Documentation CY36R1 - Part IV: Physical Processes*. available at: https://www.ecmwf.int/en/elibrary/74350-ifs-documentation-cy36r1-part-iv-physical-processes/. last access: 1 May 2023. DOI: 10.21957/2loi3bxcz.

Emanuel, K. A. and D. S. Nolan (2004). "Tropical cyclone activity and the global climate system". In: *Proceedings of the 26th Conference on Hurricanes and Tropical Meteorology*.

Enfield, D. B. and D. A. Mayer (1997). "Tropical Atlantic sea surface temperature variability and its relation to El Niño-Southern Oscillation". In: *Journal of Geophysical Research: Oceans* 102.C1, pp. 929–945.

ESGF node (2023). *The NSC ESGF node (Sweden)*. available at: https://esg-dn1.nsc.liu.se/search/cmip6-liu/. last access: 1 May 2023.

EUCP (2022a). "EUCP: Outer-European domain simulations D3.5". In: *The EUCP project*.

— (2022b). "EUCP: Outlook of future hazards for the outermost regions D4.6". In: *The EUCP project*.

Eyring, V. et al. (2016). "Overview of the Coupled Model Intercomparison Project Phase 6 (CMIP6) experimental design and organization". In: *Geoscientific Model Development* 9.5, pp. 1937–1958. DOI: 10.5194/gmd-9-1937-2016.

Feigenwinter, I. et al. (2018). *Exploring quantile mapping as a tool to produce user-tailored climate scenarios for Switzerland*. MeteoSchweiz.

Fettweis, X. et al. (Mar. 2013). "Estimating the Greenland ice sheet surface mass balance contribution to future sea level rise using the regional atmospheric climate model MAR". English. In: *The Cryosphere* 7.2. Publisher: Copernicus GmbH, pp. 469–489. ISSN: 1994-0416. DOI: https://doi.org/10.5194/tc-7-469-2013.

Fiedler, S. et al. (2019). "First forcing estimates from the future CMIP6 scenarios of anthropogenic aerosol optical properties and an associated Twomey effect". In: *Geoscientific Model Development* 12.3, pp. 989–1007. DOI: 10.5194/gmd-12-989-2019.

Findeisen, W. et al. (July 1938). "Colloidal meteorological processes in the formation of precipitation". In: *Meteorologische Zeitschrift* 24.4, pp. 443–454. DOI: 10.1127/metz/2015/0675.

Fischer, E. M., S. Sippel, and R. Knutti (Aug. 2021). "Increasing probability of record-shattering climate extremes". In: *Nature Climate Change* 11 (8), pp. 689–695. ISSN: 17586798. DOI: 10.1038/s41558-021-01092-9.

Forbes, R. M. and M. Ahlgrimm (2014). "On the Representation of High-Latitude Boundary Layer Mixed-Phase Cloud in the ECMWF Global Model". In: *Monthly Weather Review* 142.9, pp. 3425–3445. DOI: 10.1175/MWR-D-13-00325.1.

Fowler, H. J. et al. (2021). "Anthropogenic intensification of short-duration rainfall extremes". In: *Nature Reviews Earth & Environment* 2.2, pp. 107–122. ISSN: 2662-138X. DOI: 10.1038/s43017-020-00128-6.

Fox-Kemper, B. et al. (Aug. 2021). *Ocean, Cryosphere and Sea Level Change. In: Climate Change 2021: The Physical Science Basis. Contribution of Working Group I to the Sixth Assessment Report of the Intergovernmental Panel on Climate Change [Masson-Delmotte, V., P. Zhai, A. Pirani, S. L. Connors, C. Péan, S. Berger, N. Caud, Y. Chen, L. Goldfarb, M. I. Gomis, M. Huang, K. Leitzell, E. Lonnoy, J.B.R. Matthews, T. K. Maycock, T. Waterfield, O. Yelekçi, R. Yu and B. Zhou (eds.)]* Cambridge University Press.

François, B. et al. (2020). "Multivariate bias corrections of climate simulations: which benefits for which losses?" In: *Earth System Dynamics* 11.2, pp. 537–562.

Frederikse, T. et al. (Oct. 2016). "Closing the sea level budget on a regional scale: Trends and variability on the Northwestern European continental shelf". In: *Geophysical Research Letters* 43.20, pp. 10, 864–10, 872. ISSN: 00948276. DOI: 10.1002/2016GL070750.

Frederikse, T. et al. (Aug. 2020). "The causes of sea-level rise since 1900". In: *Nature* 584.7821. Publisher: Nature Publishing Group, pp. 393–397. ISSN: 1476-4687. DOI: 10.1038/s41586-020-2591-3.

Fredriksen, H.-B. et al. (2020). "How does El Niño–Southern Oscillation change under global warming—A first look at CMIP6". In: *Geophysical Research Letters* 47.22, e2020GL090640.

Friedlingstein, P. et al. (2014). "Uncertainties in CMIP5 Climate Projections due to Carbon Cycle Feedbacks". In: *J. Clim.* 27, pp. 511–526. DOI: 10.1175/JCLI-D-12-00579.1.

Fuglestvedt, H. F. and J. O. Haerter (2020). "Cold Pools as Conveyor Belts of Moisture". In: *Geophysical Research Letters* 47.12. ISSN: 0094-8276. DOI: 10.1029/2020GL087319.

Fyfe, J. et al. (2021). *Summary for Policymakers of the Working Group I Contribution to the IPCC Sixth Assessment Report - data for Figure SPM.8*. DOI: 10.5285/98af2184e13e4b91893ab72f301790db.

Gerritsen, H., H. de Vries, and M. Philippart (1995). "The Dutch Continental Shelf Model". In: *Quantitative Skill Assessment for Coastal Ocean Models*. American Geophysical Union (AGU). Chap. 19, pp. 425–467. DOI: 10.1029/CE047p0425.

Giannini, A., Y. Kushnir, and M. Cane (2001a). "Seasonality in the impact of ENSO and the North Atlantic high on Caribbean rainfall". In: *Physics and Chemistry of the Earth, Part B: Hydrology, Oceans and Atmosphere* 26.2, pp. 143–147.

Giannini, A., Y. Kushnir, and M. A. Cane (2000). "Interannual variability of Caribbean rainfall, ENSO, and the Atlantic Ocean". In: *Journal of Climate* 13.2, pp. 297–311.

Giannini, A. et al. (2001b). "The ENSO teleconnection to the tropical Atlantic Ocean: Contributions of the remote and local SSTs to rainfall variability in the tropical Americas". In: *Journal of Climate* 14.24, pp. 4530–4544.

Gilford, D. M. (2021). "pyPI (v1.3): Tropical Cyclone Potential Intensity Calculations in Python". In: *Geoscientific Model Development* 14.5, pp. 2351–2369. ISSN: 1991-9603. DOI: 10.5194/gmd-14-2351-2021.

Giorgi, F. et al. (2016). "Enhanced summer convective rainfall at Alpine high elevations in response to climate warming". In: *Nature Geoscience* 9, pp. 584–589. DOI: 10.1038/ngeo2761.

GISTEMP Team (2023). *GISS Surface Temperature Analysis (GISTEMP)*. available at: https://data.giss.nasa.gov/gistemp/. last access: 1 May 2023.

Goelzer, H. et al. (Sept. 2020). "The future sea-level contribution of the Greenland ice sheet: a multi-model ensemble study of ISMIP6". English. In: *The Cryosphere* 14.9. Publisher: Copernicus GmbH, pp. 3071–3096. ISSN: 1994-0416. DOI: https://doi.org/10.5194/tc-14-3071-2020.

Golledge, N. R. et al. (Feb. 2019). "Global environmental consequences of twenty-first-century ice-sheet melt". In: *Nature* 566.7742, pp. 65–72. ISSN: 0028-0836, 1476-4687. DOI: 10.1038/s41586-019-0889-9.

Good, S. A., M. J. Martin, and N. A. Rayner (2013). "EN4: Quality controlled ocean temperature and salinity profiles and monthly objective analyses with uncertainty estimates". en. In: *Journal of Geophysical Research: Oceans* 118.12, pp. 6704–6716. DOI: 10.1002/2013JC009067.

Greatbatch, R. J. (1994). "A note on the representation of steric sea level in models that conserve volume rather than mass". en. In: *Journal of Geophysical Research* 99.C6, p. 12767. ISSN: 0148-0227. DOI: 10.1029/94JC00847.

Gregory, J. M. et al. (Nov. 2019). "Concepts and Terminology for Sea Level: Mean, Variability and Change, Both Local and Global". en. In: *Surveys in Geophysics* 40.6, pp. 1251–1289. ISSN: 0169-3298, 1573-0956. DOI: 10.1007/s10712-019-09525-z.

Griffies, S. M. and R. J. Greatbatch (July 2012). "Physical processes that impact the evolution of global mean sea level in ocean climate models". en. In: *Ocean Modelling* 51, pp. 37–72. ISSN: 14635003. DOI: 10.1016/j.ocemod.2012.04.003.

Gutmann, E. D. et al. (2018). "Changes in Hurricanes from a 13-Yr Convection-Permitting Pseudo Global Warming Simulation". In: *Journal of Climate* 31.9, pp. 3643–3657. ISSN: 0894-8755, 1520-0442. DOI: 10.1175/JCLI-D-17-0391.1.

Haarsma, R., F. Selten, and G. J. Van Oldenborgh (2013). "Anthropogenic changes of the thermal and zonal flow structure over Western Europe and Eastern North Atlantic in CMIP3 and CMIP5 models". In: *Climate Dynamics* 41, pp. 2577–2588.

Haarsma, R. J., F. M. Selten, and S. S. Drijfhout (2015). "Decelerating Atlantic meridional overturning circulation main cause of future west European summer atmospheric circulation changes". In: *Environmental Research Letters* 10.9, p. 094007. DOI: 10.1088/1748-9326/10/9/094007.

Haarsma, R. J. et al. (2009). "Drier Mediterranean soils due to greenhouse warming bring easterly winds over summertime central Europe". In: *Geophysical Research Letters* 36.4, pp. 1–7. ISSN: 00948276. DOI: 10.1029/2008GL036617.

Haasnoot, M. et al. (Oct. 2015). "Transient scenarios for robust climate change adaptation illustrated for water management in The Netherlands". In: *Environmental Research Letters* 10.10, p. 105008. ISSN: 1748-9326. DOI: 10.1088/1748-9326/10/10/105008.

Haasnoot, M. et al. (Feb. 2020). "Adaptation to uncertain sea-level rise: how uncertainty in Antarctic mass-loss impacts the coastal adaptation strategy of the Netherlands". en. In: *Environmental Research Letters* 15.3, p. 034007. ISSN: 1748-9326. DOI: 10.1088/1748-9326/ab666c.

Haerter, J. O. and L. Schlemmer (2018). "Intensified Cold Pool Dynamics Under Stronger Surface Heating". In: *Geophysical Research Letters* 45.12, pp. 6299–6310. ISSN: 19448007. DOI: 10.1029/2017GL076874.

Hahmann, A. N., O. Garcıa-Santiago, and A. Peña (2022). "Current and future wind energy resources in the North Sea according to CMIP6". In: *Wind Energy Science* 7.6, pp. 2373–2391. DOI: 10.5194/wes-7-2373-2022.

Hausfather, Z. and G. P. Peters (2020). "Emissions – the 'business as usual' story is misleading". In: *Nature* 577, pp. 618–620. DOI: 10.1038/d41586-020-00177-3.

Hausfather, Z. et al. (2022). "Climate simulations: recognize the 'hot model' problem". In: *Nature* 605.7908, pp. 26–29.

Hazeleger, W. et al. (Dec. 2012). "EC-Earth V2.2: description and validation of a new seamless earth system prediction model". In: *Climate Dynamics* 39.11, pp. 2611–2629. ISSN: 1432-0894. DOI: 10.1007/s00382-011-1228-5.

He, C. et al. (Aug. 2022). "The Effects of Night-Time Warming on Mortality Burden under Future Climate Change Scenarios: A Modelling Study". In: *The Lancet Planetary Health* 6.8, e648–e657. ISSN: 2542–5196. DOI: 10.1016/S2542-5196(22)00139-5.

Herrera, D. and T. Ault (2017). "Insights from a new high-resolution drought atlas for the Caribbean spanning 1950–2016". In: *Journal of Climate* 30.19, pp. 7801–7825.

Hersbach, H. et al. (2020). "The ERA5 global reanalysis". In: *Quarterly Journal of the Royal Meteorological Society* 146.730, pp. 1999–2049. DOI: https://doi.org/10.1002/qj.3803.

Hinkel, J. et al. (Mar. 2019). "Meeting User Needs for Sea Level Rise Information: A Decision Analysis Perspective". In: *Earth's Future* 7.3, pp. 320–337. ISSN: 2328-4277, 2328-4277. DOI: 10.1029/2018EF001071.

Hobbs, W., M. D. Palmer, and D. Monselesan (Mar. 2016). "An Energy Conservation Analysis of Ocean Drift in the CMIP5 Global Coupled Models". EN. In: *Journal of Climate* 29.5. Publisher: American Meteorological Society Section: Journal of Climate, pp. 1639–1653. ISSN: 0894-8755, 1520-0442. DOI: 10.1175/JCLI-D-15-0477.1.

Hoffmann, P. et al. (2022). "High-resolution land use and land cover dataset for regional climate modelling : Historical and future changes in Europe". In: *Earth System Science Data Discussions* 2022, pp. 1–50. DOI: 10.5194/essd-2022-431.

Hohenegger, C. et al. (Oct. 2009). "The Soil Moisture–Precipitation Feedback in Simulations with Explicit and Parameterized Convection". In: *Journal of Climate* 22.19, pp. 5003–5020. ISSN: 0894-8755. DOI: 10.1175/2009JCLI2604.1.

Holmes, C. R. et al. (2016). "Robust future changes in temperature variability under greenhouse gas forcing and the relationship with thermal advection". In: *Journal of Climate* 29.6, pp. 2221–2236.

Houghton et al. (2001). "IPCC (2001): Climate Change 2001: The Scientific Basis. Contribution of Working Group I to the Third Assessment Report of the Intergovernmental Panel on Climate Change". In: *Cambridge University Press, Cambridge, United Kingdom and New York, NY, USA* ISBN 052-1014956, 881 pp.

Hourdin, F. et al. (2017). "The Art and Science of Climate Model Tuning". In: *Bulletin of the American Meteorological Society* 98.3, pp. 589–602. DOI: 10.1175/BAMS-D-15-00135.1.

Howard, L. (1833). *Climate of London*. Ed. by G. Mills. URL: https://urban-climate.org/documents/LukeHoward_Climate-of-London-V1.pdf.

Hurtt, G. C. et al. (2020). "Harmonization of global land use change and management for the period 850–2100 (LUH2) for CMIP6". In: *Geoscientific Model Development* 13.11, pp. 5425–5464. DOI: 10.5194/gmd-13-5425-2020.

Hyder, P. et al. (Sept. 2018). "Critical Southern Ocean climate model biases traced to atmospheric model cloud errors". In: *Nature Communications* 9.1, p. 3625. ISSN: 2041-1723. DOI: 10.1038/s41467-018-05634-2.

IPCC (2013). *The physical science basis*. URL: https://www.ipcc.ch/report/ar5/wg1/.

— (2021a). "Summary for Policymakers". In: *Climate Change 2021: The Physical Science Basis. Contribution of Working Group I to the Sixth Assessment Report of the Intergovernmental Panel on Climate Change*. Ed. by V. Masson-Delmotte et al. Cambridge, United Kingdom and New York, NY, USA: Cambridge University Press, pp. 3–32. DOI: 10.1017/9781009157896.001.

— (2021b). *The physical science basis*. URL: https://www.ipcc.ch/report/ar6/wg1/ (visited on 10/08/2022).

Jiang, W., G. Gastineau, and F. Codron (2021). "Multicentennial Variability Driven by Salinity Exchanges Between the Atlantic and the Arctic Ocean in a Coupled Climate Model". In: *Journal of Advances in Modeling Earth Systems* 13.3. e2020MS002366 2020MS002366, e2020MS002366. DOI: https://doi.org/10.1029/2020MS002366.

Joshi, M. M. et al. (2008). "Mechanisms for the land/sea warming contrast exhibited by simulations of climate change". In: *Climate Dynamics* 30.5, pp. 455–465. DOI: 10.1007/s00382-007-0306-1.

Kahraman, A. et al. (July 2021). "Quasi-Stationary Intense Rainstorms Spread Across Europe Under Climate Change". In: *Geophysical Research Letters* 48.13. ISSN: 0094-8276, 1944-8007. DOI: 10.1029/2020GL092361.

Kahraman, A. et al. (Nov. 2022). "Contrasting future lightning stories across Europe". In: *Environmental Research Letters* 17.11, p. 114023. ISSN: 1748-9326. DOI: 10.1088/1748-9326/ac9b78.

Katsman, C. A. et al. (Dec. 2008). "Climate scenarios of sea level rise for the northeast Atlantic Ocean: a study including the effects of ocean dynamics and gravity changes induced by ice melt". In: *Climatic Change* 91.3-4, pp. 351–374. ISSN: 0165-0009, 1573-1480. DOI: 10.1007/s10584-008-9442-9.

Keizer, I. et al. (Oct. 2022). "The acceleration of sea-level rise along the coast of the Netherlands started in the 1960s". In: *EGUsphere*. Publisher: Copernicus GmbH, pp. 1–21. DOI: 10.5194/egusphere-2022-935.

Kendon, E. J. et al. (Apr. 2021). "Challenges and outlook for convection-permitting climate modelling". In: *Philosophical Transactions of the Royal Society A: Mathematical, Physical and Engineering Sciences* 379.2195, p. 20190547. ISSN: 1364-503X, 1471-2962. DOI: 10.1098/rsta.2019.0547.

Kendon, E. J. et al. (Jan. 2017). "Do Convection-Permitting Regional Climate Models Improve Projections of Future Precipitation Change?" In: *Bulletin of the American Meteorological Society* 98.1. ISBN: 0003-0007, pp. 79–93. ISSN: 0003-0007. DOI: 10.1175/BAMS-D-15-0004.1.

Kendon, E. J. et al. (2020). "Greater future U.K. winter precipitation increase in new convection-permitting scenarios". In: *Journal of Climate* 33.17, pp. 7303–7318. ISSN: 08948755. DOI: 10.1175/JCLI-D-20-0089.1.

Kleidon, A. and M. Renner (2017). "An explanation for the different climate sensitivities of land and ocean surfaces based on the diurnal cycle". In: *Earth System Dynamics* 8.3, pp. 849–864. DOI: 10.5194/esd-8-849-2017.

Knaff, J. A. et al. (2021). "Estimating Tropical Cyclone Surface Winds: Current Status, Emerging Technologies, Historical Evolution, and a Look to the Future". In: *Tropical Cyclone Research and Review* 10.3, pp. 125–150. ISSN: 2225-6032. DOI: 10.1016/j.tcrr.2021.09.002.

Knapp, K. R. et al. (Mar. 2010). "The International Best Track Archive for Climate Stewardship (IBTrACS)". In: *Bulletin of the American Meteorological Society* 91.3, pp. 363–376. DOI: 10.1175/2009bams2755.1.

KNMI daggegevens (2022). *Daggegevens van het weer in Nederland.* URL: https://www.knmi.nl/nederland-nu/klimatologie/daggegevens (visited on 08/22/2022).

KNMI uurgegevens (2023). *Uurgegevens van het weer in Nederland.* URL: https://www.knmi.nl/nederland-nu/klimatologie/uurgegevens (visited on 05/23/2023).

Knutson, T. et al. (2020). "Tropical cyclones and climate change assessment: Part II: Projected response to anthropogenic warming". In: *Bulletin of the American Meteorological Society* 101.3, E303–E322.

Kociuba, G. and S. B. Power (2015). "Inability of CMIP5 models to simulate recent strengthening of the Walker circulation: Implications for projections". In: *Journal of Climate* 28.1, pp. 20–35.

Kohyama, T., D. L. Hartmann, and D. S. Battisti (2017). "La Niña–like mean-state response to global warming and potential oceanic roles". In: *Journal of Climate* 30.11, pp. 4207–4225.

Können, G. (2001). "Climate scenarios IRMA and perspectives". In: *Scientific report, KNMI.*

Kuma, P., F. A.-M. Bender, and A. R. J onsson (2023). "Climate Model Code Genealogy and its Relation to Climate Feedbacks and Sensitivity". In: *ESS Open Archive.* DOI: 10.22541/essoar.167422929.96660814/v1.

Kwadijk, J. et al. (Aug. 2010). "Using adaptation tipping points to prepare for climate change and sea level rise: A case study in the Netherlands". In: *Wiley Interdisciplinary Reviews: Climate Change* 1, pp. 729–740. DOI: 10.1002/wcc.64.

Lambert, E. et al. (2021). "Correlations Between Sea-Level Components Are Driven by Regional Climate Change". en. In: *Earth's Future* 9.2, e2020EF001825. ISSN: 2328-4277.

Le Bars, D. (Sept. 2018). "Uncertainty in Sea Level Rise Projections Due to the Dependence Between Contributors". In: *Earth's Future* 6.9, pp. 1275–1291. ISSN: 23284277. DOI: 10.1029/2018EF000849.

Le Bars, D., S. Drijfhout, and H. de Vries (Apr. 2017). "A high-end sea level rise probabilistic projection including rapid Antarctic ice sheet mass loss". en. In: *Environmental Research Letters* 12.4, p. 044013. ISSN: 1748-9326. DOI: 10.1088/1748-9326/aa6512.

Lee, C.-Y. et al. (Jan. 2018). "An Environmentally Forced Tropical Cyclone Hazard Model". In: *Journal of Advances in Modeling Earth Systems* 10.1, pp. 223–241. DOI: 10.1002/2017ms001186.

Lee, J. Y. et al. (2021). "Future Global Climate: Scenario-42 Based Projections and Near-Term Information. In: Climate Change 2021: The Physical Science Basis. 43 Contribution of Working Group I to the Sixth Assessment Report of the Intergovernmental Panel on Climate 44 Change [Masson-Delmotte, V., P. Zhai, A. Pirani, S. L. Connors, C. Pèan, S. Berger, N. Caud, Y. Chen, L. 45 Goldfarb, M. I. Gomis, M. Huang, K. Leitzell, E. Lonnoy, J. B. R. Matthews, T. K. Maycock, T. Waterfield, 46 O.Yelekçi, R. Yu and B. Zhou (eds.)]" In: Cambridge University Press.

Lenderink, G. et al. (2014). "Preparing local climate change scenarios for the Netherlands using resampling of climate model output". In: *Environmental Research Letters* 9.11, p. 115008.

Lenderink, G. et al. (2003). *Simulation of present-day climate in RACMO2: first results and model developments*. Technical report TR-252. KNMI.

Lenderink, G. et al. (Aug. 2007). "A study on combining global and regional climate model results for generating climate scenarios of temperature and precipitation for the Netherlands". In: *Climate Dynamics* 29.2-3, pp. 157–176. ISSN: 0930-7575. DOI: 10.1007/s00382-007-0227-z.

Lenderink, G. et al. (2011). "Scaling and trends of hourly precipitation extremes in two different climate zones – Hong Kong and the Netherlands". In: *Hydrology and Earth System Sciences* 15.9, pp. 3033–3041. ISSN: 1607-7938. DOI: 10.5194/hess-15-3033-2011.

Lenderink, G. et al. (2017). "Super-Clausius–Clapeyron Scaling of Extreme Hourly Convective Precipitation and Its Relation to Large-Scale Atmospheric Conditions". In: *Journal of Climate* 30.15, pp. 6037–6052. ISSN: 0894-8755. DOI: 10.1175/JCLI-D-16-0808.1.

Lenderink, G. et al. (2019a). "Systematic increases in the thermodynamic response of hourly precipitation extremes in an idealized warming experiment with a convection-permitting climate model". In: *Environmental Research Letters*.

Lenderink, G. et al. (Apr. 2021a). "Scaling and responses of extreme hourly precipitation in three climate experiments with a convection-permitting model". In: *Philosophical Transactions of the Royal Society A:Mathematical, Physical and Engineering Sciences* 379, p. 20190544. ISSN: 1364-503X, 1471-2962. DOI: 10.1098/rsta.2019.0544.

— (Apr. 2021b). "Scaling and responses of extreme hourly precipitation in three climate experiments with a convection-permitting model". In: *Philosophical Transactions of the Royal Society A: Mathematical, Physical and Engineering Sciences* 379.2195, p. 20190544. ISSN: 1364-503X, 1471-2962. DOI: 10.1098/rsta.2019.0544.

Lenderink, G. and J. Attema (2015). "A simple scaling approach to produce climate scenarios of local precipitation extremes for the Netherlands". In: *Environmental Research Letters* 10.8, p. 085001. ISSN: 1748-9326. DOI: 10.1088/1748-9326/10/8/085001.

Lenderink, G. and E. van Meijgaard (2008). "Increase in hourly precipitation extremes beyond expectations from temperature changes". In: *Nature Geoscience* 1.8, pp. 511–514. ISSN: 1752-0894. DOI: 10.1038/ngeo262.

Lenderink, G. et al. (Aug. 2018). "Reply to comments on "Temperature-extreme precipitation scaling: a two-way causality?"" In: *International Journal of Climatology* May, pp. 8–10. ISSN: 08998418. DOI: 10.1002/joc.5799.

Lenderink, G. et al. (July 2019b). "Systematic increases in the thermodynamic response of hourly precipitation extremes in an idealized warming experiment with a convection-permitting cli-

mate model". In: *Environmental Research Letters* 14.7, p. 074012. ISSN: 1748-9326. DOI: 10.1088/1748-9326/ab214a.

Lenderink, G. et al. (Aug. 2022). "A perfect model study on the reliability of the added small-scale information in regional climate change projections". In: *Climate Dynamics*. ISSN: 0930-7575, 1432-0894. DOI: 10.1007/s00382-022-06451-6.

Lenssen, N. J. L. et al. (2019). "Improvements in the GISTEMP Uncertainty Model". In: *Journal of Geophysical Research: Atmospheres* 124.12, pp. 6307–6326. DOI: https://doi.org/10.1029/2018JD029522. eprint: https://agupubs.onlinelibrary.wiley.com/doi/pdf/10.1029/2018JD029522.

Lenton, T. M. et al. (2014). "Climate tipping points — too risky to bet against". In: *Nature* 575, pp. 592–595. DOI: 10.1038/d41586-019-03595-0.

Levermann, A. et al. (Feb. 2020). "Projecting Antarctica's contribution to future sea level rise from basal ice shelf melt using linear response functions of 16 ice sheet models (LARMIP-2)". In: *Earth System Dynamics* 11.1. Publisher: Copernicus GmbH, pp. 35–76. ISSN: 2190-4979. DOI: https://doi.org/10.5194/esd-11-35-2020.

Lhermitte, S. et al. (Oct. 2020). "Damage accelerates ice shelf instability and mass loss in Amundsen Sea Embayment". In: *Proceedings of the National Academy of Sciences* 117.40. Publisher: Proceedings of the National Academy of Sciences, pp. 24735–24741. DOI: 10.1073/pnas.1912890117.

Liang, Y., N. P. Gillett, and A. H. Monahan (2020). "Climate model projections of 21st century global warming constrained using the observed warming trend". In: *Geophysical Research Letters* 47.12, e2019GL086757.

Liljegren, J. C. et al. (2008). "Modeling the Wet Bulb Globe Temperature Using Standard Meteorological Measurements". In: *Journal of Occupational and Environmental Hygiene* 5.10, pp. 645–655. DOI: 10.1080/15459620802310770.

Lipscomb, W. H. et al. (Feb. 2021). "ISMIP6-based projections of ocean-forced Antarctic Ice Sheet evolution using the Community Ice Sheet Model". English. In: *The Cryosphere* 15.2. Publisher: Copernicus GmbH, pp. 633–661. ISSN: 1994-0416. DOI: https://doi.org/10.5194/tc-15-633-2021.

Little, C. M., M. Oppenheimer, and N. M. Urban (July 2013a). "Upper bounds on twenty-first-century Antarctic ice loss assessed using a probabilistic framework". In: *Nature Climate Change* 3.7, pp. 654–659. ISSN: 1758-678X, 1758-6798. DOI: 10.1038/nclimate1845.

Little, C. M., N. M. Urban, and M. Oppenheimer (Feb. 2013b). "Probabilistic framework for assessing the ice sheet contribution to sea level change". In: *Proceedings of the National Academy of Sciences* 110.9, pp. 3264–3269. ISSN: 0027-8424, 1091-6490. DOI: 10.1073/pnas.1214457110.

Lochbihler, K., G. Lenderink, and A. P. Siebesma (Aug. 2017). "The spatial extent of rainfall events and its relation to precipitation scaling". In: *Geophysical Research Letters* 44.16, pp. 8629–8636. ISSN: 00948276. DOI: 10.1002/2017GL074857.

— (July 2019). "Response of Extreme Precipitating Cell Structures to Atmospheric Warming". In: *Journal of Geophysical Research: Atmospheres*, 2018JD029954. ISSN: 2169-897X. DOI: 10.1029/2018JD029954.

— (2021). "Cold Pool Dynamics Shape the Response of Extreme Rainfall Events to Climate Change". In: *Journal of Advances in Modeling Earth Systems* 13.2, pp. 1–16. ISSN: 1942-2466. DOI: 10.1029/2020MS002306.

Loriaux, J. M. et al. (2013). "Understanding Convective Extreme Precipitation Scaling Using Observations and an Entraining Plume Model". In: *Journal of the Atmospheric Sciences* 70.11, pp. 3641–3655. ISSN: 0022-4928. DOI: 10.1175/JAS-D-12-0317.1.

Lucas-Picher, P. et al. (Aug. 2021). "Convection-permitting modeling with regional climate models: Latest developments and next steps". In: *WIREs Climate Change*, pp. 1–59. ISSN: 1757-7780. DOI: 10.1002/wcc.731.

Luu, L. N. et al. (2023). "Impact of Surface Roughness Changes on Surface Wind Speed over Western Europe: A Study with a Regional Climate Model". In: *Journal of Geophysical Research: Atmospheres)* 128, pp. 1–18. DOI: 10.1029/2022JD038426.

Maat, H. ter et al. (Apr. 2013). "Exploring the Impact of Land Cover and Topography on Rainfall Maxima in the Netherlands". In: *Journal of Hydrometeorology* 14, pp. 524–542. DOI: 10.1175/JHM-D-12-036.1.

Martinez, C. et al. (2019). "Seasonal climatology and dynamical mechanisms of rainfall in the Caribbean". In: *Climate dynamics* 53.1, pp. 825–846.

Masson, V. (Mar. 1, 2000). "A Physically-Based Scheme For The Urban Energy Budget In Atmospheric Models". In: *Boundary-Layer Meteorology* 94.3, pp. 357–397. DOI: 10.1023/A:1002463829265.

Mauritsen, T. et al. (2012). "Tuning the climate of a global model". In: *Journal of Advances in Modeling Earth Systems* 4.3. DOI: https://doi.org/10.1029/2012MS000154.

Mayers, D. and C. Ruf (2020). "Estimating the True Maximum Sustained Wind Speed of a Tropical Cyclone from Spatially Averaged Observations". In: *Journal of Applied Meteorology and Climatology* 59.2, pp. 251–262. ISSN: 1558-8424, 1558-8432. DOI: 10.1175/JAMC-D-19-0177.1.

McKee, T. B., N. J. Doesken, J. Kleist, et al. (1993). "The relationship of drought frequency and duration to time scales". In: *Proceedings of the 8th Conference on Applied Climatology*. Vol. 17. 22. Boston, pp. 179–183.

Meccia, V. L. et al. (Oct. 2022). "Internal multi-centennial variability of the Atlantic Meridional Overturning Circulation simulated by EC-Earth3". In: *Climate Dynamics*. ISSN: 1432-0894. DOI: 10.1007/s00382-022-06534-4.

Meehl, G. A. et al. (2020). "Context for interpreting equilibrium climate sensitivity and transient climate response from the CMIP6 Earth system models". In: *Science Advances* 6.26, eaba1981. DOI: 10.1126/sciadv.aba1981.

Meijers, A. J. S. (2014). "The Southern Ocean in the Coupled Model Intercomparison Project phase 5". In: *Philos Trans A Math Phys Eng Sci.* 372.2019, p. 20130296. DOI: 10.1098/rsta.2013.0296.

Meijgaard, E. van et al. (2008). *The KNMI regional atmospheric climate model RACMO, version 2.1*. Tech. rep. TR-302. KNMI, pp43.

Meijgaard, E. van et al. (2012). *Refinement and application of a regional atmospheric model for climate scenario calculations of Western Europe*. KvR 054/12, ISBN/EAN 978-90-8815-046-3. also available at http://climexp.knmi.nl/publications/FinalReport_KvR-CS06.pdf. Climate changes Spatial Planning.

Meijgaard, E. v. (2019). *A closer look at the snow accumulation issue in RACMO*. available at: https://wiki.gerics.de/euro-cordex/NinthMeeting?action=AttachFile&do=view&target=Meijgaard-EuroCordex-20190128.pptx. presented at the 9th EURO-CORDEX General Assembly, Hamburg, Germany, 28–30 January 2019.

Min, E. et al. (2013). "Evaluation of trends in high temperature extremes in north-western Europe in regional climate models". In: *Environmental Research Letters* 8.1, p. 014011. DOI: 10.1088/1748-9326/8/1/014011.

Mironov, D. et al. (2010). "Implementation of the lake parameterisation scheme FLake into the numerical weather prediction model COSMO". In: *Boreal Environmental Research* 15, pp. 218–230. ISSN: 1797–2469.

Morice, C. P. et al. (2021). "An Updated Assessment of Near-Surface Temperature Change From 1850: The HadCRUT5 Data Set". In: *Journal of Geophysical Research: Atmospheres* 126.3, e2019JD032361. DOI: 10.1029/2019JD032361.

Morrison, H. et al. (2020). "Confronting the Challenge of Modeling Cloud and Precipitation Microphysics". In: *Journal of Advances in Modeling Earth Systems* 12.8. e2019MS001689 2019MS001689, e2019MS001689. DOI: https://doi.org/10.1029/2019MS001689.

Moseley, C., P. Berg, and J. O. Haerter (Dec. 2013). "Probing the precipitation life cycle by iterative rain cell tracking". In: *Journal of Geophysical Research: Atmospheres* 118.November, n/a–n/a. ISSN: 2169897X. DOI: 10.1002/2013JD020868.

Nice, K. A. et al. (2022). "Isolating the impacts of urban form and fabric from geography on urban heat and human thermal comfort". In: *Building and Environment* 224, p. 109502.

Nie, J. et al. (Sept. 2018). "Dynamic amplification of extreme precipitation sensitivity". In: *Proceedings of the National Academy of Sciences* 115.38, pp. 9467–9472. ISSN: 0027-8424, 1091-6490. DOI: 10.1073/pnas.1800357115.

Noije, T. van et al. (2021). "EC-Earth3-AerChem: a global climate model with interactive aerosols and atmospheric chemistry participating in CMIP6". In: *Geoscientific Model Development* 14.9, pp. 5637–5668. DOI: 10.5194/gmd-14-5637-2021.

Noije, T. P. C. van et al. (2014). "Simulation of tropospheric chemistry and aerosols with the climate model EC-Earth". In: *Geoscientific Model Development* 7.5, pp. 2435–2475. DOI: 10.5194/gmd-7-2435-2014.

Nolan, D. S., E. D. Rappin, and K. A. Emanuel (2007). "Tropical cyclogenesis sensitivity to environmental parameters in radiative?convective equilibrium". In: *Quarterly Journal of the Royal Meteorological Society* 133.629, pp. 2085–2107. ISSN: 1477-870X. DOI: 10.1002/qj.170.

O'Neill, B. C. et al. (2016). "The Scenario Model Intercomparison Project (ScenarioMIP) for CMIP6". In: *Geoscientific Model Development* 9.9, pp. 3461–3482. DOI: 10.5194/gmd-9-3461-2016.

O'Gorman, P. A. (Oct. 2012). "Sensitivity of tropical precipitation extremes to climate change". In: *Nature Geoscience* 5.10, pp. 697–700. ISSN: 1752-0894, 1752-0908. DOI: 10.1038/ngeo1568.

Oke, T. R. (1982). "The energetic basis of the urban heat island". In: *Quarterly Journal of the Royal Meteorological Society* 108.455, pp. 1–24. ISSN: 0035-9009. DOI: https://doi.org/10.1002/qj.49710845502.

Oldenborgh, G. J. van et al. (2009). "Western Europe is warming much faster than expected". In: *Climate of the Past* 5.1, pp. 1–12. DOI: 10.5194/cp-5-1-2009.

Oldenborgh, G. J. van (2019). "De extreme hitte van eind juli 2019". In: *Meteorologica* (3), pp. 28–29.

Oldenborgh, G. J. van et al. (2017). "Attribution of extreme rainfall from Hurricane Harvey, August 2017". In: *Environmental Research Letters* 12.12, p. 124009. ISSN: 1748-9326. DOI: 10.1088/1748-9326/aa9ef2.

Oldenborgh, G. J. van et al. (2019). *Human contribution to the record-breaking June 2019 heat wave in France*.

Otosaka, I. N. et al. (Apr. 2023). "Mass balance of the Greenland and Antarctic ice sheets from 1992 to 2020". English. In: *Earth System Science Data* 15.4. Publisher: Copernicus GmbH, pp. 1597–1616. ISSN: 1866-3508. DOI: 10.5194/essd-15-1597-2023.

Overeem, A. (2014). "Radar bebouwd gebied". In: *Ervaringen met de aanpak van regenwateroverlast in bebouwd gebied.* Ed. by H. Luijtelaar. Vol. 18. RIONEDreeks. Stichting RIONED: Ede, the Netherlands. Chap. 21, 284:305.

Palmer, M. D. et al. (2020). "Exploring the Drivers of Global and Local Sea-Level Change Over the 21st Century and Beyond". en. In: *Earth's Future* 8.9, e2019EF001413.

Patterson, M. (2023). "North-West Europe Hottest Days Are Warming Twice as Fast as Mean Summer Days". In: *Geophysical Research Letters* 50.10. DOI: 10.1029/2023GL102757.

Peltier, W. R., D. F. Argus, and R. Drummond (Jan. 2015). "Space geodesy constrains ice age terminal deglaciation: The global ICE-6G_C (VM5a) model: Global Glacial Isostatic Adjustment". In: *Journal of Geophysical Research: Solid Earth* 120.1, pp. 450–487. ISSN: 21699313. DOI: 10.1002/2014JB011176.

Pfeifroth, U. et al. (2018). "Trends and variability of surface solar radiation in Europe based on surface- and satellite-based data records". In: *Journal of Geophysical Research: Atmospheres* 123, pp. 1735–1754. DOI: 10.1002/2017JD027418.

Pfeifroth, U. et al. (2023). *Surface Radiation Data Set - Heliosat (SARAH) - Edition 3*. DOI: 10.5676/EUM_SAF_CM/SARAH/V003.

Pichelli, E. et al. (June 2021). "The first multi-model ensemble of regional climate simulations at kilometer-scale resolution part 2: historical and future simulations of precipitation". In: *Climate Dynamics* 56.11-12. ISBN: 0123456789 Publisher: Springer Berlin Heidelberg, pp. 3581–3602. ISSN: 0930-7575. DOI: 10.1007/s00382-021-05657-4.

Poujol, B. et al. (2020). "A physically based precipitation separation algorithm for convection-permitting models over complex topography". In: *Quarterly Journal of the Royal Meteorological Society* 146.727, pp. 748–761. ISSN: 1477870X. DOI: 10.1002/qj.3706.

Prein, A. F. et al. (2021). "Sensitivity of organized convective storms to model grid spacing in current and future climates". In: *Philosophical Transactions of the Royal Society A: Mathematical, Physical and Engineering Sciences* 379.2195, p. 20190546. ISSN: 1364503X. DOI: 10.1098/rsta.2019.0546.

Prein, A. F. et al. (Dec. 2017). "Increased rainfall volume from future convective storms in the US". In: *Nature Climate Change* 7.12, pp. 880–884. ISSN: 1758-678X, 1758-6798. DOI: 10.1038/s41558-017-0007-7.

Purr, C., E. Brisson, and B. Ahrens (2019). "Convective shower characteristics simulated with the convection-permitting climate model COSMO-CLM". In: *Atmosphere* 10.12. ISSN: 20734433. DOI: 10.3390/ATMOS10120810.

Rädler, A. T. et al. (Aug. 2019). "Frequency of severe thunderstorms across Europe expected to increase in the 21st century due to rising instability". In: *npj Climate and Atmospheric Science* 2.1, p. 30. ISSN: 2397-3722. DOI: 10.1038/s41612-019-0083-7.

Rahmstorf, S. and D. Coumou (Nov. 2011). "Increase of extreme events in a warming world". In: *Proceedings of the National Academy of Sciences of the United States of America* 108 (44), pp. 17905–17909. ISSN: 00278424. DOI: 10.1073/pnas.1101766108.

Rasmussen, K. L. et al. (July 2020). "Changes in the convective population and thermodynamic environments in convection-permitting regional climate simulations over the United States". In: *Climate Dynamics* 55.1-2, pp. 383–408. ISSN: 0930-7575, 1432-0894. DOI: 10.1007/s00382-017-4000-7.

Raupach, T. H. et al. (Feb. 2021). "The effects of climate change on hailstorms". In: *Nature Reviews Earth & Environment* 2.3, pp. 213–226. ISSN: 2662-138X. DOI: 10.1038/s43017-020-00133-9.

Rauthe, M. et al. (July 2013). "A Central European precipitation climatology – Part I: Generation and validation of a high-resolution gridded daily data set (HYRAS)". In: *Meteorologische Zeitschrift* 22, pp. 235–256. DOI: 10.1127/0941-2948/2013/0436.

Reerink, T. J. et al. (2023). "Retuning the EC-Earth3 CMIP6 version". In: *Geosci. Model. Dev. Discuss., in preparation*.

Reinhart, V. et al. (2022). "High-resolution land use and land cover dataset for regional climate modelling: a plant functional type map for Europe 2015". In: *Earth Syst. Sci. Data* 14.4, pp. 1735–1794. DOI: 10.5194/essd-14-1735-2022.

Riahi, K. et al. (2017). "The Shared Socioeconomic Pathways and their energy, land use, and greenhouse gas emissions implications: An overview". In: *Global environmental change* 42, pp. 153–168.

Ribes, A., S. Qasmi, and N. P. Gillett (2021). "Making climate projections conditional on historical observations". In: *Science Advances* 7.4, eabc0671.

Rignot, E. et al. (Jan. 2019). "Four decades of Antarctic Ice Sheet mass balance from 1979–2017". en. In: *Proceedings of the National Academy of Sciences* 116.4, pp. 1095–1103. ISSN: 0027-8424, 1091-6490. DOI: 10.1073/pnas.1812883116.

Roberts, M. J. et al. (2020). "Projected Future Changes in Tropical Cyclones Using the CMIP6 HighResMIP Multimodel Ensemble". In: *Geophysical Research Letters* 47.14, e2020GL088662. DOI: https://doi.org/10.1029/2020GL088662.

Rodehacke, C. B. et al. (Dec. 2020). "Future sea level contribution from Antarctica inferred from CMIP5 model forcing and its dependence on precipitation ansatz". English. In: *Earth System Dynamics* 11.4. Publisher: Copernicus GmbH, pp. 1153–1194. ISSN: 2190-4979. DOI: 10.5194/esd-11-1153-2020.

Rodriguez-Vera, G. et al. (2019). "Coupled interannual variability of wind and sea surface temperature in the Caribbean Sea and the Gulf of Mexico". In: *Journal of Climate* 32.14, pp. 4263–4280.

Rogelj, J. et al. (2018). "Scenarios towards limiting global mean temperature increase below 1.5 C". In: *Nature Climate Change* 8.4, pp. 325–332.

Rooy, W. C. de et al. (Feb. 2022). "Model development in practice: a comprehensive update to the boundary layer schemes in HARMONIE-AROME cycle 40". In: *Geoscientific Model Development* 15.4, pp. 1513–1543. ISSN: 1991-959X. DOI: 10.5194/gmd-15-1513-2022.

Rotstayn, L. D. (2000). "On the 201ctuning201d of autoconversion parameterizations in climate models". In: *Journal of Geophysical Research: Atmospheres* 105.D12, pp. 15495–15507. DOI: https://doi.org/10.1029/2000JD900129.

Sallée, J.-B. et al. (2013). "Assessment of Southern Ocean water mass circulation and characteristics in CMIP5 models: Historical bias and forcing response". In: *Journal of Geophysical Research: Oceans* 118.4, pp. 1830–1844. DOI: https://doi.org/10.1002/jgrc.20135.

Sanchez-Benitez, A. et al. (2022). "The July 2019 European Heat Wave in a Warmer Climate: Storyline Scenarios with a Coupled Model Using Spectral Nudging". In: *Journal of Climate* 35, pp. 2373–2390. DOI: 10.1175/JCLI-D-21.

Sangelantoni, L. et al. (2023). "Investigating the representation of heatwaves from an ensemble of km-scale regional climate simulations within CORDEX-FPS convection". In: *Climate Dynamics*. ISSN: 0930-7575. DOI: 10.1007/s00382-023-06769-9.

Schär, C. et al. (Mar. 1996a). "Surrogate climate-change scenarios for regional climate models". In: *Geophysical Research Letters* 23.6, pp. 669–672. ISSN: 00948276. DOI: 10.1029/96GL00265.

— (Mar. 1996b). "Surrogate climate-change scenarios for regional climate models". In: *Geophysical Research Letters* 23.6, pp. 669–672. ISSN: 00948276. DOI: 10.1029/96GL00265.

Schär, C. et al. (2016). "Percentile indices for assessing changes in heavy precipitation events". In: *Climatic Change* 137.1, pp. 201–216. ISSN: 0165-0009, 1573-1480. DOI: 10.1007/s10584-016-1669-2.

Schneider, T., P. A. O'Gorman, and X. J. Levine (July 2010). "Water vapor and the dynamics of climate changes". In: *Reviews of Geophysics* 48.3, RG3001. ISSN: 8755-1209. DOI: 10.1029/2009RG000302.

Schwingshackl, C. et al. (2021). "Heat Stress Indicators in CMIP6: Estimating Future Trends and Exceedances of Impact-Relevant Thresholds". In: *Earth's Future* 9.3. e2020EF001885 2020EF001885, e2020EF001885. DOI: https://doi.org/10.1029/2020EF001885. eprint: https://agupubs.onlinelibrary.wiley.com/doi/pdf/10.1029/2020EF001885.

Screen, J. A. et al. (2022). "Net Equatorward Shift of the Jet Streams When the Contribution From Sea-Ice Loss Is Constrained by Observed Eddy Feedback". In: *Geophysical Research Letters* 49.23, e2022GL100523.

Seager, R. et al. (2019). "Strengthening tropical Pacific zonal sea surface temperature gradient consistent with rising greenhouse gases". In: *Nature Climate Change* 9.7, pp. 517–522.

Selten, F. M. et al. (2020). "Future continental summer warming constrained by the present-day seasonal cycle of surface hydrology". In: *Scientific reports* 10.1, p. 4721.

Shepherd, T. G. et al. (2018). "Storylines: an alternative approach to representing uncertainty in physical aspects of climate change". In: *Climatic change* 151, pp. 555–571.

Sherwood, S. C. et al. (2020). "An Assessment of Earth's Climate Sensitivity Using Multiple Lines of Evidence". In: *Reviews of Geophysics* 58.4. e2019RG000678 2019RG000678, e2019RG000678. DOI: https://doi.org/10.1029/2019RG000678.

Simulated Annealing (Nov. 17, 2022). In: *Wikipedia*.

Slangen, A. B. A., M. Haasnoot, and G. Winter (2022). "Rethinking Sea-Level Projections Using Families and Timing Differences". en. In: *Earth's Future* 10.4. _eprint: https://onlinelibrary.wiley.com/doi/pdf/10.1 e2021EF002576. ISSN: 2328-4277. DOI: 10.1029/2021EF002576.

Slangen, A. B. A. et al. (May 2014). "Projecting twenty-first century regional sea-level changes". en. In: *Climatic Change* 124.1-2, pp. 317–332. ISSN: 0165-0009, 1573-1480. DOI: 10.1007/s10584-014-1080-9.

Smith, C. (2021). *Supporting datasets (v0.1.0)*. DOI: 10.5281/zenodo.4539914.

Smith, C. J. et al. (2018). "FAIR v1. 3: a simple emissions-based impulse response and carbon cycle model". In: *Geoscientific Model Development* 11.6, pp. 2273–2297.

Sousa, P. M. et al. (Jan. 2018). "European temperature responses to blocking and ridge regional patterns". In: *Climate Dynamics* 50 (1-2), pp. 457–477. ISSN: 14320894. DOI: 10.1007/s00382-017-3620-2.

Sousa, P. M. et al. (Dec. 2020). "Distinct influences of large-scale circulation and regional feedbacks in two exceptional 2019 European heatwaves". In: *Communications Earth and Environment* 1 (1). ISSN: 26624435. DOI: 10.1038/s43247-020-00048-9.

Steffelbauer, D. B. et al. (June 2022). "Evidence of regional sea-level rise acceleration for the North Sea". In: *Environmental Research Letters* 17.7. Publisher: IOP Publishing, p. 074002. ISSN: 1748-9326. DOI: 10.1088/1748-9326/ac753a.

Sterl, A., C. Severijns, and H. Dijkstra et al. (2008). "When can we expect extremely high surface temperatures?" In: *Geophys. Res. Lett.* 35.L14703. DOI: 10.1029/2008GL034071.

Stevens, B. et al. (2017). "MACv2-SP: a parameterization of anthropogenic aerosol optical properties and an associated Twomey effect for use in CMIP6". In: *Geoscientific Model Development* 10.1, pp. 433–452. DOI: 10.5194/gmd-10-433-2017.

Stewart, I. D. (2011). "A systematic review and scientific critique of methodology in modern urban heat island literature". In: *International Journal of Climatology* 31.2, pp. 200–217. ISSN: 0899-8418. DOI: https://doi.org/10.1002/joc.2141.

Stewart, I. D. et al. (Oct. 1, 2021). "Time Evolution of the Surface Urban Heat Island". In: *Earth's Future* 9.10, e2021EF002178. ISSN: 2328-4277. DOI: https://doi.org/10.1029/2021EF002178.

Stolte, W. et al. (2023). *Zeespiegelmonitor 2022*. Tech. rep.

Storelvmo, T. and I. Tan (July 2015). "The Wegener-Bergeron-Findeisen process – Its discovery and vital importance for weather and climate". In: *Meteorologische Zeitschrift* 24.4, pp. 455–461. DOI: 10.1127/metz/2015/0626.

Suarez-Gutierrez, L. et al. (May 2020). "Dynamical and thermodynamical drivers of variability in European summer heat extremes". In: *Climate Dynamics* 54 (9-10), pp. 4351–4366. ISSN: 14320894. DOI: 10.1007/s00382-020-05233-2.

Sundqvist, H. (1978). "A parameterization scheme for non-convective condensation including prediction of cloud water content". In: *Quarterly Journal of the Royal Meteorological Society* 104.441, pp. 677–690. DOI: https://doi.org/10.1002/qj.49710444110.

Sutton, R. T., B. Dong, and J. M. Gregory (2007). "Land/sea warming ratio in response to climate change: IPCC AR4 model results and comparison with observations". In: *Geophysical Research Letters* 34.2. DOI: https://doi.org/10.1029/2006GL028164.

Tallaksen, L. M. and H. A. Van Lanen (2004). "Hydrological drought: processes and estimation methods for streamflow and groundwater". In.

Tebaldi, C. and R. Knutti (2007). "The use of the multi-model ensemble in probabilistic climate projections". In: *Philosophical transactions of the royal society A: mathematical, physical and engineering sciences* 365.1857, pp. 2053–2075.

Theeuwes, N. E. et al. (2017). "A diagnostic equation for the daily maximum urban heat island effect for cities in northwestern Europe". In: *International Journal of Climatology* 37.1, pp. 443–454. ISSN: 0899-8418. DOI: https://doi.org/10.1002/joc.4717.

Tiedtke, M. (1993). "Representation of Clouds in Large-Scale Models". In: *Monthly Weather Review* 121.11, pp. 3040–3061. DOI: 10.1175/1520-0493(1993)121<3040:ROCILS>2.0.CO;2.

Tokarska, K. B. et al. (2020). "Past warming trend constrains future warming in CMIP6 models". In: *Science advances* 6.12, eaaz9549.

Truchelut, R. E. et al. (2022). "Earlier onset of North Atlantic hurricane season with Warming Oceans". In: *Nature Communications* 13.1. DOI: 10.1038/s41467-022-31821-3.

Valk, C. de (2020). *Standard method for determining a climatological trend*. Tech. rep. TR-389. KNMI, 32pp.

Van Breedam, J., H. Goelzer, and P. Huybrechts (Nov. 2020). "Semi-equilibrated global sea-level change projections for the next 10 000 years". English. In: *Earth System Dynamics* 11.4. Publisher: Copernicus GmbH, pp. 953–976. ISSN: 2190-4979. DOI: 10.5194/esd-11-953-2020.

van de Wal, R. S. W. et al. (2022). "A High-End Estimate of Sea Level Rise for Practitioners". In: *Earth's Future* 10.11, e2022EF002751. ISSN: 2328-4277. DOI: 10.1029/2022EF002751.

Van den Hurk, B. et al. (2007). "New climate change scenarios for the Netherlands". In: *Water science and technology* 56.4, pp. 27–33.

van der Linden, E. C. et al. (Jan. 2023). "Antarctic contribution to future sea level from ice shelf basal melt as constrained by ice discharge observations". English. In: *The Cryosphere* 17.1. Publisher: Copernicus GmbH, pp. 79–103. ISSN: 1994-0416. DOI: 10.5194/tc-17-79-2023.

Van Loon, A. F. (2015). "Hydrological drought explained". In: *Wiley Interdisciplinary Reviews: Water* 2.4, pp. 359–392.

Van Meerbeeck, C. (2020). *Climate Trends and Projections for the OECS Region*. URL: https://www.oecs.org/en/our-work/knowledge/library/climate-change/climate-trends-and-projections-for-the-oecs-region (visited on 10/08/2022).

Van Nieuwenhuyse, J. et al. (2023). "Air-stagnation episodes based on regional climate models part I: evaluation over Europe". In: *Clim. Dyn.*, pp. 1432–0894. DOI: 10.1007/s00382-023-06665-2.

Van Oostenbrugge, R. et al. (2015). "Aanpassen aan klimaatverandering – Kwetsbaarheden zien, kansen grijpen". In: *PBL* 1454. DOI: ISBN:978-94-91506-90-1.

Vautard, R. et al. (2010). "Northern Hemisphere atmospheric stilling partly attributed to an increase in surface roughness". In: *Nat. Geosci.* 3, pp. 756–61.

Vautard, R. et al. (2018). "Attribution of Wintertime Anticyclonic Stagnation Contributing to Air Pollution in Western Europe". In: *Bulletin of the American Meteorological Society* 99.1, S70–S75. DOI: https://doi.org/10.1175/BAMS-D-17-0113.1.

Vautard, R. et al. (Sept. 2020). "Human contribution to the record-breaking June and July 2019 heatwaves in Western Europe". In: *Environmental Research Letters* 15 (9). ISSN: 17489326. DOI: 10.1088/1748-9326/aba3d4.

Vecchi, G. A. and B. J. Soden (2007). "Increased tropical Atlantic wind shear in model projections of global warming: ATLANTIC WIND SHEAR AND GLOBAL WARMING". In: *Geophysical Research Letters* 34.8. ISSN: 00948276. DOI: 10.1029/2006GL028905.

Vermeersen, B. L. et al. (Sept. 2018). "Sea-level change in the Dutch Wadden Sea". en. In: *Netherlands Journal of Geosciences* 97.3, pp. 79–127. ISSN: 0016-7746, 1573-9708. DOI: 10.1017/njg.2018.7.

Verseveld, W. J. van et al. (2022). "Wflow$_s$*bmv*0.6.1, *aspatiallydistributedhydrologicmodel* : *fromglobaldatatolocalapplications*". In: *Geoscientific Model Development Discussions* 2022, pp. 1–52. DOI: 10.5194/gmd-2022-182.

Vicente-Serrano, S. M., S. Begueria, and J. I. López-Moreno (2010). "A multiscalar drought index sensitive to global warming: the standardized precipitation evapotranspiration index". In: *Journal of climate* 23.7, pp. 1696–1718.

Vries, H. de et al. (2022). "Quantifying the role of the large-scale circulation on European summer precipitation change". In: *Climate Dynamics*. ISSN: 0930-7575, 1432-0894. DOI: 10.1007/s00382-022-06250-z.

Vries, I. de and H. de Vries (2022). "Waarom langjarige hitterecords soms verpletterd worden". In: *Meteorologica* (3), pp. 8–11.

Walker, J. S. et al. (Feb. 2022). "Timing of emergence of modern rates of sea-level rise by 1863". In: *Nature Communications* 13.1. Publisher: Nature Publishing Group, p. 966. ISSN: 2041-1723. DOI: 10.1038/s41467-022-28564-6.

Wang, B. and H. Murakami (2020). "Dynamic genesis potential index for diagnosing present-day and future global tropical cyclone genesis". In: *Environmental Research Letters* 15.11, p. 114008. ISSN: 1748-9326. DOI: 10.1088/1748-9326/abbb01.

WCRP (2017). *The World Climate Research Programme (WCRP) Grand Challenge on Clouds, Circulation and Climate Sensitivity*. available at: https://wcrp-climate.org/component/content/article/61-gc-clouds-circulation. last access: 1 May 2023.

— (Aug. 2018). "Global sea-level budget 1993–present". In: *Earth System Science Data* 10.3, pp. 1551–1590. ISSN: 1866-3508. DOI: https://doi.org/10.5194/essd-10-1551-2018.

Wever, N. (2012). "Quantifying trends in surface roughness and the effect on surface wind speed observations". In: *J. Geophys. Res.* 117 (D11). DOI: 10.1029/2011JD017118.

Whan, K. et al. (2021). "Novel multivariate quantile mapping methods for ensemble post-processing of medium-range forecasts". In: *Weather and climate extremes* 32, p. 100310.

Wiel, K. van der and R. Bintanja (2021). "Contribution of climatic changes in mean and variability to monthly temperature and precipitation extremes". In: *Communications Earth & Environment*, pp. 1–11. ISSN: 2662-4435. DOI: 10.1038/s43247-020-00077-4.

Wild, M. et al. (2021). "Evidence for clear-sky dimming and brightening in central Europe". In: *Geophysical Research Letters* 48, e2020GL092216. DOI: 10.1029/2020GL092216.

Wills, R. C. et al. (2022). "Systematic Climate Model Biases in the Large-Scale Patterns of Recent Sea-Surface Temperature and Sea-Level Pressure Change". In: *Geophysical Research Letters* 49.17, e2022GL100011.

WMO (2022). *State of the Global Climate 2021*. URL: https://library.wmo.int/doc_num.php?explnum_id=11178 (visited on 08/22/2022).

Woodworth, P. L. (Mar. 2012). "A Note on the Nodal Tide in Sea Level Records". In: *Journal of Coastal Research* 28.2. Publisher: Coastal Education and Research Foundation, pp. 316–323. ISSN: 0749-0208, 1551-5036. DOI: 10.2112/JCOASTRES-D-11A-00023.1.

Wouters, H. et al. (2017). "Heat stress increase under climate change twice as large in cities as in rural areas: A study for a densely populated midlatitude maritime region". In: *Geophysical Research Letters* 44.17, pp. 8997–9007. DOI: https://doi.org/10.1002/2017GL074889. eprint: https://agupubs.onlinelibrary.wiley.com/doi/pdf/10.1002/2017GL074889.

Wyser, K. et al. (2020). "On the increased climate sensitivity in the EC-Earth model from CMIP5 to CMIP6". In: *Geoscientific Model Development* 13.8, pp. 3465–3474. DOI: 10.5194/gmd-13-3465-2020.

Yin, J. et al. (2022). "Representation of the autoconversion from cloud to rain using a weighted ensemble approach: a case study using WRF v4.1.3". In: *Geoscientific Model Development* 15.2, pp. 771–786. DOI: 10.5194/gmd-15-771-2022.

Appendix A

Availability of KNMI'23 ensemble data

The data request for the KNMI'23 ensemble

A uniform data request has been used for the historical and all SSP experiments for the time interval 1949-2167. For the historical 1850-1948 interval the 3D variables on 23 pressure levels (and a few others) are omitted, which heavily reduces the output volume. The same applies for the r1 members which have been continued from 2168-2301. A compact request, which improves the EC-Earth3 CPU performance (and keeps cmorisation limited to a small amount of data) generates a very small output volume as discussed in Sect. 2.3.2, this request has been used for the piControl and the spin-up experiments.

Listing A.1 shows the KNMI'23 data request for all experiments between 1949-2167, and which are delivered after cmorisation. The variable names, long_names, dimensions and units are all according to the CMOR3 conventions (2023) & CMIP6 CMOR Tables (2023).

Listing A.1: Overview KNMI'23 data request

table	variable	dimensions	unit	long_name	code name
SIday	siconc	lon lat time typesi	%	Sea-Ice Area Percentage (Ocean Grid)	nemo: siconc
SIday	siconca	lon lat time typesi	%	Sea-Ice Area Percentage (Atmospheric Grid)	ifs: 31.129
Amon	cl	lon lat alevel time	%	Percentage Cloud Cover	ifs: 248.128
Amon	cli	lon lat alevel time	kg kg-1	Mass Fraction of Cloud Ice	ifs: 247.128
Amon	clivi	lon lat time	kg m-2	Ice Water Path	ifs: 79.128
Amon	clt	lon lat time	%	Total Cloud Cover Percentage	ifs: 164.128
Amon	clw	lon lat alevel time	kg kg-1	Mass Fraction of Cloud Liquid Water	ifs: 246.128
Amon	clwvi	lon lat time	kg m-2	Condensed Water Path	ifs: 116.129
Amon	evspsbl	lon lat time	kg m-2 s-1	Evaporation Including Sublimation and Transpiration	ifs: 182.128
Amon	hfls	lon lat time	W m-2	Surface Upward Latent Heat Flux	ifs: 147.128
Amon	hfss	lon lat time	W m-2	Surface Upward Sensible Heat Flux	ifs: 146.128
Amon	hur	lon lat plev19 time	%	Relative Humidity	ifs: 157.128
Amon	hurs	lon lat time height2m	%	Near-Surface Relative Humidity	ifs: 80.129
Amon	hus	lon lat plev19 time	1	Specific Humidity	ifs: 133.128
Amon	huss	lon lat time height2m	1	Near-Surface Specific Humidity	ifs: 81.129
Amon	pfull	lon lat alevel time2	Pa	Pressure at Model Full-Levels	ifs: 54.128
Amon	pr	lon lat time	kg m-2 s-1	Precipitation	ifs: 228.128
Amon	prc	lon lat time	kg m-2 s-1	Convective Precipitation	ifs: 143.128
Amon	prsn	lon lat time	kg m-2 s-1	Snowfall Flux	ifs: 144.128
Amon	prw	lon lat time	kg m-2	Water Vapor Path	ifs: 137.128
Amon	ps	lon lat time	Pa	Surface Air Pressure	tm5: ps|ifs: 134.128
Amon	psl	lon lat time	Pa	Sea Level Pressure	ifs: 151.128
Amon	rlds	lon lat time	W m-2	Surface Downwelling Longwave Radiation	ifs: 175.128
Amon	rldscs	lon lat time	W m-2	Surface Downwelling Clear-Sky Longwave Radiation	ifs: 104.129
Amon	rlus	lon lat time	W m-2	Surface Upwelling Longwave Radiation	ifs: 96.129
Amon	rlut	lon lat time	W m-2	TOA Outgoing Longwave Radiation	ifs: 179.128
Amon	rlutcs	lon lat time	W m-2	TOA Outgoing Clear-Sky Longwave Radiation	ifs: 209.128
Amon	rsds	lon lat time	W m-2	Surface Downwelling Shortwave Radiation	ifs: 169.128
Amon	rsdscs	lon lat time	W m-2	Surface Downwelling Clear-Sky Shortwave Radiation	ifs: 132.129
Amon	rsdt	lon lat time	W m-2	TOA Incident Shortwave Radiation	ifs: 212.128
Amon	rsus	lon lat time	W m-2	Surface Upwelling Shortwave Radiation	ifs: 95.129
Amon	rsuscs	lon lat time	W m-2	Surface Upwelling Clear-Sky Shortwave Radiation	ifs: 131.129
Amon	rsut	lon lat time	W m-2	TOA Outgoing Shortwave Radiation	ifs: 97.129
Amon	rsutcs	lon lat time	W m-2	TOA Outgoing Clear-Sky Shortwave Radiation	ifs: 103.129
Amon	rtmt	lon lat time	W m-2	Net Downward Radiative Flux at Top of Model	ifs: 98.129
Amon	sbl	lon lat time	kg m-2 s-1	Surface Snow and Ice Sublimation Flux	ifs: 44.128
Amon	sfcWind	lon lat time height10m	m s-1	Near-Surface Wind Speed	ifs: 214.129
Amon	ta	lon lat plev19 time	K	Air Temperature	ifs: 130.128
Amon	tas	lon lat time height2m	K	Near-Surface Air Temperature	ifs: 167.128
Amon	tasmax	lon lat time height2m	K	Daily Maximum Near-Surface Air Temperature	ifs: 201.128
Amon	tasmin	lon lat time height2m	K	Daily Minimum Near-Surface Air Temperature	ifs: 202.128
Amon	tauu	lon lat time	Pa	Surface Downward Eastward Wind Stress	ifs: 180.128
Amon	tauv	lon lat time	Pa	Surface Downward Northward Wind Stress	ifs: 181.128

```
     Amon      ts              lon lat time             K          Surface Temperature                                        ifs: 139.128
     Amon      ua              lon lat plev19 time      m s-1      Eastward Wind                                              ifs: 131.128
8810 Amon      uas             lon lat time height10m   m s-1      Eastward Near-Surface Wind                                 ifs: 165.128
     Amon      va              lon lat plev19 time      m s-1      Northward Wind                                             ifs: 132.128
     Amon      vas             lon lat time height10m   m s-1      Northward Near-Surface Wind                                ifs: 166.128
     Amon      wap             lon lat plev19 time      Pa s-1     Omega (=dp/dt)                                             ifs: 135.128
     Amon      zg              lon lat plev19 time      m          Geopotential Height                                        ifs: 129.128
8815
     6hrLev    ps              lon lat time1            Pa         Surface Air Pressure                                       tm5: ps|ifs: 134.128

     fx        areacella       lon lat                  m2         Grid-Cell Area for Atmospheric Grid Variables              ifs: 129.128
     fx        orog            lon lat                  m          Surface Altitude                                           ifs: 129.128
8820 fx        sftlf           lon lat                  %          Percentage of the Grid Cell Occupied by Land (+ Lakes)     ifs: 172.128

     Omon      evs             lon lat time             kg m-2 s-1 Water Evaporation Flux Where Ice Free Ocean over Sea       nemo: evs
     Omon      friver          lon lat time             kg m-2 s-1 Water Flux into Sea Water from Rivers                      nemo: friver
     Omon      fsitherm        lon lat time             kg m-2 s-1 Water Flux into Sea Water Due to Sea Ice Thermodynamics    nemo: fsitherm
8825 Omon      hfbasin         lat basin time           W          Northward Ocean Heat Transport                             nemo: hfbasin
     Omon      hfds            lon lat time             W m-2      Downward Heat Flux at Sea Water Surface                    nemo: hfds
     Omon      hfevapds        lon lat time             W m-2      Temperature Flux Due to Evaporation Expressed as           nemo: hfevapds
                                                                   Heat Flux out of Sea Water
     Omon      hfgeou          lon lat time             W m-2      Upward Geothermal Heat Flux at Sea Floor                   nemo: hfgeou
8830 Omon      hfrainds        lon lat time             W m-2      Temperature Flux Due to Rainfall Expressed as              nemo: hfrainds
                                                                   Heat Flux into Sea Water
     Omon      htovgyre        lat basin time           W          Northward Ocean Heat Transport Due to Gyre                 nemo: htovgyre
     Omon      htovovrt        lat basin time           W          Northward Ocean Heat Transport Due to Overturning          nemo: htovovrt
     Omon      masscello       lon lat olevel time      kg m-2     Ocean Grid-Cell Mass per Area                              nemo: masscello
8835 Omon      masso           time                     kg         Sea Water Mass                                             nemo: masso
     Omon      mlotst          lon lat time             m          Ocean Mixed Layer Thickness Defined by Sigma T             nemo: mlotst
     Omon      msftbarot       lon lat time             kg s-1     Ocean Barotropic Mass Streamfunction                       nemo: msftbarot
     Omon      msftyz          gridlat olevel basin time kg s-1    Ocean Y Overturning Mass Streamfunction                    nemo: msftyz
     Omon      pbo             lon lat time             Pa         Sea Water Pressure at Sea Floor                            nemo: pbo
8840 Omon      prsn            lon lat time             kg m-2 s-1 Snowfall Flux where Ice Free Ocean over Sea                ifs: 144.128
     Omon      pso             lon lat time             Pa         Sea Water Pressure at Sea Water Surface                    nemo: pso
     Omon      rsntds          lon lat time             W m-2      Net Downward Shortwave Radiation at Sea Water Surface      nemo: rsntds
     Omon      sfdsi           lon lat time             kg m-2 s-1 Downward Sea Ice Basal Salt Flux                           nemo: sfdsi
     Omon      sltovgyre       lat basin time           kg s-1     Northward Ocean Salt Transport Due to Gyre                 nemo: sltovgyre
8845 Omon      sltovovrt       lat basin time           kg s-1     Northward Ocean Salt Transport Due to Overturning          nemo: sltovovrt
     Omon      so              lon lat olevel time      0.001      Sea Water Salinity                                         nemo: so
     Omon      soga            time                     0.001      Global Mean Sea Water Salinity                             nemo: soga
     Omon      sos             lon lat time             0.001      Sea Surface Salinity                                       nemo: sos
     Omon      talknat         lon lat olevel time      mol m-3    Natural Total Alkalinity                                   nemo: talknat
8850 Omon      thetao          lon lat olevel time      degC       Sea Water Potential Temperature                            nemo: thetao
     Omon      thetaoga        time                     degC       Global Average Sea Water Potential Temperature             nemo: thetaoga
     Omon      thkcello        lon lat olevel time      m          Ocean Model Cell Thickness                                 nemo: thkcello
     Omon      tos             lon lat time             degC       Sea Surface Temperature                                    nemo: tos
     Omon      tossq           lon lat time             degC2      Square of Sea Surface Temperature                          nemo: tossq
8855 Omon      umo             lon lat olevel time      kg s-1     Ocean Mass X Transport                                     nemo: umo
     Omon      uo              lon lat olevel time      m s-1      Sea Water X Velocity                                       nemo: uo
     Omon      vmo             lon lat olevel time      kg s-1     Ocean Mass Y Transport                                     nemo: vmo
     Omon      vo              lon lat olevel time      m s-1      Sea Water Y Velocity                                       nemo: vo
     Omon      volo            time                     m3         Sea Water Volume                                           nemo: volo
8860 Omon      wfo             lon lat time             kg m-2 s-1 Water Flux into Sea Water                                  nemo: wfo
     Omon      wfonocorr       lon lat time             kg m-2 s-1 Water Flux into Sea Water Without Flux Correction          nemo: wfonocorr
     Omon      wmo             lon lat olevel time      kg s-1     Upward Ocean Mass Transport                                nemo: wmo
     Omon      zhalfo          lon lat olevhalf time    m          Depth Below Geoid of Interfaces Between Ocean Layers       nemo: zhalfo
     Omon      zos             lon lat time             m          Sea Surface Height Above Geoid                             nemo: zos
8865 Omon      zossq           lon lat time             m2         Square of Sea Surface Height Above Geoid                   nemo: zossq
     Omon      zostoga         time                     m          Global Average Thermosteric Sea Level Change               nemo: zostoga

     Oyr       dissicnat       lon lat olevel time      mol m-3    Natural Dissolved Inorganic Carbon Concentration           nemo: dissicnat

8870 6hrPlev   siconca         lon lat time typesi      %          Sea-Ice Area Percentage (Atmospheric Grid)                 ifs:  31.129

     day       clt             lon lat time             %          Total Cloud Cover Percentage                               ifs: 164.128
     day       hfls            lon lat time             W m-2      Surface Upward Latent Heat Flux                            ifs: 147.128
     day       hfss            lon lat time             W m-2      Surface Upward Sensible Heat Flux                          ifs: 146.128
8875 day       hurs            lon lat time height2m    %          Near-Surface Relative Humidity                             ifs:  80.129
     day       hursmax         lon lat time height2m    %          Daily Maximum Near-Surface Relative Humidity               ifs:  80.129
     day       hursmin         lon lat time height2m    %          Daily Minimum Near-Surface Relative Humidity               ifs:  80.129
     day       hus             lon lat plev8 time       1          Specific Humidity                                          ifs: 133.128
     day       huss            lon lat time height2m    1          Near-Surface Specific Humidity                             ifs:  81.129
8880 day       mrso            lon lat time             kg m-2     Total Soil Moisture Content                                lpjg: mrso|ifs:  43.129
     day       pr              lon lat time             kg m-2 s-1 Precipitation                                              ifs: 228.128
     day       prc             lon lat time             kg m-2 s-1 Convective Precipitation                                   ifs: 143.128
     day       prsn            lon lat time             kg m-2 s-1 Snowfall Flux                                              ifs: 144.128
     day       psl             lon lat time             Pa         Sea Level Pressure                                         ifs: 151.128
8885 day       rlds            lon lat time             W m-2      Surface Downwelling Longwave Radiation                     ifs: 175.128
     day       rlus            lon lat time             W m-2      Surface Upwelling Longwave Radiation                       ifs:  96.129
     day       rlut            lon lat time             W m-2      TOA Outgoing Longwave Radiation                            ifs: 179.128
     day       rsds            lon lat time             W m-2      Surface Downwelling Shortwave Radiation                    ifs: 169.128
     day       sfcWind         lon lat time height10m   m s-1      Daily-Mean Near-Surface Wind Speed                         ifs: 214.129
8890 day       sfcWindmax      lon lat time height10m   m s-1      Daily Maximum Near-Surface Wind Speed                      ifs: 214.129
     day       snc             lon lat time             %          Snow Area Percentage                                       ifs: 119.129
     day       snw             lon lat time             kg m-2     Surface Snow Amount                                        ifs: 141.128
     day       ta              lon lat plev8 time       K          Air Temperature                                            ifs: 130.128
     day       tas             lon lat time height2m    K          Near-Surface Air Temperature                               ifs: 167.128
8895 day       tasmax          lon lat time height2m    K          Daily Maximum Near-Surface Air Temperature                 ifs: 201.128
     day       tasmin          lon lat time height2m    K          Daily Minimum Near-Surface Air Temperature                 ifs: 202.128
     day       tslsi           lon lat time             K          Surface Temperature Where Land or Sea Ice                  ifs: 235.128
     day       ua              lon lat plev8 time       m s-1      Eastward Wind                                              ifs: 131.128
     day       uas             lon lat time height10m   m s-1      Eastward Near-Surface Wind                                 ifs: 165.128
8900 day       va              lon lat plev8 time       m s-1      Northward Wind                                             ifs: 132.128
     day       vas             lon lat time height10m   m s-1      Northward Near-Surface Wind                                ifs: 166.128
     day       zg              lon lat plev8 time       m          Geopotential Height                                        ifs: 129.128

     Emon      mrsol           lon lat sdepth time      kg m-2     Total Water Content of Soil Layer                          lpjg: mrsol|ifs: 118.129
8905
     Oday      tos             lon lat time             degC       Sea Surface Temperature                                    nemo: tos

     SImon     siage           lon lat time             s          Age of Sea Ice                                             nemo: siage
     SImon     sicompstren     lon lat time             N m-1      Compressive Sea Ice Strength                               nemo: sicompstren
8910 SImon     siconc          lon lat time typesi      %          Sea-Ice Area Percentage (Ocean Grid)                       nemo: siconc
     SImon     siconca         lon lat time typesi      %          Sea-Ice Area Percentage (Atmospheric Grid)                 ifs:  31.129
     SImon     sidivvel        lon lat time1            s-1        Divergence of the Sea-Ice Velocity Field                   nemo: sidivvel
     SImon     sidmassevapsubl lon lat time             kg m-2 s-1 Sea-Ice Mass Change Through Evaporation and Sublimation    nemo: sidmassevapsubl
     SImon     sidmassgrowthbot lon lat time            kg m-2 s-1 Sea-Ice Mass Change Through Basal Growth                   nemo: sidmassgrowthbot
```

```
SImon     sidmassgrowthwat lon lat time            kg m-2 s-1 Sea-Ice Mass Change Through Growth in                 nemo: sidmassgrowthwat
                                                                Supercooled Open Water (Frazil)
SImon     sidmassmeltbot   lon lat time            kg m-2 s-1 Sea-Ice Mass Change Through Bottom Melting            nemo: sidmassmeltbot
SImon     sidmassmelttop   lon lat time            kg m-2 s-1 Sea-Ice Mass Change Through Surface Melting           nemo: sidmassmelttop
SImon     sidmasssi        lon lat time            kg m-2 s-1 Sea-Ice Mass Change Through Snow-to-Ice Conversion    nemo: sidmasssi
SImon     sidmasstranx     lon lat time            kg s-1     X-Component of Sea-Ice Mass Transport                 nemo: sidmasstranx
SImon     sidmasstrany     lon lat time            kg s-1     Y-Component of Sea-Ice Mass Transport                 nemo: sidmasstrany
SImon     siflswdtop       lon lat time            W m-2      Downwelling Shortwave Flux over Sea Ice               nemo: siflswdtop
SImon     sihc             lon lat time            J m-2      Sea-Ice Heat Content per Unit Area                    nemo: sihc
SImon     simass           lon lat time            kg m-2     Sea-Ice Mass per Area                                 nemo: simass
SImon     sisali           lon lat time            0.001      Sea Ice Salinity                                      nemo: sisali
SImon     sisnmass         lon lat time            kg m-2     Snow Mass per Area                                    nemo: sisnmass
SImon     sisnthick        lon lat time            m          Snow Thickness                                        nemo: sisnthick
SImon     sistrxdtop       lon lat time            N m-2      X-Component of Atmospheric Stress on Sea Ice          nemo: sistrxdtop
SImon     sistrydtop       lon lat time            N m-2      Y-Component of Atmospheric Stress on Sea Ice          nemo: sistrydtop
SImon     sitempsnic       lon lat time            K          Temperature at Snow-Ice Interface                     nemo: sitempsnic
SImon     sitemptop        lon lat time            K          Surface Temperature of Sea Ice                        nemo: sitemptop
SImon     sithick          lon lat time            m          Sea Ice Thickness                                     nemo: sithick
SImon     siu              lon lat time            m s-1      X-Component of Sea-Ice Velocity                       nemo: siu
SImon     siv              lon lat time            m s-1      Y-Component of Sea-Ice Velocity                       nemo: siv
SImon     sivol            lon lat time            m          Sea-Ice Volume per Area                               nemo: sivol
SImon     sndmassmelt      lon lat time            kg m-2 s-1 Snow Mass Rate of Change Through Melt                 nemo: sndmassmelt
SImon     sndmasssnf       lon lat time            kg m-2 s-1 Snow Mass Change Through Snow Fall                    nemo: sndmasssnf

Lmon      mrfso            lon lat time            kg m-2     Soil Frozen Water Content                             ifs:  85.129
Lmon      mrro             lon lat time            kg m-2 s-1 Total Runoff                                          lpjg: mrro|ifs: 205.128
Lmon      mrros            lon lat time            kg m-2 s-1 Surface Runoff                                        lpjg: mrros|ifs: 8.128
Lmon      mrso             lon lat time            kg m-2     Total Soil Moisture Content                           lpjg: mrso|ifs:  43.129
Lmon      mrsos            lon lat time sdepth1     kg m-2     Moisture in Upper Portion of Soil Column              lpjg: mrsos|ifs:  99.129
Lmon      tsl              lon lat sdepth time      K          Temperature of Soil                                   lpjg: tsl|ifs: 117.129

LImon     hfdsn            lon lat time            W m-2      Downward Heat Flux into Snow Where Land over Land     ifs: 120.129
LImon     lwsnl            lon lat time            kg m-2     Liquid Water Content of Snow Layer                    ifs: 141.128
LImon     sbl              lon lat time            kg m-2 s-1 Surface Snow and Ice Sublimation Flux                 ifs:  44.128
LImon     snc              lon lat time            %          Snow Area Percentage                                  ifs: 119.129
LImon     snd              lon lat time            m          Snow Depth                                            ifs: 115.129
LImon     snm              lon lat time            kg m-2 s-1 Surface Snow Melt                                     ifs:  45.128
LImon     snw              lon lat time            kg m-2     Surface Snow Amount                                   ifs: 141.128
LImon     tsn              lon lat time            K          Snow Internal Temperature                             ifs: 238.128

Oclim     difvho           lon lat olevel time2    m2 s-1     Ocean Vertical Heat Diffusivity                       nemo: difvho
Oclim     difvmo           lon lat olevel time2    m2 s-1     Ocean Vertical Momentum Diffusivity                   nemo: difvmo
Oclim     difvso           lon lat olevel time2    m2 s-1     Ocean Vertical Salt Diffusivity                       nemo: difvso

Ofx       areacello        lon lat                 m2         Grid-Cell Area for Ocean Variables                    nemo: areacello
Ofx       basin            lon lat                 1          Region Selection Index                                nemo: basin
Ofx       deptho           lon lat                 m          Sea Floor Depth Below Geoid                           nemo: Bathymetry
Ofx       hfgeou           lon lat                 W m-2      Upward Geothermal Heat Flux at Sea Floor              nemo: hfgeou
Ofx       sftof            lon lat                 %          Sea Area Percentage                                   nemo: sftof

6hrPlevPt hus23r           lon lat plev23r time1   1          Specific Humidity                                     ifs: 133.128
6hrPlevPt mrsol            lon lat sdepth time1    kg m-2     Total Water Content of Soil Layer                     lpjg: mrsol|ifs: 118.129
6hrPlevPt ta23r            lon lat plev23r time1   K          Air Temperature                                       ifs: 130.128
6hrPlevPt tosa             lon lat time1           degC       Sea Surface Temperature                               ifs:  34.128
6hrPlevPt tsl4sl           lon lat sdepth time1    K          Temperature of Soil                                   ifs: 215.129
6hrPlevPt ua23r            lon lat plev23r time1   m s-1      Eastward Wind                                         ifs: 131.128
6hrPlevPt va23r            lon lat plev23r time1   m s-1      Northward Wind                                        ifs: 132.128

Eday      mrros            lon lat time            kg m-2 s-1 Surface Runoff                                        lpjg: mrros|ifs: 8.128
```

The specific *table - variable* combinations that have been created in line with the CMOR framework for the RCM downscaling, and which include the four variables on 23 pressure levels, are summarized in Listing A.2.

Listing A.2: Essential added variables for the downscaling in the json dat request file

```
{
    "ifs": {
        "6hrLev": [
            "ps"
        ],
        "6hrPlev": [
            "siconca"
        ],
        "6hrPlevPt": [
            "ta23r",
            "va23r",
            "ua23r",
            "hus23r",
            "tosa",
            "tsl4sl",
            "mrsol"
        ]
    },
}
```

The archived KNMI'23 ensemble data

The 800 TB of global data which has been produced with the retuned EC-Earth3$_{p5}$ version, consists of 16 historical, SSP1-2.6, SSP2-4.5, SSP3-7.0 & SSP5-8.5 and 6 SSP1-1.9 members, and thus include the large volume 23 pressure level data for RCM downscaling.

The EC-Earth3 KNMI'23 data at SURF archive (tape storage with backup) is available at:

```
/archive/climate/dutch-climate-scenarios/ec-earth-3/cmorised-results/dutch-climate
-scenarios/CMIP6/
```

the data here is entirely conform the CMOR directory structure archived.

Note that via:

```
/archive/climate/dutch-climate-scenarios/
```

all KNMI'23 data (EC-Earth3 & RACMO) can be found.

The 13 TB data set requested by the resampling group has been synced on a disk connected to the SURF VM: The KNMI'23 historical, SSP126, SSP245 & SSP585 data, are available via the VM connected disk:

```
~/shared_data/volume_3/Common/ecearth3bis/dcs-bwi/CMIP6
```

following entirely the CMOR directory structure.

The 804 TB cmorised EC-Earth3 data on the KNMI HPC are located at the two additional NFS disks: /scratch (0.5 PB) & /scratch2 (1.1 PB):

```
/scratch/projects/dutch_scen/reerink/cmorised-results/dutch-scenarios/
/scratch2/projects/dutch_scen/reerink/cmorised-results/dutch-scenarios/
```

Included in the 804 TB cmorised EC-Earth3 data is the large volume 23 pressure level data which contains the forcing boundaries for the dynamical downscaling with RACMO.

We plan to publish from the KNMI'23 ensemble a subset of monthly climatological relevant variables on the ESGF node. A way to select the entire published KNMI'23 dataset on the ESGF node (2023) would be to ask for: *Source ID*: EC-Earth3 & *Variant Label*: r*i1p5f1.

Appendix B

Retuning EC-Earth: comparing historical simulations

This appendix contains a list of figures on the following pages that show the effect of the retuning on the historical climate simulation (in addition to Sect. 2.3.4).

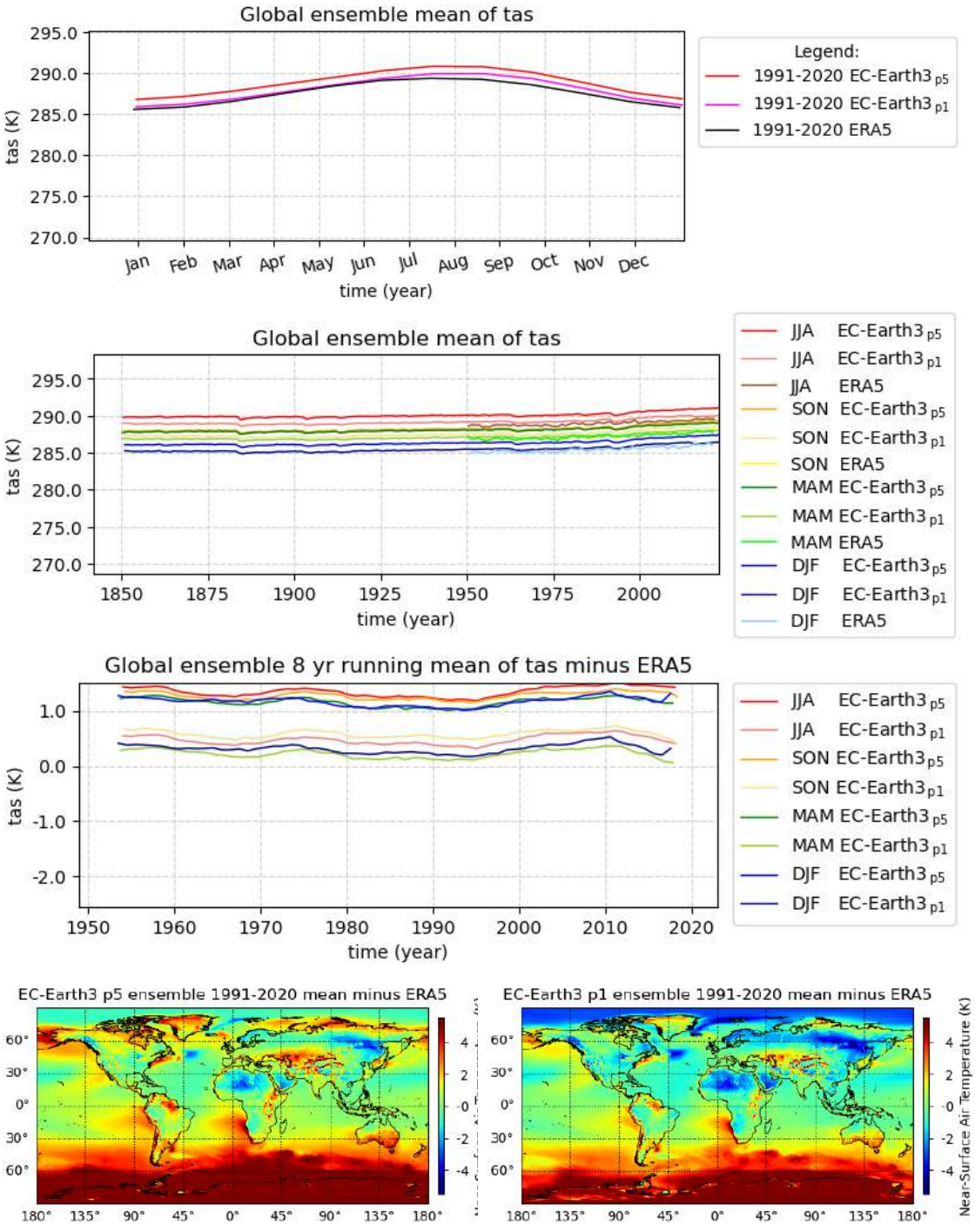

Figure B.1: Near-Surface Air Temperature (**tas**) for **Global**. The ensemble mean for the **1991-2020** climatology, the season record relative to ERA5, the season record and the 1991-2020 mean for p5 & p1. Observations: Both p1 & p5 are substantial too warm (about 0.45° and 1.25° respectively). All seasons are warmer with p5 and thus further away from ERA5.The NH has improved with p5, while as expected, the SH deteriorates (even warmer) for p5. Tuning aim confirmed.

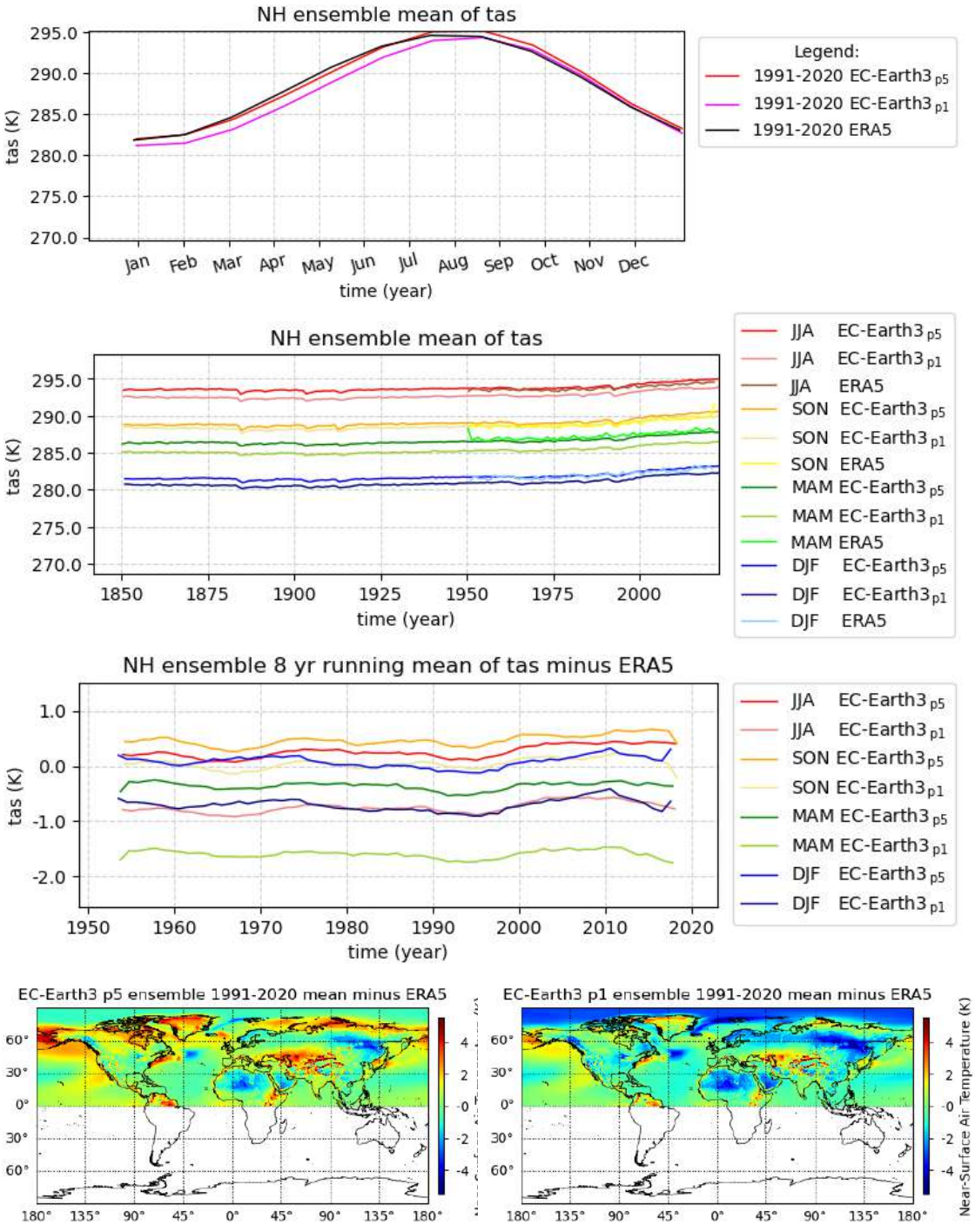

Figure B.2: Near-Surface Air Temperature (**tas**) for **NH**. The ensemble mean for the **1991-2020** climatology, the season record relative to ERA5, the season record and the 1991-2020 mean for p5 & p1. Observations: MAM, JJA & DJF warmer and closer to ERA5 with p5. SON bit overcorrected.The NH has improved with p5, while as expected, the SH deteriorates (even warmer) for p5. Tuning aim confirmed.

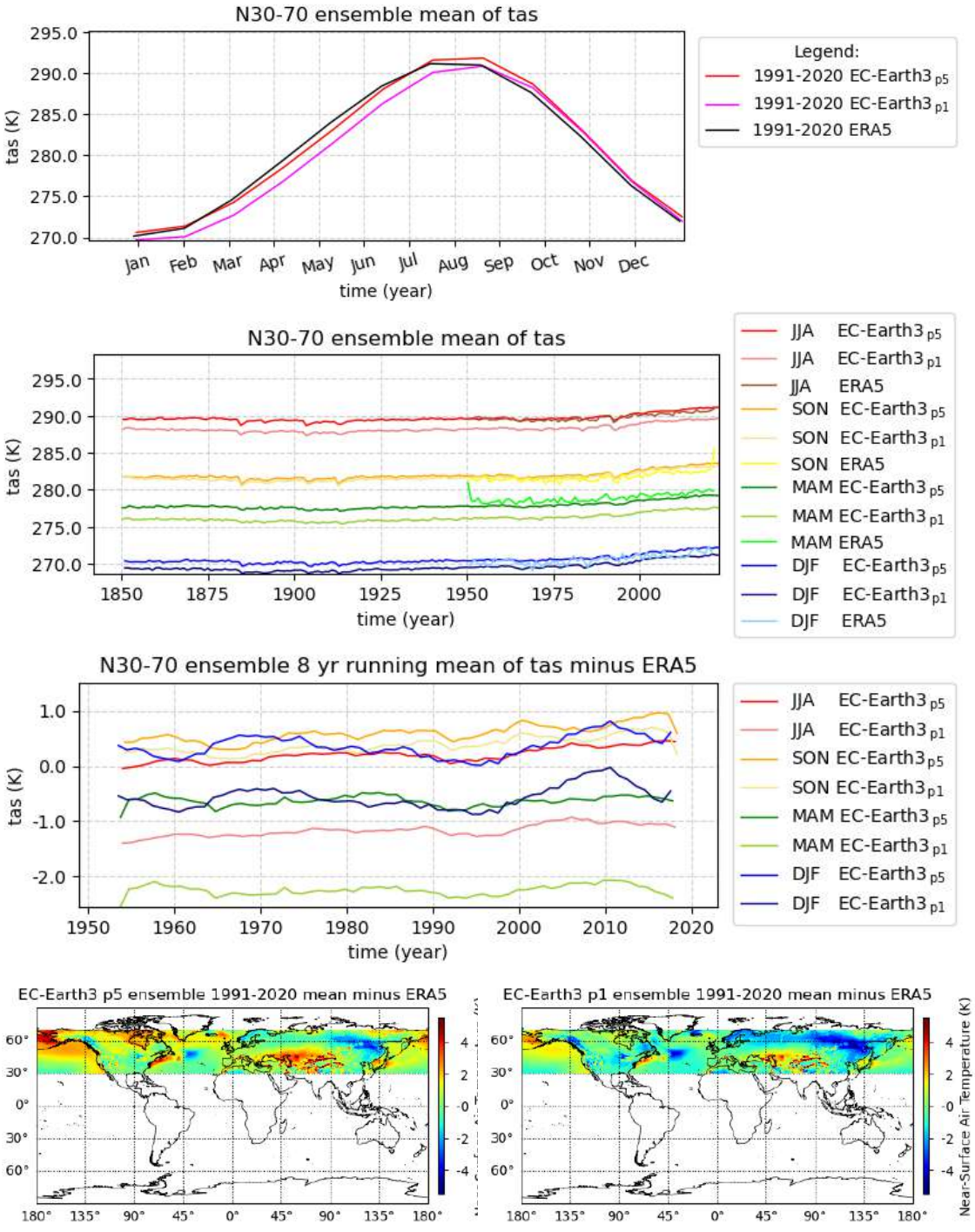

Figure B.3: Near-Surface Air Temperature (**tas**) for **N30-70**. The ensemble mean for the **1991-2020** climatology, the season record relative to ERA5, the season record and the 1991-2020 mean for p5 & p1. Observations: MAM, JJA & DJF warmer and closer to ERA5 with p5. SON bit overcorrected.The NH has improved with p5, while as expected, the SH deteriorates (even warmer) for p5. Tuning aim confirmed.

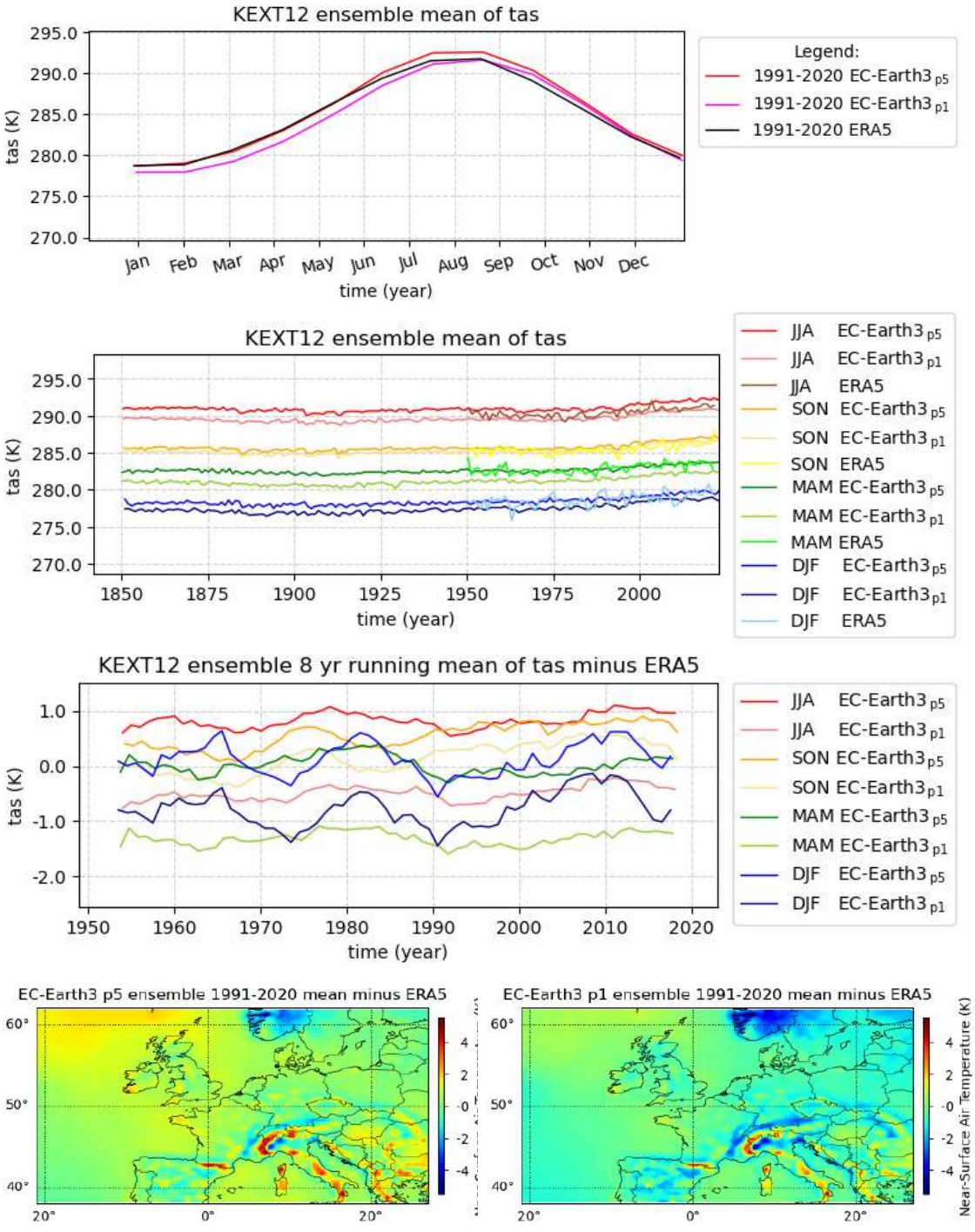

Figure B.4: Near-Surface Air Temperature (**tas**) for **KEXT12**. The ensemble mean for the **1991-2020** climatology, the season record relative to ERA5, the season record and the 1991-2020 mean for p5 & p1. Observations: MAM & DJF warmer and closer to ERA5 with p5 (for AS p1 bit closer to ERA5, JJA overcorrected). The NH has improved with p5, while as expected, the SH deteriorates (even warmer) for p5. Tuning aim confirmed.

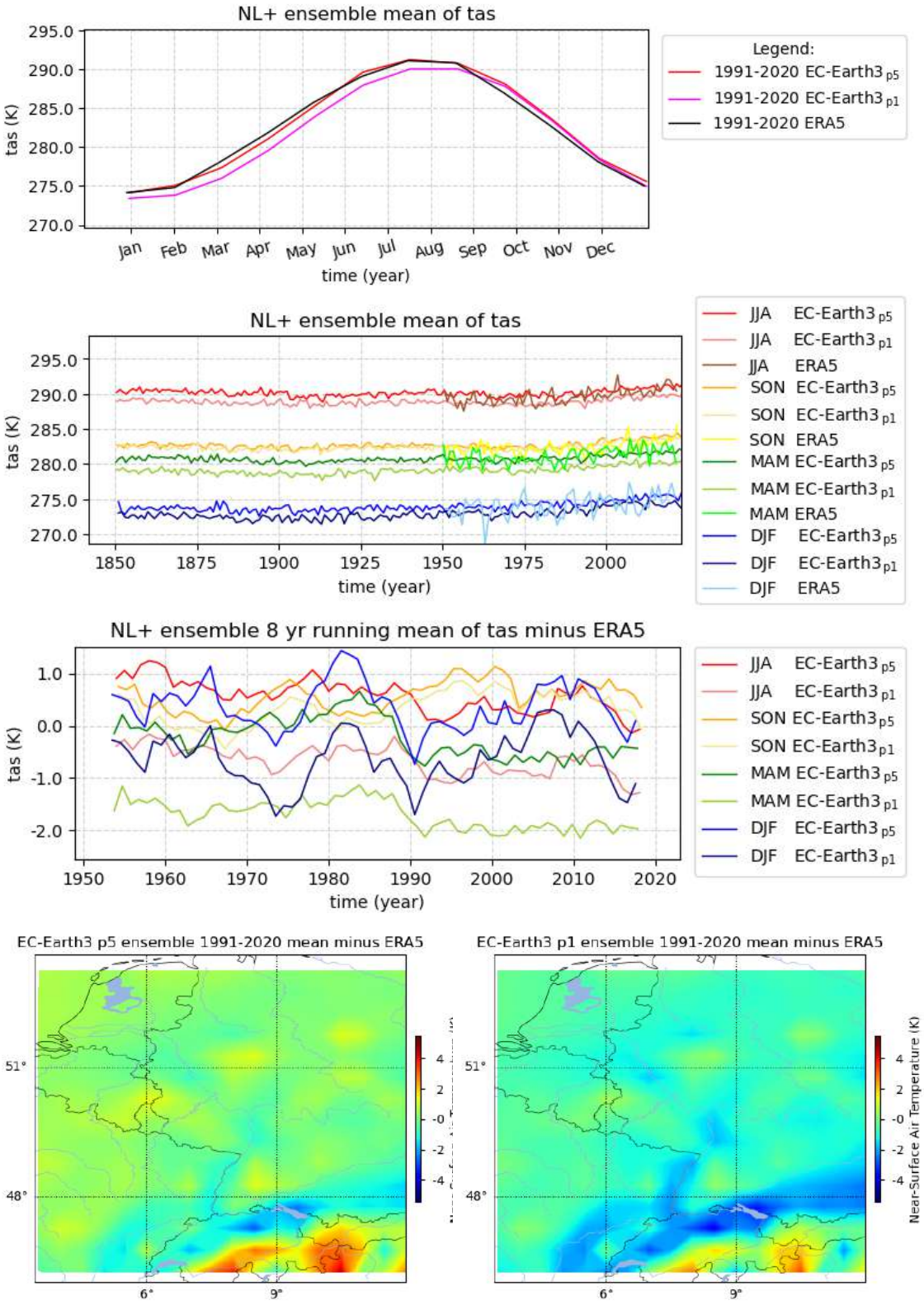

Figure B.5: Near-Surface Air Temperature (**tas**) for **NL+**. The ensemble mean for the **1991-2020** climatology, the season record relative to ERA5, the season record and the 1991-2020 mean for p5 & p1. Observations: For NL+ p5 does well,except for S & D where p1 is slightly closer to ERA5.The NH has improved with p5, while as expected, the SH deteriorates (even warmer) for p5. Tuning aim confirmed.

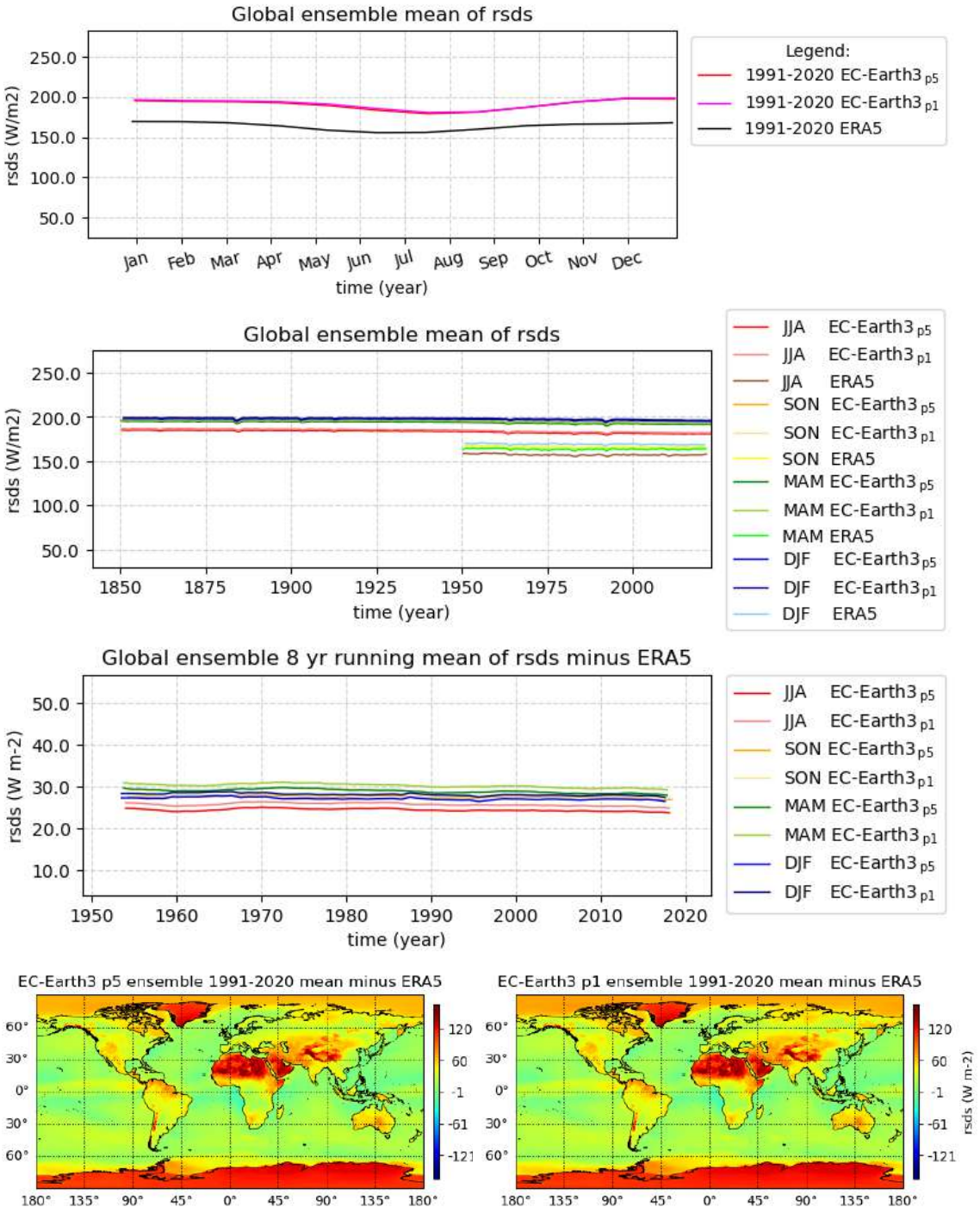

Figure B.6: Surface Downwelling Shortwave Radiation (**rsds**) for **Global**. The ensemble mean for the **1991-2020** climatology, the season record relative to ERA5, the season record and the 1991-2020 mean for p5 & p1. Observations: Both p5 & p1 are similar and overestimate ERA5. For all seasons p5 is (sligthly) closer to ERA5.

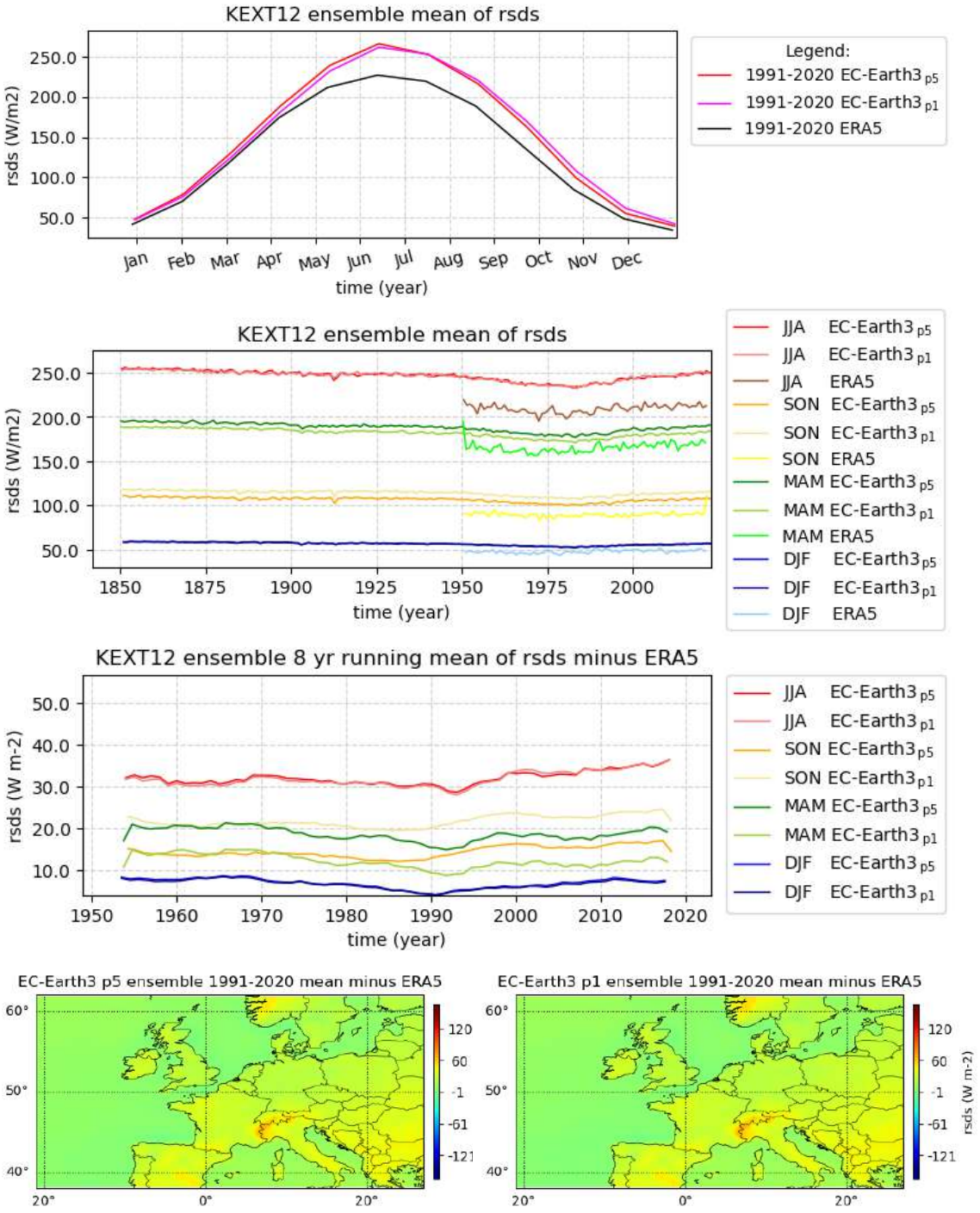

Figure B.7: Surface Downwelling Shortwave Radiation (**rsds**) for **KEXT12**. The ensemble mean for the **1991-2020** climatology, the season record relative to ERA5, the season record and the 1991-2020 mean for p5 & p1. Observations: Both p5 & p1 are similar and overestimate ERA5 (most in NH-summer). For MAMJ p1 is sligthly closer to ERA5. For ASOND p5 is sligthly closer to ERA5.

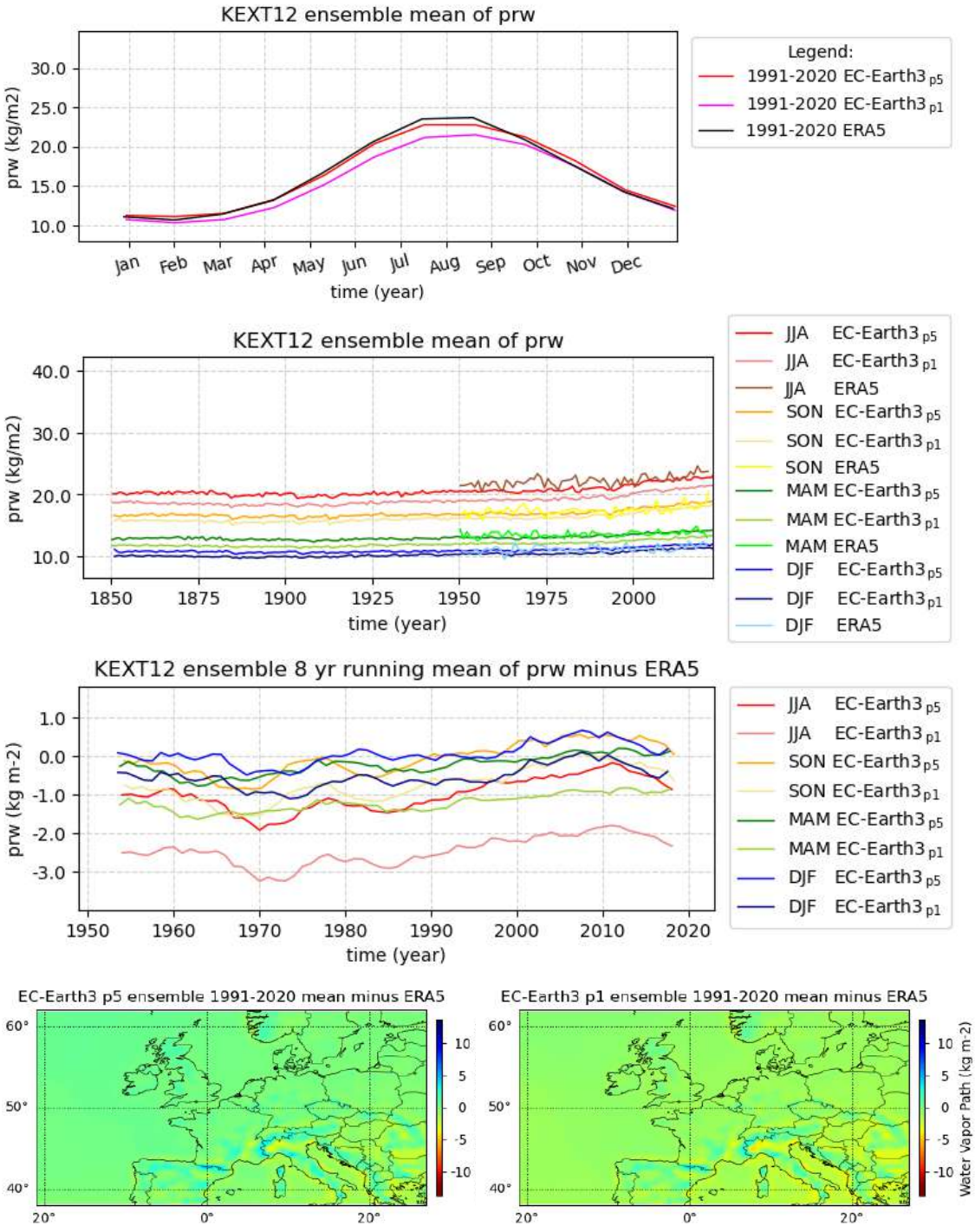

Figure B.8: Water Vapor Path (**prw**) for **KEXT12**. The ensemble mean for the **1991-2020** climatology, the season record relative to ERA5, the season record and the 1991-2020 mean for p5 & p1. Observations: NH, N30-70, Europe, KEXT12 & NL+ are closer to ERA5 with p5.

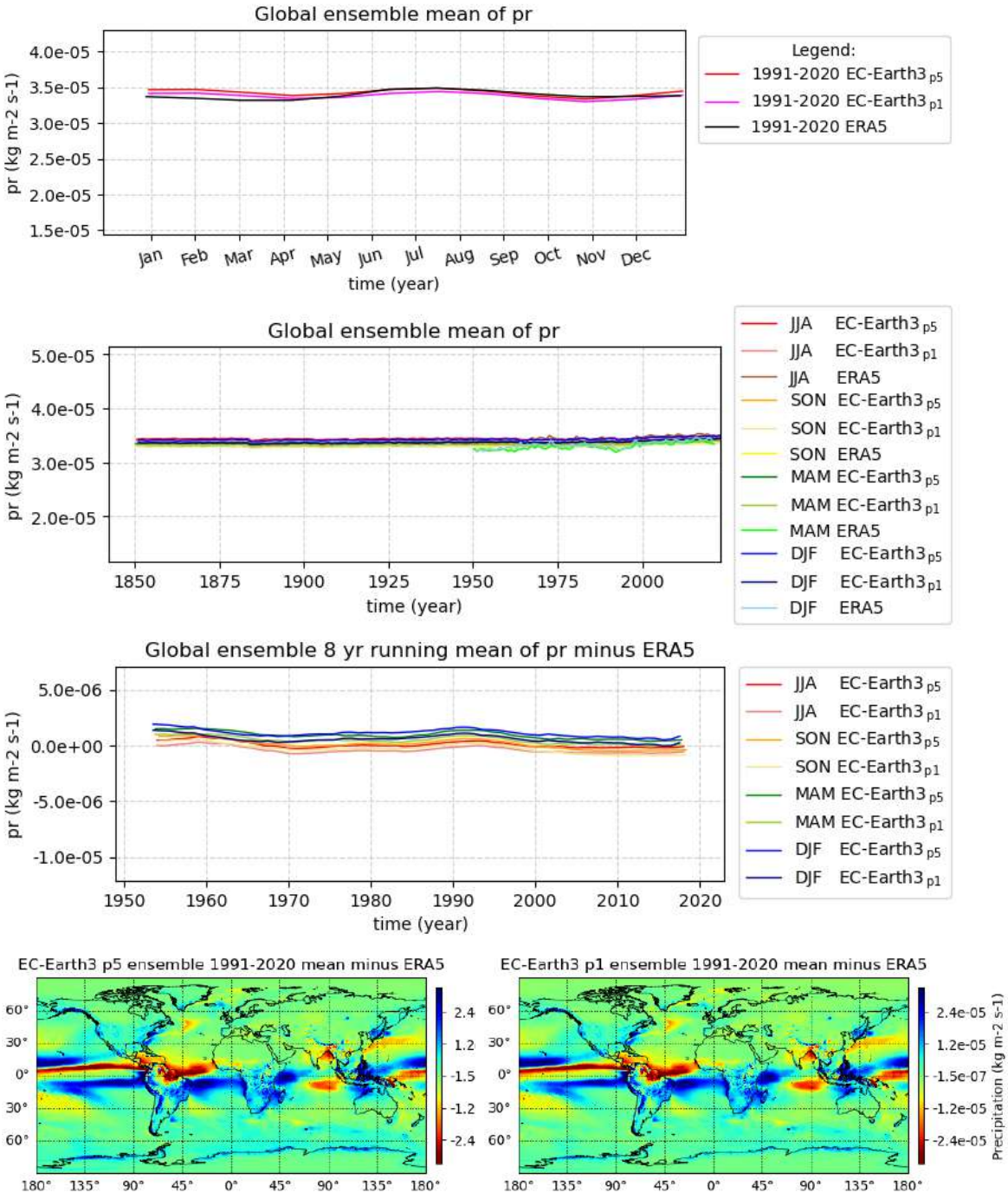

Figure B.9: Precipitation (**pr**) for **Global**. The ensemble mean for the **1991-2020** climatology, the season record relative to ERA5, the season record and the 1991-2020 mean for p5 & p1. Observations: Both p5 & p1 are similar and close to ERA5.

Note that ERA5 pr is considered less reliable than ERA5 tas.

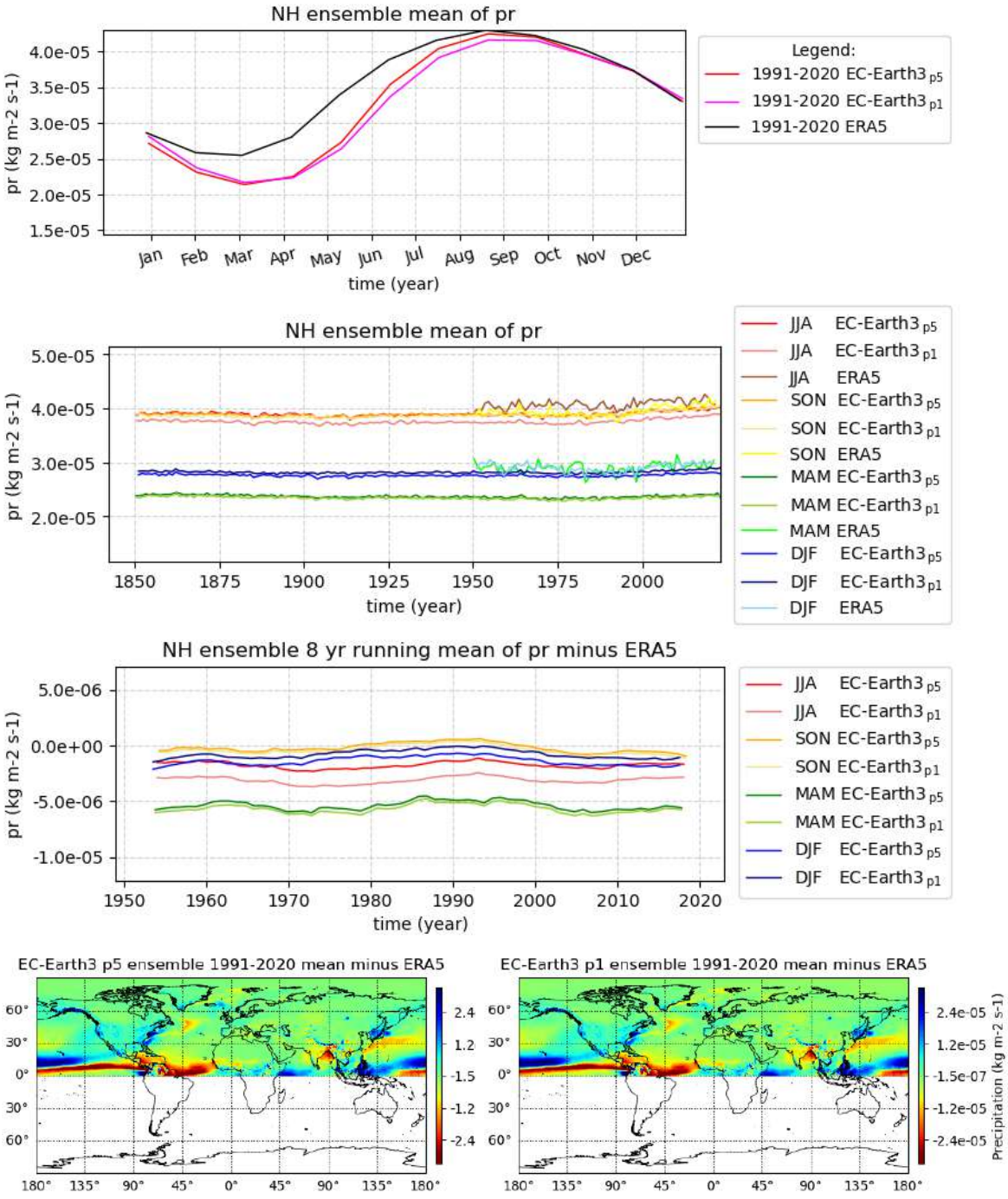

Figure B.10: Precipitation (**pr**) for **NH**. The ensemble mean for the **1991-2020** climatology, the season record relative to ERA5, the season record and the 1991-2020 mean for p5 & p1. Observations: For JFMAMJJ p5 & p1 underestimate ERA5. For MJJAS p5 is wetter & better (closer to ERA5). For OND p5, p1 & ERA are nearly equal.

Note that ERA5 pr is considered less reliable than ERA5 tas.

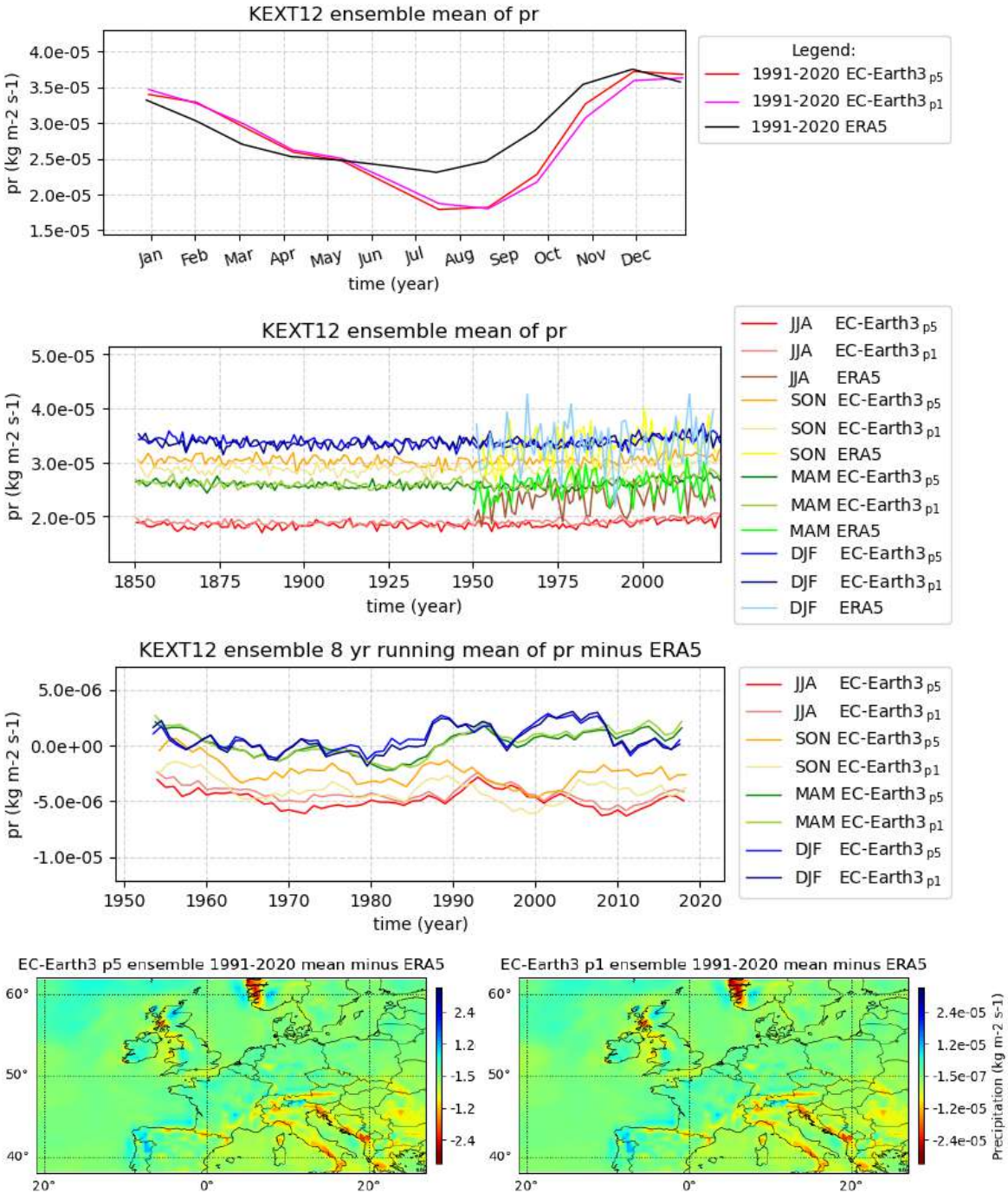

Figure B.11: Precipitation (**pr**) for **KEXT12**. The ensemble mean for the **1991-2020** climatology, the season record relative to ERA5, the season record and the 1991-2020 mean for p5 & p1. Observations: For JJASON p5 & p1 underestimate ERA5. For SON p5 is wetter & better (closer to ERA5). For the other seasons p5 & p1 are rather equal.

Note that ERA5 pr is considered less reliable than ERA5 tas.

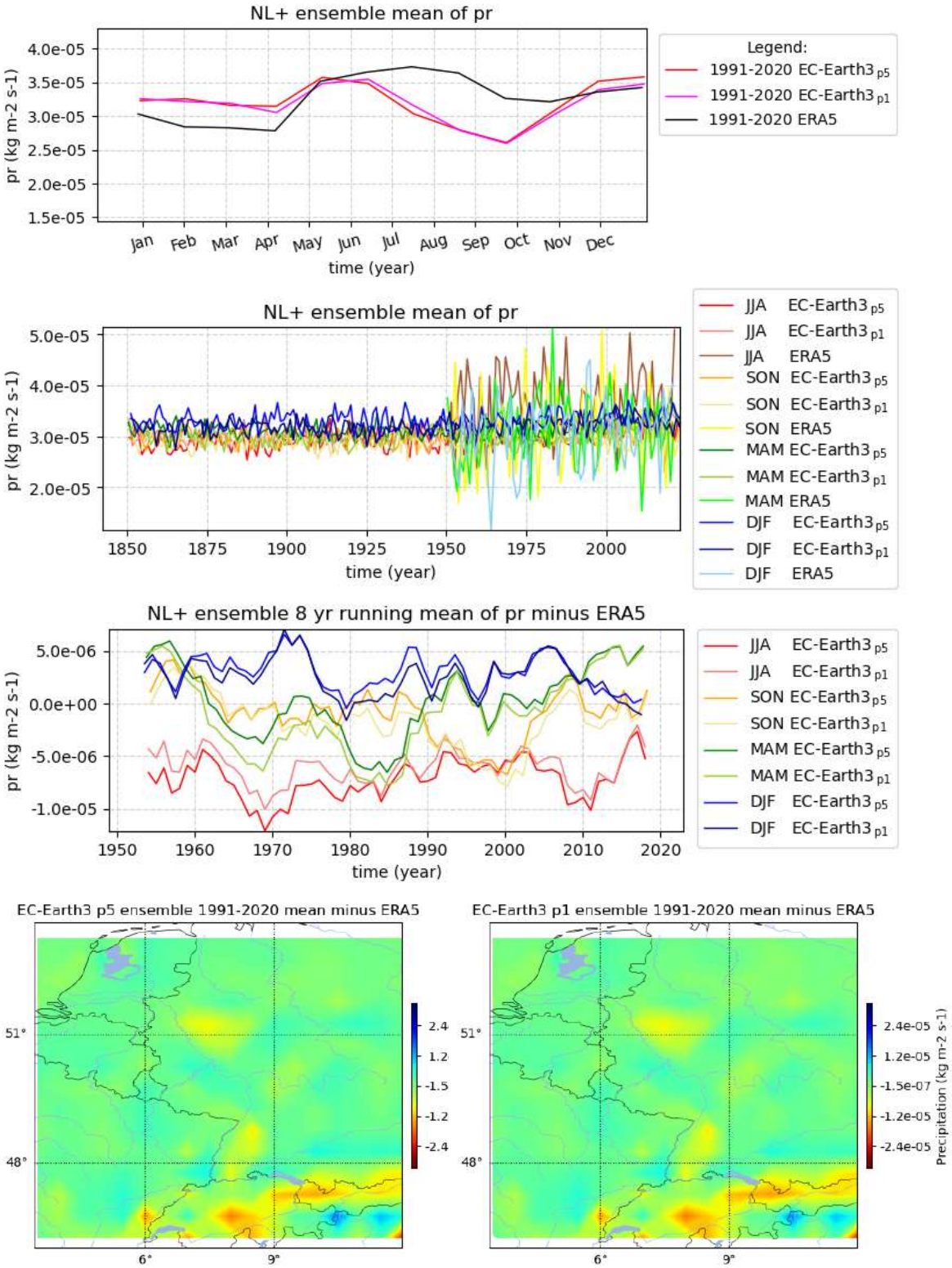

Figure B.12: Precipitation (**pr**) for **NL+**. The ensemble mean for the **1991-2020** climatology, the season record relative to ERA5, the season record and the 1991-2020 mean for p5 & p1. Observations: For JJASO p5 & p1 underestimate ERA5. For JFMA p5 & p1 overestimate ERA5.

Note that ERA5 pr is considered less reliable than ERA5 tas.

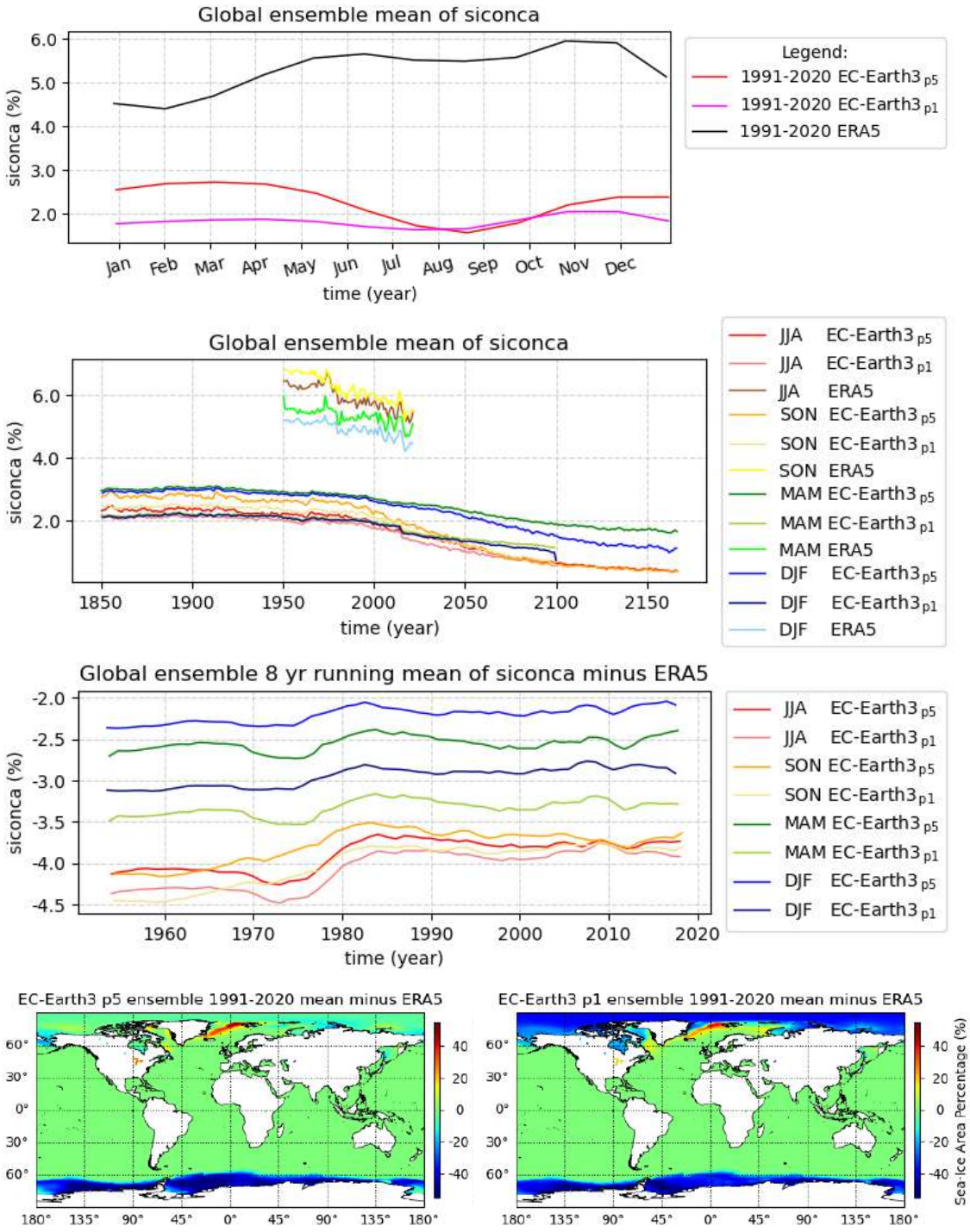

Figure B.13: Sea-Ice Area Percentage (Atmospheric Grid) (**siconca**) for **Global**. The ensemble mean for the **1991-2020** climatology, the season record relative to ERA5, the season record and the 1991-2020 mean for p5 & p1. Observations: NH is closer to ERA5 and less underestimated with p5. Almost equal for SH.

Remarkable for this warmed NH tuning.

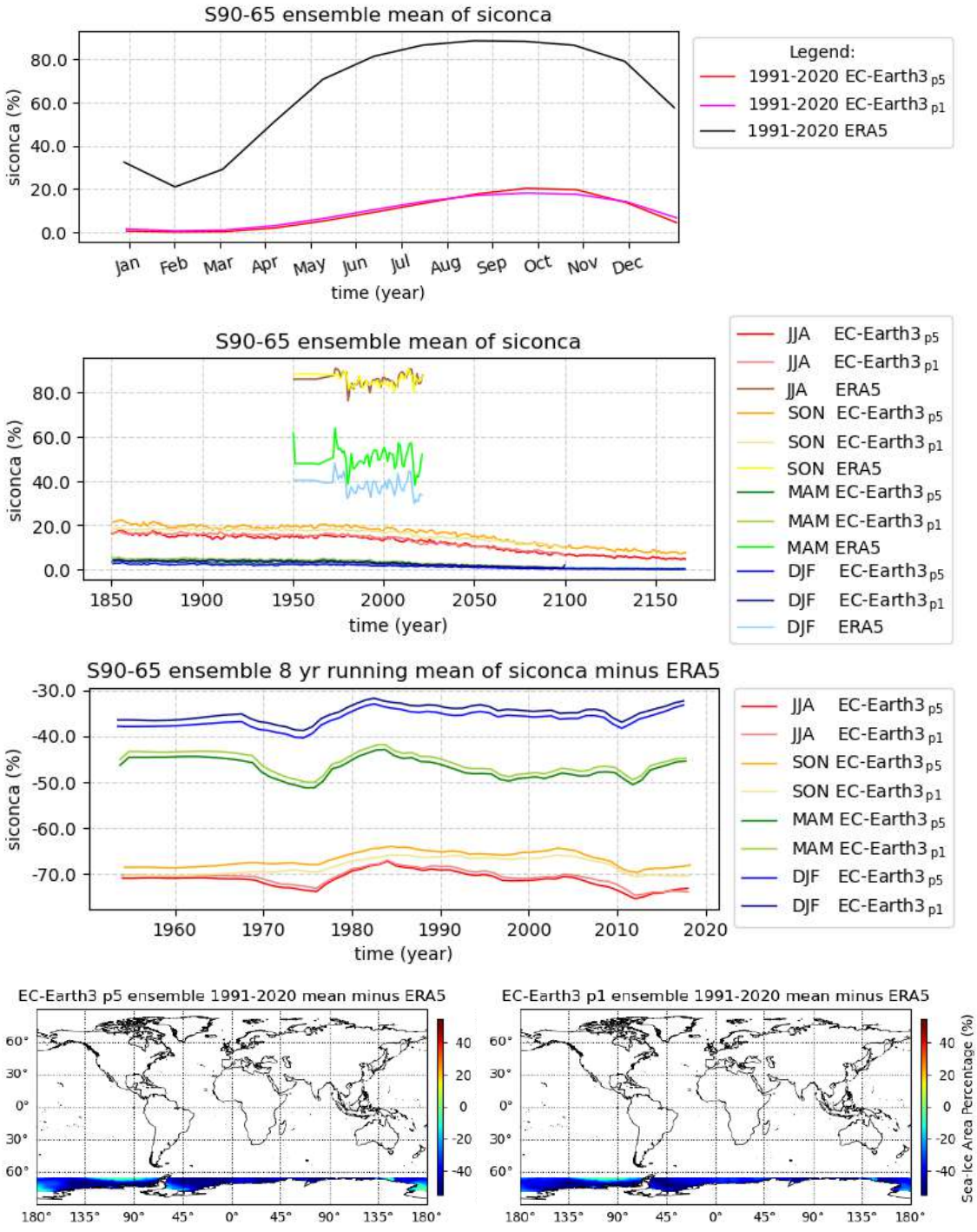

Figure B.14: Sea-Ice Area Percentage (Atmospheric Grid) (**siconca**) for **S90-65**. The ensemble mean for the **1991-2020** climatology, the season record relative to ERA5, the season record and the 1991-2020 mean for p5 & p1. Observations: NH is closer to ERA5 and less underestimated with p5. Almost equal for SH.

Remarkable for this warmed NH tuning.

Appendix C

List of GCMs

Model name	Variant-id	Data	Wind	BES
ACCESS-CM2	r1i1p1f1	M,D	x	x
ACCESS-ESM1-5	r1i1p1f1	M,D	x	x
AWI-CM-1-1-MR	r1i1p1f1	M,D	x	x
BCC-CSM2-MR	r1i1p1f1	M,D	x	x
CanESM5	r10i1p1f1	M,D	x	x
CanESM5-CanOE	r1i1p2f1	M		
CESM2	r4i1p1f1	M,D		x
CESM2-WACCM	r1i1p1f1	M,D		x
CIESM	r1i1p1f1	M		
CMCC-CM2-SR5	r1i1p1f1	M,D	x	x
CNRM-CM6-1	r1i1p1f2	M,D	x	x
CNRM-CM6-1-HR	r1i1p1f2	M,D	x	x
CNRM-ESM2-1	r1i1p1f2	M,D	x	x
EC-Earth3	r1i1p1f1	M	x	x
EC-Earth3-Veg	r1i1p1f1	M	x	x
FGOALS-f3-L	r1i1p1f1	M		
FGOALS-g3	r1i1p1f1	M		x
GFDL-ESM4	r1i1p1f1	M,D	x	x
GISS-E2-1-G	r1i1p3f1	M		
HadGEM3-GC31-LL	r1i1p1f3	M,D	x	x
INM-CM4-8	r1i1p1f1	M,D	x	x
INM-CM5-0	r1i1p1f1	M,D	x	x
IPSL-CM6A-LR	r1i1p1f1	M,D	x	x
KACE-1-0-G	r1i1p1f1	M,D	x	x
MIROC6	r1i1p1f1	M,D	x	x
MIROC-ES2L	r1i1p1f2	M,D	x	x
MPI-ESM1-2-HR	r1i1p1f1	M,D	x	x
MPI-ESM1-2-LR	r10i1p1f1	M,D	x	x
MRI-ESM2-0	r1i1p1f1	M,D	x	x
NESM3	r1i1p1f1	M,D	x	x
NorESM2-LM	r1i1p1f1	M,D		x
NorESM2-MM	r1i1p1f1	M,D		x
UKESM1-0-LL	r1i1p1f2	M,D	x	x

Table C.1: CMIP6 models included in the KNMI'23 CMIP6 standard set. Noted are model names, the specific variant-id of the published run, and temporal resolution of data available (monthly and/or daily), whether they were used in Section 3.3 (*Wind*) or in Chapter 9 (*BES*).

Royal Netherlands Meteorological Institute

PO Box 201 | NL-3730 AE De Bilt
Netherlands | www.knmi.nl